

**AFRL-VA-WP-TR-2005-3060**

**AIR VEHICLES TECHNOLOGY  
INTEGRATION PROGRAM (AVTIP)**



**Delivery Order 0020 : Prediction Of  
Manufacturing Tolerances For Laminar Flow**

**Aaron Drake  
Anne M. Bender  
William D. Solomon, Jr.  
Andrea J. Vavra**

**Northrop Grumman Corporation  
Air Combat Systems  
1 Hornet Way  
El Segundo, CA 90245**

**JUNE 2005**

**Final Report for 1 December 2003 – 30 June 2005**

**Approved for public release; distribution unlimited.**

**STINFO FINAL REPORT**

**AIR VEHICLES DIRECTORATE  
AIR FORCE RESEARCH LABORATORY  
AIR FORCE MATERIEL COMMAND  
WRIGHT-PATTERSON AIR FORCE BASE, OH 45433-7542**

# NOTICE

Using Government drawings, specifications, or other data included in this document for any purpose other than Government procurement does not in any way obligate the U.S. Government. The fact that the Government formulated or supplied the drawings, specifications, or other data does not license the holder or any other person or corporation; or convey any rights or permission to manufacture, use, or sell any patented invention that may relate to them.

This report was cleared for public release by the Air Force Research Laboratory Wright Site (AFRL/WS) Public Affairs Office (PAO) and is releasable to the National Technical Information Service (NTIS). It will be available to the general public, including foreign nationals.

PAO Case Number: AFRL/WS-05-2282, 3 Oct 2005]

THIS TECHNICAL REPORT IS APPROVED FOR PUBLICATION.

\_\_\_\_\_/s/  
Jeffrey R. Komives, 2d Lt, USAF  
Aerospace Engineer  
Aerodynamic Configuration Branch

\_\_\_\_\_/s/  
Christopher P. Remillard  
Chief  
Aerodynamic Configuration Branch

\_\_\_\_\_/s/  
Tim J. Schumacher  
Chief  
Aeronautical Sciences Division

This report is published in the interest of scientific and technical information exchange and its publication does not constitute the Government's approval or disapproval of its ideas or findings.

REPORT DOCUMENTATION PAGE				Form Approved OMB No. 0704-0188	
Public reporting burden for this collection of information is estimated to average 1 hour per response, including the time for reviewing instructions, searching existing data sources, gathering and maintaining the data needed, and completing and reviewing this collection of information. Send comments regarding this burden estimate or any other aspect of this collection of information, including suggestions for reducing this burden to Department of Defense, Washington Headquarters Services, Directorate for Information Operations and Reports (0704-0188), 1215 Jefferson Davis Highway, Suite 1204, Arlington, VA 22202-4302. Respondents should be aware that notwithstanding any other provision of law, no person shall be subject to any penalty for failing to comply with a collection of information if it does not display a currently valid OMB control number. <b>PLEASE DO NOT RETURN YOUR FORM TO THE ABOVE ADDRESS.</b>					
1. REPORT DATE (DD-MM-YYYY) <b>June 2005</b>		2. REPORT TYPE <b>Final</b>		3. DATES COVERED (From - To) <b>1 Dec 2003 – 30 Jun 2005</b>	
4. TITLE AND SUBTITLE  <b>Air Vehicle Technology Integration Program (AVTIP)</b>  <b>Delivery Order 0020 : Prediction Of Manufacturing Tolerances For Laminar Flow</b>				5a. CONTRACT NUMBER <b>F33615-00-D-3054-0020</b>	
				5b. GRANT NUMBER	
				5c. PROGRAM ELEMENT NUMBER <b>0602201</b>	
6. AUTHOR(S)  <b>Aaron Drake</b> <b>Anne M. Bender</b>  <b>William D. Solomon, Jr.</b> <b>Andrea J. Vavra</b>				5d. PROJECT NUMBER <b>A071</b>	
				5e. TASK NUMBER	
				5f. WORK UNIT NUMBER <b>0A</b>	
7. PERFORMING ORGANIZATION NAME(S) AND ADDRESS(ES)  <b>Northrop Grumman Corporation</b> <b>Air Combat Systems</b> <b>1 Hornet Way</b> <b>El Segundo, CA 90245</b>				8. PERFORMING ORGANIZATION REPORT NUMBER	
9. SPONSORING / MONITORING AGENCY NAME(S) AND ADDRESS(ES) <b>AIR VEHICLES DIRECTORATE</b>  <b>AIR FORCE RESEARCH LABORATORY</b>  <b>AIR FORCE MATERIEL COMMAND</b> <b>WRIGHT-PATTERSON AFB, OH 45433-7542</b>				10. SPONSOR/MONITOR'S ACRONYM(S)  <b>AFRL/VAAA</b>	
				11. SPONSOR/MONITOR'S REPORT NUMBER(S)  <b>AFRL-VA-WP-TR-2005-3060</b>	
12. DISTRIBUTION / AVAILABILITY STATEMENT <b>Approved for public release; distribution unlimited.</b>					
13. SUPPLEMENTARY NOTES <b>This document contains color.</b>					
14. ABSTRACT An examination of the effects of surface excrescences on boundary layer transition has been performed, including both experimental and computational components. The experimental study focused on stagnation-line starting condition boundary layers in incompressible flow without sweep effects. The study was performed at low-Reynolds number—less than 106—and included the effects of both adverse and favorable pressure gradients. The results for both forward and aft-facing steps indicate a substantial stabilizing effect of favorable pressure gradient on excrescence-induced boundary layer transition. These findings suggest that manufacturing tolerances for laminar flow aircraft could be loosened in areas where even mild favorable pressure gradients exist. The present study, due to its limited scope, does not provide sufficient basis for setting actual manufacturing tolerances; however, it provides a solid foundation on which follow-on examinations including compressibility effects can be built.					
15. SUBJECT TERMS: laminar flow, laminar, manufacturing tolerances, excrescence, drag					
16. SECURITY CLASSIFICATION OF:			17. LIMITATION OF ABSTRACT	18. NUMBER OF PAGES	19a. NAME OF RESPONSIBLE PERSON
a. REPORT	b. ABSTRACT	c. THIS PAGE			2Lt Jeffrey R. Komives
Unclassified	Unclassified	Unclassified	SAR	288	19b. TELEPHONE NUMBER (include area code) <b>937-255-1190</b>

## Table of Contents

Section	Page
<b>1.0 Introduction.....</b>	<b>1</b>
1.1 Types of Surface Excrescences .....	1
1.2 Excrescence Nomenclature and Nondimensionalization.....	2
1.3 Excrescence Effects Background.....	4
1.4 Previous Recommendations .....	6
1.5 Project Overview.....	8
<b>2.0 Low-Speed Experimental Database Development.....</b>	<b>10</b>
2.1 Test Facility .....	10
2.2 Model.....	13
2.3 Low-Speed Experimental Results.....	19
2.3.1 Pressure Distributions .....	19
2.3.2 Pressure Gradients.....	20
2.3.3 Boundary Layer Velocity Profiles .....	26
2.3.4 Skin Friction Distributions.....	65
2.3.5 Boundary Layer Transition Trends.....	201
<b>3.0 Computational Examination of Excrescence Flow Fields.....</b>	<b>216</b>
3.1 CFD Modeling the Clean Plate in the Tunnel .....	216
3.2 CFD Modeling of Plate with Excrescences .....	238
3.3 Assessment of Computational Study.....	278
<b>4.0 Conclusions.....</b>	<b>279</b>
4.1 Allowable Excrescences for Global Hawk-Type Aircraft .....	279
<b>5.0 Recommended Follow-On Activities.....</b>	<b>281</b>
5.1 Experimental Investigation at Full-Scale Reynolds Numbers .....	281
5.2 Assessment of Compressibility Effects.....	281
5.3 Initial Experimental Assessment of Sweep Effects .....	282
5.4 Integrated Demonstration of Critical Results .....	283
5.5 Investigation of Combined Sweep and Compressibility Effects .....	284
<b>6.0 References.....</b>	<b>285</b>
<b>LIST OF ACRONYMS, ABBREVIATIONS, AND SYMBOLS.....</b>	<b>286</b>



## 1.0 Introduction

Drag reduction is critical for long-endurance aircraft such as the RQ-4A Global Hawk and the SensorCraft concept. One approach to reducing drag currently employed on Global Hawk and the SensorCraft concept is the use of a wing designed for laminar flow. By careful design, the boundary layer on a laminar flow wing can have a transition location that is significantly further downstream than on a conventional wing, resulting in a much smaller fraction of the aircraft wetted area being covered by higher drag turbulent flow. The exploitation of laminar flow on flight vehicles, though, requires more stringent manufacturing tolerances than nonlaminar flow vehicles. Specifically, these more stringent manufacturing requirements include tighter tolerances on the allowable heights of steps, widths of gaps, and surface waviness. However, the existing literature on laminar flow does not provide sufficient criteria on manufacturing tolerances for a surface in a pressure gradient. Therefore, the required tolerances must be determined from conducting a test specific to the geometry of interest, or they must be extrapolated from the existing literature on flow effects in the absence of a pressure gradient. The former method is inefficient, laborious, and untimely. The latter method is also highly undesirable as the pressure gradient can be expected to have a profound effect on boundary layer transition. Thus, the determination of manufacturing tolerances is fraught with uncertainty, often leading to requirements that are tighter than necessary to ensure that laminar flow is achieved.

To be generally applicable, manufacturing tolerance criteria must be developed as a function of pressure distribution and sweep angle in order for wings to be designed and built to achieve laminar flow under actual operating conditions. Starting with the existing literature on laminar flow, this study developed general criteria for manufacturing tolerances. Thus the results are applicable to a broad range of future operational vehicle designs. Additionally, the results are immediately applicable and of great utility to current programs such as Global Hawk.

The ultimate goal of the program was to develop generalized criteria for the allowable size of surface imperfections on a laminar flow wing to prevent premature transition. The criteria developed are a function of the pressure gradient, allowing the results to be applicable to future projects and not merely to one specific airframe. Of particular interest in this program was steps and waves—the most commonly occurring manufacturing excrescences of interest. This study was, however, intended to be only the first part of an overall effort to generate the needed detailed understanding of manufacturing tolerances. As such, it examined constant pressure gradients at relatively low Reynolds numbers in incompressible flow. This, then, can form the foundation of subsequent activities that expand the understanding.

### 1.1 Types of Surface Excrescences

Surface excrescences are any variation from the nominal outer mold line (OML) of an aerodynamic surface. The most common source of surface excrescences is the real world manufacturing process. On aircraft wings, surface steps and waves are the most commonly encountered excrescence that must be controlled for laminar flow. Surface gaps, about which there is some data in the literature, are less of an issue since they can be controlled and/or filled in most typical manufacturing processes.

The excrescences examined in this study were forward facing steps, aft-facing steps and surface waves. All of these excrescences were two-dimensional (2-D)—the geometry was constant in the spanwise direction—making these idealized representations of those found on actual aircraft.

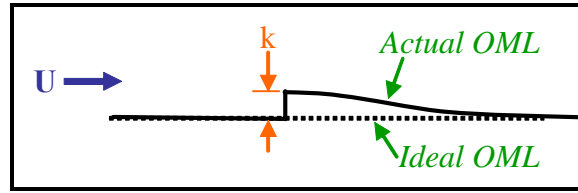


**Figure 1. Forward-facing step**

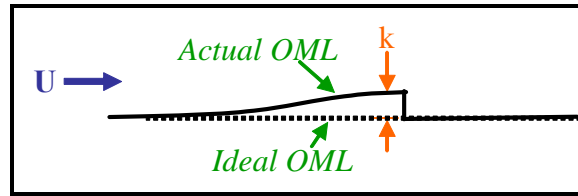


**Figure 2. Aft-facing step**

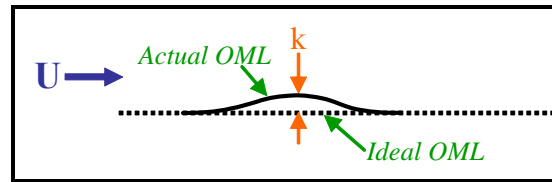


**Figure 3. Surface wave**

## 1.2 Excrescence Nomenclature and Nondimensionalization

Key to producing relations between surface excrescences and boundary layer transition is identifying those parameters on which the relations depend in such a way that they can be applied to other situations. To do this, the geometry and the results were nondimensionalized. Careful selection of dimensionless parameters ensured that the results are as useful as possible to the aerodynamic designer. The results have been formulated in such a way that the parameters needed are ones that either the wing designer will have readily available or can easily be obtained.

Excrescence geometries are defined by their height,  $k$ . In the case of waves, this is the maximum height from the idealized surface geometry. For steps, this is the height of the face of the step. The location of the step is described by the chordwise position  $x_k$ , measured from the leading edge to the position at which the height is measured. Or, by a surface distance,  $s_k$ , which is measured along the surface contour from the stagnation point to the location at which the excrescence height was measured.

The nondimensionalized excrescence height is expressed as an excrescence Reynolds number,  $Re_k$ :

$$\text{Re}_k = \frac{u_k k}{\nu_k}, \quad (1)$$

where  $k$  is the excrescence height,  $u_k$  is the velocity that would be observed at a height  $k$  above the surface in an undisturbed (no excrescence present) laminar boundary layer at the location of the excrescence ( $x_k$ ), and,  $\nu_k$  is the viscosity at that same location in the undisturbed boundary layer. This nondimensionalization is common in the literature and the parameters can be easily obtained from the measurement of the boundary layer velocity profile in an experimental situation, or by the use of simple 2-D boundary layer computational methods.

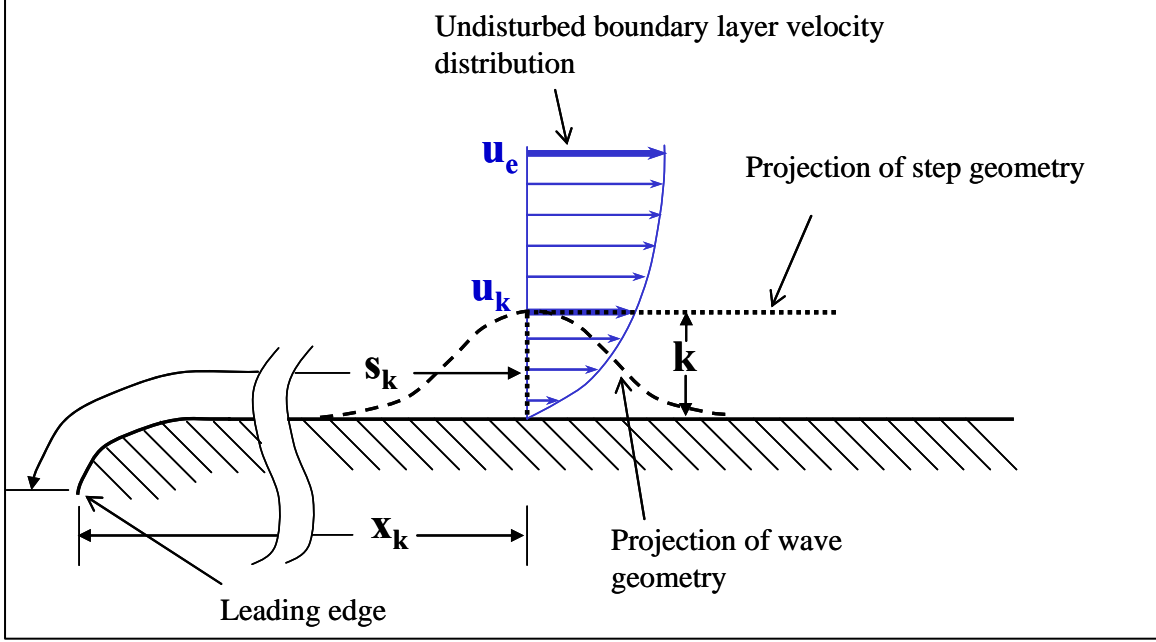


**Figure 4. Excrescence geometry parameters**

The nondimensionalized location of the excrescence is expressed as an excrescence location Reynolds number,  $\text{Re}_{xk}$ . This Reynolds number is formed by integrating the flow properties from the stagnation point to the location of the excrescence along the surface:

$$\text{Re}_{xk} = \int_0^{s_k} \frac{u_e}{\nu_e} ds, \quad (2)$$

where  $u_e$  is the boundary layer edge velocity (corresponding to the  $\delta_{99}$  height of the boundary layer) and  $\nu_e$  is the viscosity at that location. Using  $\text{Re}_{xk}$  to describe the location of the excrescences allows those flow properties that directly affect the development of the boundary layer to be accounted for. With known pressure distributions, the parameters required to determine  $\text{Re}_{xk}$  are easily obtained.

Similar to the description of the excrescence location, the transition location is described by a transition Reynolds number,  $\text{Re}_{tr}$ , that is formed from the integrated boundary layer edge properties from the stagnation point to the transition location,  $x_{tr}$ :

$$\text{Re}_{tr} = \int_0^{s_{tr}} \frac{u_e}{\nu_e} ds. \quad (3)$$

The actual location of transition,  $x_{tr}$ , is not necessarily straightforward to determine. In reality, transition is not an instantaneous process. Rather, the transition region separating the clearly laminar boundary layer from the clearly turbulent boundary layer is finite and can be substantial in length. However, for the aerodynamic designer it is often much more convenient to think of a single transition location that divides laminar flow from turbulent. The above formulation is based on identifying such a single point of transition. A discussion of how this transition location was determined, and the assumptions implicit in doing so, in the present study is contained in Section 2.3.4.

Pressure gradients were nondimensionalized using parameters that would be readily available to the aerodynamic designer. In the literature, using the Falkner-Skan wedge flow parameter  $\beta$  is the most common form of nondimensionalized pressure gradient. However, while  $\beta$  is convenient for basic experiments and analytical studies of boundary layer flows, it is not convenient for the aerodynamic designer. Therefore, the pressure gradient parameter  $K$  was selected.<sup>1</sup>

$$K = \frac{\nu_e}{u_e^2} \frac{du_e}{dx}. \quad (4)$$

### 1.3 Excrescence Effects Background

Work in 1943 by Fage<sup>2</sup> examined the effects of built-up ridges, essentially an integral forward and aft facing step, 1 inch wide (in the streamwise direction). This low-speed work did not examine forward facing steps in isolation; however, it is valuable to consider since the integrated forward- and aft-facing step should represent a limiting case for the effects of isolated forward-facing steps. The work of Fage did not identify any significant influence of pressure gradient—though this is likely an erroneous conclusion. The results were not expressed in terms of  $\text{Re}_k$ , however the published data allows a determination of  $\text{Re}_{k_{crit}} = 900$ .

A summary of a number of experimental data sets was prepared by Braslow<sup>3</sup> in 1960, from which he concluded that 2-D roughness, of the type incorporating an integrated forward and aft facing steps has an  $\text{Re}_{k_{crit}}$  of approximately 200. There is, however, significant scatter in the source data, most likely due to varying flow quality in the various facilities used. The value of 200 is near the upper end of the scatter band, as would be appropriate for a flight environment.

A low-speed study of 2-D and 3-D surface excrescences by Smith and Clutter<sup>4</sup> in 1954 concluded that the critical  $\text{Re}_k$  for a 2-D wire trip was in the range of 43 to 260. One of their conclusions was that pressure distribution did not seem to affect the critical  $\text{Re}_k$ ; however, their data appears ambiguous on this point.

Flight experiments conducted by Drake, et al.<sup>5</sup> in 1996 investigated the effects of integral steps and gaps on boundary layer transition in flight on a wing with a favorable pressure gradient designed to mimic that of a laminar flow airfoil. This work was done at Mach numbers of 0.50 to 0.80. All surface disturbance geometries tested included a forward facing step with an aft

facing step one inch downstream. The results of these tests indicated  $Re_{k,crit}$  values of approximately 500.

**Table 1 Forward-facing step criteria**

Reference	Disturb.	Test Article	Mach	Pres. Grad.	$Re_{k,crit}$
Fage, 1943	Ridge	Flat Plate	Incompressible	0	900
Braslow, 1960	Ridge	Flat Plate	Incompressible	0	200
Smith, 1954	Wire	NACA 65010	Incompressible	Unspecified	43-260
Drake, 1996	Ridge	Flight	$M = 0.5 - 0.8$	Favorable	500

There is essentially no literature for isolated aft-facing steps. As such, the best guidance comes from work on wire trips—the mechanism for a wire trip, namely a leeward separation bubble, is likely similar to that of an aft-facing step. However, an aft-facing step likely to be somewhat worse, due to the lack of boundary layer stabilizing effects from initial compression. From the literature,  $Re_{k,crit}$  for wire trips is approximately 120. Therefore, aft-facing steps can be expected to have  $Re_{k,crit} = 80$ .

Work in 1939 by Hood<sup>6</sup> examined surface waves on a NACA 23012 airfoil model in a wind tunnel at a  $C_l$  of 0.15. Two wave heights were examined on the 5-foot chord model. Chord Reynolds numbers varied up to  $10.3 \times 10^6$ . The primary focus of the work was overall drag of the airfoil and how it was influenced by surface imperfections. However, the key result was that waves in the leading edge region could induce premature transition, leading to higher skin friction drag. The waves tested were sinusoidal cross-sections with a streamwise length (width of wave piece) of 3 inches. The critical height for a wave at 10.5 percent chord was 0.020 inches. This corresponds to  $Re_{k,crit} = 3850$ . The Falkner-Skan pressure gradient parameter ( $\beta$ ) was  $-0.006$  at the center of the wave.

Work by Fage<sup>2</sup> in 1943 looked at spanwise bulges and their effects on transition locations. Because of the way Fage's bulges were formed, the presented the flow with a wave geometry almost identical to the sinusoidal shape of Hood's experiments. Experiments were carried out in a wind tunnel using both a flat plate (with zero pressure gradient and with imposed pressure gradients) and an airfoil model. One of Fage's conclusions was that the critical size of the wave was essentially independent of the local pressure gradient. Fage expressed his results for critical height as a function of distance from the leading edge and streamwise width of the wave:

$$k_{crit} = s_{tr} 9.0 \times 10^6 Re_k^{-3/2} (w/s_{tr})^{1/2} \quad (5)$$

for cases where  $w^{1/2} s_k^{1/2} / s_{tr} > 0.09$ , based on the flat plate experiments. From the airfoil experiments, a similar relation was determined:

$$k_{crit} = s_{tr} 13.5 \times 10^6 Re_k^{-3/2} (w/s_{tr})^{1/2} (s_k/s_{tr})^{1/2}, \quad (6)$$

where the stated valid range is  $w^{1/2} s_k^{1/2} / s_{tr} < 0.09$ . These relations correspond to an  $Re_k$  of approximately 2,000, based on the experimental results reported. However, there is substantial scatter in Fage's data. It is likely that despite the fact that considerable care was taken to ensure a low-disturbance environment, the turbulence levels were higher than expected and tended to obscure the pressure gradient effects.

**Table 2 Surface wave criteria**

Reference	Test Article	Environment	Mach	Pres. Grad.	$Re_{k,crit}$
Hood, 1939	NACA 23012	Wind Tunnel	Incompressible	$\beta = -0.006$	3850
Fage, 1943	Flat Plate	Wind Tunnel	Incompressible	Independent	2000

## 1.4 Previous Recommendations

Based on the existing literature, recommendations for steps and waves had previously been produced. In the course of producing these recommendations, it became clear that the lack of pressure gradient effect data would result in overly conservative manufacturing tolerance criteria. This is because favorable pressure gradients are known to stabilize boundary layers, thus delaying transition and, likely, permitting a larger excrescence to exist without effect on transition. However, the degree to which favorable pressure gradients of the type present on a laminar flow aircraft's wing stabilize the boundary layer was unknown. Hence, it was necessary to base the criteria on the flat plate (no pressure gradient) data, despite knowing it was conservative. The similar lack of data for adverse pressure gradients was not of as great concern because, in practice for these wing designs, it is generally assumed that boundary layers will transition once the pressure gradient becomes adverse, regardless of the presence of—or lack thereof—surface excrescences.

**Table 3 Tolerance Recommendations**

Excrescence	$Re_{k,crit}$
Forward-Facing Step	150
Aft-Facing Step	80
Wave	2000

While specifying overly conservative manufacturing tolerances may seem of little consequence since they do not hurt the performance of the aircraft, that is not the case. Having to meet a particular tolerance criteria has profound effects on the design of the tooling and the overall production approach. This, then, has direct implications on not just cost, but production time and field support and aircraft mission availability.

For a Global Hawk-type aircraft—with typical values of chord = 4.7 ft, Mach = 0.60, altitude = 55,000 ft—these tolerance recommendations fairly tight restrictions on the allowable size of excrescences (see table 3 through figure 7).

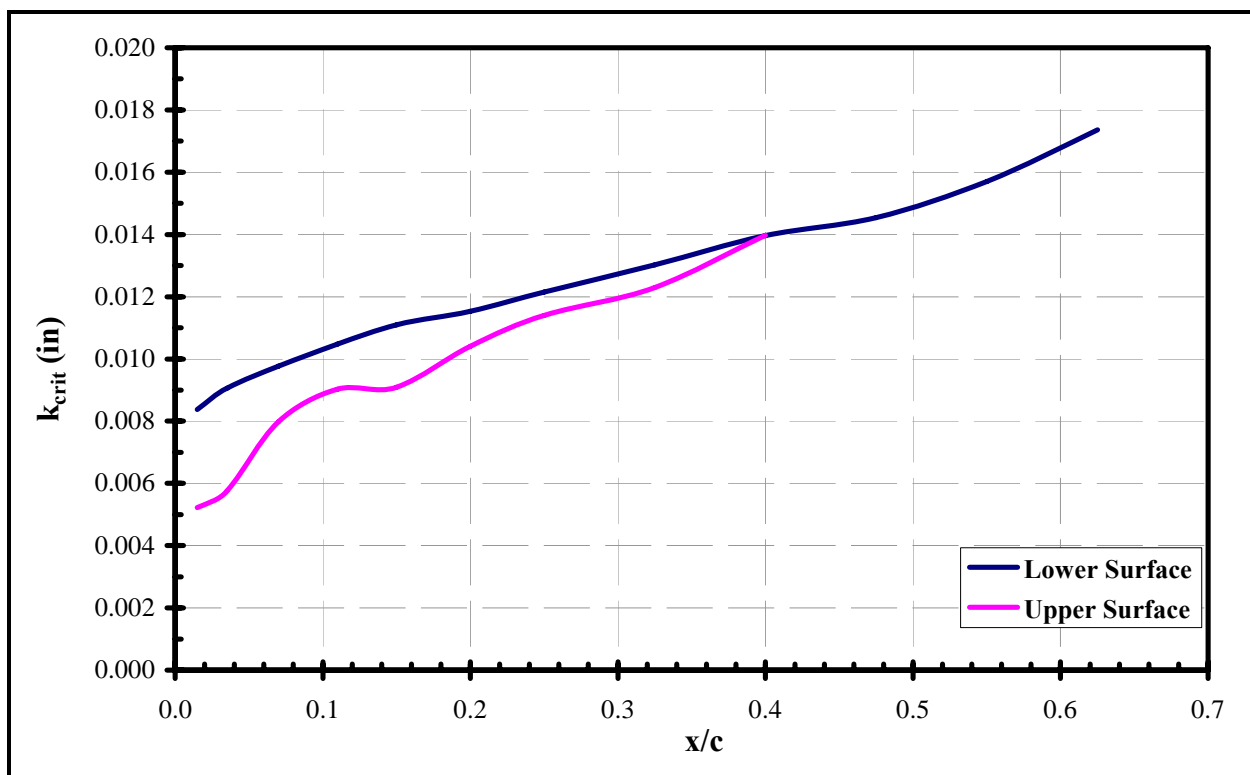


Figure 5. Forward-facing step recommendations for a Global Hawk-type vehicle

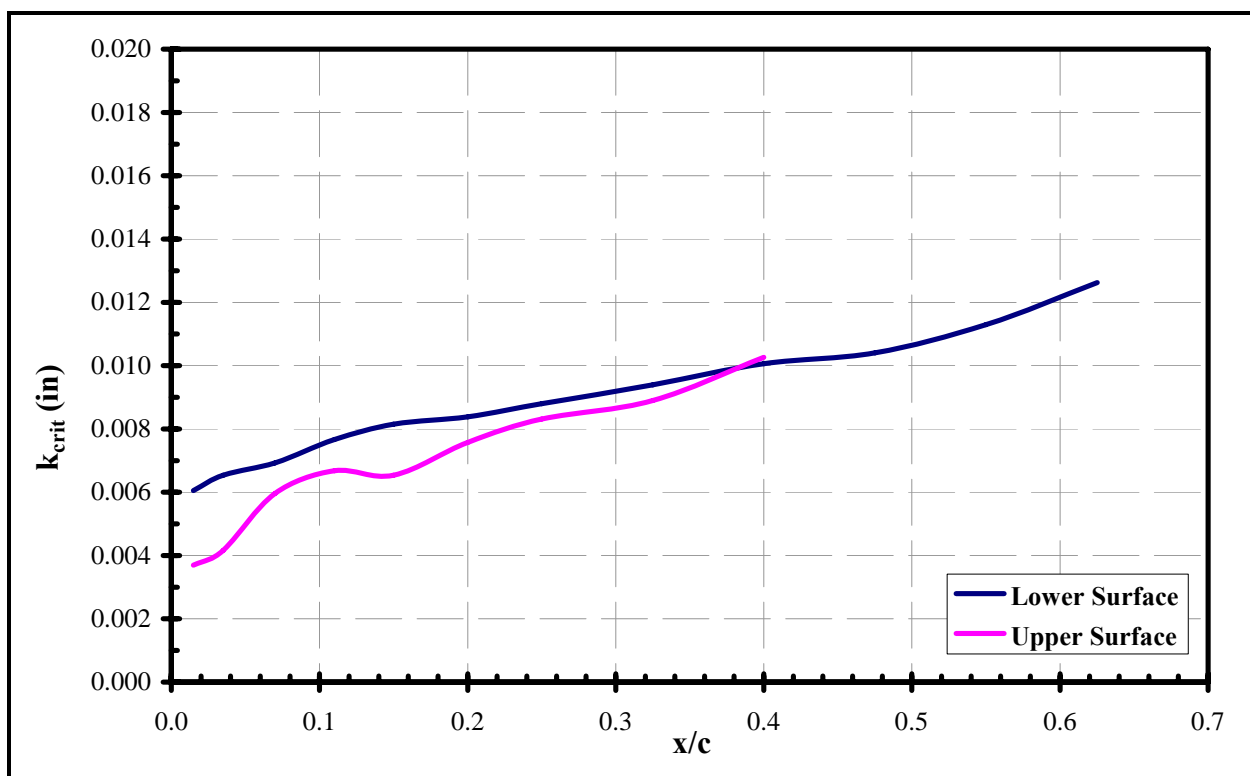
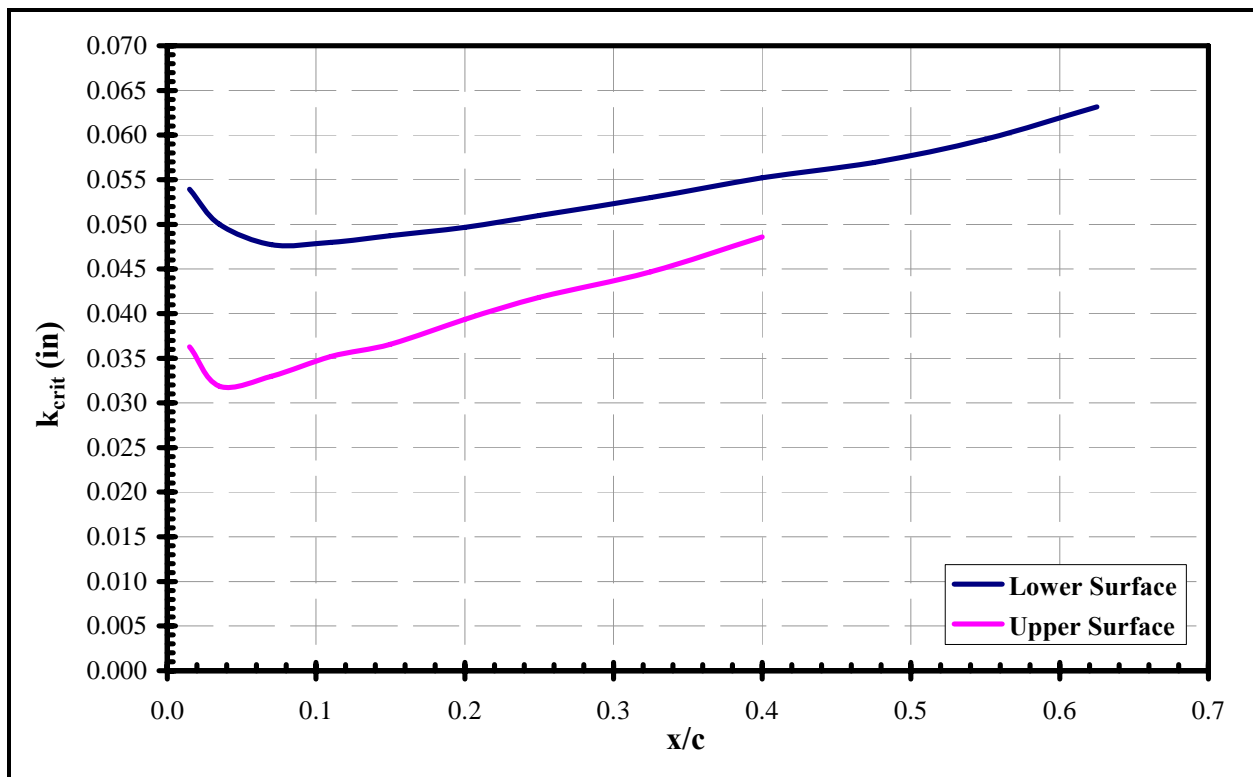


Figure 6. Aft-facing step recommendations for a Global Hawk-type vehicle



**Figure 7. Surface wave recommendations for a Global Hawk-type vehicle**

## 1.5 Project Overview

The study focused on unswept wings, with a broad range of pressure distributions (the area of greatest interest for platforms like Global Hawk). The approach used made use of both experimental and computational studies. Extensive series of low-speed experiments, augmented by computation, were used to efficiently develop the generalized surface quality requirements. The use of both computational and experimental approaches was a key aspect of this study and helped ensure that a more complete foundation of understanding of the detailed flow effects was produced and could be built upon with subsequent activities to expand the Reynolds number range and introduce compressibility and sweep effects.

The original plan for this study was to make use of the Northrop Grumman Low-Speed Research Wind Tunnel for the low-speed experiments. However, during preparations for this task, it was discovered that the wind tunnel was significantly out of specification. The specifications for the wind tunnel included a maximum freestream turbulence level of 0.10 percent, which is the level required to undertake such a study. Some early testing in the wind tunnel raised doubts as to the actual turbulence level. Subsequent investigations determined that the turbulence level had never been actually measured. Measurements then undertaken showed actual turbulence levels of approximately 0.25 percent, significantly too high for this study. Some efforts were made to improve these levels but they were unsuccessful and, for reasons unrelated to this study, it was decided not to bring the wind tunnel into specification.

An alternate facility for this study was identified at Washington State University (WSU). Northrop Grumman had recently used this facility for a similar study of step effects on boundary layer transition and it was known that the flow quality was sufficiently high to use for this



activity. However, the capabilities of the WSU Contractionless Boundary Layer Wind Tunnel were significantly different from the Northrop Grumman Low-Speed Research Wind Tunnel. In particular, the smaller test section size and notably lower dynamic pressure meant that the experimental study would be limited in Reynolds number—falling short of the full-scale transition Reynolds numbers for Global Hawk or SensorCraft—and the compound pressure gradients more-representative of real airfoils could not be tested. It was determined that, even with these limitations, a meaningful first step could be taken with this study in the WSU wind tunnel.

Computational studies to examine the detailed flow behavior in the presence of the surface steps were performed using the Northrop Grumman Generalized Compressible Navier-Stokes (GCNS) code. GCNS is widely used for design and the investigation of detailed flow features. The resulting modeling was used in an attempt to identify key similarity parameters governing the transition behavior in the presence of the surface imperfections, and can be used for integrating the resulting criteria for surface quality into the wing design.

## **2.0 Low-Speed Experimental Database Development**

Task 1 of the Prediction of Manufacturing Tolerances for Laminar Flow contract was to build a low-speed experimental database of surface excrescence effects on boundary layer transition. This database would then form the basis of subsequent extensions to compressible flow conditions and sweep effects.

The approach used was to develop a test apparatus that allowed the pressure gradient to be varied without having to change the physical excrescence parts or the actual test surface. To accomplish this, a special flat plate model was mounted in a wind tunnel with a movable upper wall. The positioning of the wall determined the static pressure variation over the test plate. The test plate itself had provisions for excrescence inserts that allowed various step and wave geometries to be tested. A row of pressure taps in the model allowed measurement of the static pressure distribution on the plate and a traversing Preston tube was used to measure the chordwise distribution of skin friction. From these skin friction distributions, the transition location was determined.

### **2.1 Test Facility**

The WSU, Tri-Cities Low Speed Contractionless Wind Tunnel was used for the Task 1 experimental work. The wind tunnel is located at the WSU campus in Richland, WA. The wind tunnel was designed and constructed especially for boundary layer research. Powered by a five horsepower motor, the forward-swept blade centrifugal fan provides unit Reynolds numbers from zero to  $0.2 \times 10^6$  per foot in the 2- by 2-ft test section. The motor and fan unit is controlled by a variable frequency drive unit. The overall layout of the wind tunnel is shown in Figure 8

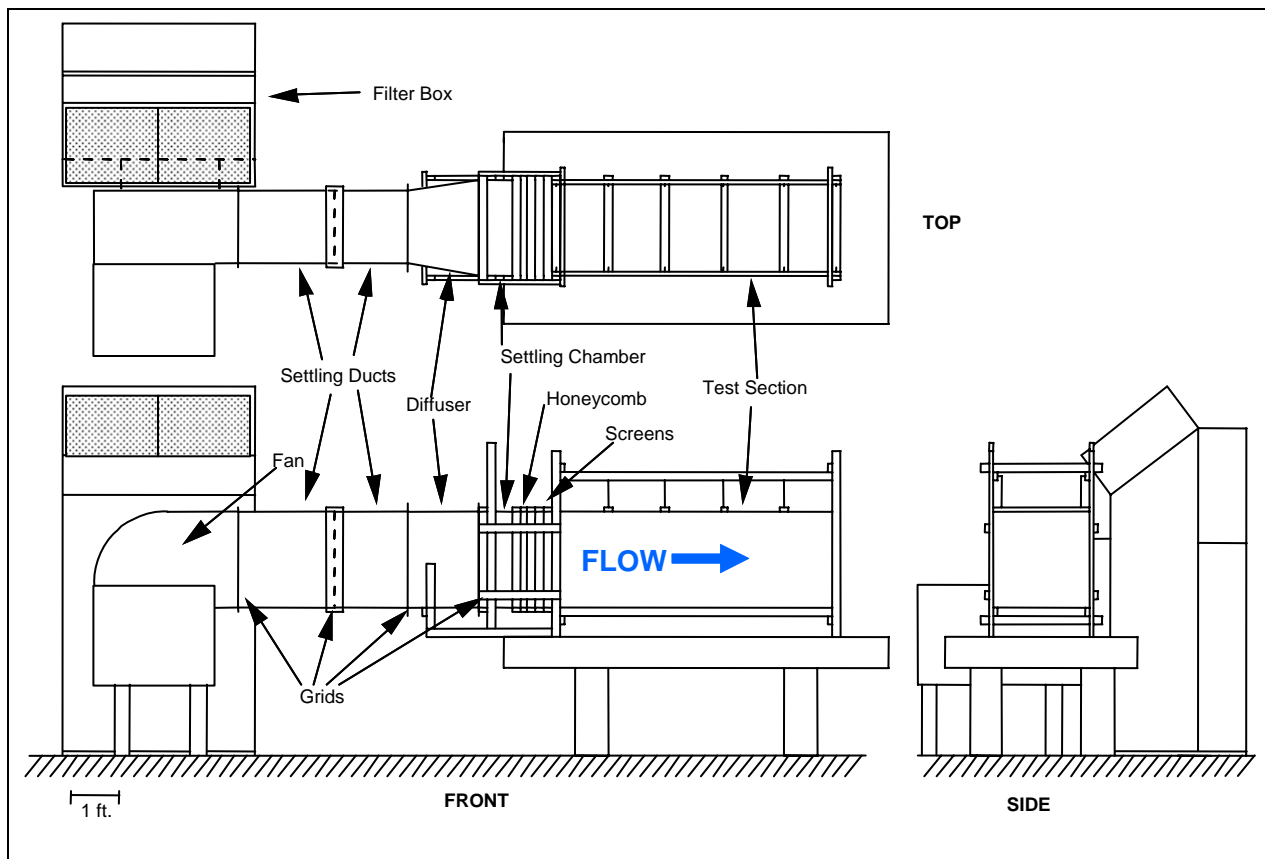


**Figure 8. WSU Low-Speed Contractionless Boundary Layer Wind Tunnel**

The wind tunnel's blower-type design positions the 2- by 2-ft cross-section, 6-foot-long test section as the downstream-most component. The upper wall is easily adjustable to allow tailoring of pressure gradients through the test section. The upper wall is supported from the upper longitudinal braces by twelve turnbuckles, six on each side. The lower wall is also moveable. The walls of the test section are constructed of 0.250-inch transparent acrylic sheet. The test section itself is mounted on a 4- by 8-foot optical table. Mounting the test section on an optical table provides a flat, rigid support and the ability to easily mount probe supports, lights, and imaging equipment at any point around the wind tunnel. The blower-type arrangement allows the static pressure at the test section exit to be known (ambient room pressure) and allows easier sealing of the test section due to the relatively small pressure difference between the outside room and the test section interior. Additionally, probe and model access is greatly facilitated by this configuration.

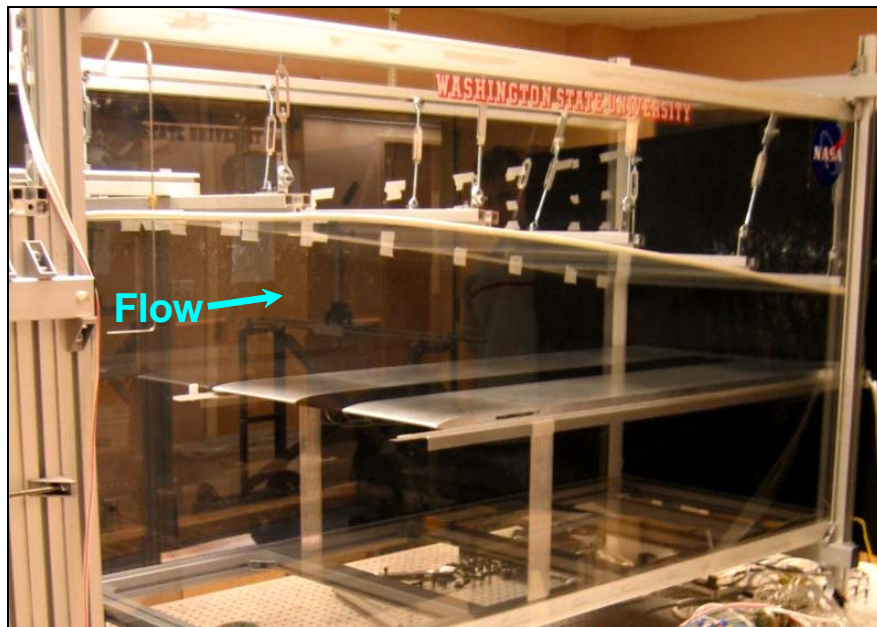


**Figure 9. Test section with flat plate model**

The structure of the test section is formed from extruded aluminum channels. The sidewalls of the wind tunnel are attached to vertical supports. The vertical supports attach to the outside of the sidewalls. The sidewalls themselves are 3 feet tall. At the lower and upper edges of the sidewall, longitudinal supports are attached to the inside surface of the sidewall. With the vertical supports in place, transverse supports above and below the test section sidewall on each of the vertical supports fixed the test section width. Six lower transverse ribs were attached between the lower longitudinal supports. The lower wind tunnel wall was then placed inside the tunnel, resting on the lower longitudinal supports and these transverse ribs. The upper wall was formed by adhering upper transverse ribs to the outside surface of the upper wall Plexiglas piece. Turnbuckles attached these transverse ribs suspended the upper wall from the upper longitudinal supports. Adjustment of the turnbuckles allowed manipulation of the upper wall position.

The air mover for the wind tunnel is a forward-swept-blade centrifugal fan with top horizontal discharge and driven by a 5-hp 230-V 3-phase motor. This air-mover is rated for a flow rate of 8,000 CFM at 2.0 inches of water. The motor is controlled by a variable frequency drive control. The forward-swept blade centrifugal fan design provides a higher blade-passing frequency than would be possible using a more-conventional backward-facing centrifugal design with fewer blades. The higher blade passing frequency results in lighter loading per blade and, thus, an overall lower level of unsteadiness. The fan exit is rectangular with dimensions of 23.1 by 17.9 inches. The inlet to the fan is on an adjacent side, thus oriented 90 degrees from the exit and is circular with a diameter of 24.25 inches. A large filter box, housing a two-stage filter array removes dust and other particulates which could interfere with experimental apparatus in the test section and foul the flow conditioning screens. Before entering the test section the flow passes through a two-stage settling duct, a diffuser, several grids, honeycomb, and a series of screens to improve flow uniformity, reduce flow angularity, and reduce freestream turbulence.

Maximum reliable performance of the wind tunnel is achieved when the motor is run at a frequency of 57 Hz. The motor can be run briefly at settings as high as 60 Hz., however, the controller occasionally senses an impending overload condition and shuts the system down. This

is a limitation not of the motor, but of the controller; this motor is the largest for which this controller was designed and has a built-in current limit lower than the maximum for the motor. Run at a motor frequency of 57 Hz, with the test section empty and set at a constant cross section, an exit dynamic pressure of 1.0 lb/ft<sup>2</sup> is achieved. At this setting, that is a speed of 30.9 ft/s, giving a unit Reynolds number of 0.20 x 10<sup>6</sup>/ft.

## 2.2 Model

A flat plate model was designed with a blunt leading edge and provisions for excrescence elements in various locations. The model was made from a single piece of aluminum. The span of the model was 23.5 inches to allow a clean fit in the 2-ft-wide test section. An existing support rail system supported the flat plate model in the center of the test section. A single chordwise row of 40 pressure taps was installed 2.5 inches from the centerline of the model and plumbed with tygon tubing taped to the lower surface of the model. The aft portion of the lower surface of the model was milled-out with a series of spars and webs left exposed to lighten the model for easier handling.

The leading edge of the test plate was shaped to be a *super ellipse* in cross section. The super ellipse is constructed similar to an ellipse, however the shape is slightly modified so that the second derivative goes to zero at the minor axes. This is important because having noncontinuous second derivatives can cause separation and transition where the elliptical leading edge meets the constant-thickness portion of the flat plate. The super ellipse is described by the equation

$$y = \left\{ \left( \frac{t}{2} \right)^2 - \left( \frac{t}{2} \right)^2 \left( \frac{c-x}{c} \right)^{2+\left( \frac{x}{c} \right)^2} \right\}^{1/2}, \quad (7)$$

where  $t$  is the thickness of the plate (equivalent to the minor axis of the ellipse),  $c$  is the chord of the leading edge (equivalent to half the major axis of the ellipse), and  $x$  is the distance from the leading edge in the streamwise direction.

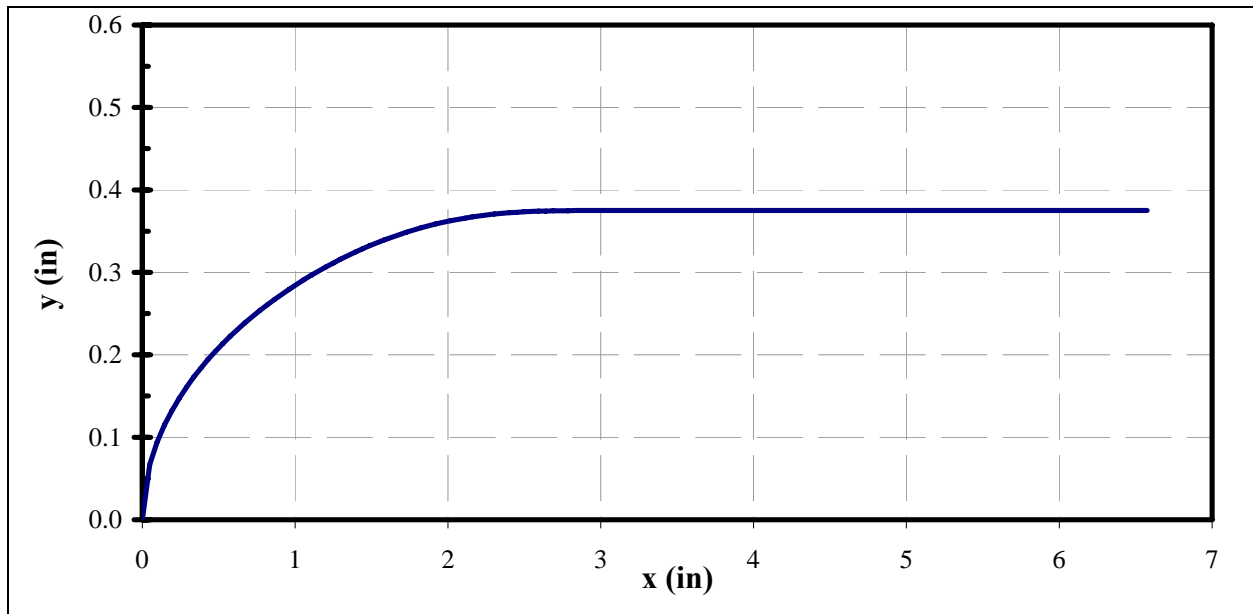


**Figure 10. Super ellipse leading edge geometry**

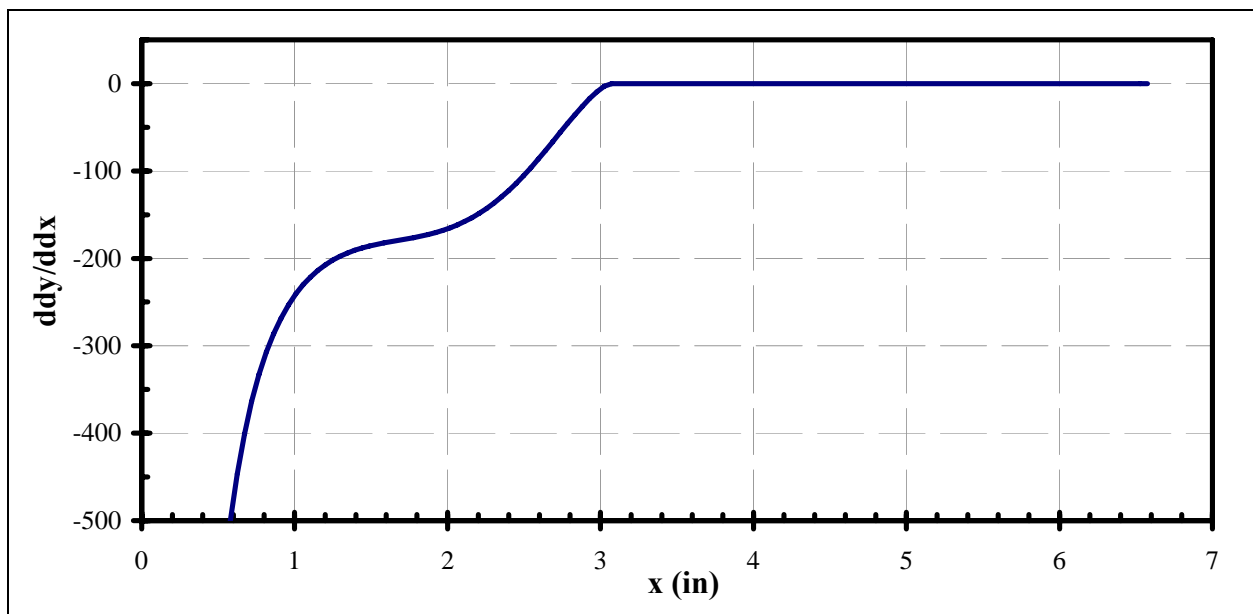


**Figure 11. Super ellipse leading edge curvature distribution**

The upper surface of the model had a 12-inch-long, full-span cavity milled in it to accept excrescence inserts. Each insert was 3 inches in chord and could be positioned at any of four locations (denoted A, B, C, and D). The remaining three locations were fitted with filler pieces. The filler pieces were designed to provide a level surface and were each equipped with a single static pressure tap.

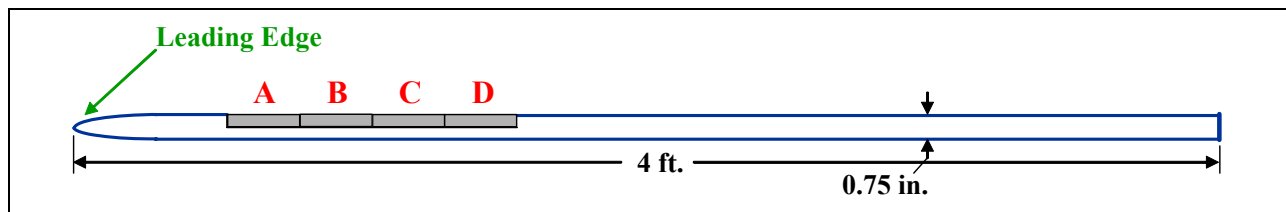


**Figure 12. Basic test plate geometry**

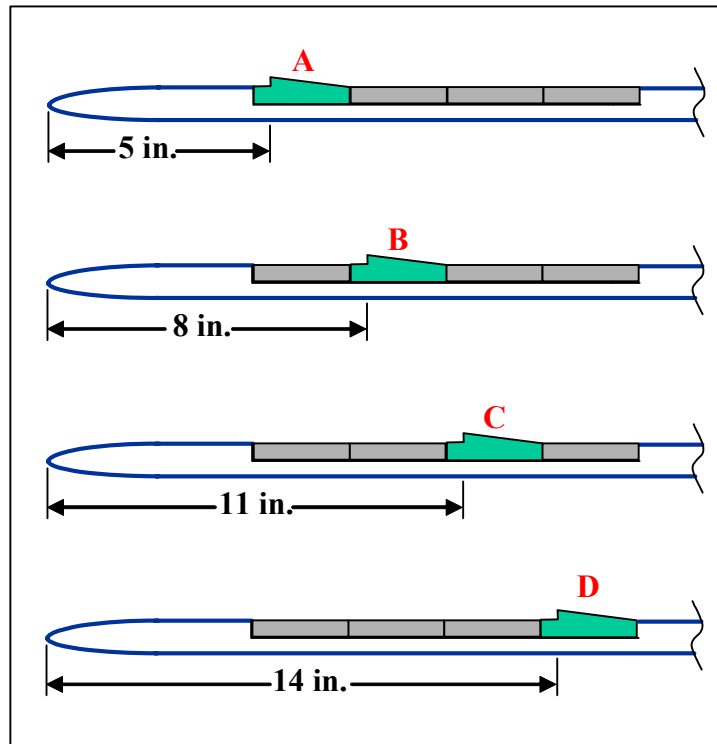


**Figure 13. Forward-facing step locations**

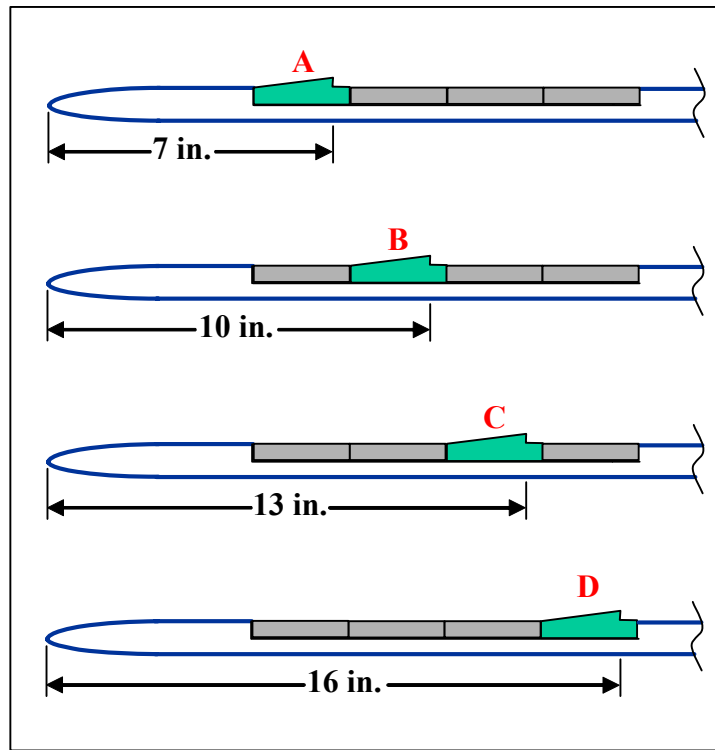


**Figure 14. Aft-facing step locations**

**Table 4 Excrescence locations**

<b>Excrescence Type</b>	<b>A</b>	<b>B</b>	<b>C</b>	<b>D</b>
Forward-Facing Step	5 inches	8 inches	11 inches	14 inches
Aft-Facing Step	7 inches	10 inches	13 inches	16 inches
Wave	6 inches	9 inches	12 inches	15 inches
Adjust-A-Wave	7.5 inches	--	--	--

**Table 5 Excrescence Piece Sizes**

<b>Step</b>	<b>Wave</b>	
<b>Height [in]</b>	<b>Height [in]</b>	<b>Length [in]</b>
0.100	0.250	2.50
0.090	0.200	2.00
0.080	0.170	1.70
0.070	0.120	1.20
0.055	Adjust-a-Wave	6.00
0.035	--	--
Adjust-a-Step	--	--



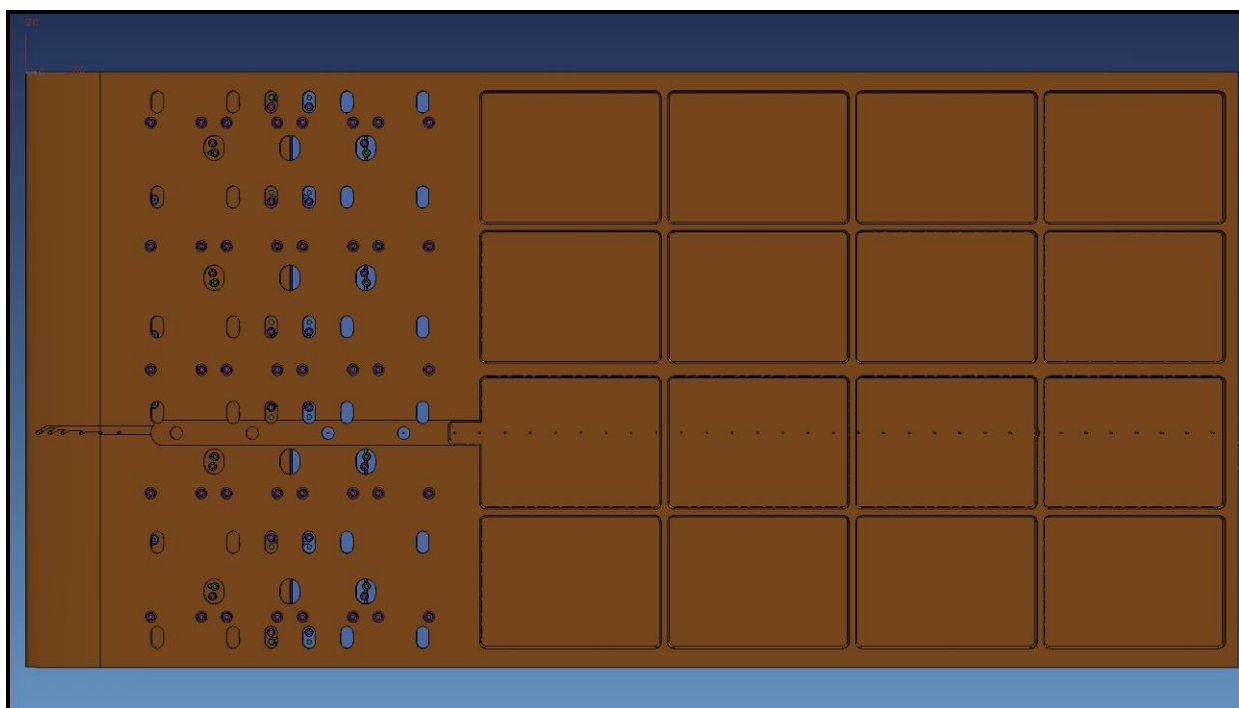


**Figure 15. Test plate lower surface showing milled webs and excrescence attachments**

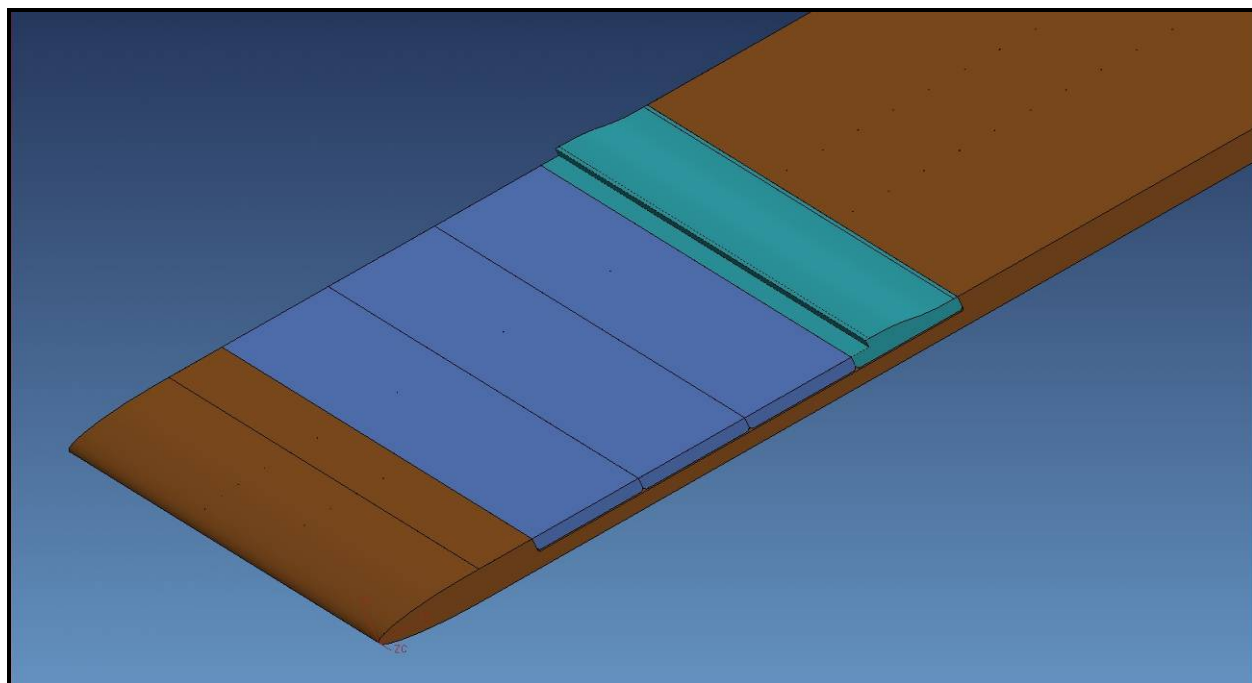


**Figure 16. Test plate upper surface with forward-facing step in position D**

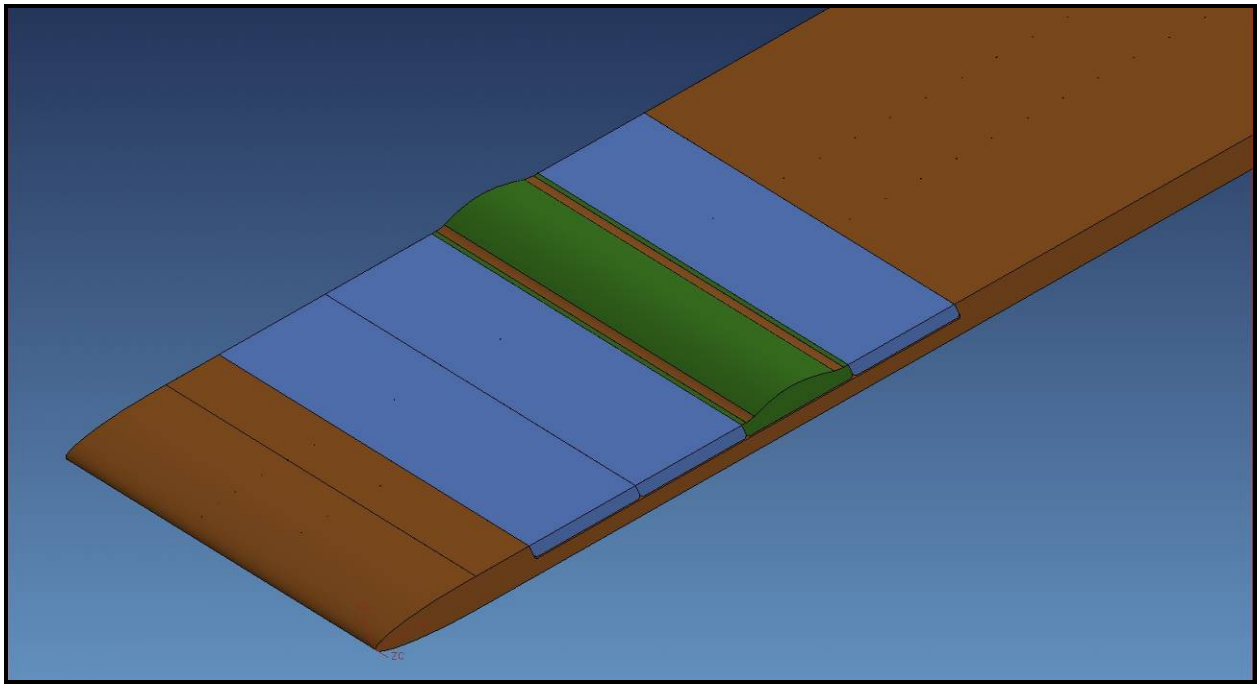


**Figure 17. Test plate upper surface with wave in position C**

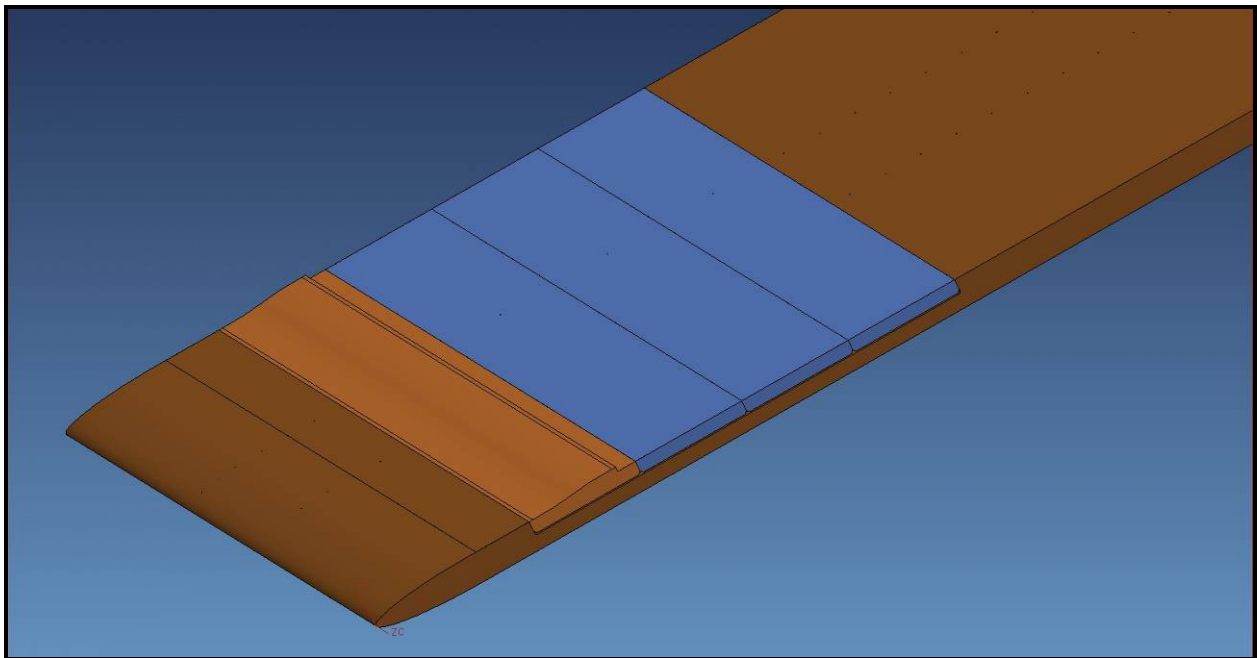


**Figure 18. Test plate upper surface with aft-facing step in position A**

## 2.3 Low-Speed Experimental Results

### ***2.3.1 Pressure Distributions***

Pressure measurements were made using a single pressure transducer connected to a mechanical multiplexer. The pressure transducer was a MKS Baratron model 698 sensor with a range of  $\pm 10$  torr (differential) operated by an MKS Baratron type 270D signal condition. The transducer accuracy is 0.15 percent of reading, and zero measurements were made with every scan to account for zero drift. The pressure transducer provided a conditioned voltage output which was measured with a 16 bit A/D converted so that the resulting accuracy of the pressure measurements should be within the 0.15 percent of reading achievable by the transducer.

A Scanivalve Corp. model SSS48C 48P/1T pressure multiplexer allowed 48 pressures to be connected sequentially to the positive port of the differential pressure sensor; the negative port was always connected to an upstream static pressure reference. For all pressure scans, the first two pressures measured were the upstream total pressure and the upstream static reference so that a reference dynamic and zero pressure were acquired at the beginning of each scan. Starting with the third port, inputs to the pressure multiplexer were connected to the static pressure taps in the surface of the test plate. The test plate provided 41 surface static pressure ports spaced 1 inch apart after 16 inches from the leading edge, more closely within the first 4 inches of the leading edge, and 3 inches apart between 6 and 15 inches from the leading edge. The last few ports of the multiplexer were used for connection of the Preston tube and boundary layer total pressure probes. Pressure connections were made using 0.062-inch ID tubing.

Selection of which input port of the multiplexer to read was done using home and step control actuated with digital outputs of the data acquisition computer. A few seconds were allowed for pressure settling after each step before reading each port pressure.

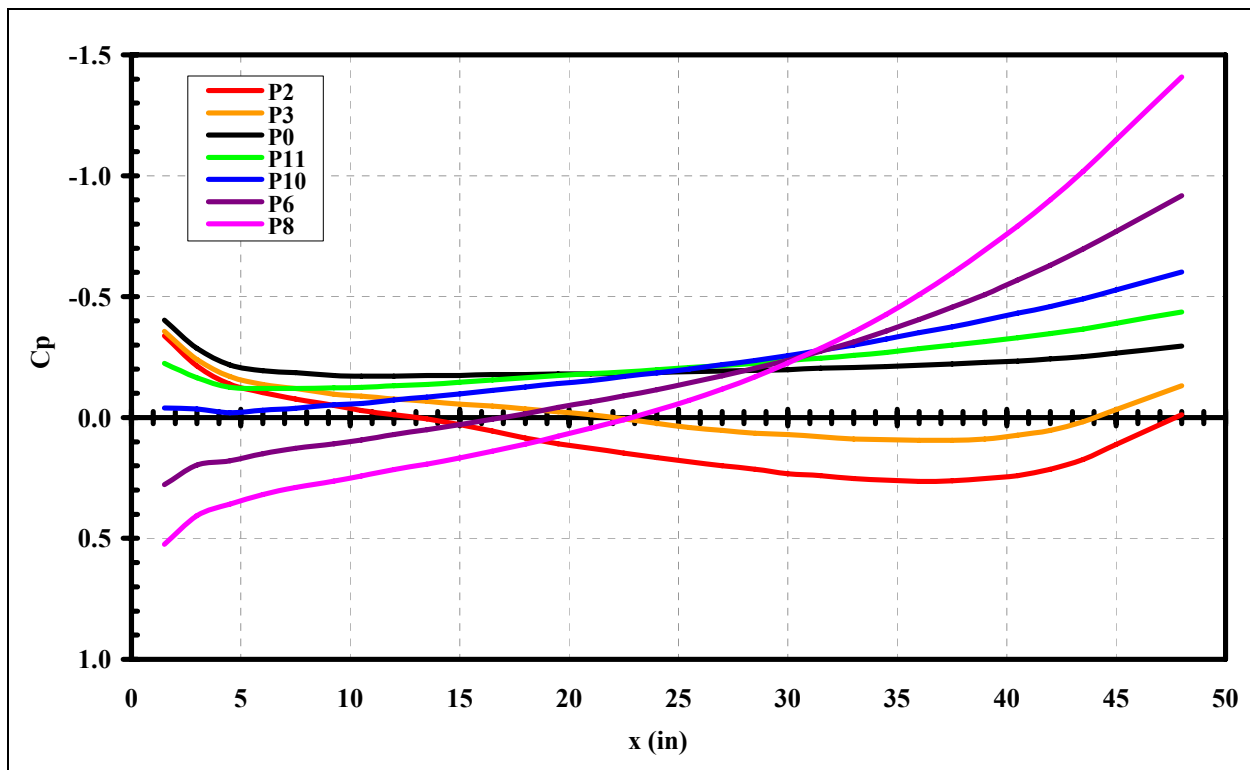


Figure 19. Static pressure distributions for tested cases

### 2.3.2 Pressure Gradients

The measured static pressure distributions were used to determine the dimensionless pressure gradients for each condition tested. The approach discussed in Section 1.2 was used to determine  $K$ . The results are shown in Figure 20. For the approximately constant region of each pressure gradient, a constant  $K$  was assigned. These dimensionless pressure gradient values are shown in Table 6.

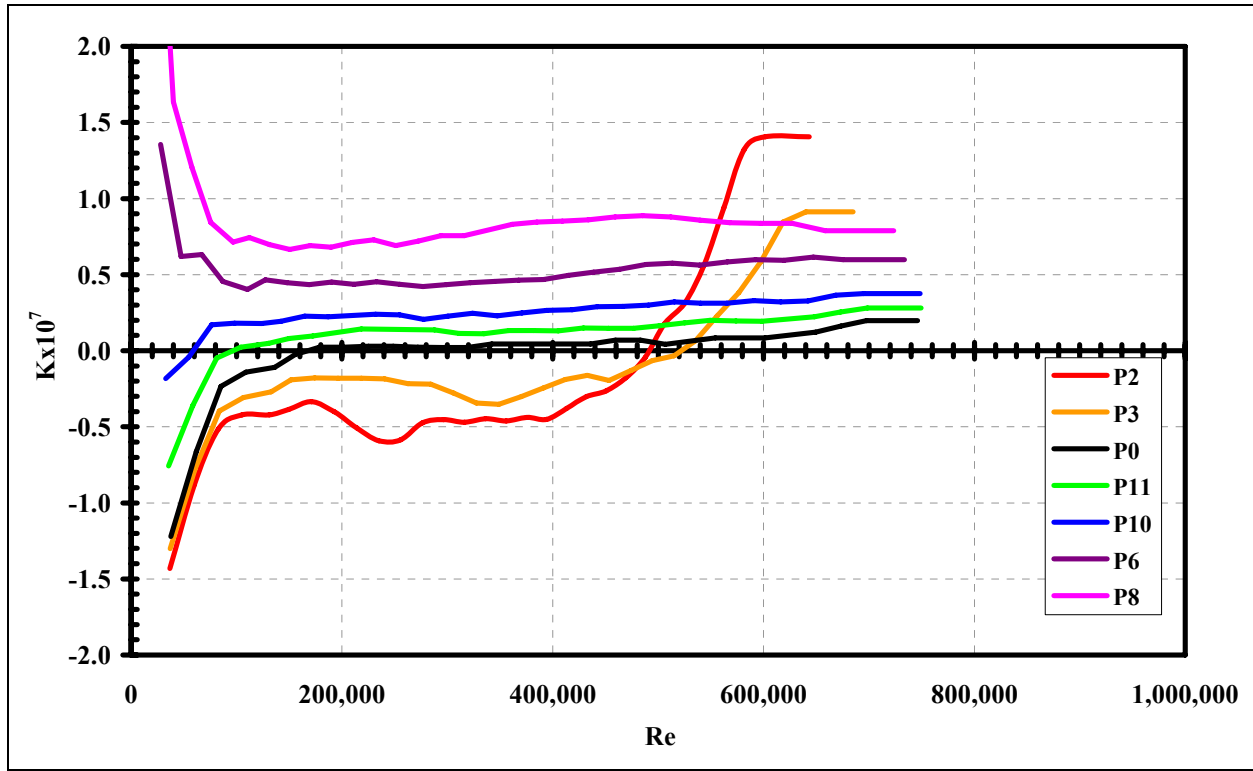


Figure 20. Dimensionless pressure gradients for tested cases

Table 6 Pressure gradient values

Setting	K	$Re_{x max}$
P2	$-0.44 \times 10^{-7}$	149,000
P3	$-0.24 \times 10^{-7}$	275,000
P0	$0.04 \times 10^{-7}$	745,000
P11	$0.15 \times 10^{-7}$	728,000
P10	$0.27 \times 10^{-7}$	744,000
P6	$0.51 \times 10^{-7}$	717,000
P8	$0.78 \times 10^{-7}$	677,000

The nondimensionalized pressure gradients that were tested are applicable to relevant systems. For comparison, the chordwise distribution of  $K$ , as a function of chordwise-integrated Reynolds number is shown for two representative wings. The first is a Global Hawk-type wing with pressure distributions shown in Figure 21 and typical flight conditions shown in Table 7. Figures 22 through 25 show the comparison with the current test conditions. It can be seen the present study fully covers the range of  $K$  values of importance to the Global Hawk-type wing. However, because of the limited Reynolds number range of the present study, the full range of Reynolds numbers is not covered. Figure 26 shows pressure distributions for an early SensorCraft wing design. While this is not the current wing design, it is generally representative of the pressure distributions (note, the SensorCraft wing has substantial amounts of sweep, those effects on surface excrescences are not included in the present study). Figures 27 and 28 show a similar comparison of dimensionless pressure gradient for SensorCraft; the result is the same, the range of applicable  $K$  values is covered, but not the full range of Reynolds numbers. In the case of the

SensorCraft wing, the Reynolds number shortfall is even more pronounced, due to its large size and resulting higher cruise Reynolds numbers.

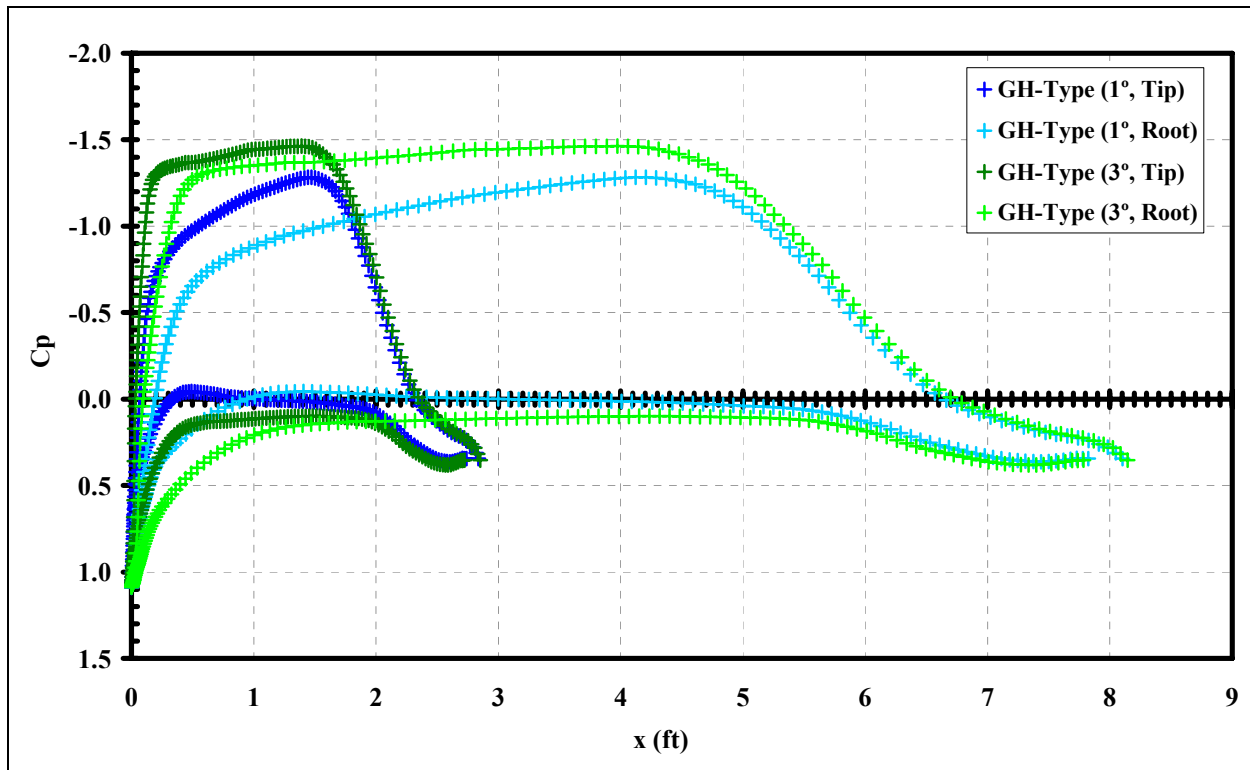


Figure 21. Pressure distributions for a Global Hawk-type wing

Table 7 Typical flight conditions for a Global Hawk-type aircraft

	M	Altitude (ft)	q (lb/ft <sup>2</sup> )	$\rho$ (sl/ft <sup>3</sup> )	$\mu$ (sl/ft-s)	u (ft/s)	Re/ft
Heavy Cruise	0.600	55,000	48	$2.85 \times 10^{-4}$	$2.97 \times 10^{-7}$	$5.80 \times 10^2$	556600
Mid Cruise	0.575	57,500	39	$2.52 \times 10^{-4}$	$2.97 \times 10^{-7}$	$5.57 \times 10^2$	473000
Light Cruise	0.550	60,000	32	$2.24 \times 10^{-4}$	$2.97 \times 10^{-7}$	$5.32 \times 10^2$	401300

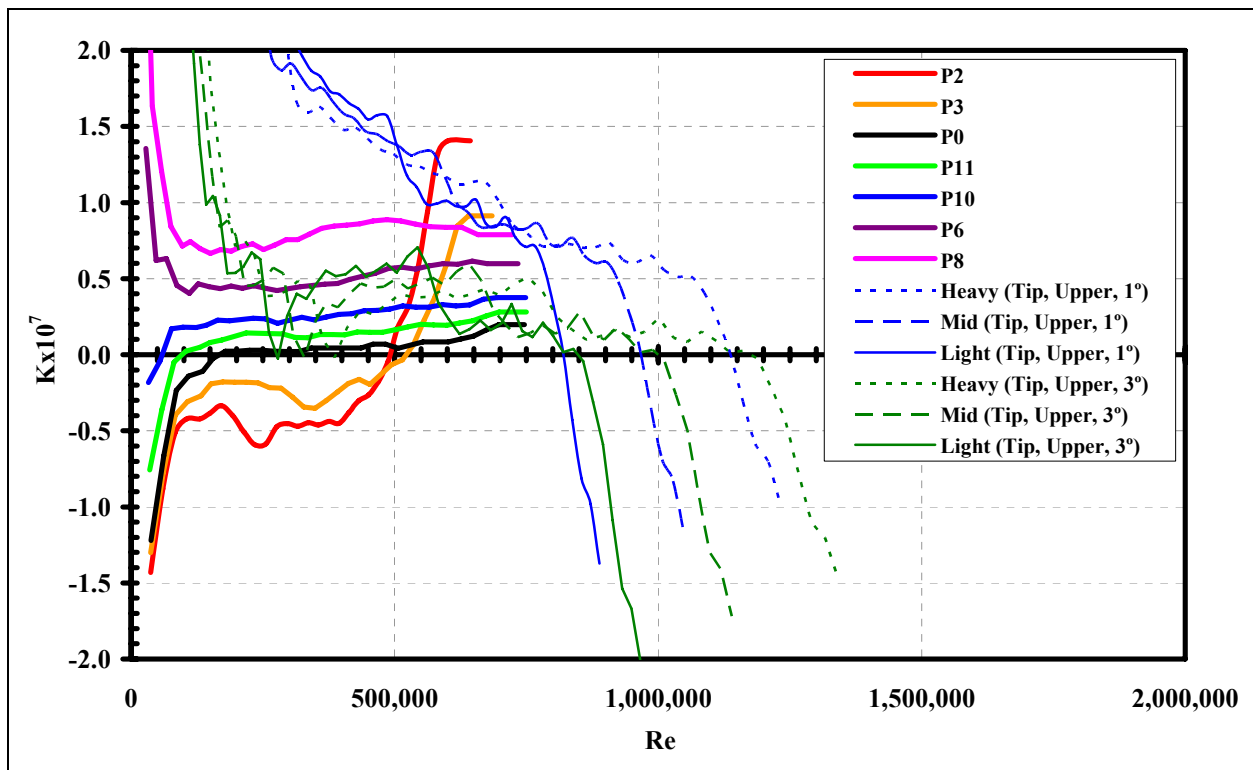


Figure 22. Pressure gradient comparison with GH-type wing tip upper surface

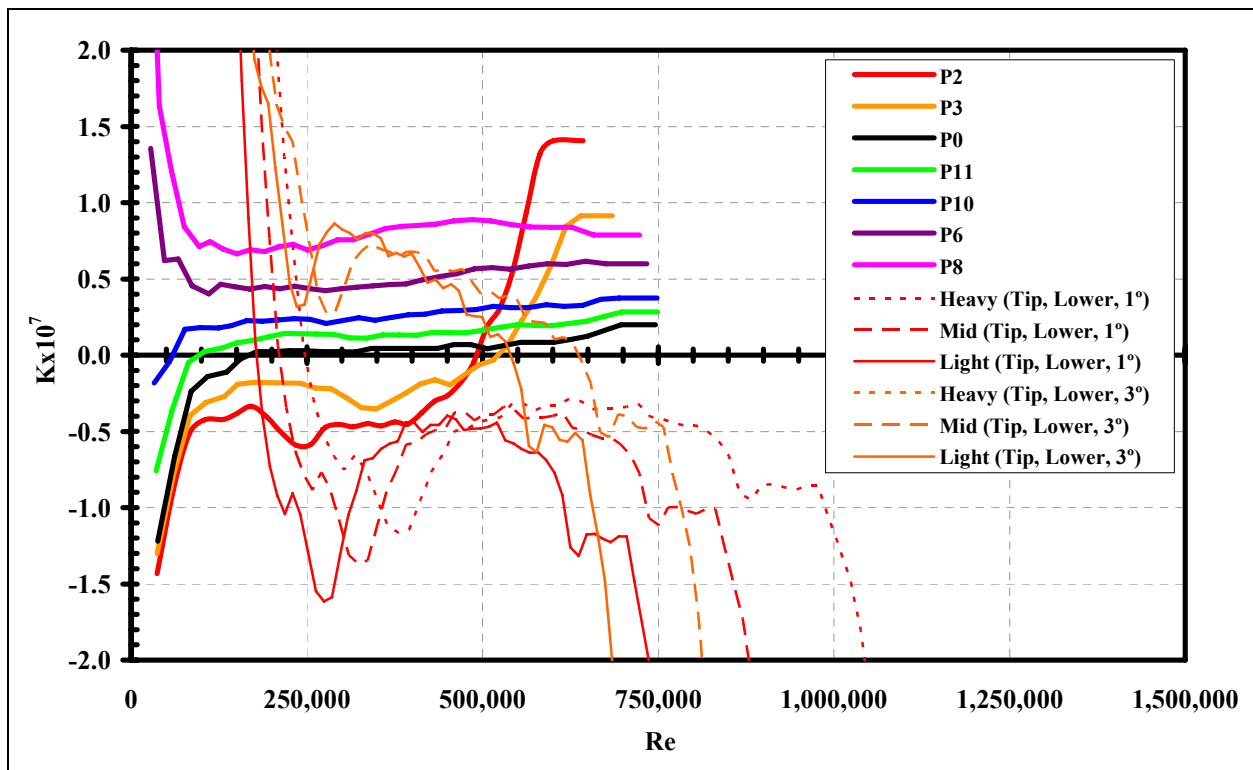


Figure 23. Pressure gradient comparison with GH-type wing tip lower surface

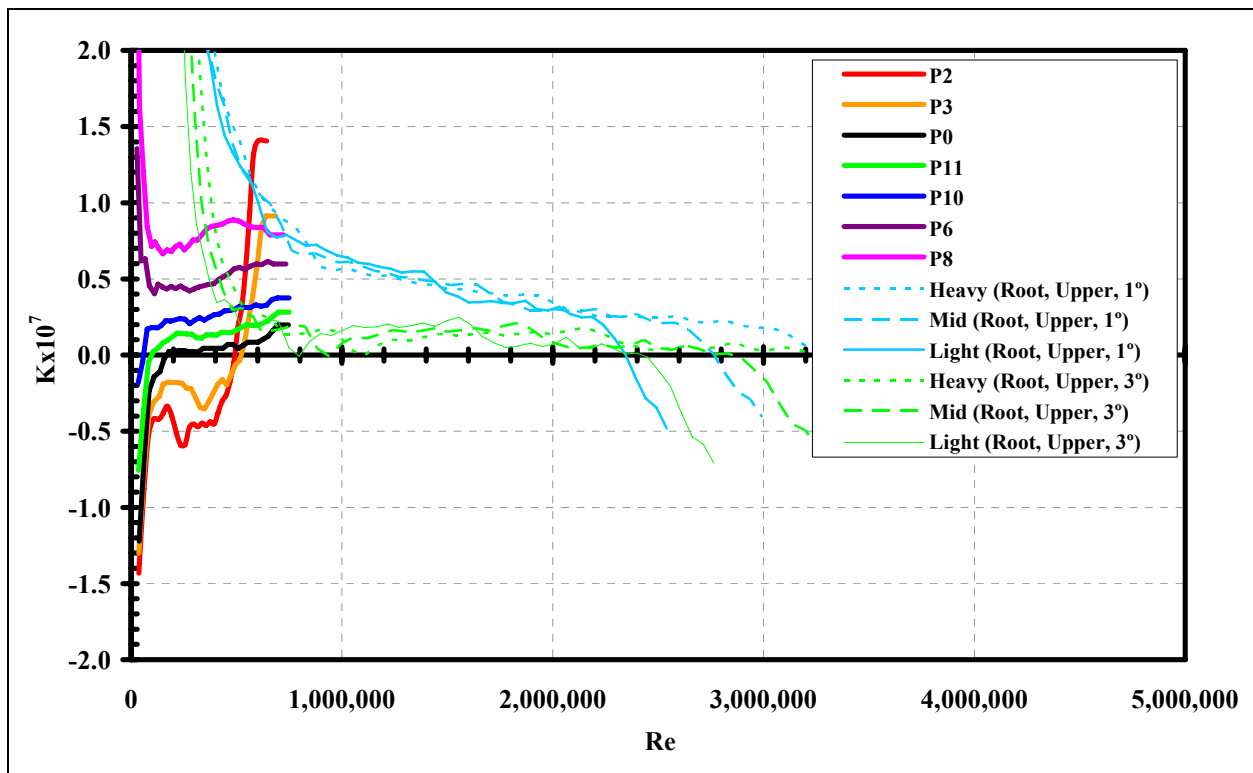


Figure 24. Pressure gradient comparison with GH-type wing root upper surface

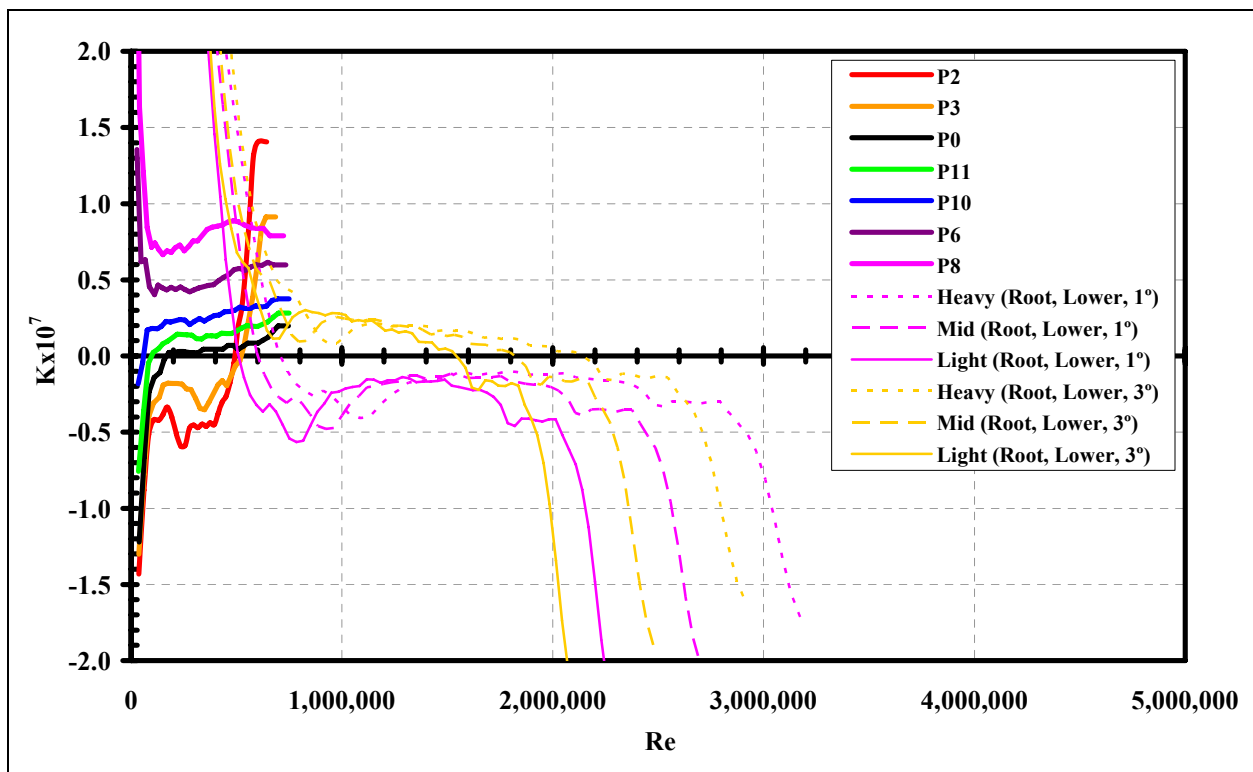


Figure 25. Pressure gradient comparison with GH-type wing root lower surface



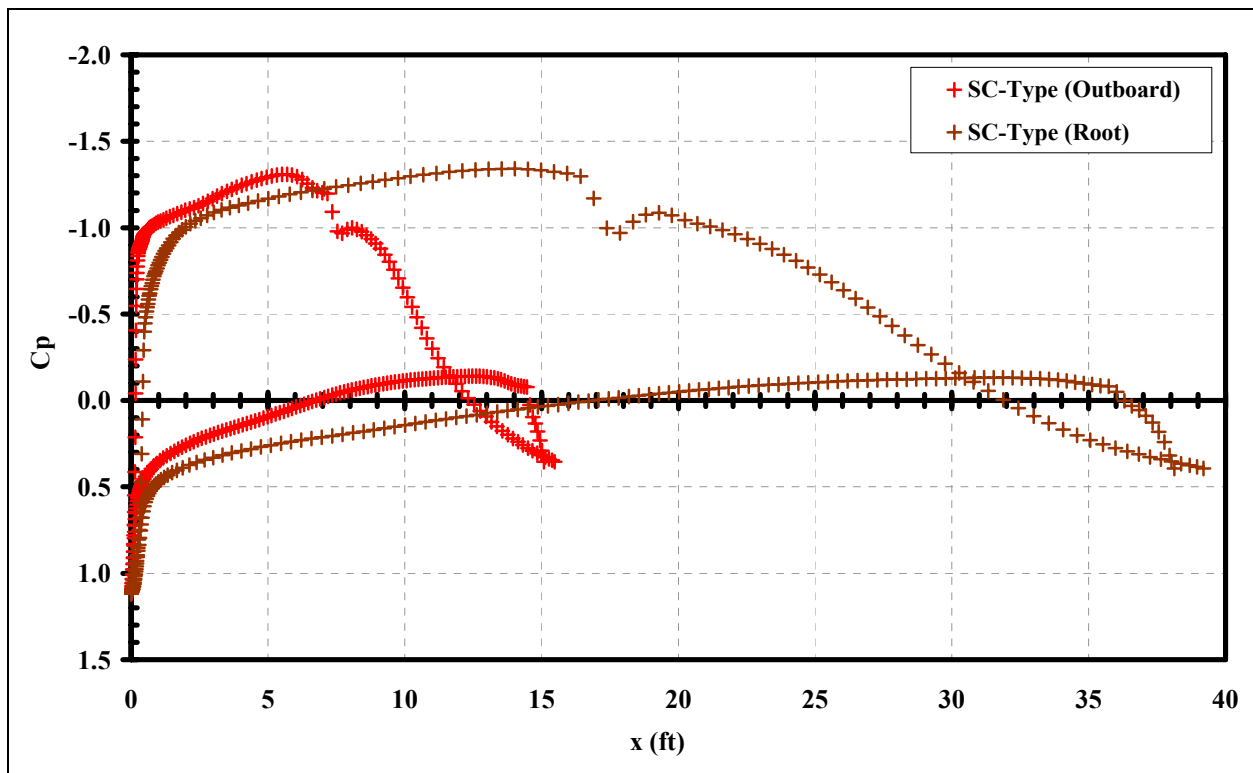


Figure 26. Pressure distributions for a SensorCraft-type wing

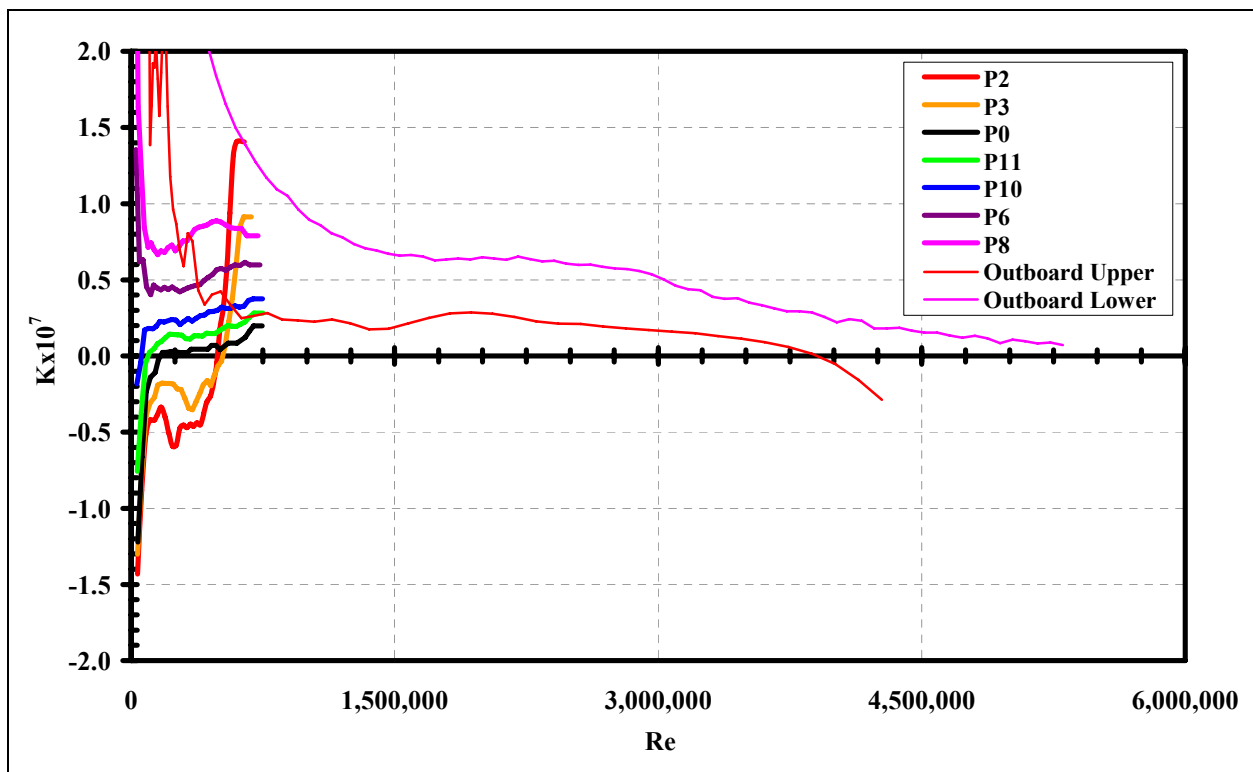


Figure 27. Pressure gradient comparison with SC-type wing tip

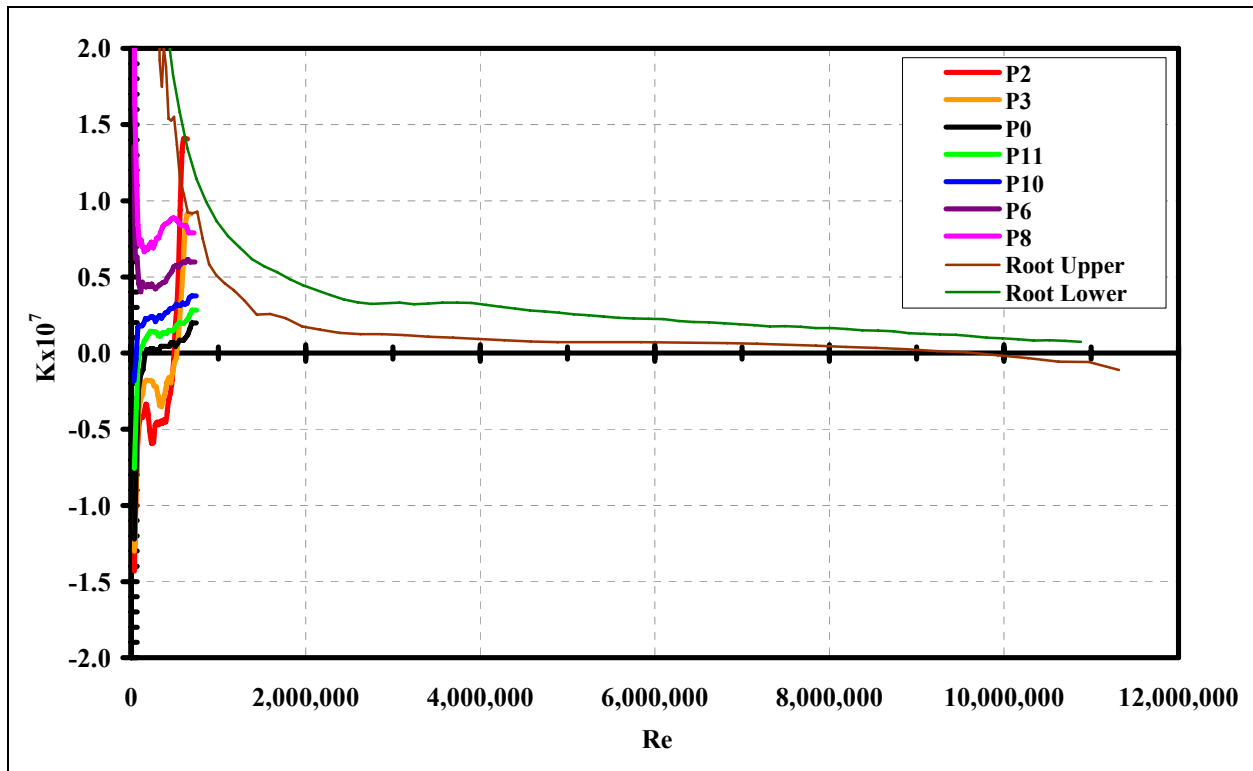


Figure 28. Pressure gradient comparison with SC-type wing root

### 2.3.3 Boundary Layer Velocity Profiles

To determine the excrescence height Reynolds number ( $Re_k$ , see Section 1.2), it was necessary to have measurements of the boundary layer velocity profile at each excrescence location for each pressure gradient. The boundary layer velocity profiles were measured with a total pressure tube mounted on an automated traverse. The resulting pressure differences (total pressure from the boundary layer traverse minus reference static pressure) were then corrected for the location of the wall and the displacement effect of the tube in the proximity of the wall. Boundary layer measurements were made with a round probe of either 0.050-inch or 0.032-inch diameter. The probe was positioned using a computer-controlled stepper motor driven probe traverse system.

Measurements made with a total pressure probe in a flow of spatially varying mean velocity are known to deviate from the true value of velocity at the probe centerline location because of averaging and flow distortion effects caused by the finite size of the probe. This effect has traditionally been accounted for by applying a correction to the location of the measurement; this has been termed a displacement correction. Early studies (summarized by Bryer and Pankhurst<sup>8</sup>, 1971, chapter 2) have proposed that a displacement of 10 to 20 percent of the probe diameter, in the direction of velocity increase, be applied for typical round pressure probes. Some confusion has remained about this correction, partly because different investigators have recommended corrections that aren't identical, and partly because there are usually additional effects from turbulence and/or the presence of a nearby wall that also cause errors in pressure probe measurements.

Recently, McKeon et al.<sup>9</sup> have extensively evaluated the application of a displacement correction to mean velocity measurements from a total pressure probe in a fully developed turbulent pipe flow. They also evaluated the influences of turbulence, and of a nearby solid surface. The latter

is known to be important for wall-bounded flows when a probe is located within about two probe diameters of a surface and corrections for this effect have been termed wall proximity corrections. Their recommended correction scheme is to use a new form of displacement correction for measurements except within two probe diameters of a surface. For the latter region, they recommend a separate wall proximity correction.

In the present experiments, total pressure probes have been used to measure the boundary layer mean velocity with a variety of pressure gradients, and with both laminar and turbulent flow. In particular, the laminar flow measurements are used to compute various dimensionless parameters that help to generalize the results, so it is desired that these be accurately determined. The objective of the present study was to evaluate whether the correction scheme recommended by McKeon et al.—developed specifically for turbulent pipe flow with a slightly favorable pressure gradient—is also adequate for laminar boundary layers in a variety of pressure gradients. The evaluation has been accomplished by measuring the same boundary layer with probes of different diameters. The figures below show measurements with seven different probes in a 3-mm laminar boundary layer with approximately zero pressure gradient on a flat, sharp-nosed plate. These data encompass a range of probe diameter to boundary layer thickness ratios of about 0.2 to 0.8. Comparing the uncorrected measurements from probes of different sizes, it is observed that the difference in the data is not large even though the probe size varies by almost a factor of four and is quite large compared to the boundary layer thickness. Comparing the corrected and uncorrected results, the scheme of McKeon et al. is seen to collapse the data from all probe sizes to a single curve with little apparent difference attributable to different probe size. Hence, we conclude that their correction method (combined displacement and wall proximity) is indeed applicable to laminar boundary layers.

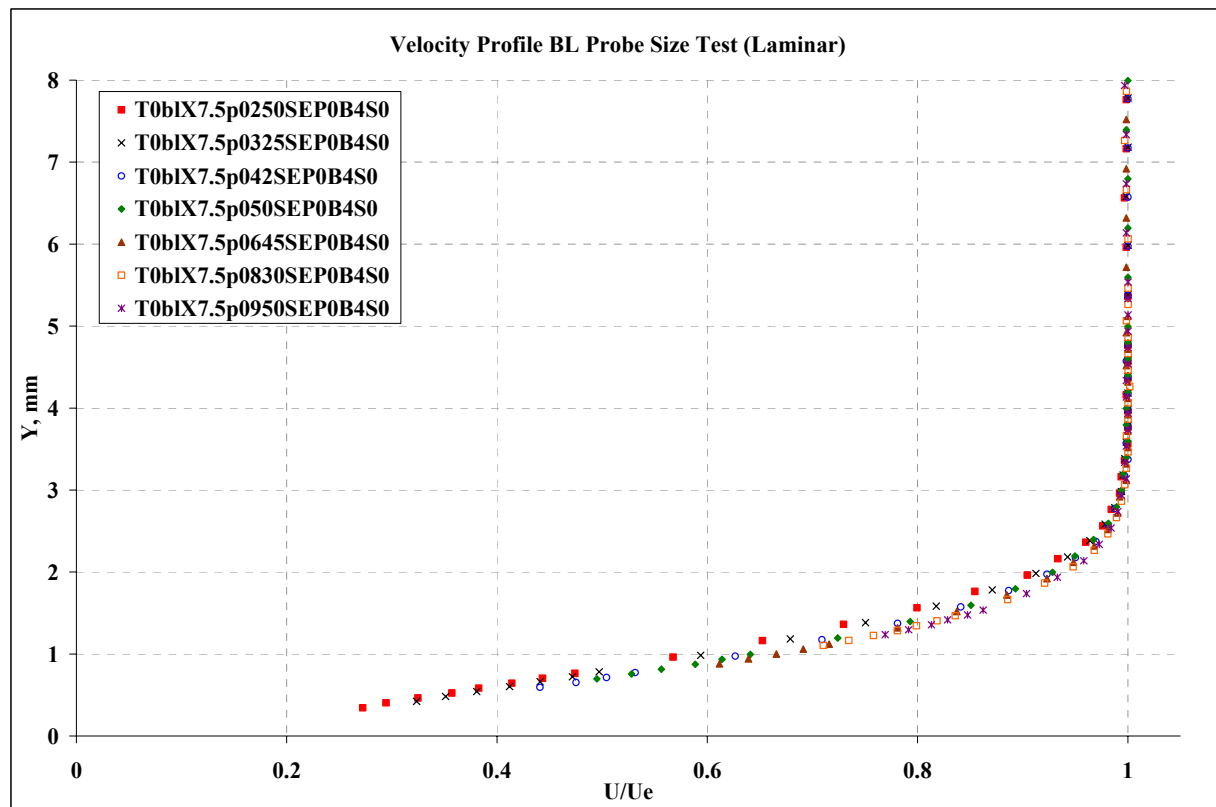


**Figure 29. Uncorrected velocity profiles with various tube diameters**

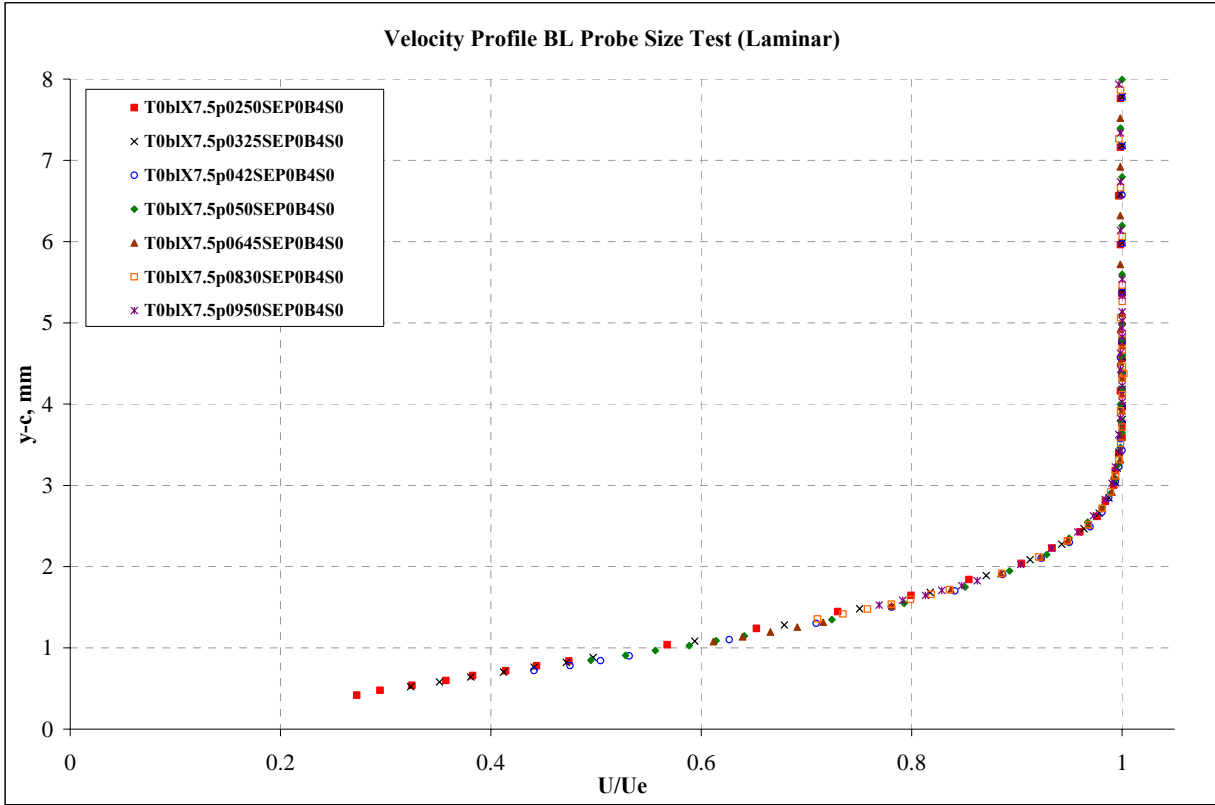


**Figure 30. Displacement-corrected velocity profiles with various tube diameters**

Boundary layer velocity profiles were measured for each of the pressure gradients. Velocity profiles were measured at  $x = 5, 6, 7, 8, 9, 10, 11, 12, 13, 14, 15$ , and  $16$  inches for all but one of the pressure gradients. Only a limited subset of the boundary layer velocity profiles necessary for data reduction was taken for pressure gradient P8. The reasons are related to the fact that this pressure gradient has the largest downward control wall deflection and to the height and installation of the traverse. For P8, boundary layer velocity profiles were measured at  $x = 6, 9$ , and  $11$  inches. To reduce the data properly, velocity profiles are needed at each of the  $x$ -stations where excrescences were located, namely:  $x = 5, 7, 8, 10, 11, 13, 14$ , and  $16$  inches.

To supplement the measured boundary layer profiles, a simple computational method was used. This method used the code IBL, which computes 2-D laminar, transitional, or turbulent boundary layers with or without prescribed arbitrary distributions of surface pressure, heat transfer, and/or mass transfer.<sup>10</sup> Computational results from IBL were compared to the measured profiles at  $x=6, 9$ , and  $11$  inches. The parameters  $\delta^*$  (momentum thickness) and  $\theta$  (displacement thickness) were compared and the IBL results were scaled by the  $\theta$  ratio in order to more accurately match the measured profiles. This scaling factor was then applied to the IBL results at the excrescence locations. The IBL results, scaled to match the measured profiles, were then used in the data reduction for pressure gradient P8.

Plots of each of the measured velocity profiles as well as the scaled velocity profiles of P8 are shown in the following plots. Note, for cases where the excrescence fell between adjacent profiles (e.g., the waves, which were centered at  $7.5$  inches), the velocity profiles were averaged.

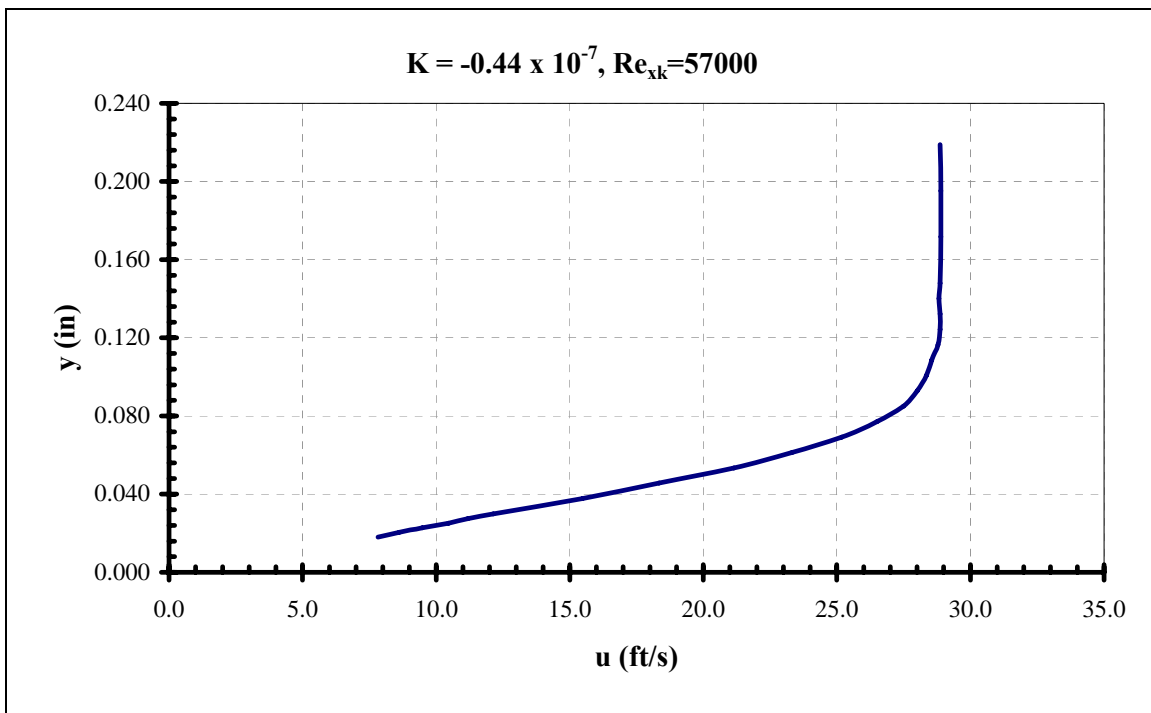


Figure 31. Boundary layer velocity profile

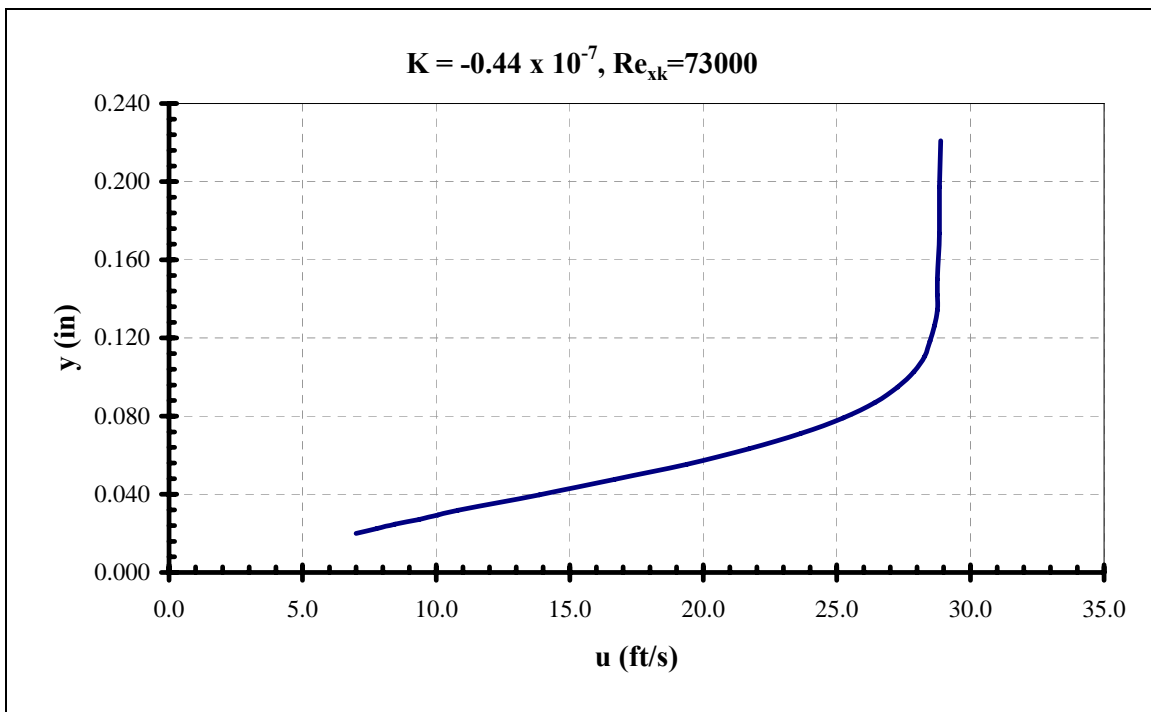


Figure 32. Boundary layer velocity profile

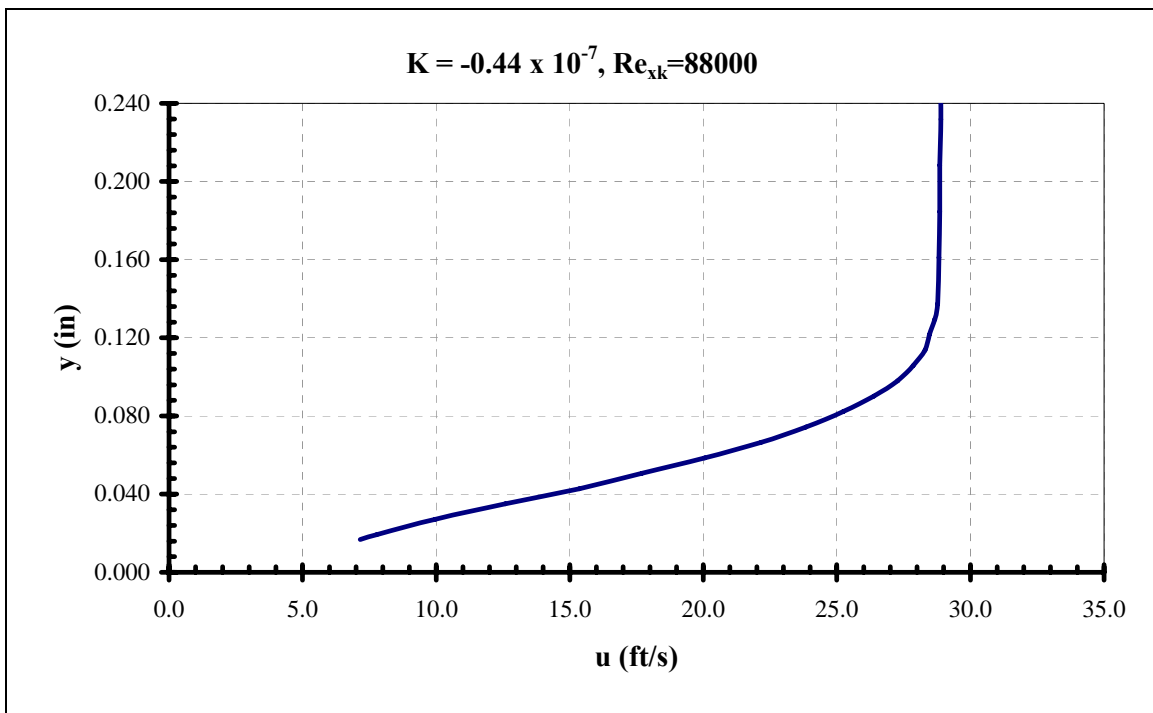


Figure 33. Boundary layer velocity profile

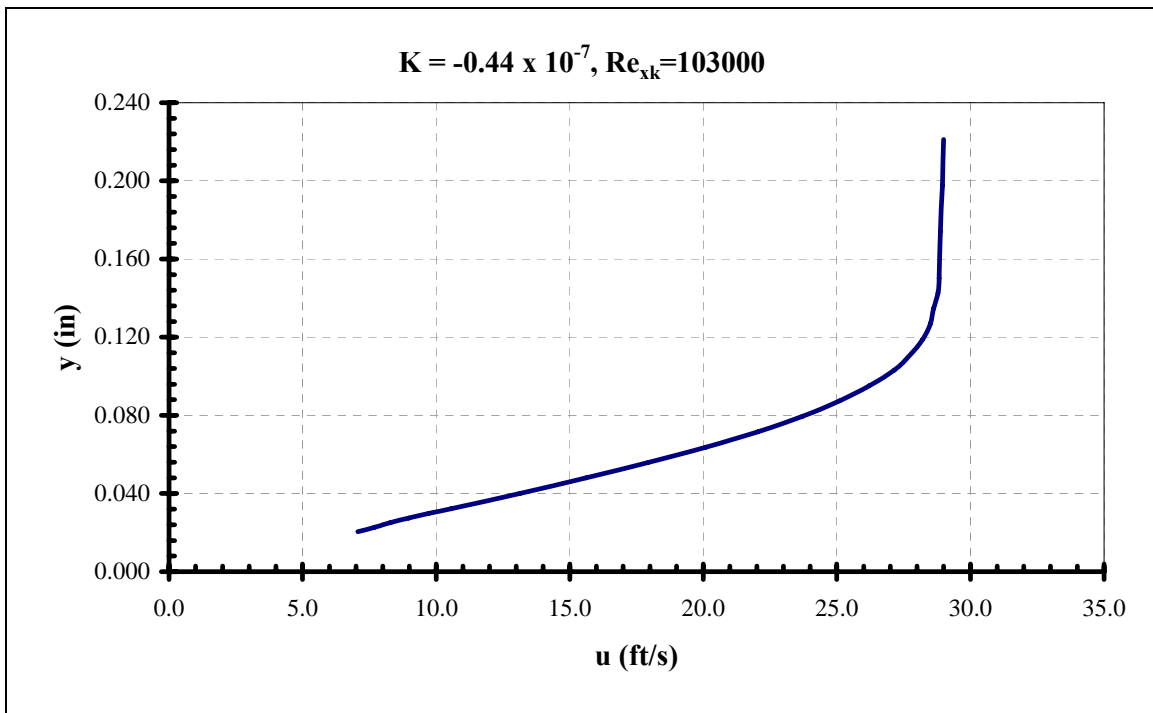
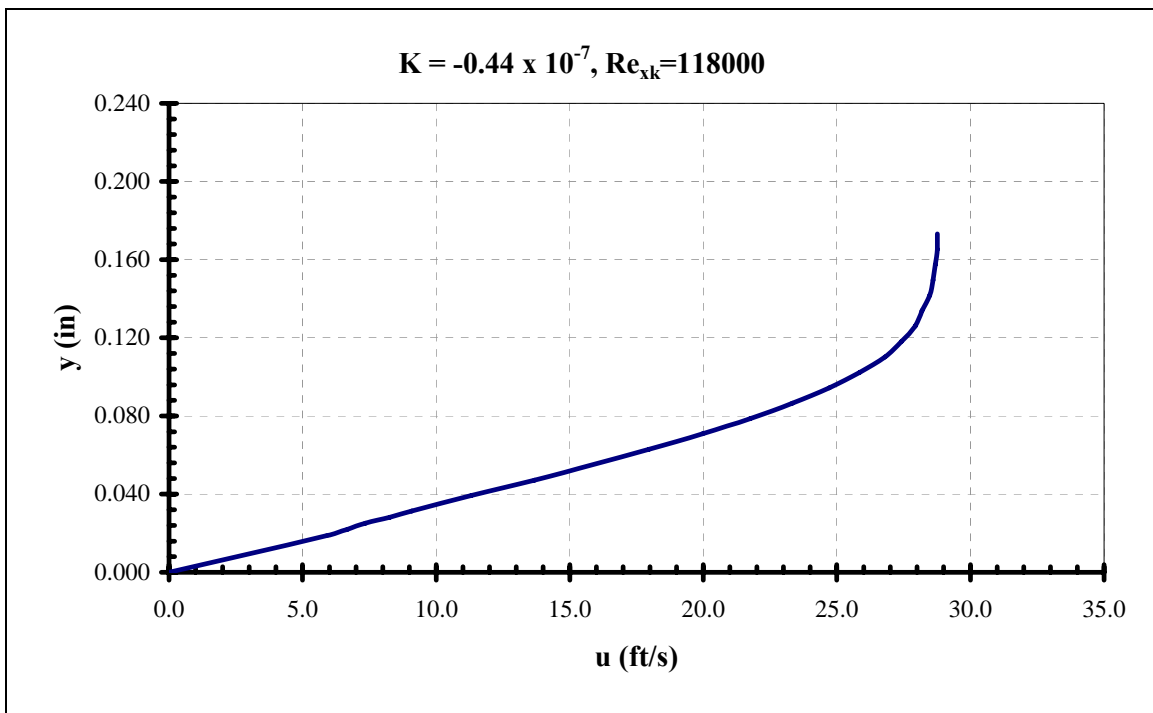
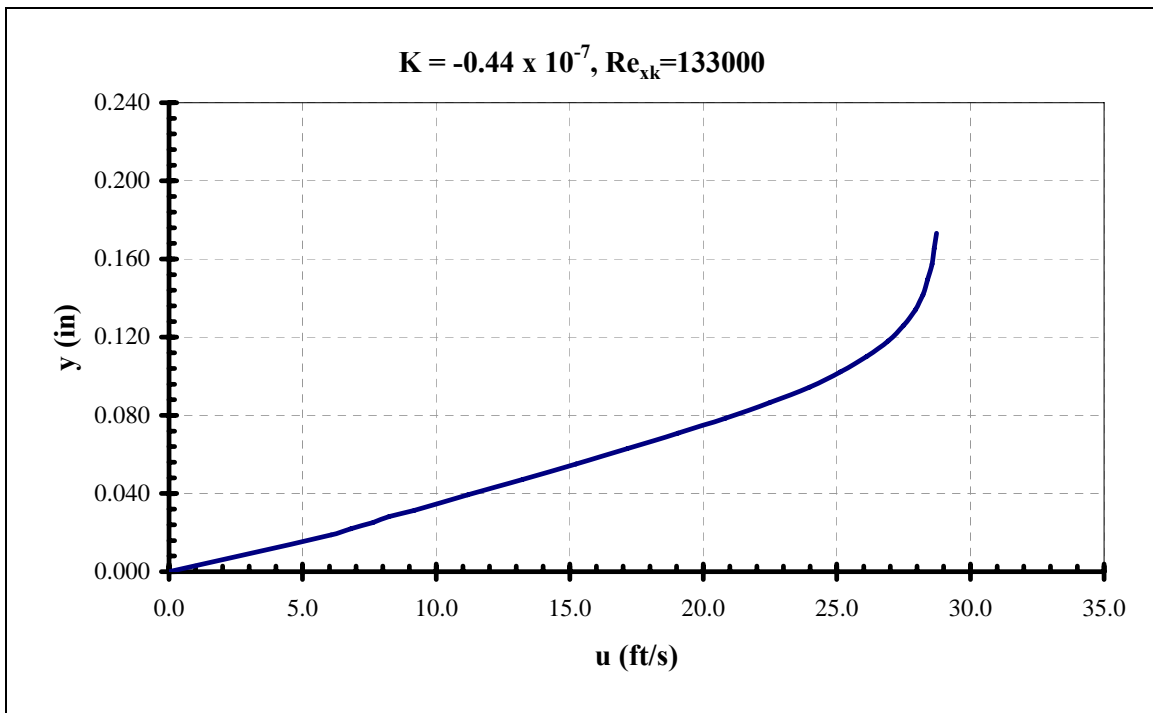


Figure 34. Boundary layer velocity profile



**Figure 35. Boundary layer velocity profile**



**Figure 36. Boundary layer velocity profile**

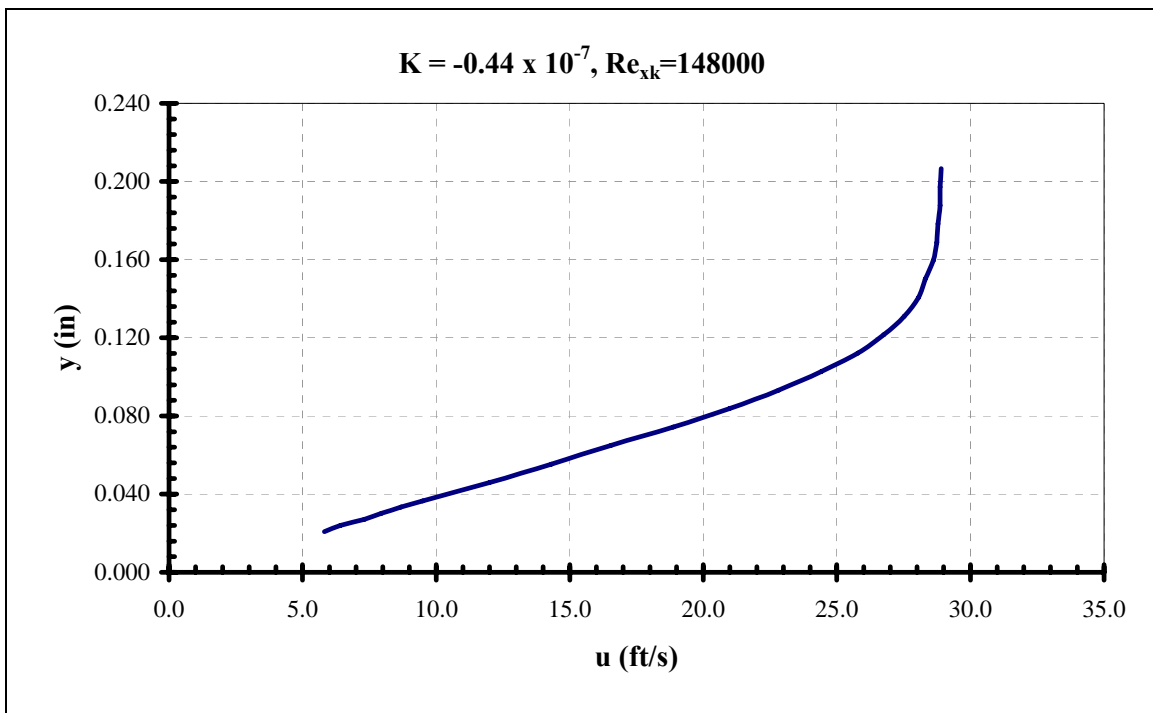


**Figure 37. Boundary layer velocity profile**

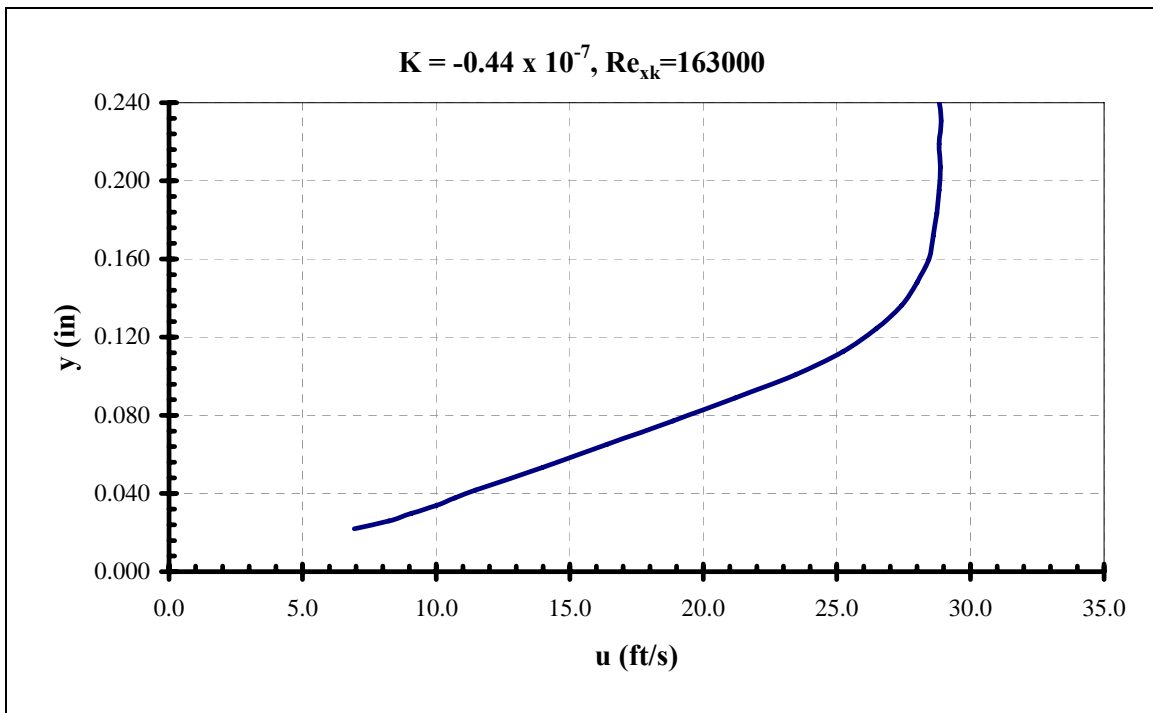


**Figure 38. Boundary layer velocity profile**



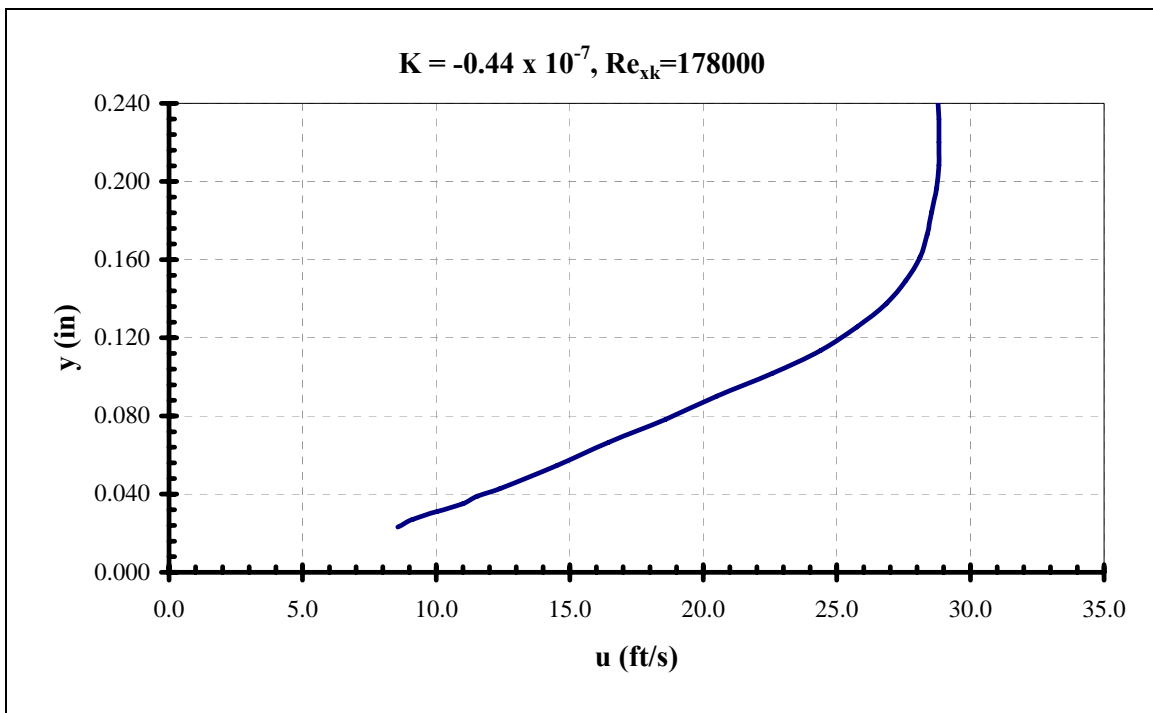


**Figure 39. Boundary layer velocity profile**

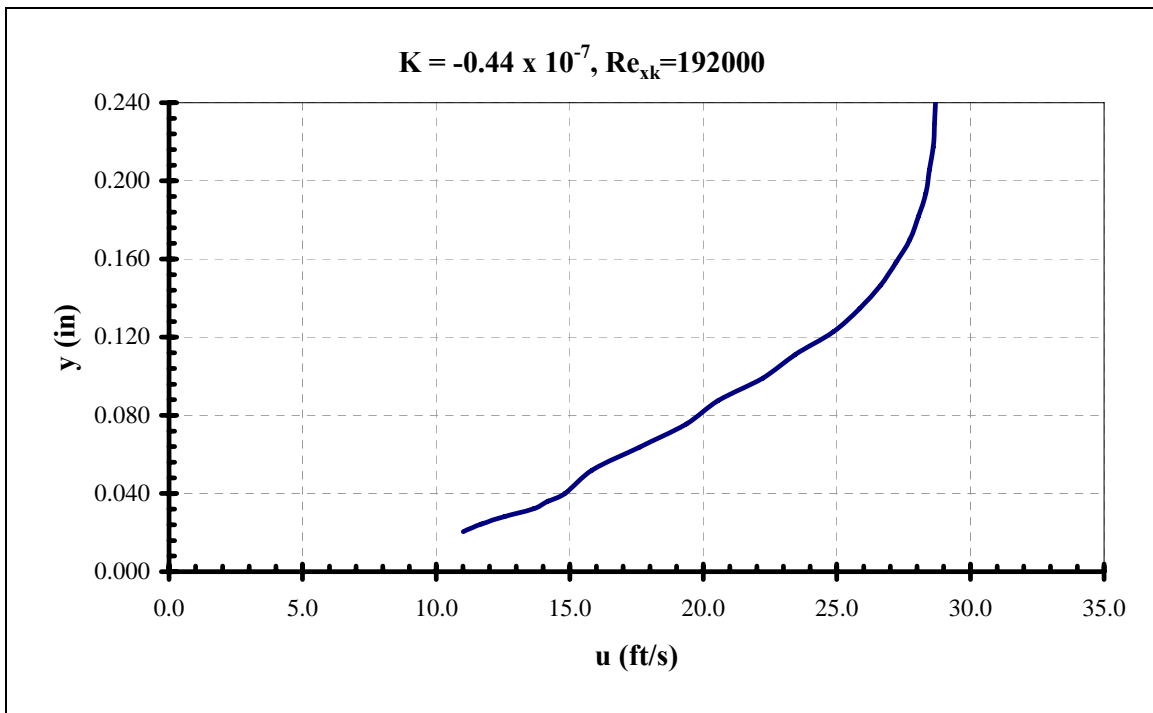


**Figure 40. Boundary layer velocity profile**

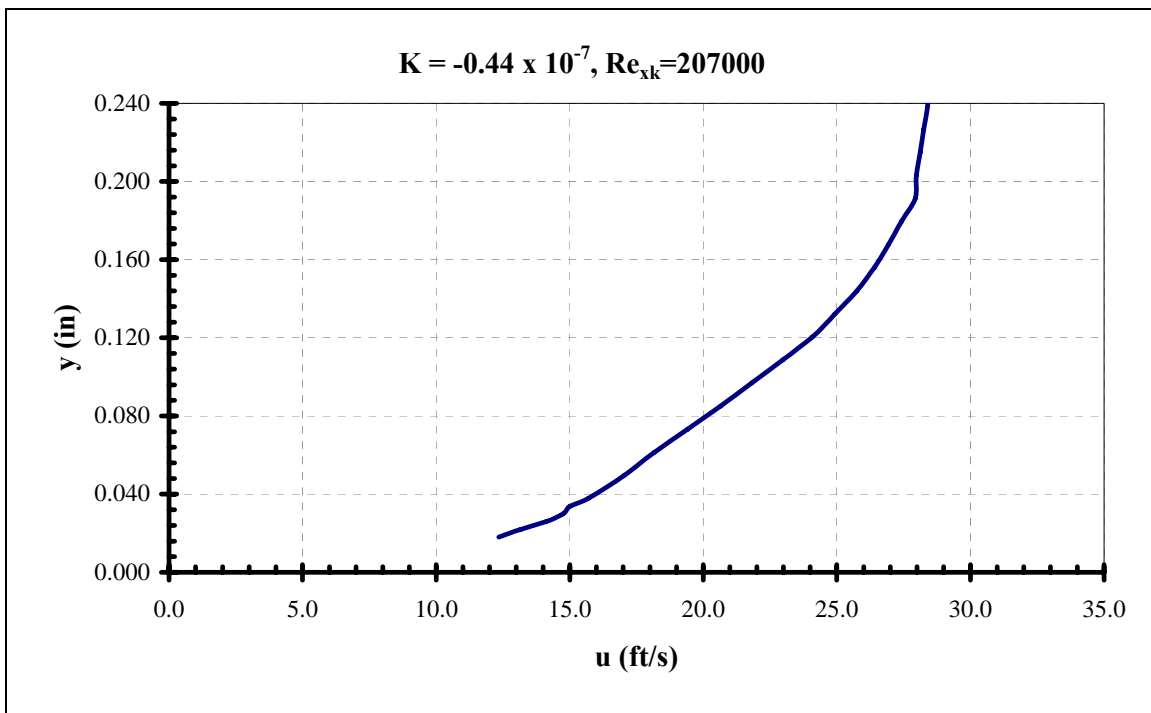


**Figure 41. Boundary layer velocity profile**

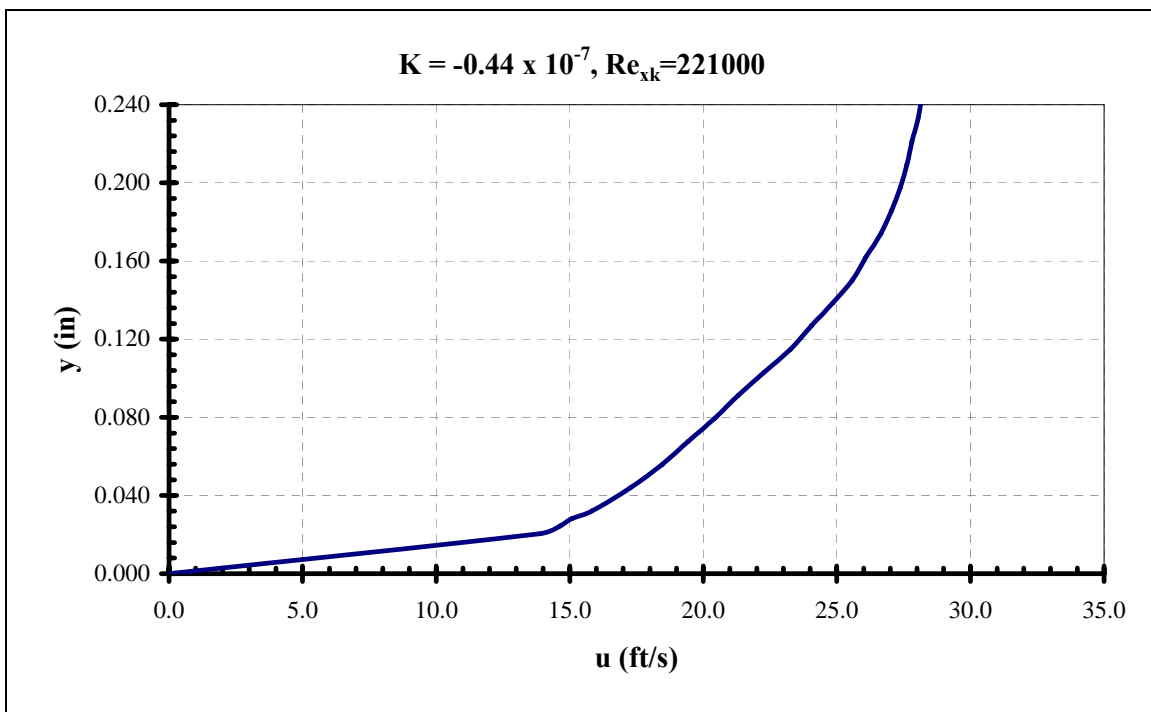


**Figure 42. Boundary layer velocity profile**

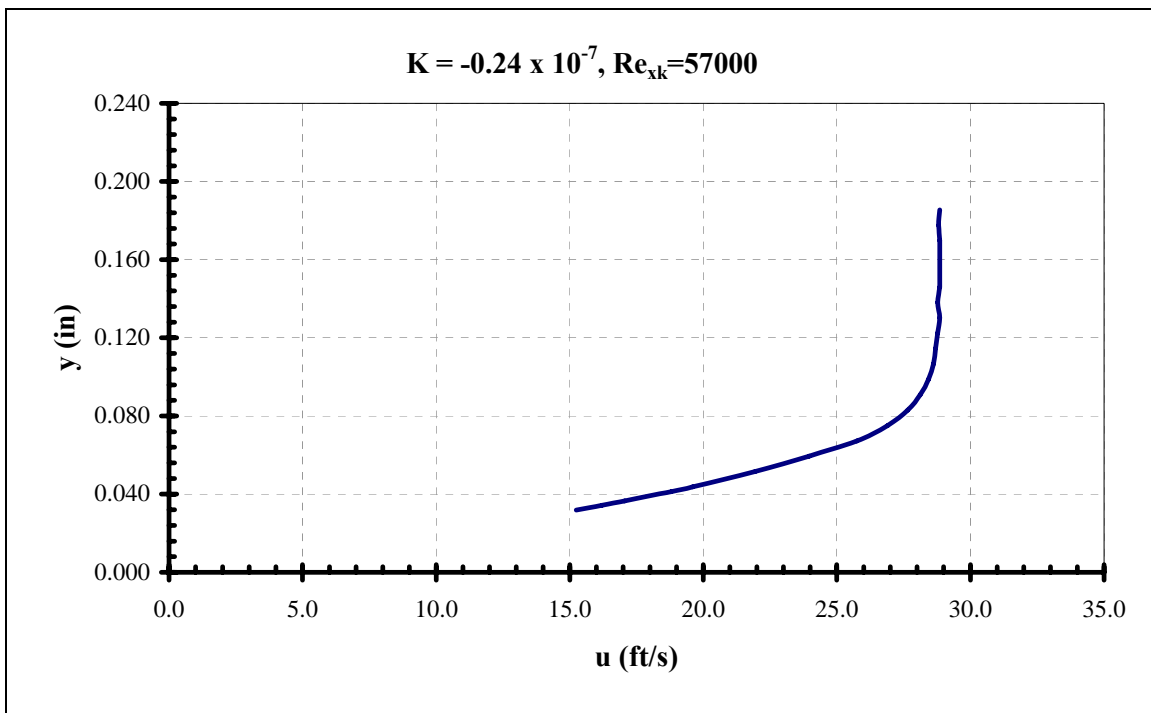


Figure 43. Boundary layer velocity profile

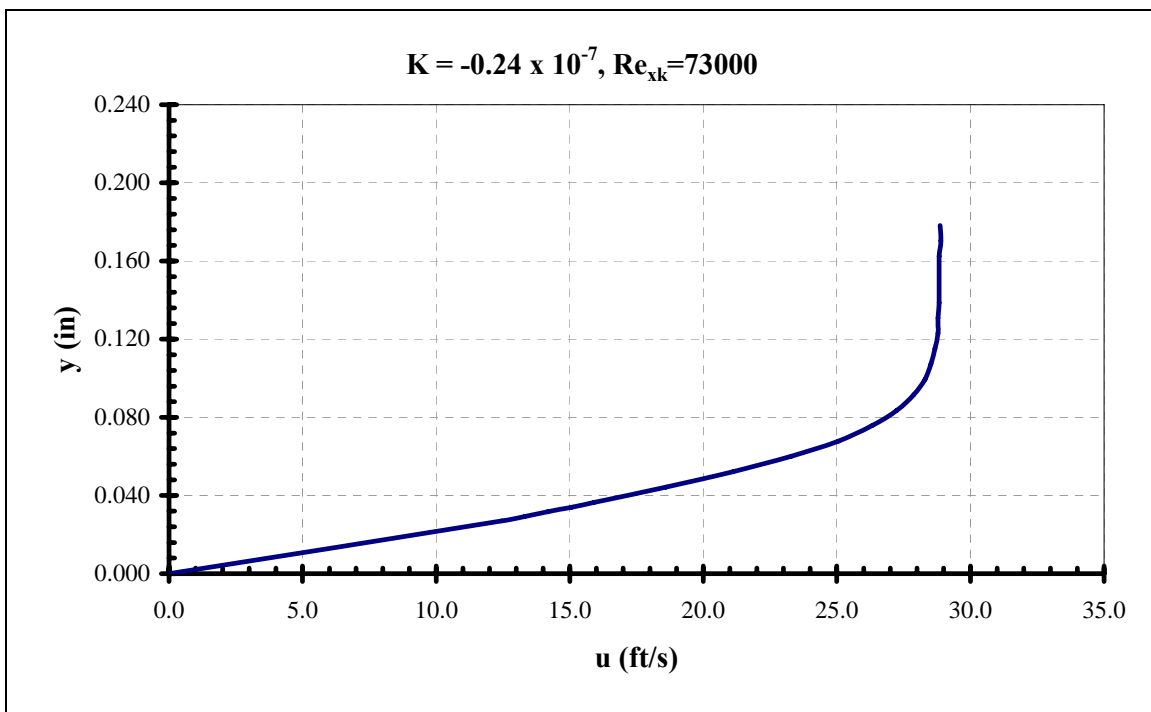


Figure 44. Boundary layer velocity profile

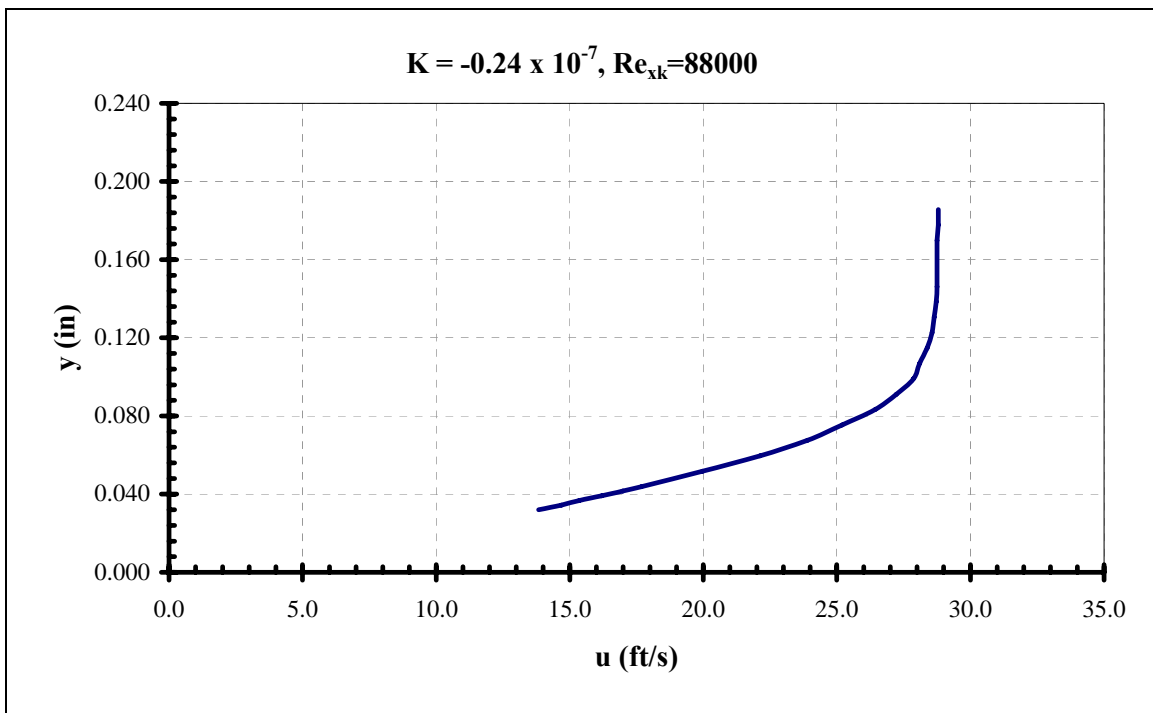


Figure 45. Boundary layer velocity profile

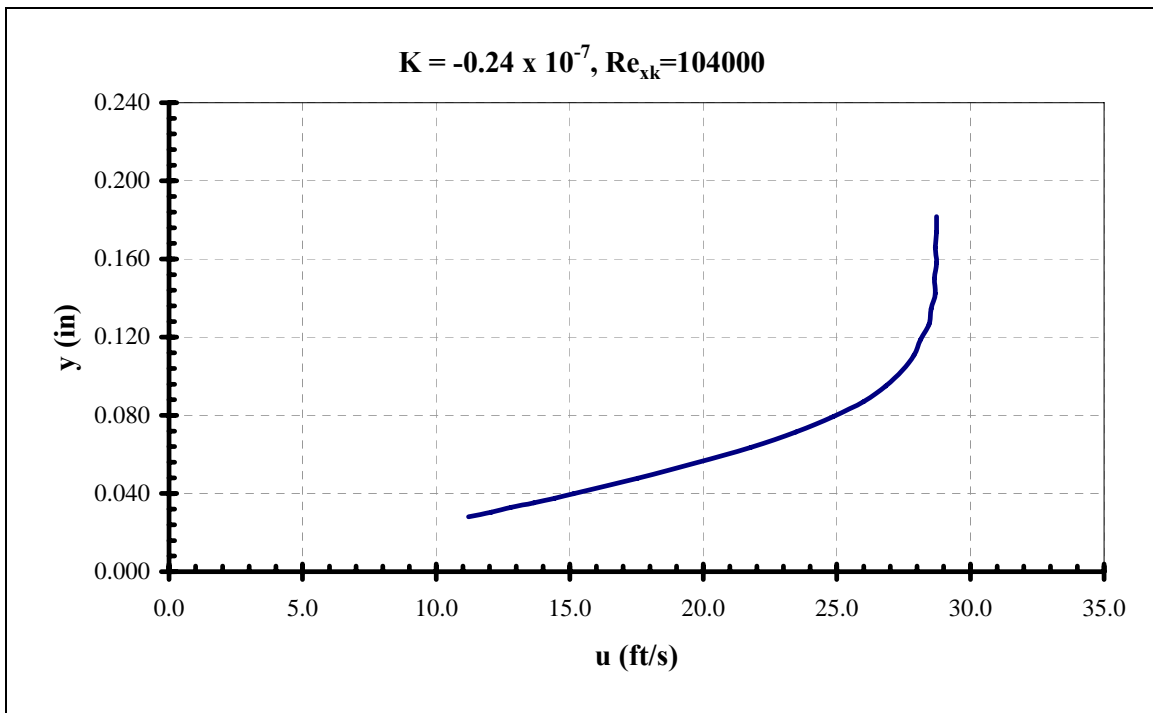
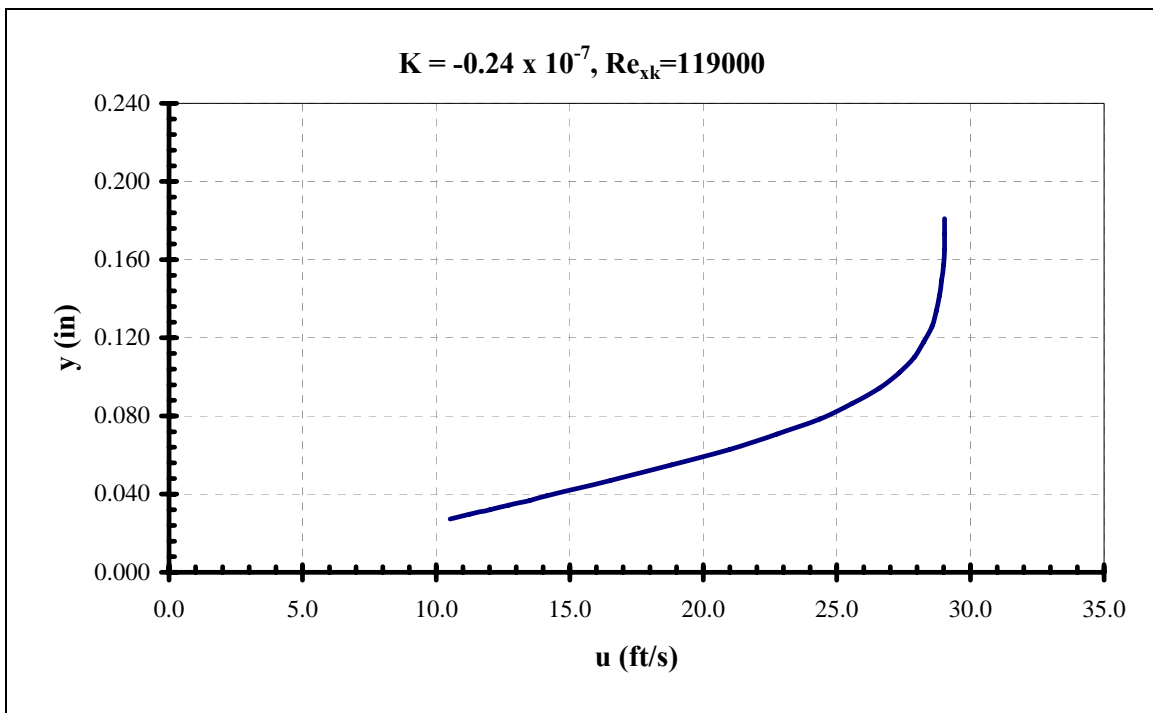
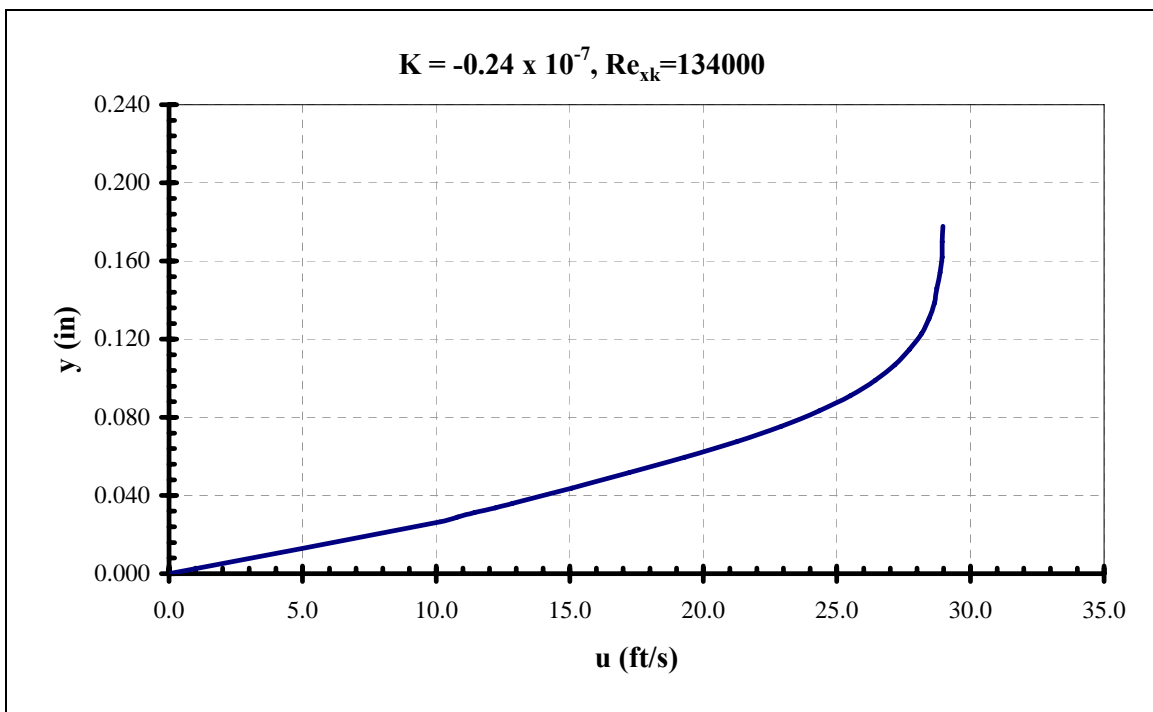


Figure 46. Boundary layer velocity profile



**Figure 47. Boundary layer velocity profile**



**Figure 48. Boundary layer velocity profile**

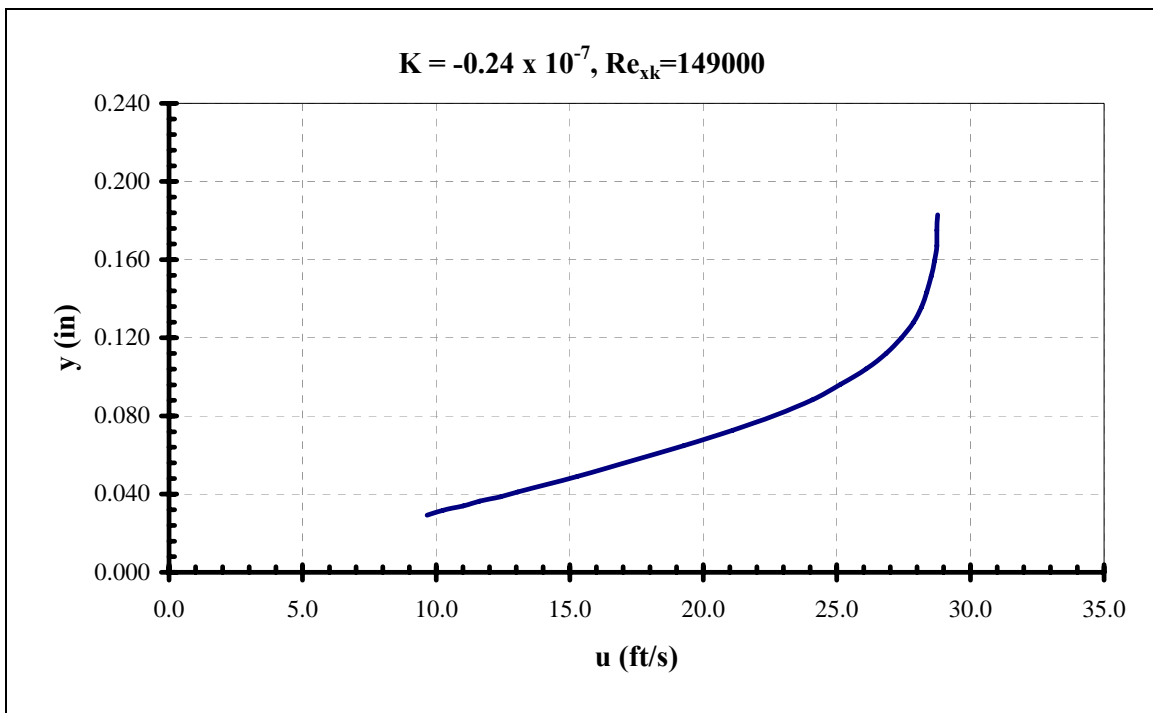


**Figure 49. Boundary layer velocity profile**

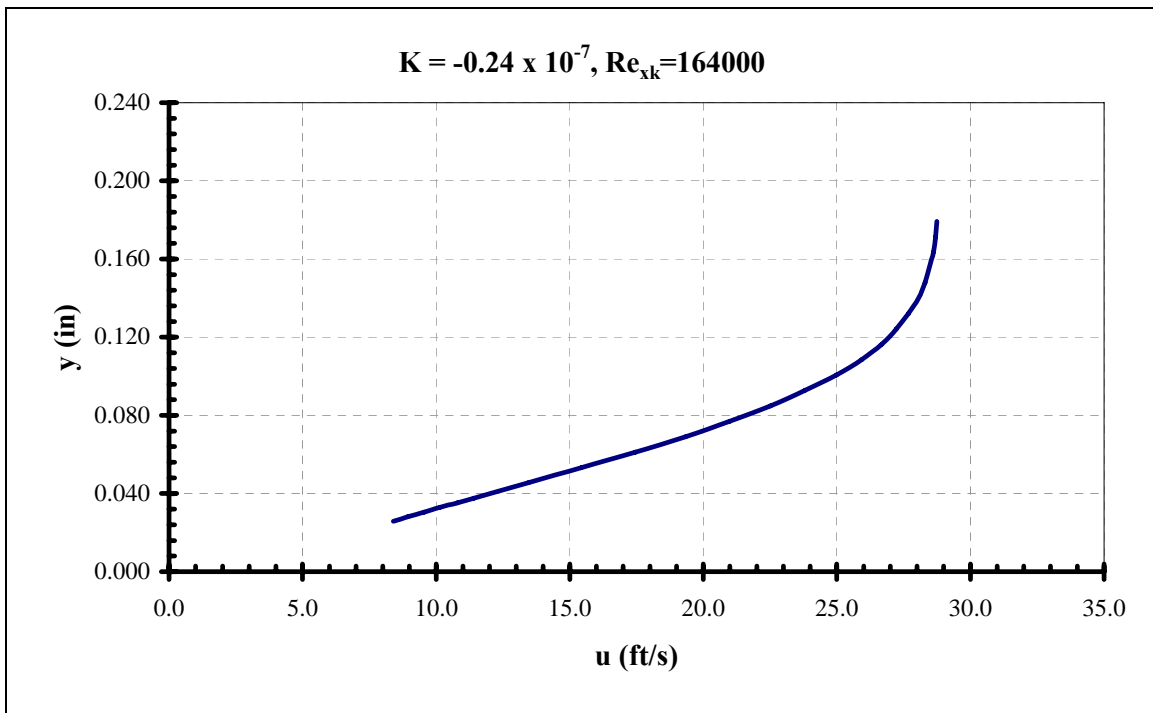


**Figure 50. Boundary layer velocity profile**

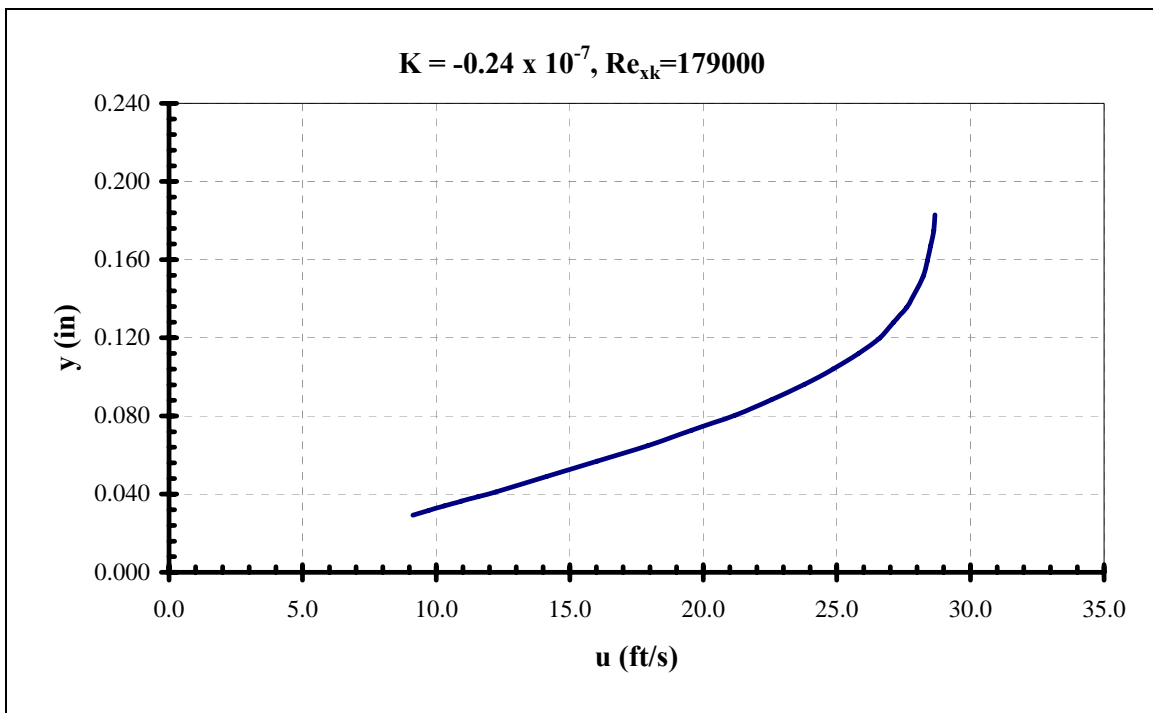


**Figure 51. Boundary layer velocity profile**

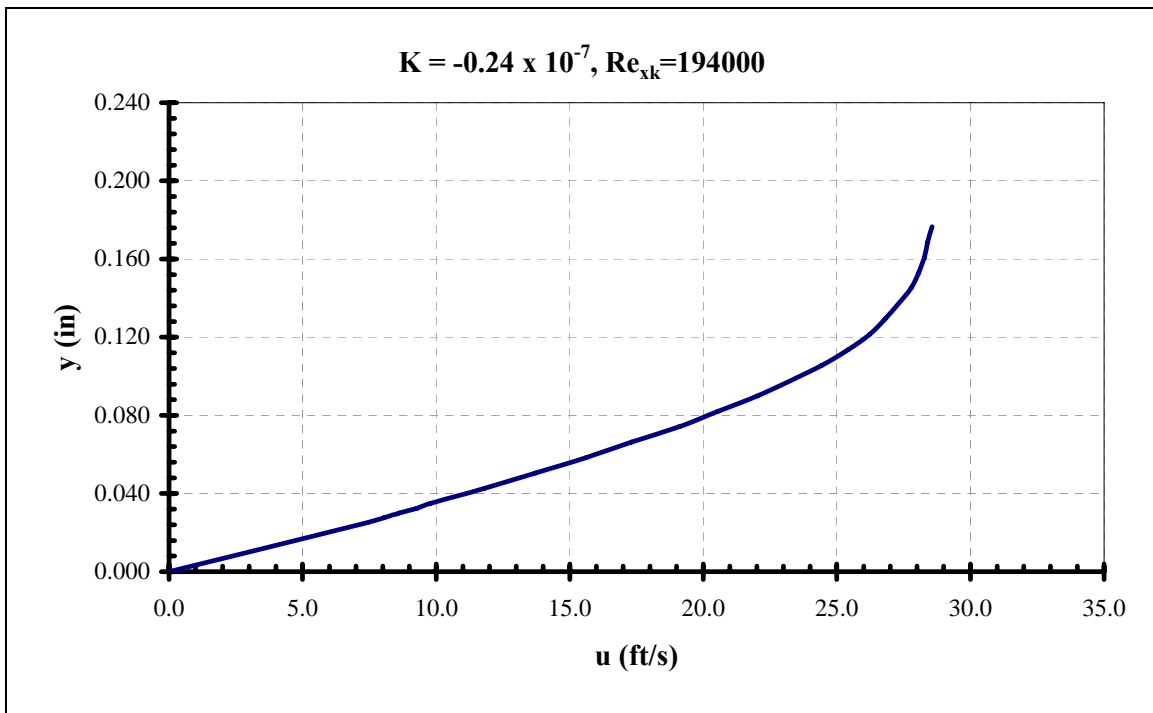


**Figure 52. Boundary layer velocity profile**

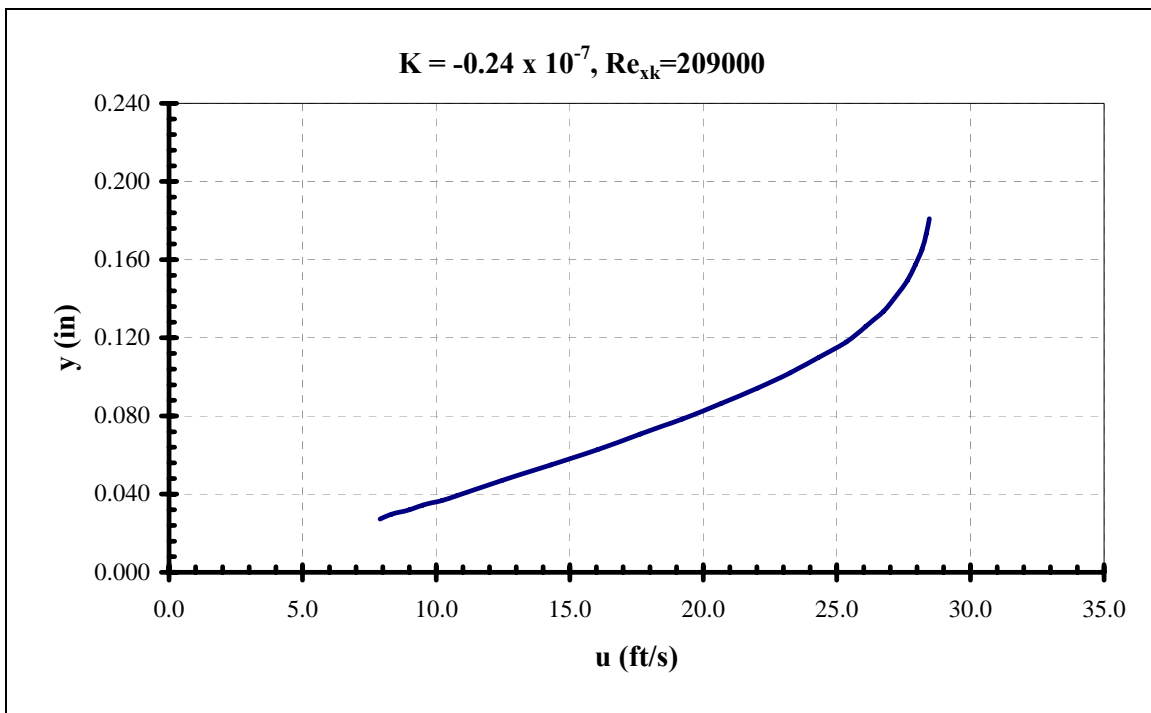


**Figure 53. Boundary layer velocity profile**

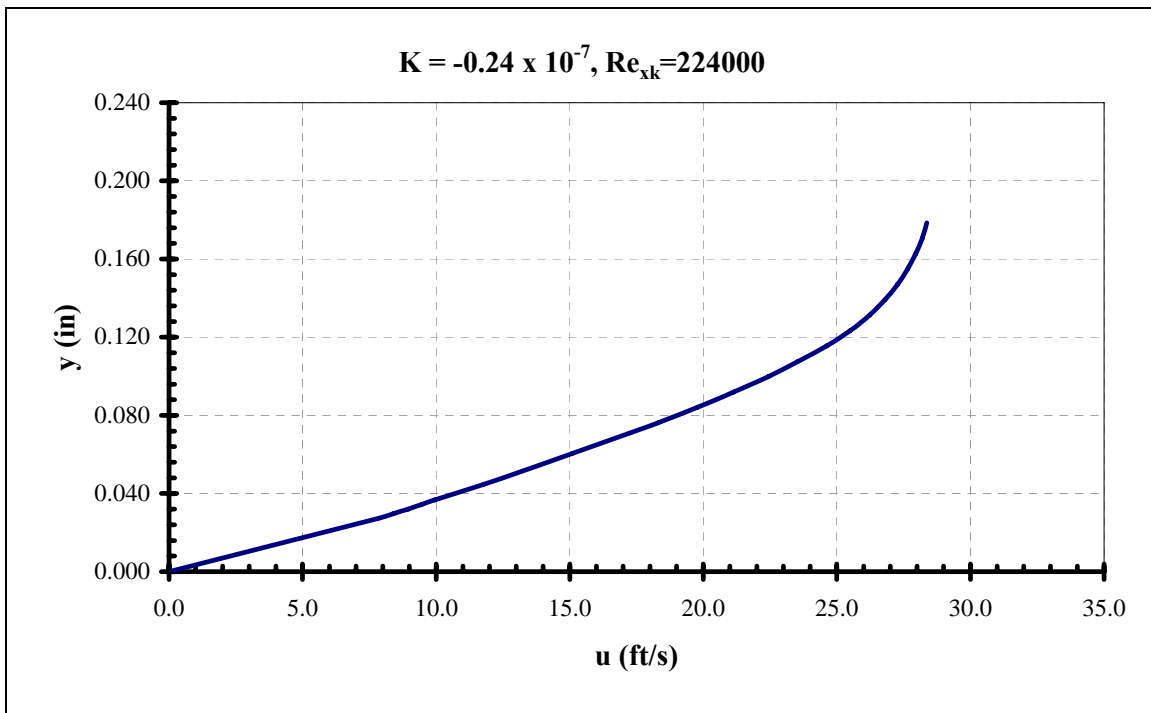


**Figure 54. Boundary layer velocity profile**



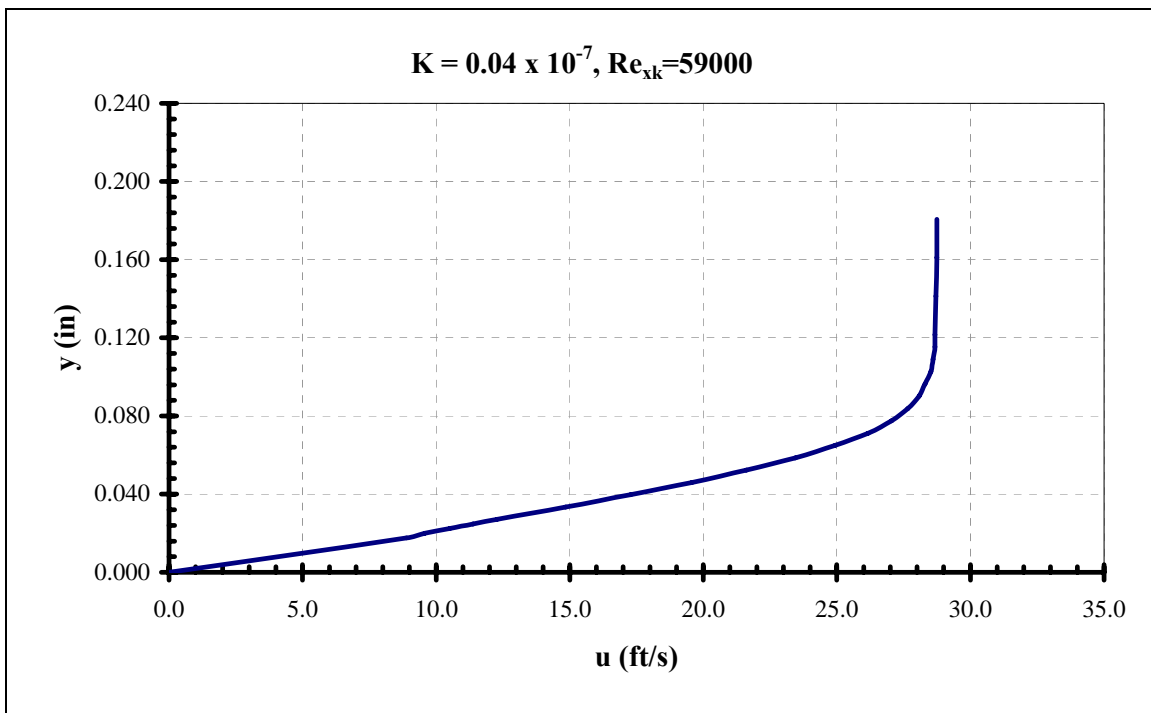


**Figure 55. Boundary layer velocity profile**

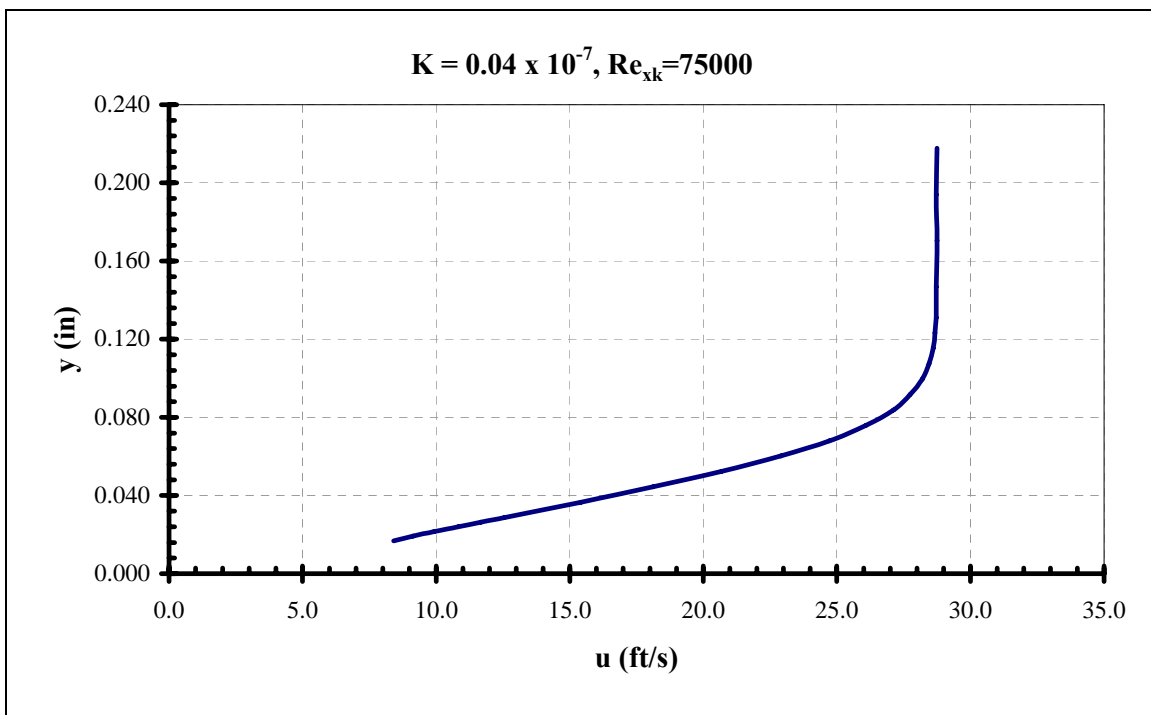


**Figure 56. Boundary layer velocity profile**

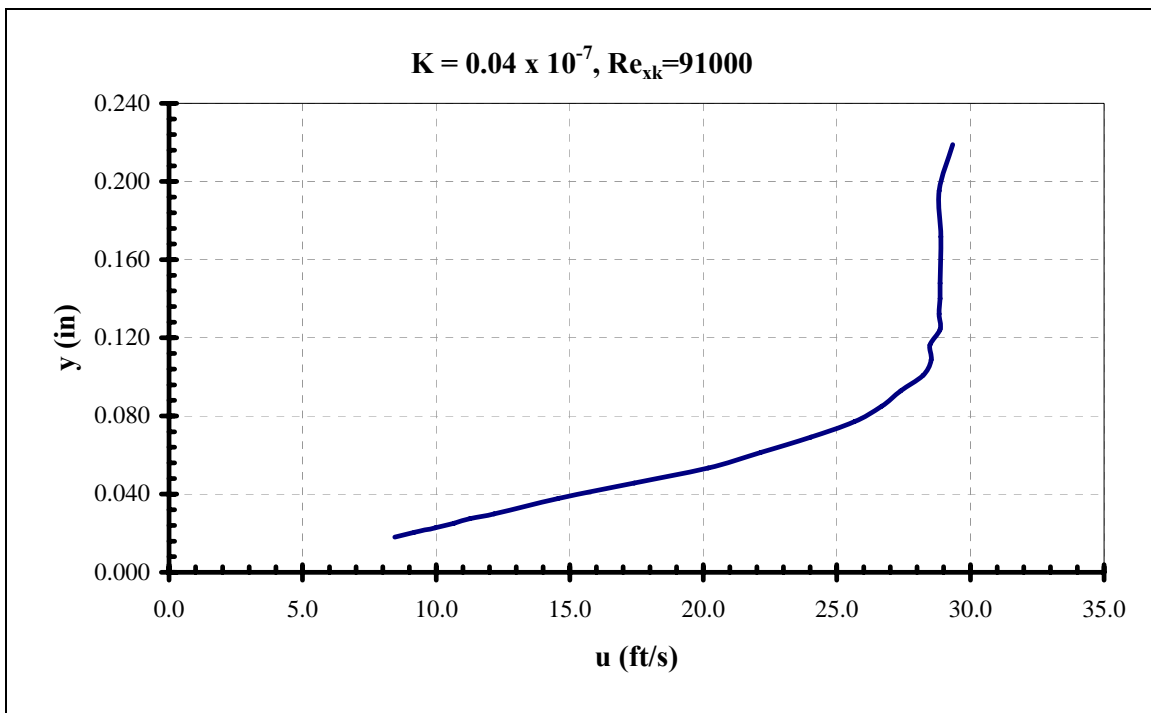


**Figure 57. Boundary layer velocity profile**

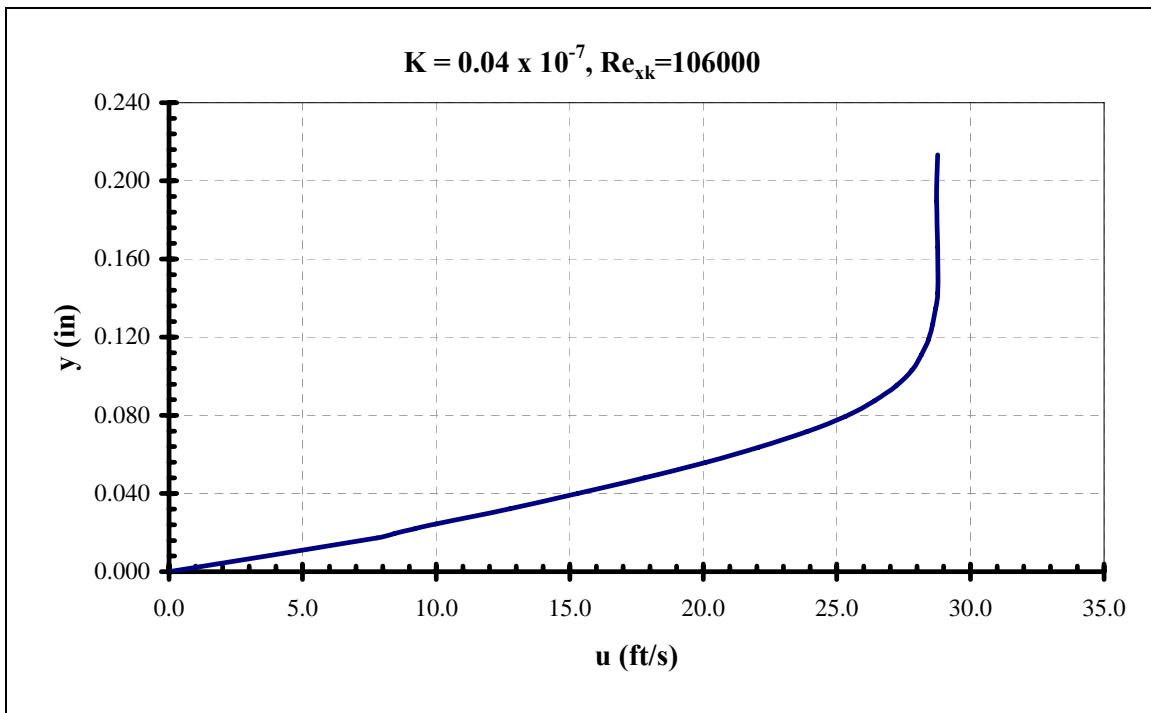


**Figure 58. Boundary layer velocity profile**

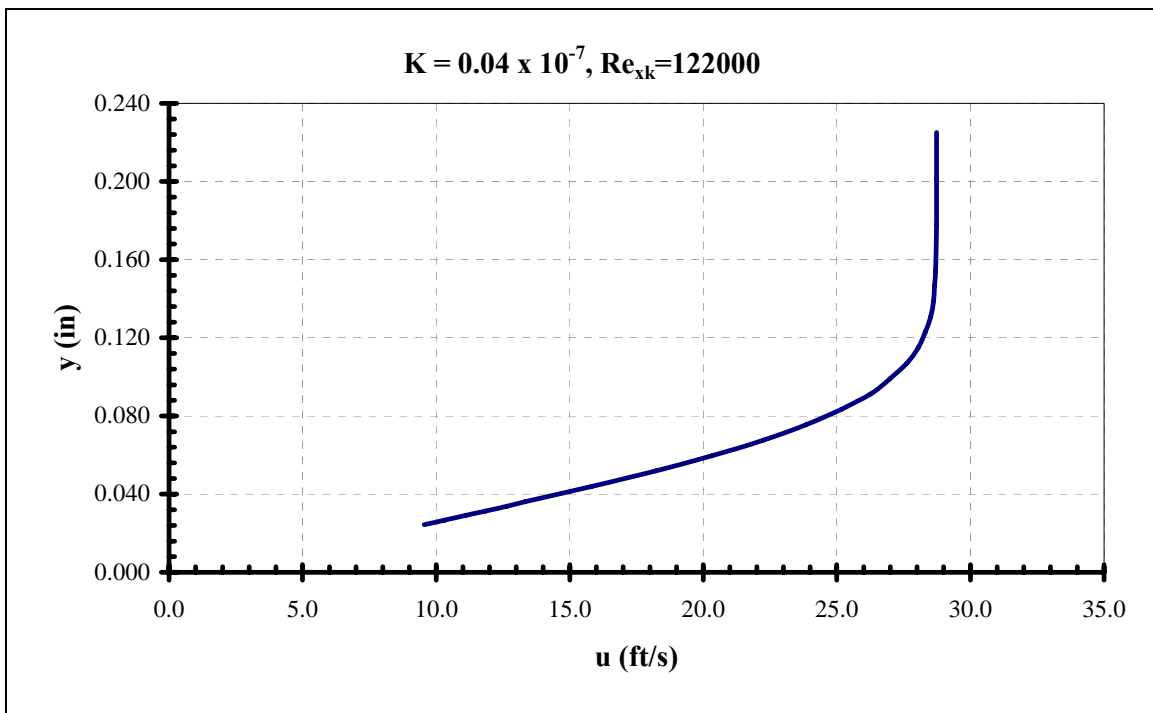


**Figure 59. Boundary layer velocity profile**

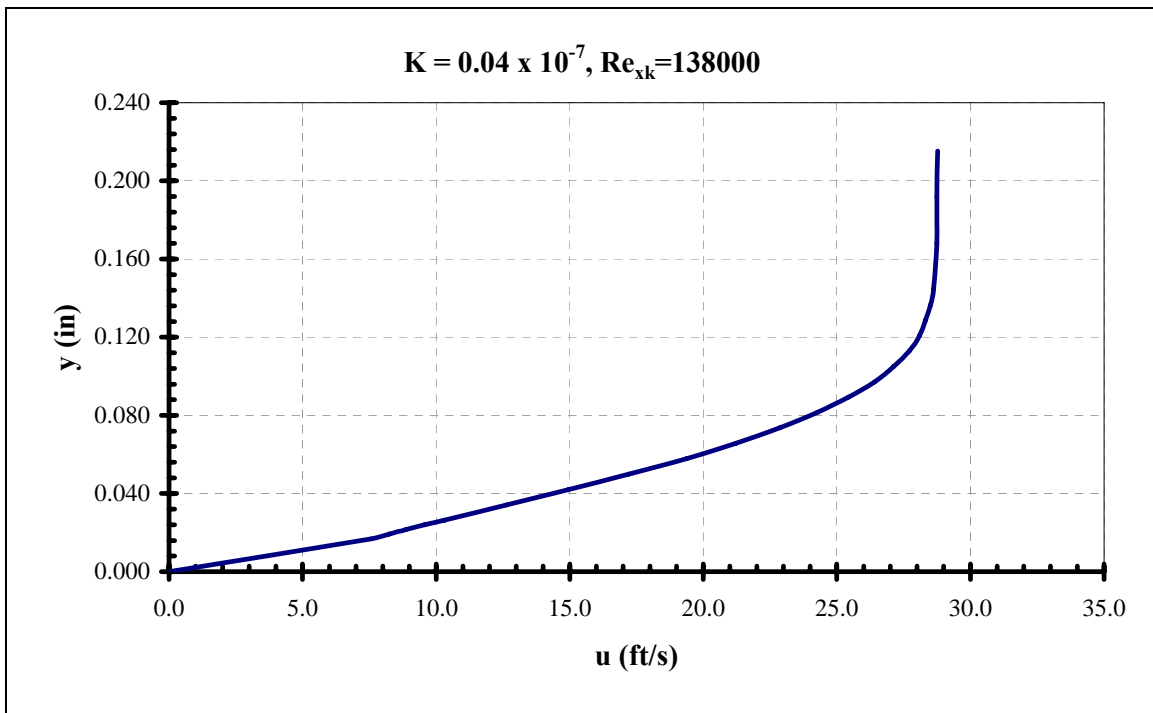


**Figure 60. Boundary layer velocity profile**

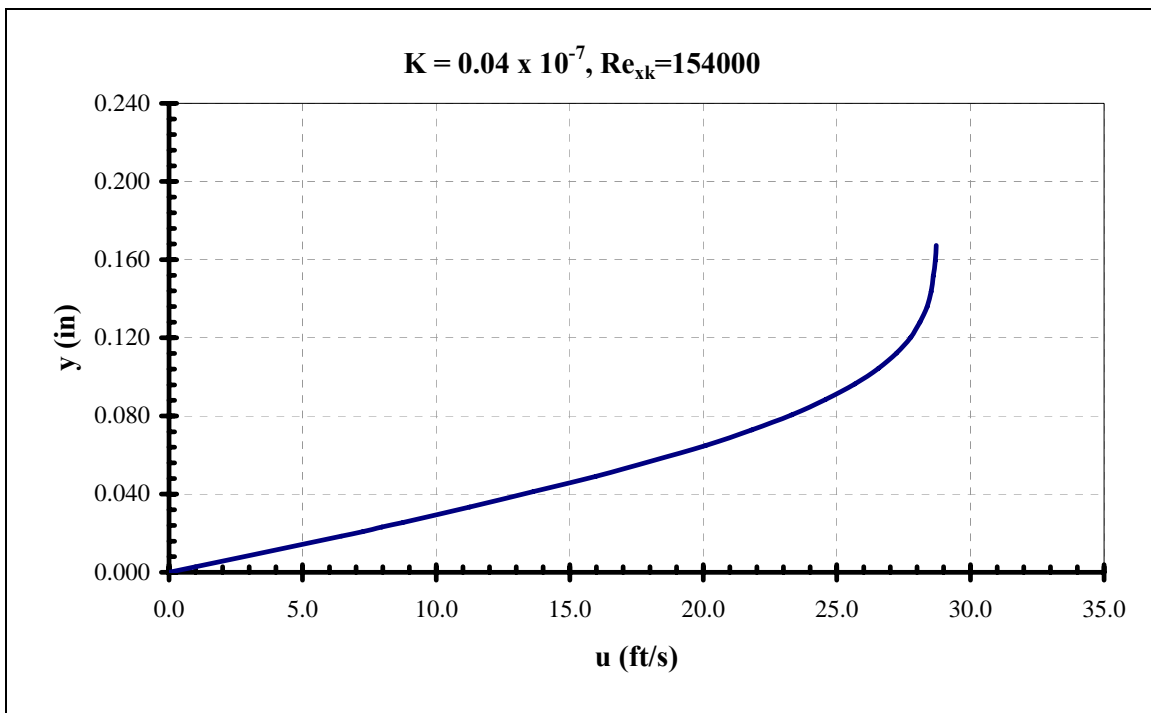


**Figure 61. Boundary layer velocity profile**

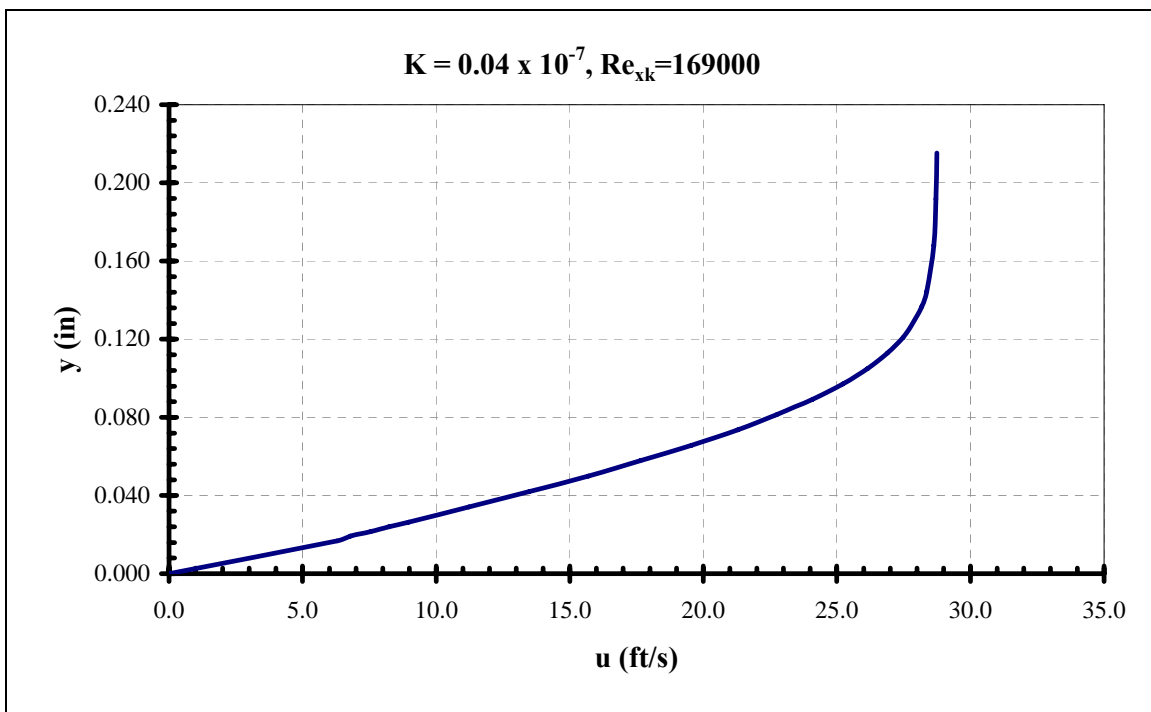


**Figure 62. Boundary layer velocity profile**

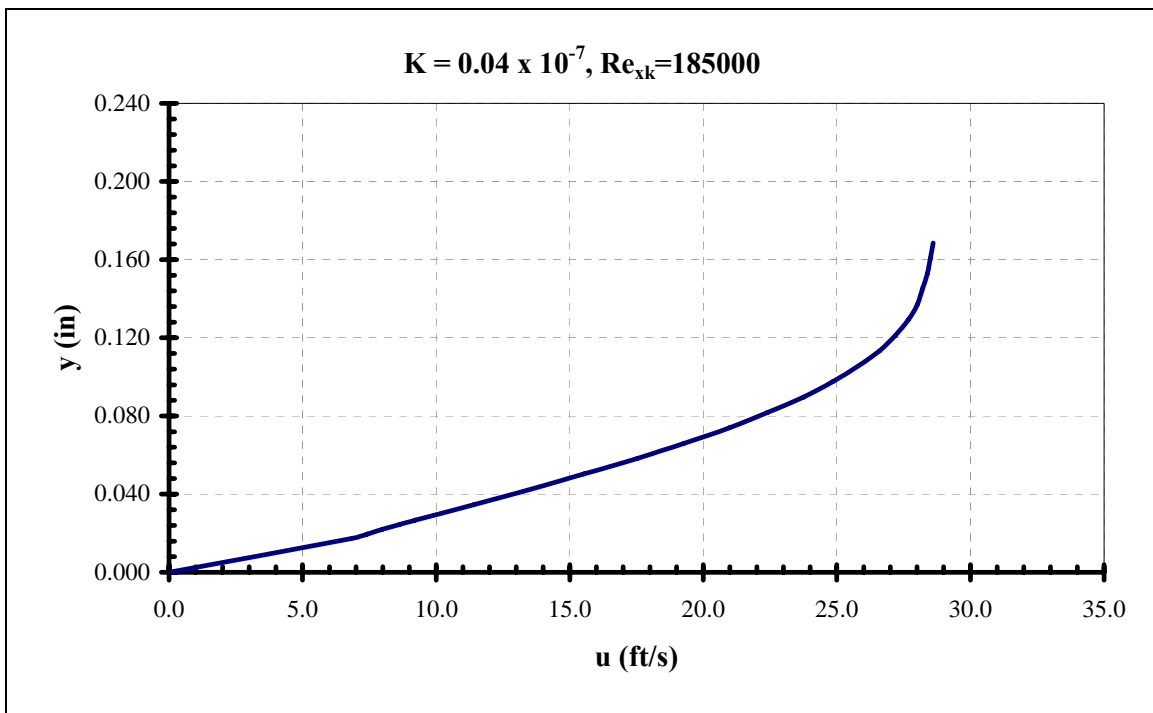


**Figure 63. Boundary layer velocity profile**

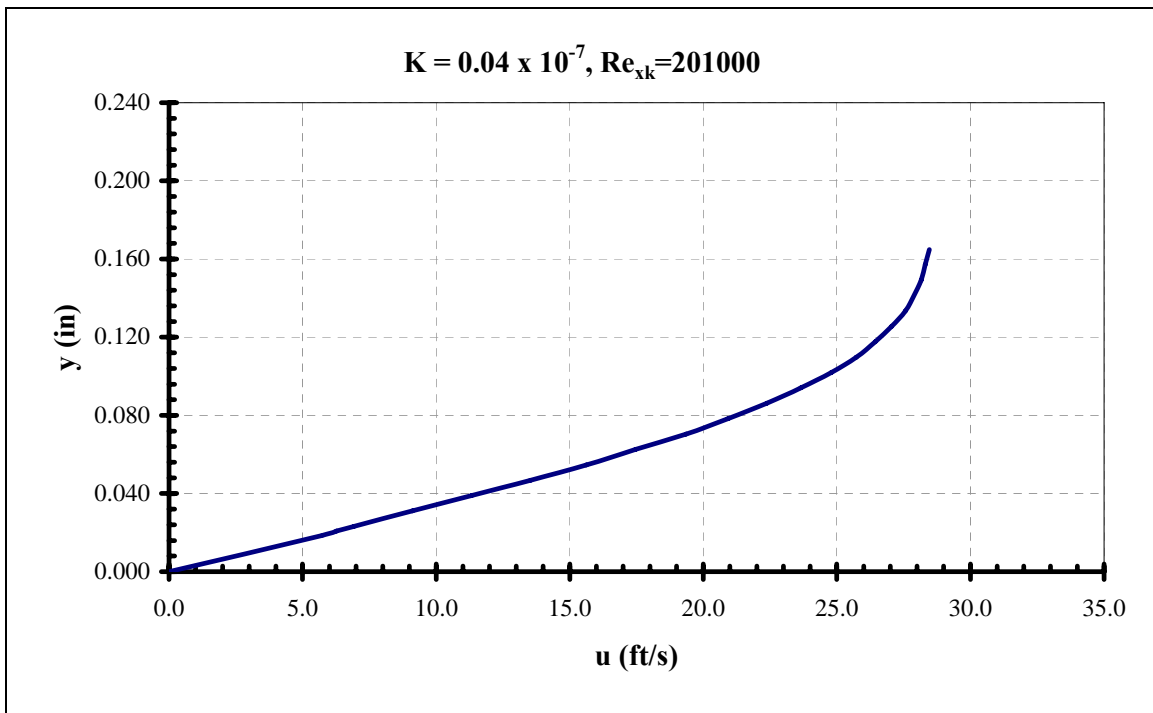


**Figure 64. Boundary layer velocity profile**

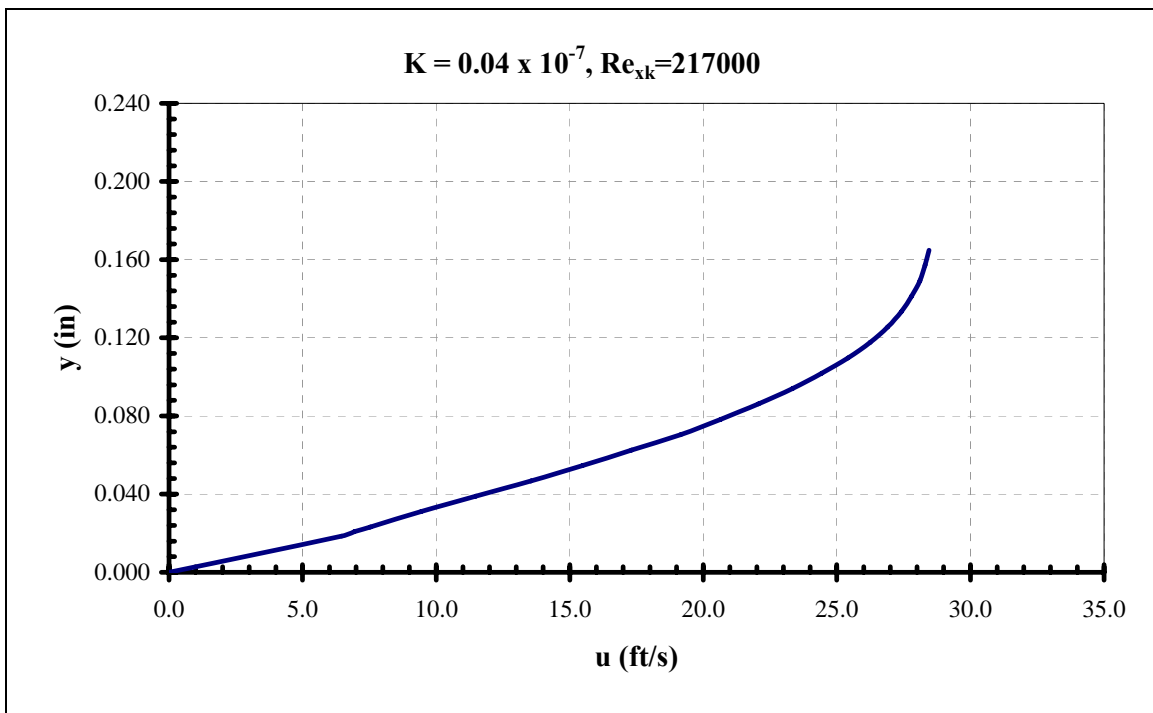


**Figure 65. Boundary layer velocity profile**

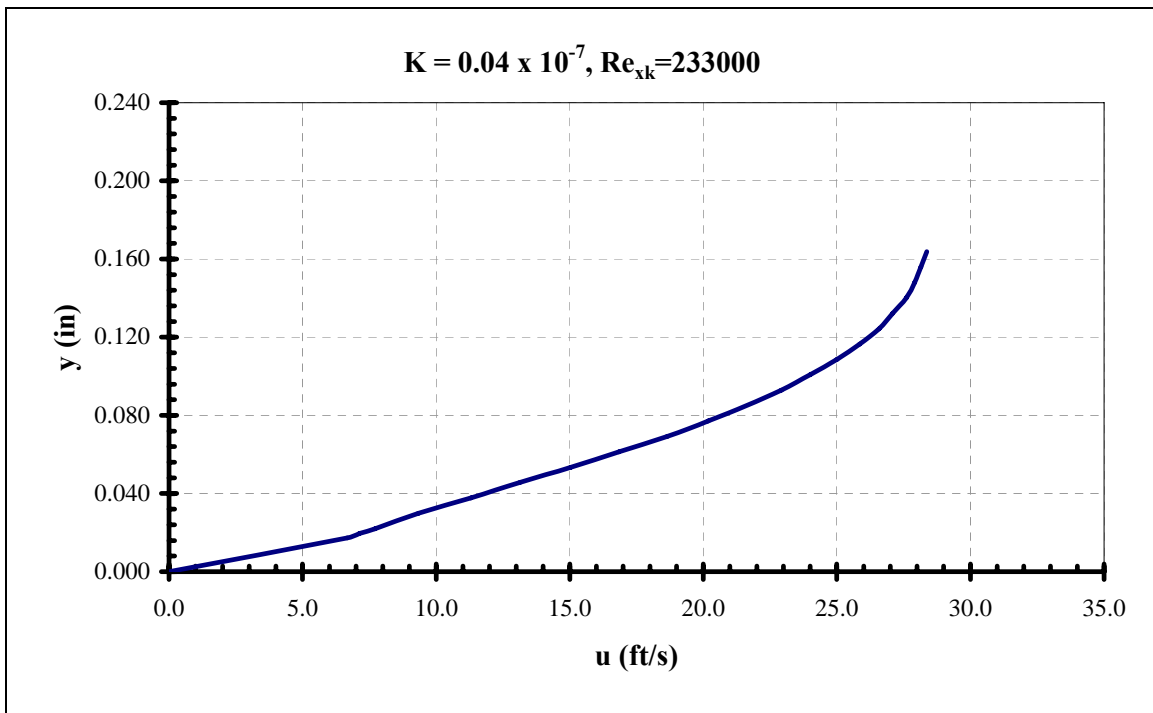


**Figure 66. Boundary layer velocity profile**

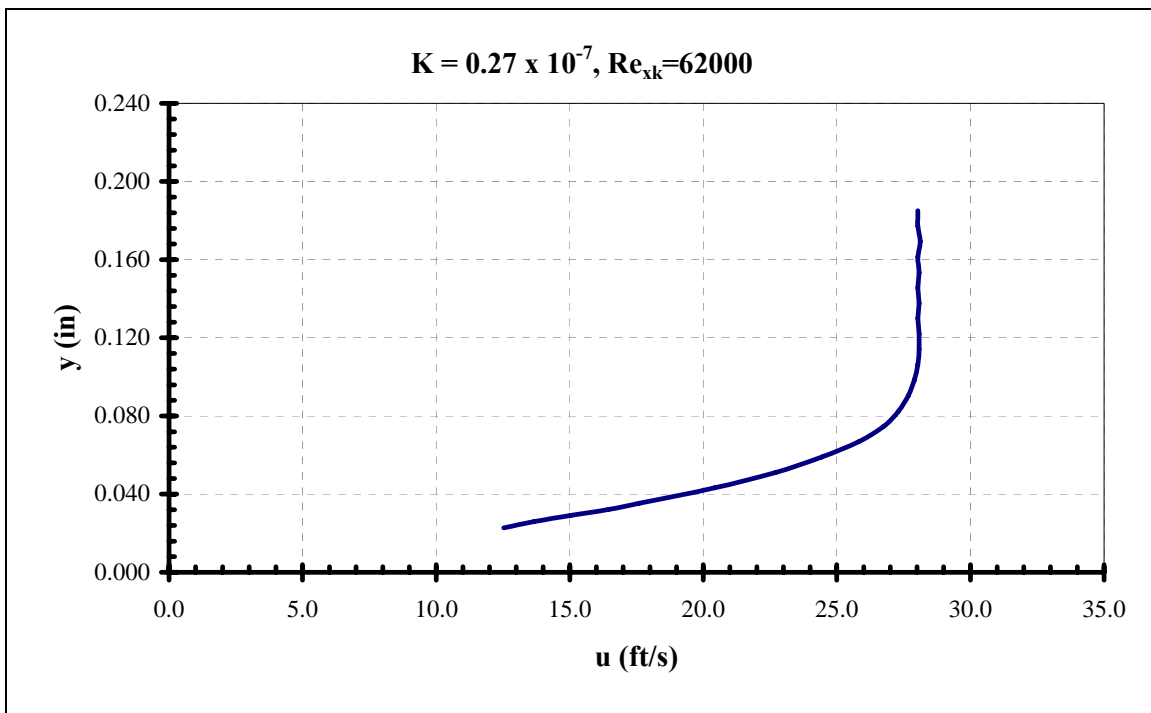


**Figure 67. Boundary layer velocity profile**

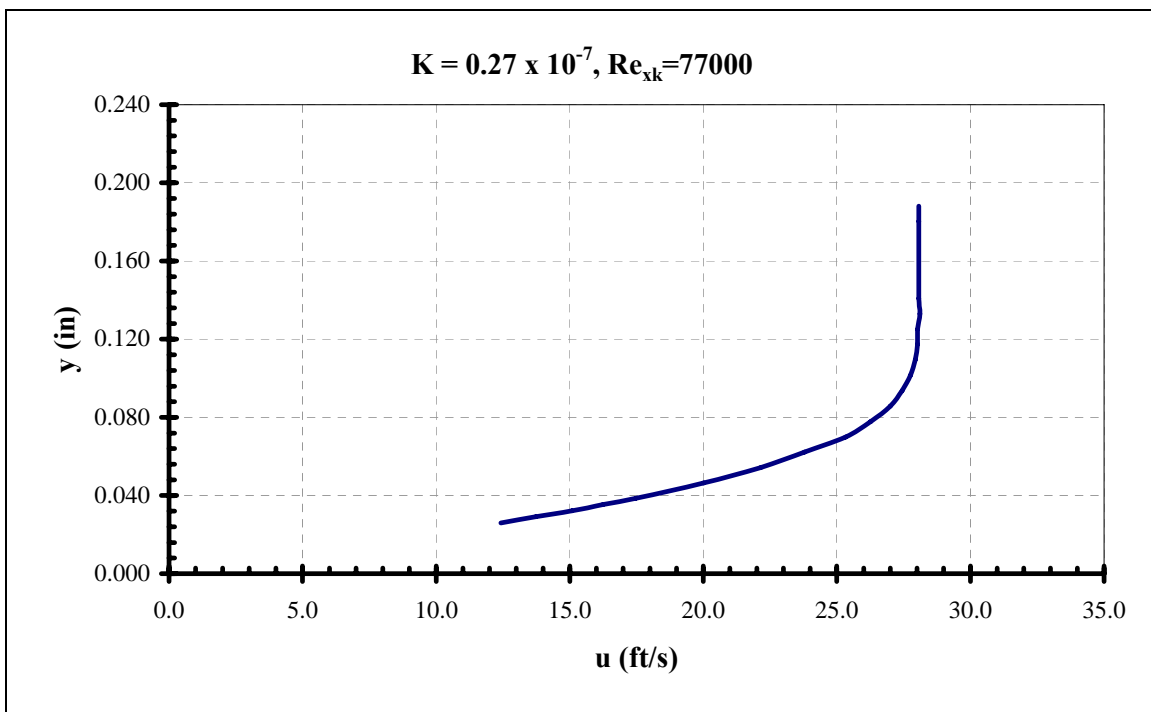


**Figure 68. Boundary layer velocity profile**

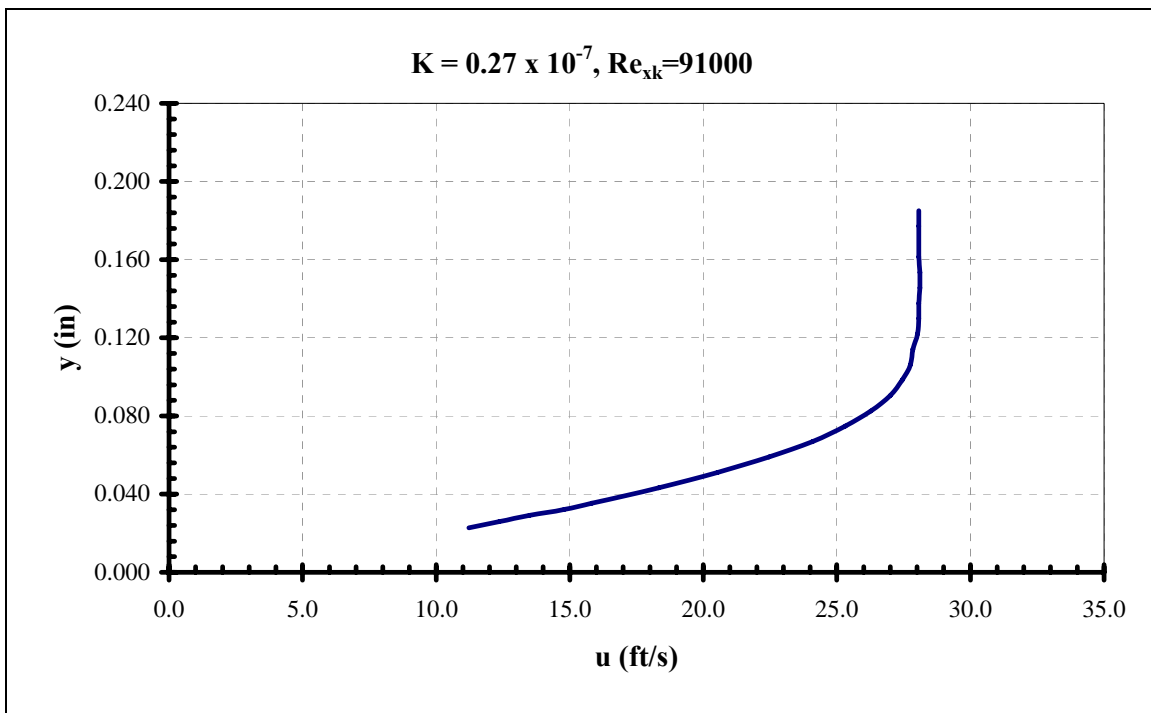


**Figure 69. Boundary layer velocity profile**

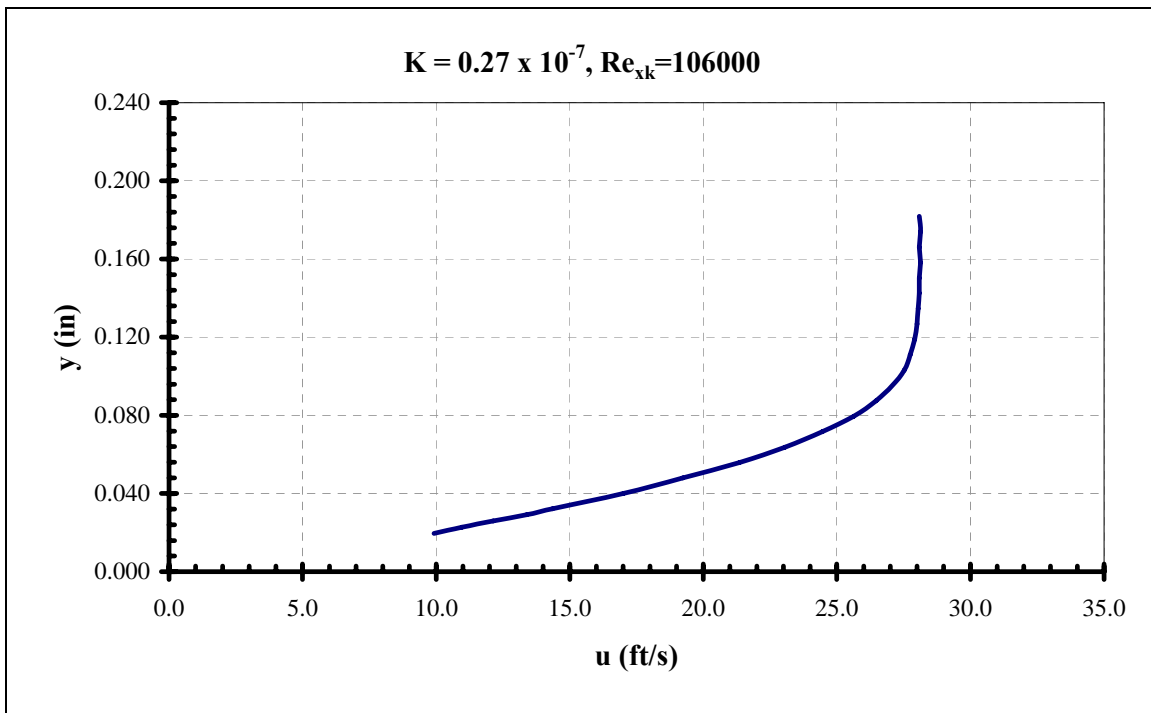


**Figure 70. Boundary layer velocity profile**



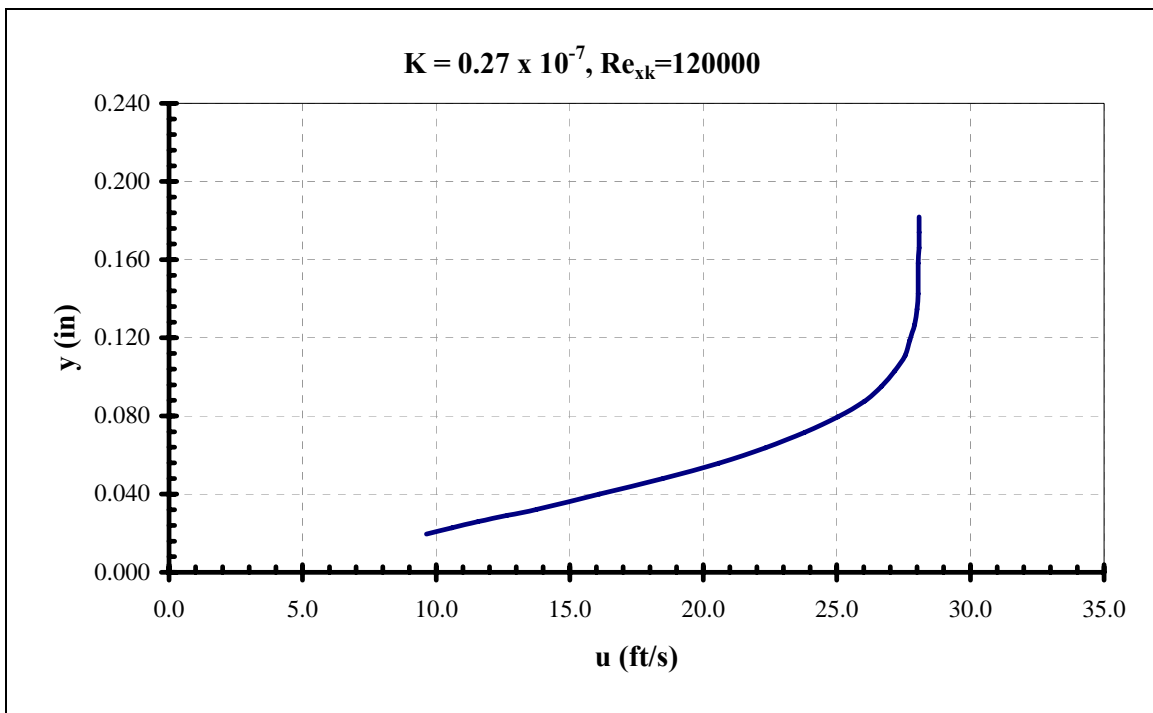


Figure 71. Boundary layer velocity profile

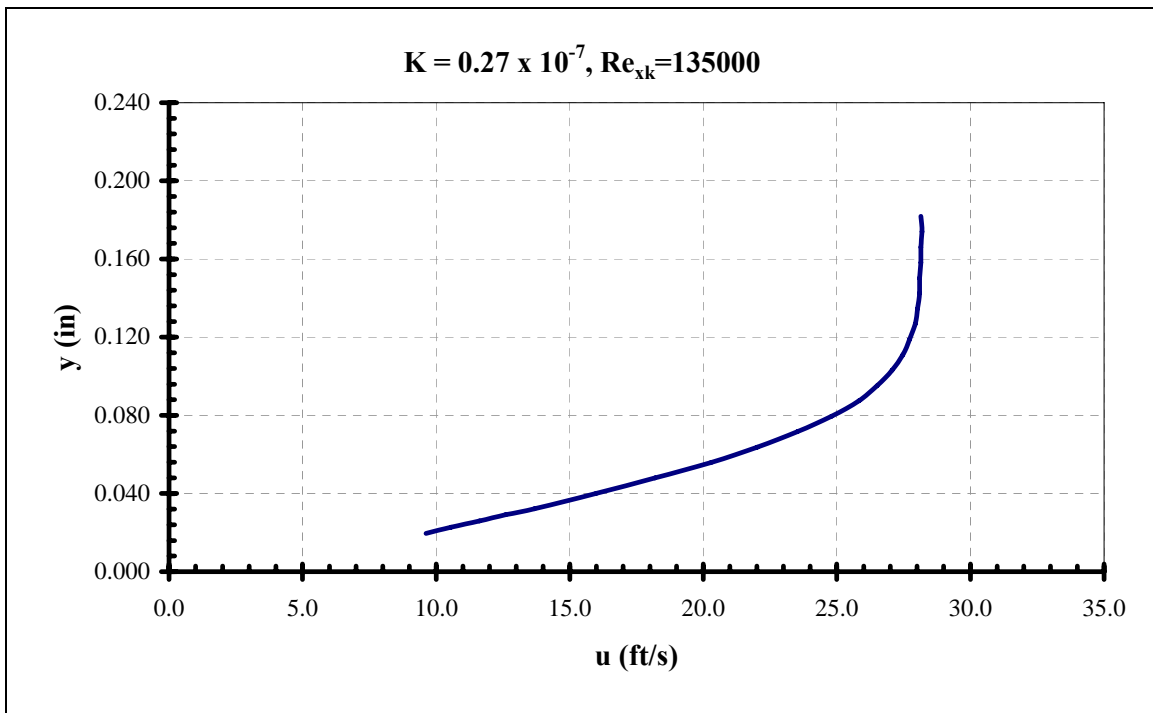
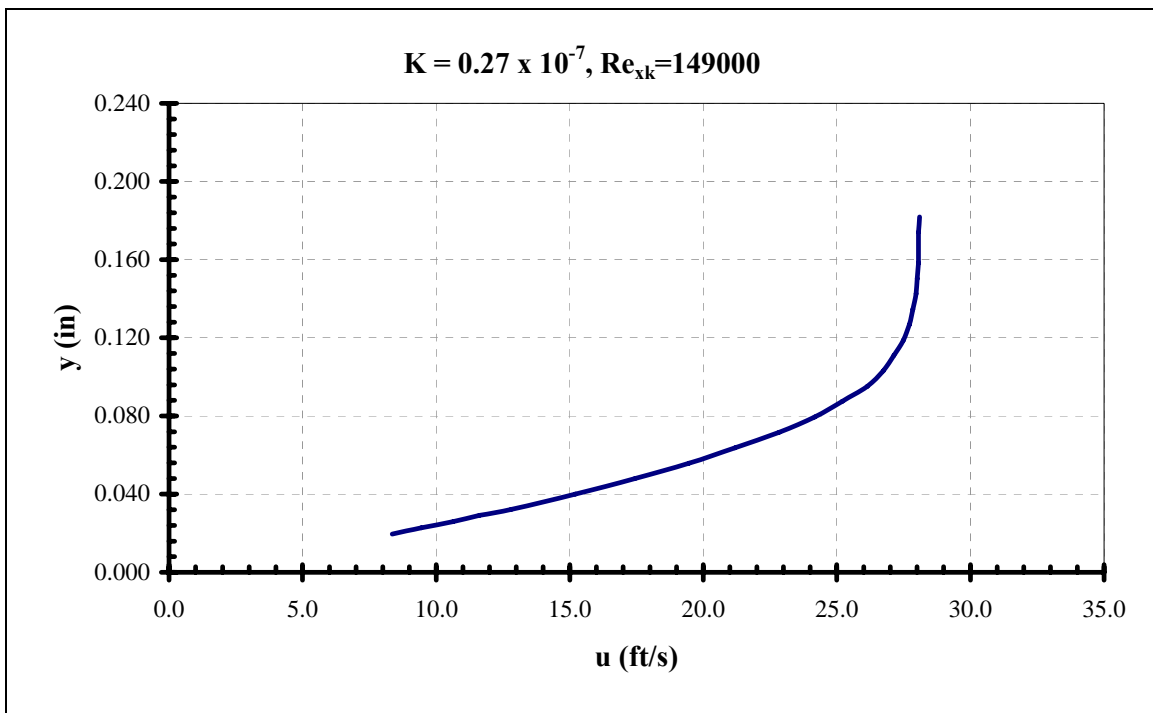
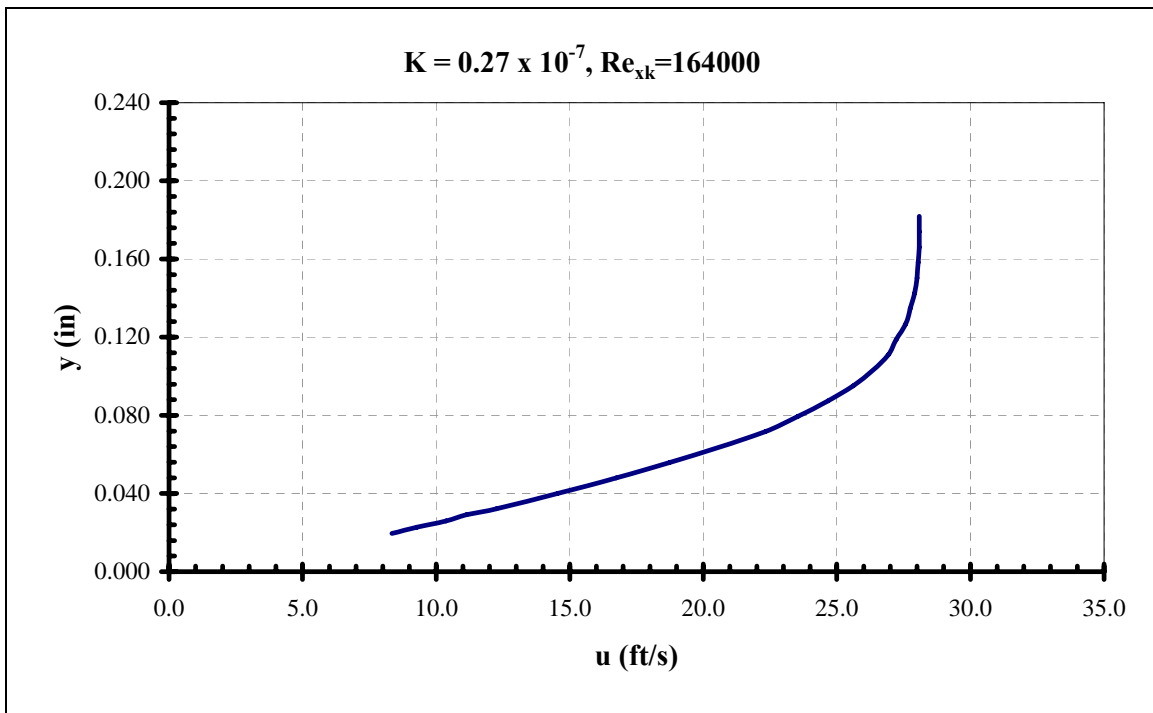


Figure 72. Boundary layer velocity profile



**Figure 73. Boundary layer velocity profile**



**Figure 74. Boundary layer velocity profile**

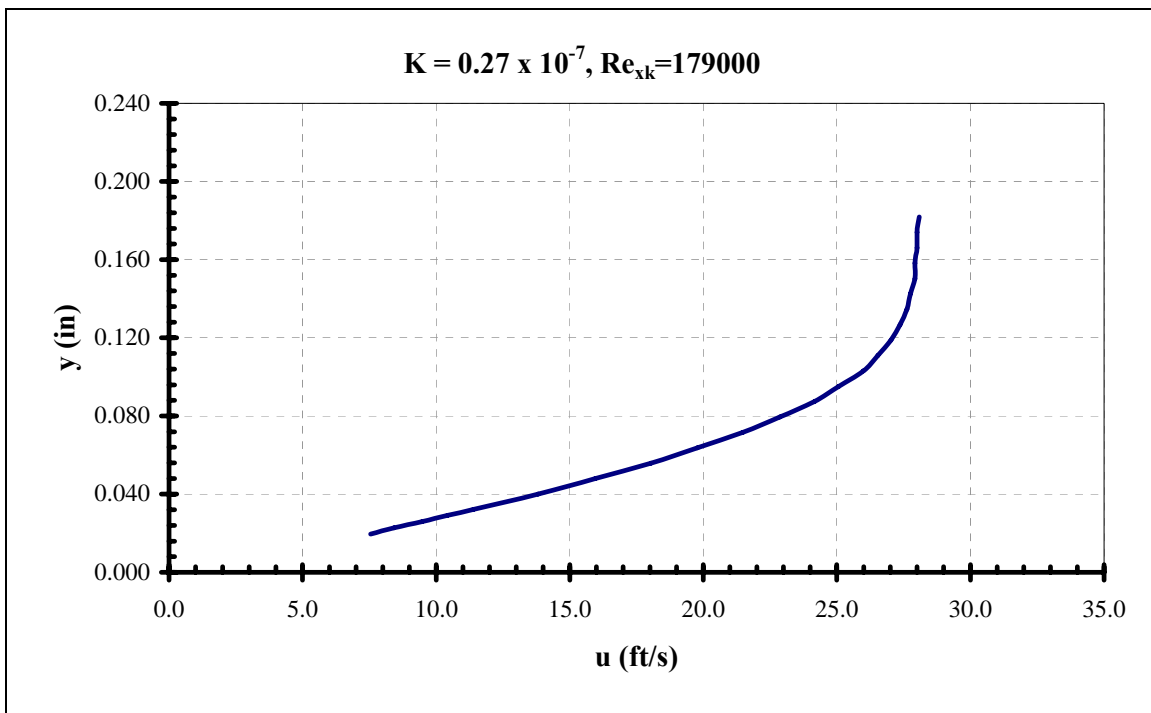


**Figure 75. Boundary layer velocity profile**

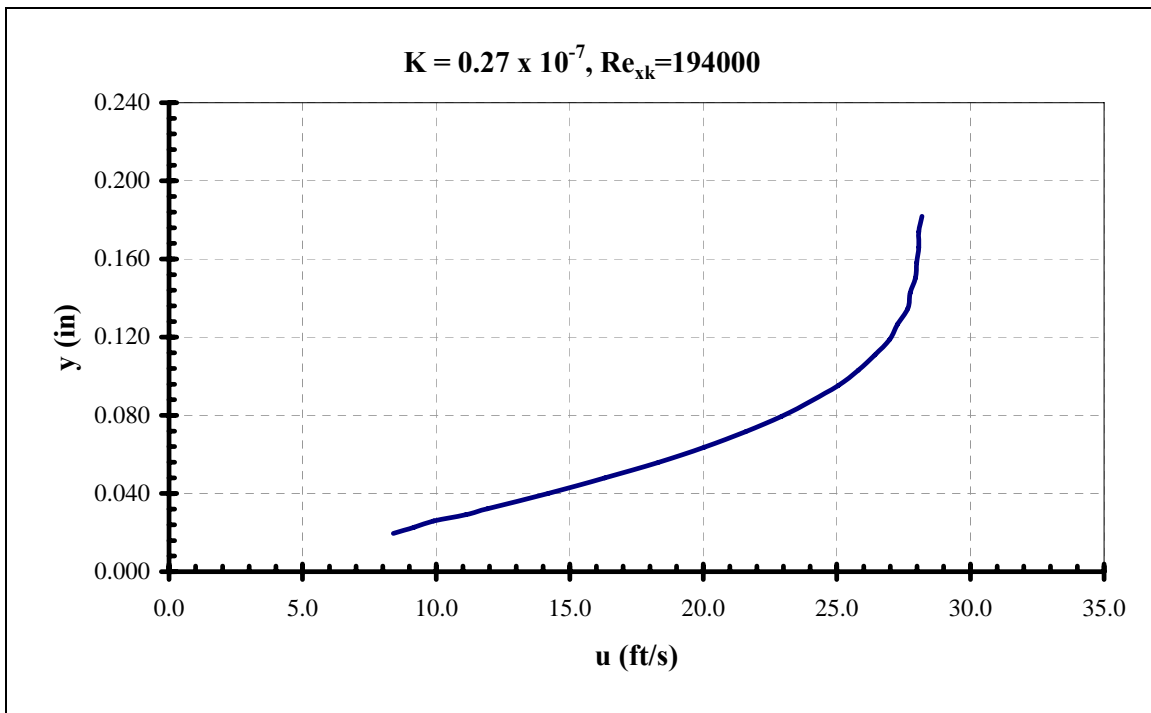


**Figure 76. Boundary layer velocity profile**

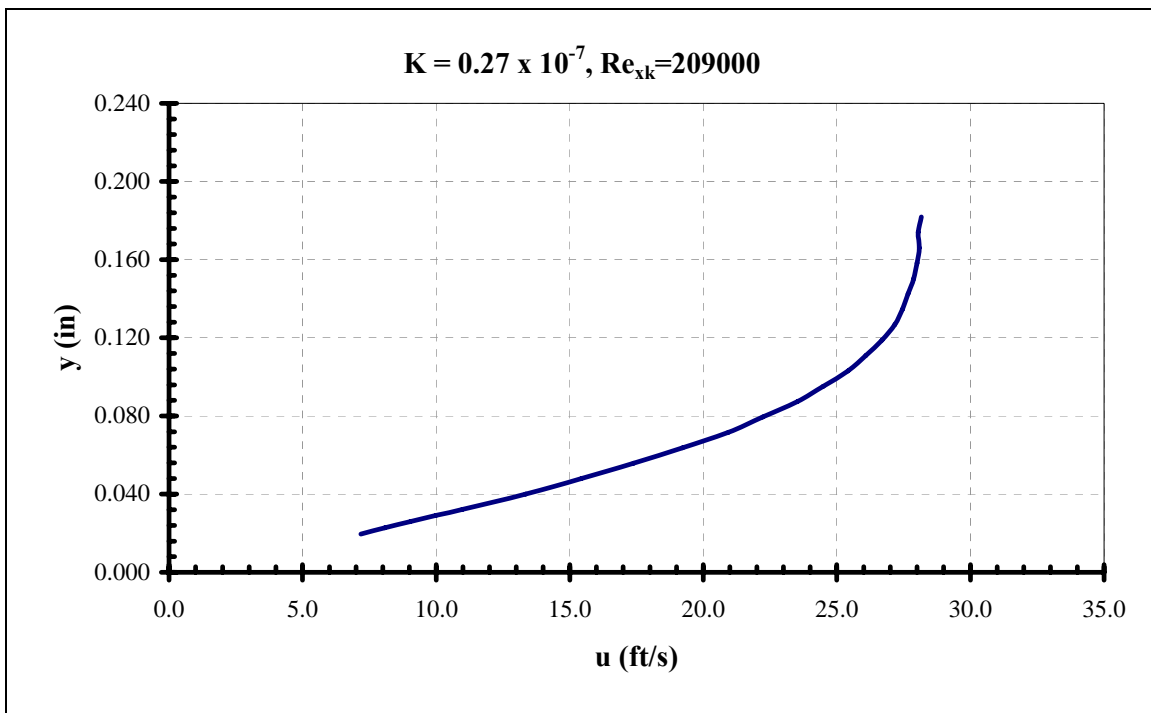


**Figure 77. Boundary layer velocity profile**

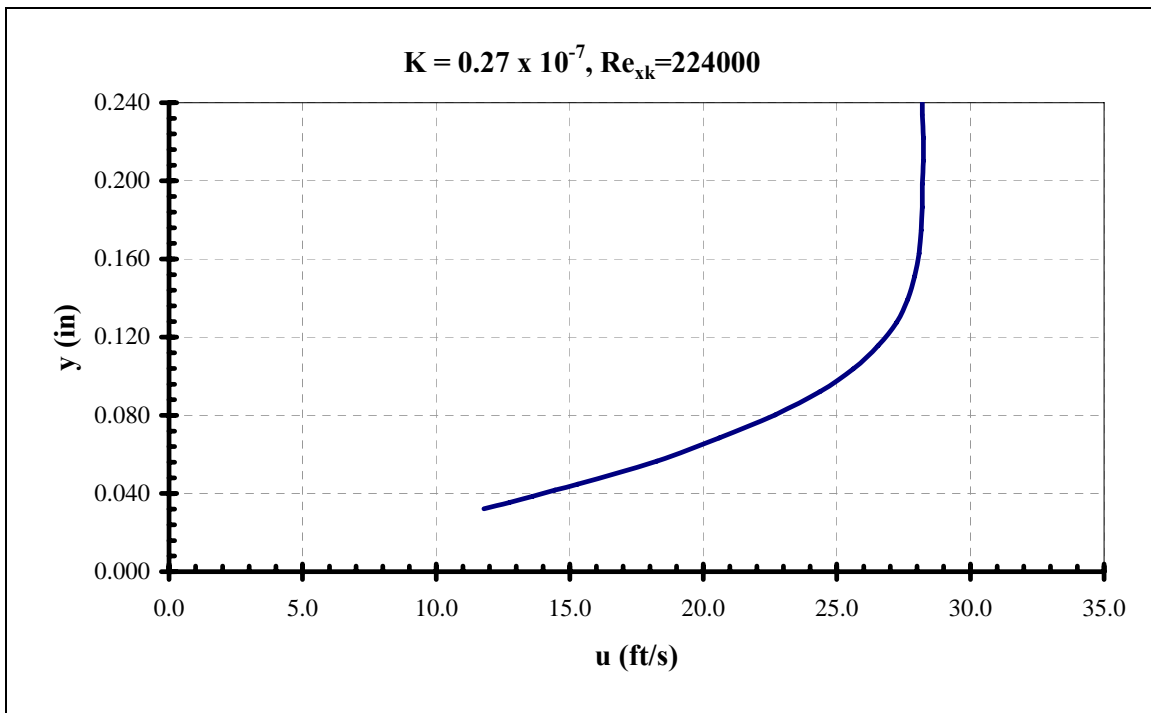


**Figure 78. Boundary layer velocity profile**

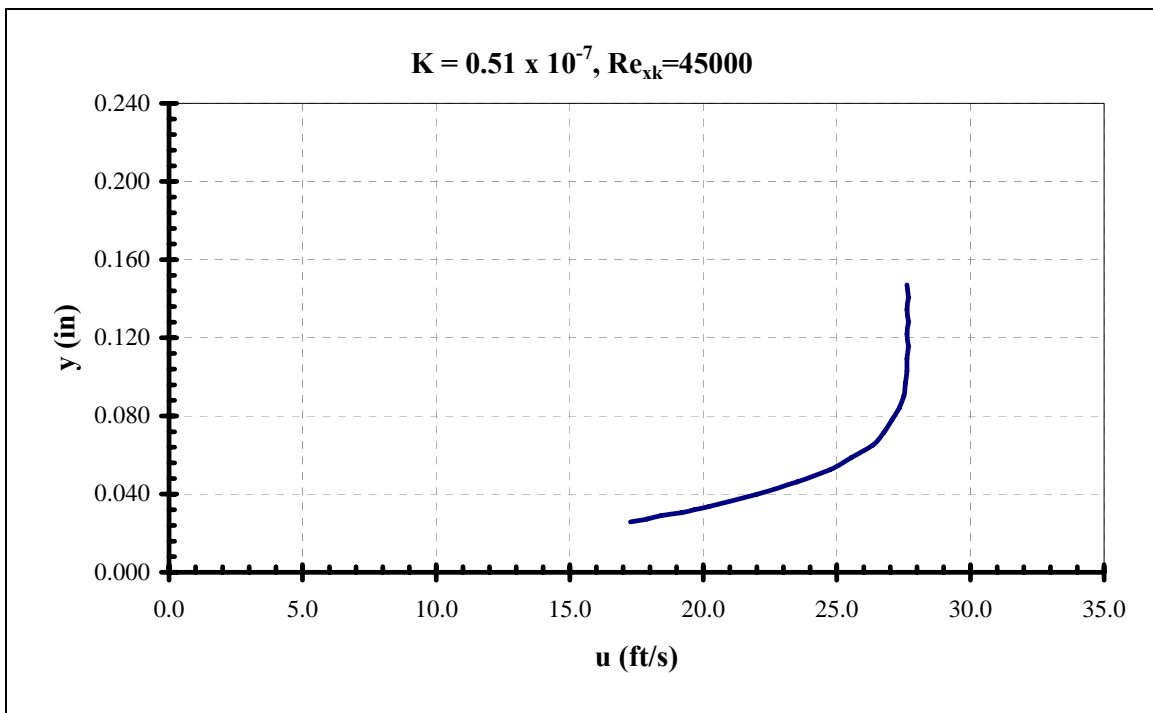


**Figure 79. Boundary layer velocity profile**

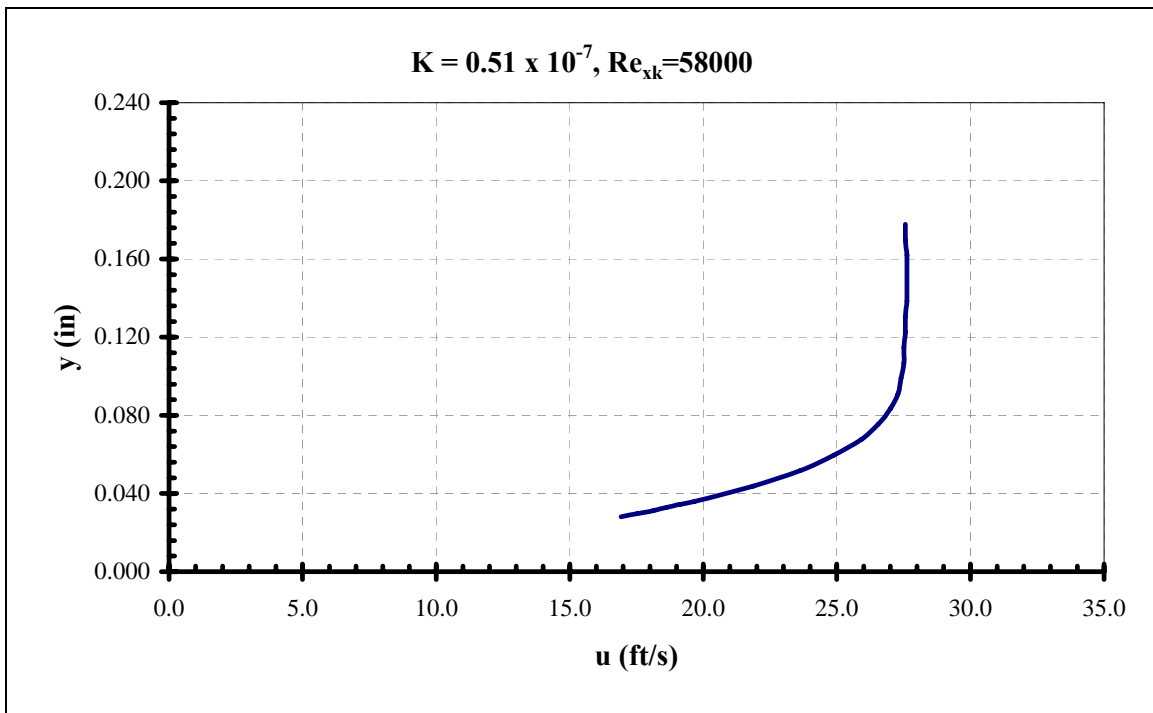


**Figure 80. Boundary layer velocity profile**

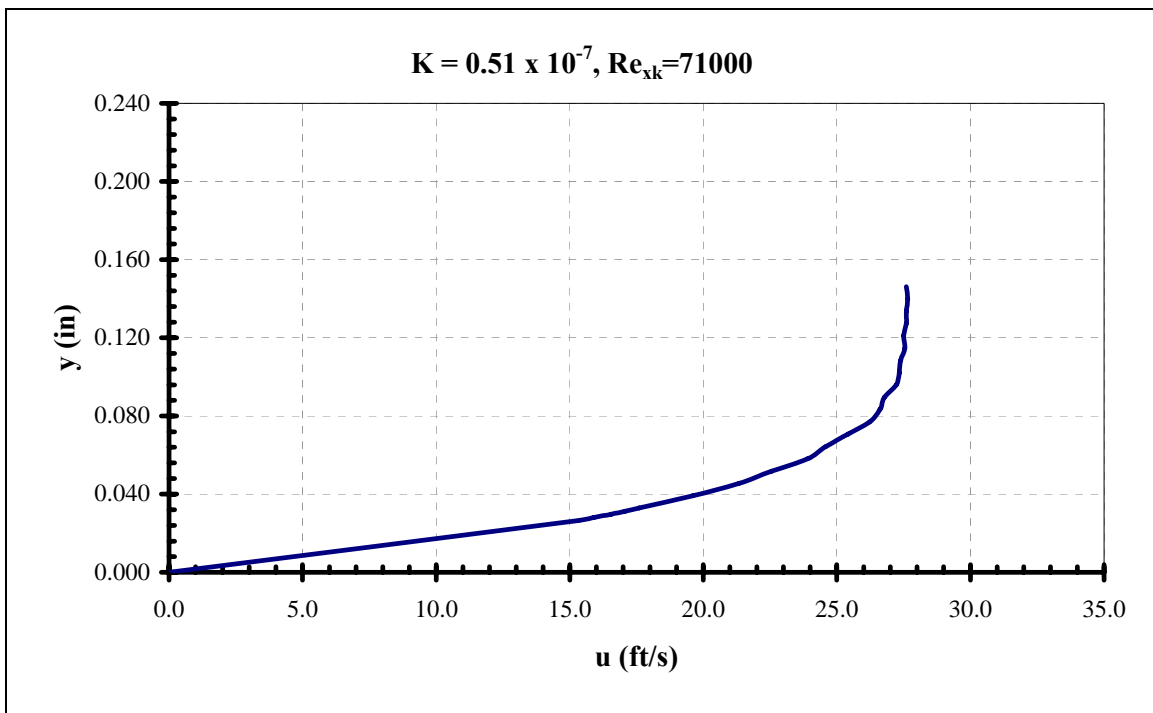


**Figure 81. Boundary layer velocity profile**

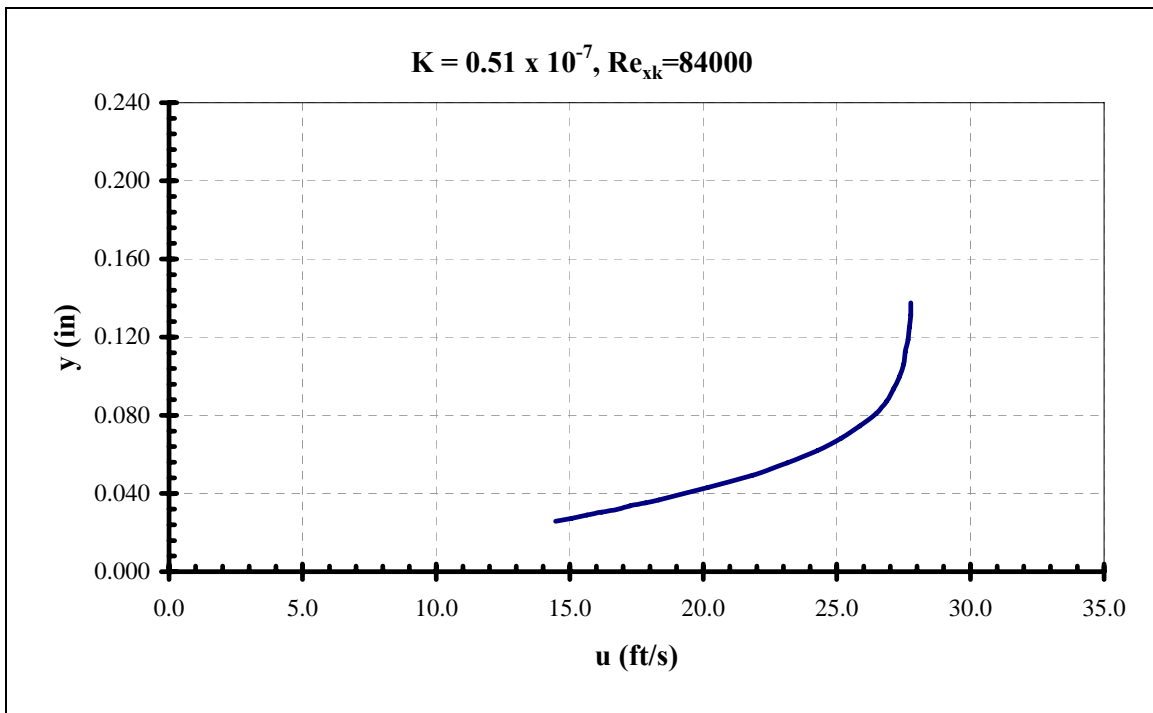


**Figure 82. Boundary layer velocity profile**

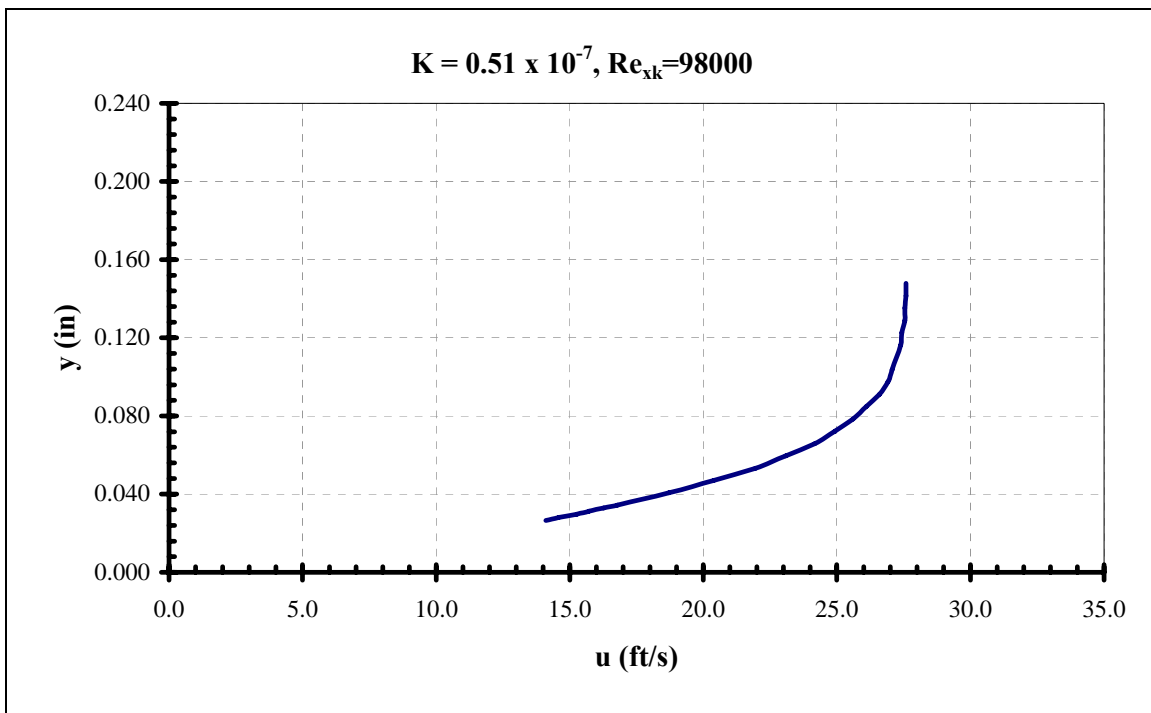


**Figure 83. Boundary layer velocity profile**

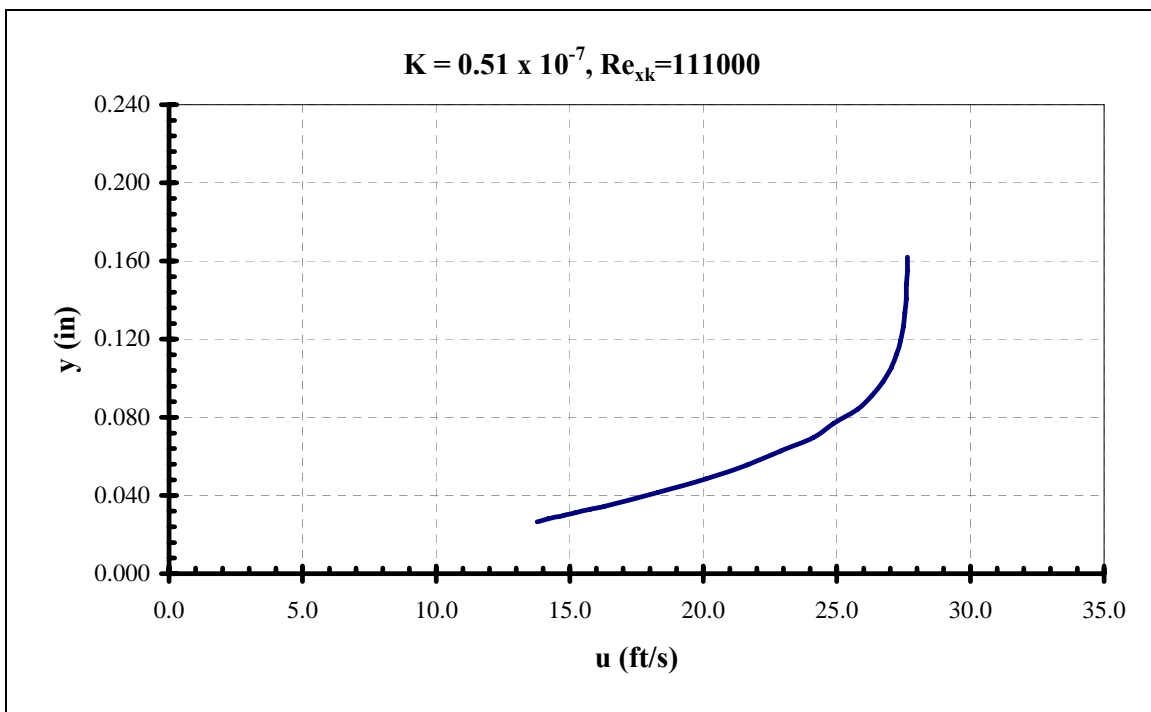


**Figure 84. Boundary layer velocity profile**

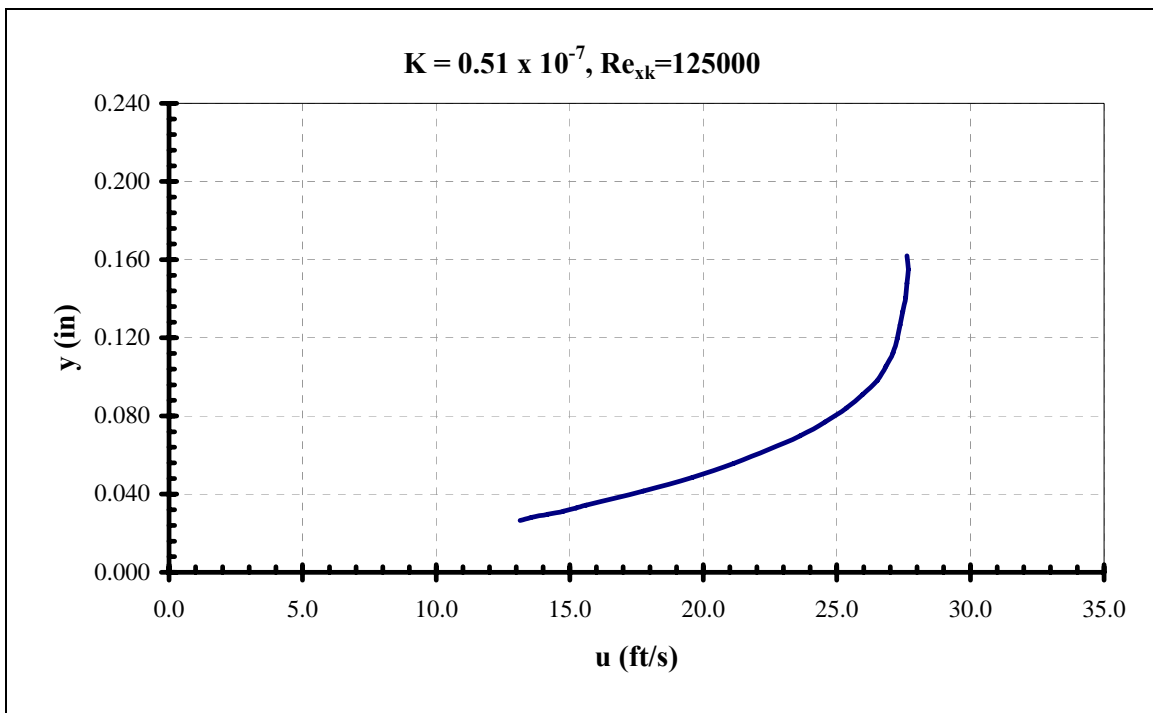


**Figure 85. Boundary layer velocity profile**

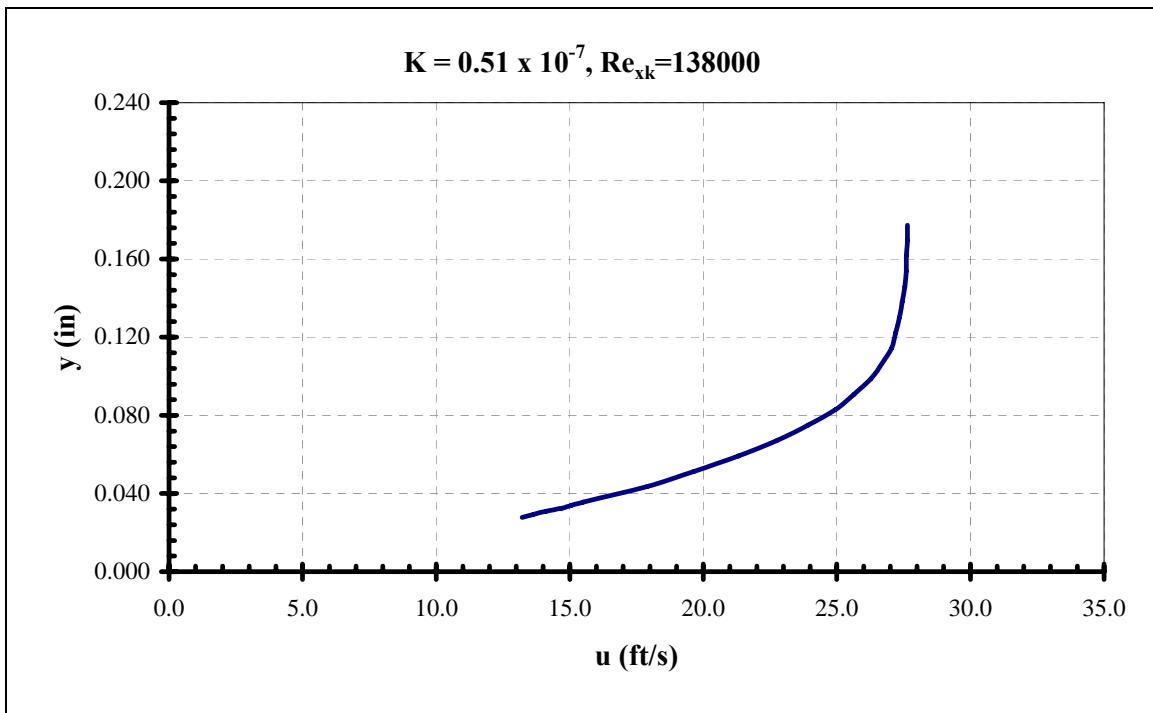


**Figure 86. Boundary layer velocity profile**



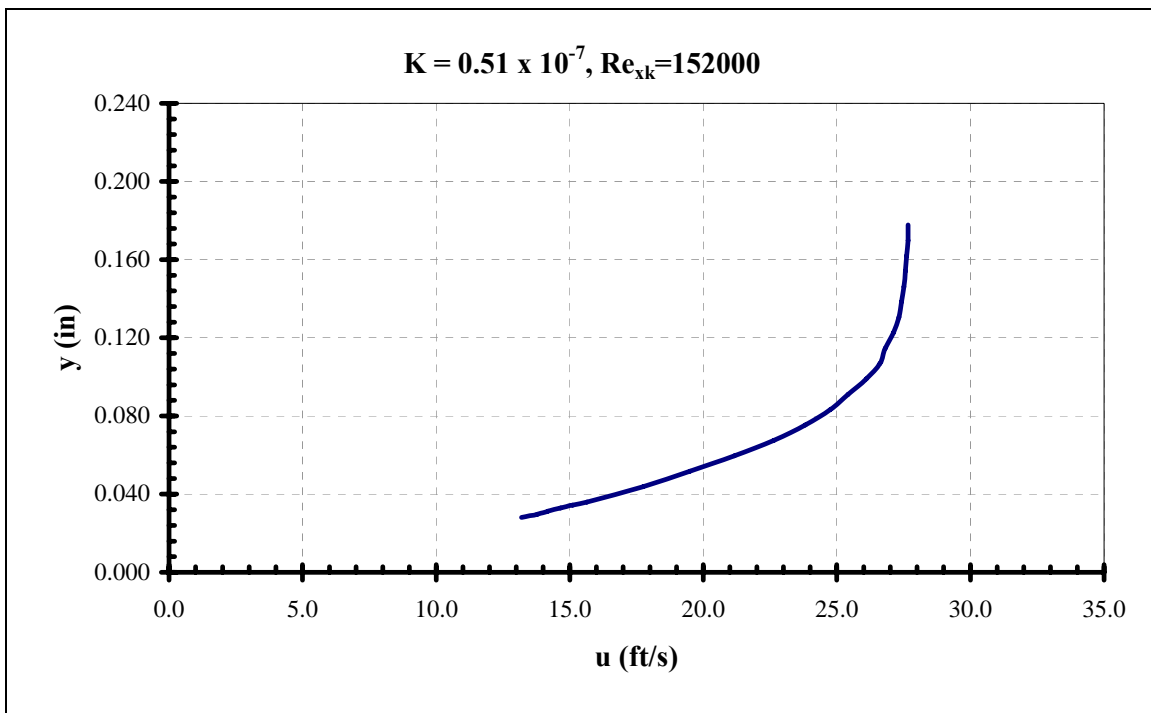


**Figure 87. Boundary layer velocity profile**

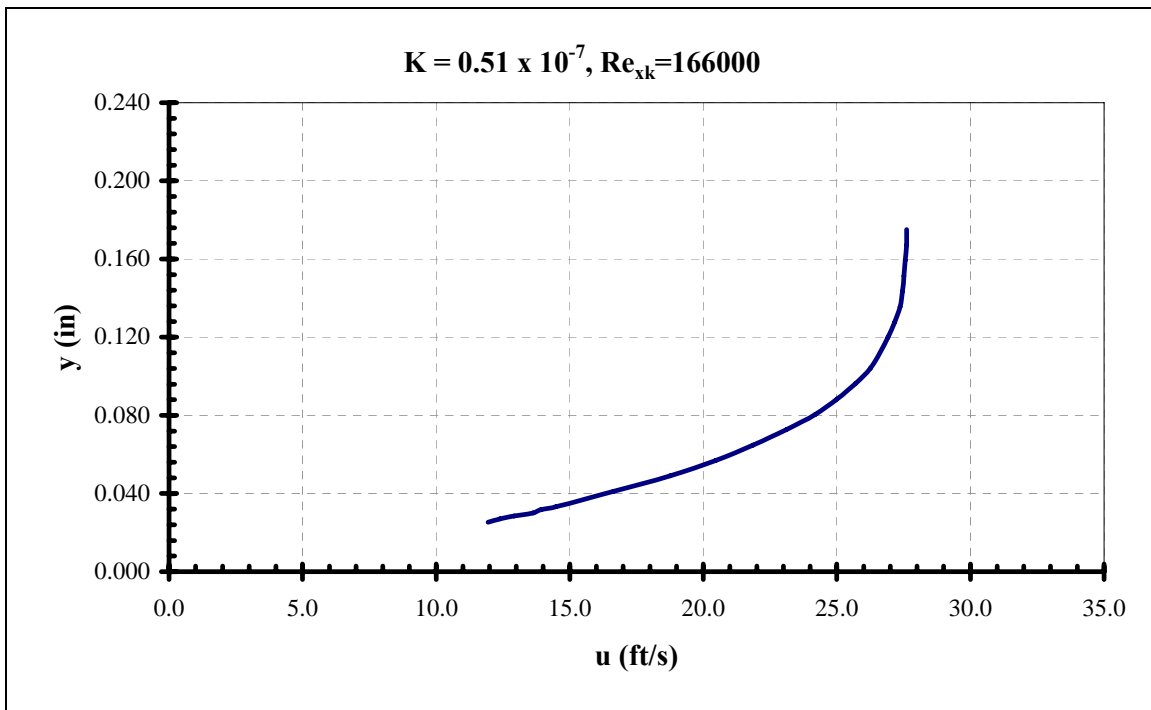


**Figure 88. Boundary layer velocity profile**

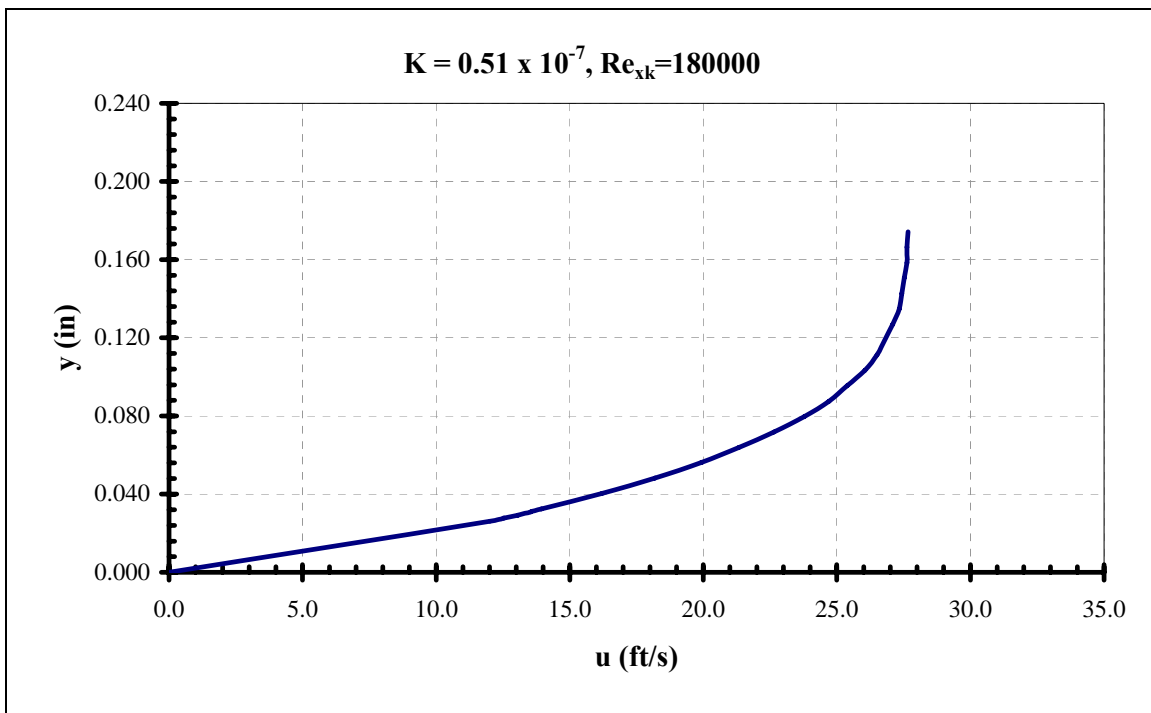


**Figure 89. Boundary layer velocity profile**

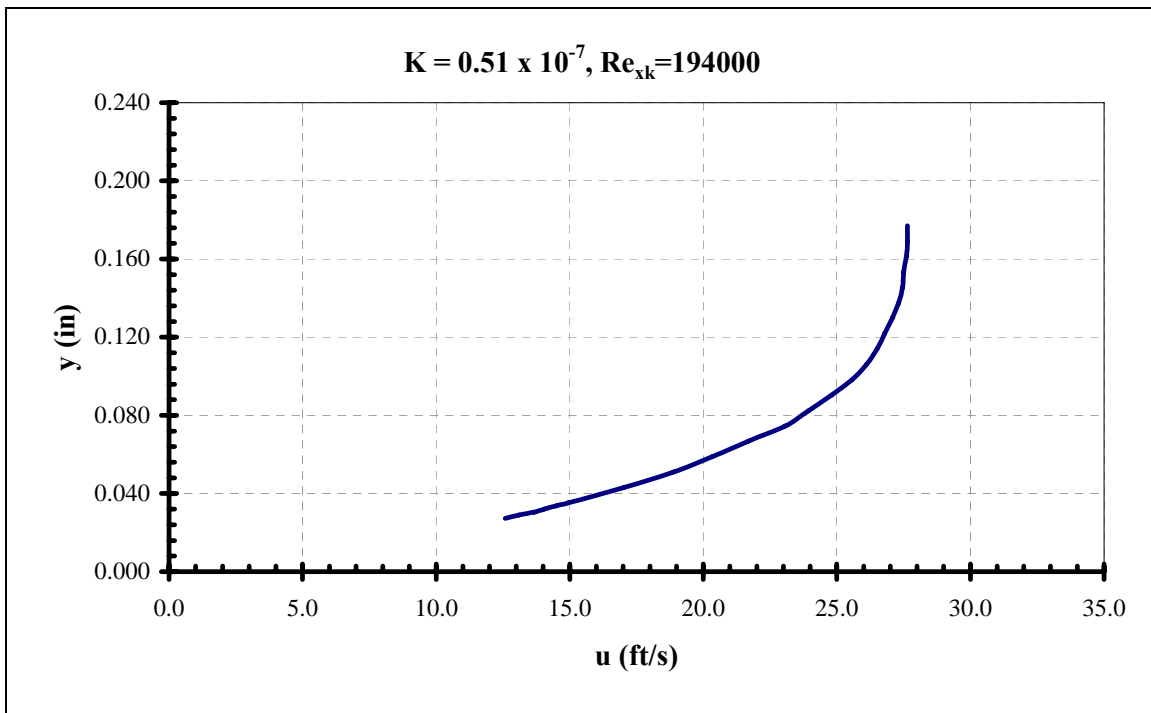


**Figure 90. Boundary layer velocity profile**

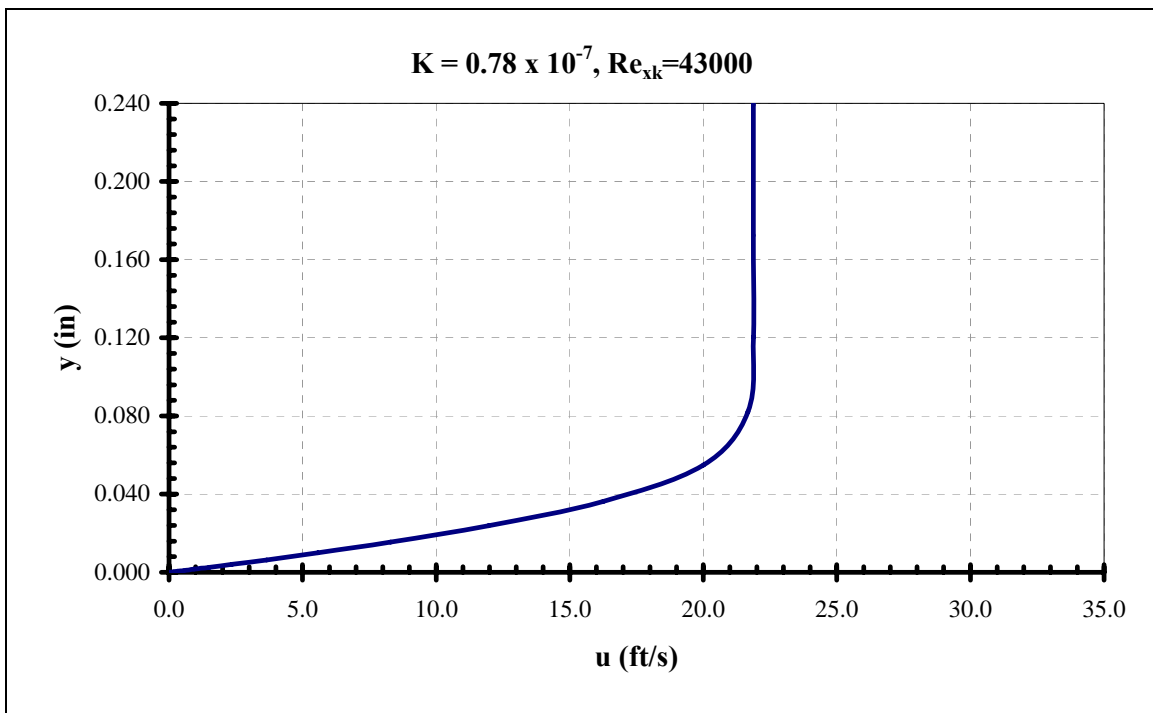


**Figure 91. Boundary layer velocity profile**

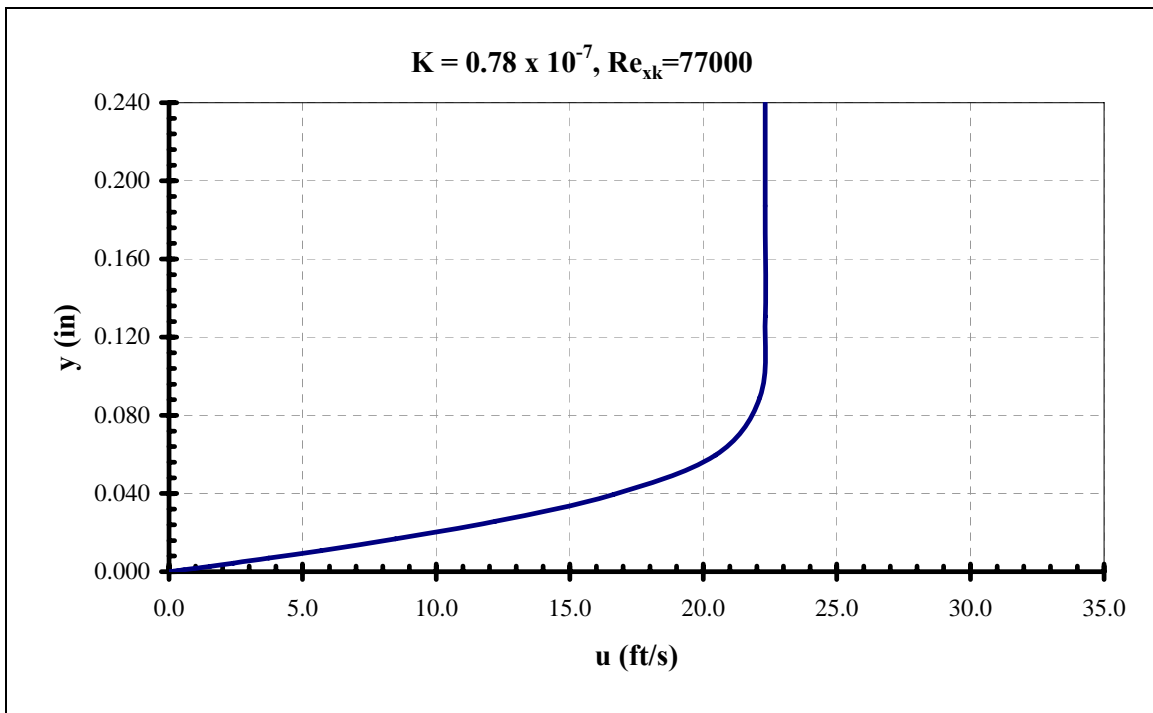


**Figure 92. Boundary layer velocity profile**

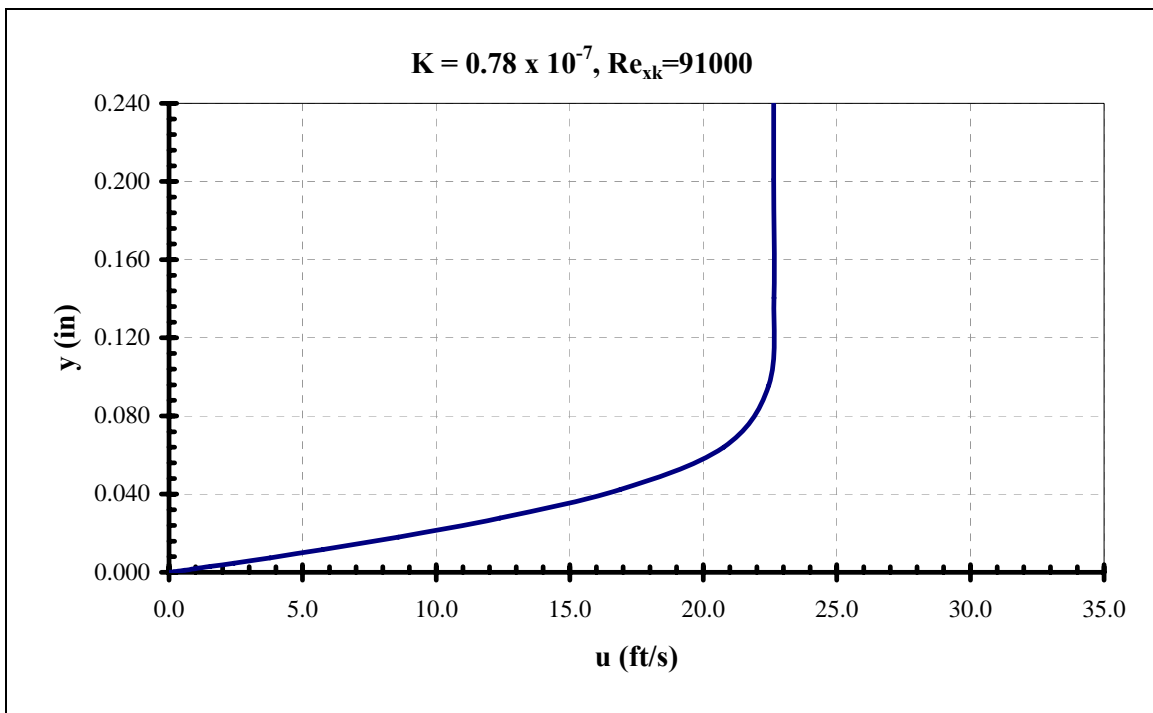


**Figure 93. Boundary layer velocity profile**

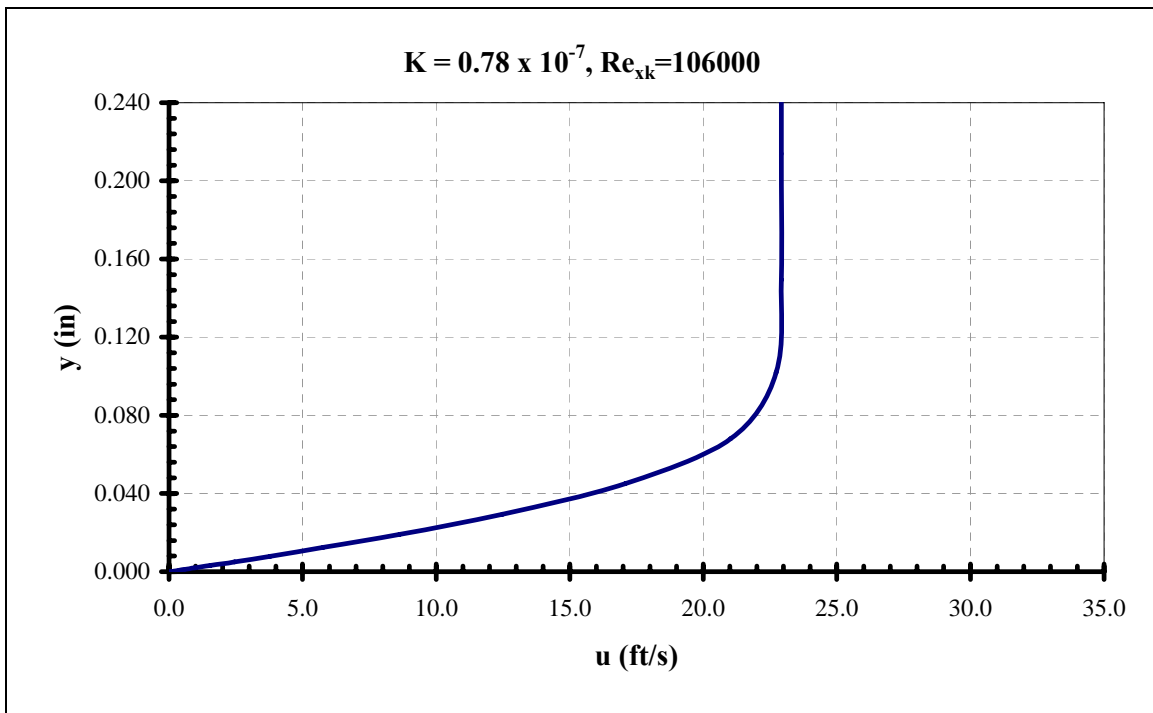


**Figure 94. Boundary layer velocity profile**

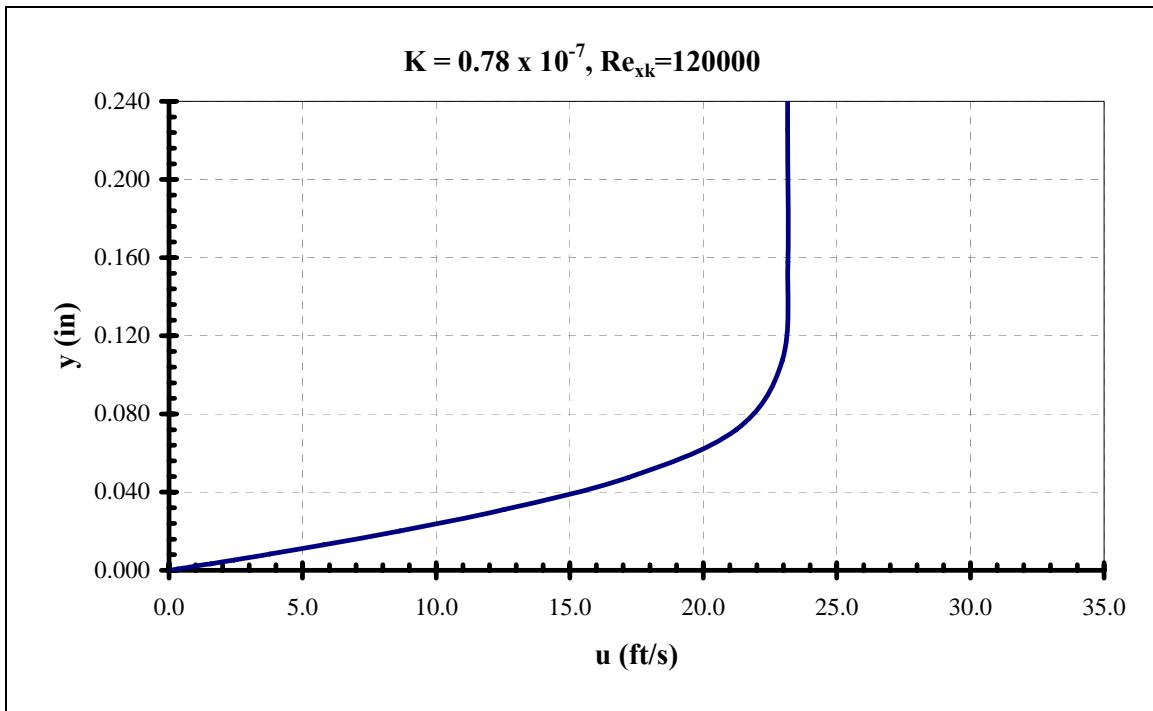


**Figure 95. Boundary layer velocity profile**

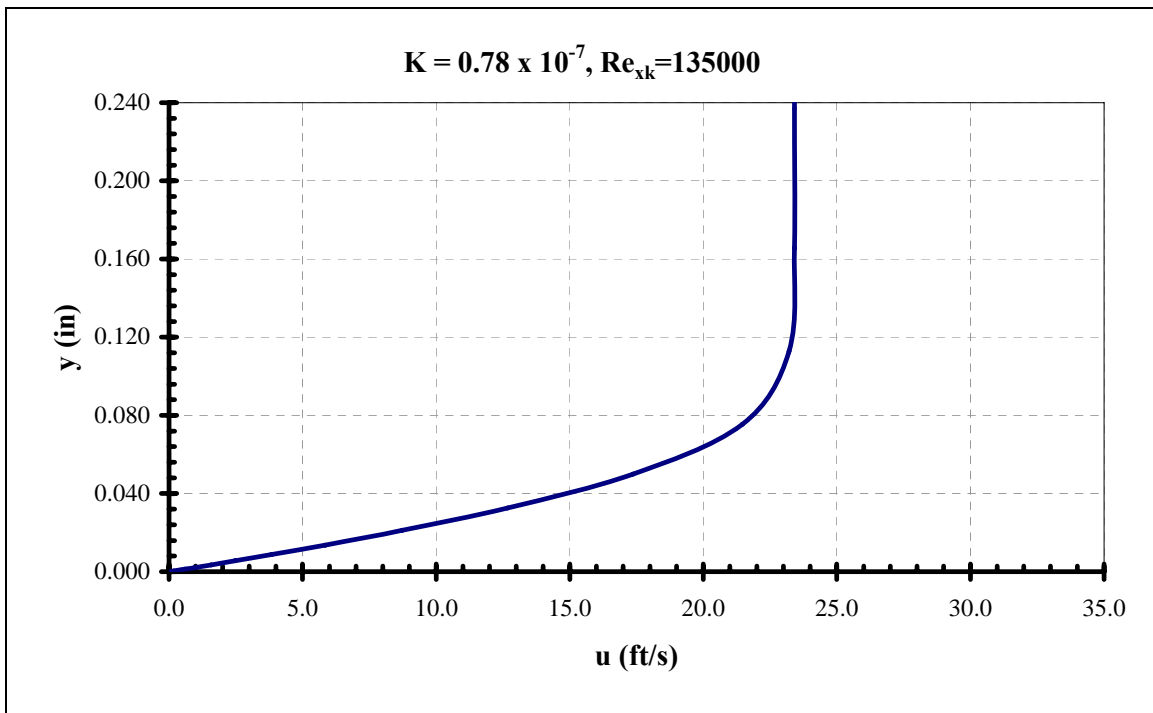


**Figure 96. Boundary layer velocity profile**

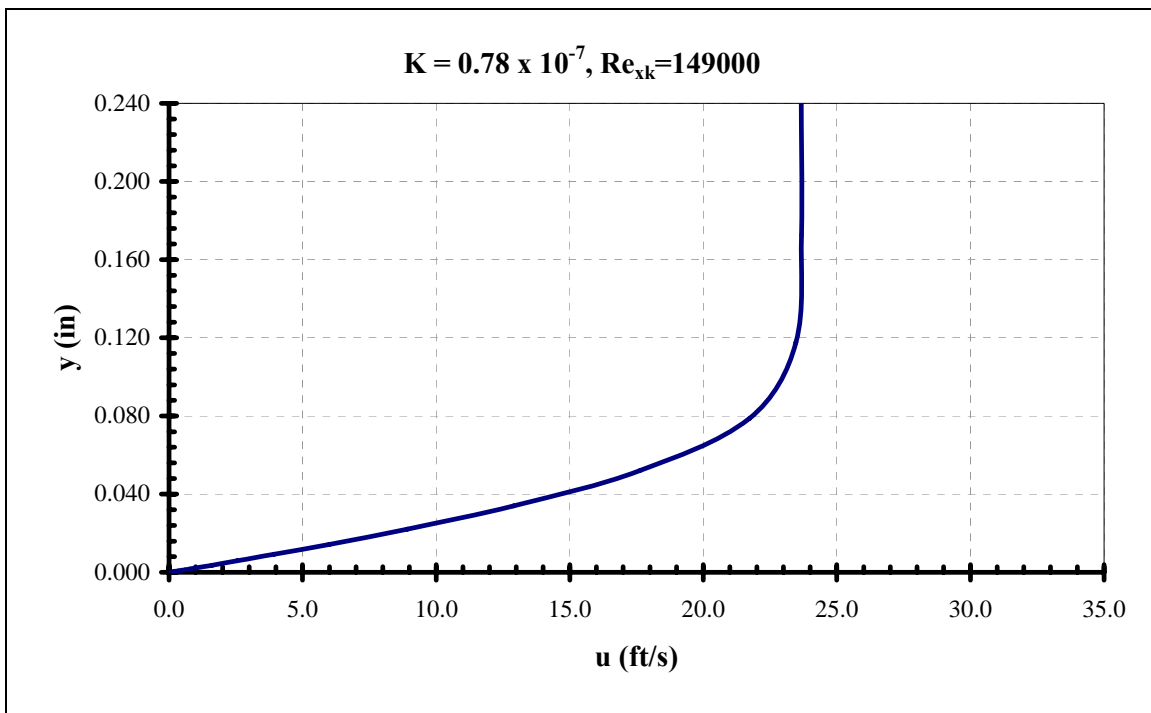


**Figure 97. Boundary layer velocity profile**

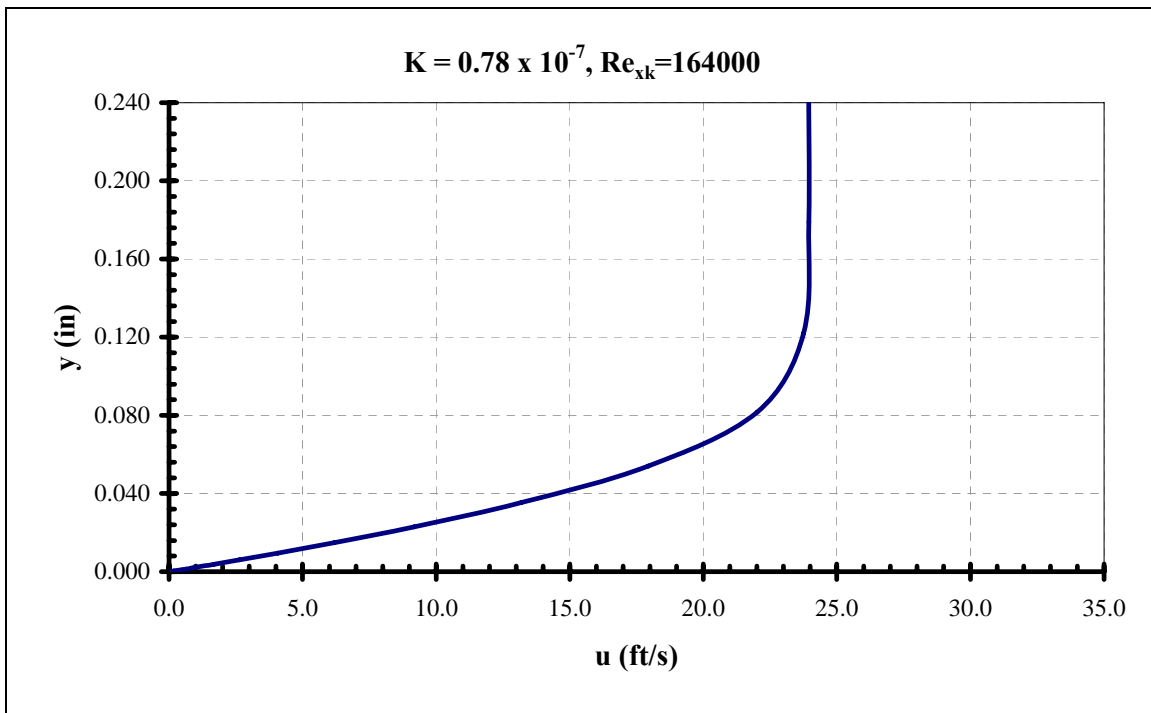


**Figure 98. Boundary layer velocity profile**

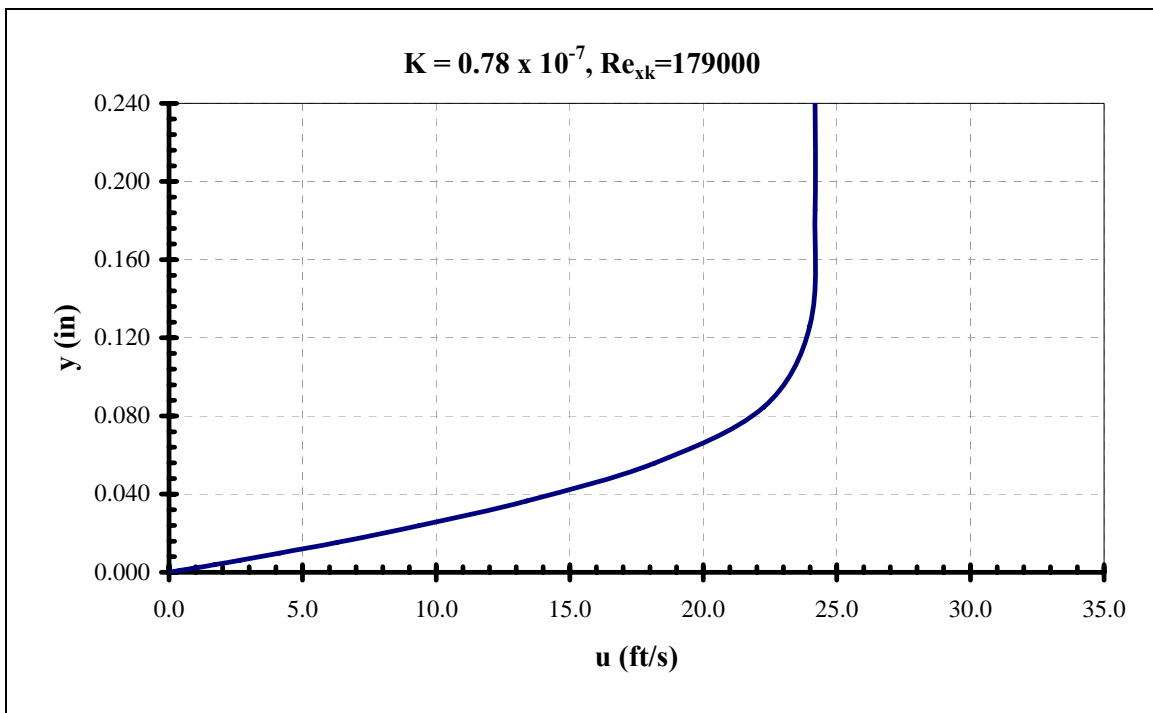


**Figure 99. Boundary layer velocity profile**

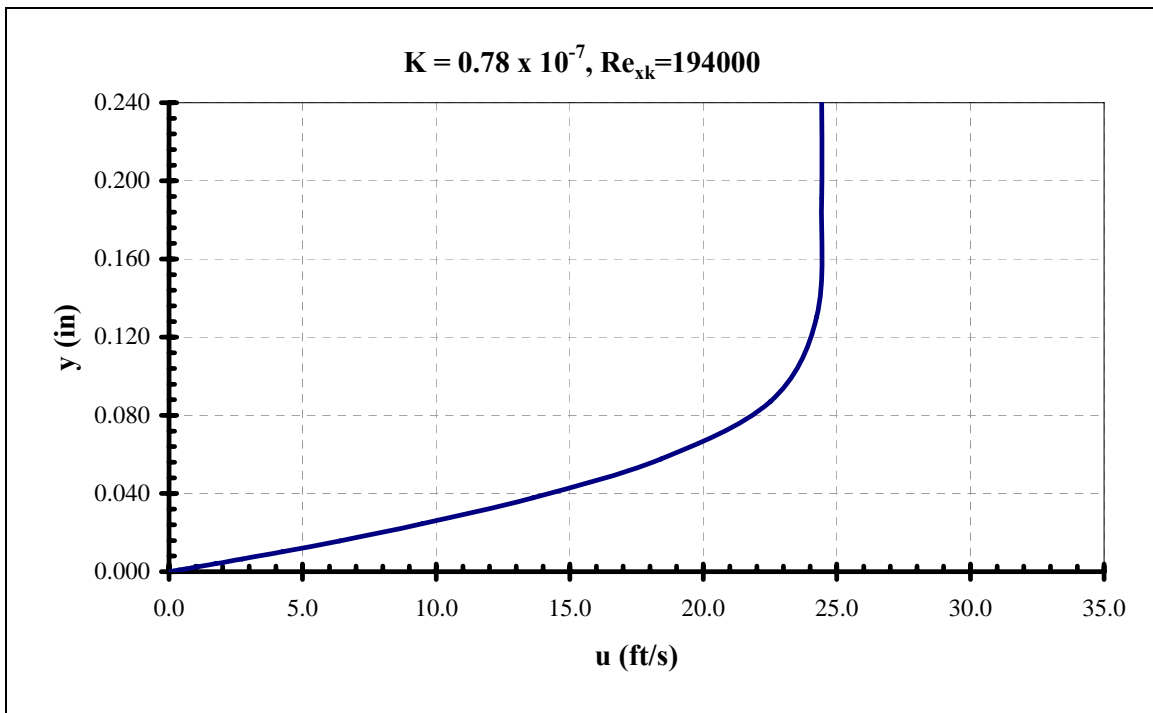


**Figure 100. Boundary layer velocity profile**

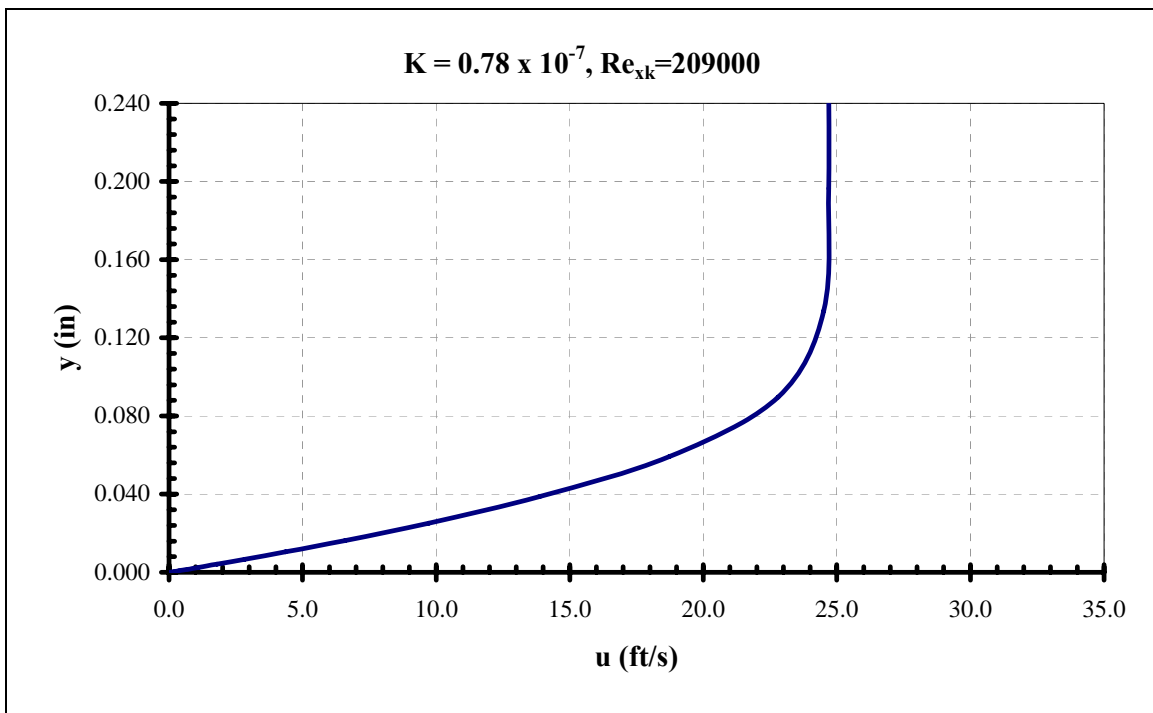


**Figure 101. Boundary layer velocity profile**

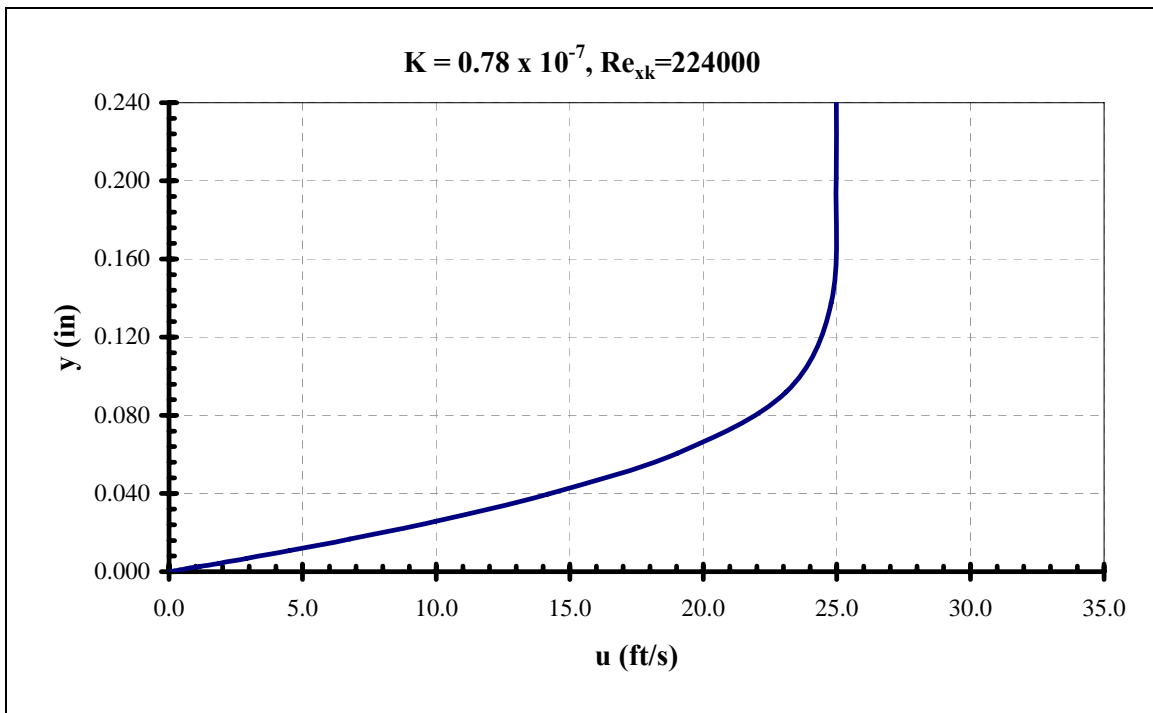


**Figure 102. Boundary layer velocity profile**



### 2.3.4 Skin Friction Distributions

Skin friction distributions for each combination of excrescence geometry and pressure distribution were measured using a Preston tube<sup>11</sup>. These Preston tube measurements were made with a probe consisting of a 0.042-inch outside diameter hypodermic needle protruding forward from a long rod. The probe tip was angled downward to that the opening would always rest touching the surface. The probe and rod assembly allowed the probe to be positioned anywhere on the test plate; the required local surface static pressure for each location was obtained by interpolating the surface pressure distribution. The resulting pressure differences were converted to skin friction coefficients using Patel's calibration<sup>12</sup> for turbulent boundary layers and Poll's calibration<sup>13</sup> for laminar boundary layers.

Poll's calibration for laminar boundary layers is as follows:

$$\bar{Y} = 1.104\bar{X}^{1/2} - \frac{18.96}{\bar{X}^{1/2}}, \quad (8)$$

where

$$\bar{X} = \frac{\Delta p d^2}{4\rho v^2} \quad (9)$$

$$\bar{Y} = \frac{\tau d^2}{4\rho v^2} \quad (10)$$

valid for,  $120 < \bar{X} < 0.033\left(\frac{du}{v}\right)^2$ .

Patel's calibration for turbulent boundary layers is as follows:

$$y^* = 0.8287 - 0.1381x^* + 0.1437x^{*2} - 0.0060x^{*3}, \quad (11)$$

where

$$x^* = \log_{10}\left(\frac{\Delta p d^2}{4\rho v^2}\right) \quad (12)$$

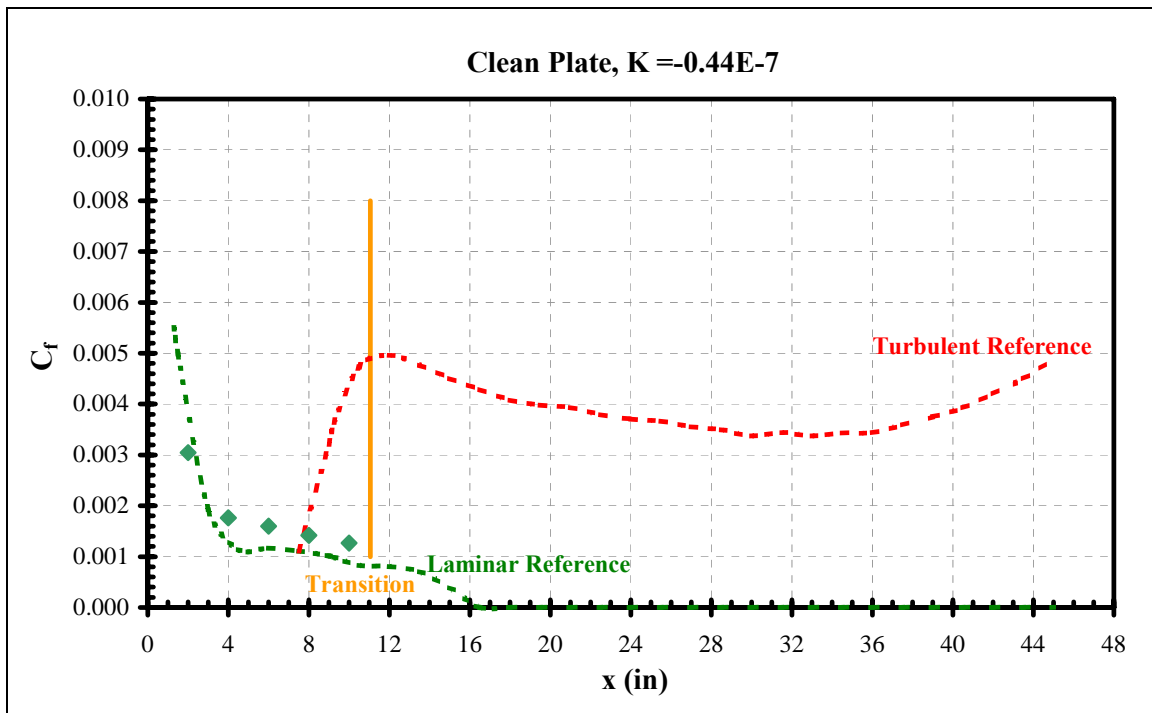
$$y^* = \log_{10}\left(\frac{\tau d^2}{4\rho v^2}\right) \quad (13)$$

valid for,  $1.5 < y^* < 3.5$ .

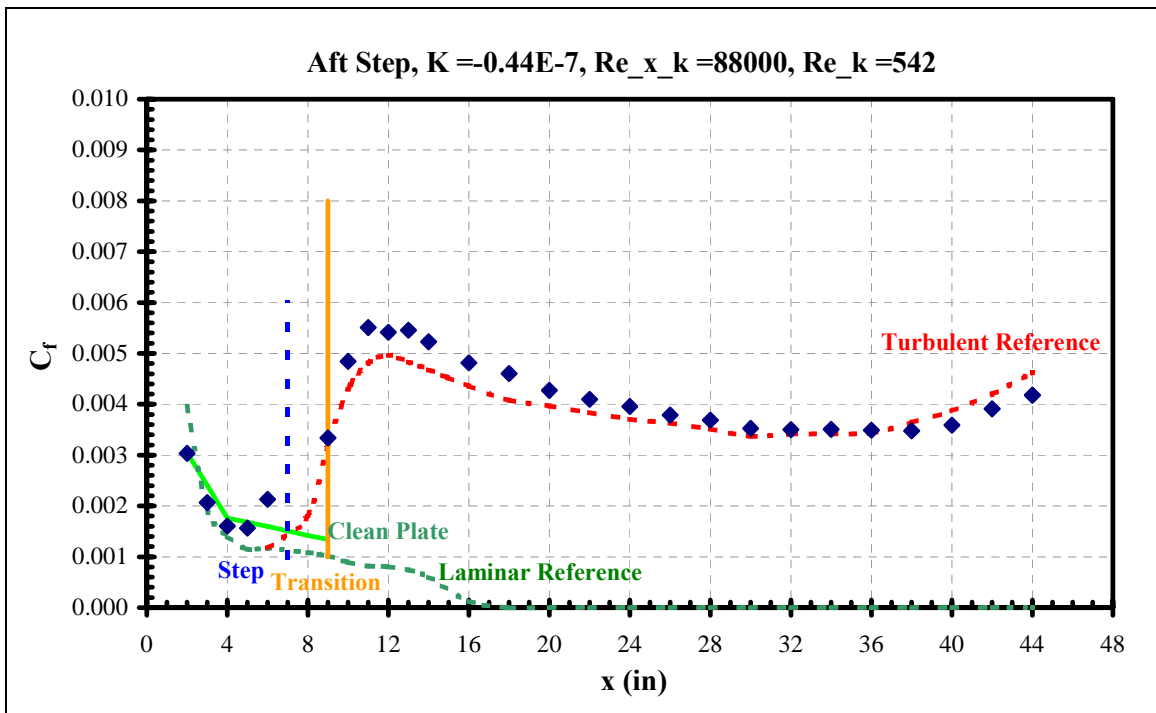
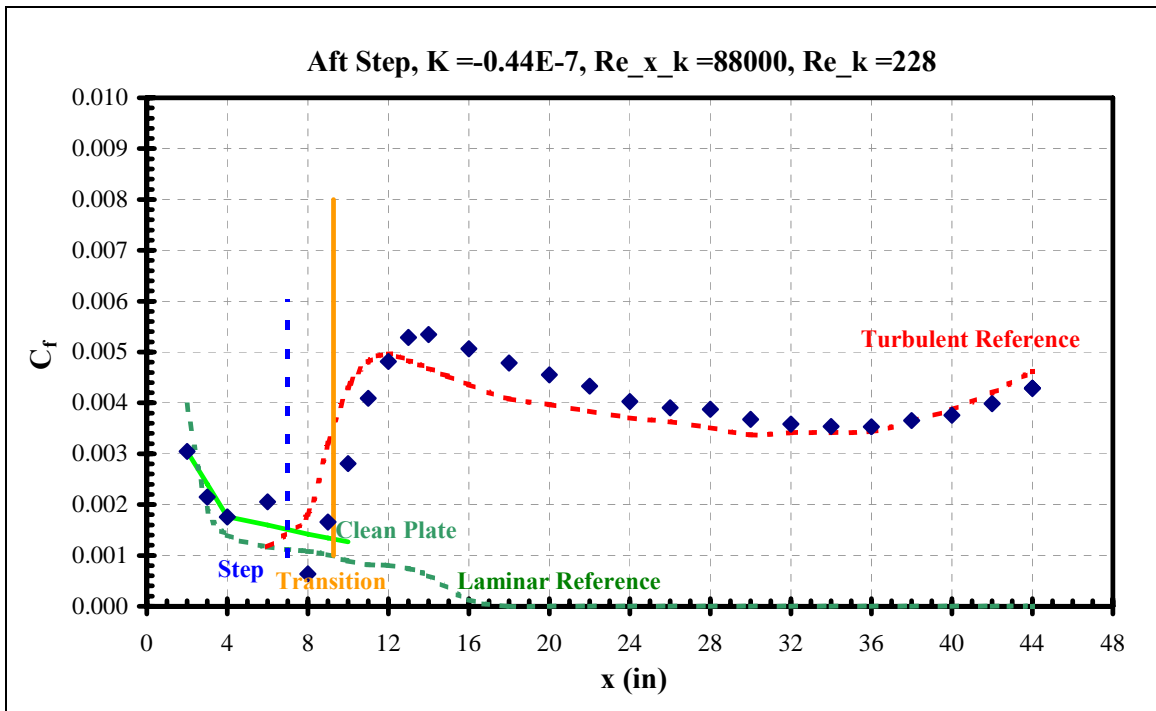
The adjust-a-wave initially had a small step aft of the wave due to the thickness of the skin. A later modification to the adjust-a-wave eliminated this step and allowed the aft end to be flush with the plate. The step was shown to have a noticeable effect on the data. Thus, the data has been separated into groups depending on whether the step was present or not.

Comparison of the adjust-a-step results with the fixed step results showed a difference attributable to the difference in the blendout. The adjust-a-step blended back to the plate distance of the plate over a distance of approximately 5 inches, whereas the fixed step blended

out over a distance of approximately 2.5 inches. The primary effects of steps have been determined from the fixed step data. The adjust-a-step data is plotted separately and comparisons are shown with the fixed step data.



**Figure 103. Clean plate skin friction distribution**



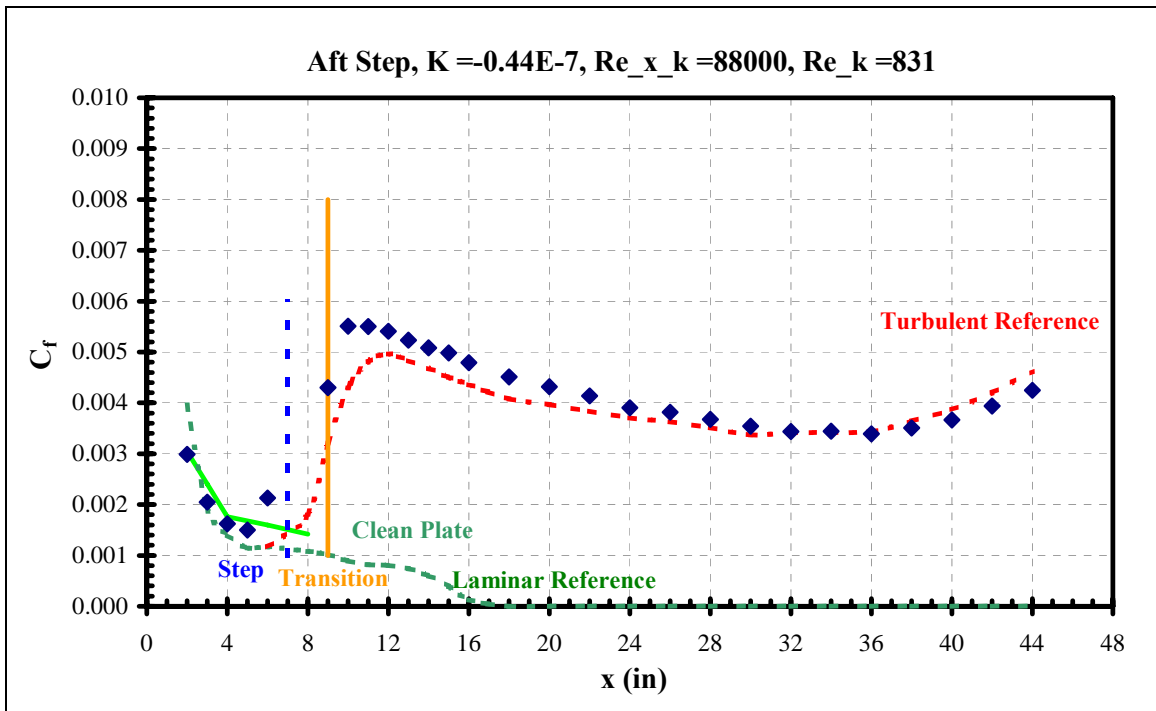


**Figure 106. Aft step skin friction distribution**

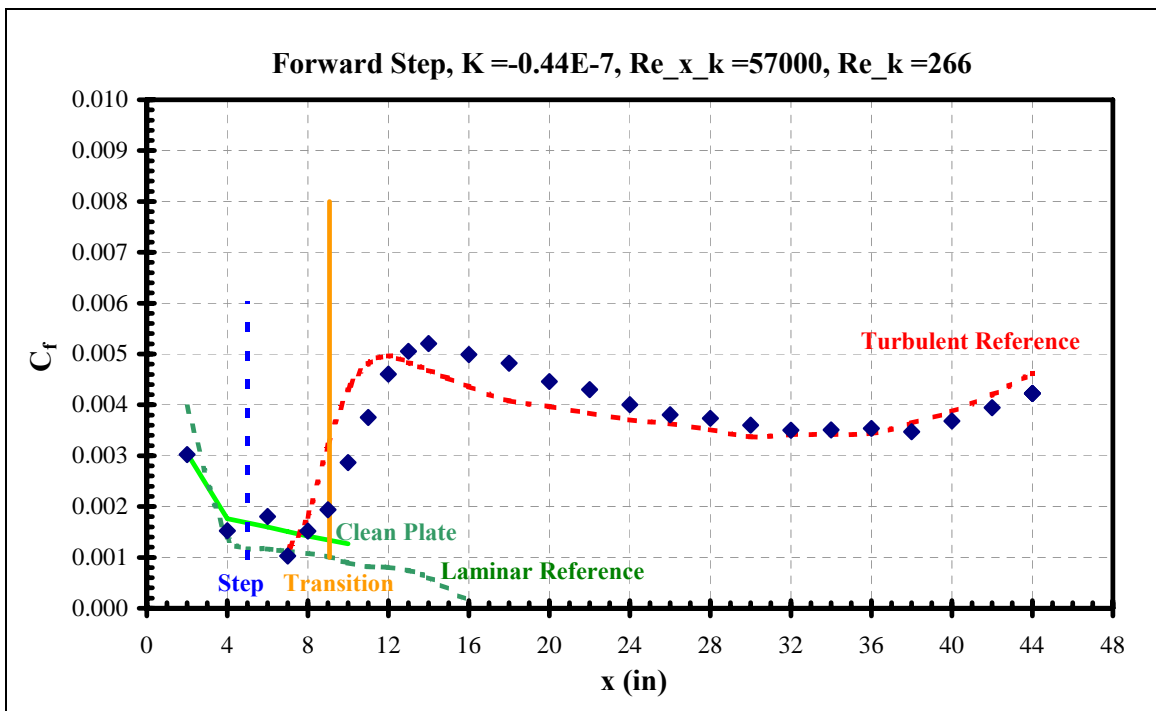
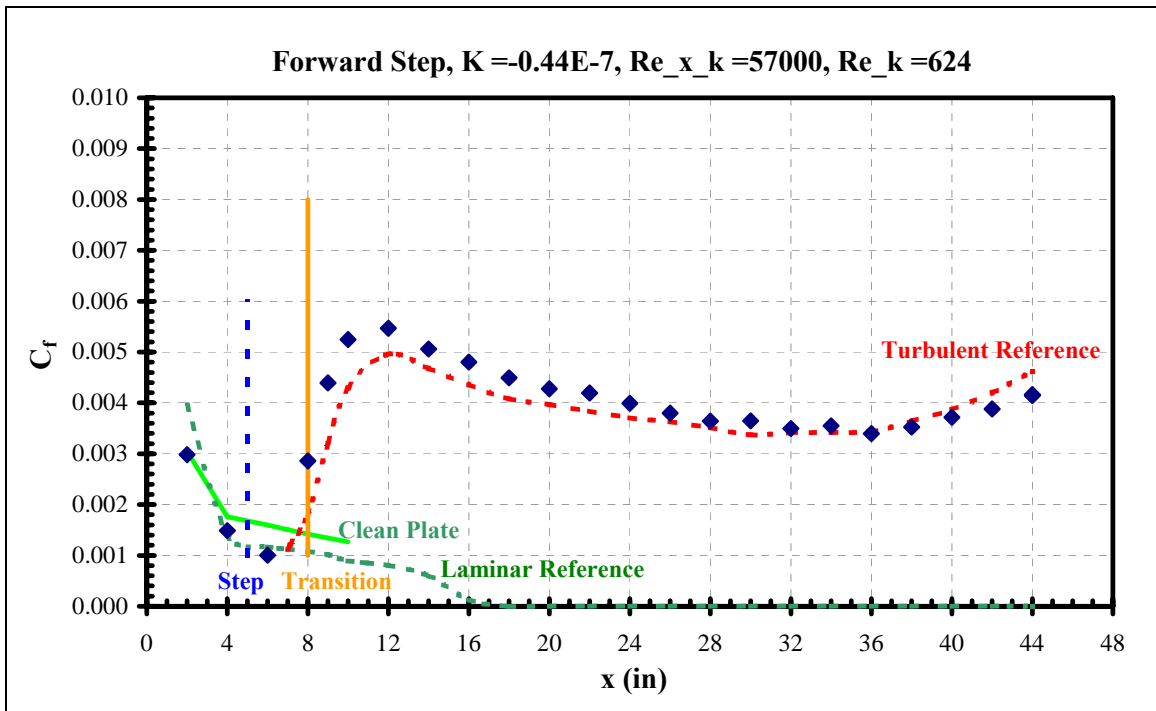


**Figure 107. Forward step skin friction distribution**



**108. Forward step skin friction distribution**

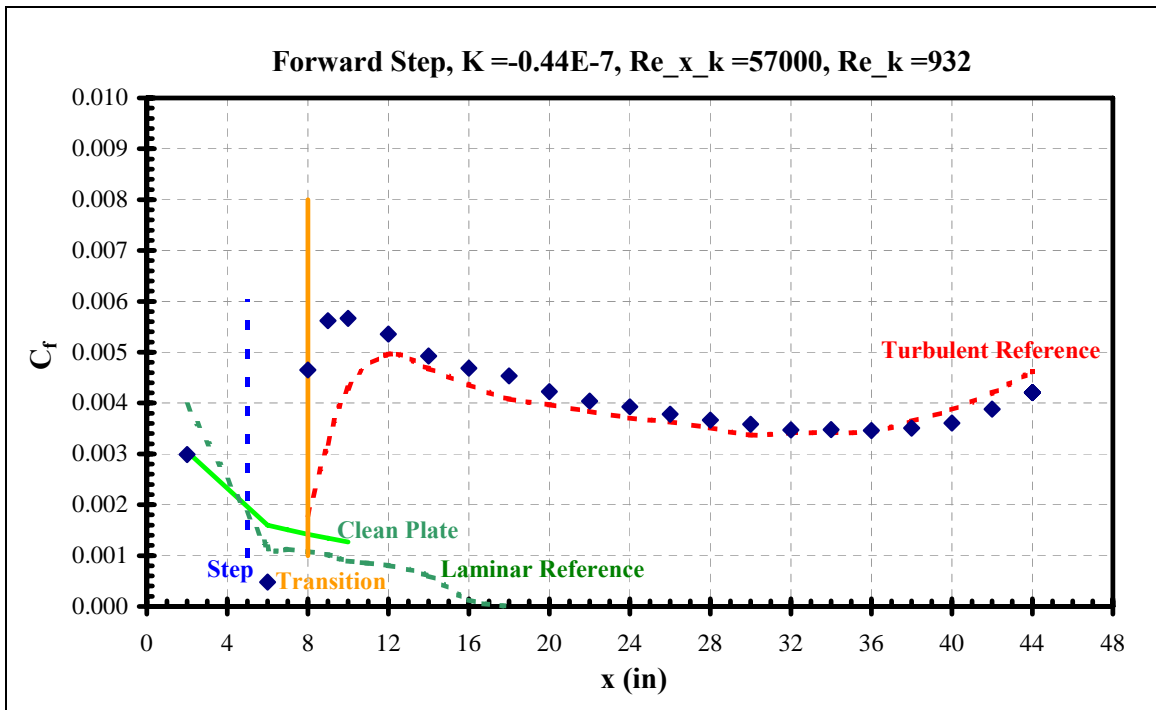


**Figure 109. Forward step skin friction distribution**

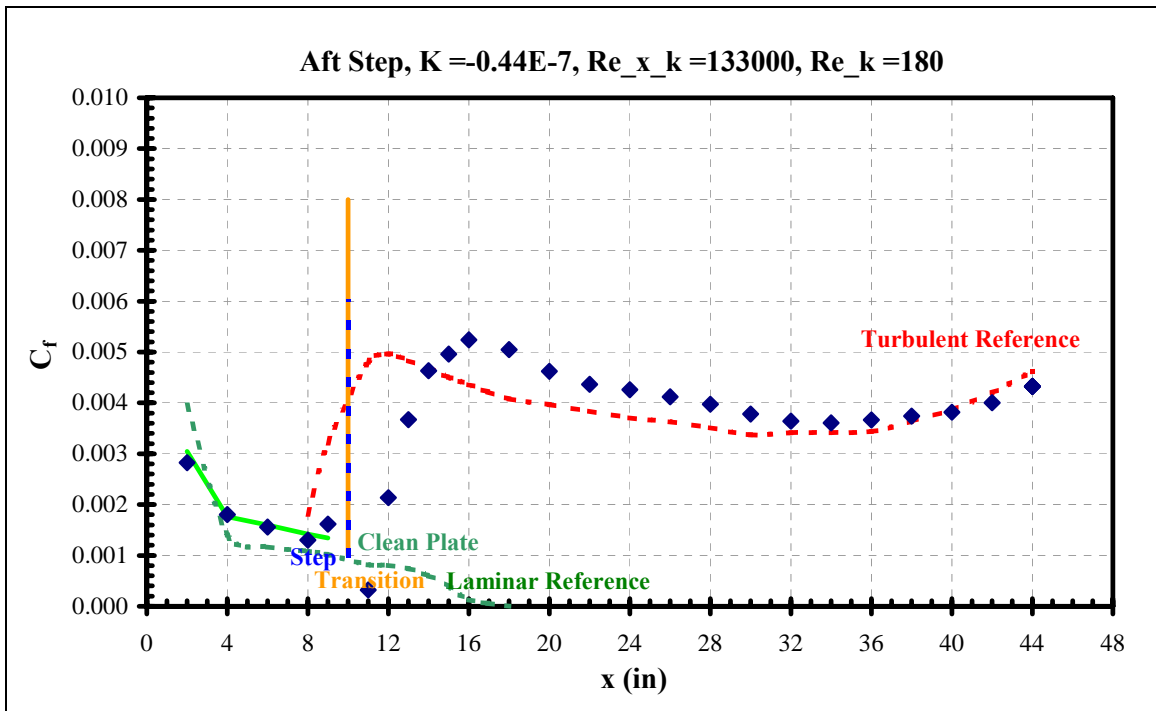


Figure 110. Aft step skin friction distribution

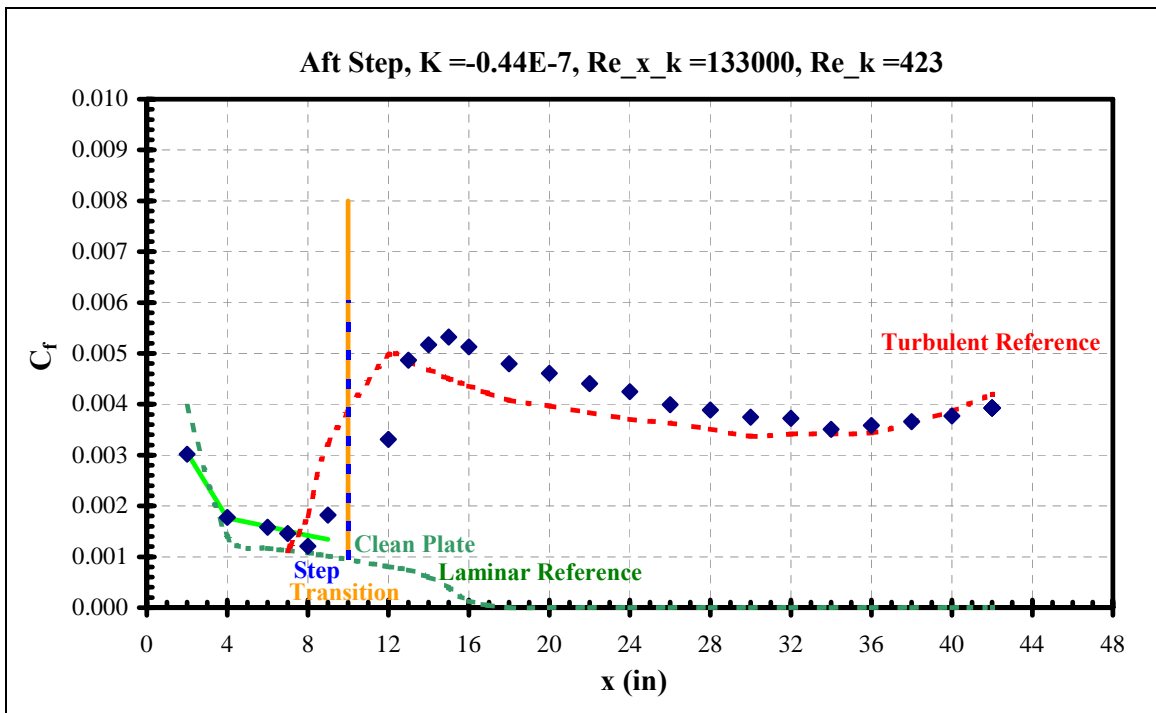
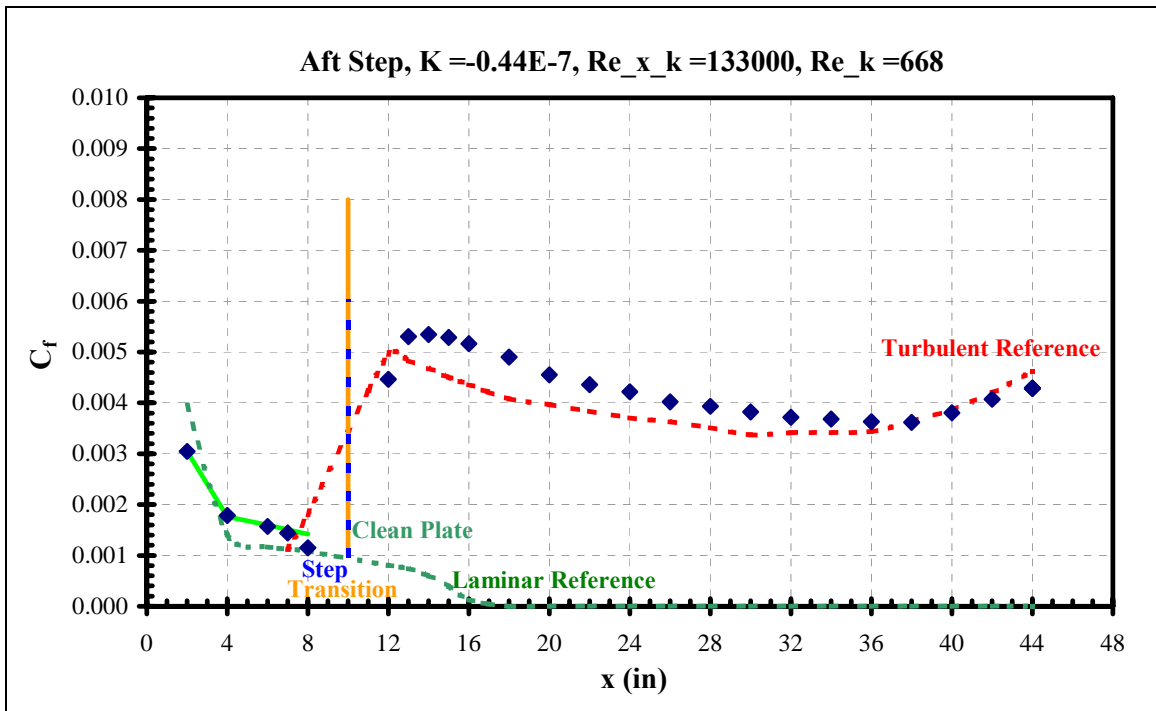
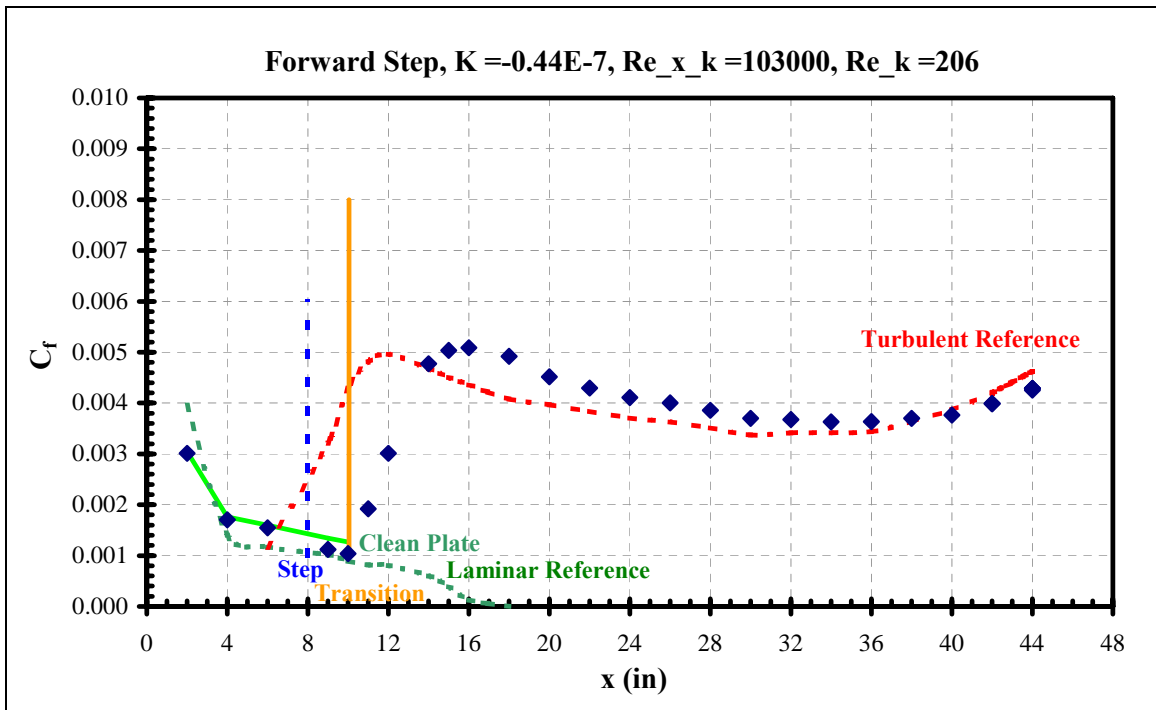


Figure 111. Aft step skin friction distribution



**Figure 112. Aft step skin friction distribution**



**Figure 113. Forward step skin friction distribution**

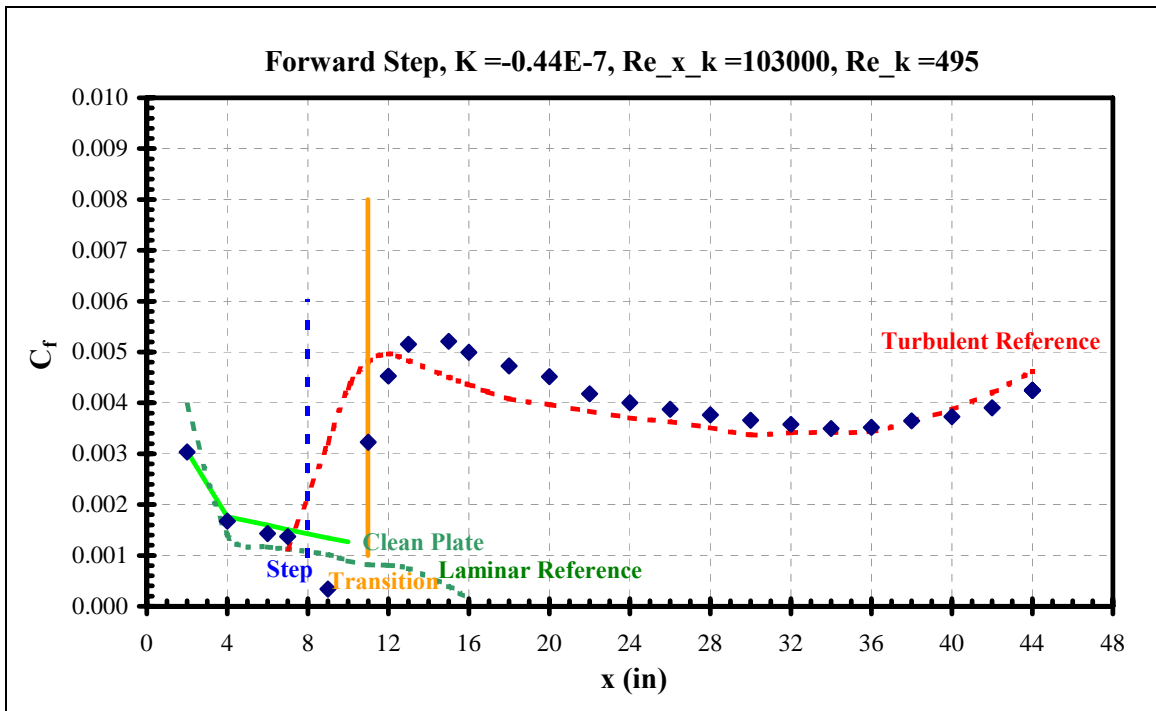


**Figure 114. Forward step skin friction distribution**

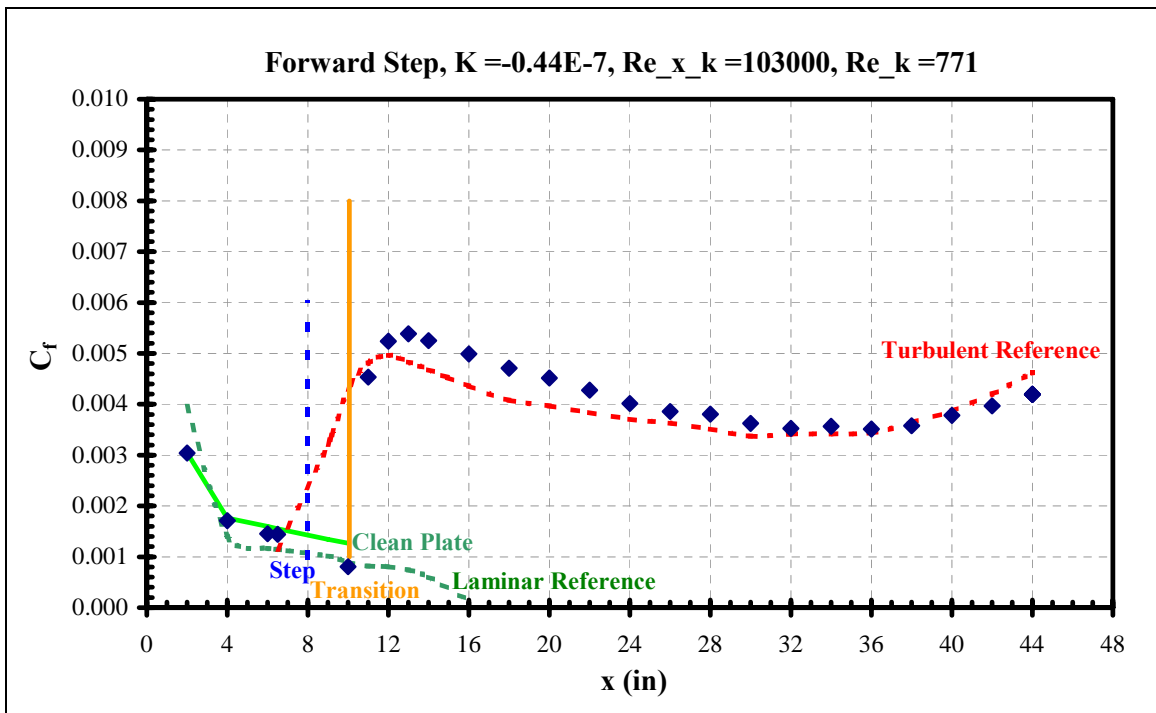


**Figure 115. Forward step skin friction distribution**



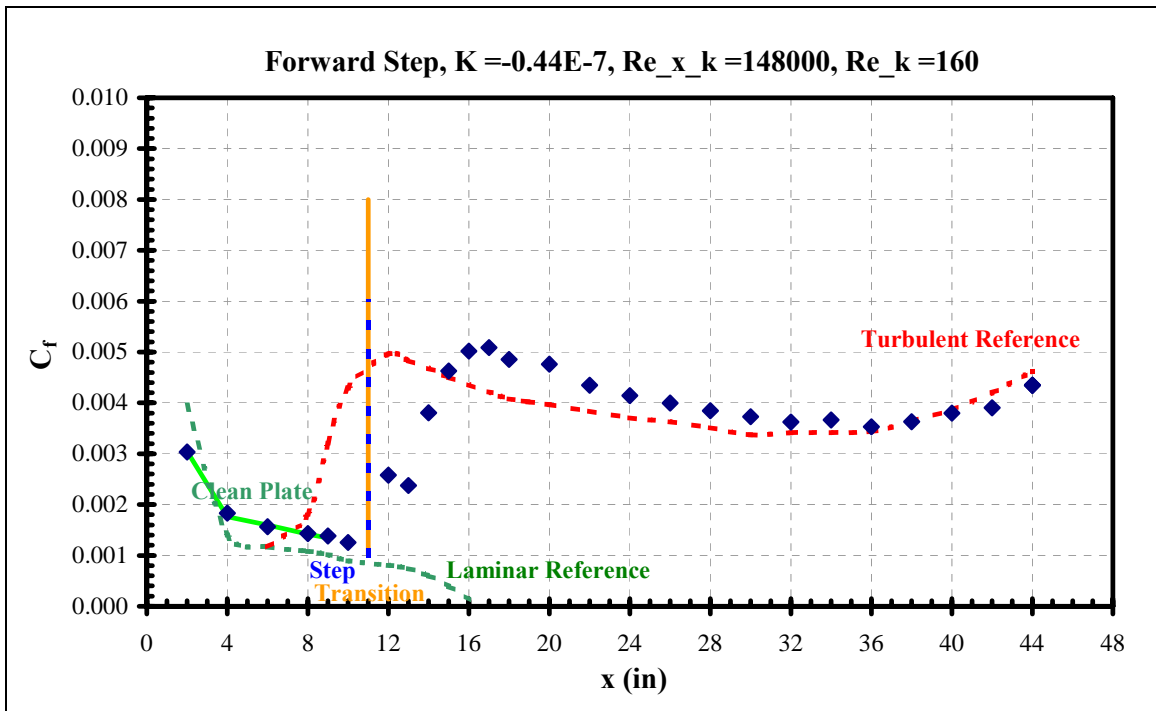


**Figure 116. Forward step skin friction distribution**

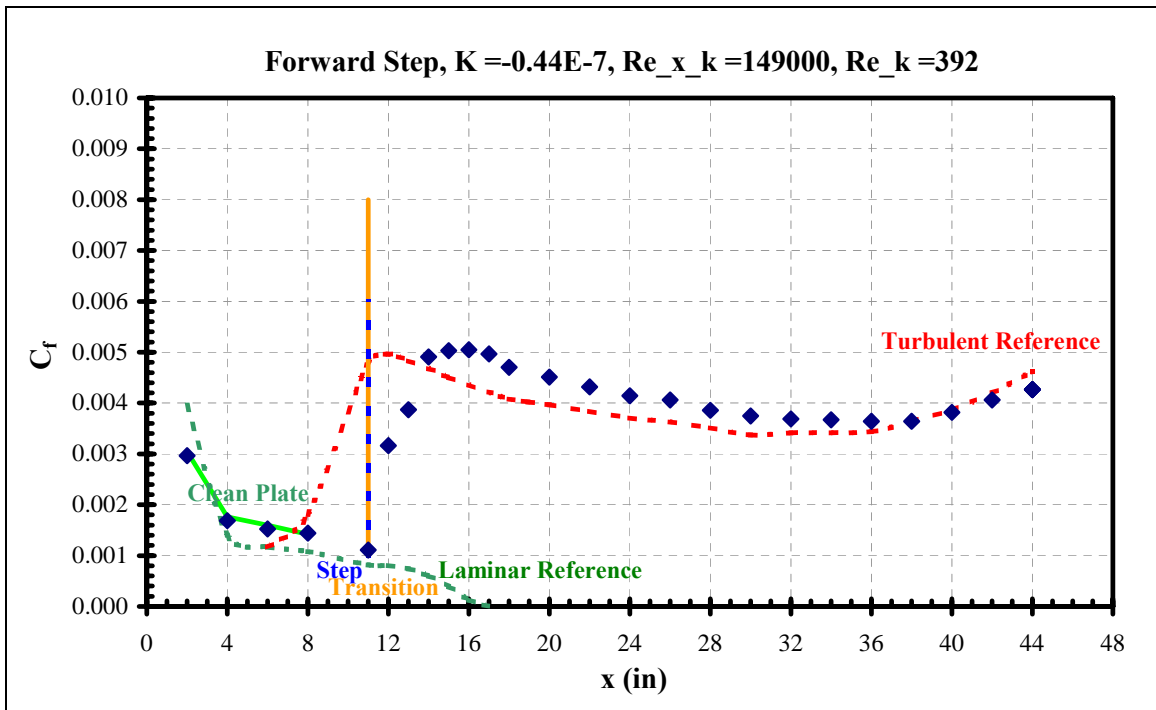


**Figure 117. Forward step skin friction distribution**

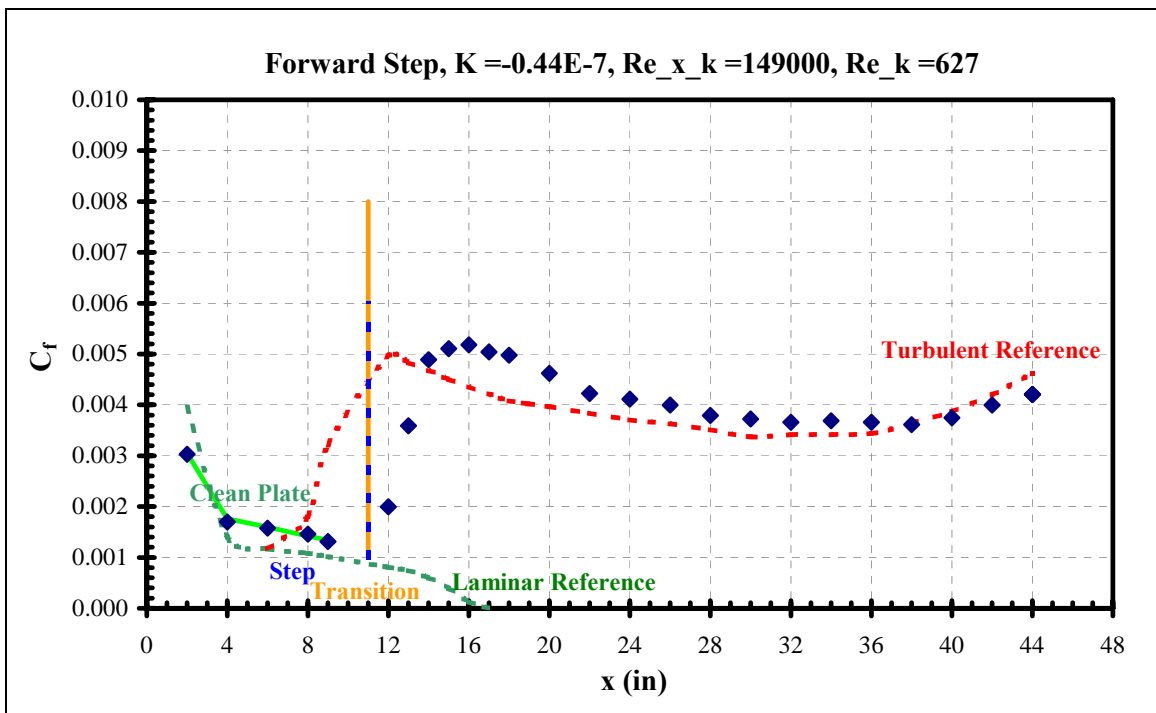


**Figure 118. Forward step skin friction distribution**

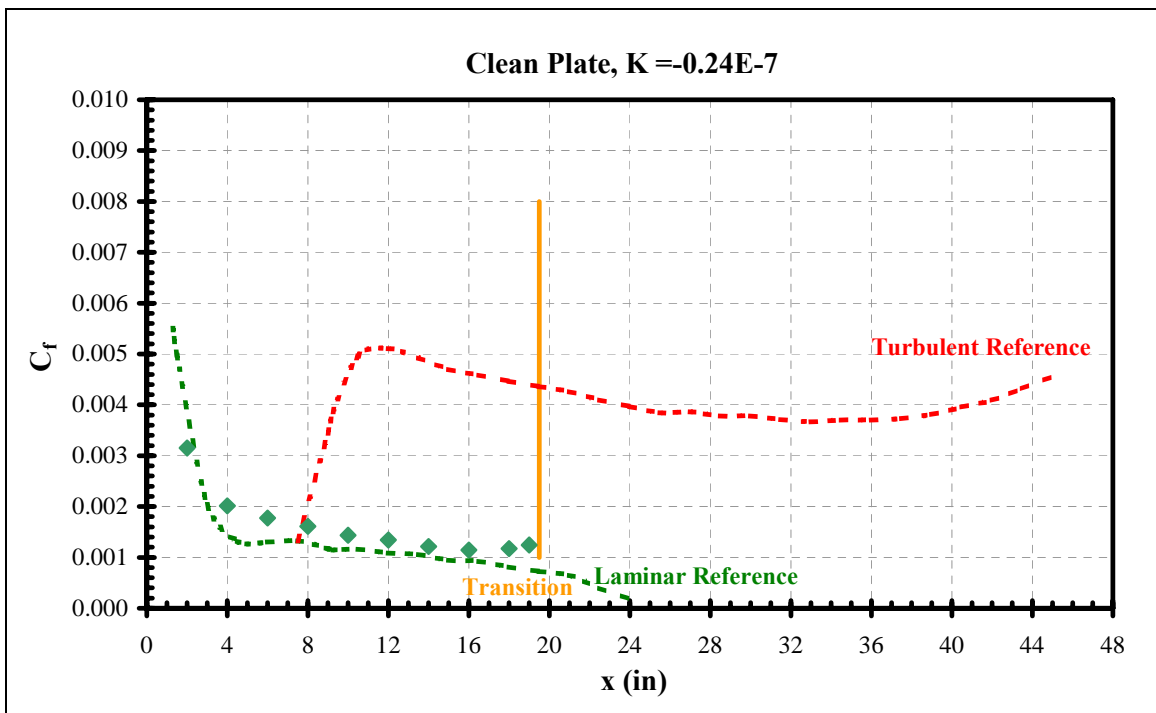


**Figure 119. Clean plate skin friction distribution**

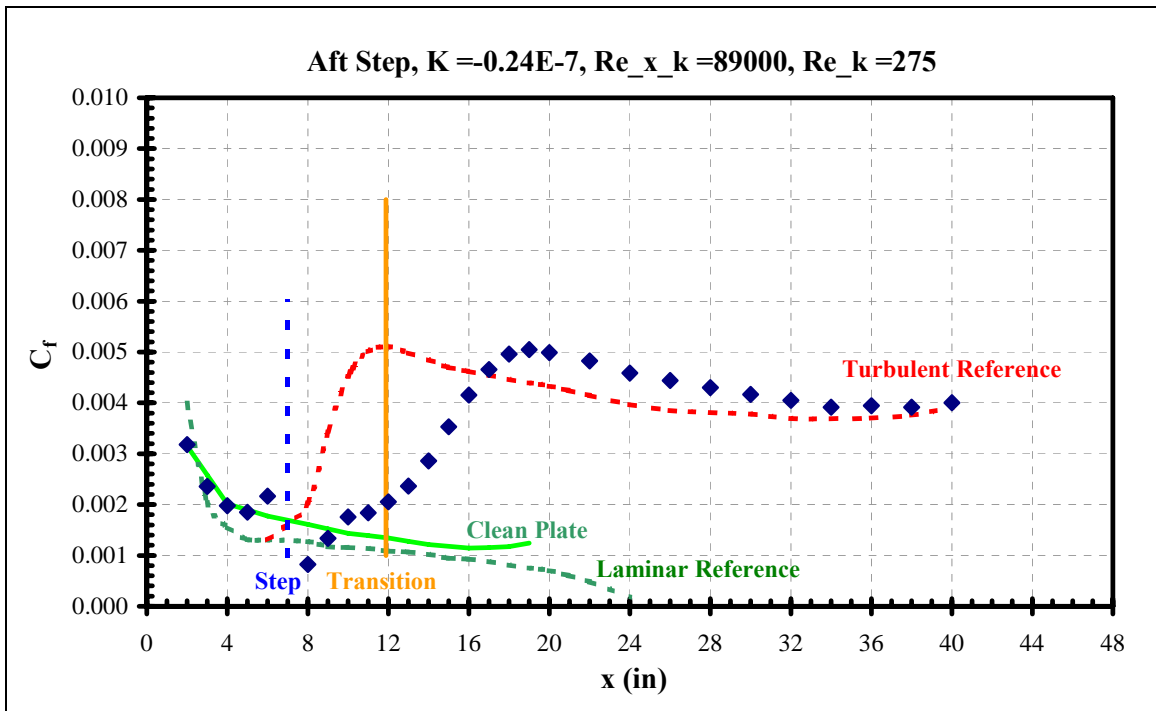


**Figure 120. Aft step skin friction distribution**

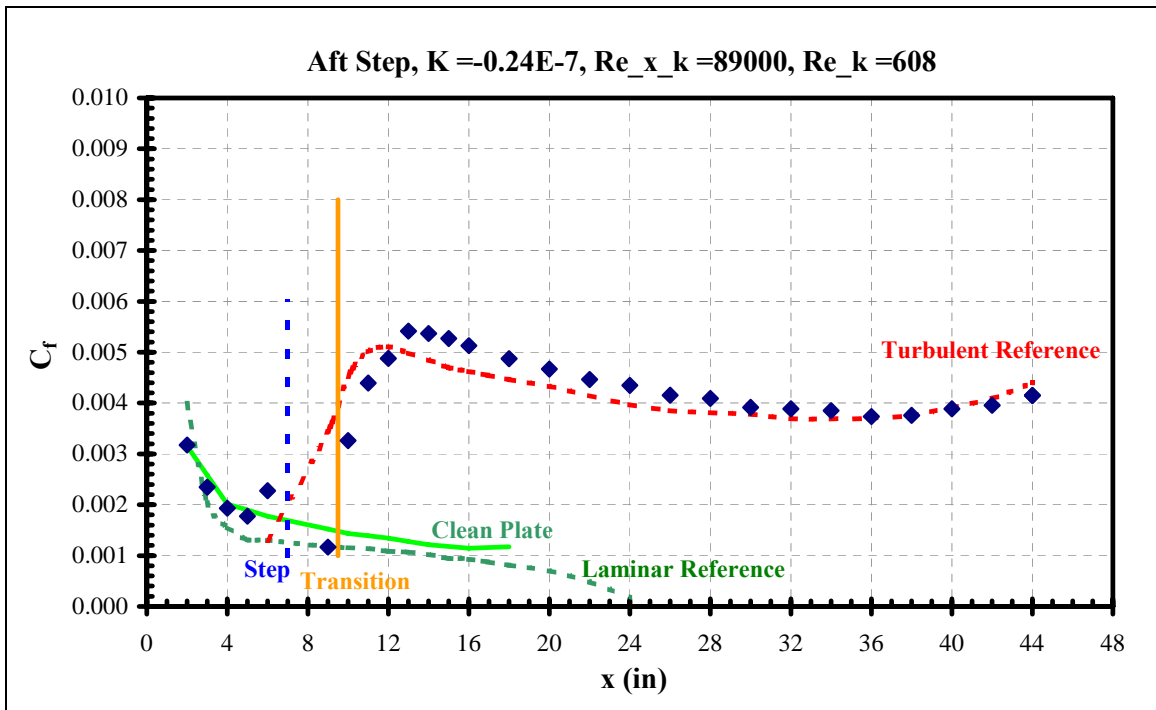


**Figure 121. Aft step skin friction distribution**

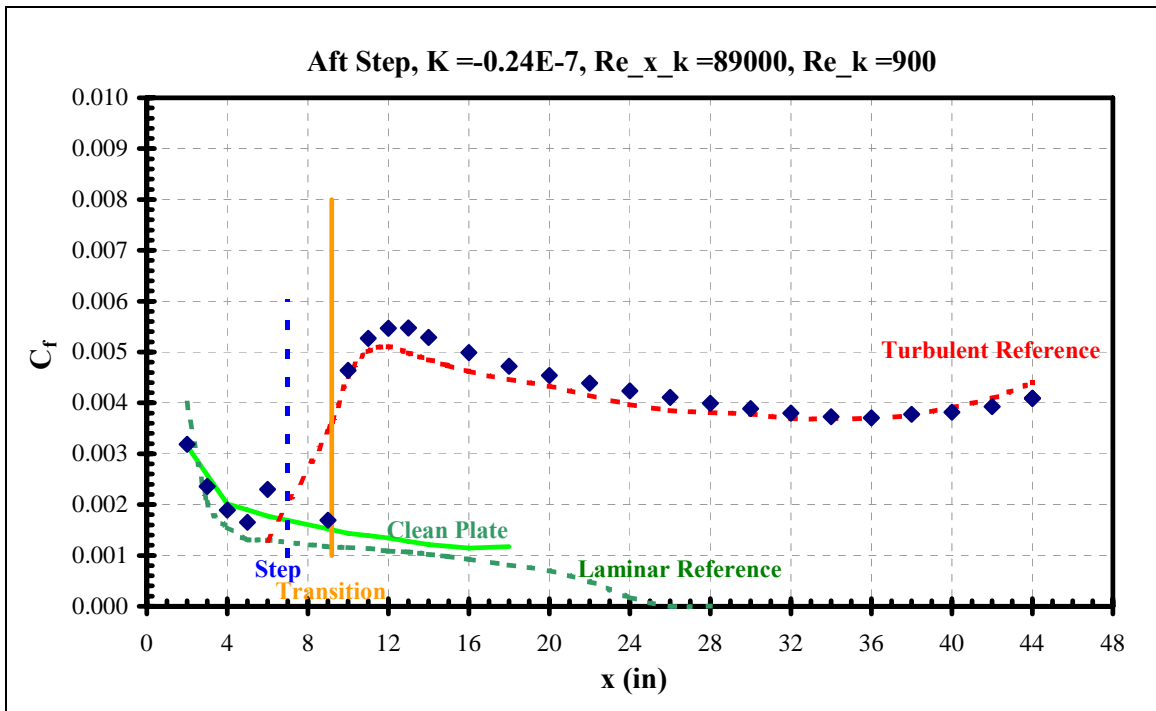


**Figure 122. Aft step skin friction distribution**

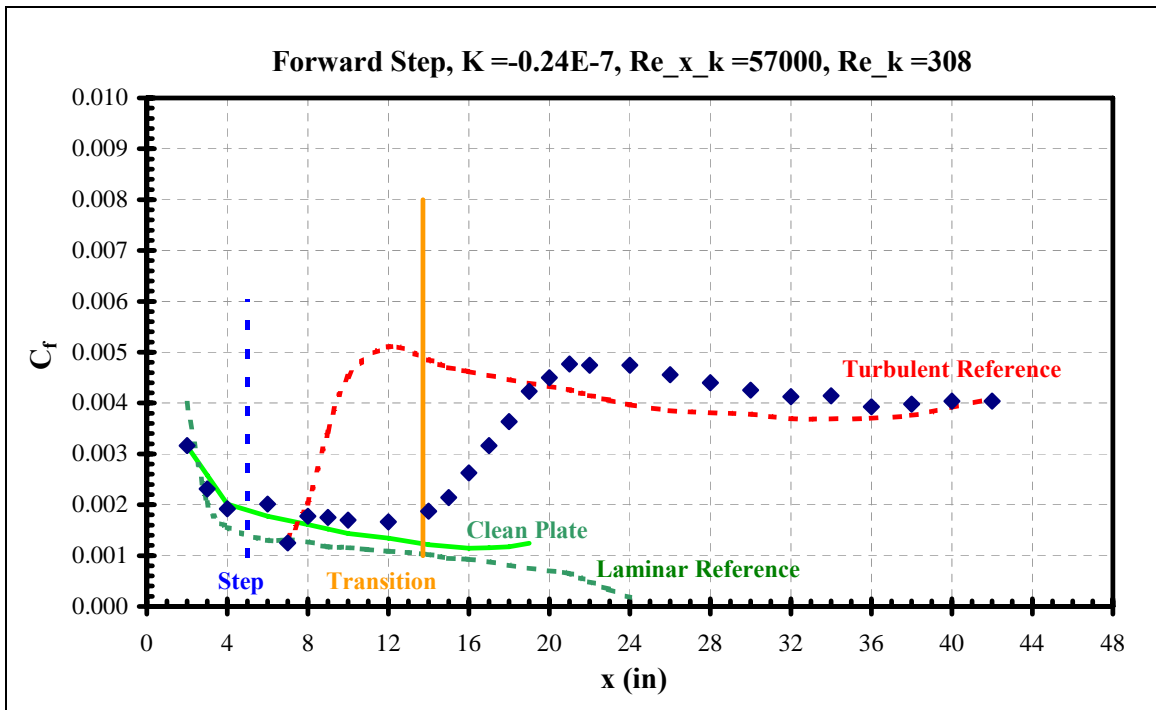


**Figure 123. Forward step skin friction distribution**

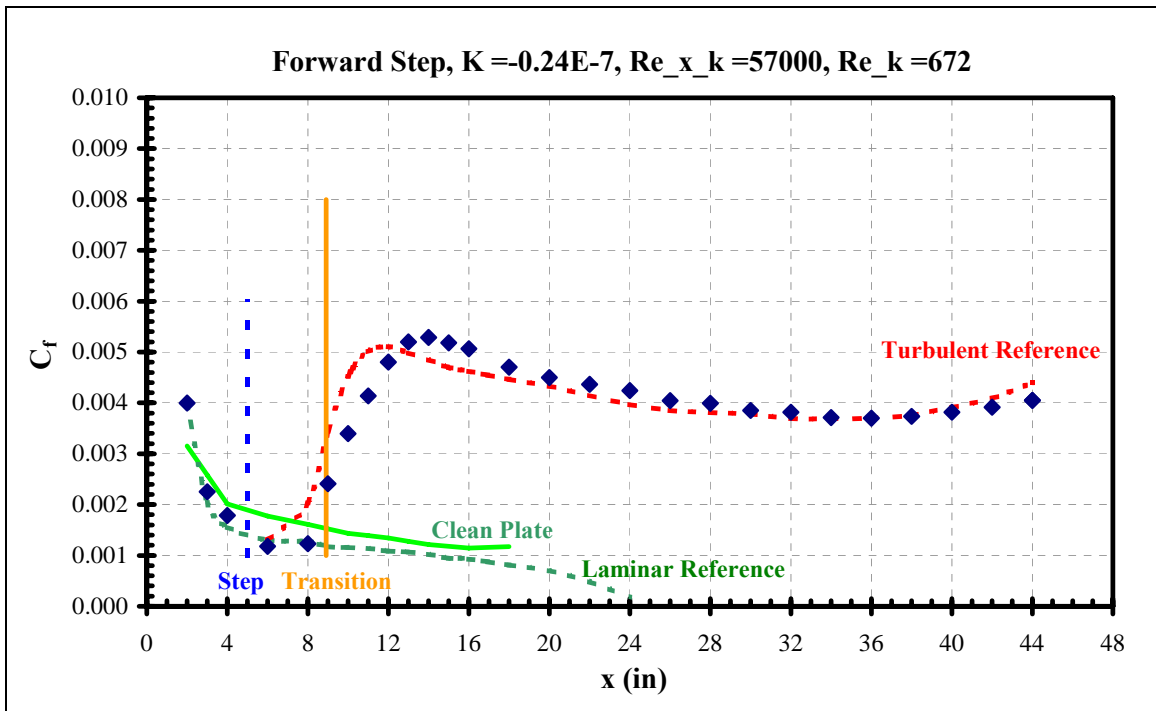


**Figure 124. Forward step skin friction distribution**

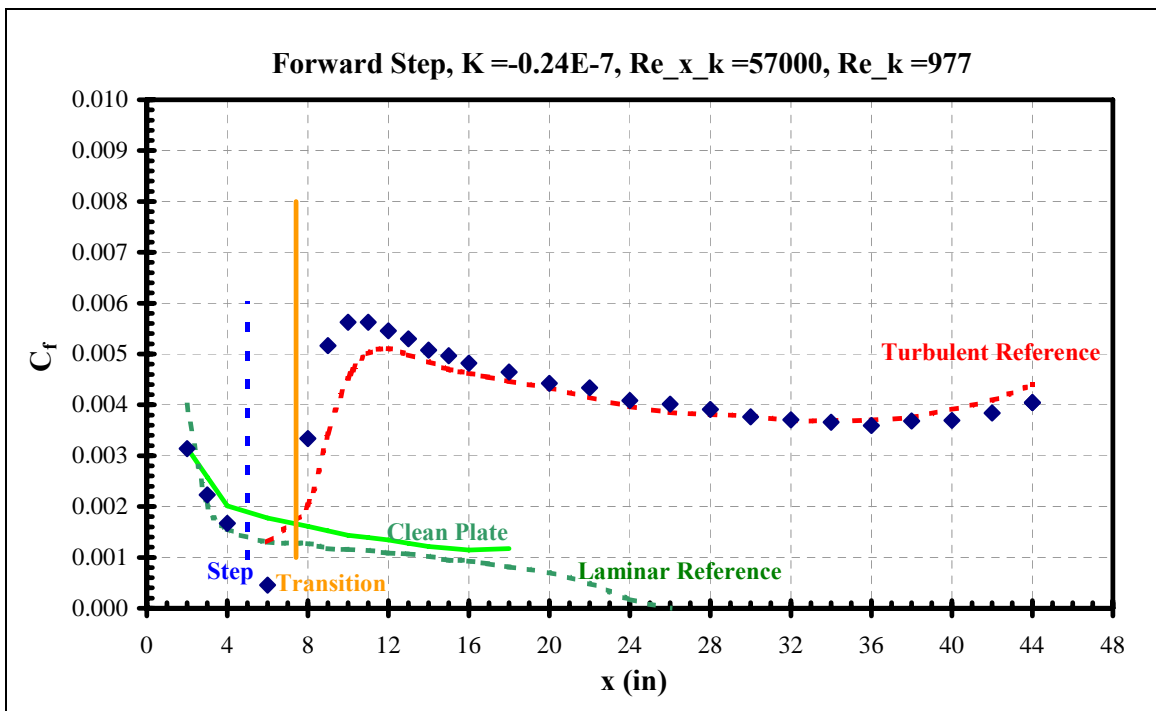


**Figure 125. Forward step skin friction distribution**

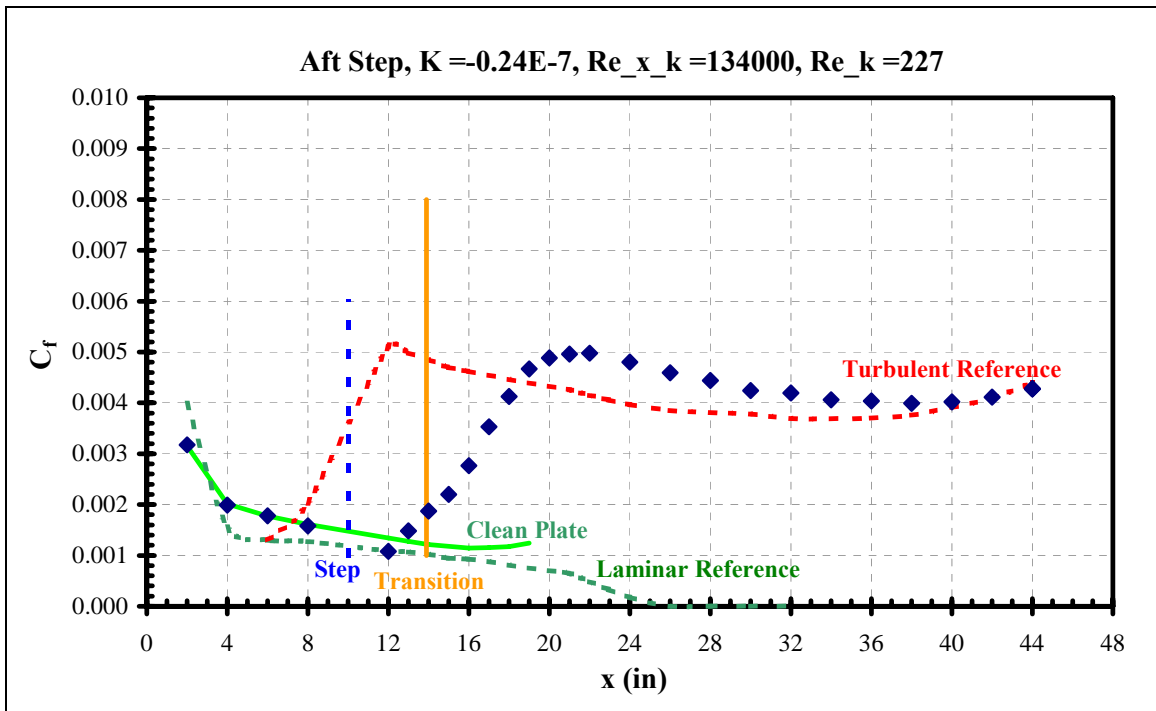


Figure 126. Aft step skin friction distribution

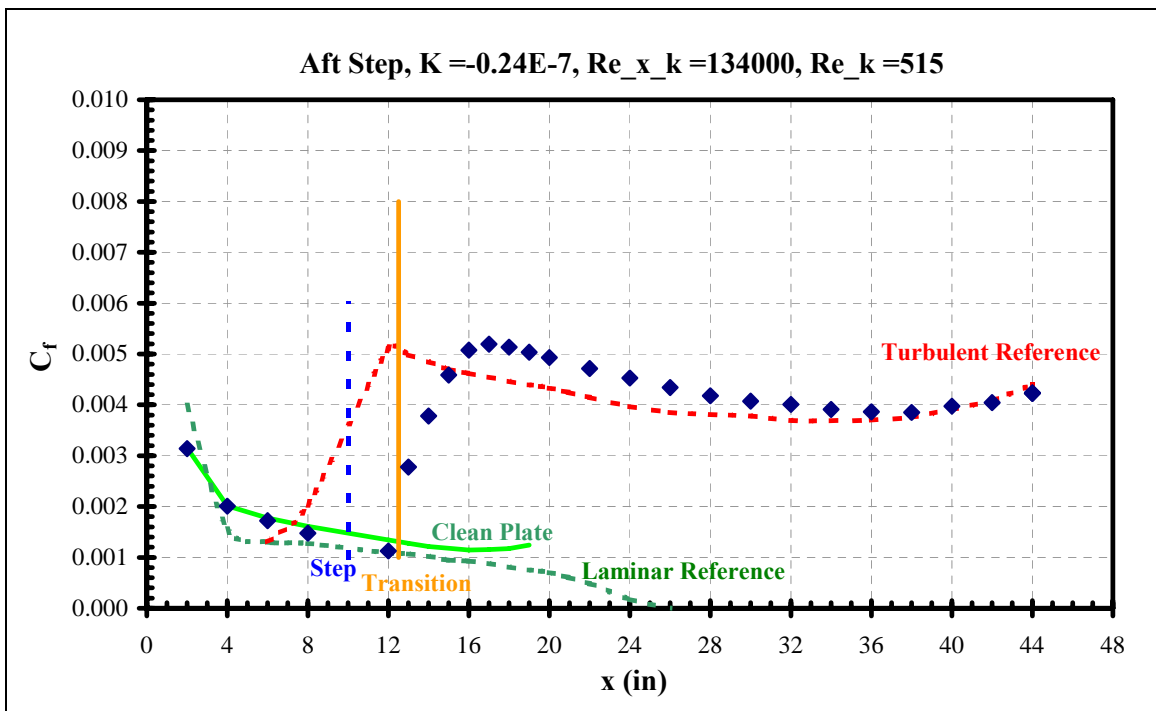
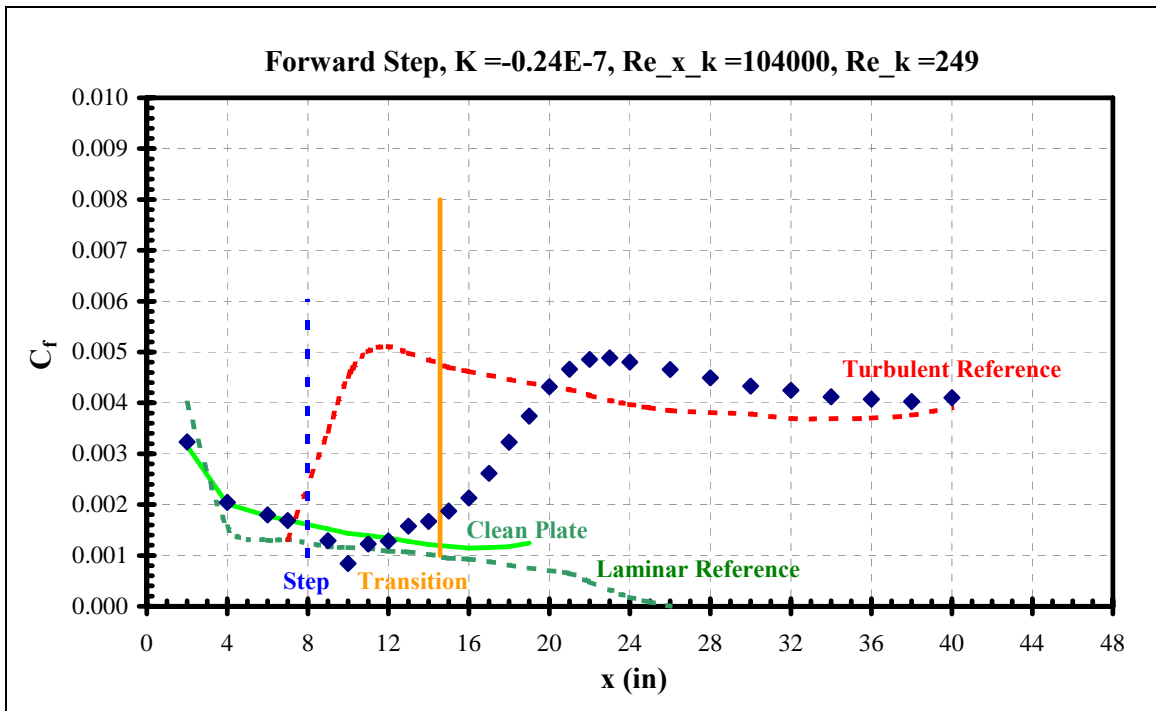
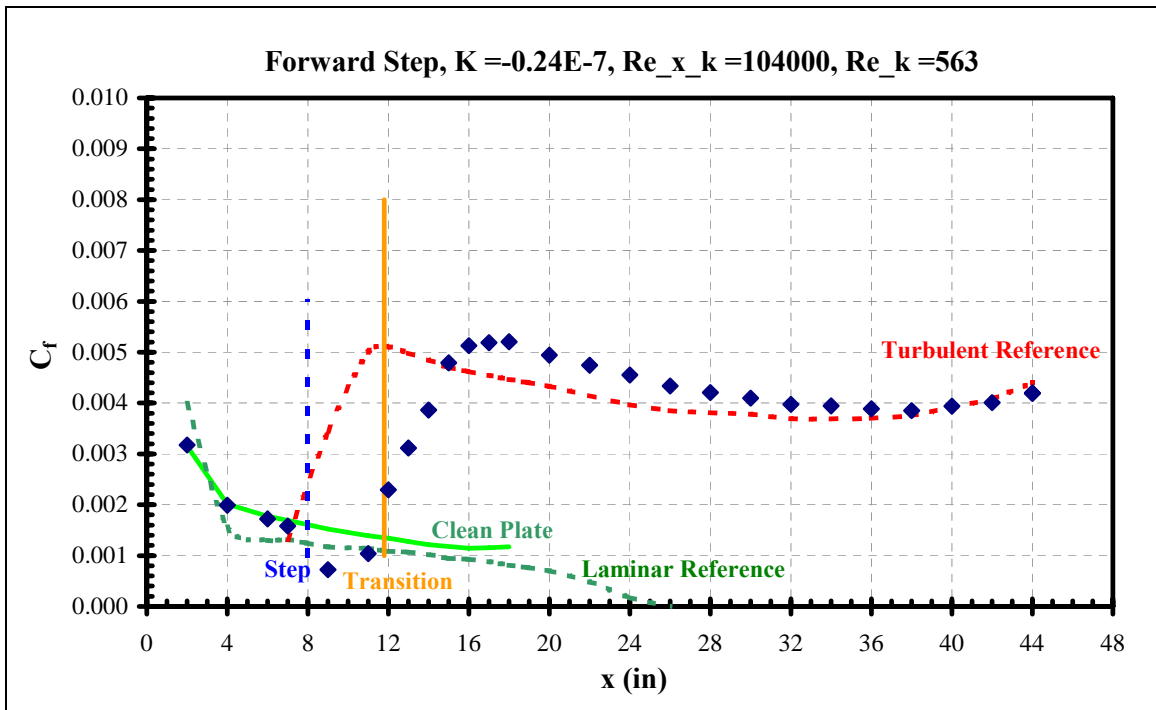


Figure 127. Aft step skin friction distribution



**Figure 128. Forward step skin friction distribution**



**Figure 129. Forward step skin friction distribution**

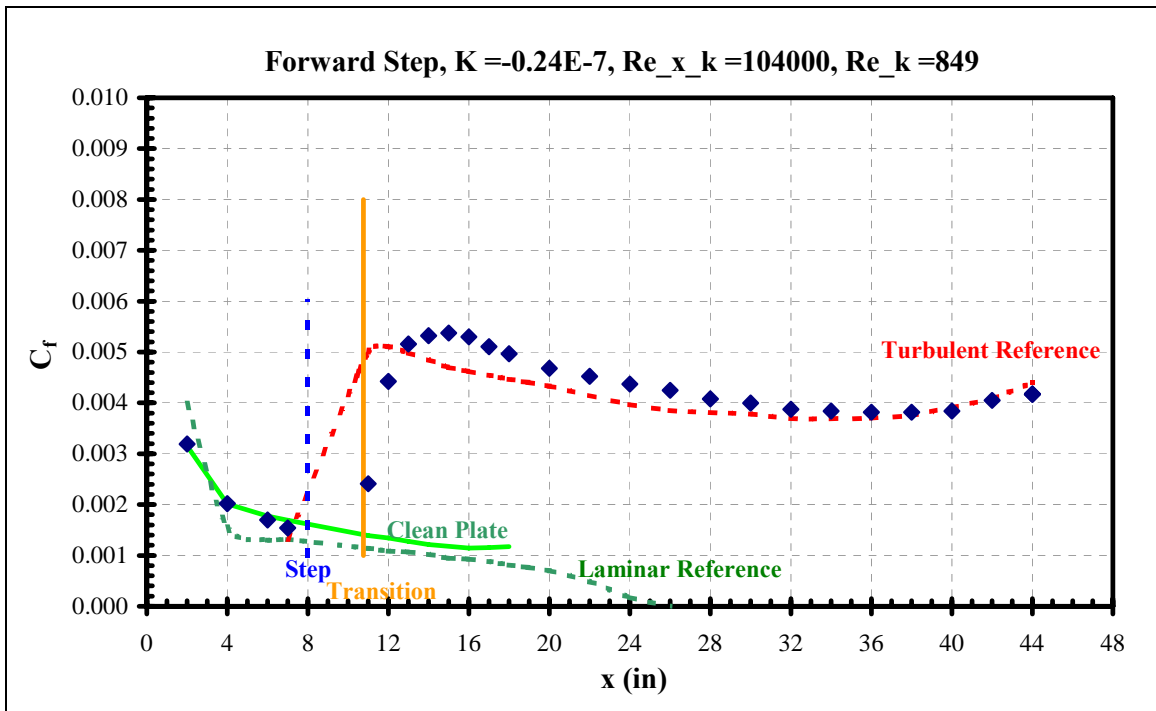


**Figure 130. Forward step skin friction distribution**

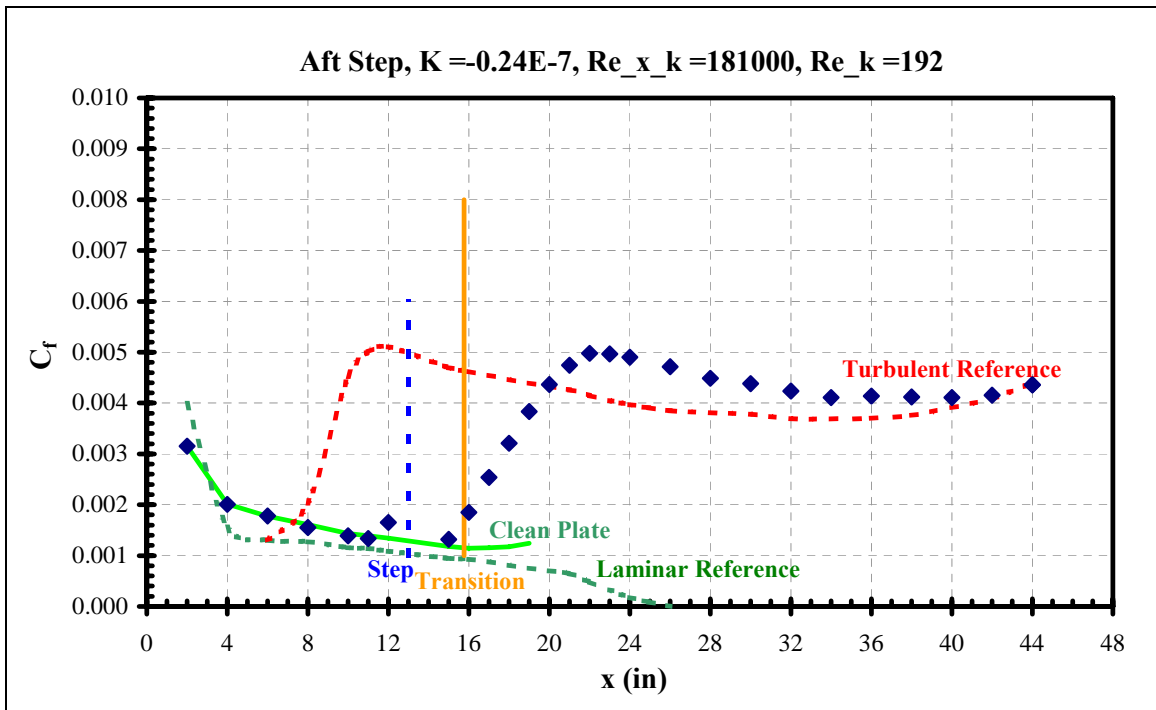


**Figure 131. Aft step skin friction distribution**



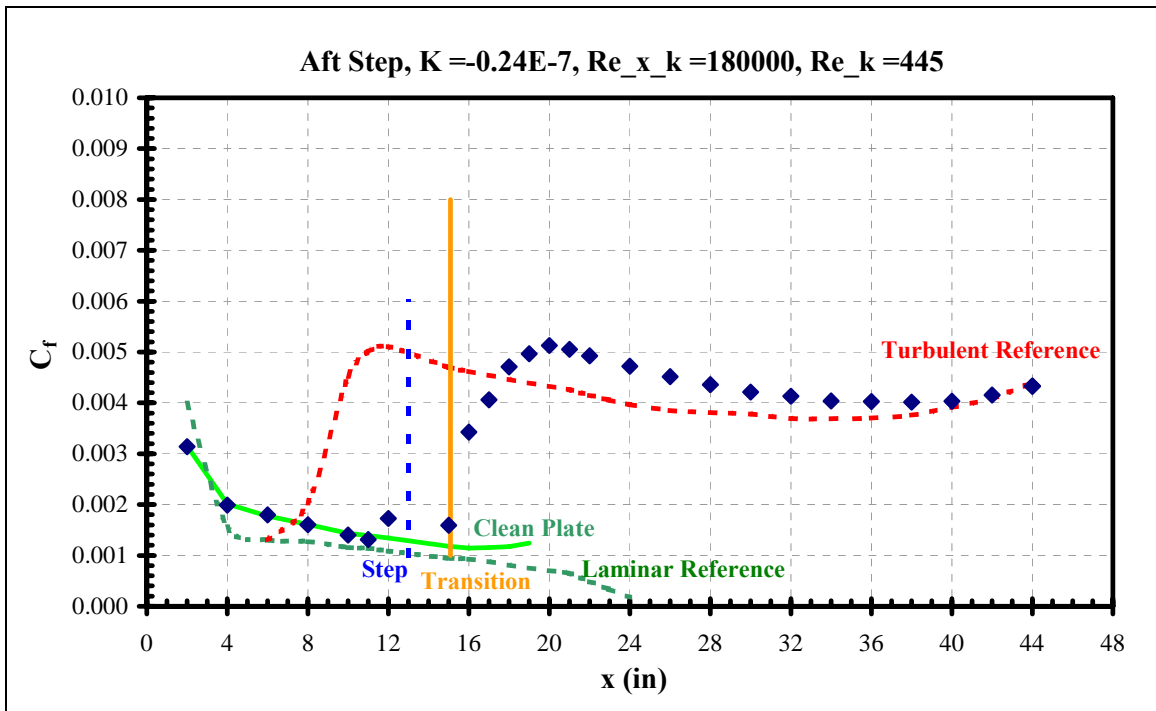


**Figure 132. Aft step skin friction distribution**

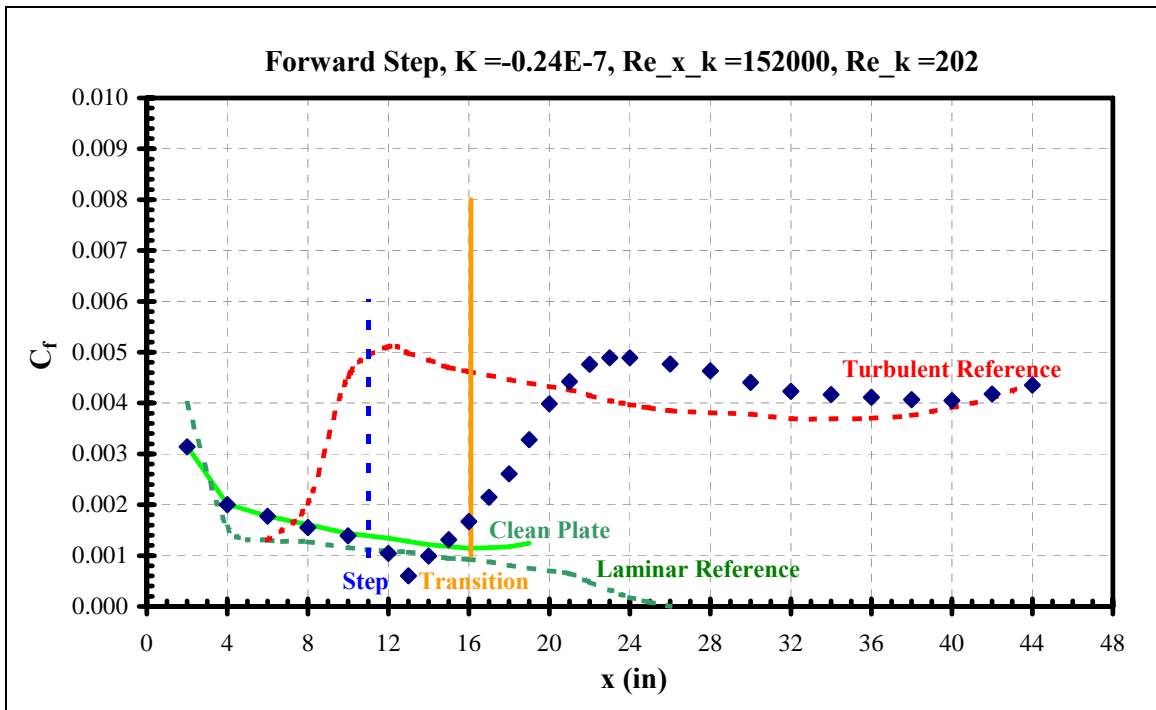


**Figure 133. Forward step skin friction distribution**

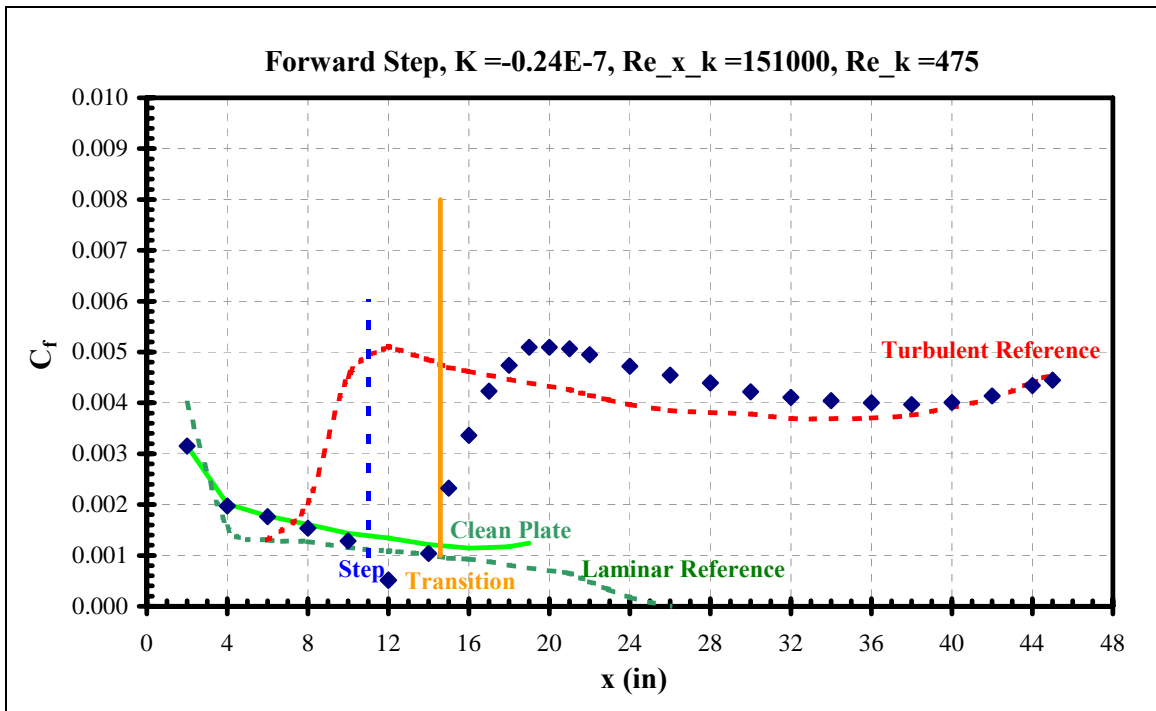


**Figure 134. Forward step skin friction distribution**

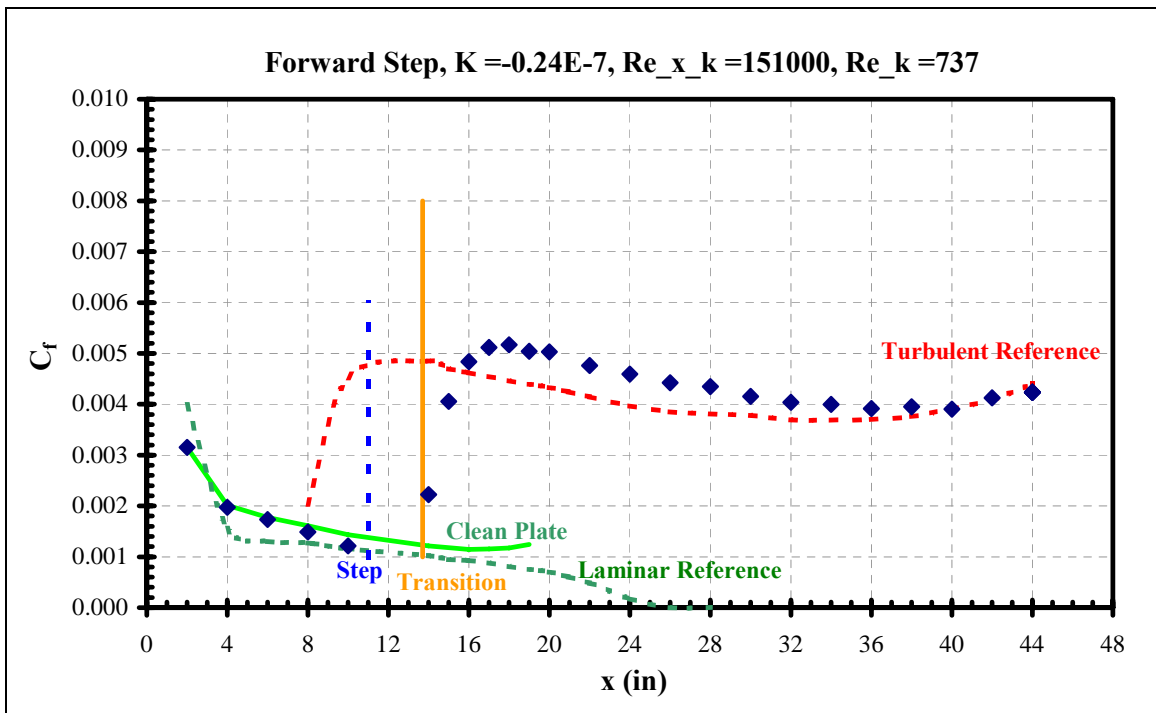


**Figure 135. Forward step skin friction distribution**

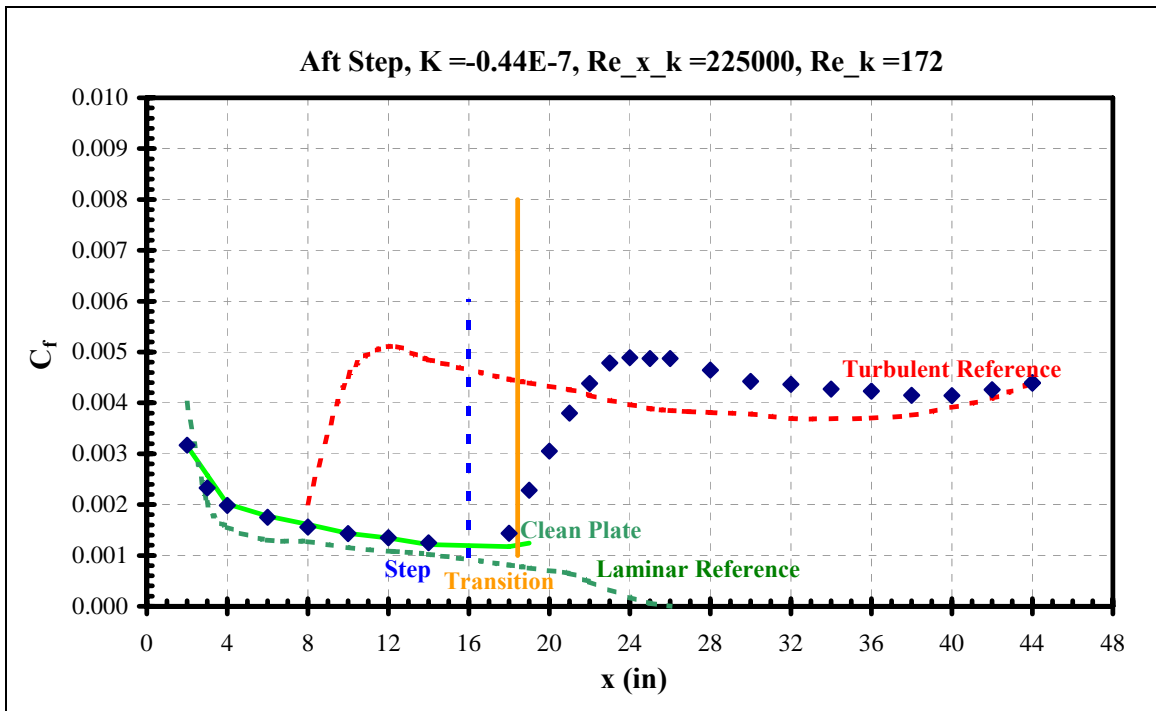


Figure 136. Aft step skin friction distribution

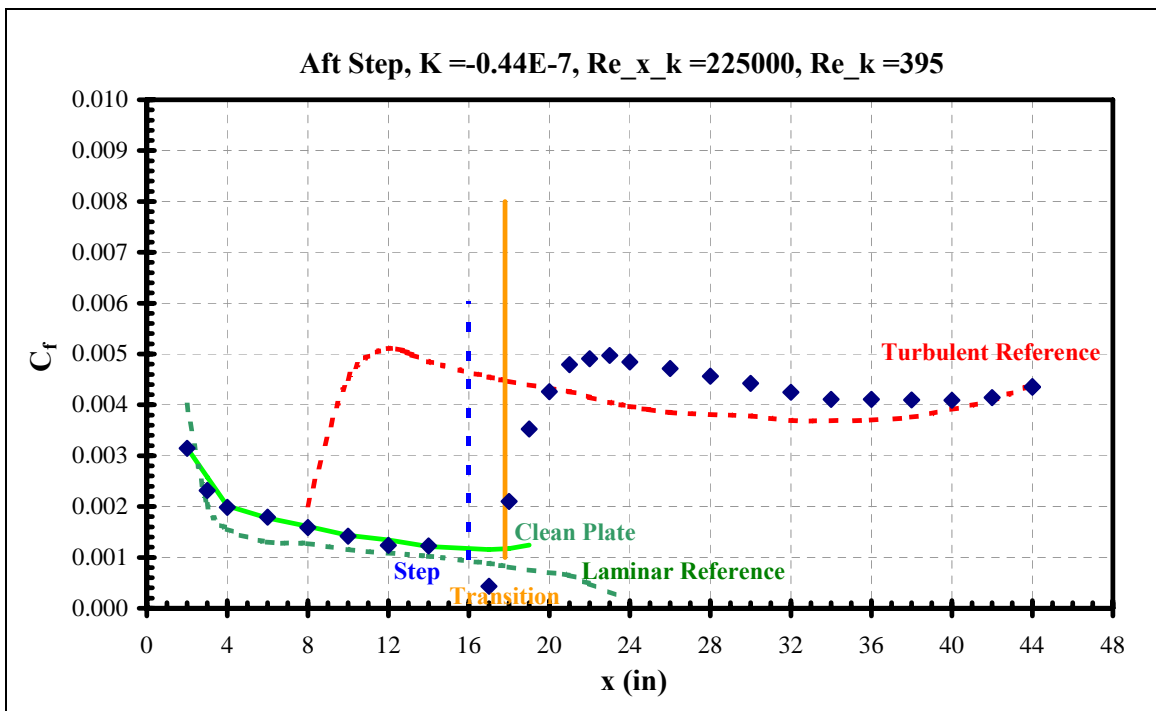
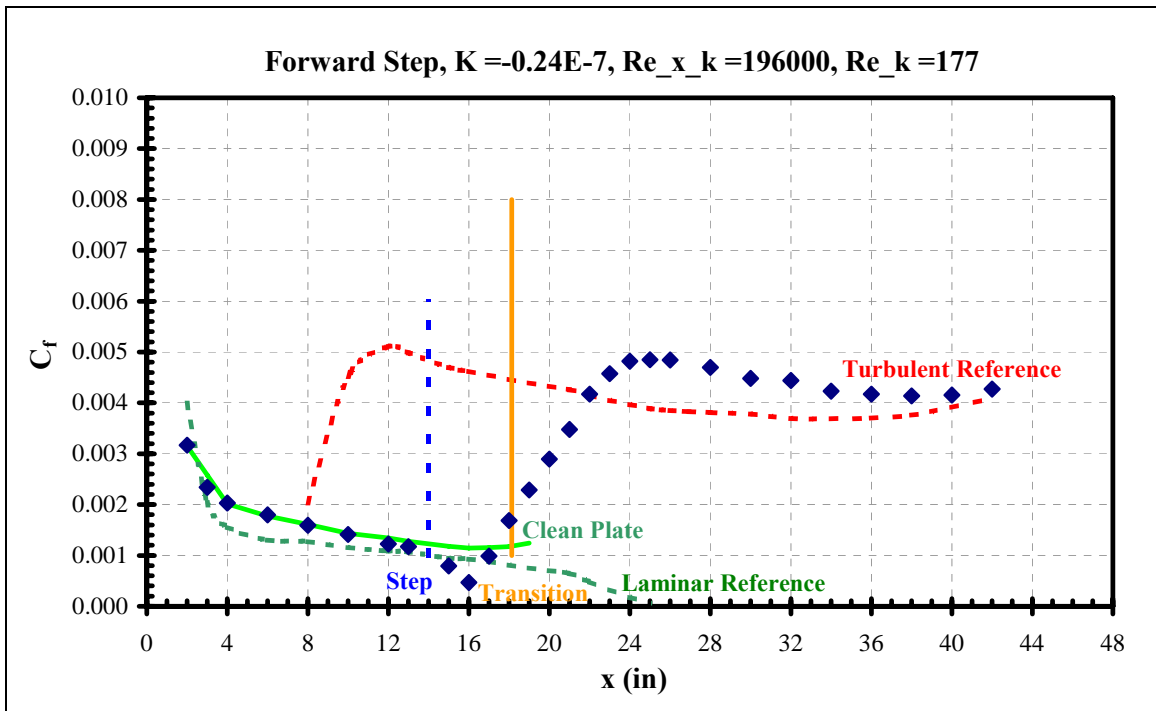
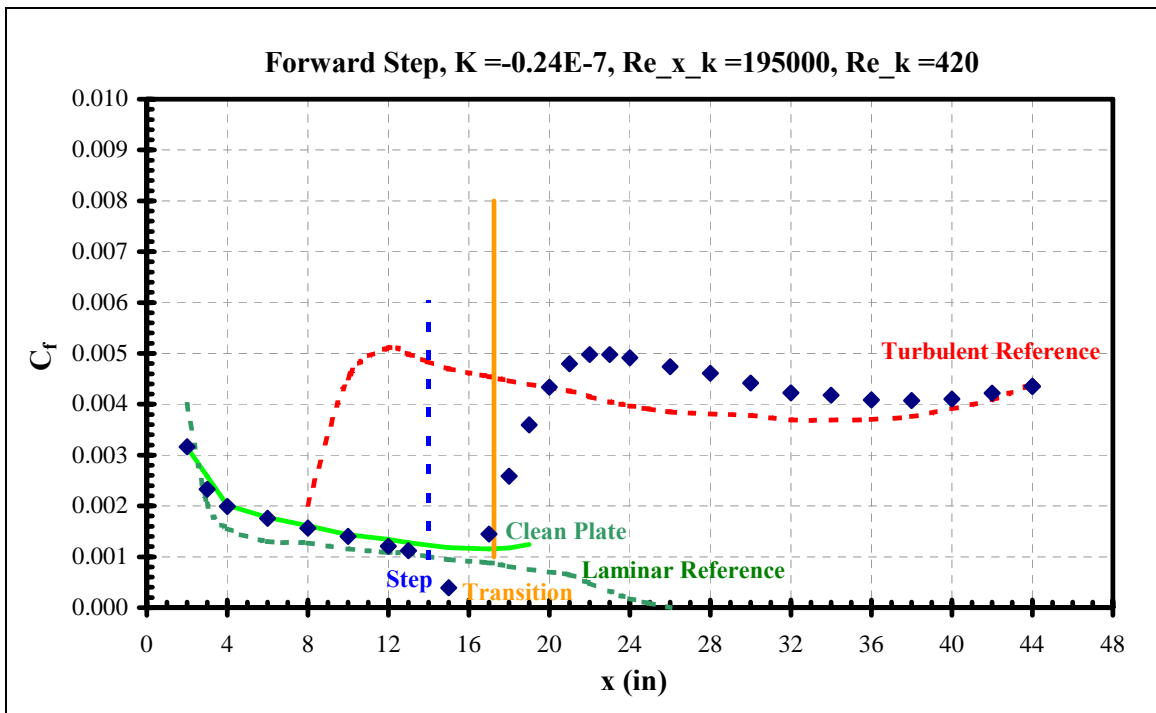


Figure 137. Aft step skin friction distribution



**Figure 138. Forward step skin friction distribution**



**Figure 139. Forward step skin friction distribution**

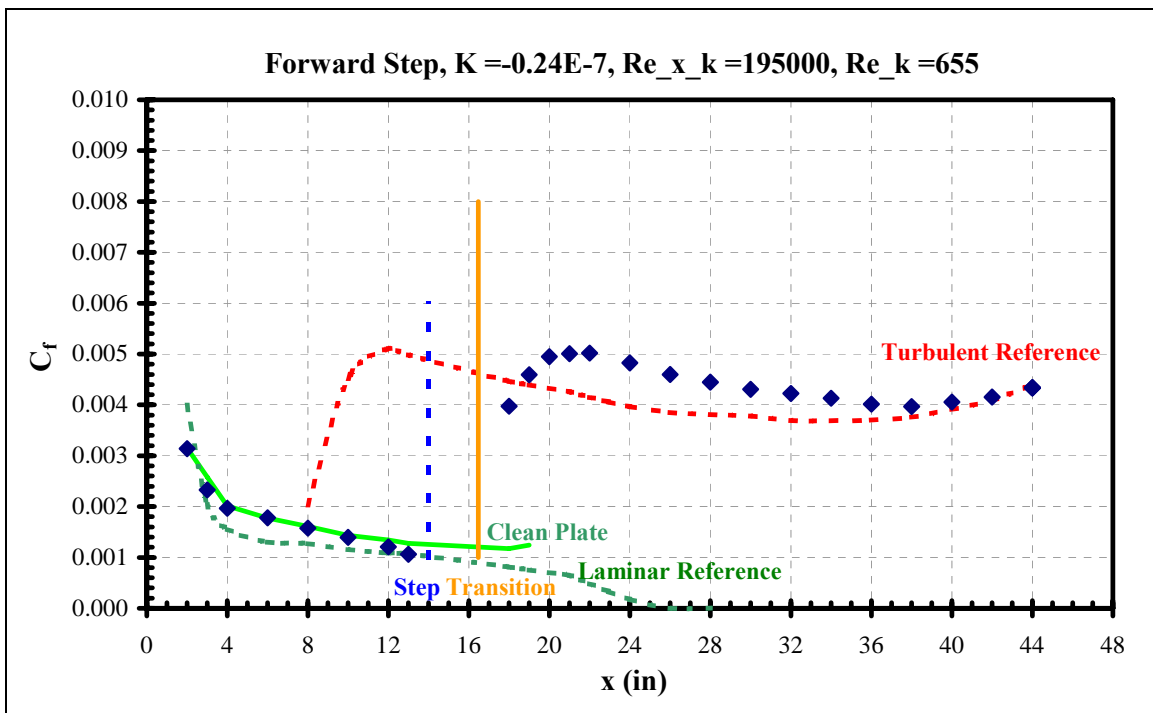


**Figure 140. Forward step skin friction distribution**

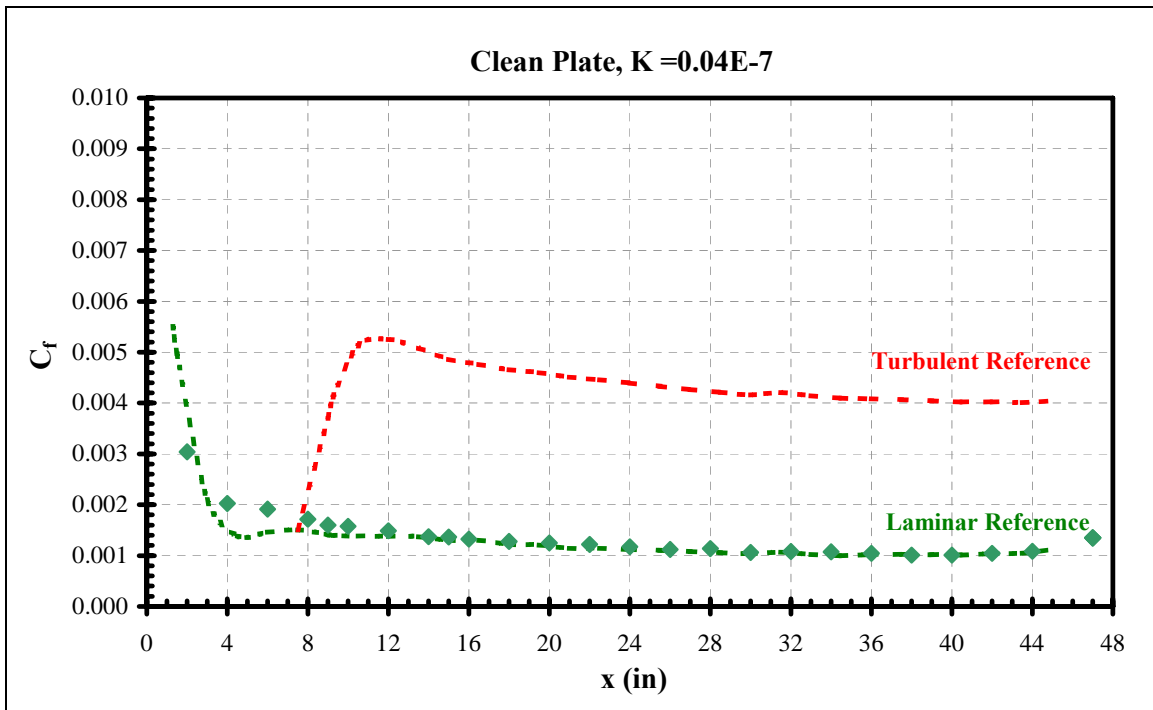


**Figure 141. Clean plate skin friction distribution**

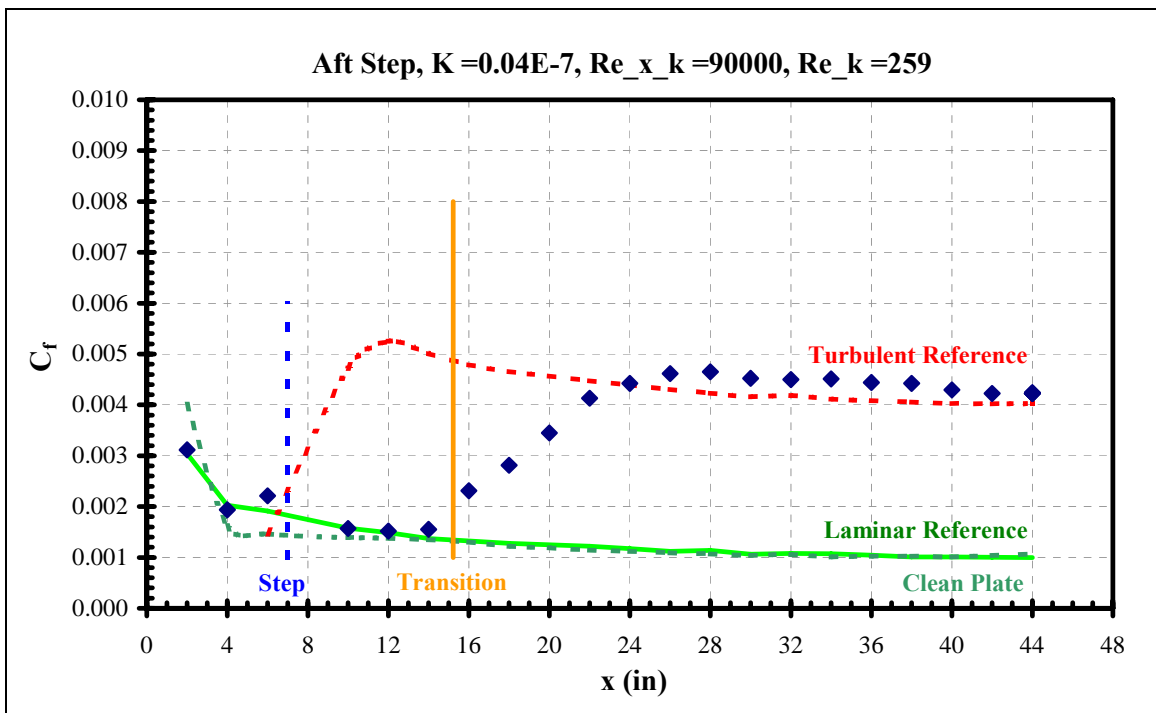


**Figure 142. Aft step skin friction distribution**

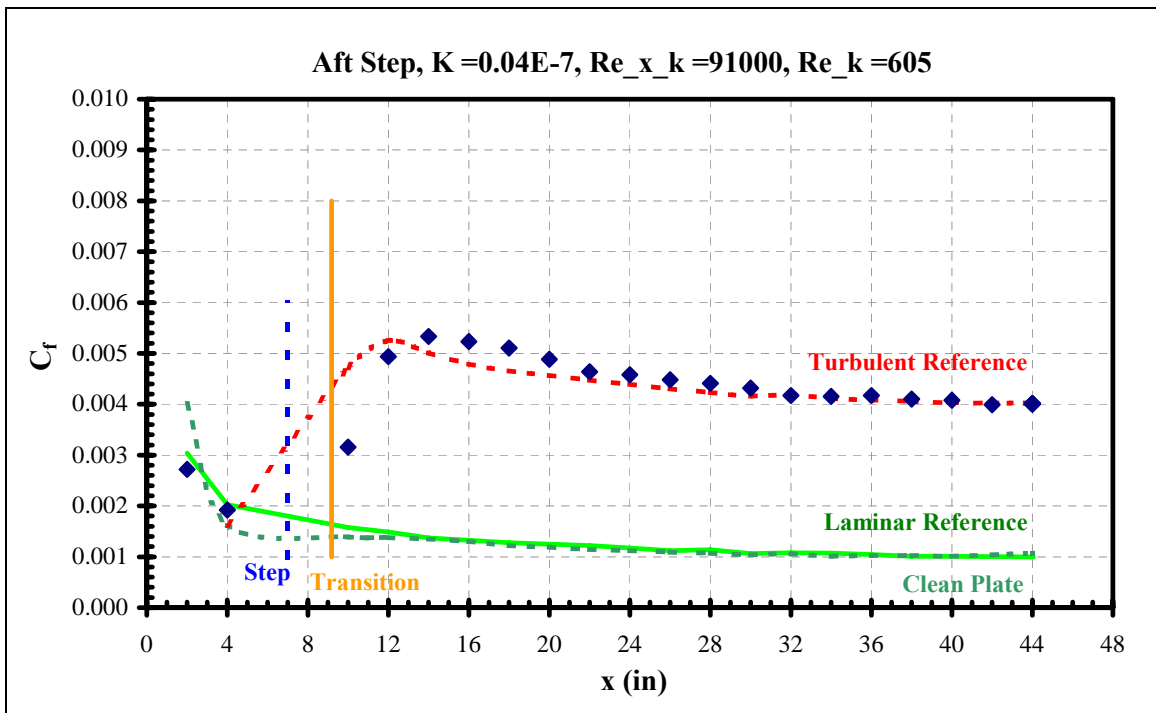


**Figure 143. Aft step skin friction distribution**

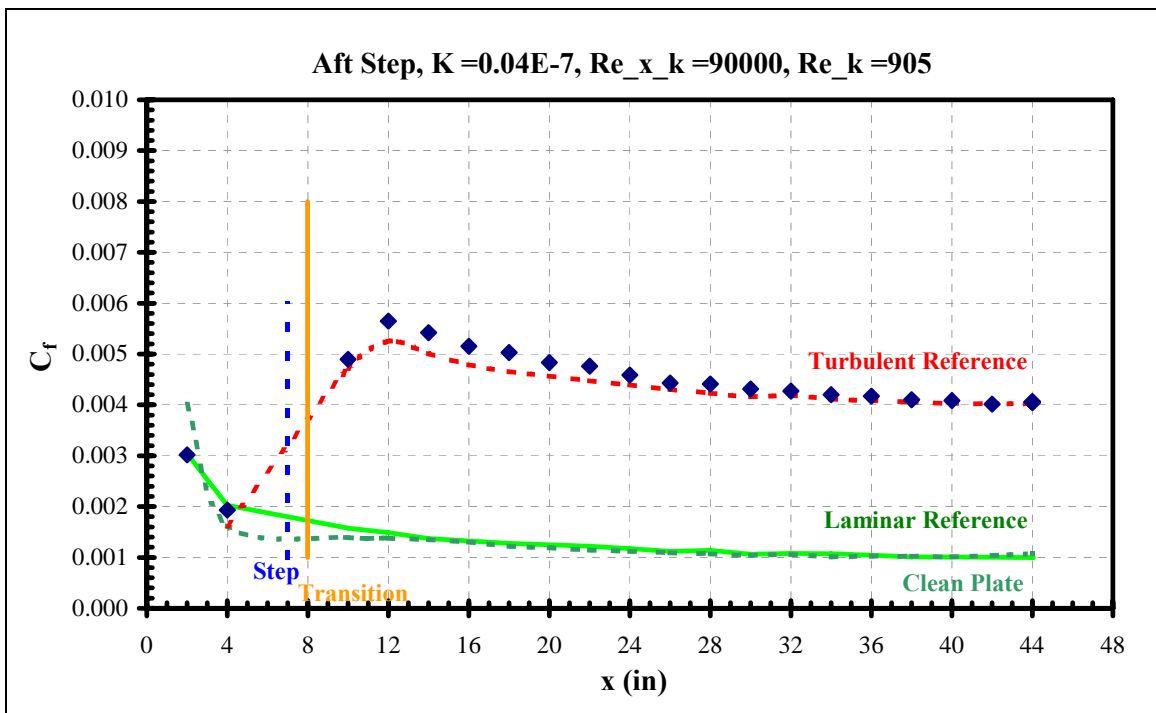


**Figure 144. Aft step skin friction distribution**

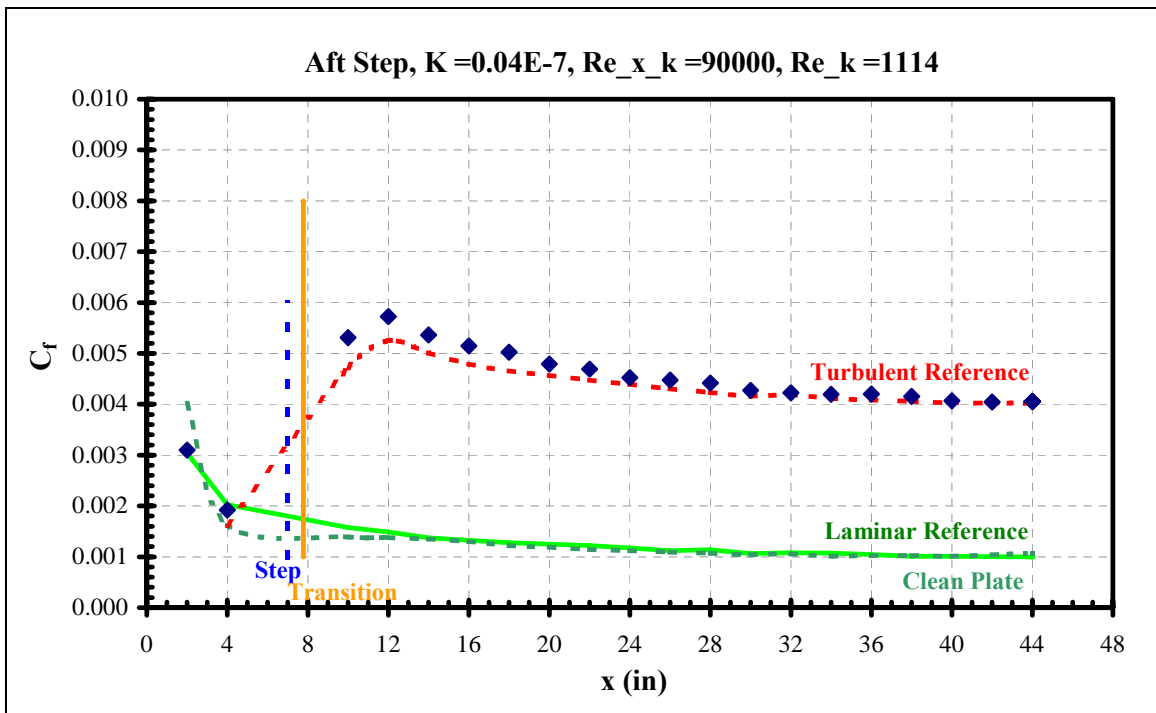


**Figure 145. Aft step skin friction distribution**

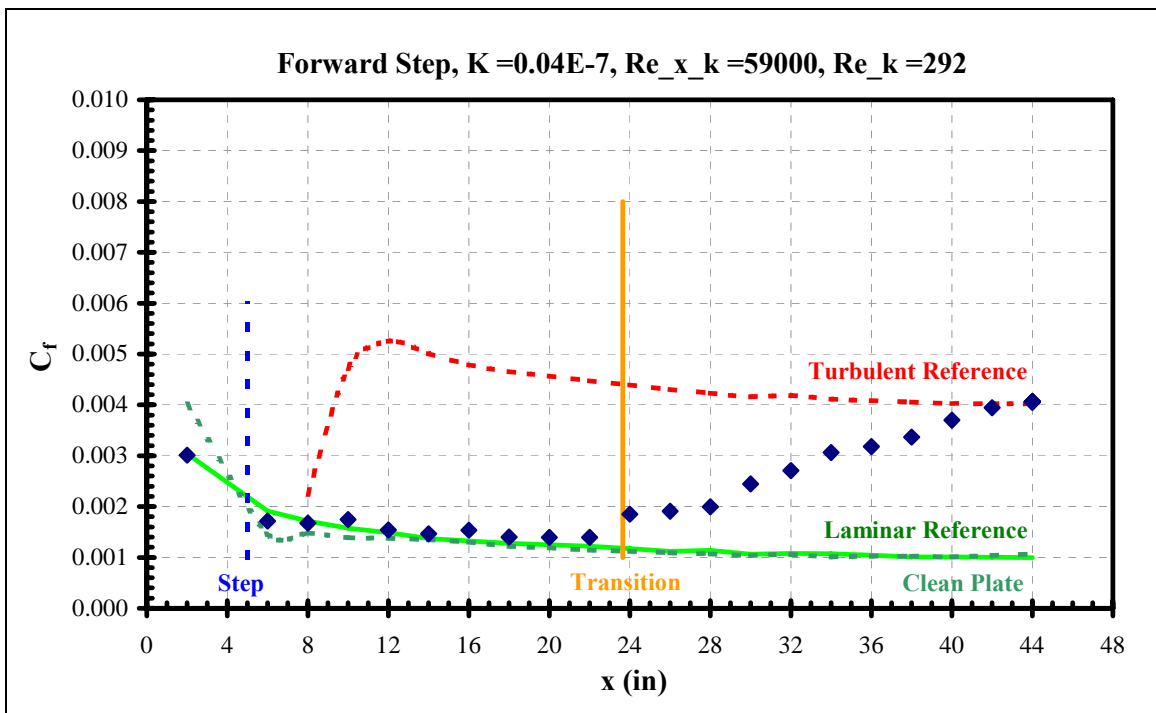


**Figure 146. Forward step skin friction distribution**

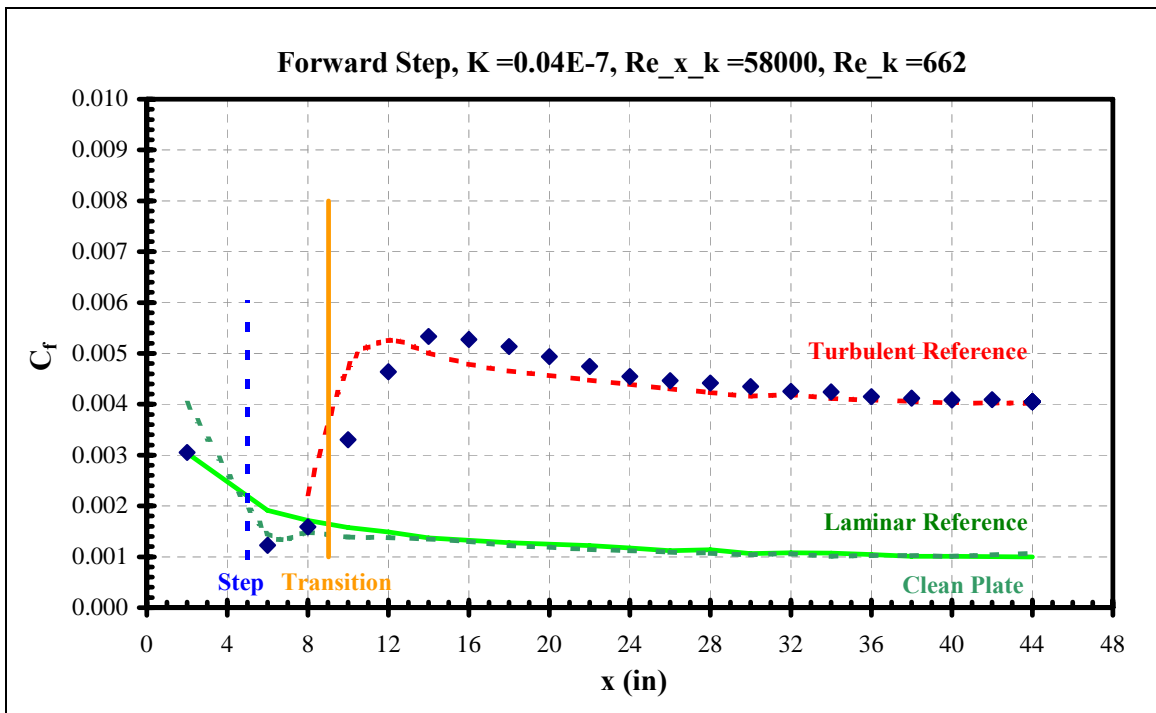


**Figure 147. Forward step skin friction distribution**



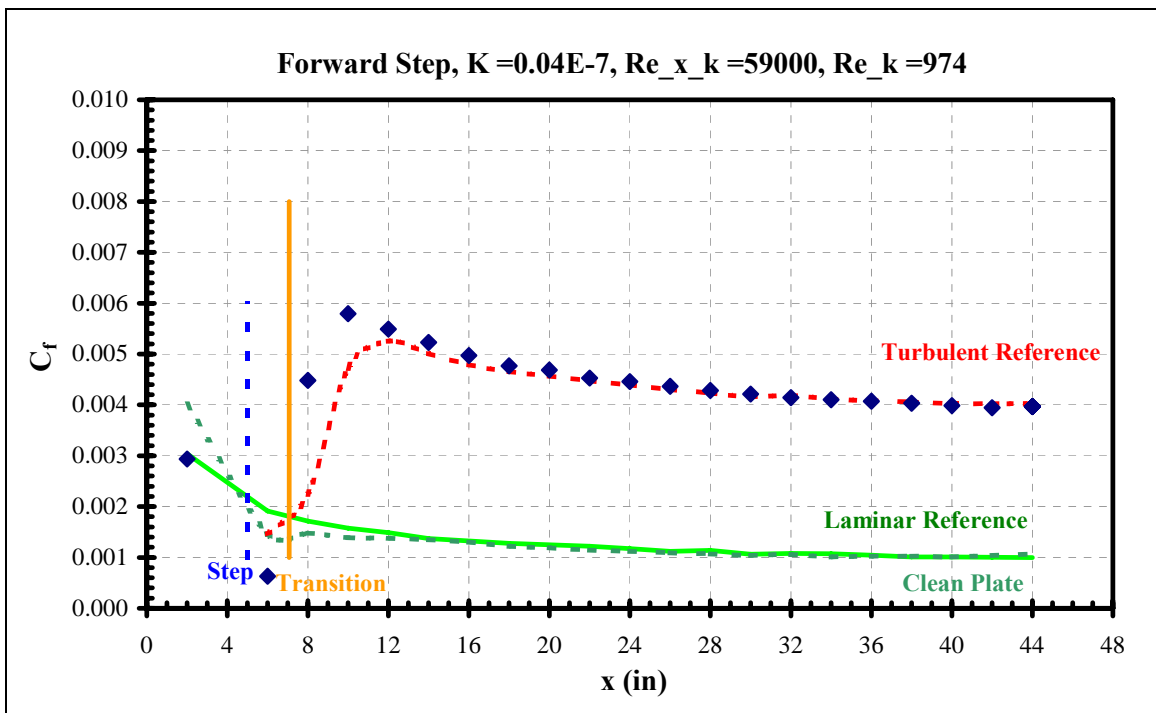


**Figure 148. Forward step skin friction distribution**

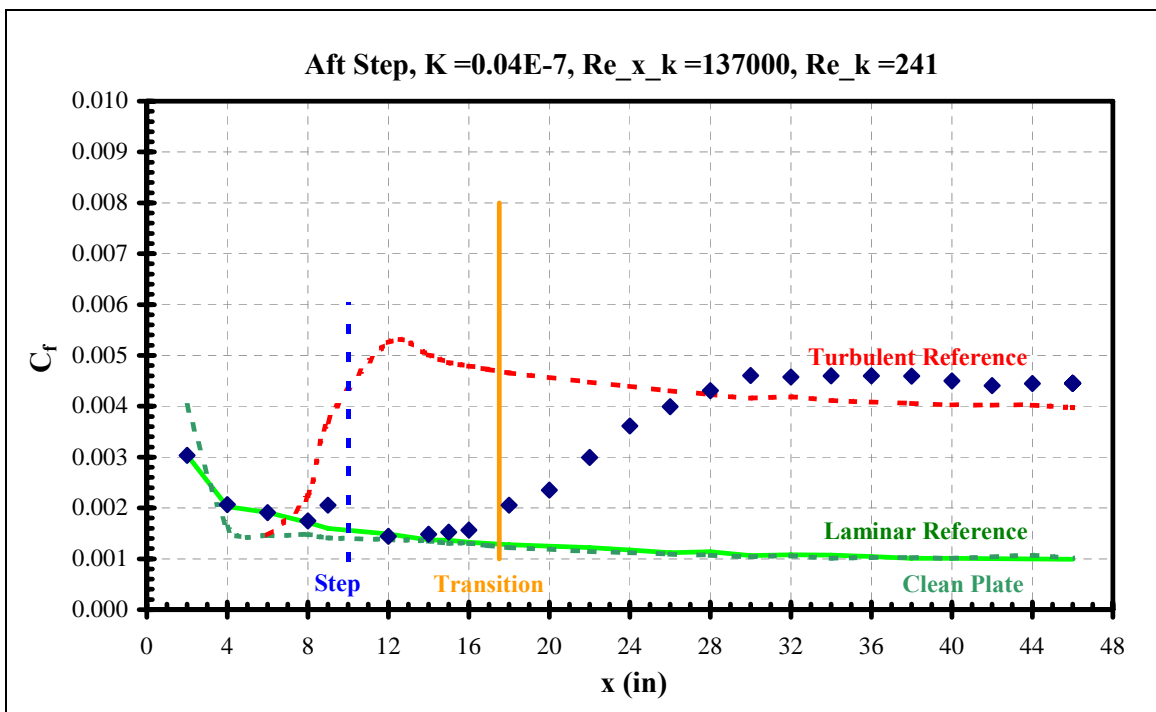


**Figure 149. Aft step skin friction distribution**

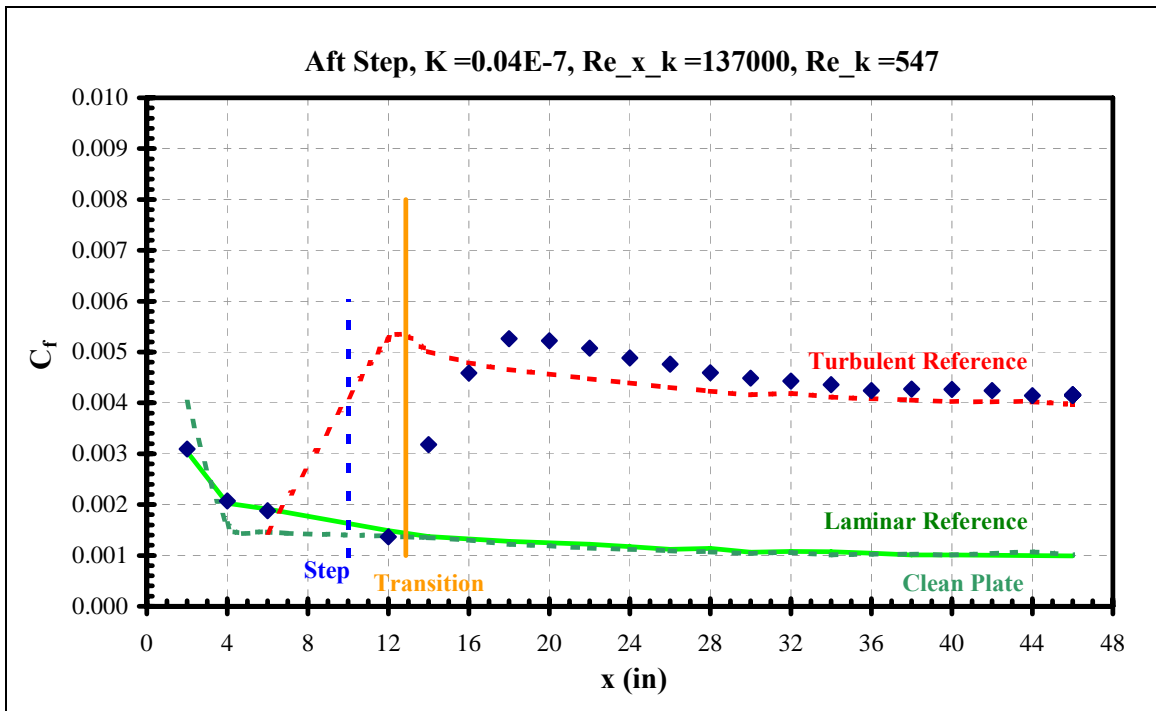


**Figure 150. Aft step skin friction distribution**

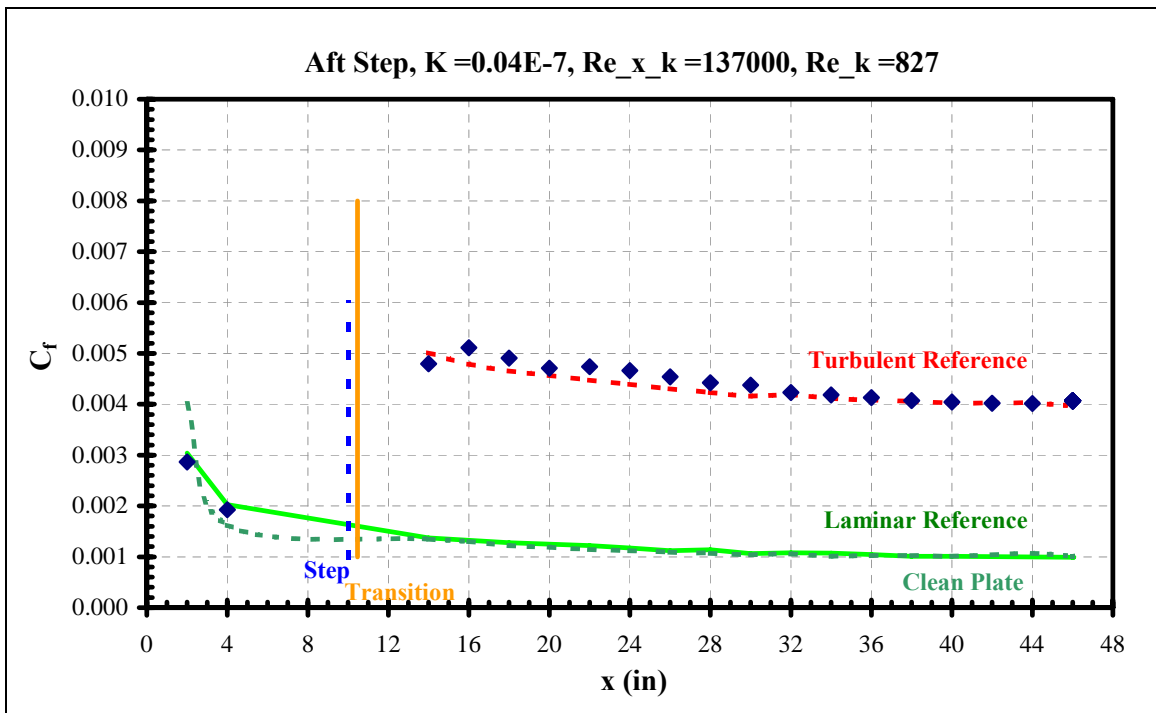


**Figure 151. Aft step skin friction distribution**

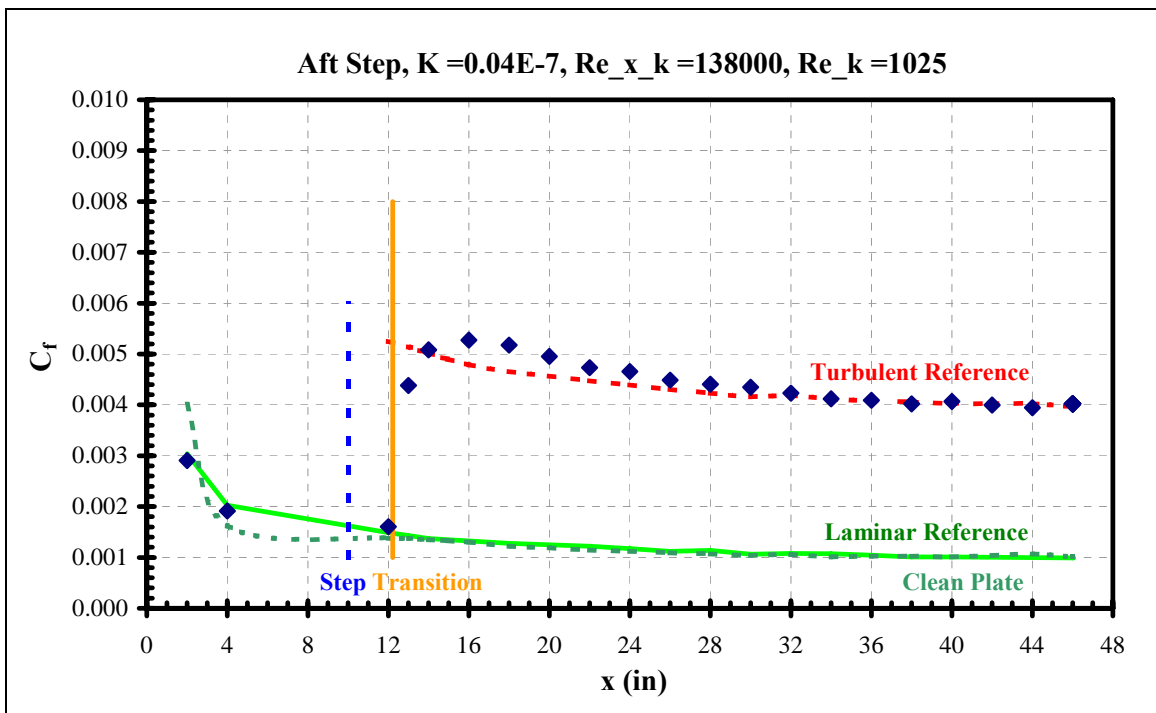


**Figure 152. Aft step skin friction distribution**

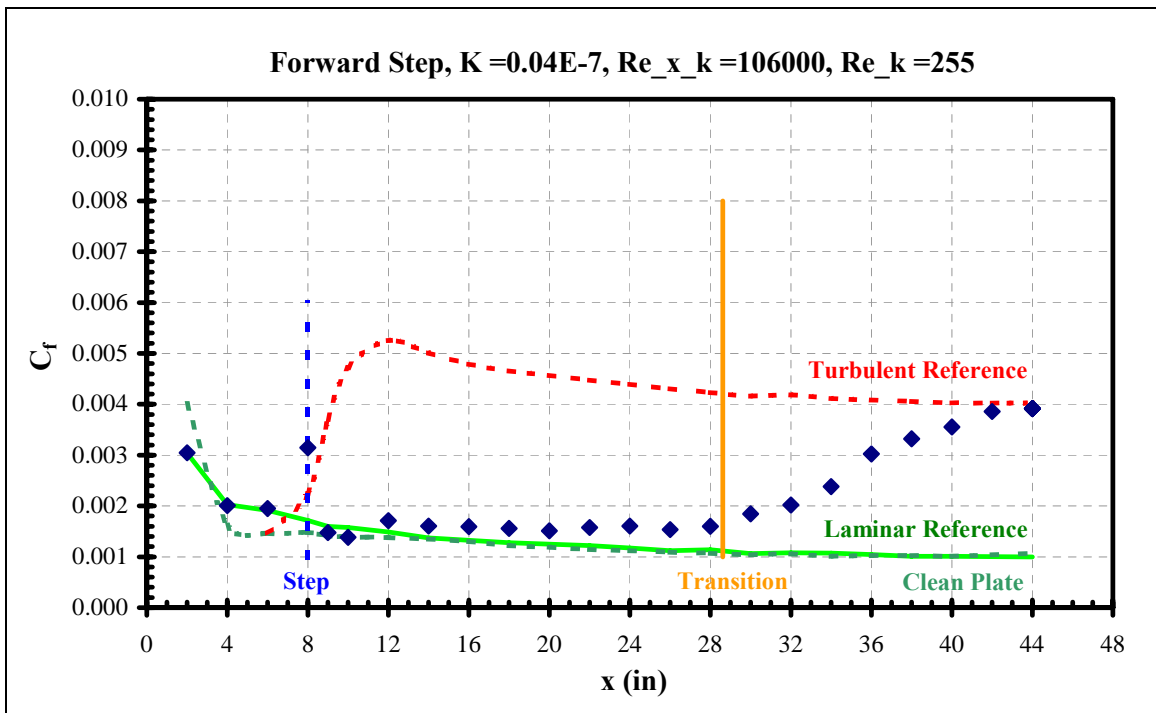


**Figure 153. Forward step skin friction distribution**

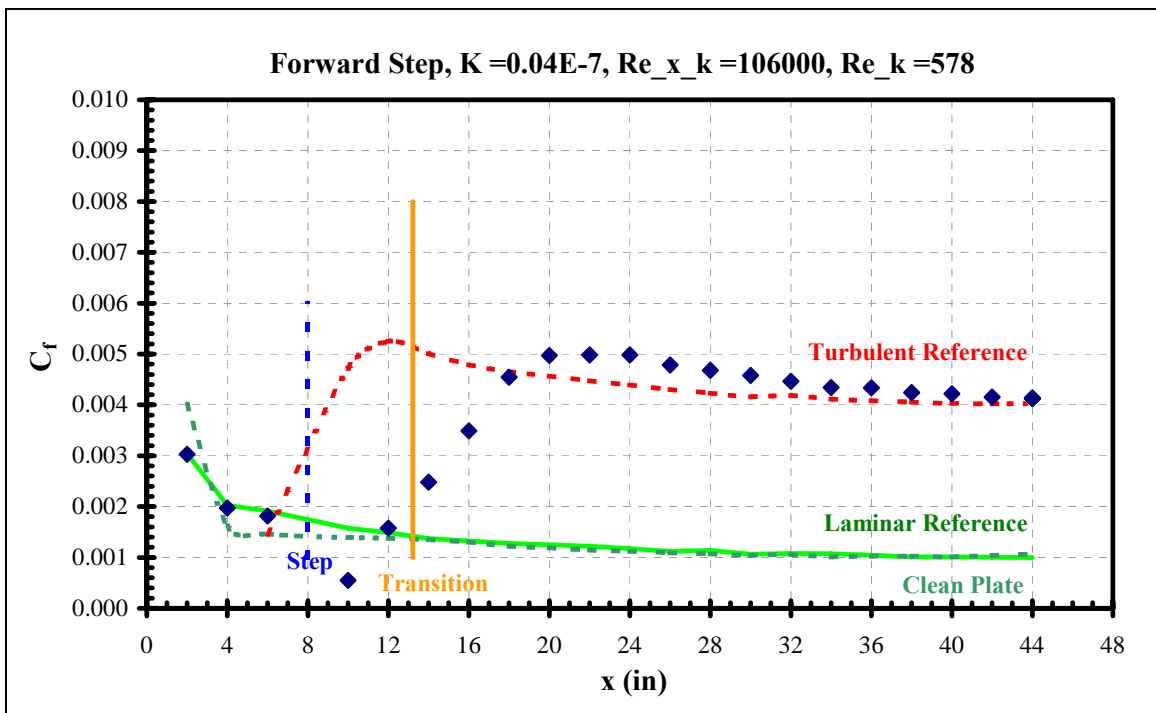


**Figure 154. Forward step skin friction distribution**

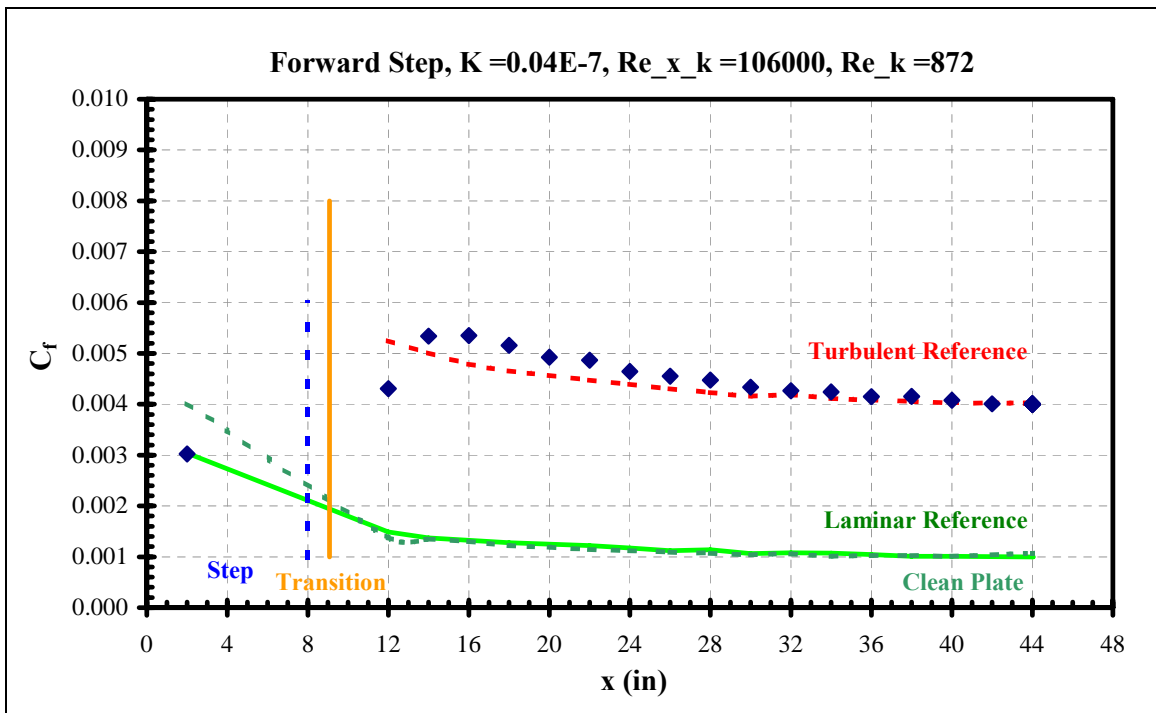


**Figure 155. Forward step skin friction distribution**

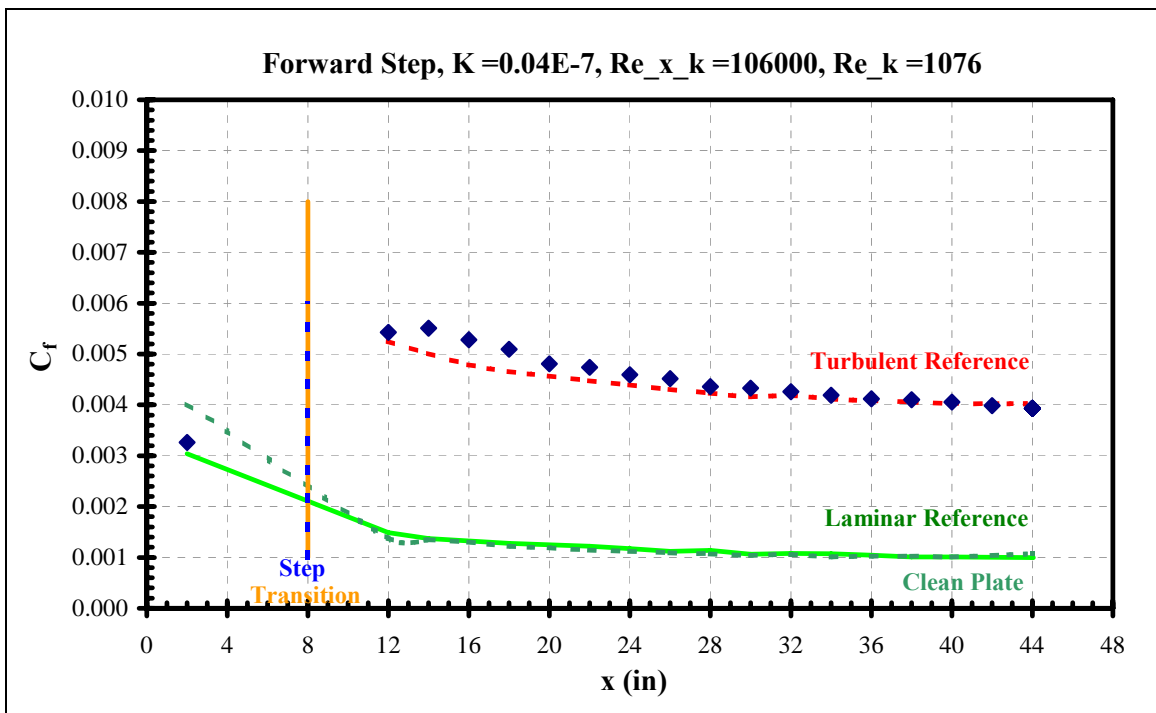


**Figure 156. Forward step skin friction distribution**

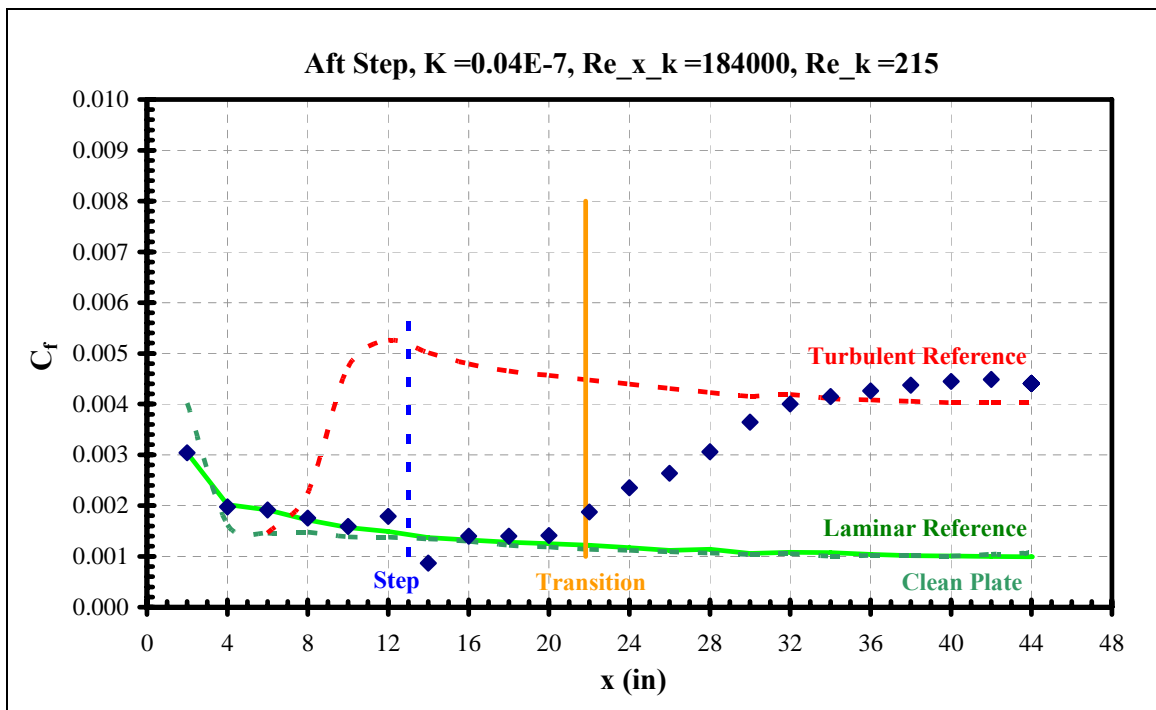


**Figure 157. Aft step skin friction distribution**

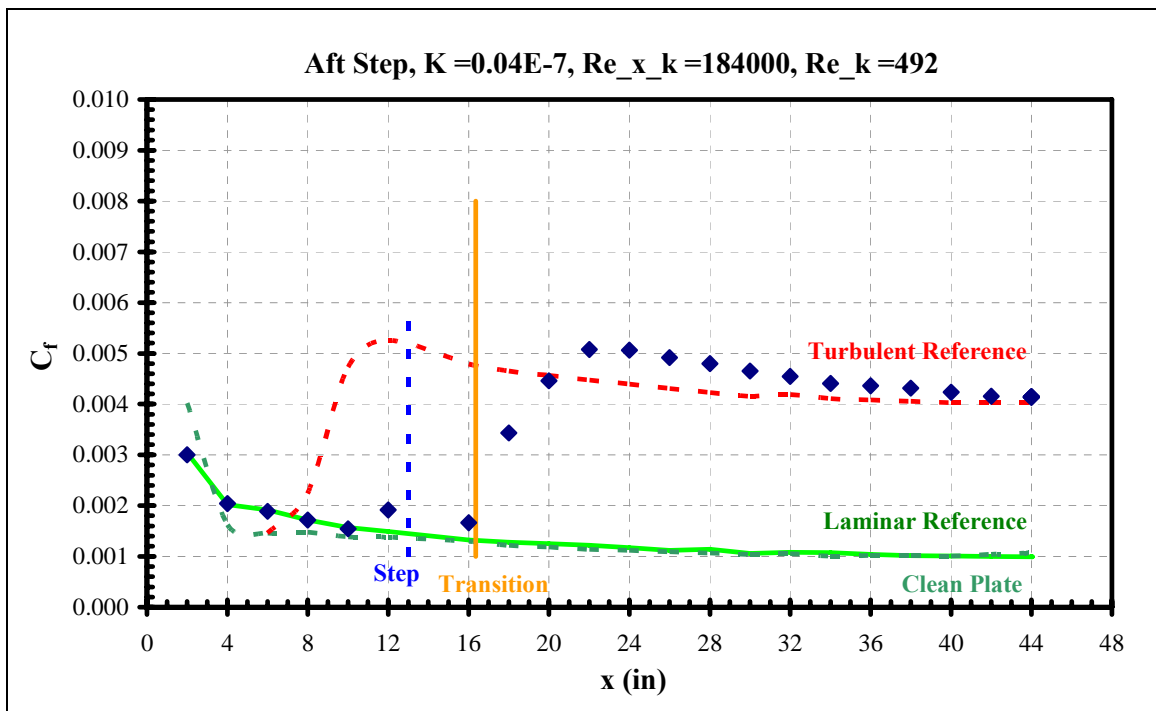


**Figure 158. Aft step skin friction distribution**

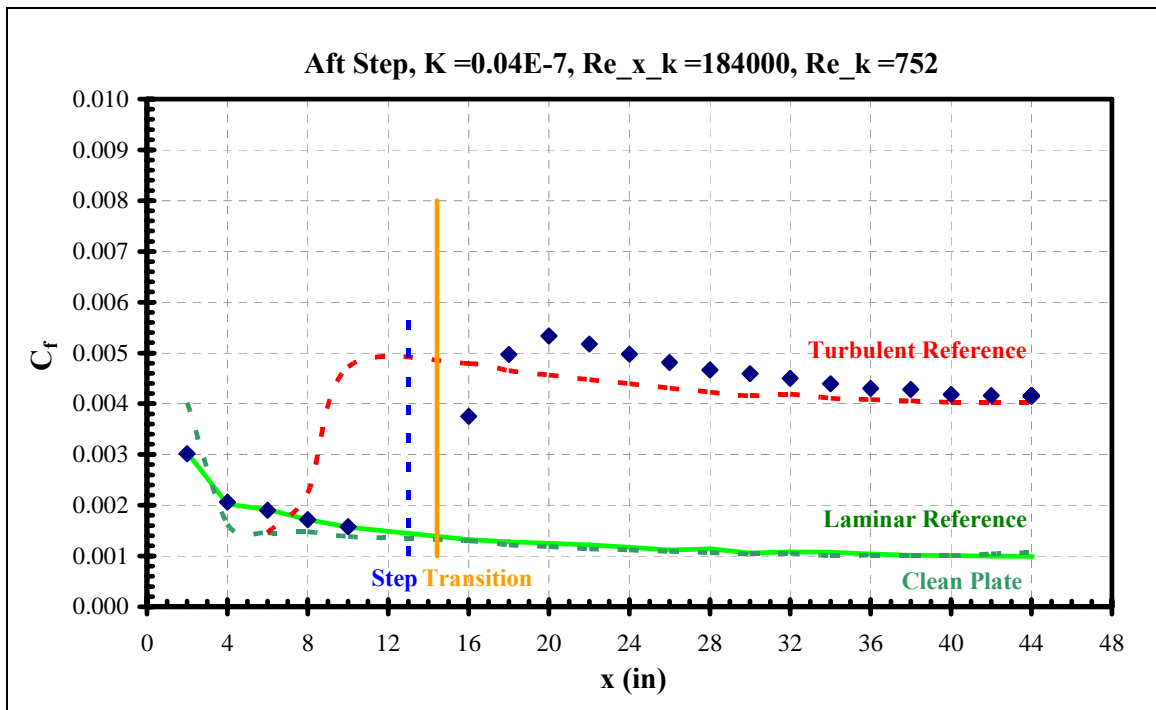


**Figure 159. Aft step skin friction distribution**

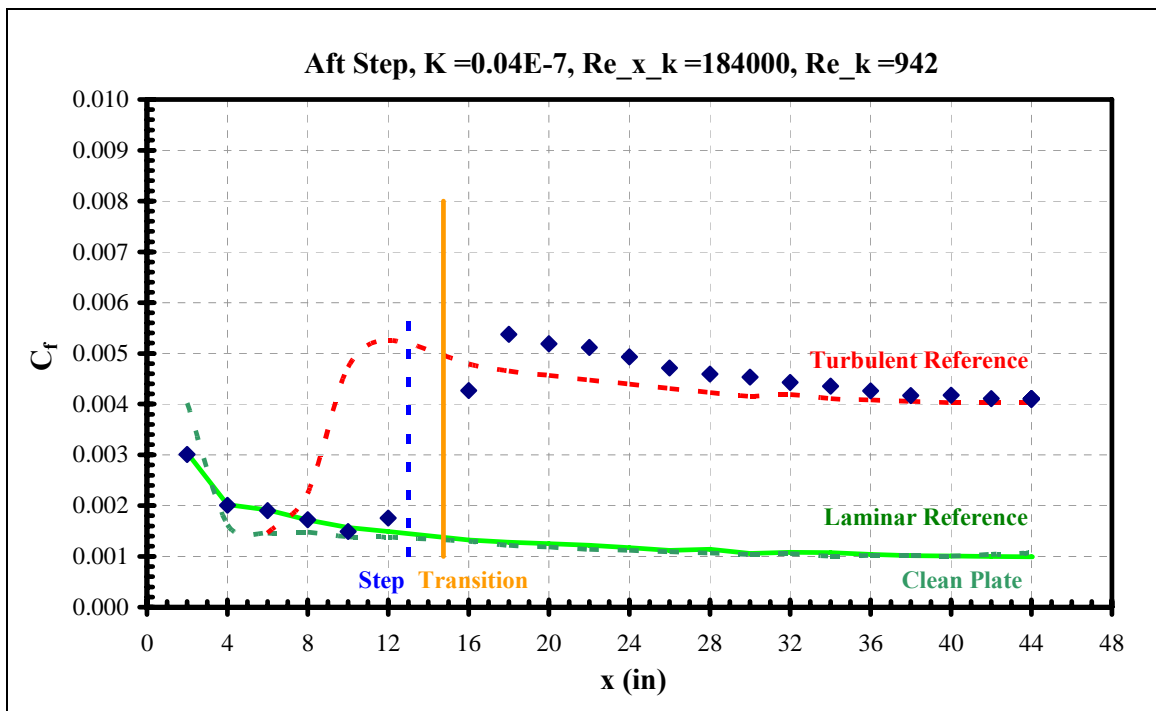


**Figure 160. Aft step skin friction distribution**

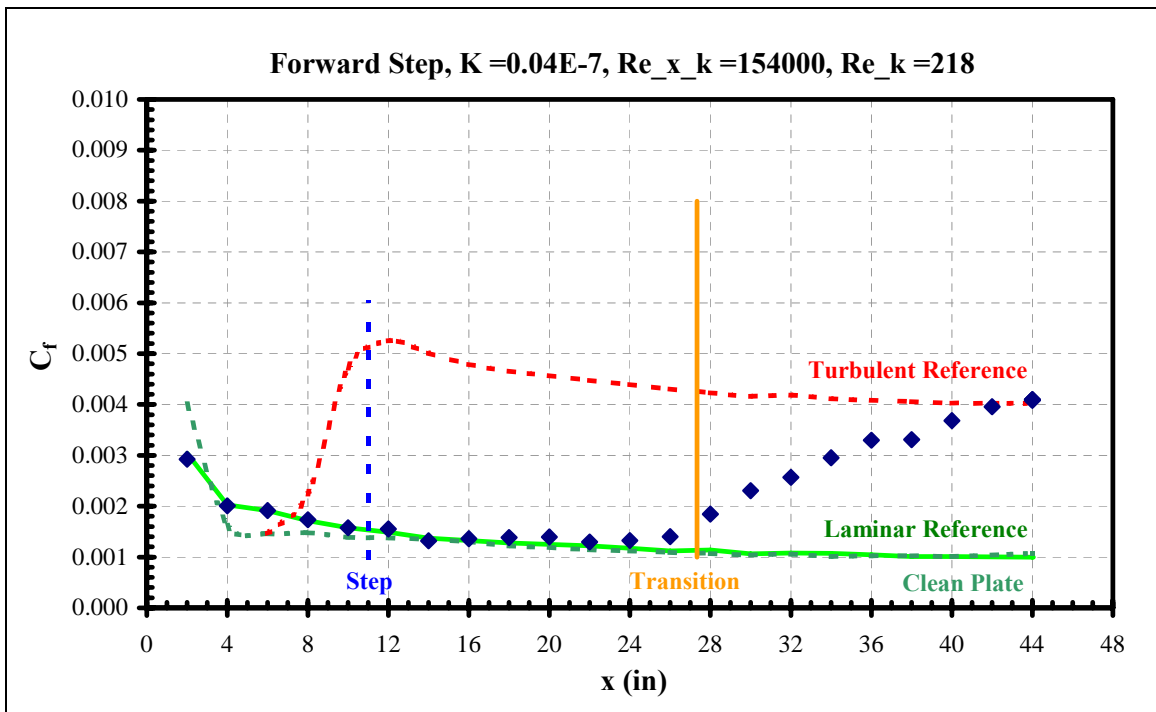


**Figure 161. Forward step skin friction distribution**

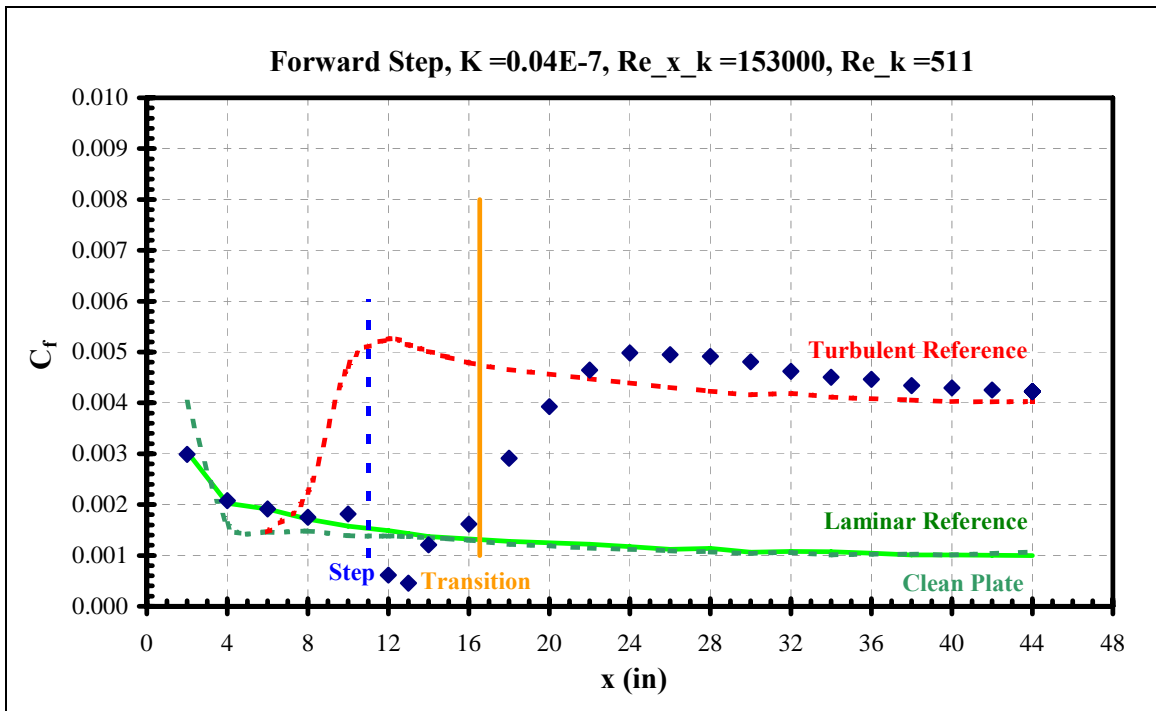


**Figure 162. Forward step skin friction distribution**

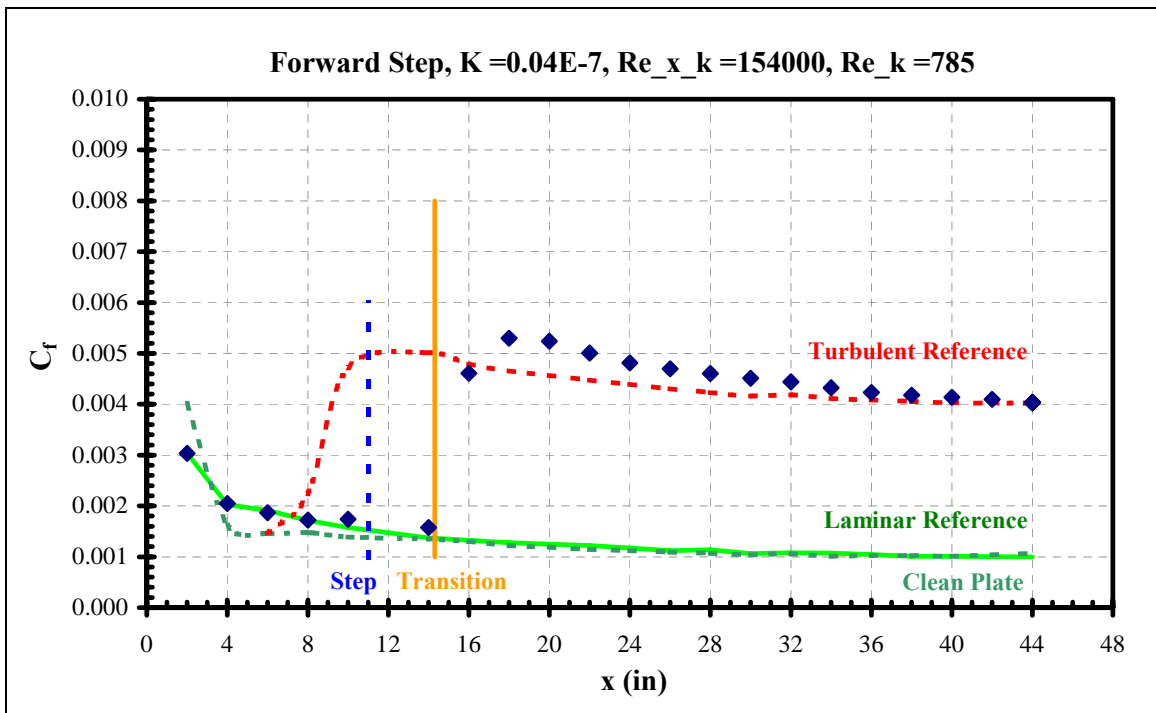


**Figure 163. Forward step skin friction distribution**



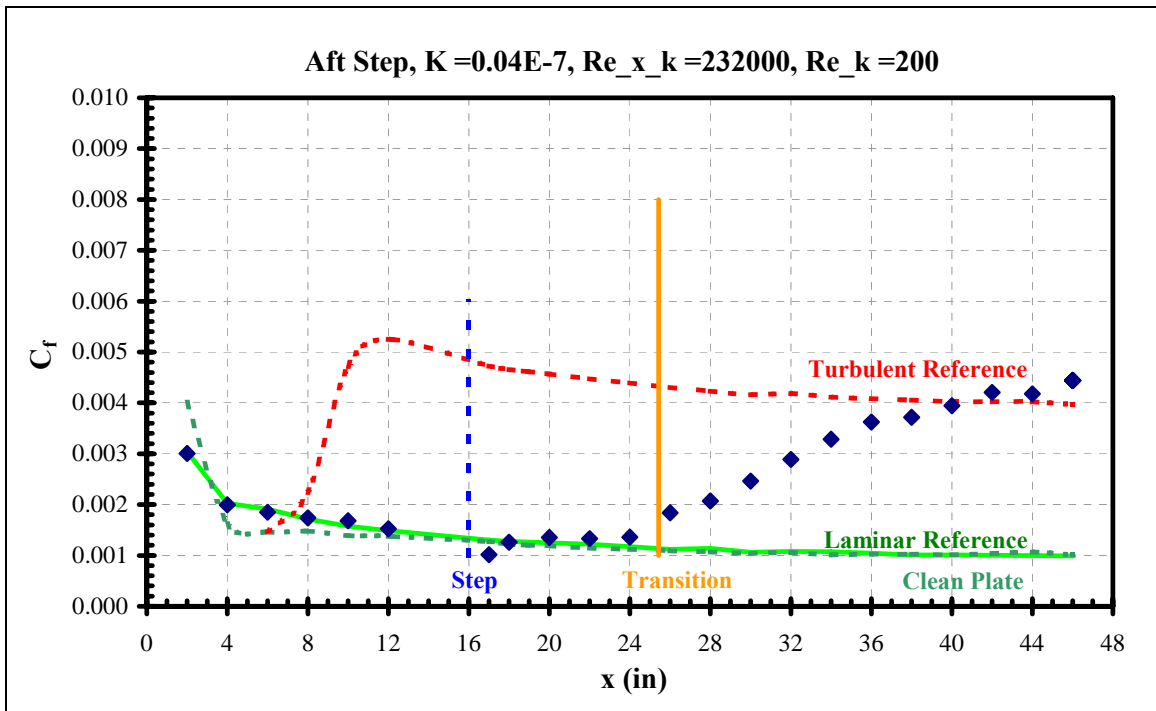


**Figure 164. Aft step skin friction distribution**

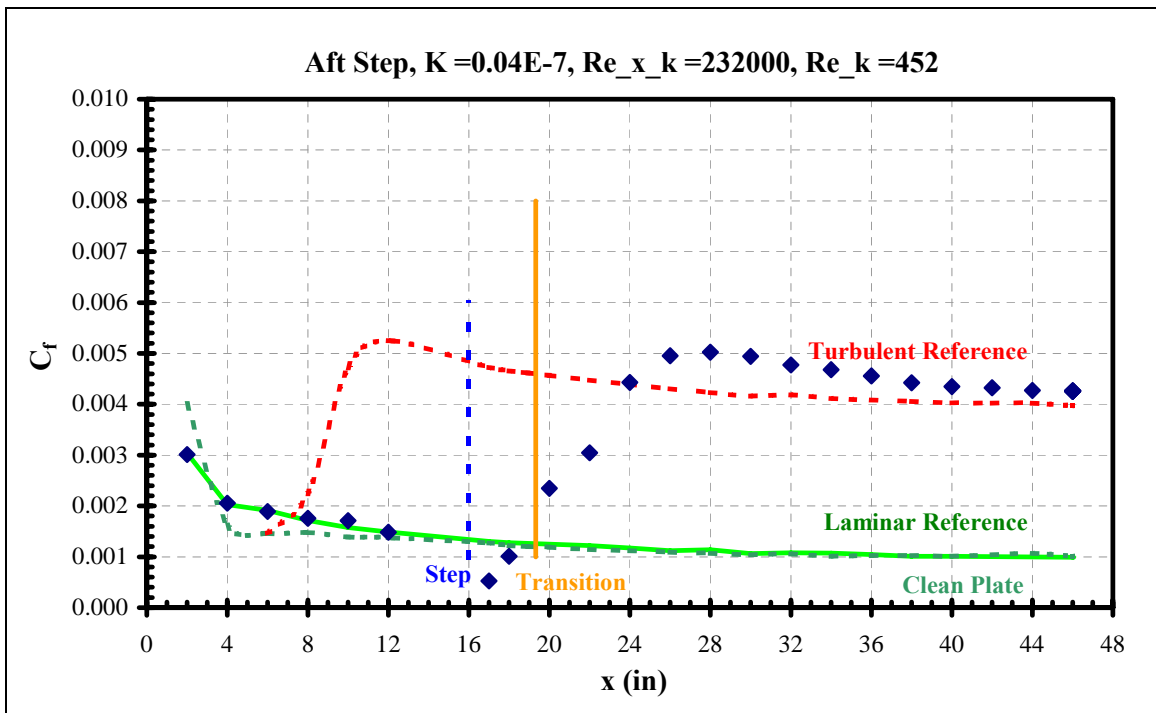


**Figure 165. Aft step skin friction distribution**

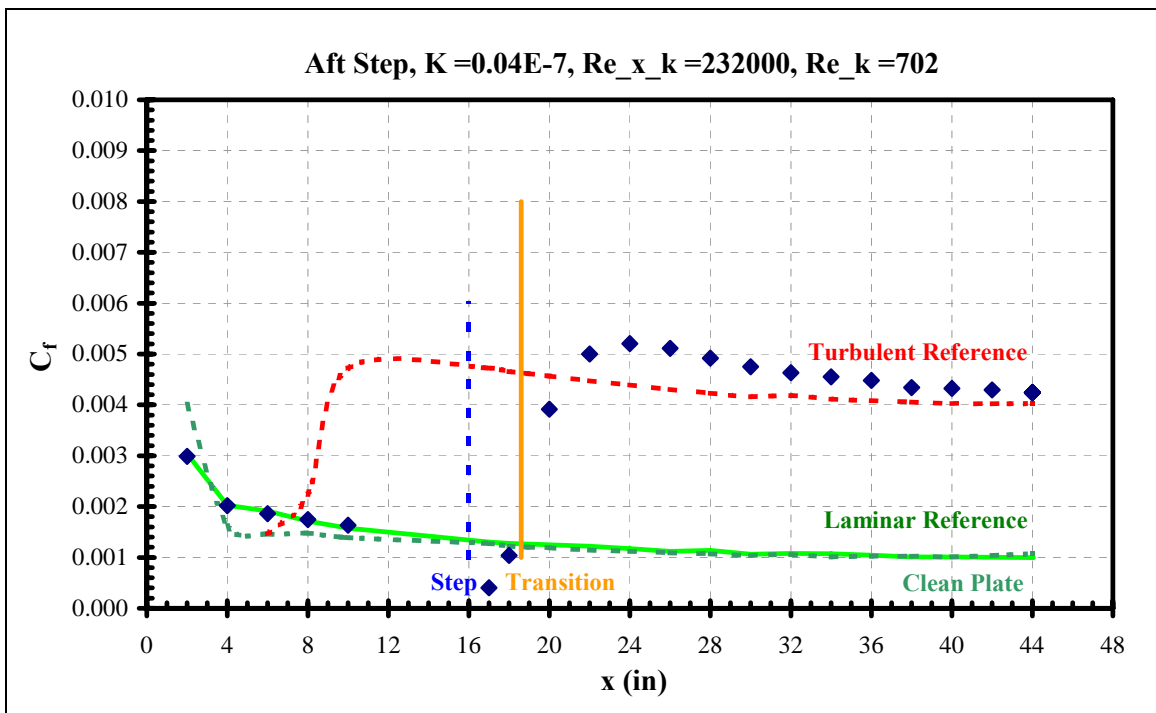


Figure 166. Aft step skin friction distribution

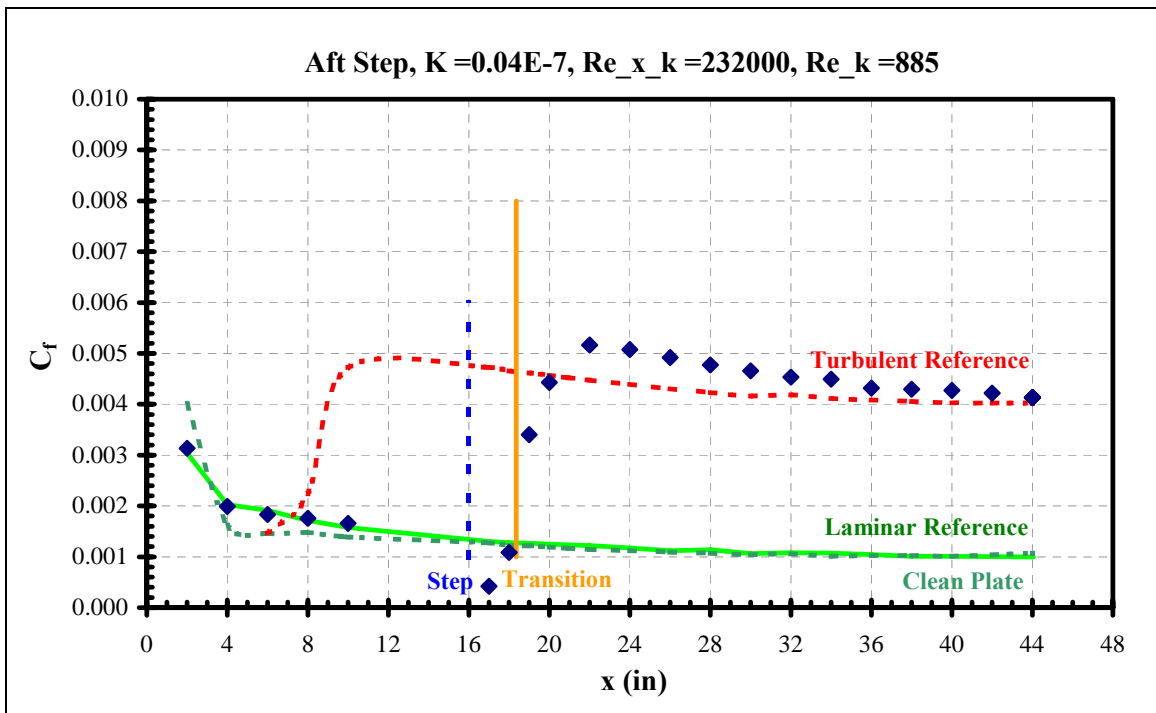
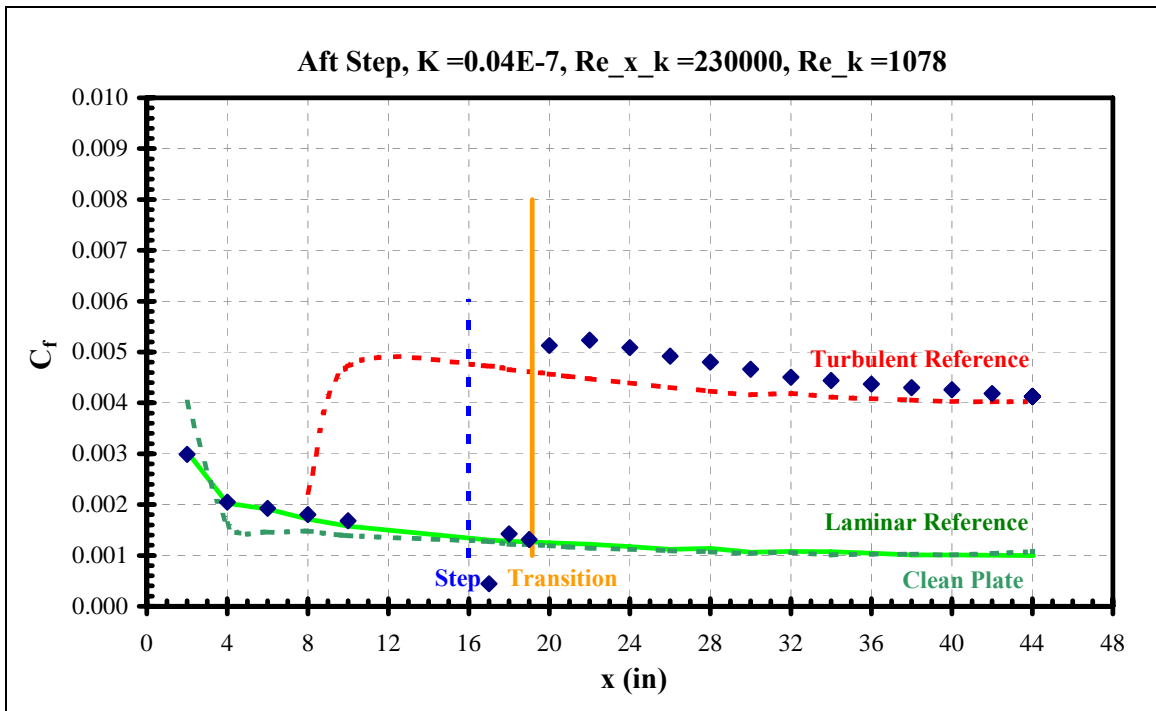
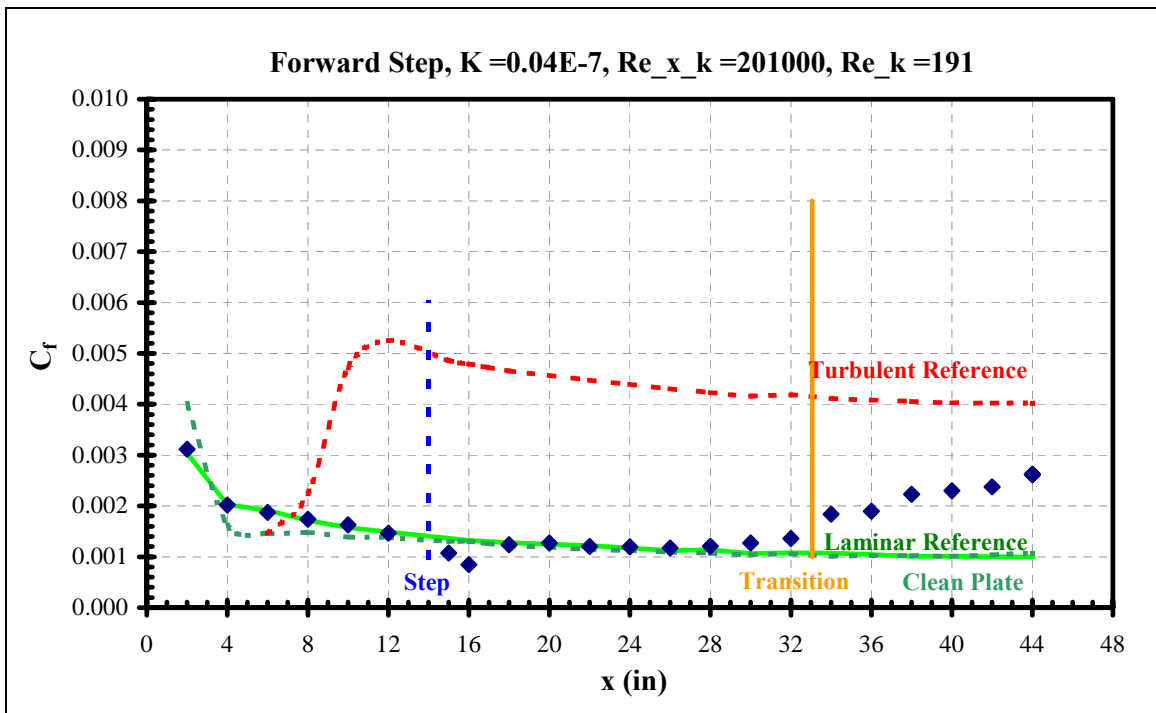


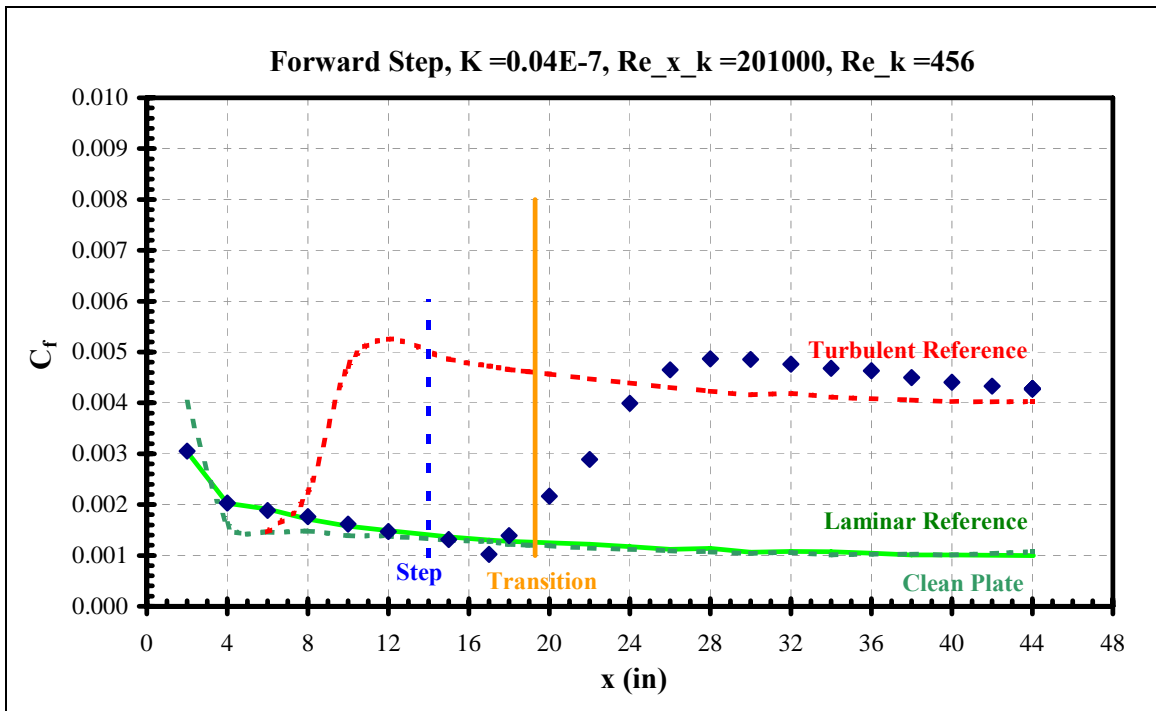
Figure 167. Aft step skin friction distribution



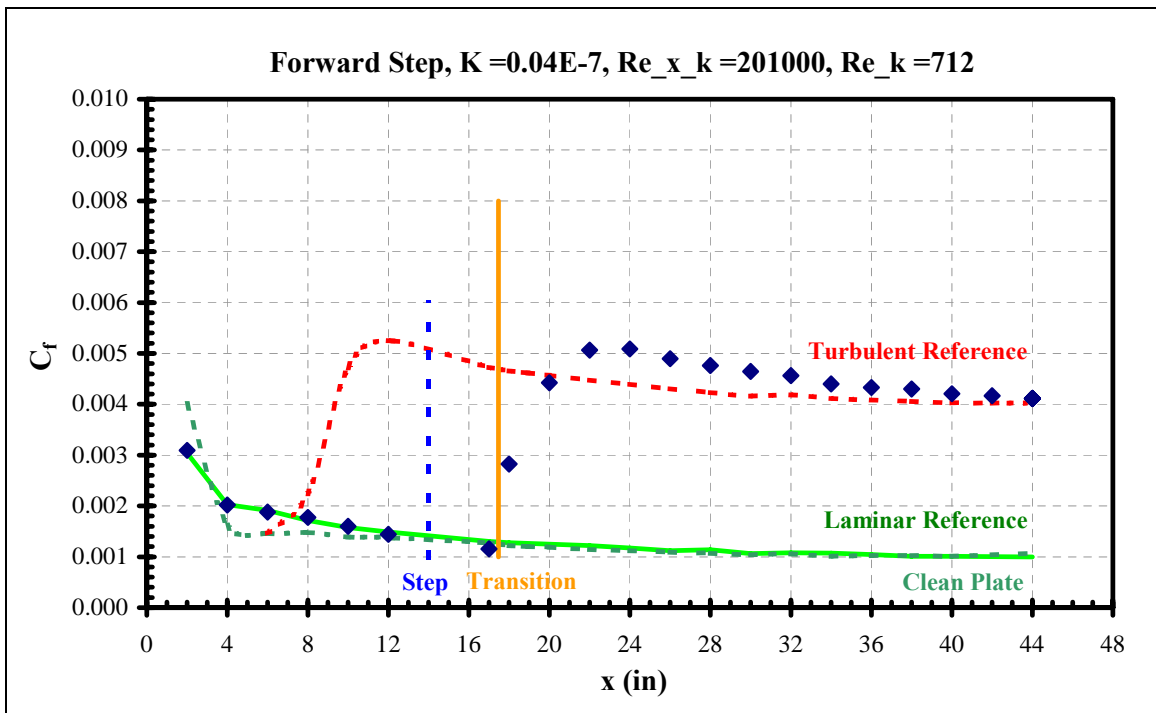
**Figure 168. Aft step skin friction distribution**



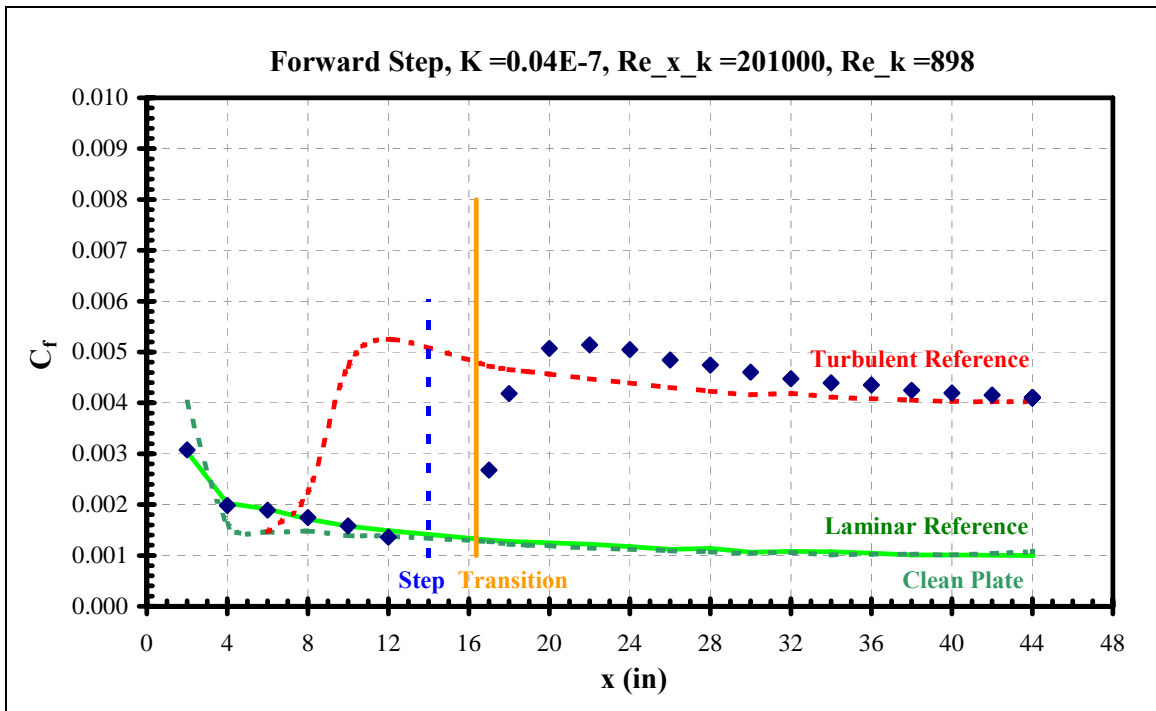
**Figure 169. Forward step skin friction distribution**



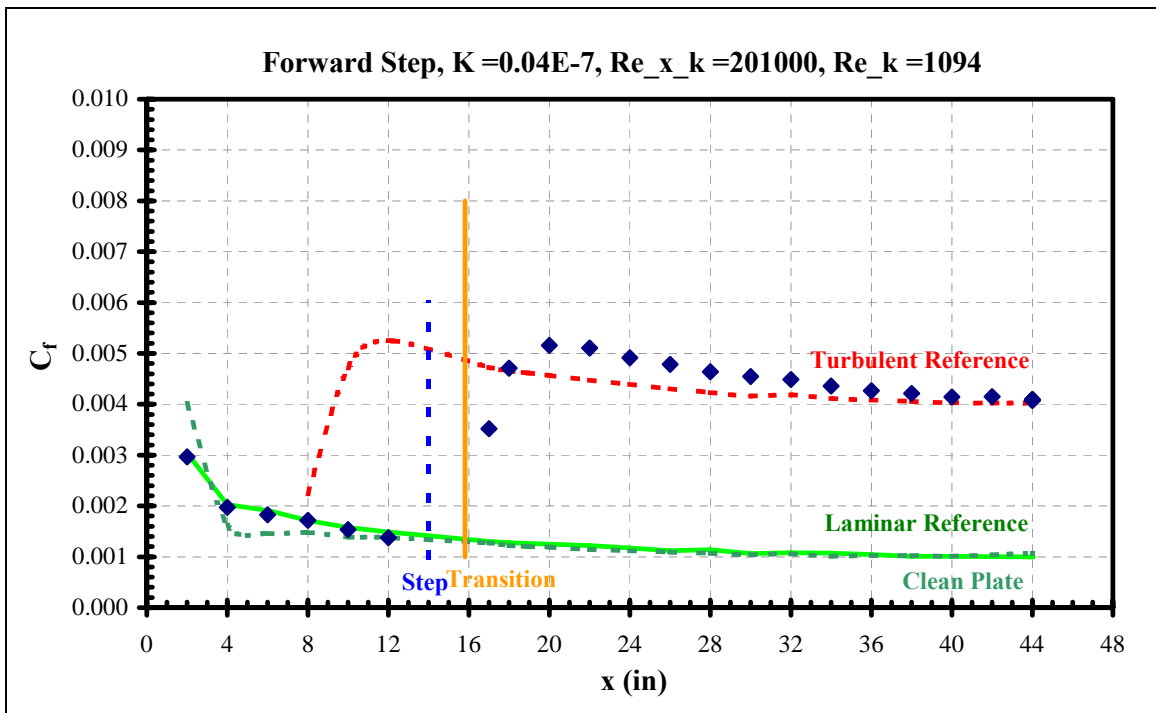
**Figure 170. Forward step skin friction distribution**



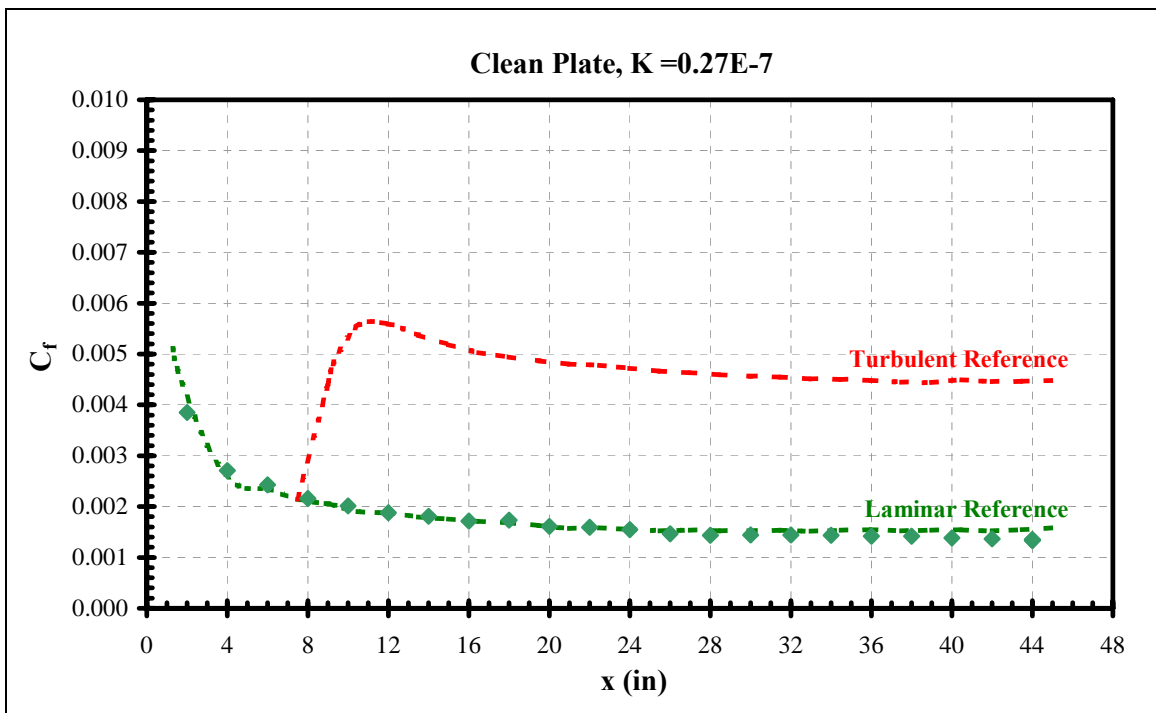
**Figure 171. Forward step skin friction distribution**



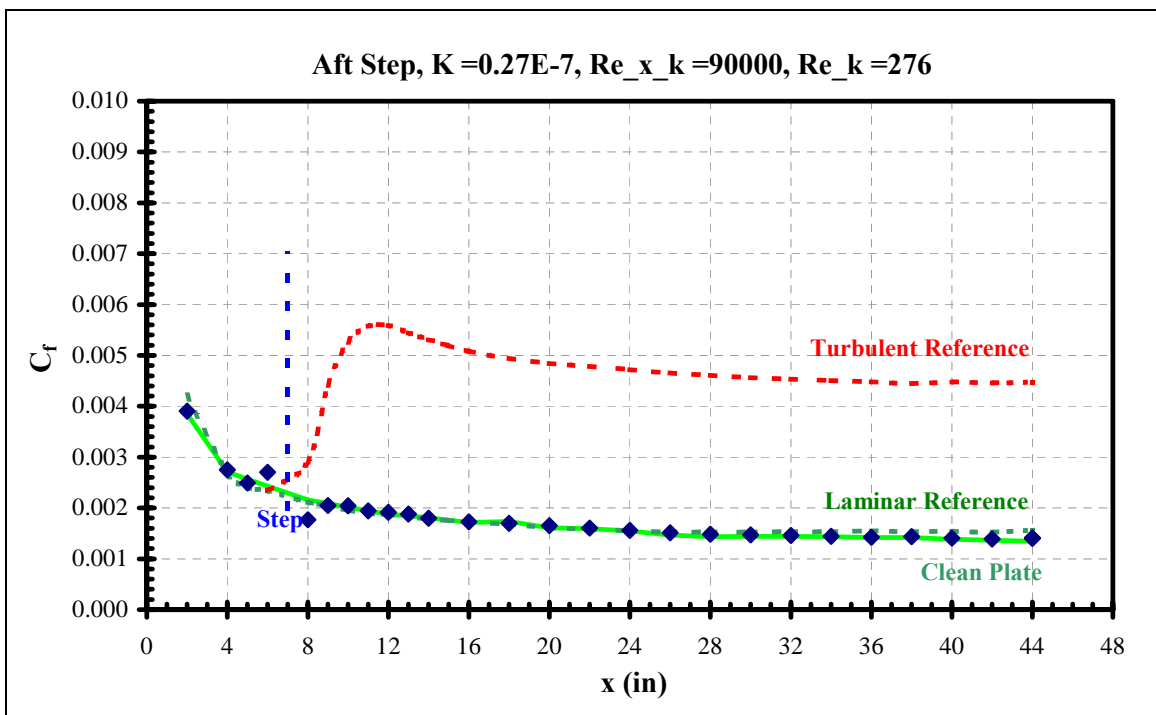
**Figure 172. Forward step skin friction distribution**



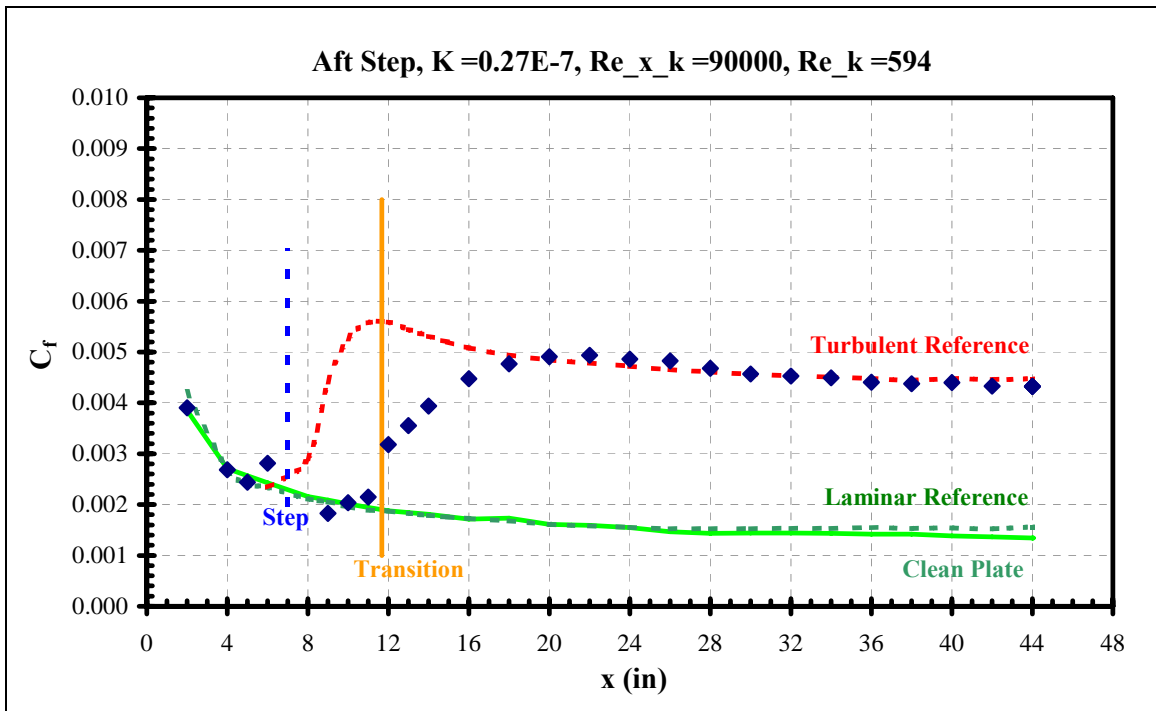
**Figure 173. Forward step skin friction distribution**



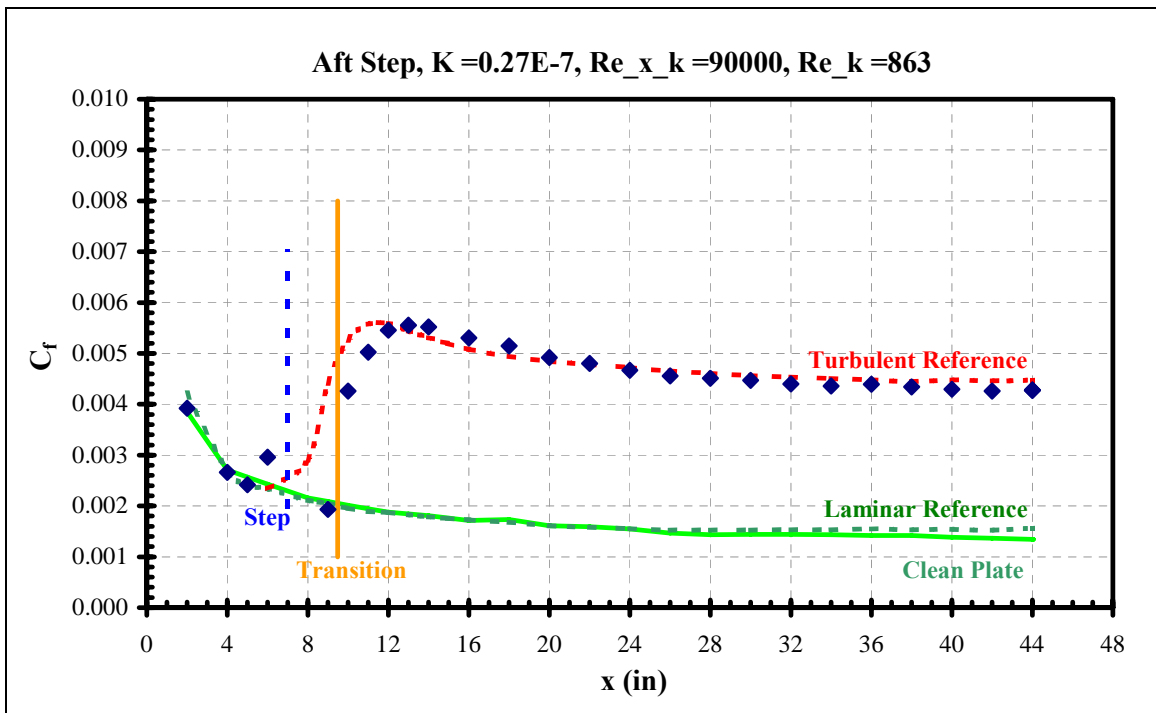
**Figure 174 Clean plate skin friction distribution**



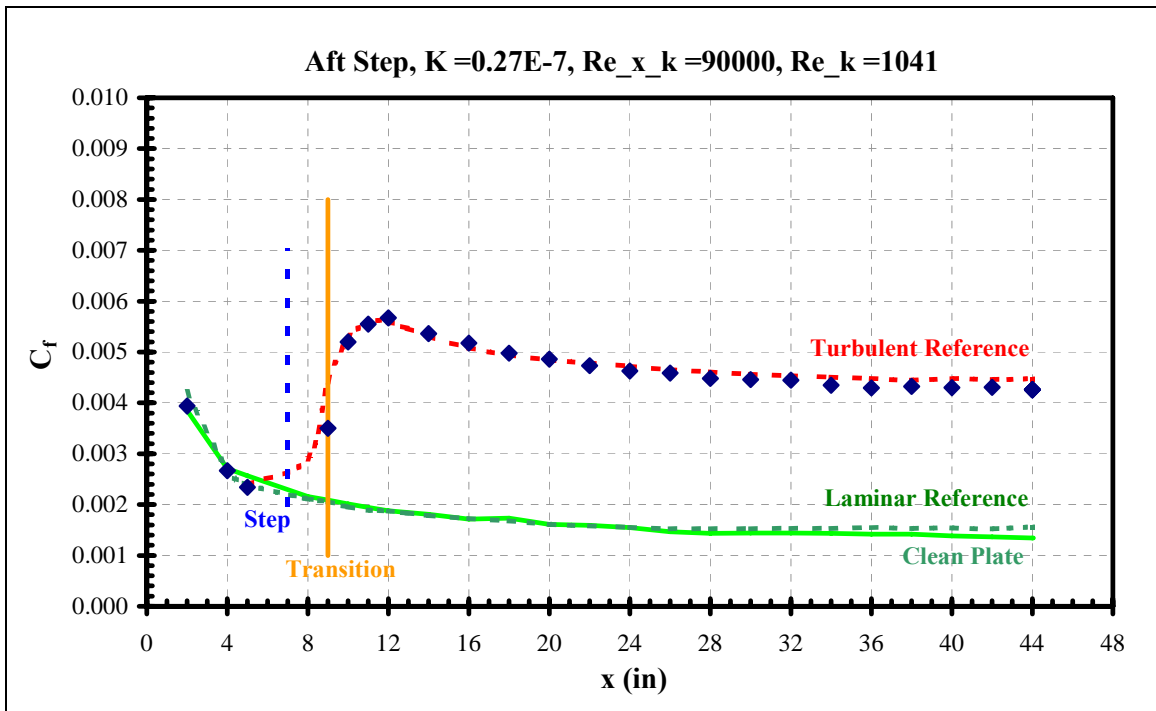
**Figure 175. Aft step skin friction distribution**



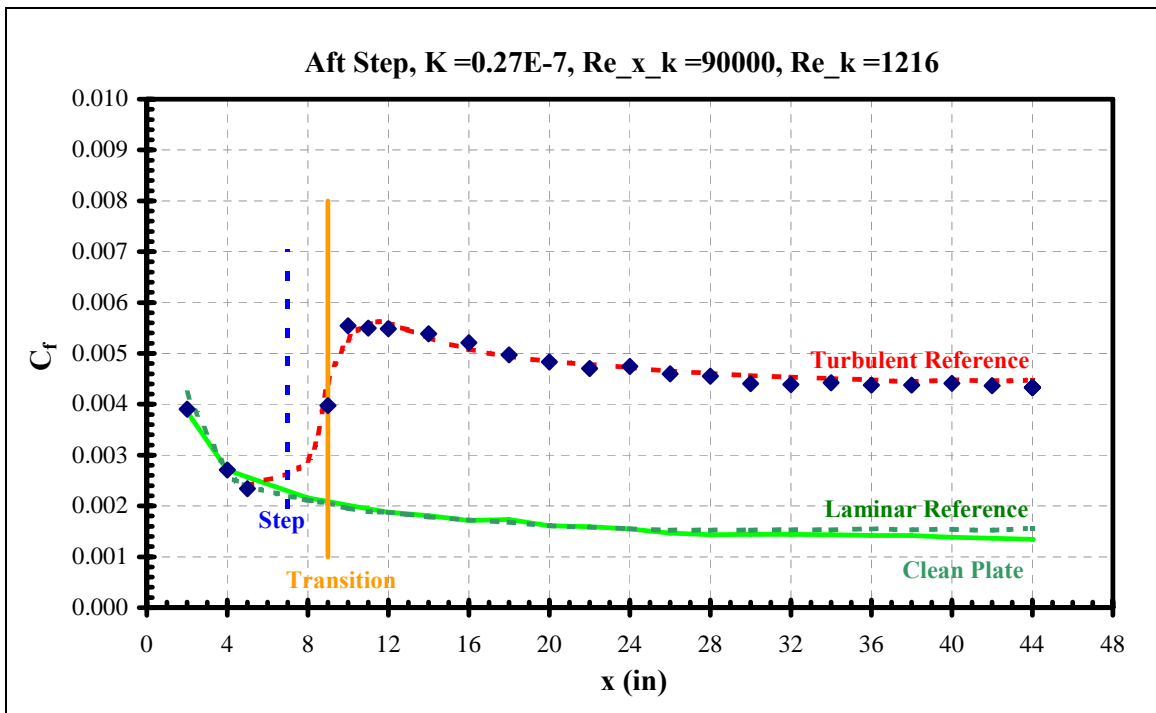
**Figure 176 Aft step skin friction distribution**



**Figure 177 Aft step skin friction distribution**

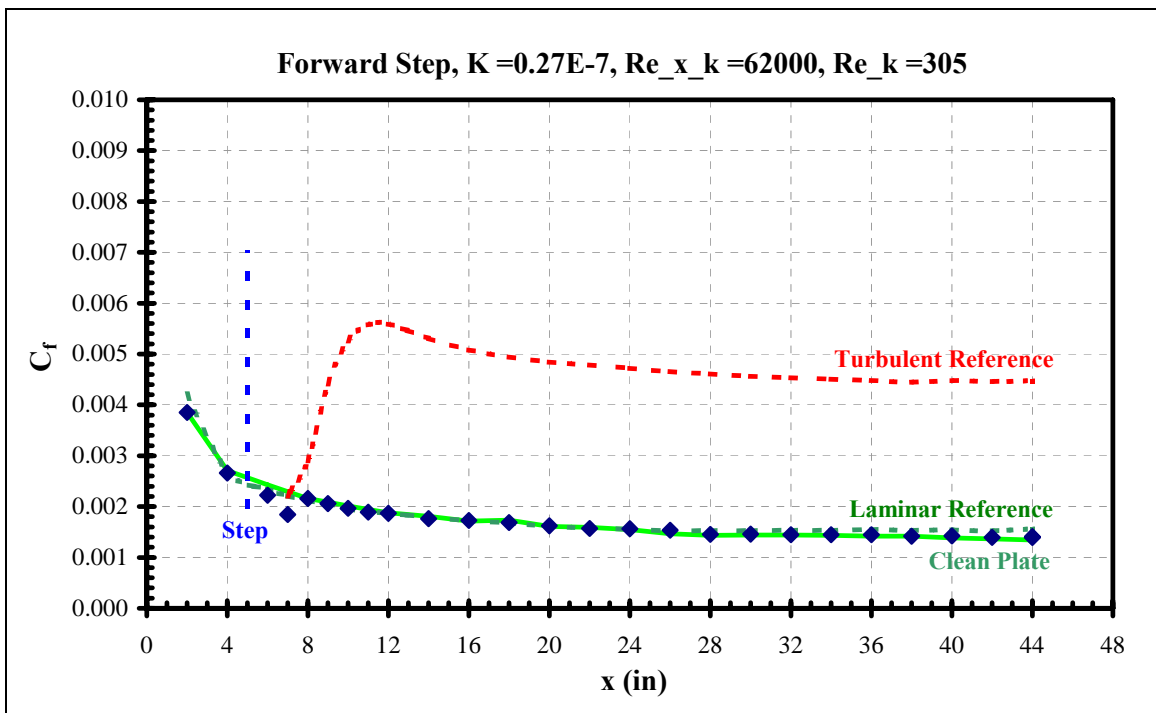


**Figure 178 Aft step skin friction distribution**

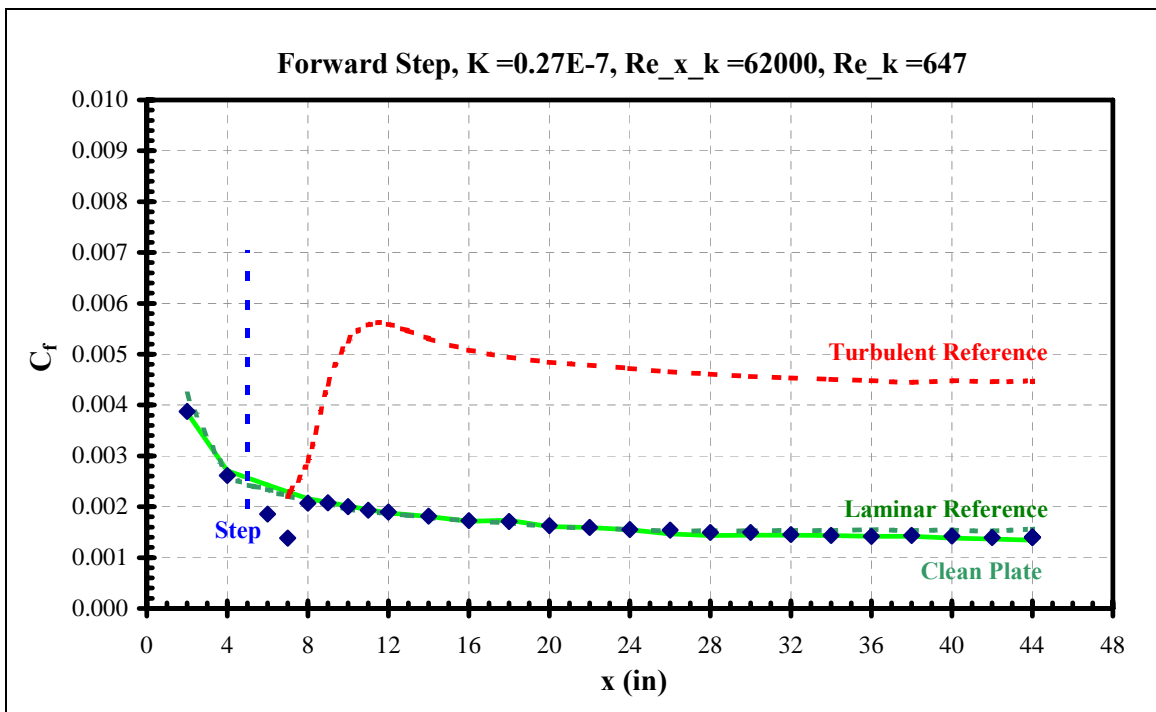


**Figure 179 Aft step skin friction distribution**

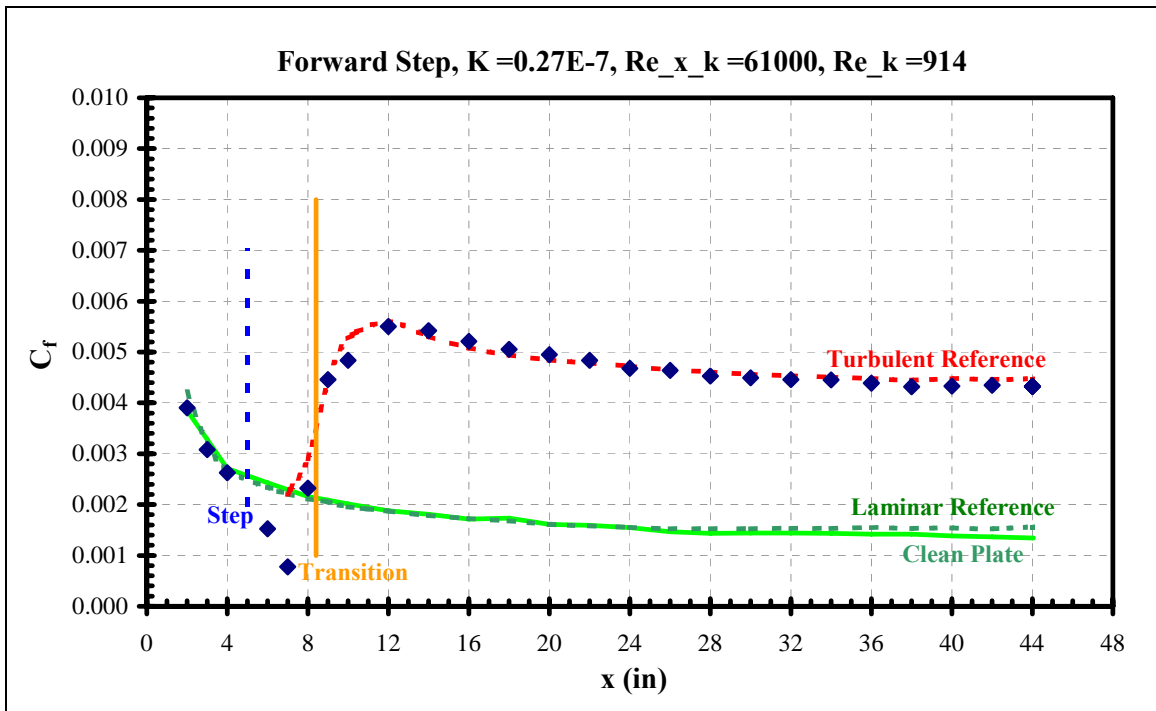




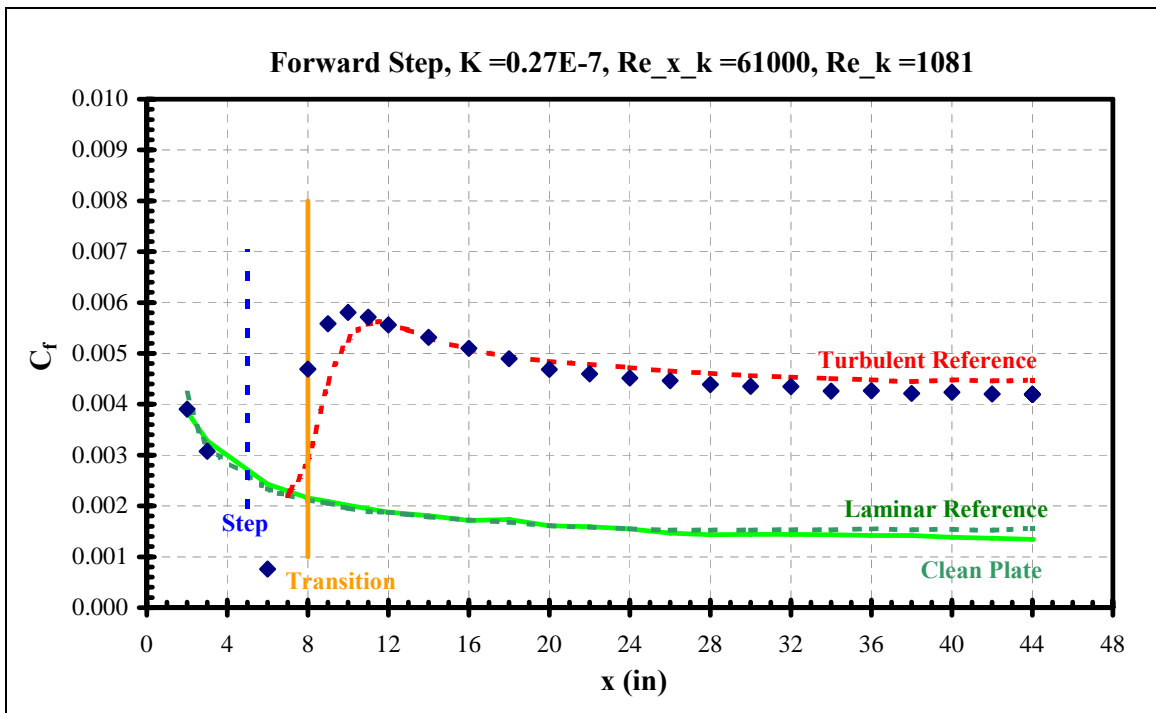
**Figure 180 Forward step skin friction distribution**



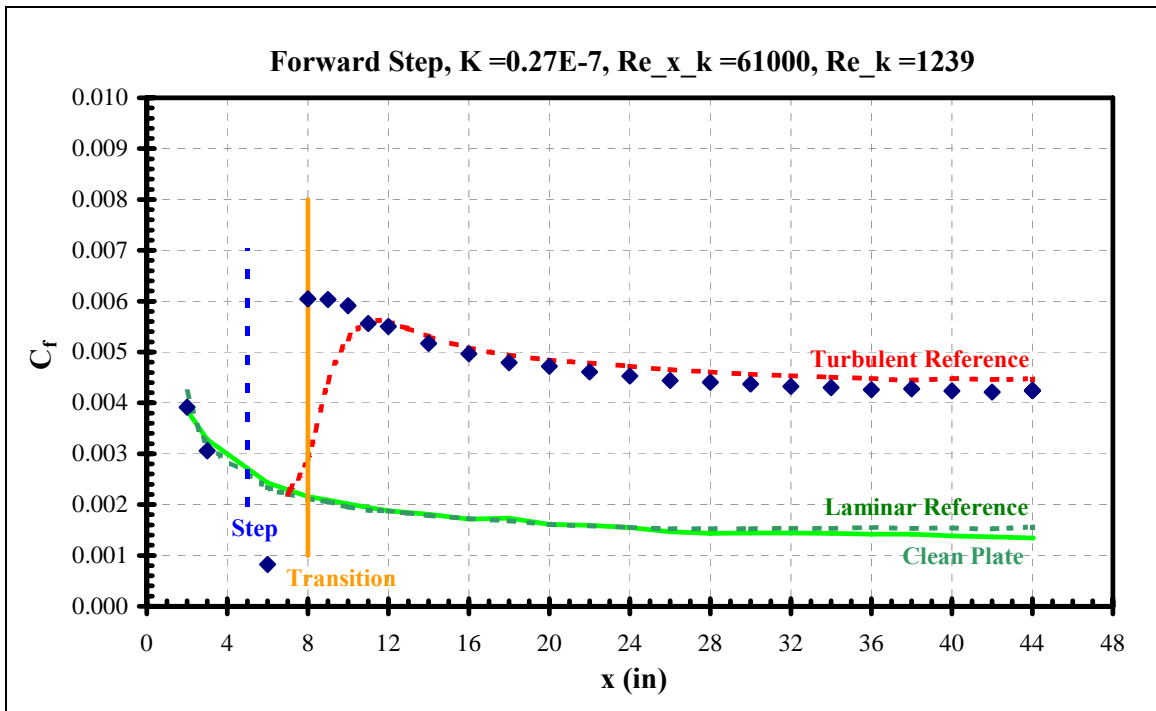
**Figure 181 Forward step skin friction distribution**



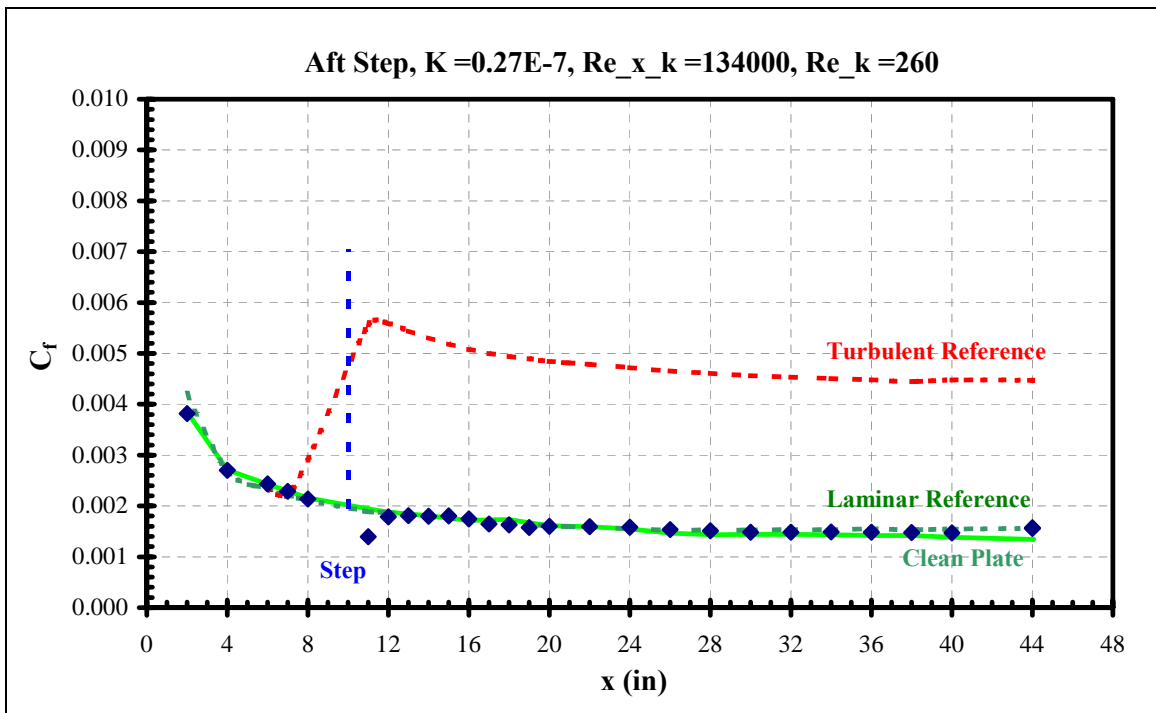
**Figure 182 Forward step skin friction distribution**



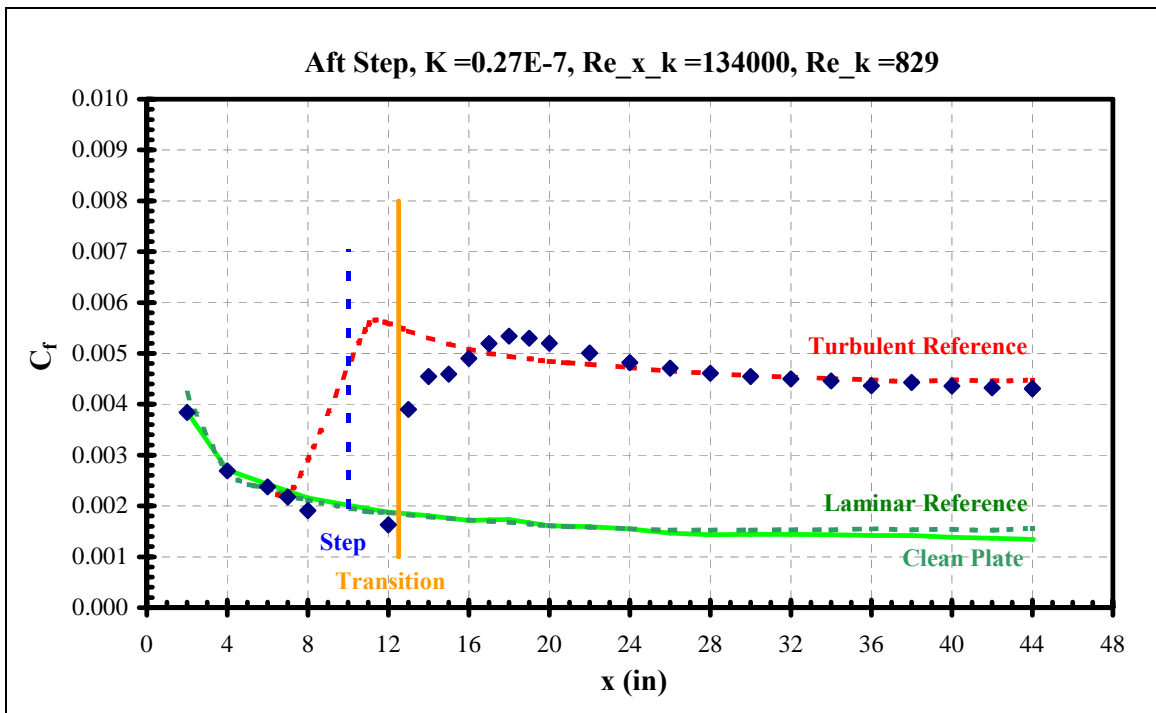
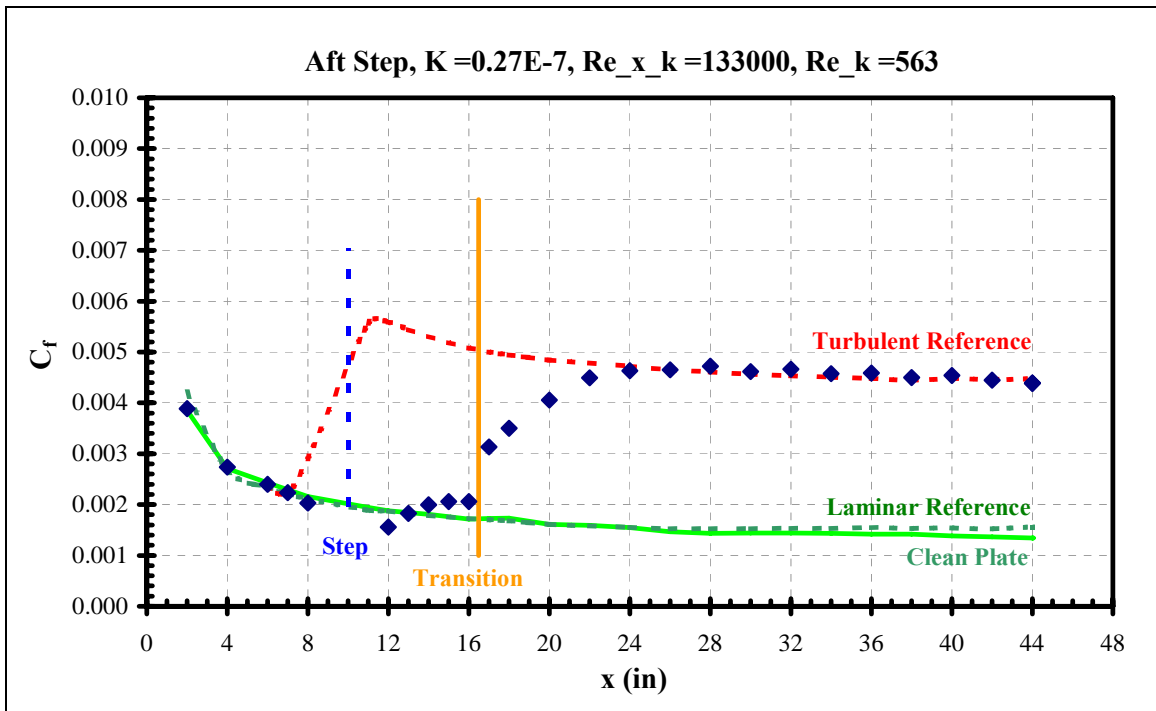
**Figure 183 Forward step skin friction distribution**



**Figure 184 Forward step skin friction distribution**



**Figure 185 Aft step skin friction distribution**



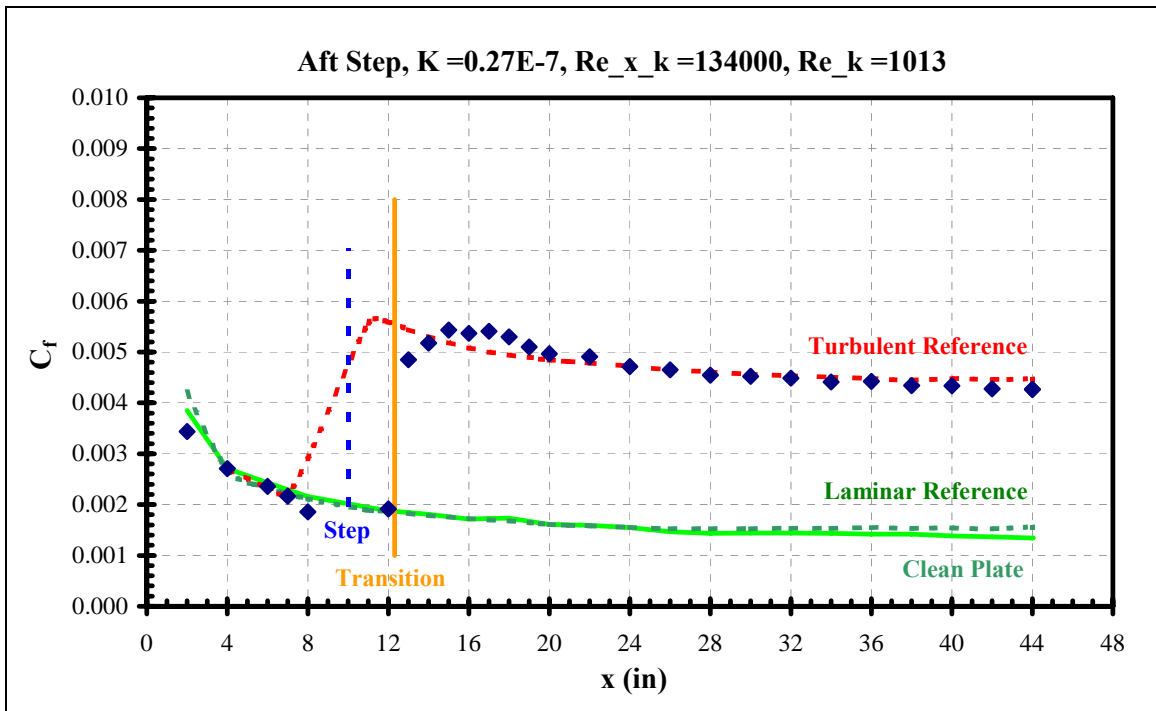


**Figure 188 Aft step skin friction distribution**

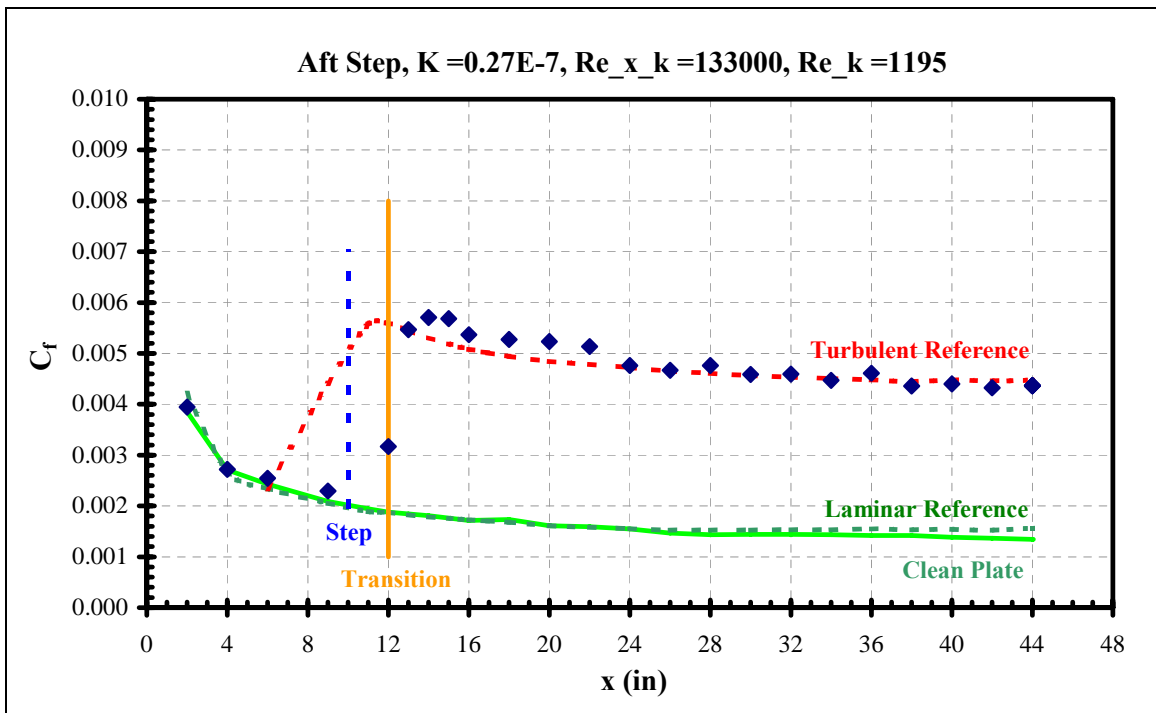


**Figure 189 Aft step skin friction distribution**

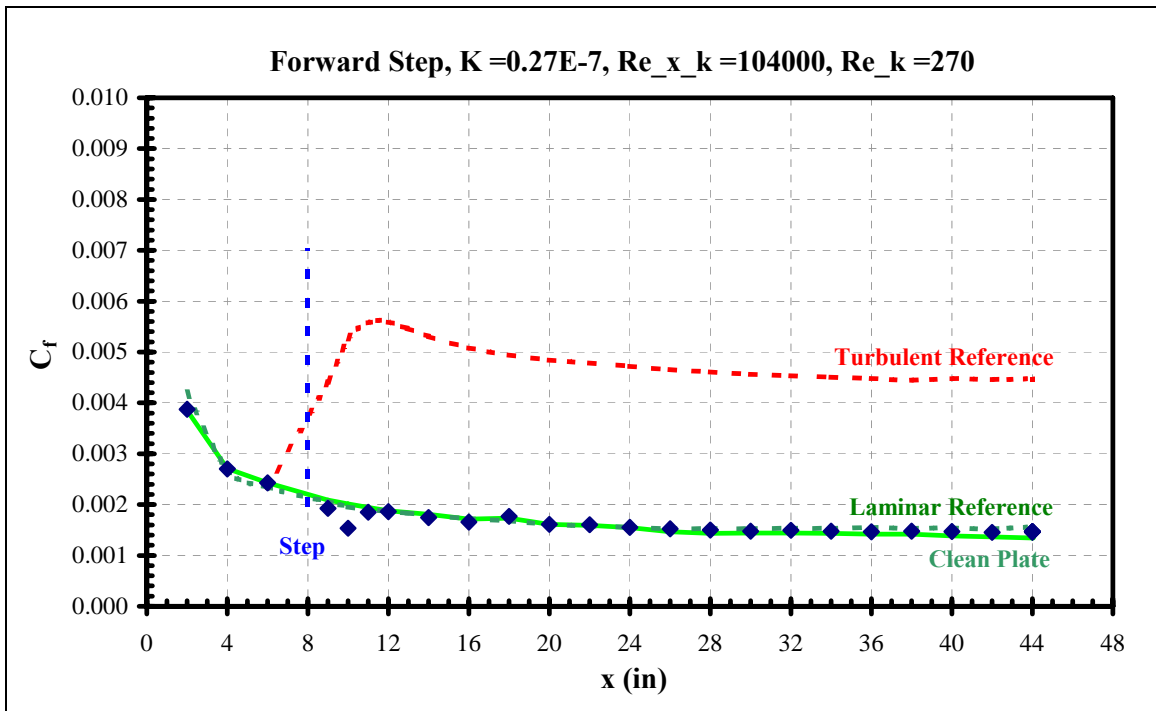


**Figure 190 Forward step skin friction distribution**

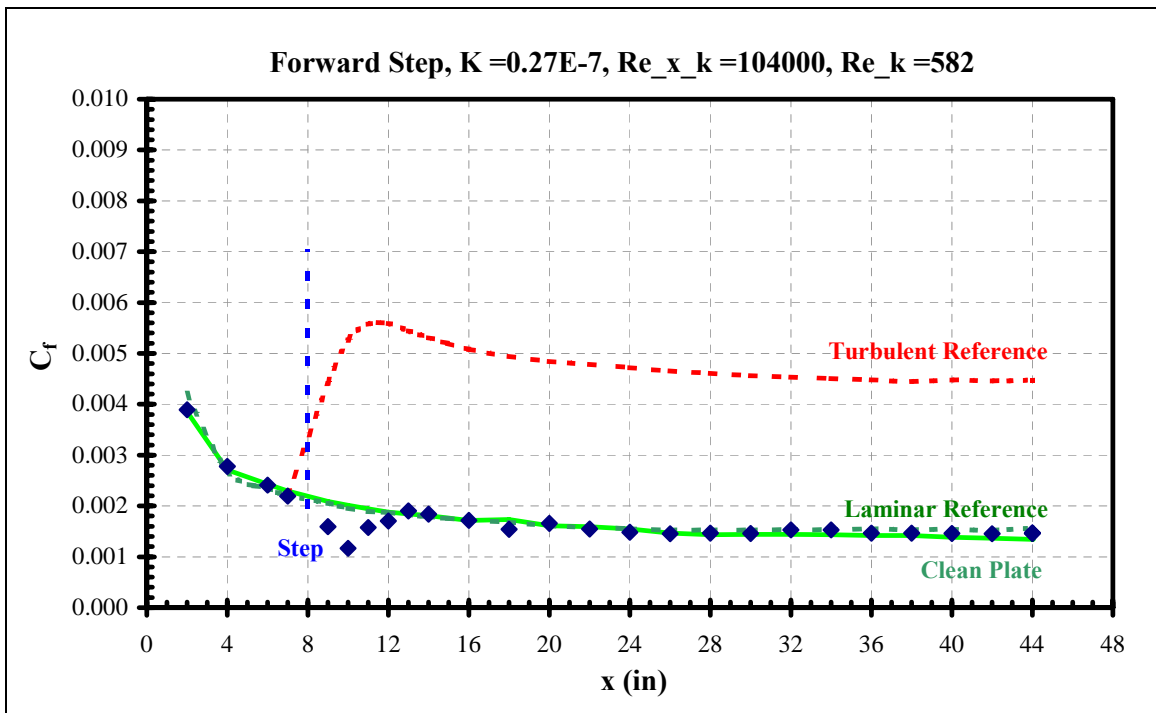


**Figure 191 Forward step skin friction distribution**

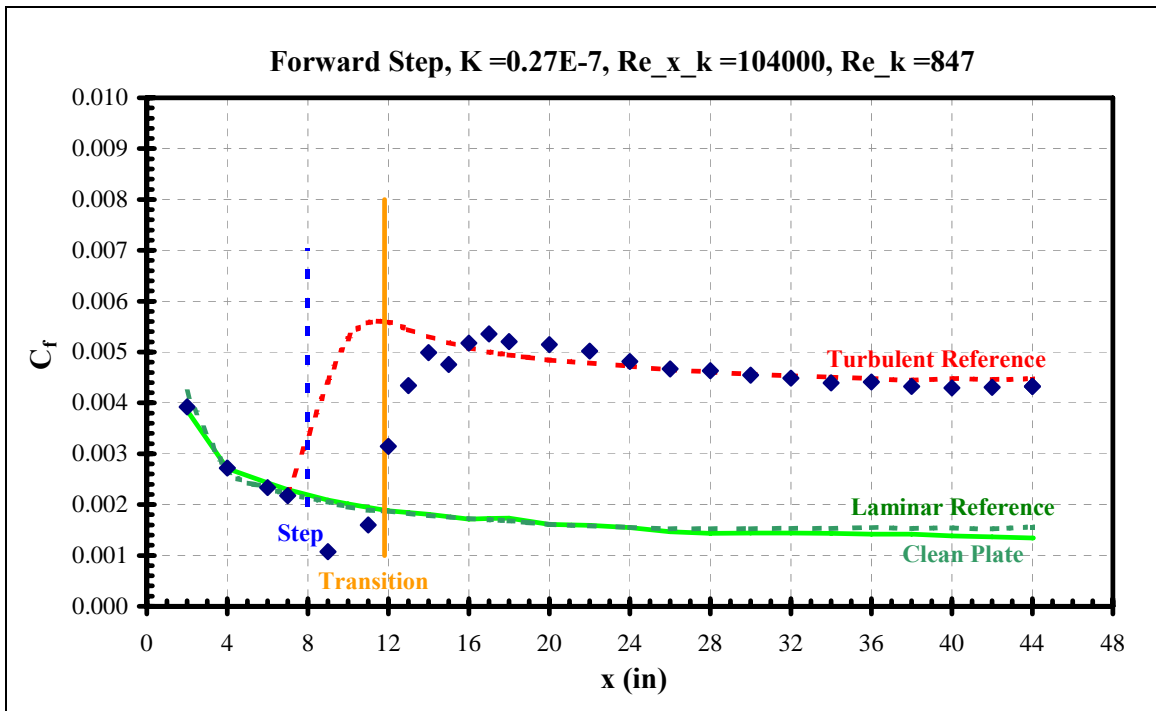


**Figure 192 Forward step skin friction distribution**

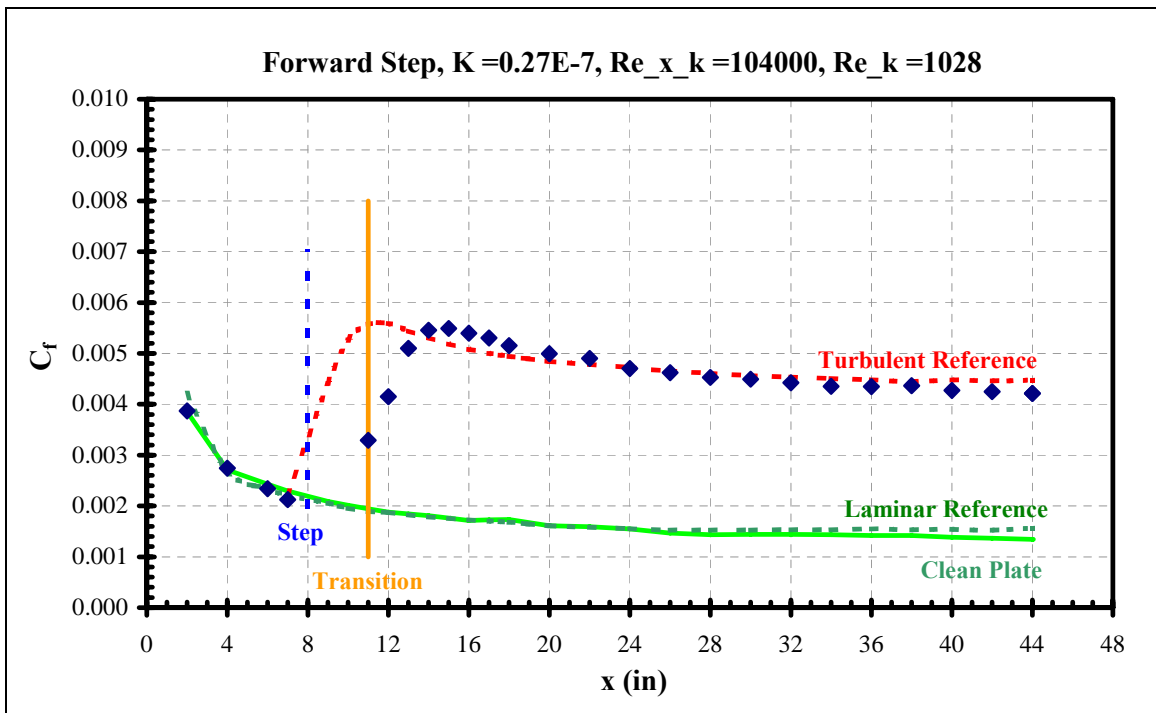


**Figure 193 Forward step skin friction distribution**

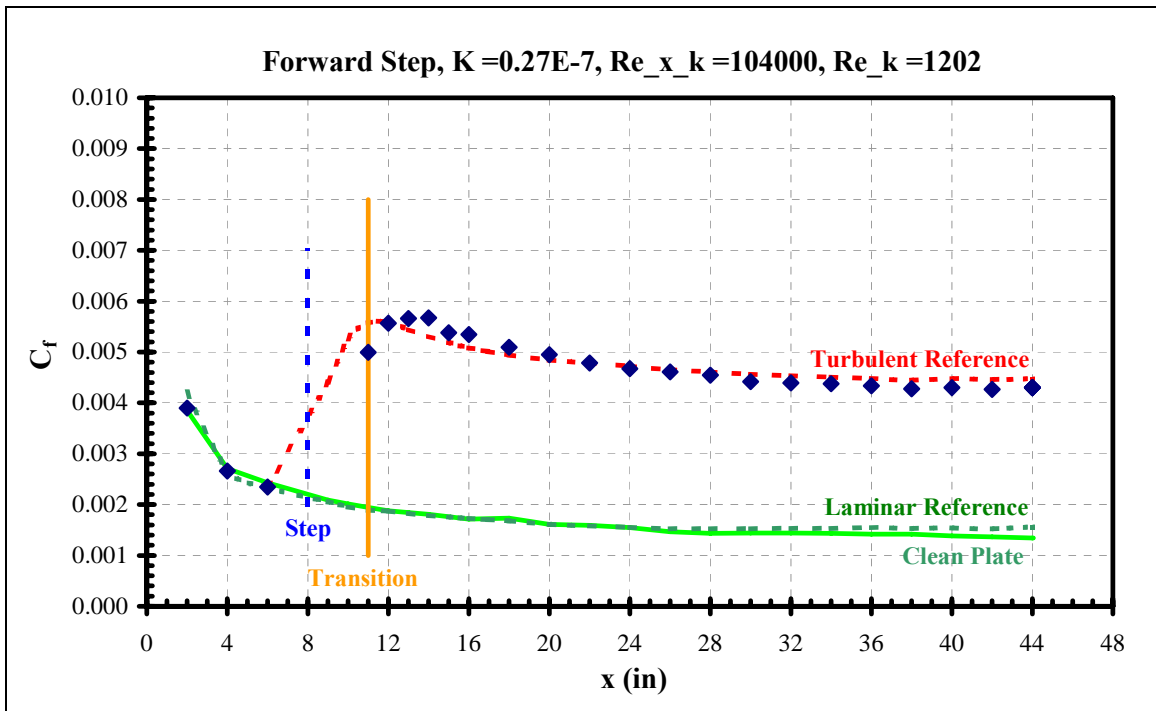


**Figure 194 Forward step skin friction distribution**

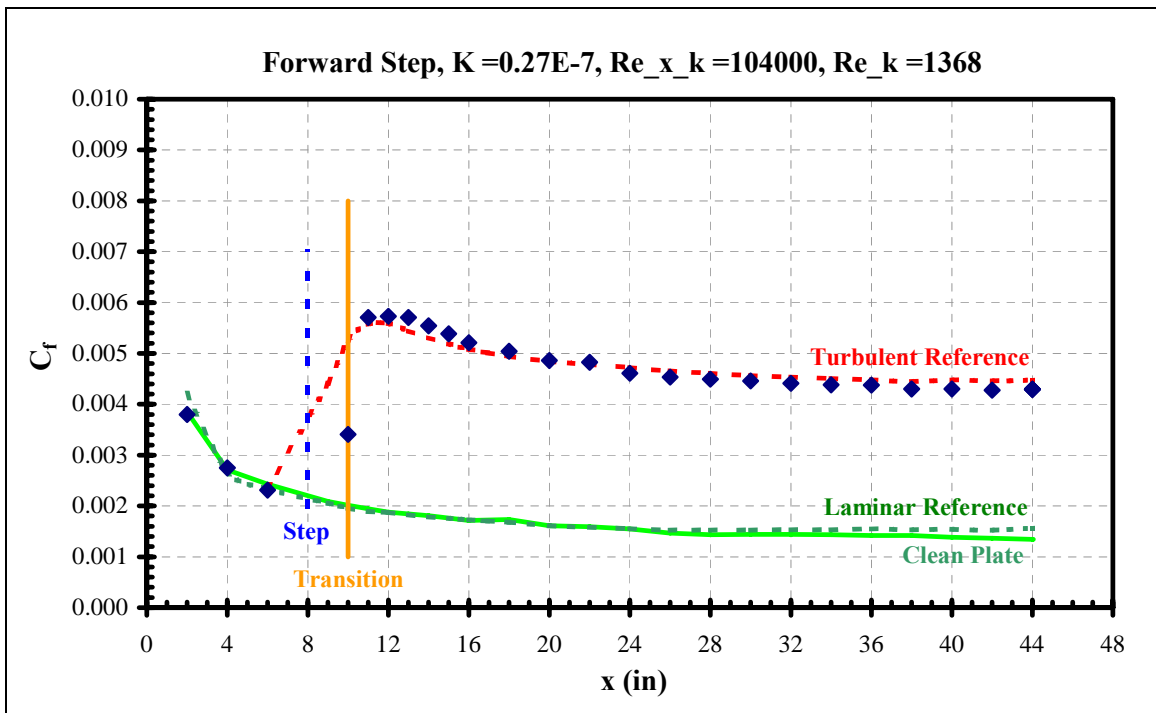


**Figure 195 Forward step skin friction distribution**



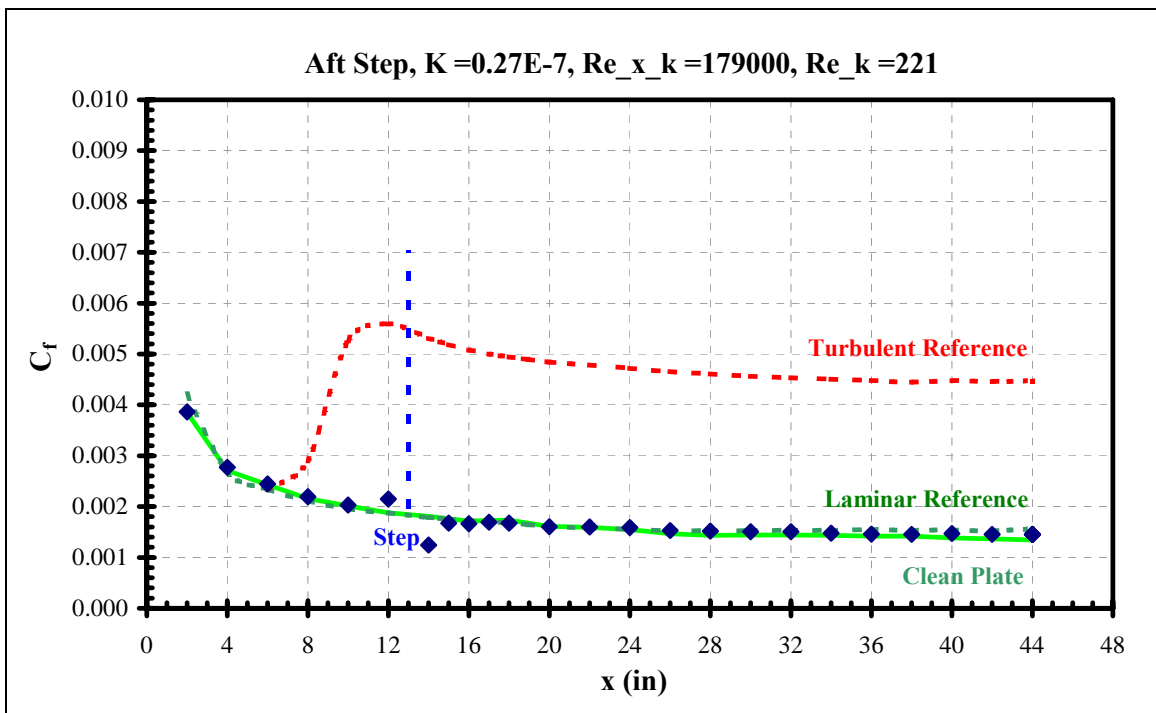


**Figure 196 Aft step skin friction distribution**

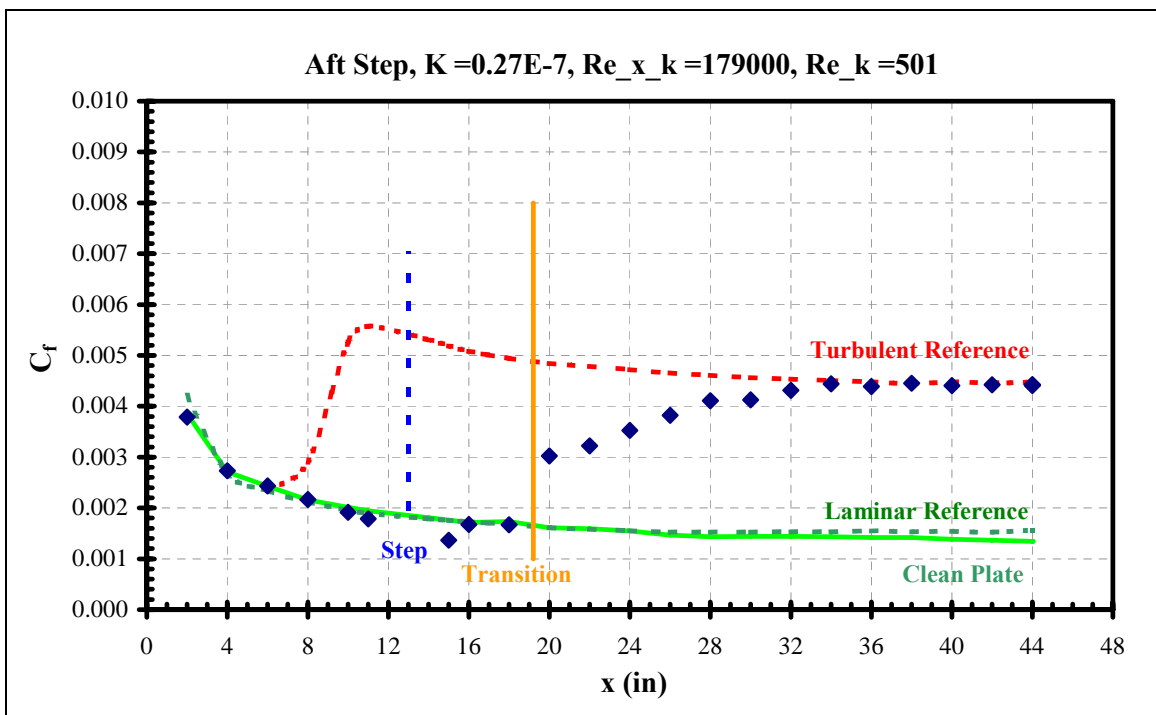


**Figure 197 Aft step skin friction distribution**

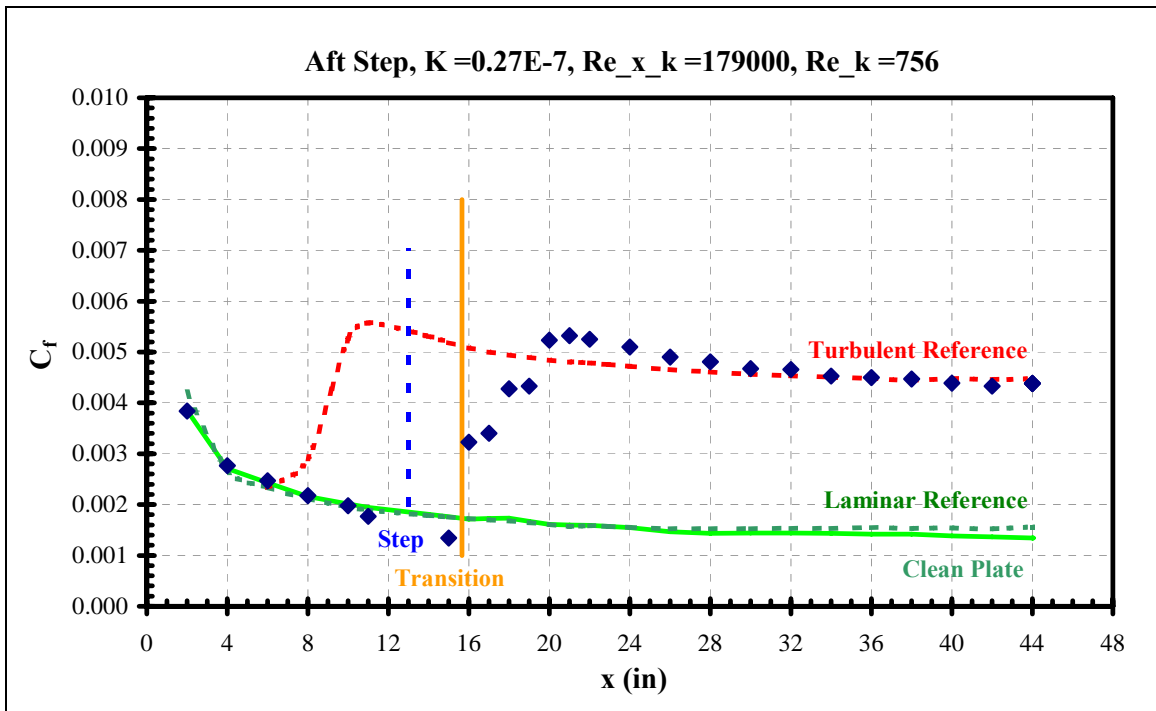


**Figure 198 Aft step skin friction distribution**

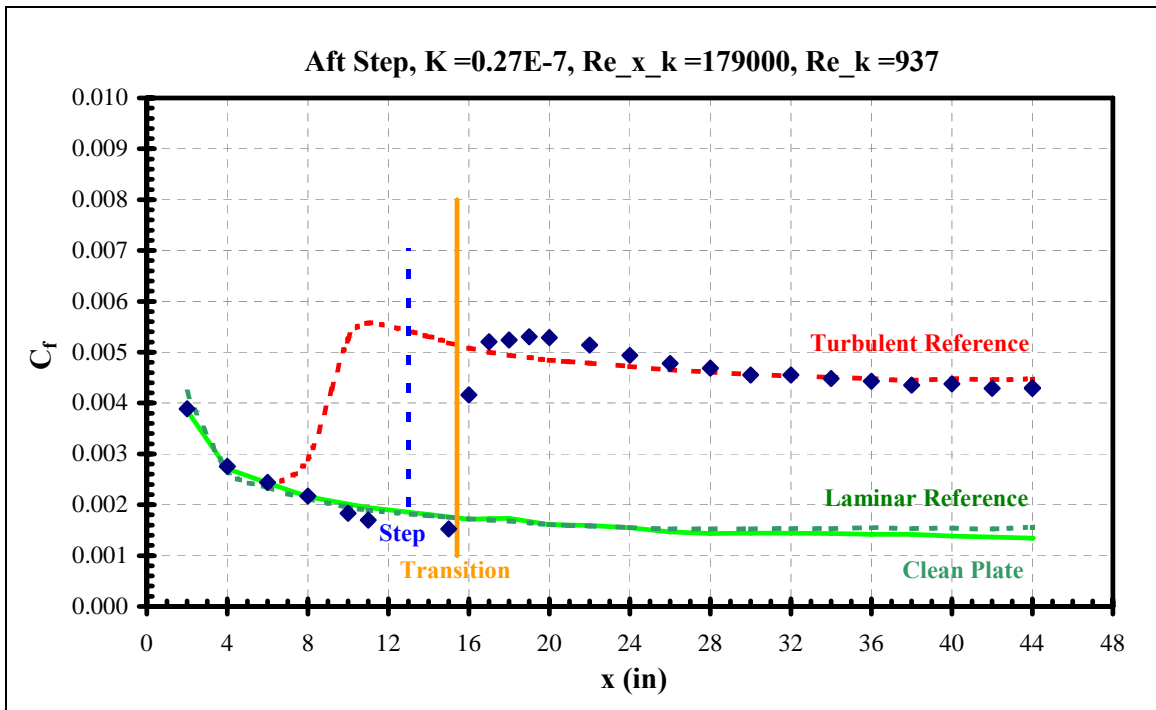


**Figure 199 Aft step skin friction distribution**

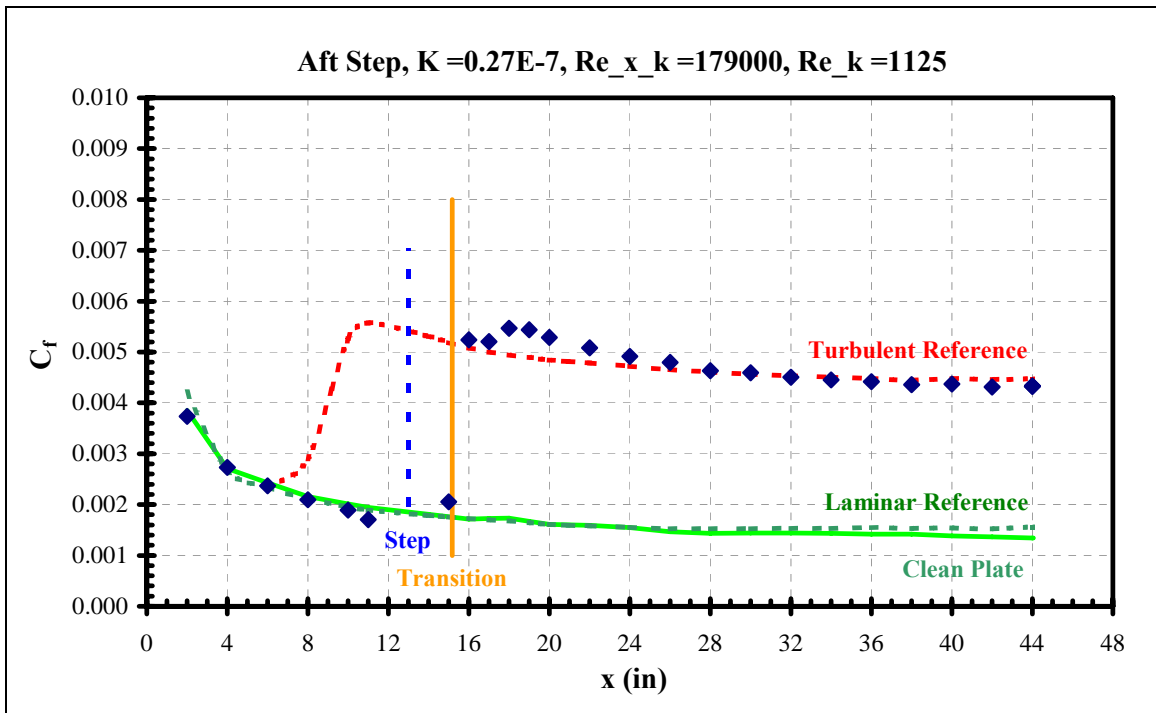


**Figure 200 Aft step skin friction distribution**

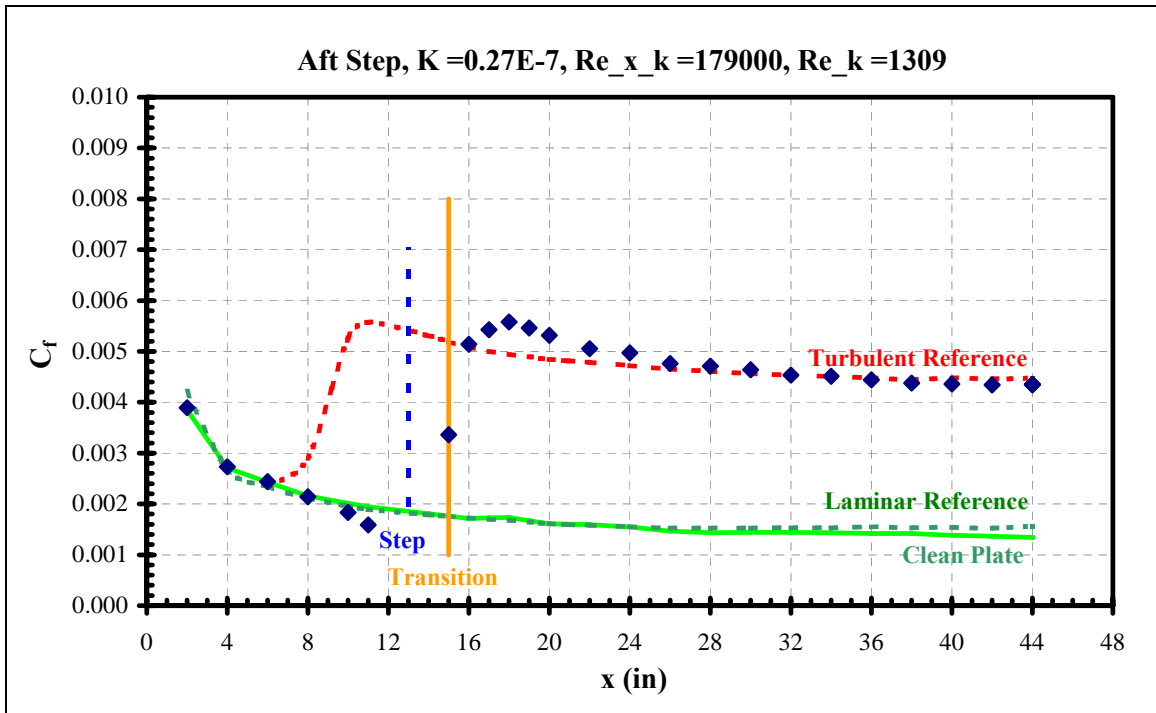


**Figure 201 Aft step skin friction distribution**

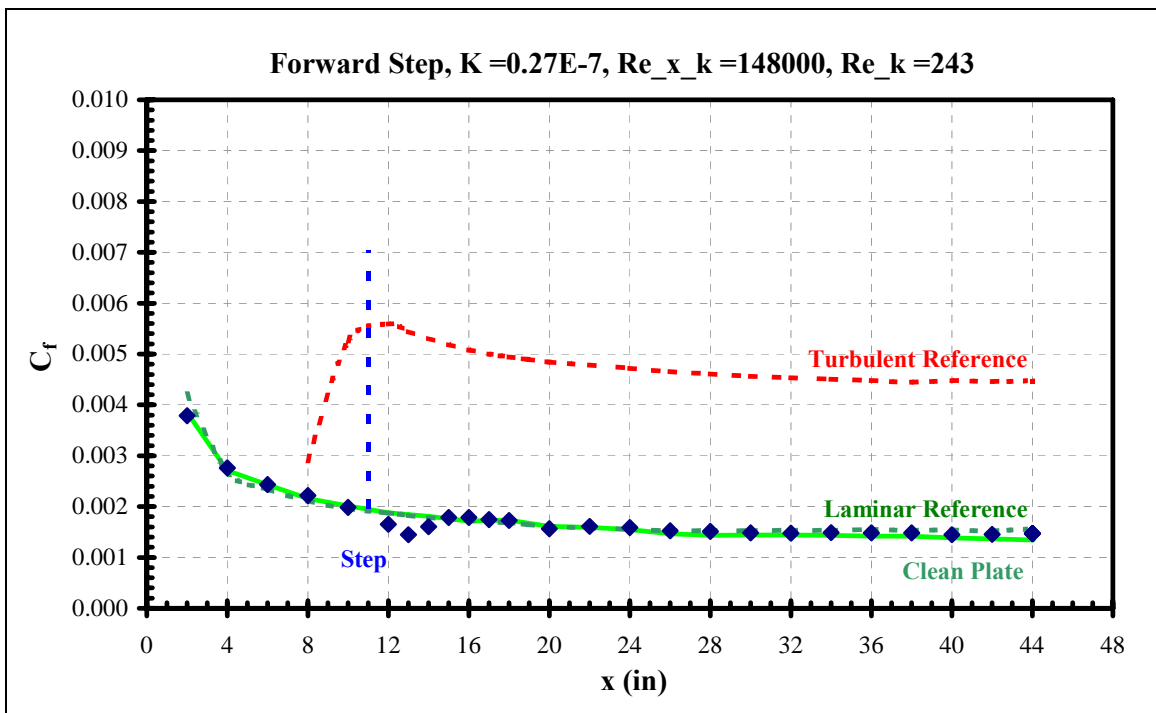


**Figure 202 Forward step skin friction distribution**

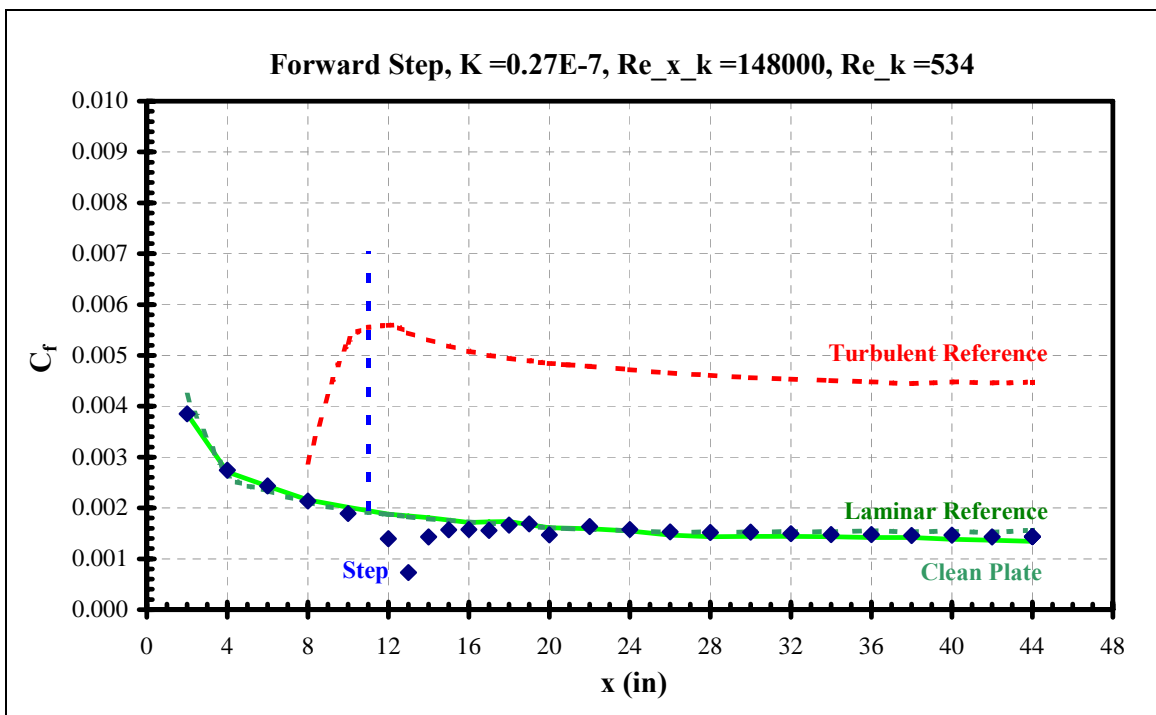


**Figure 203 Forward step skin friction distribution**

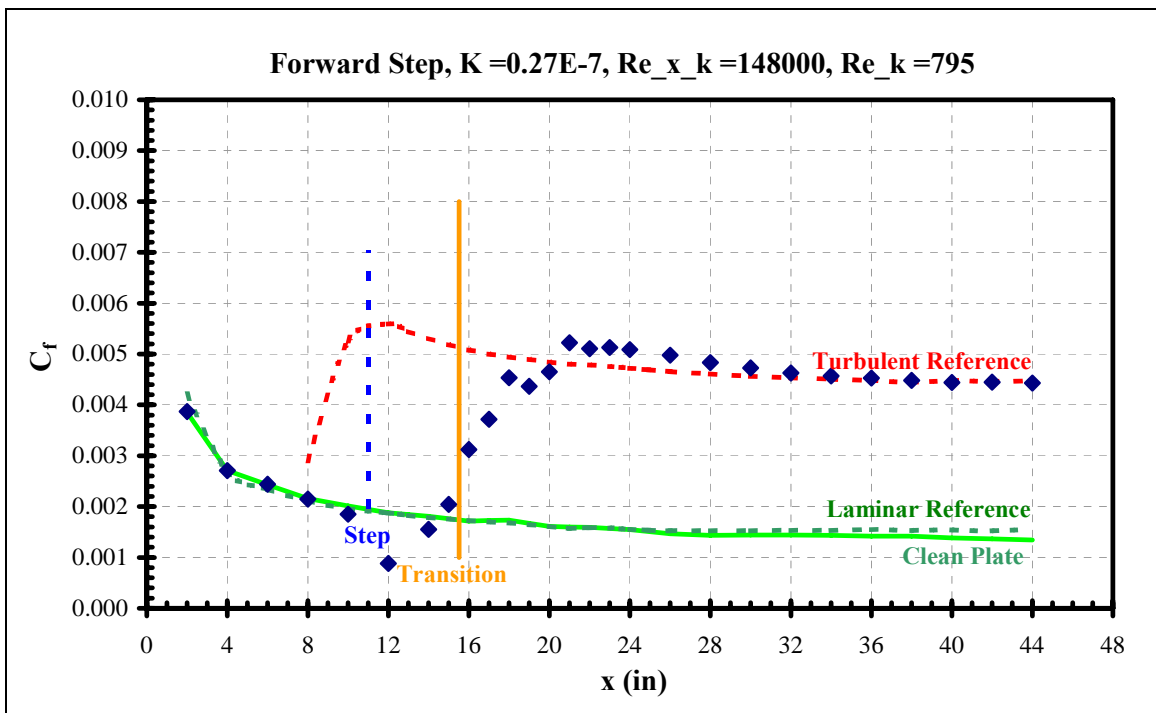


**Figure 204 Forward step skin friction distribution**

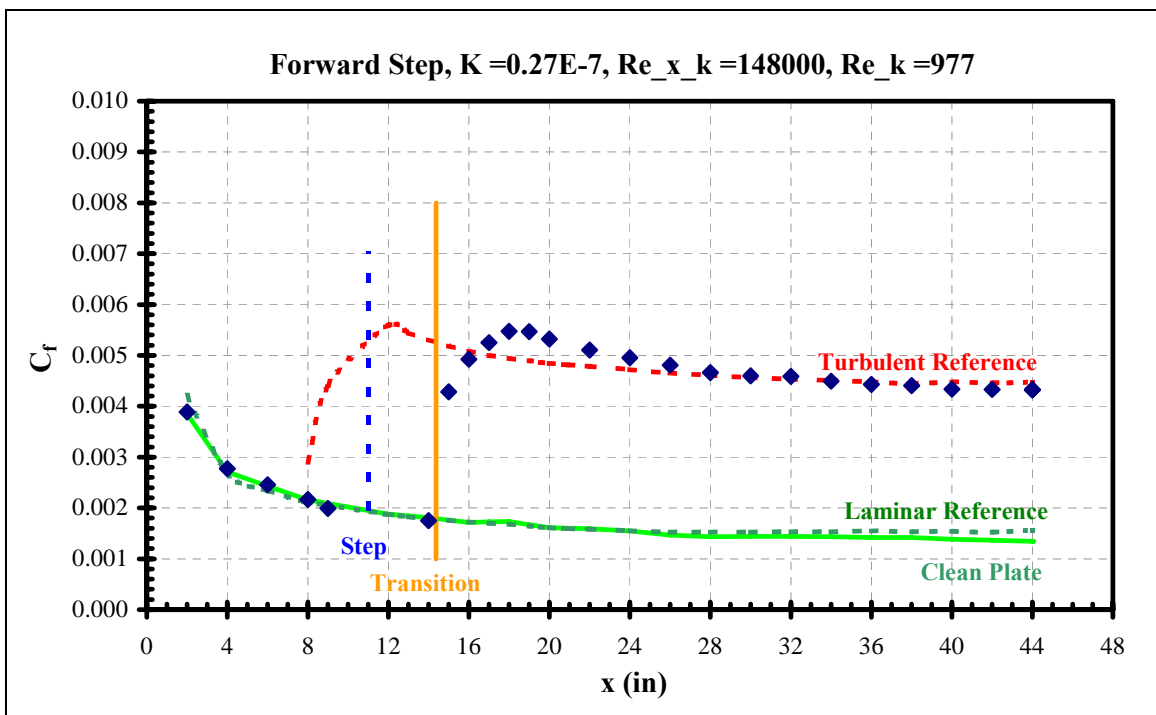


**Figure 205 Forward step skin friction distribution**

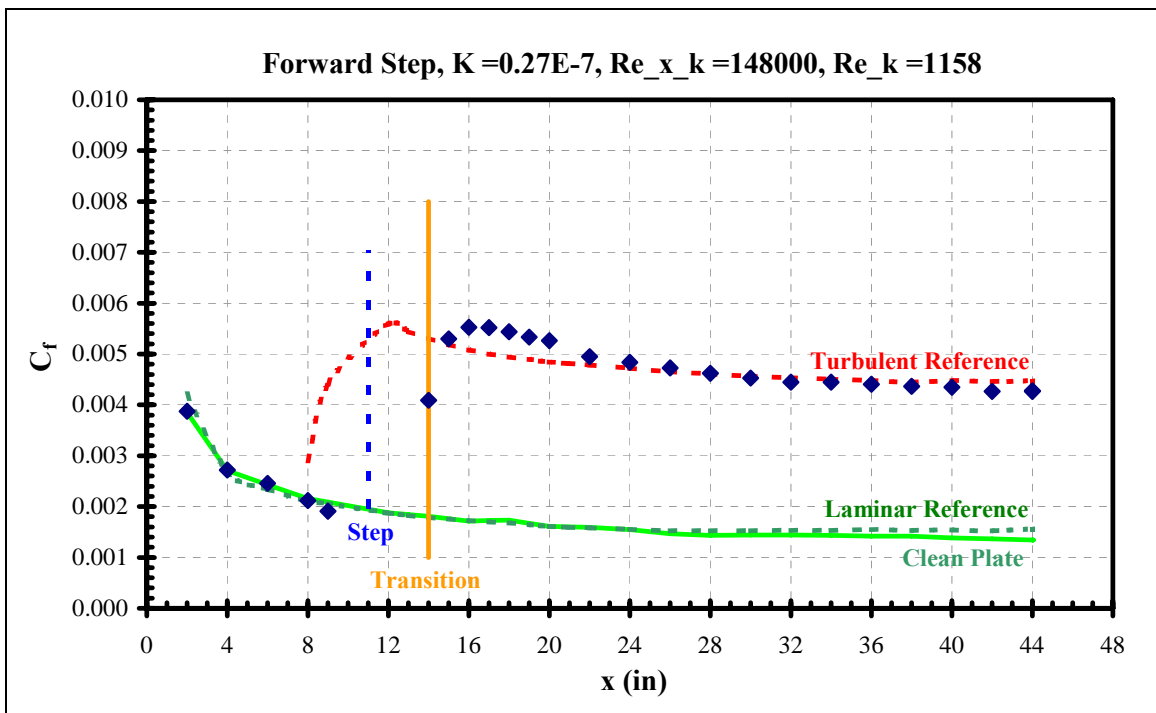


**Figure 206 Forward step skin friction distribution**

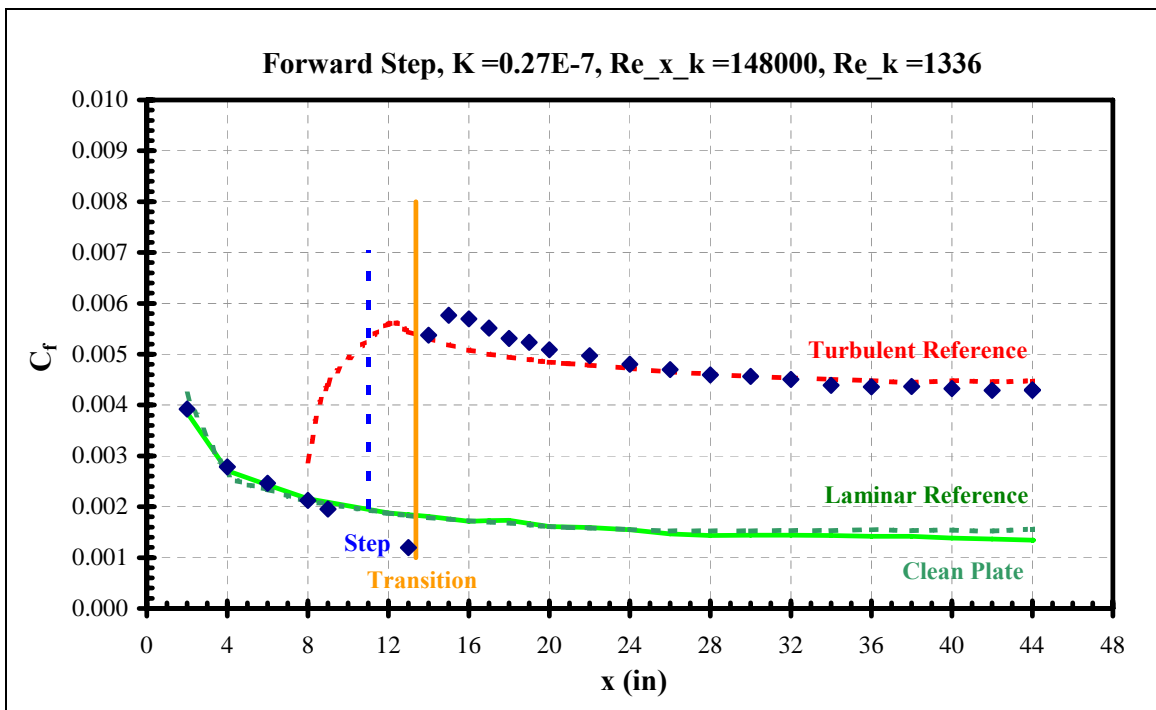


**Figure 207 Forward step skin friction distribution**

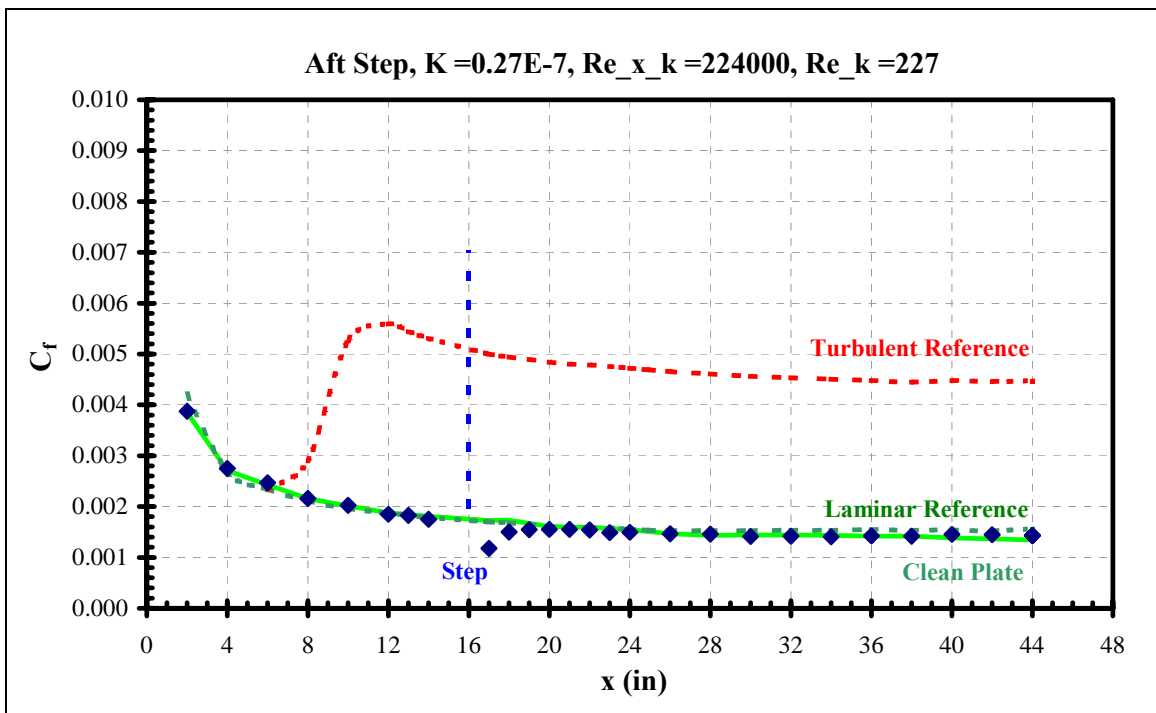


**Figure 208 Aft step skin friction distribution**

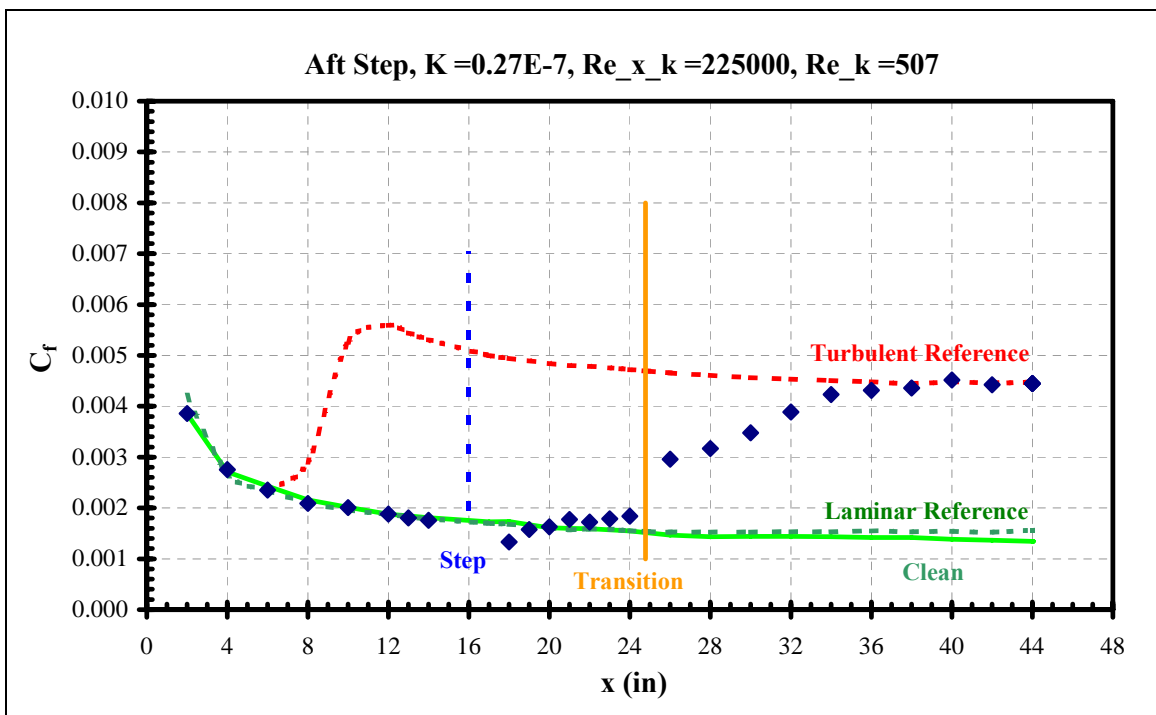


**Figure 209 Aft step skin friction distribution**

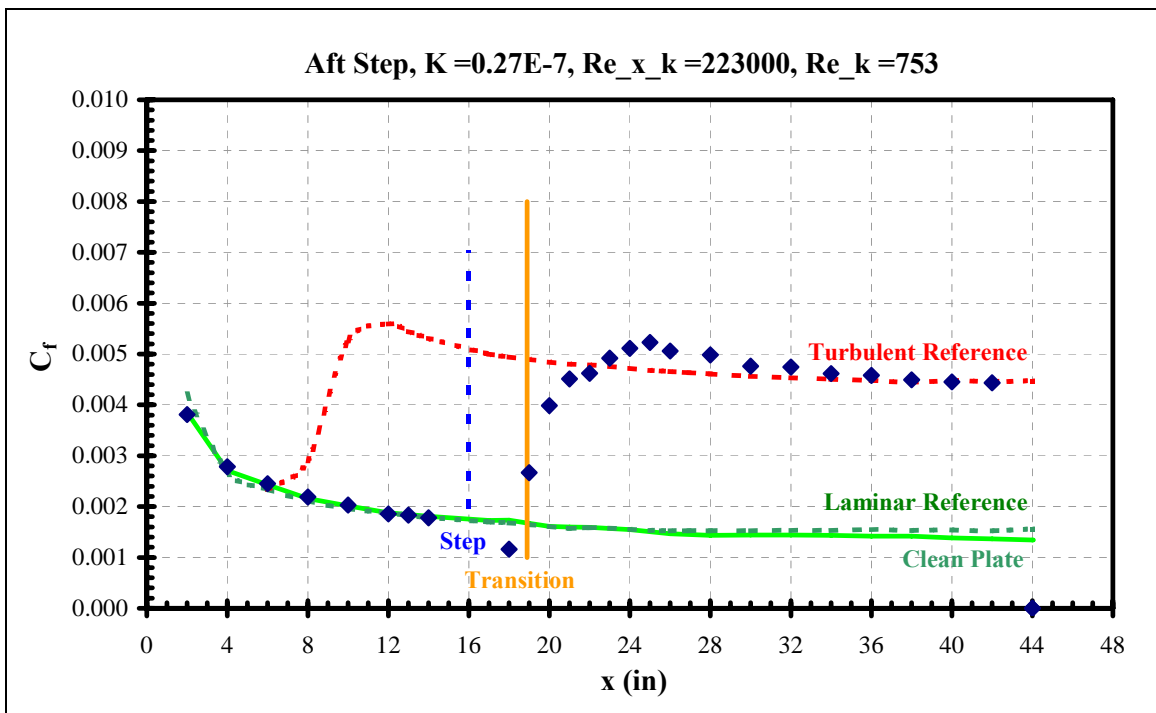


**Figure 210 Aft step skin friction distribution**

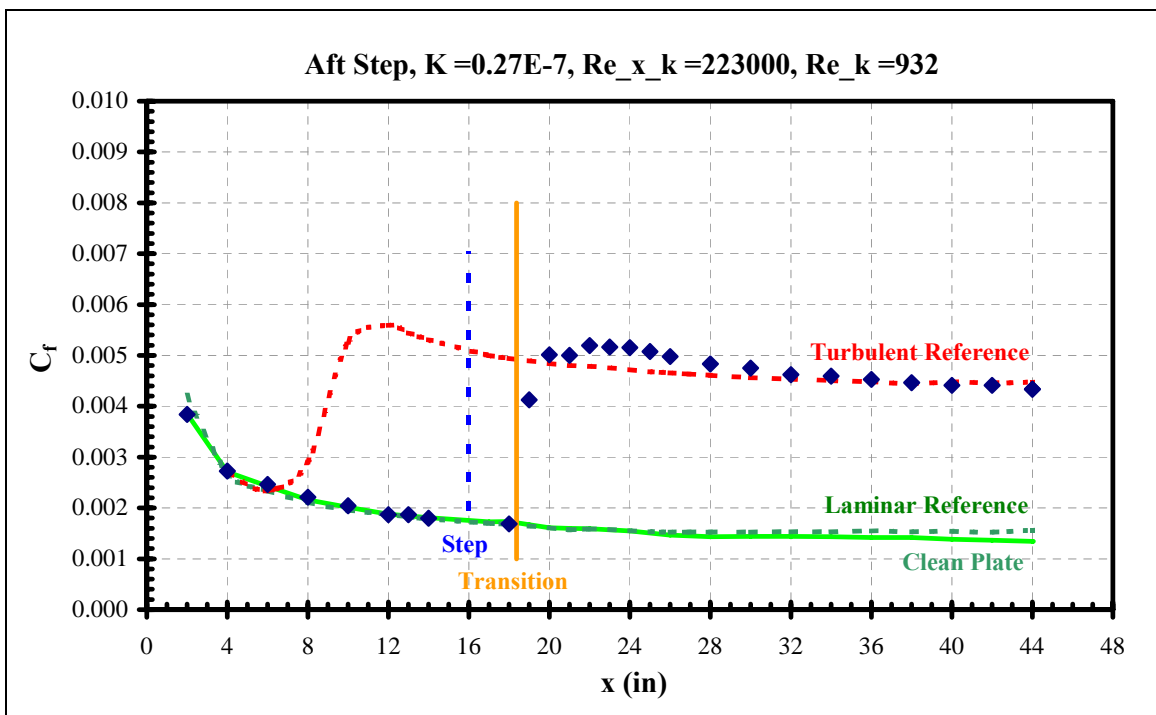


**Figure 211 Aft step skin friction distribution**



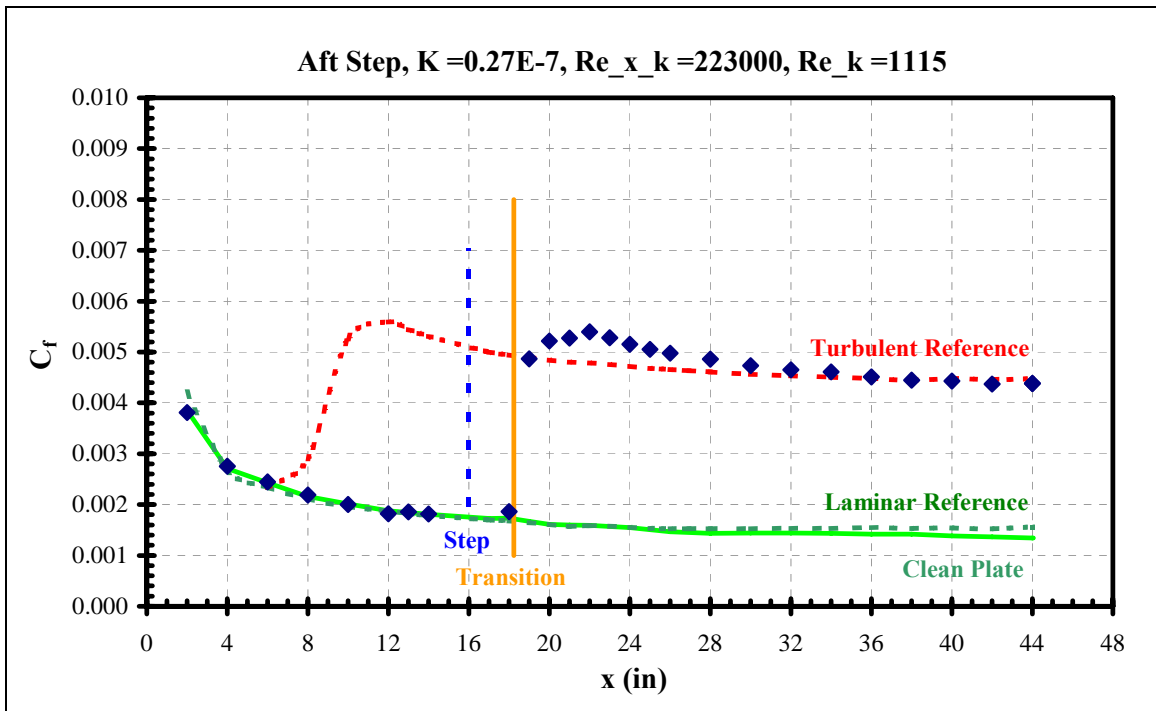


Figure 212 Aft step skin friction distribution

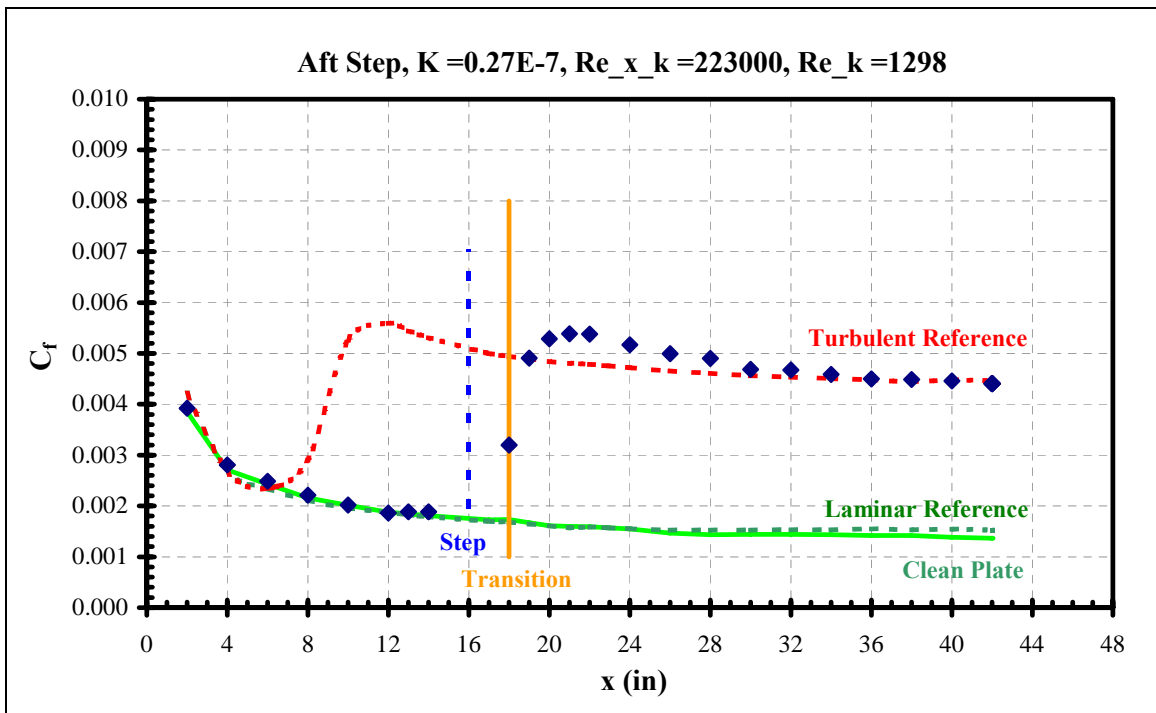
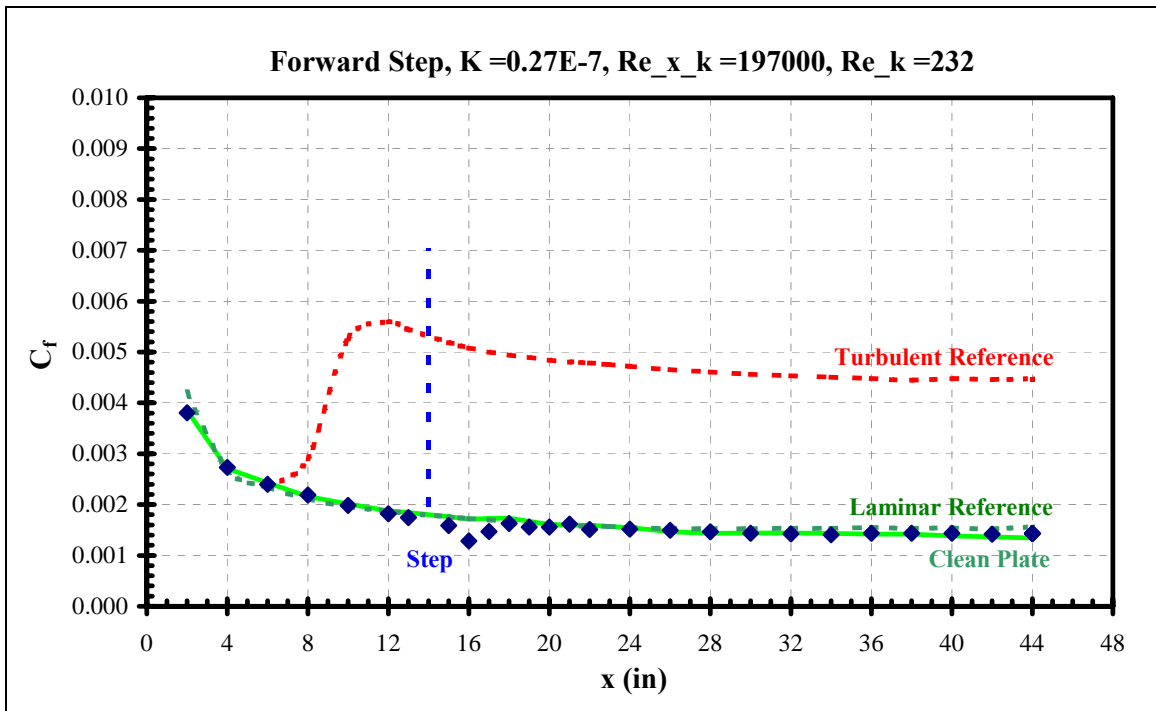
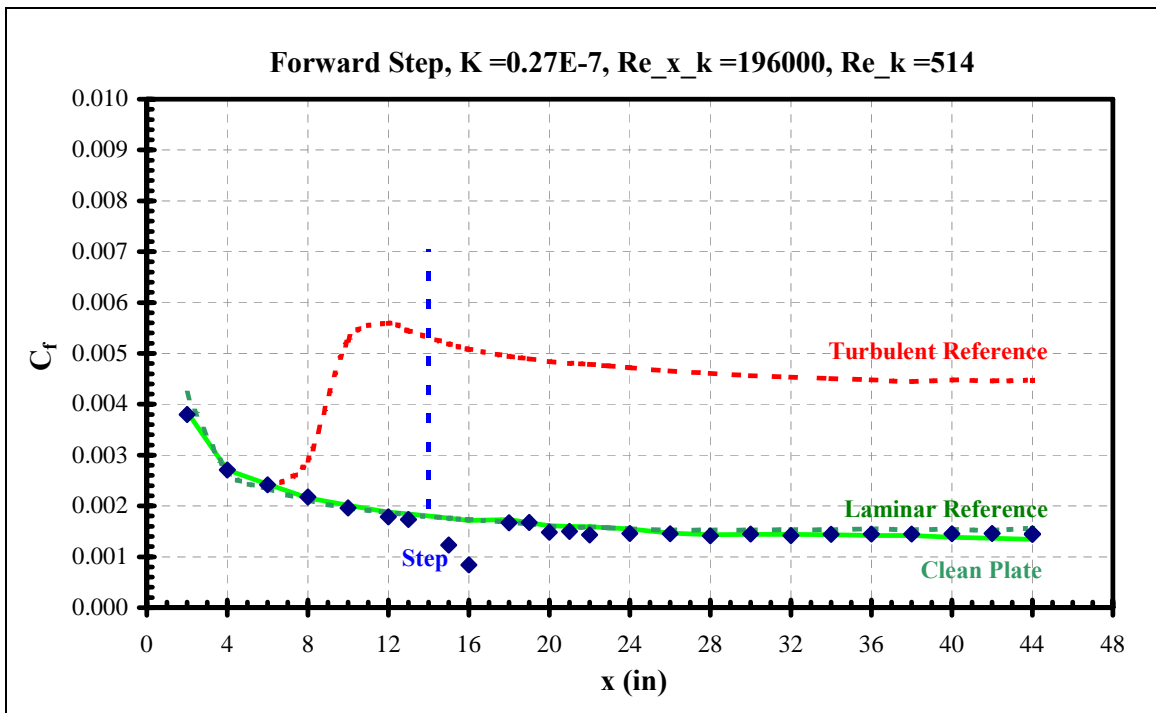


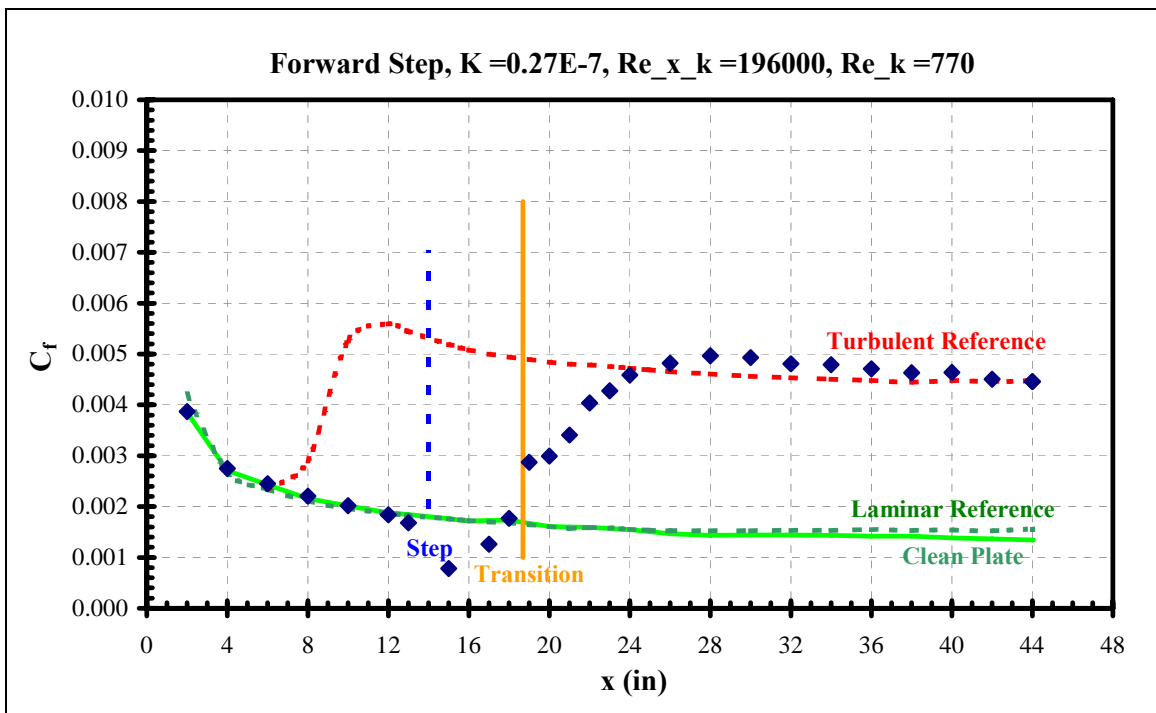
Figure 213 Aft step skin friction distribution



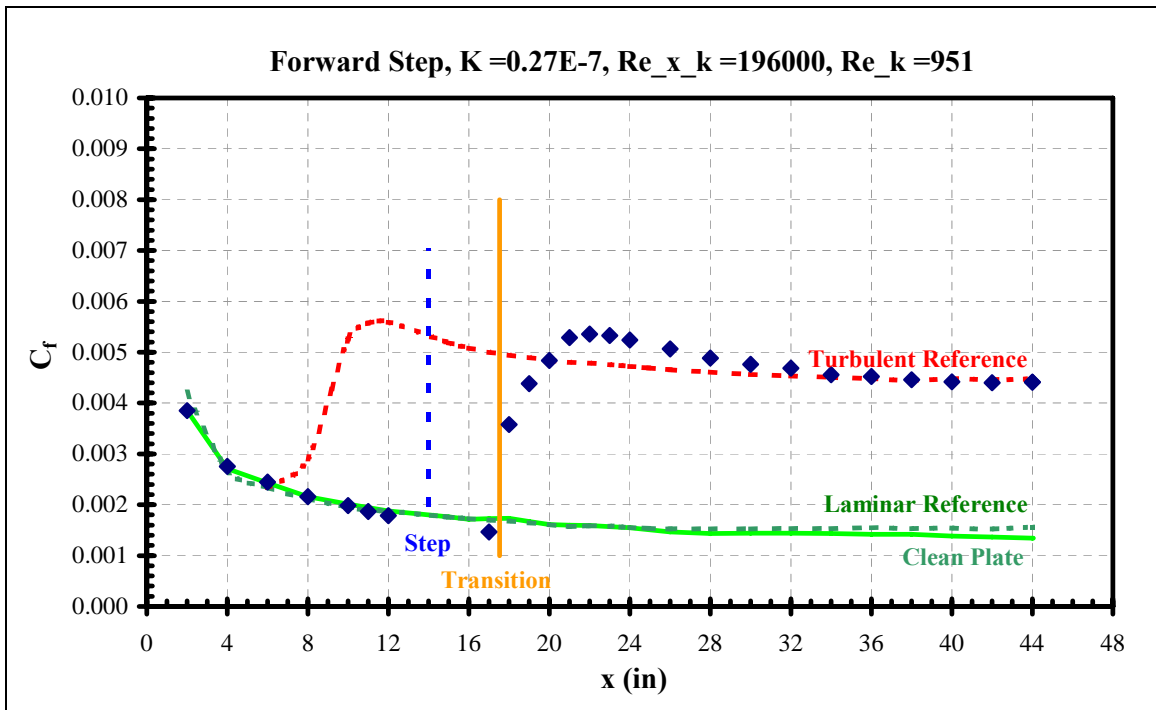
**Figure 214 Forward step skin friction distribution**



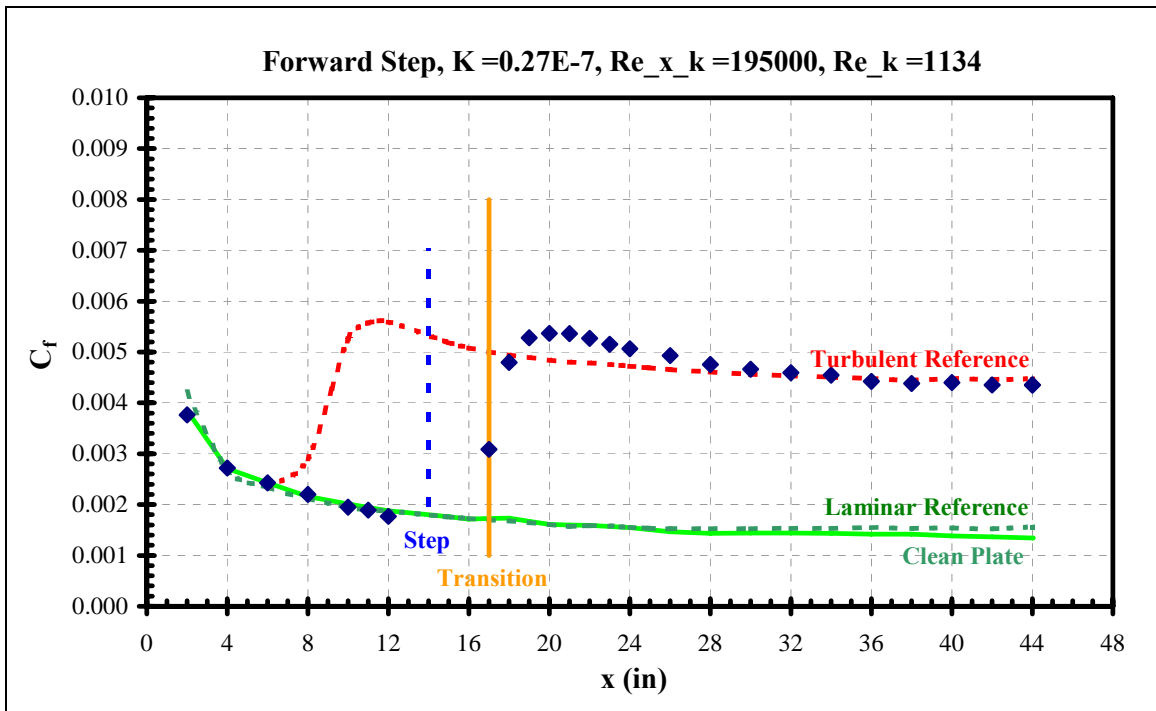
**Figure 215 Forward step skin friction distribution**



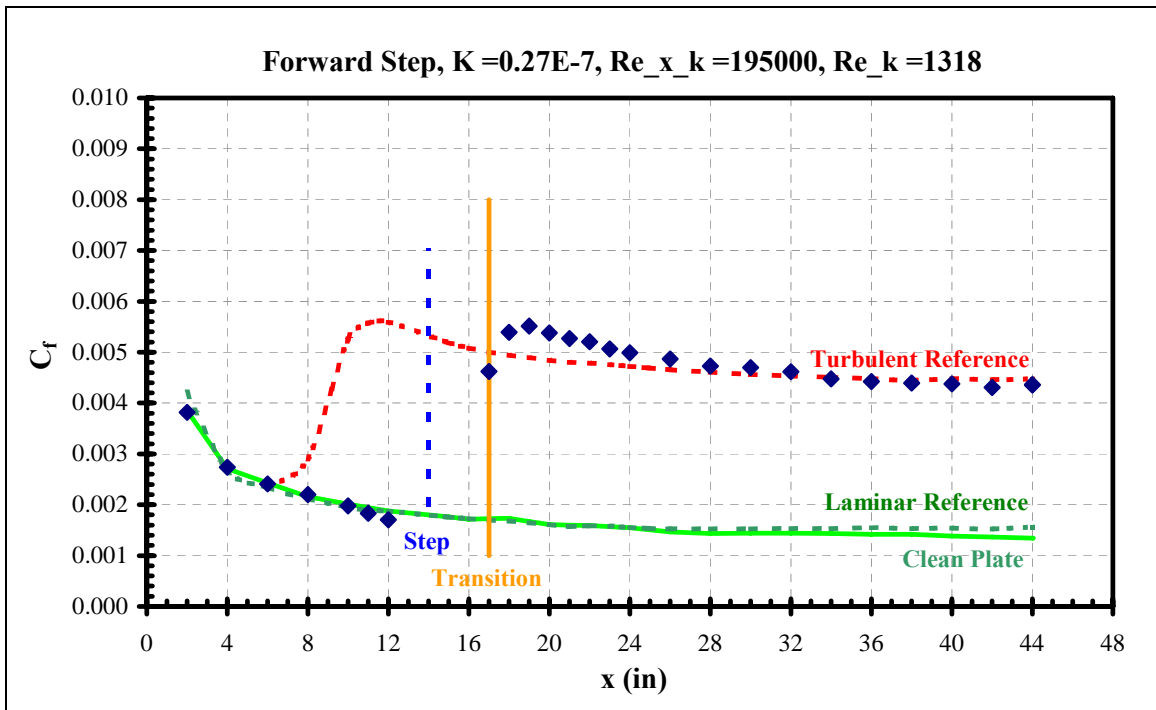
**Figure 216 Forward step skin friction distribution**



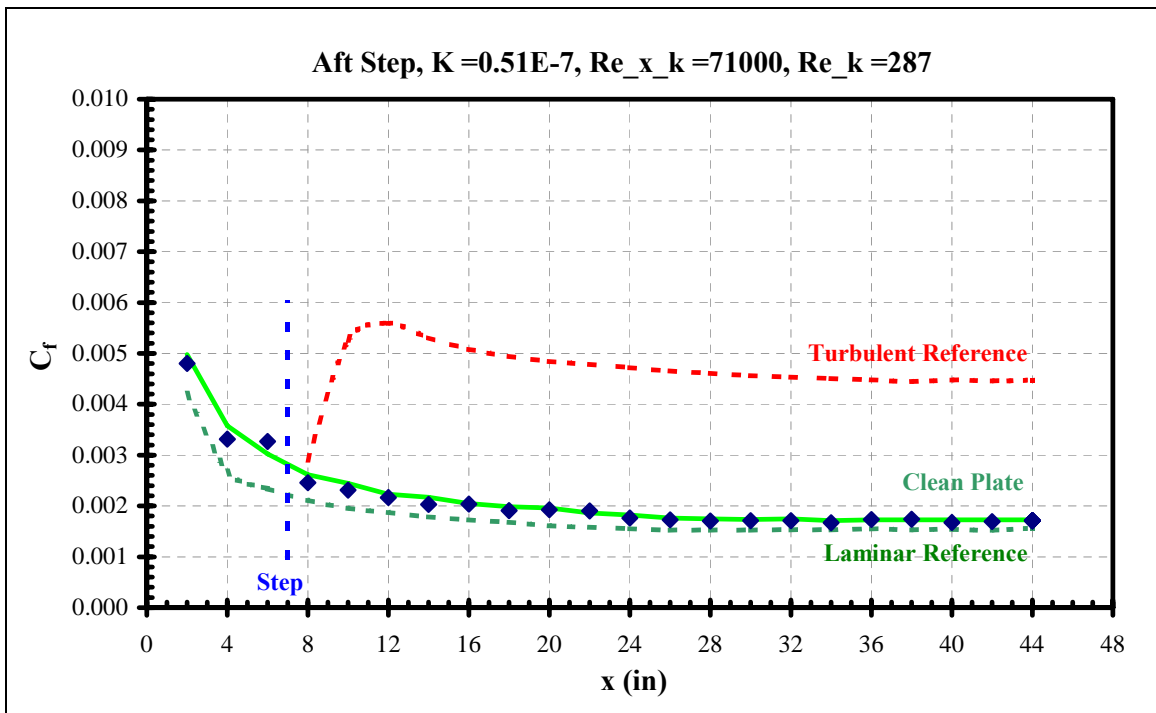
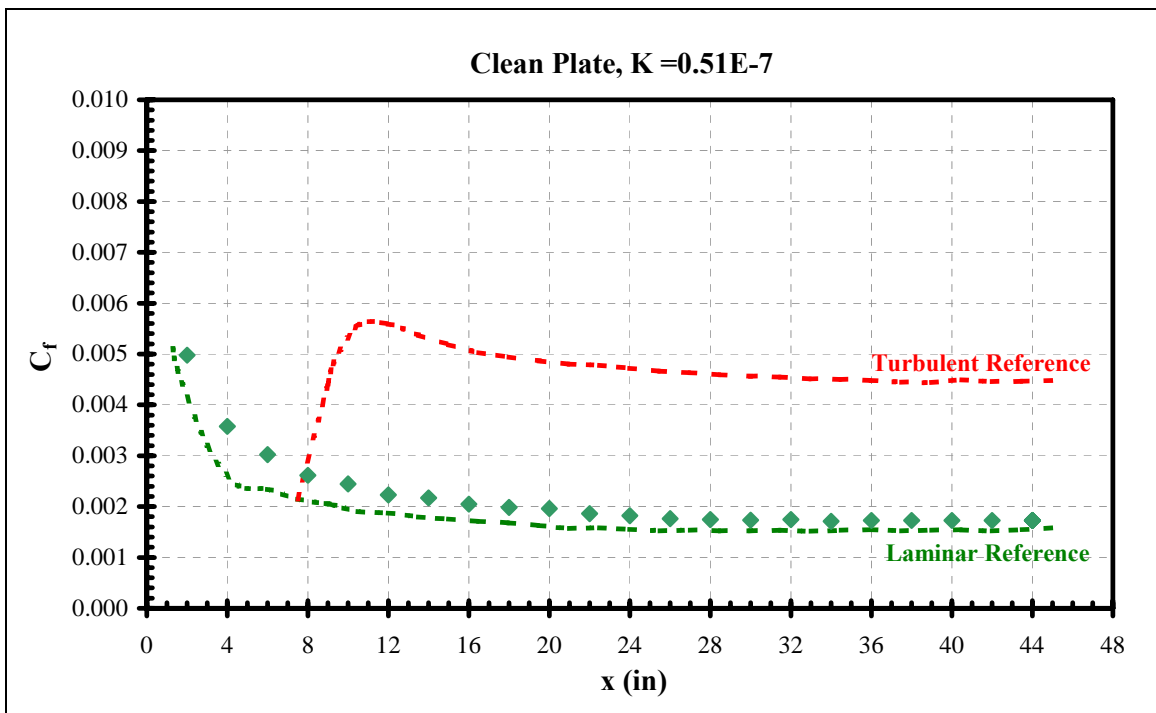
**Figure 217 Forward step skin friction distribution**

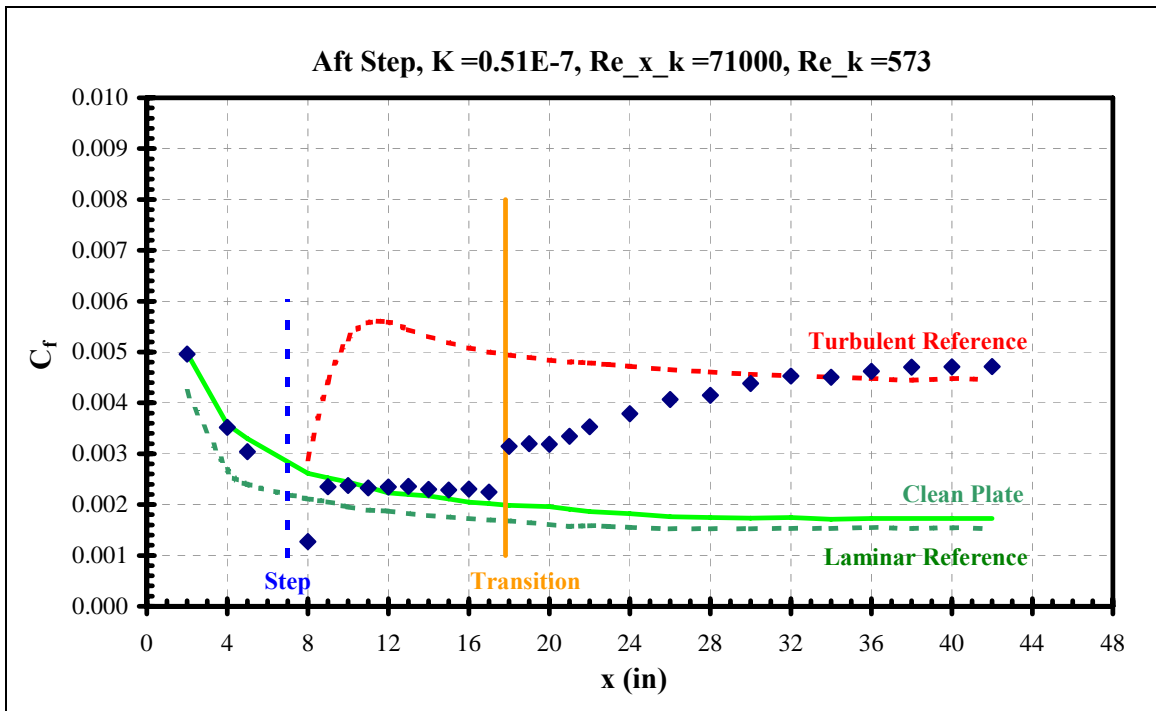


**Figure 218 Forward step skin friction distribution**

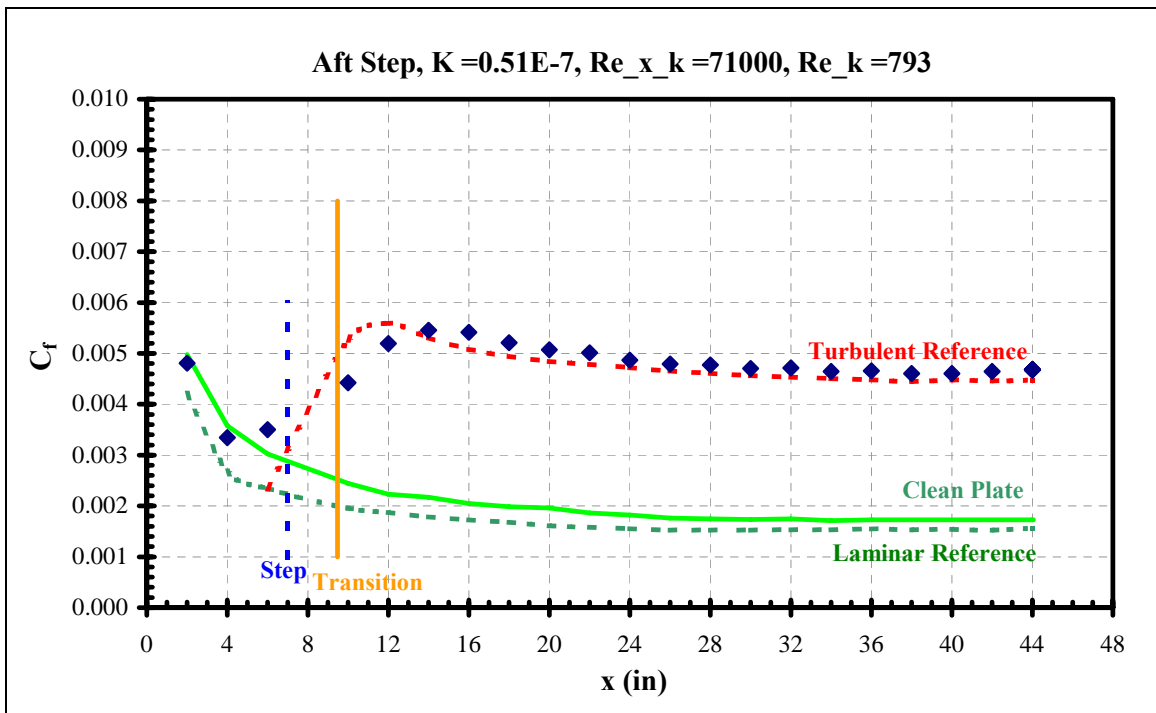


**Figure 219 Forward step skin friction distribution**

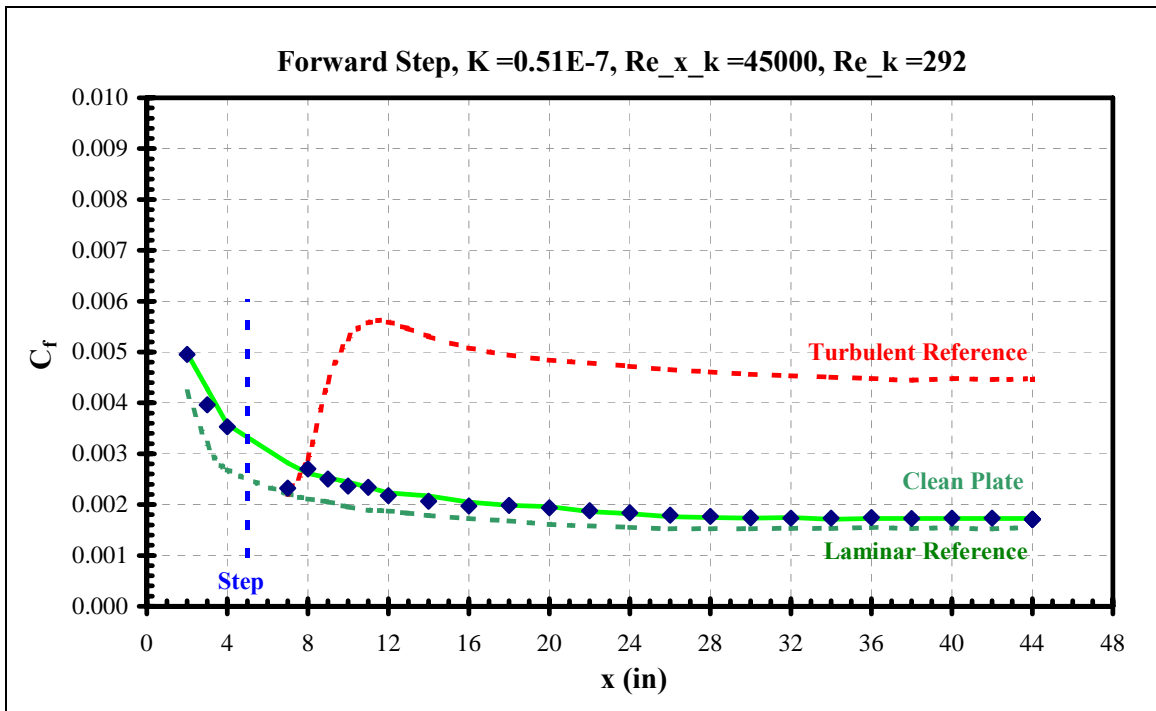




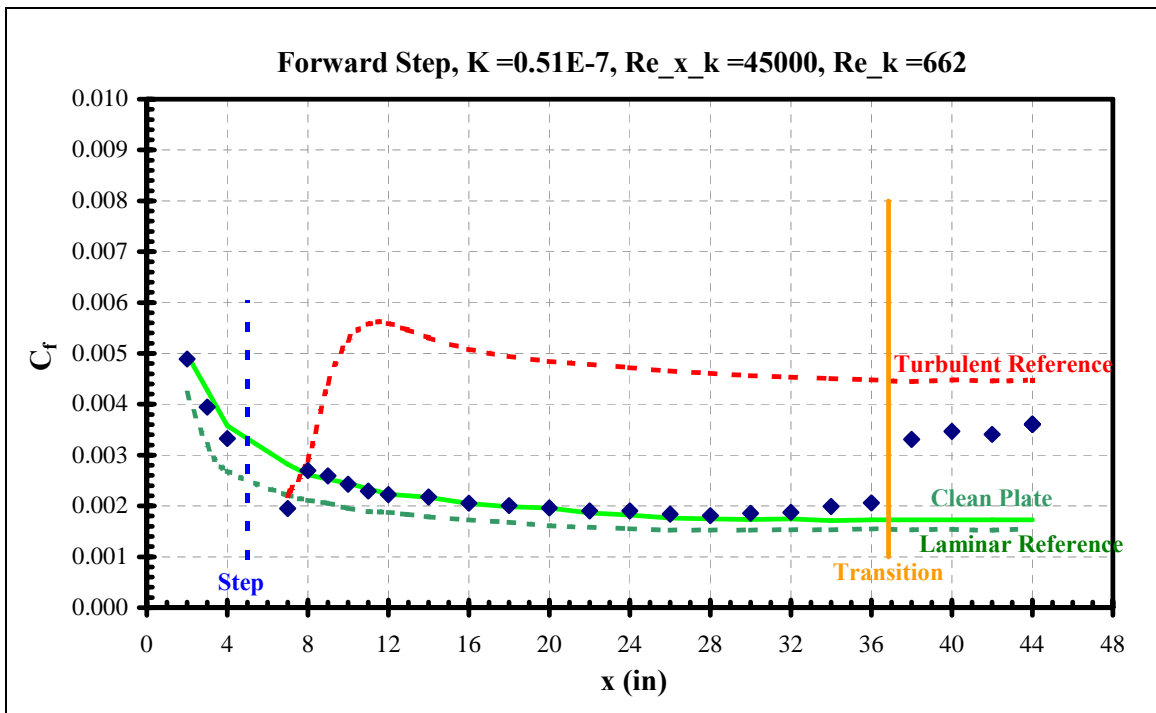
**Figure 222 Aft step skin friction distribution**



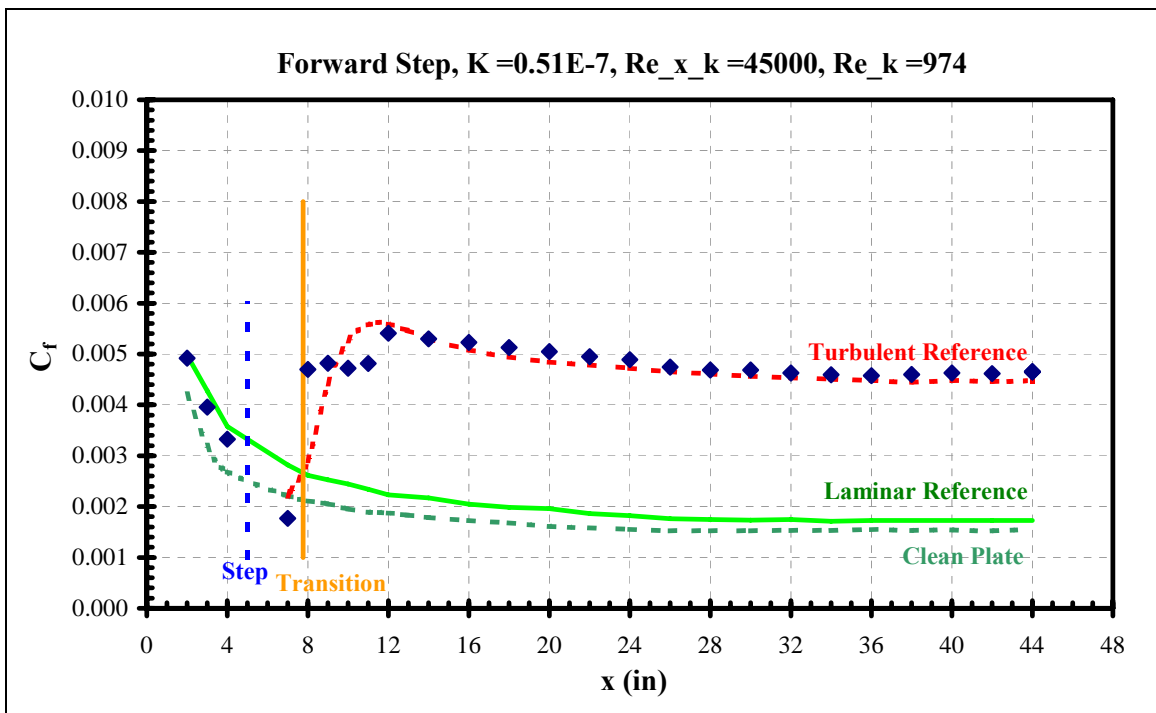
**Figure 223 Aft step skin friction distribution**



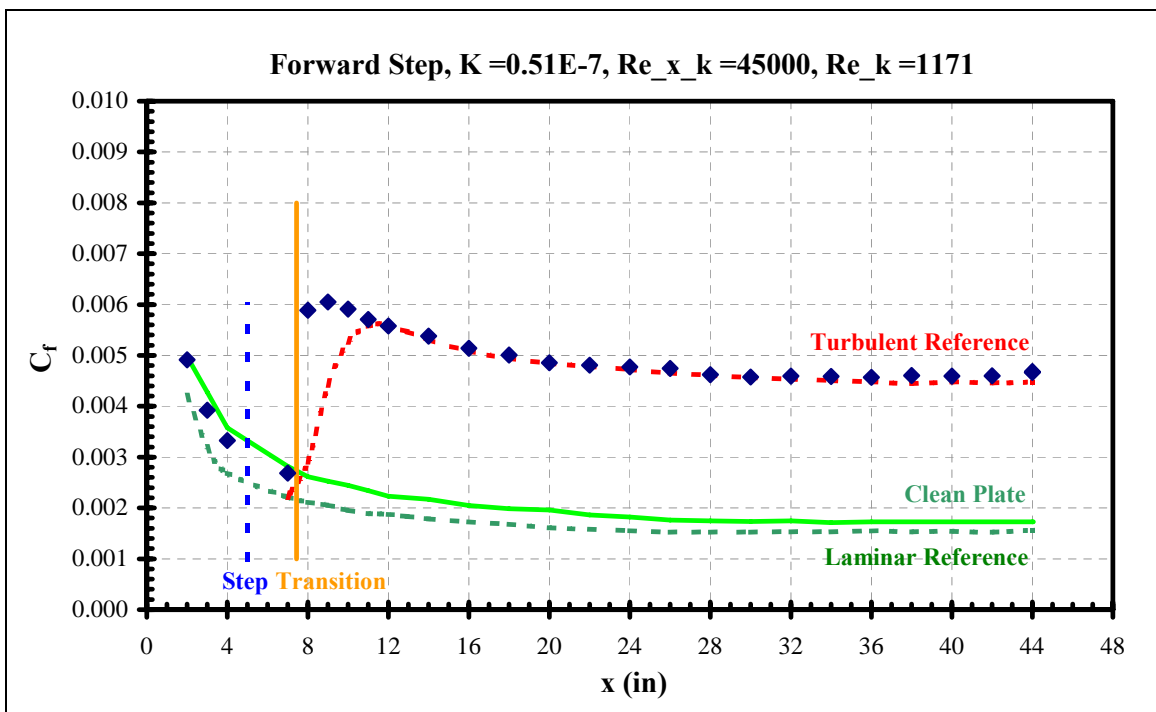
**Figure 224 Forward step skin friction distribution**



**Figure 225 Forward step skin friction distribution**

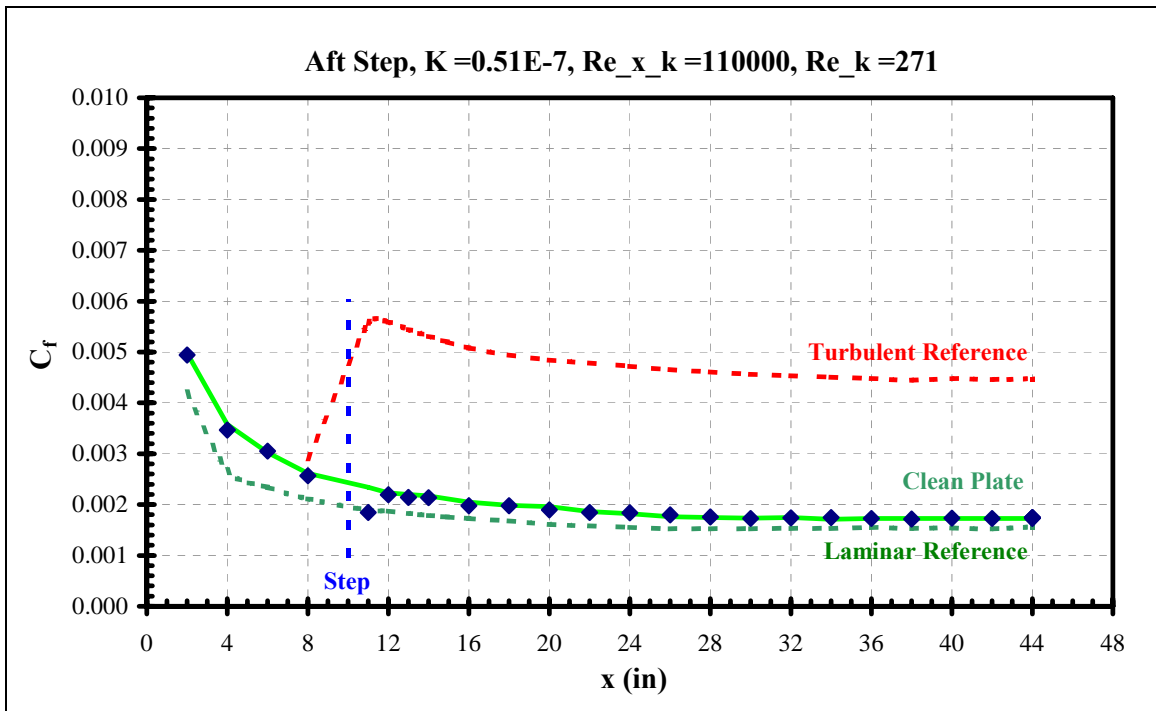


**Figure 226 Forward step skin friction distribution**

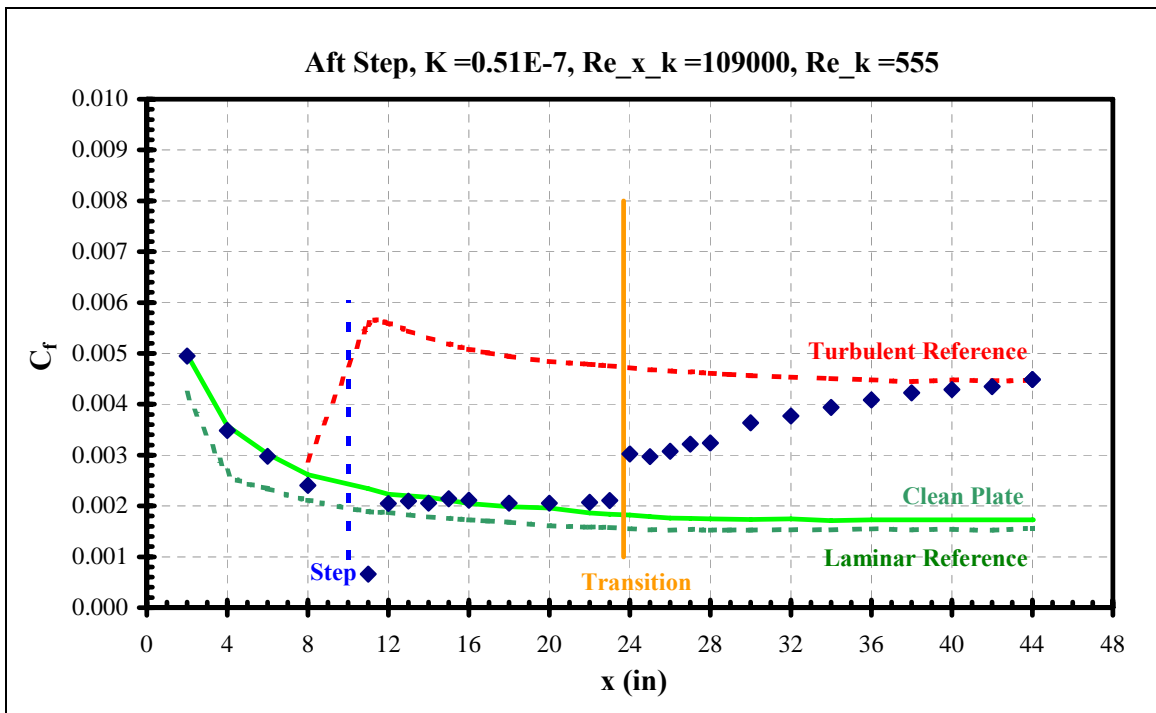


**Figure 227 Forward step skin friction distribution**

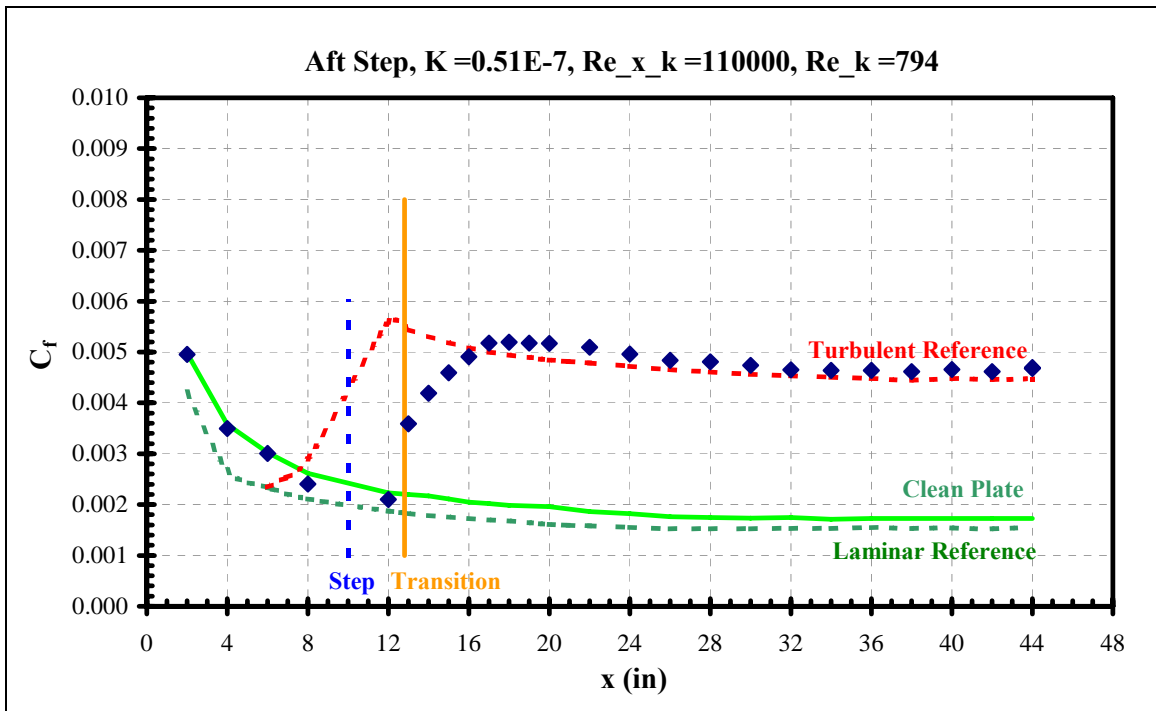




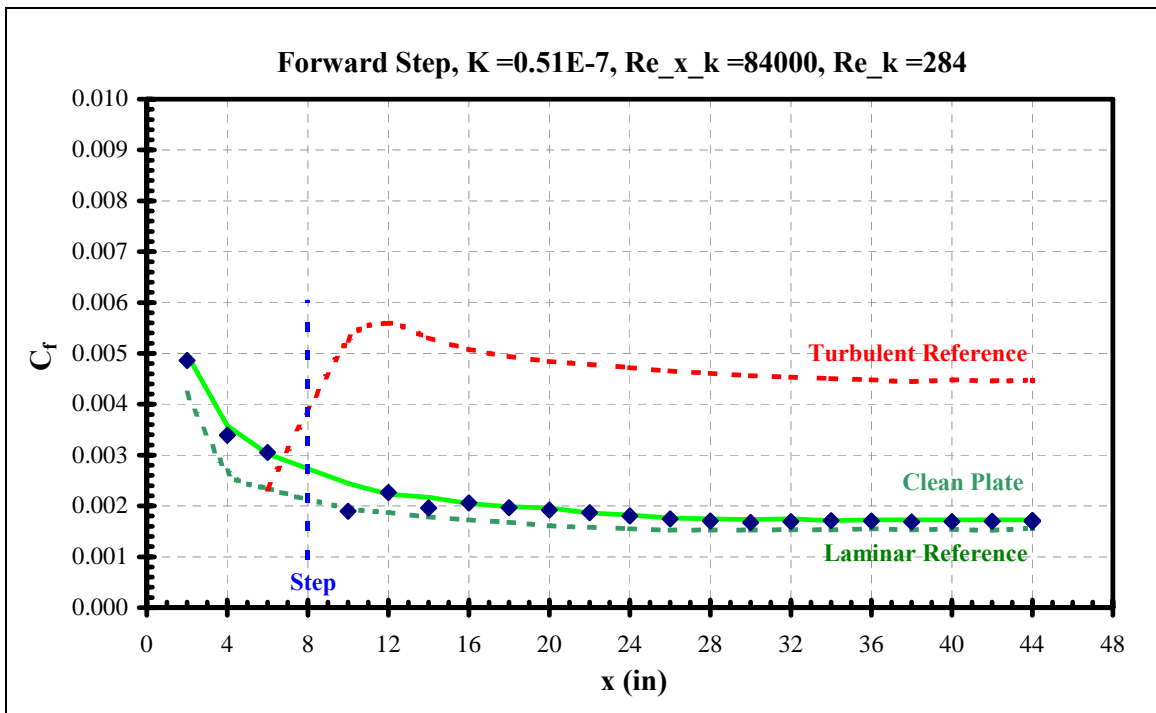
**Figure 228 Aft step skin friction distribution**



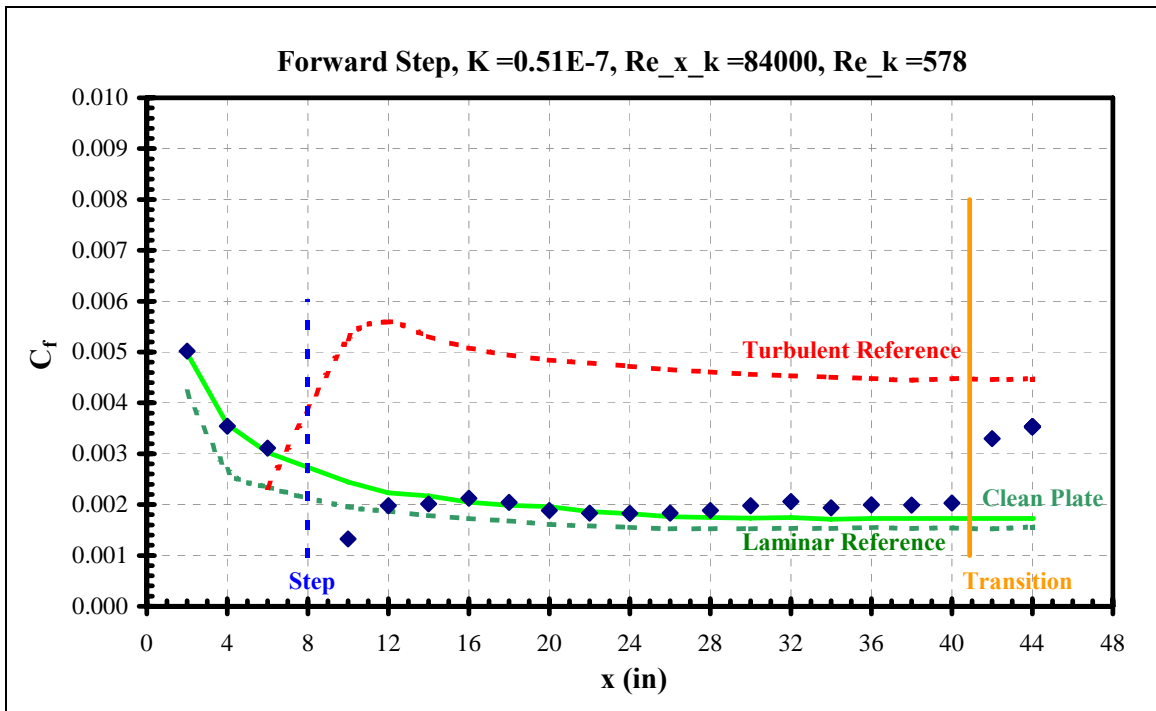
**Figure 229 -Aft step skin friction distribution**



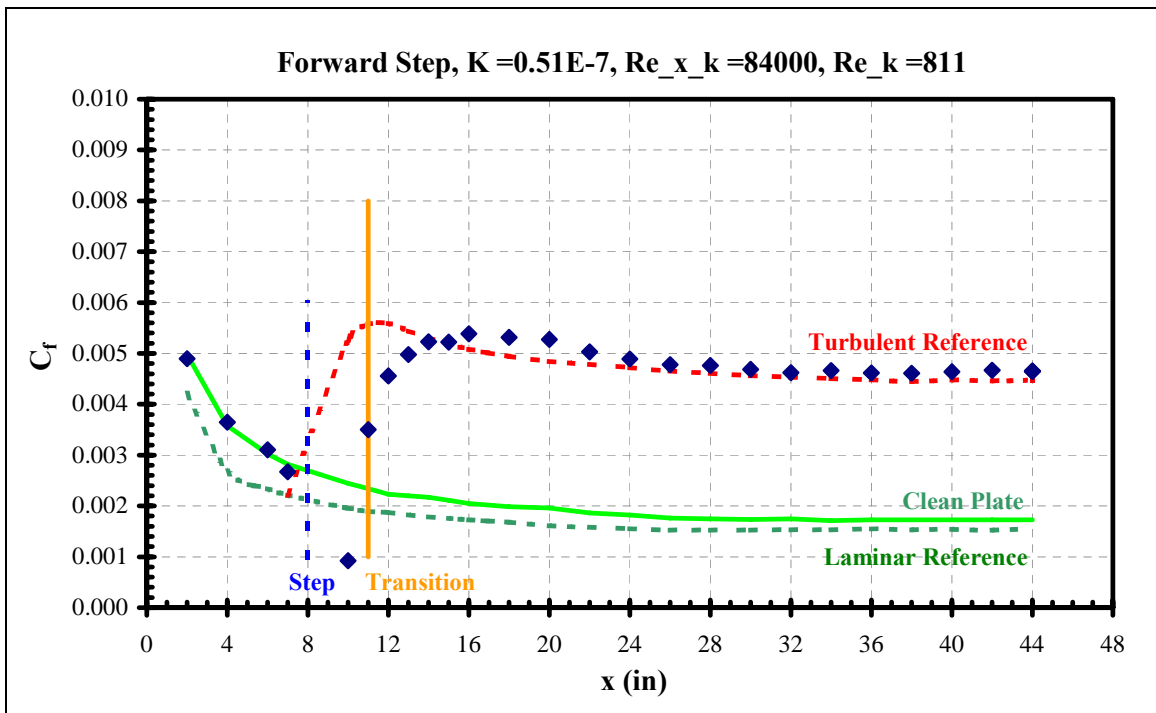
**Figure 230 Aft step skin friction distribution**



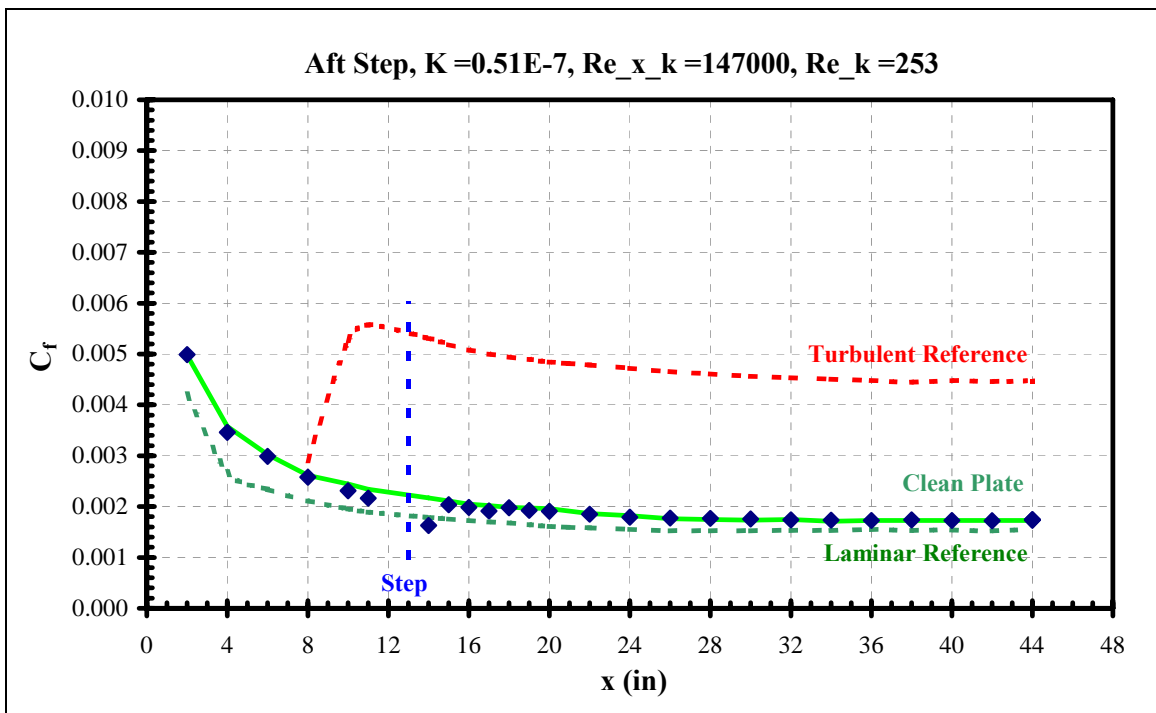
**Figure 231 Forward step skin friction distribution**



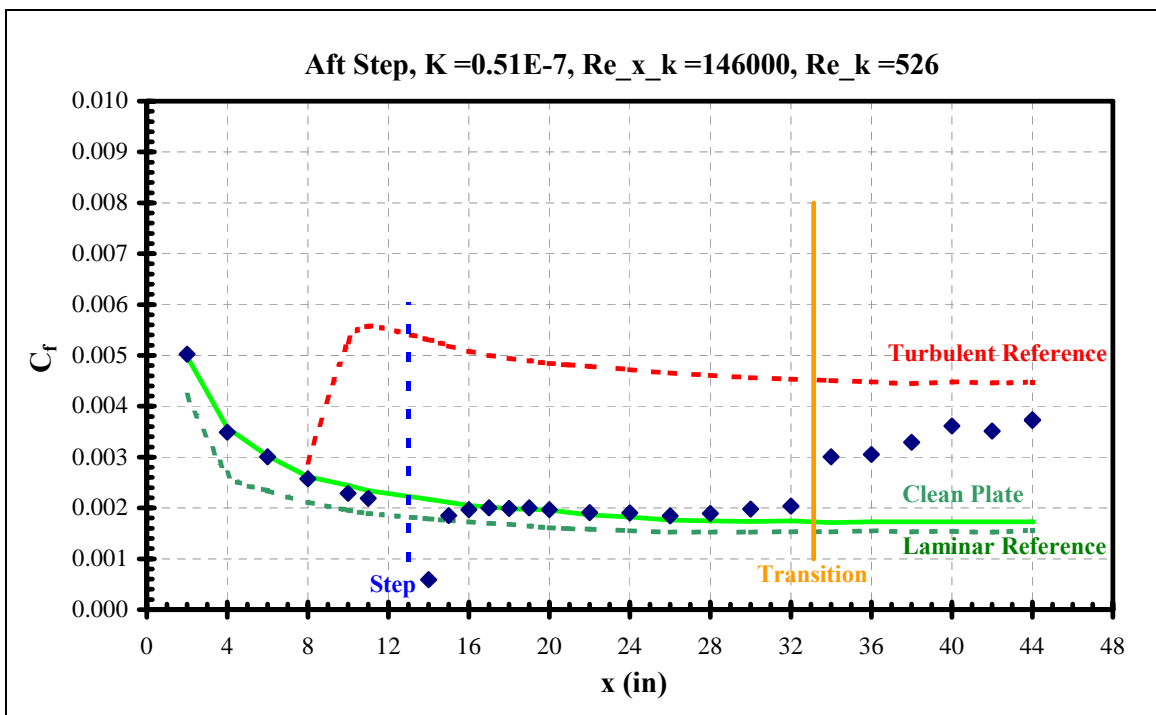
**Figure 232 Forward step skin friction distribution**



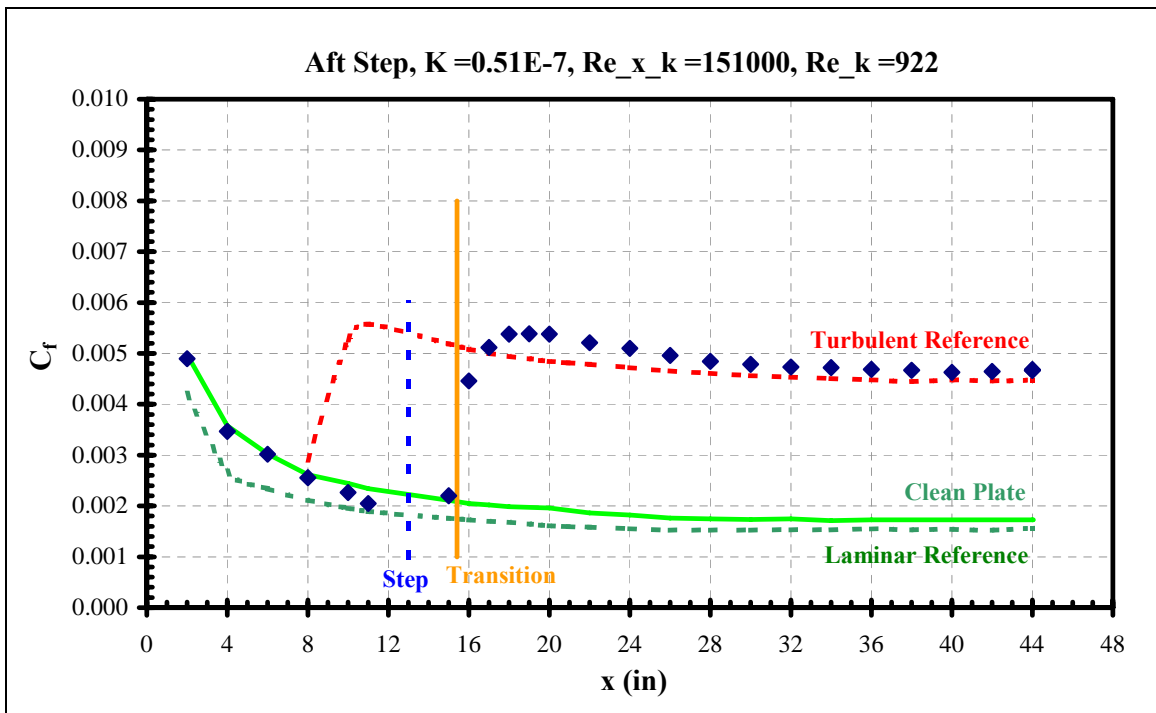
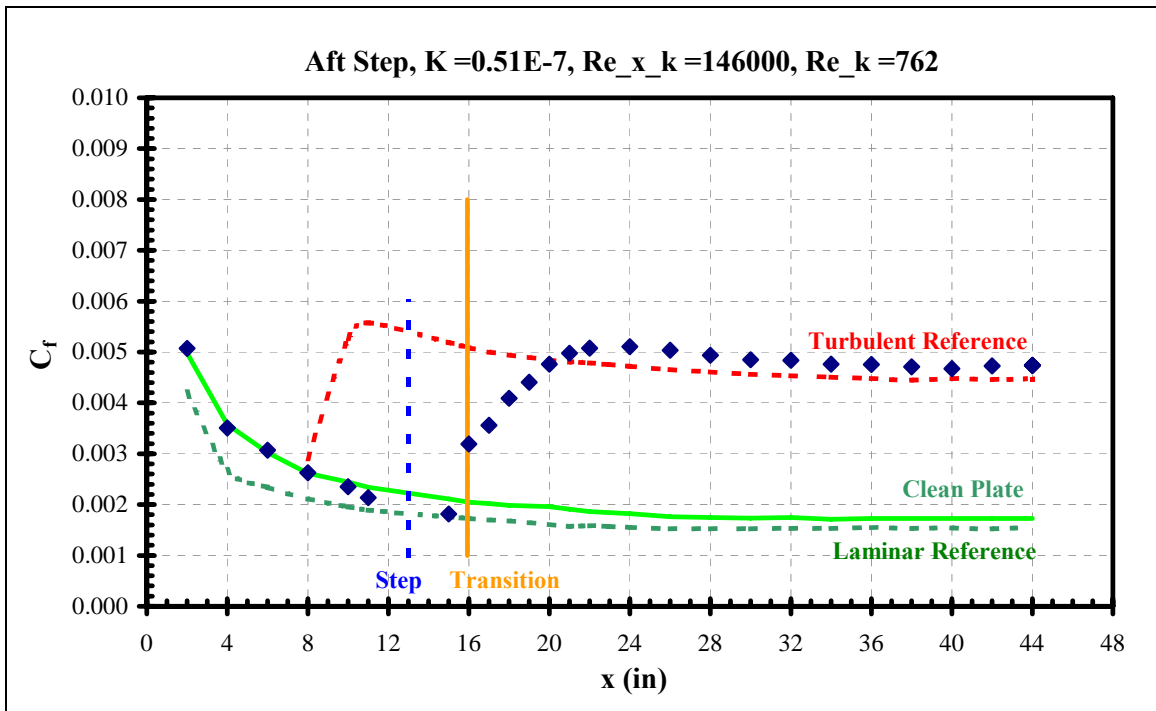
**Figure 233 Forward step skin friction distribution**

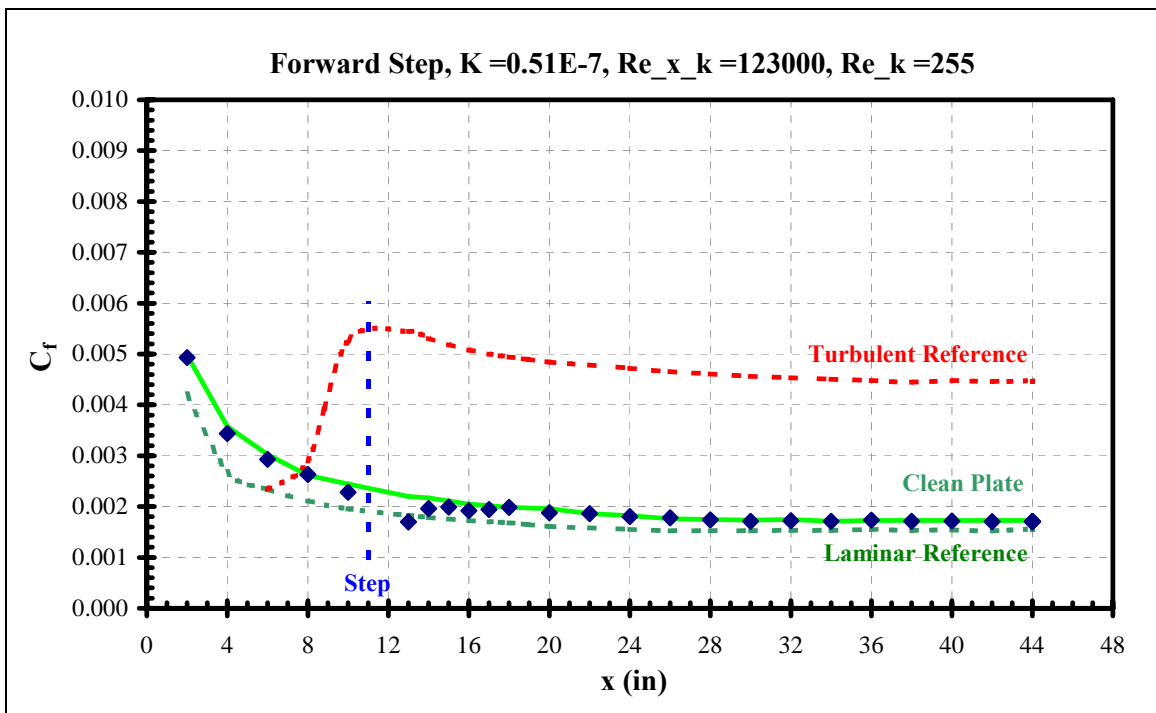


**Figure 234 Aft step skin friction distribution**

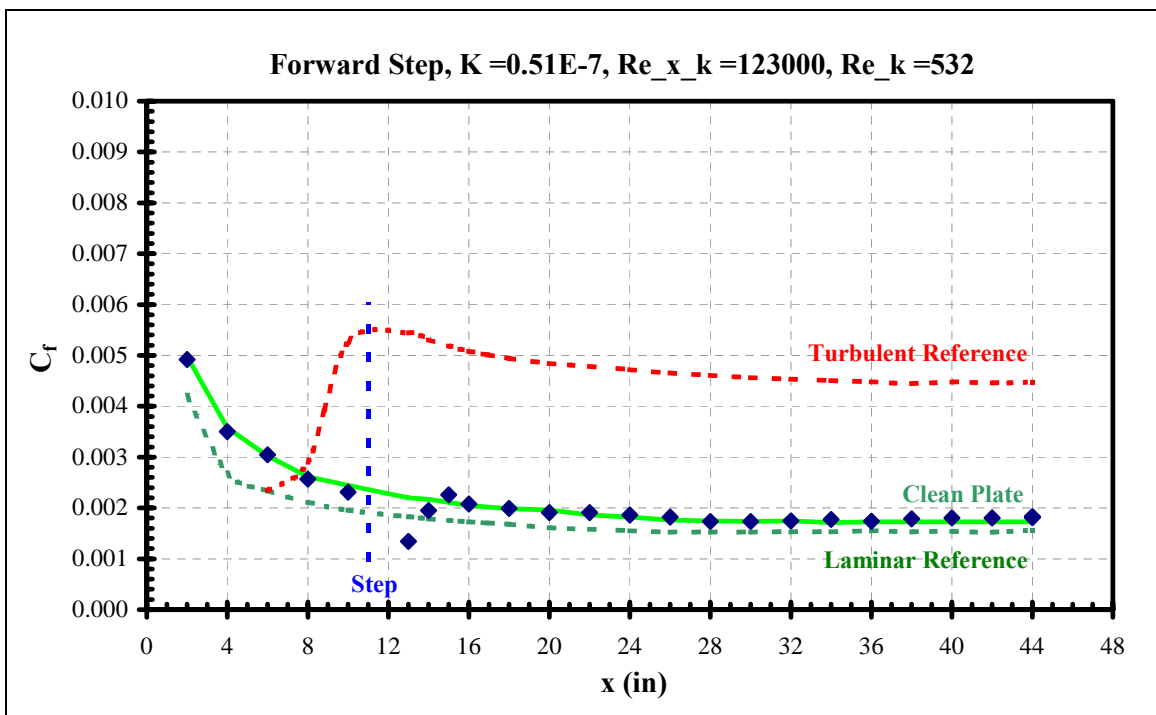


**Figure 235 Aft step skin friction distribution**

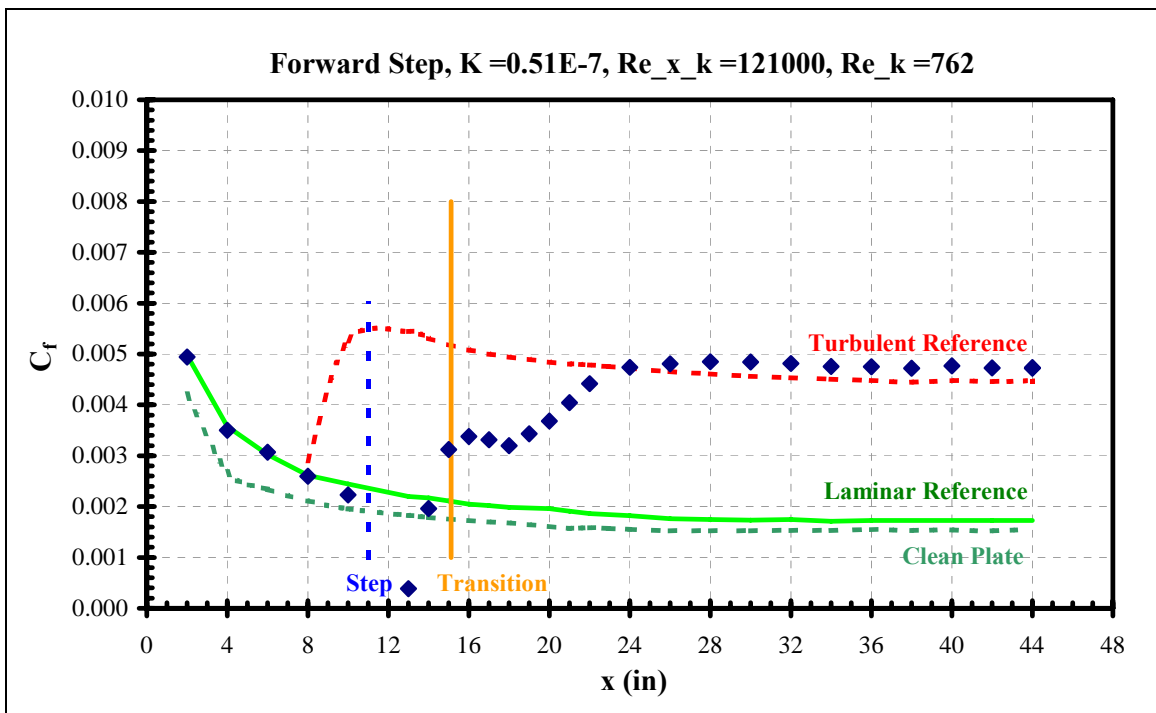




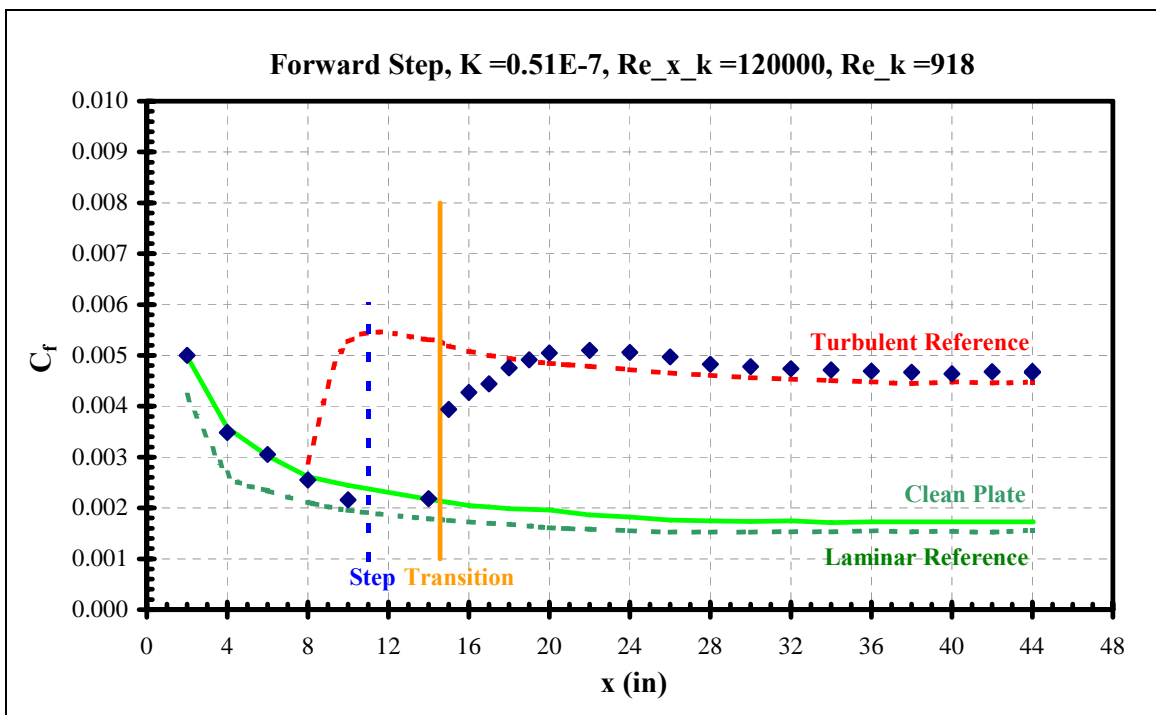
**Figure 238 Forward step skin friction distribution**



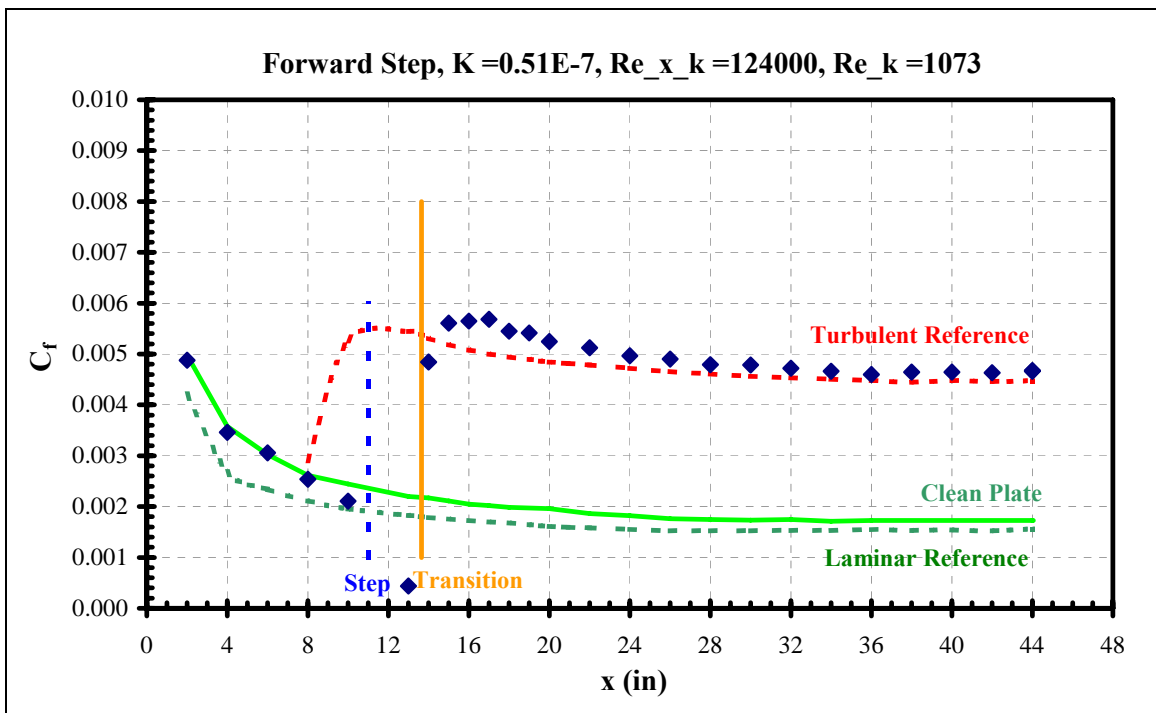
**Figure 239 Forward step skin friction distribution**



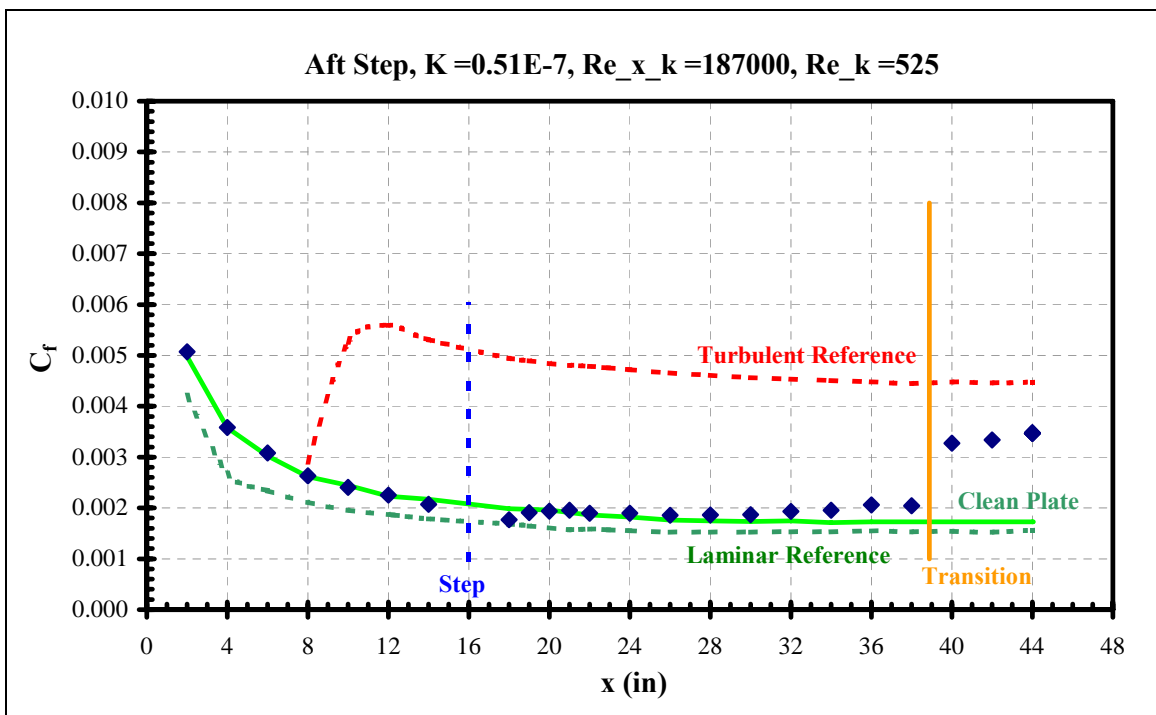
**Figure 240 Forward step skin friction distribution**



**Figure 241 Forward step skin friction distribution**

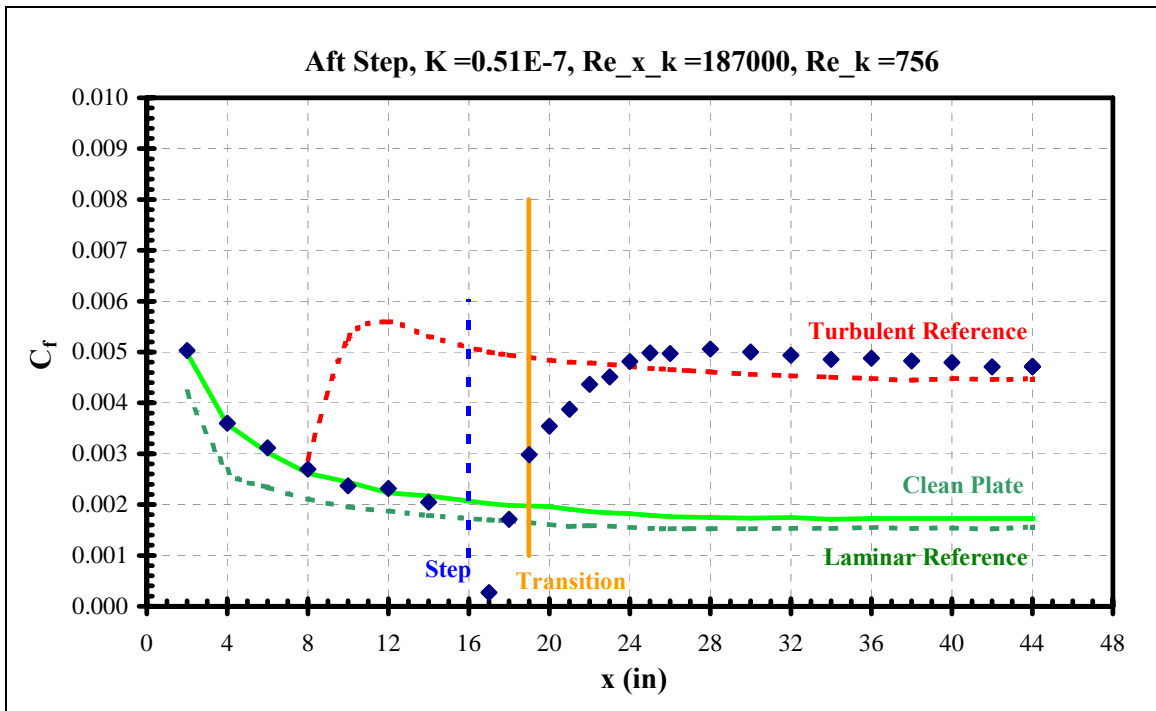


**Figure 242 Forward step skin friction distribution**

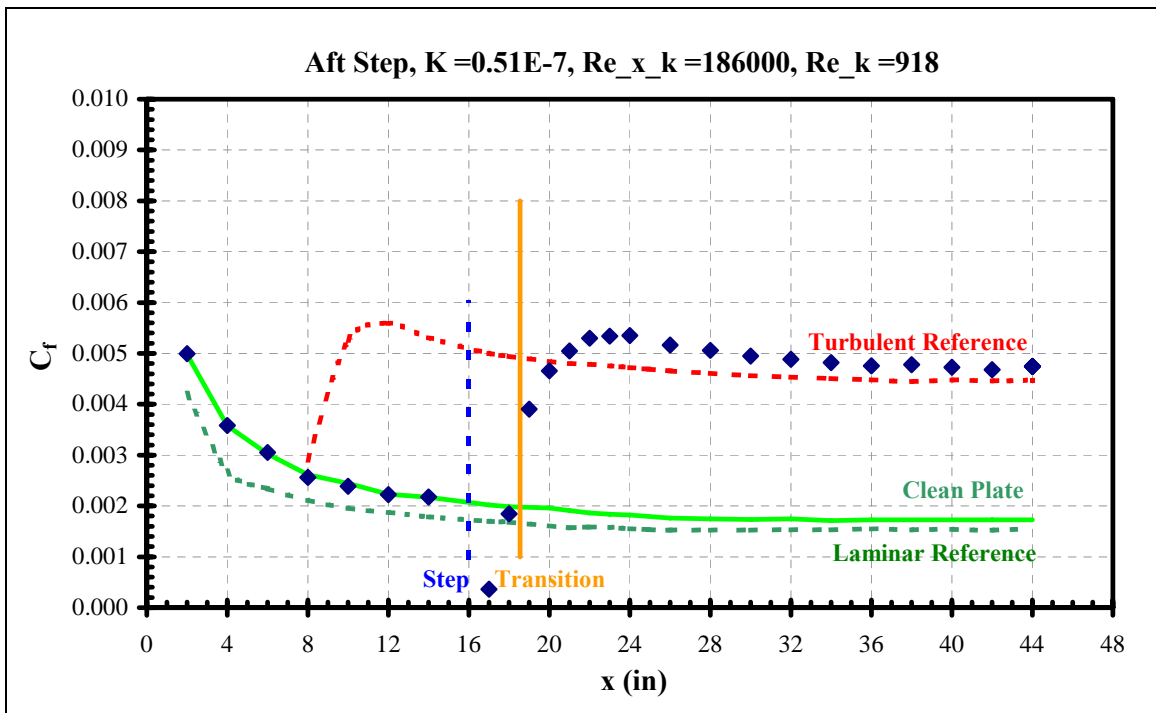


**Figure 243 Aft step skin friction distribution**

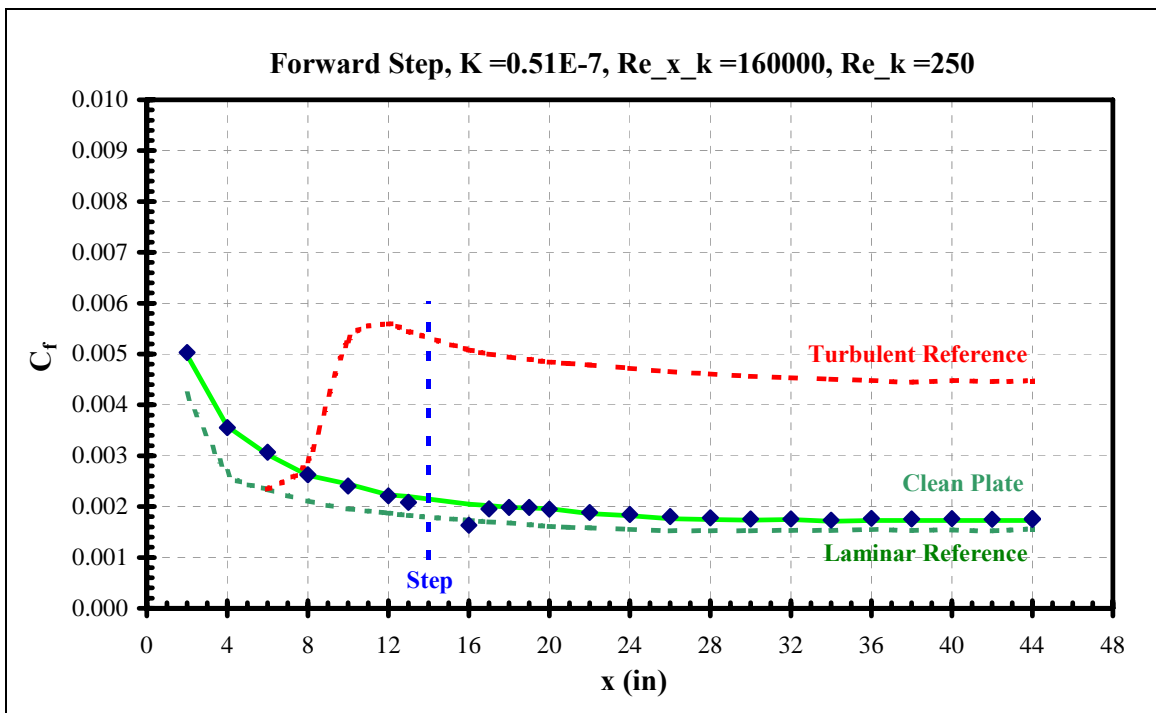




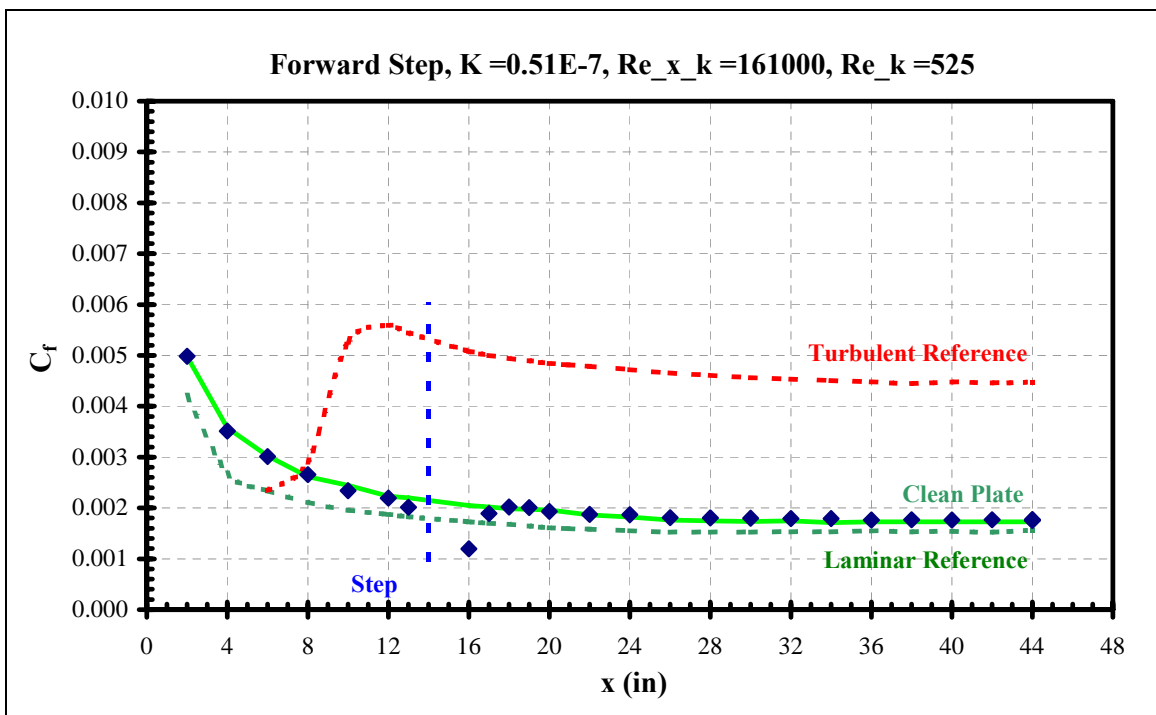
**Figure 244 Aft step skin friction distribution**



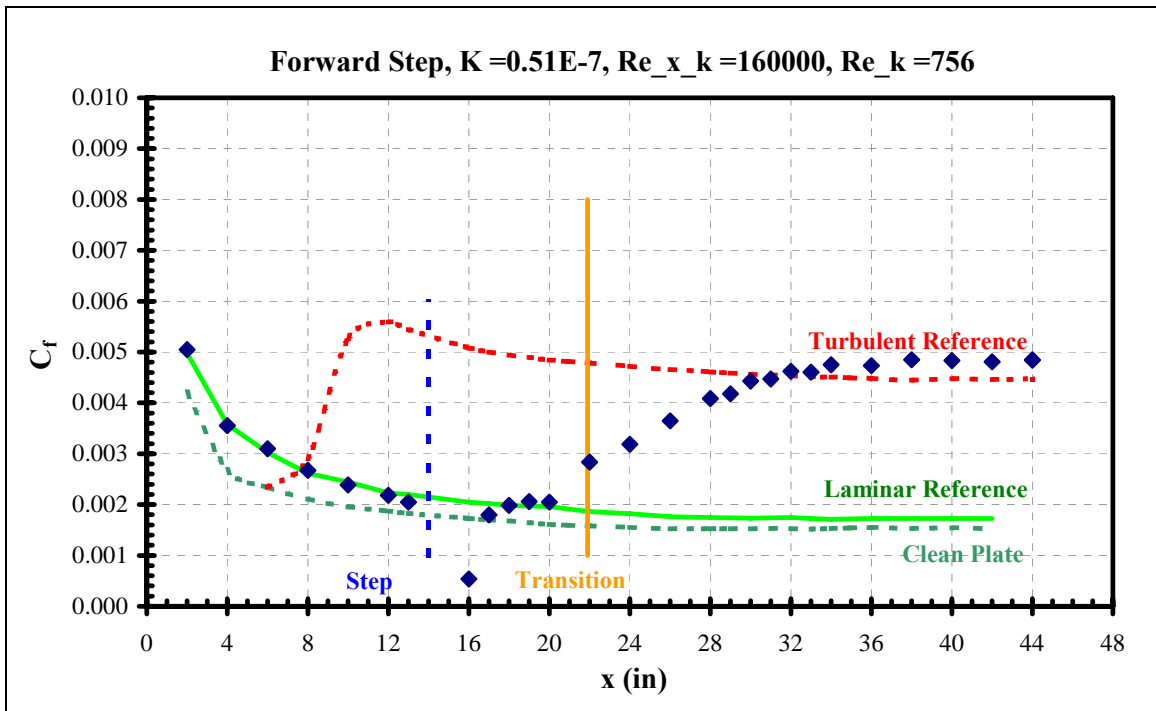
**Figure 245 Aft step skin friction distribution**



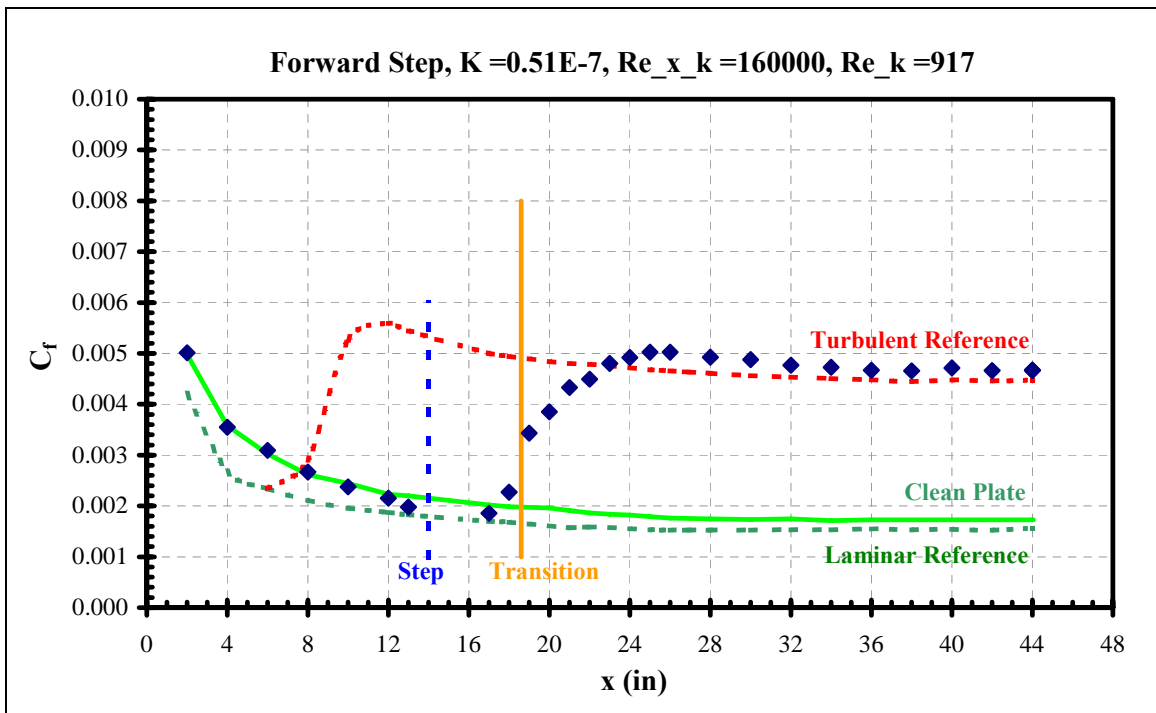
**Figure 246 Forward step skin friction distribution**



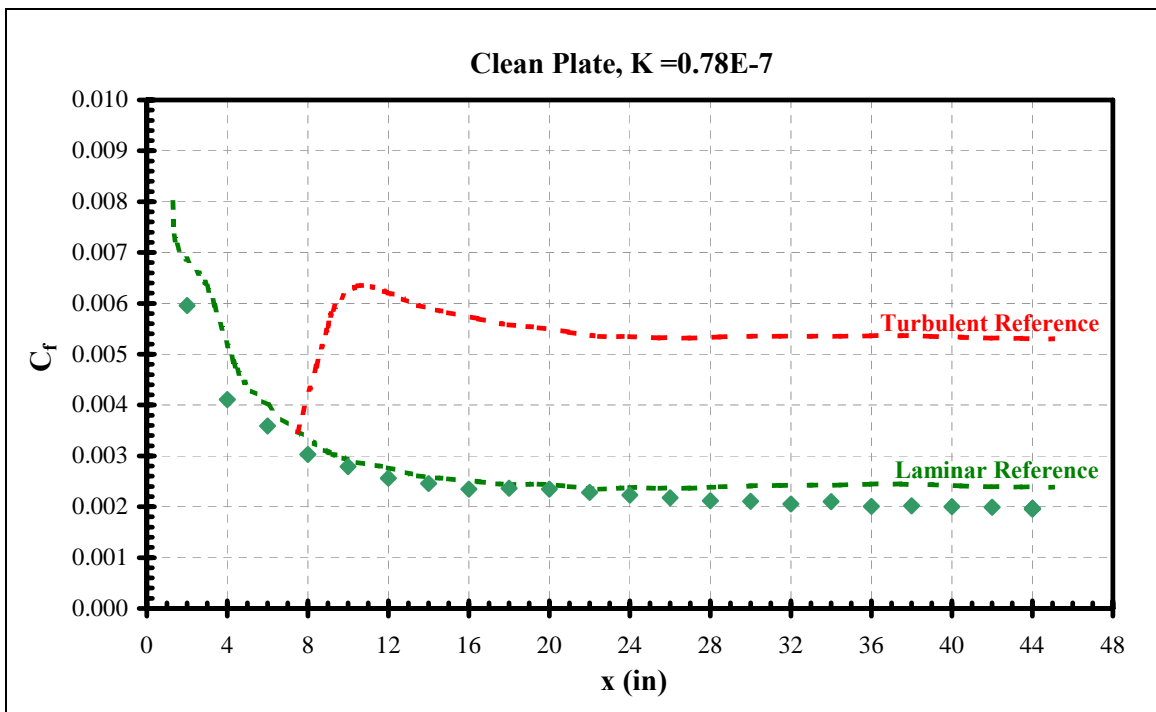
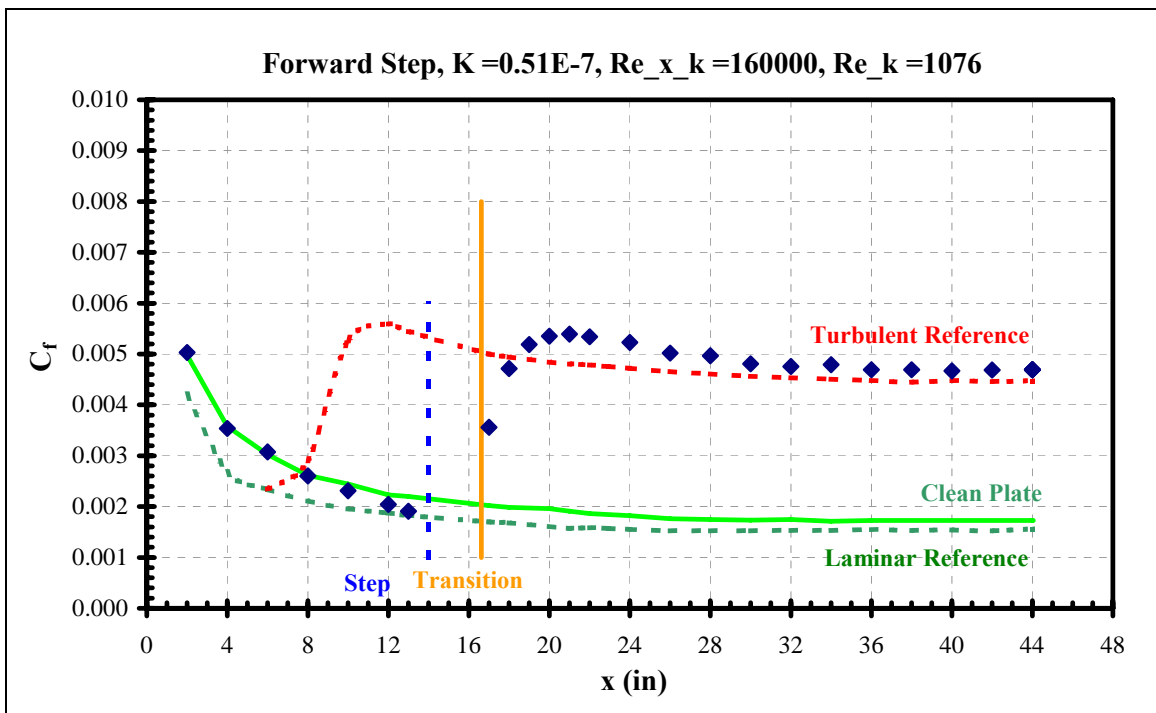
**Figure 247 Forward step skin friction distribution**

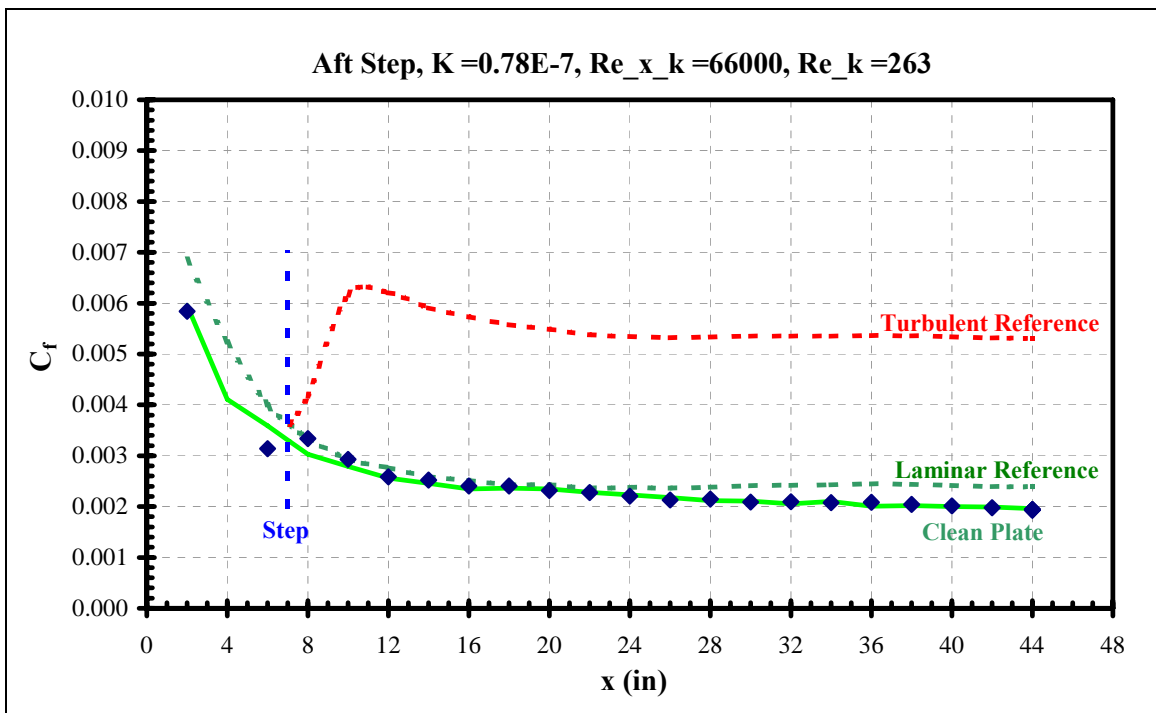


**Figure 248 Forward step skin friction distribution**

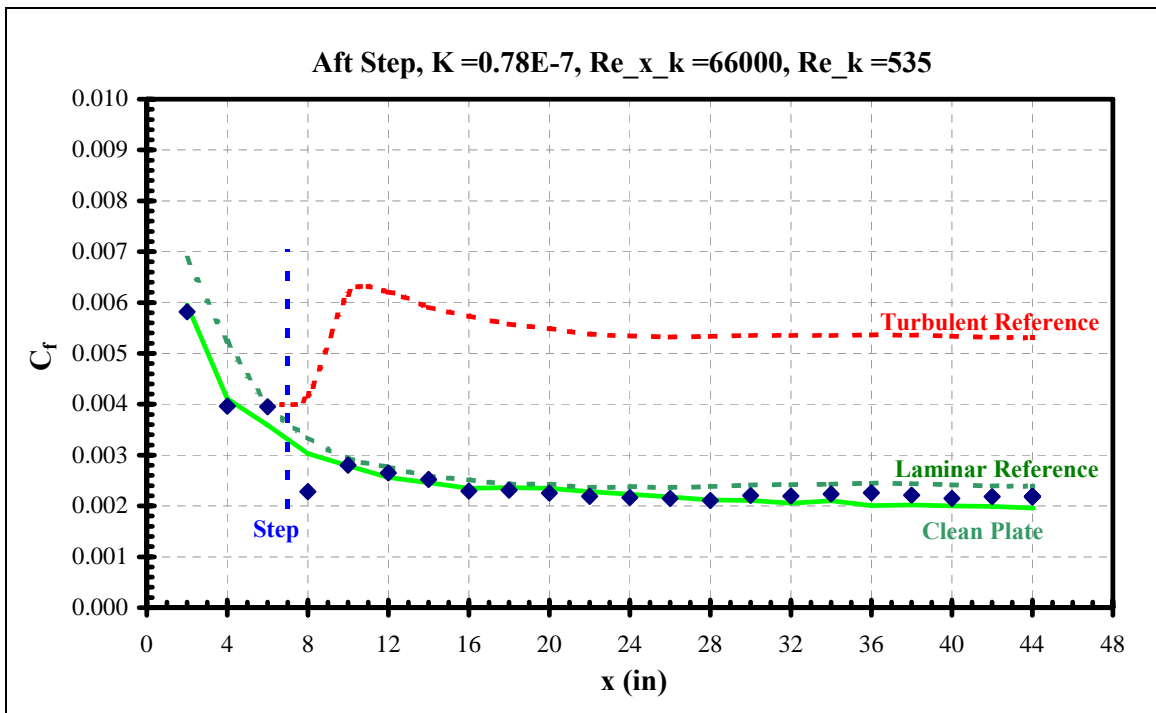


**Figure 249 Forward step skin friction distribution**

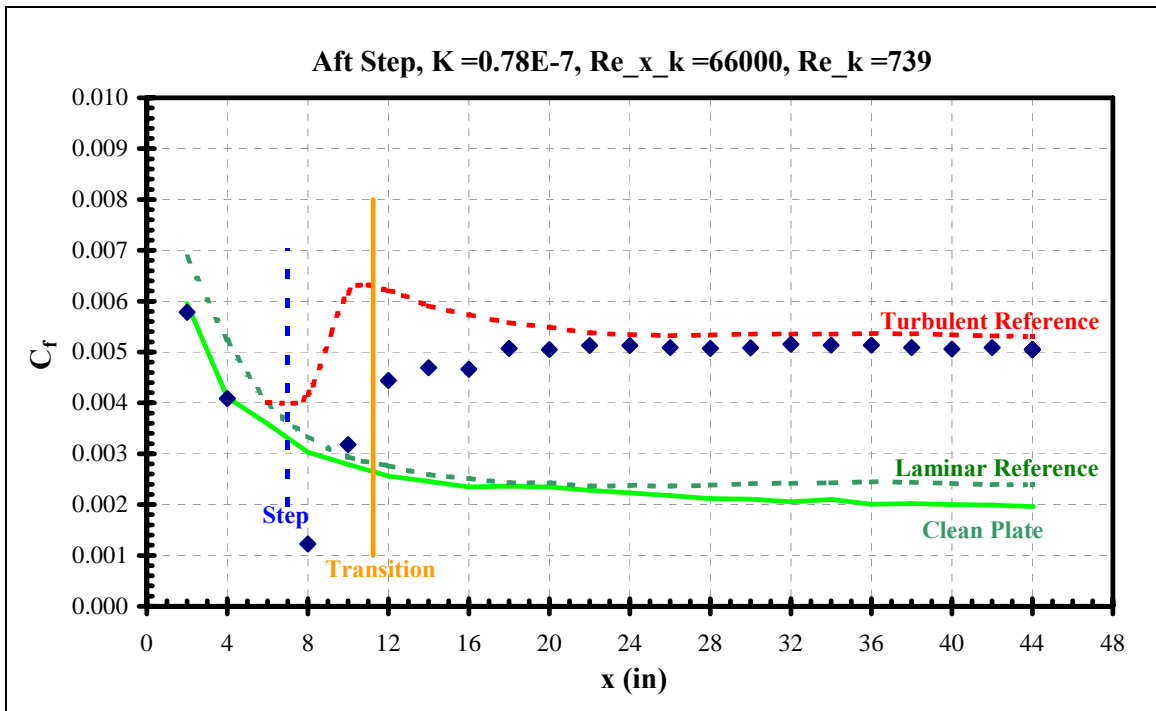




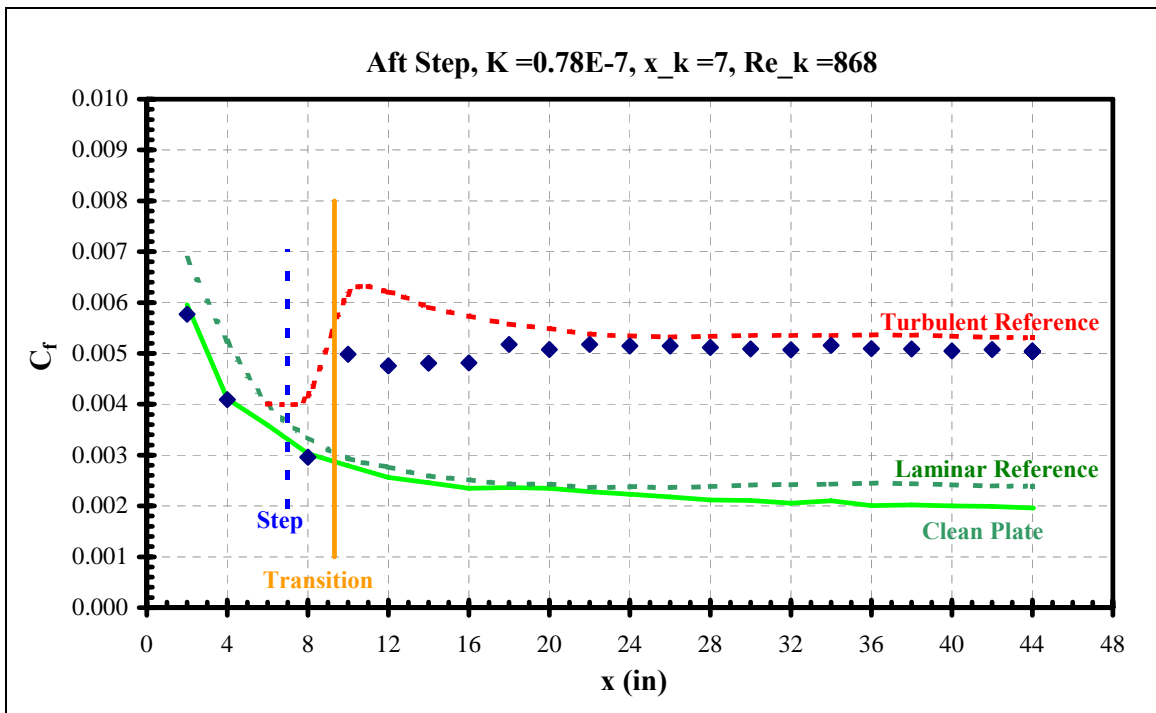
**Figure 252 Aft step skin friction distribution**



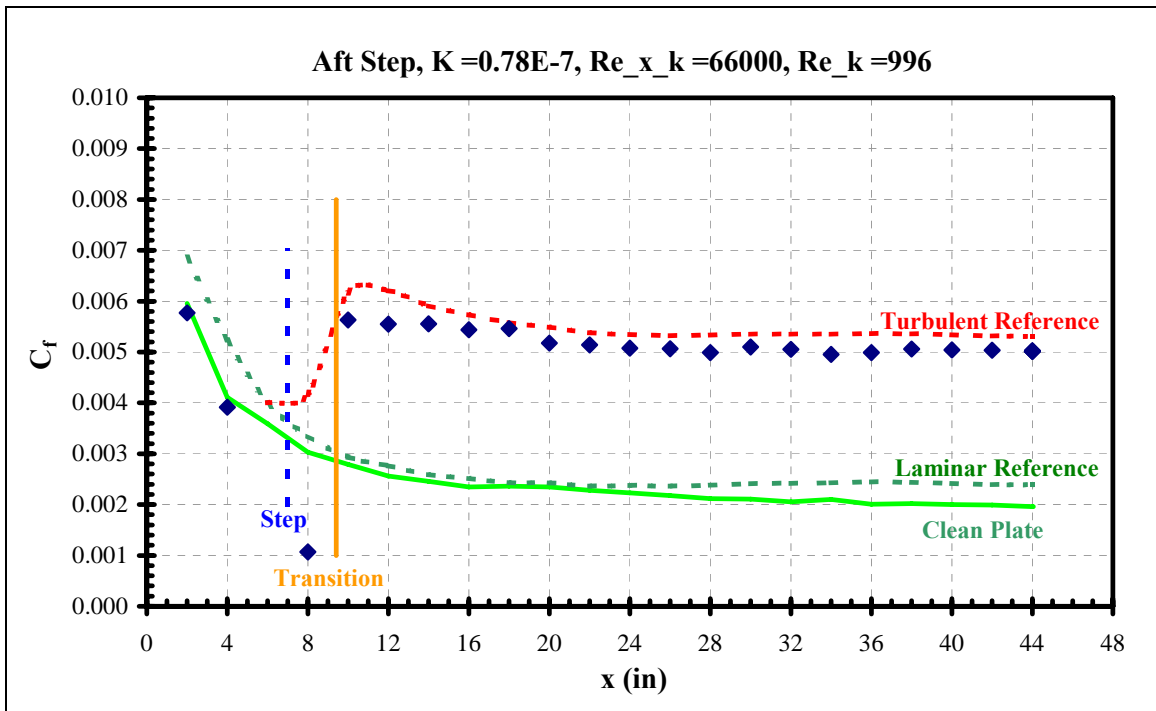
**Figure 253 Aft step skin friction distribution**



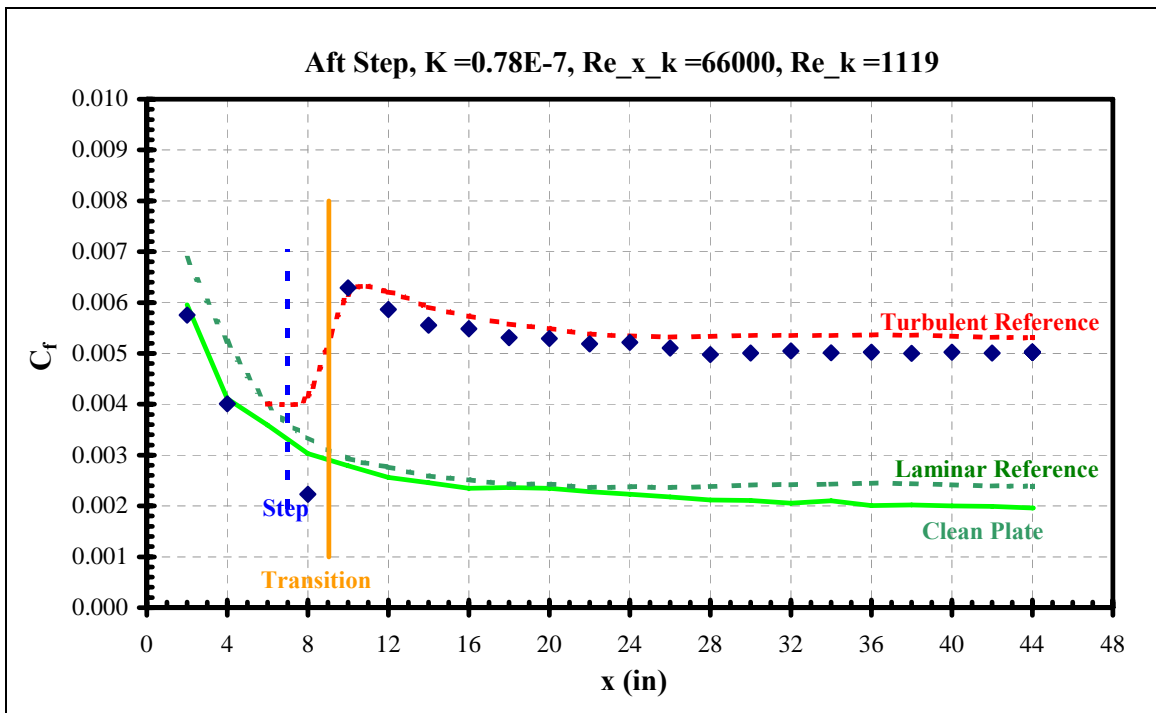
**Figure 254 Aft step skin friction distribution**



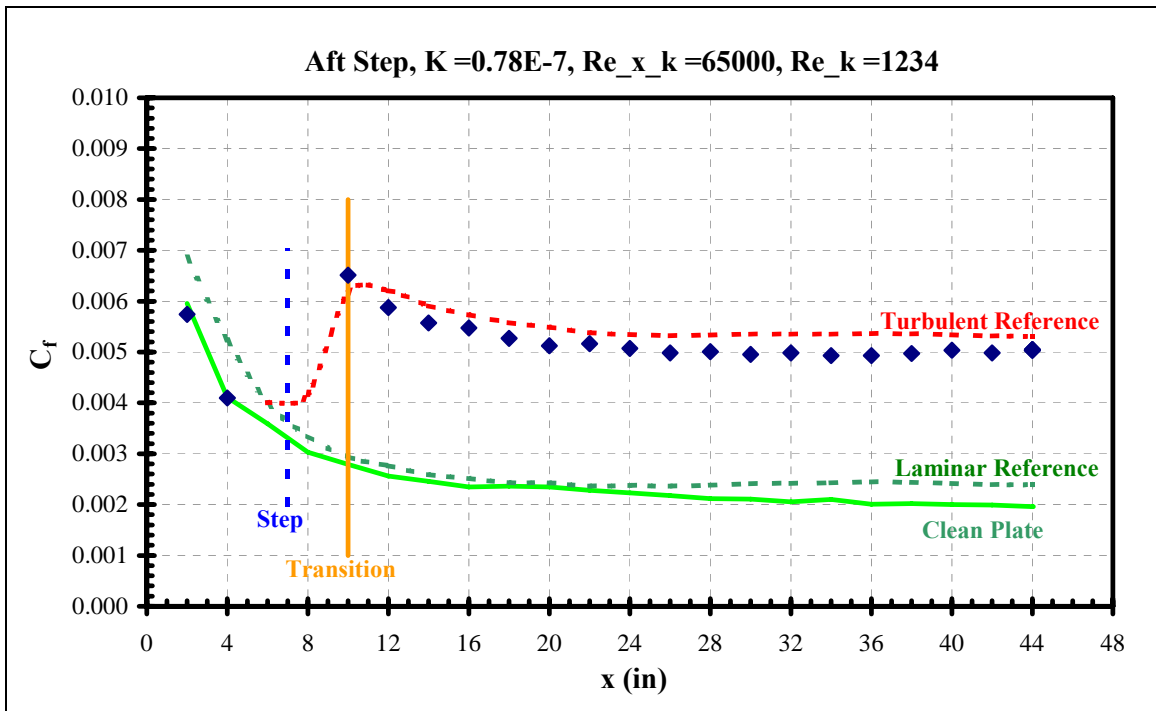
**Figure 255 Aft step skin friction distribution**



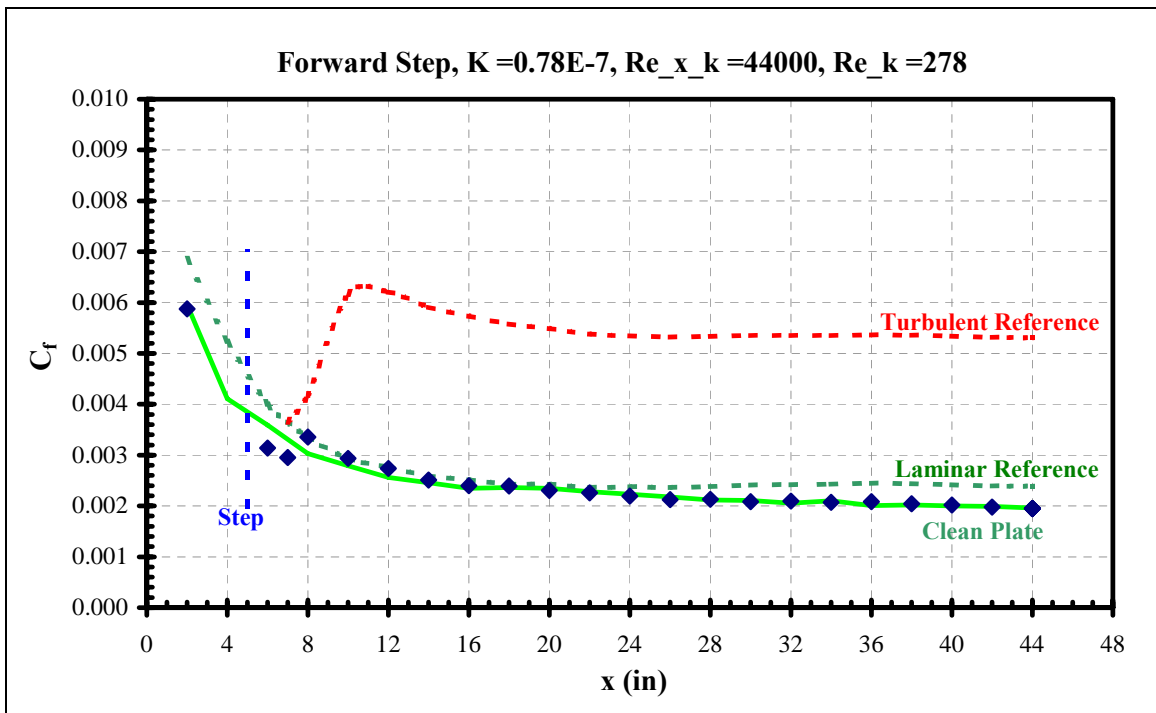
**Figure 256 Aft step skin friction distribution**



**Figure 257 Aft step skin friction distribution**

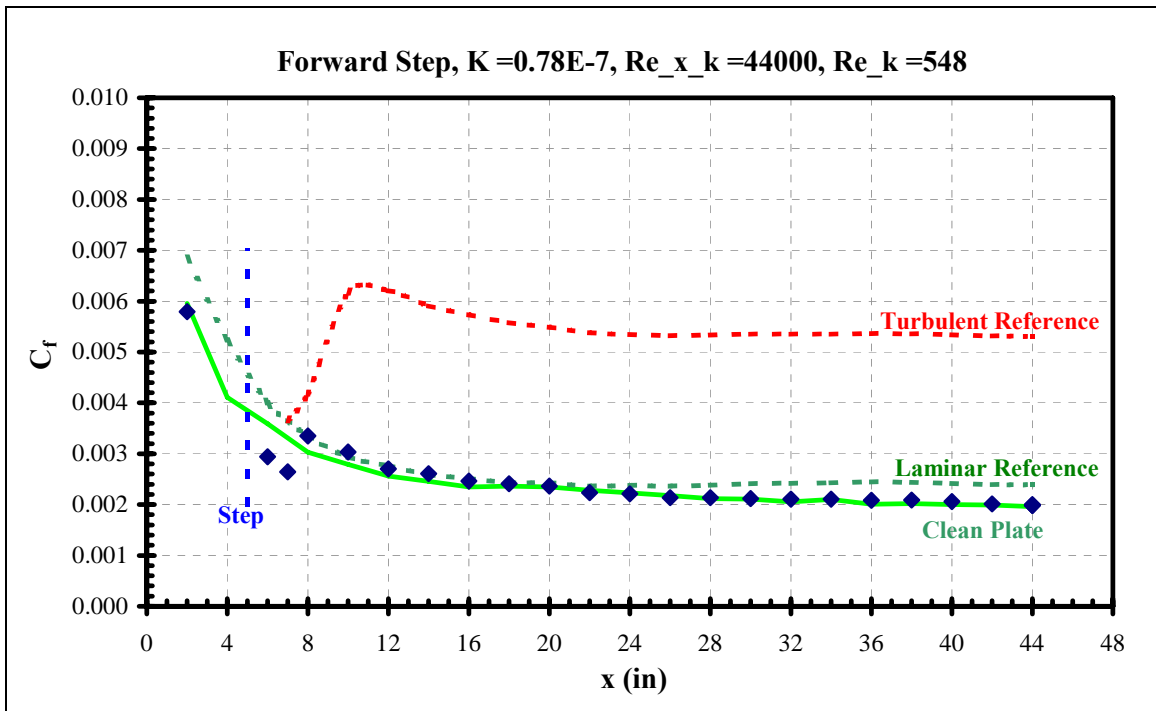


**Figure 258 Aft step skin friction distribution**

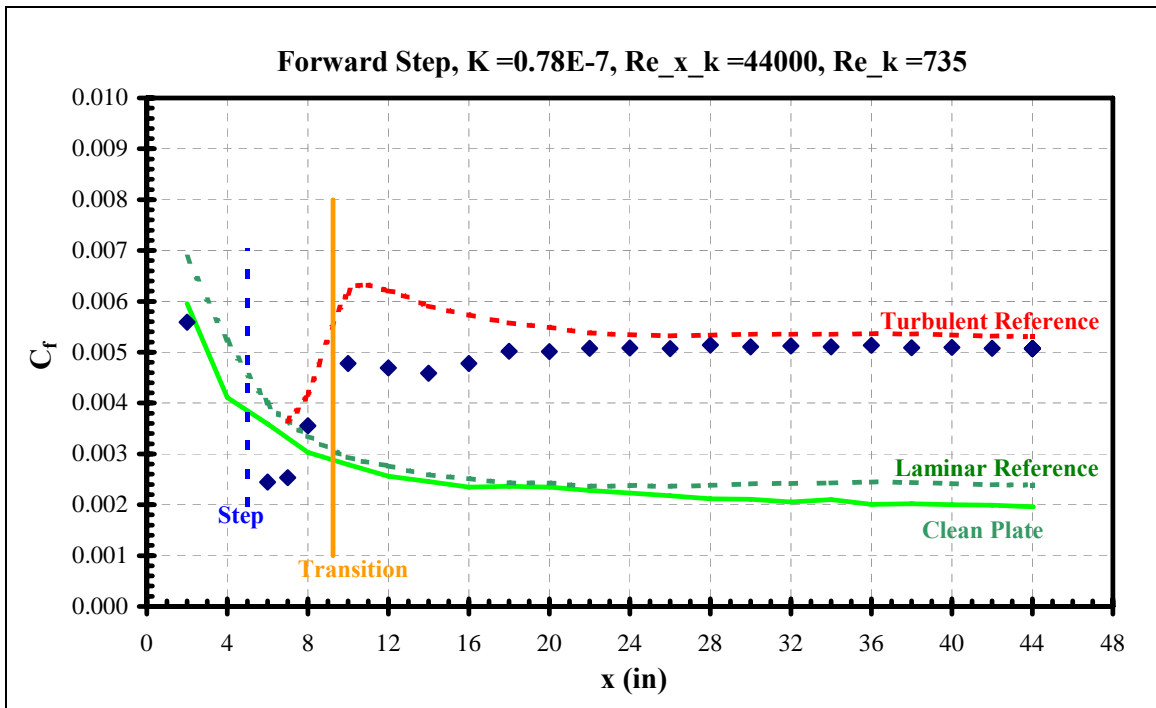


**Figure 259 Forward step skin friction distribution**

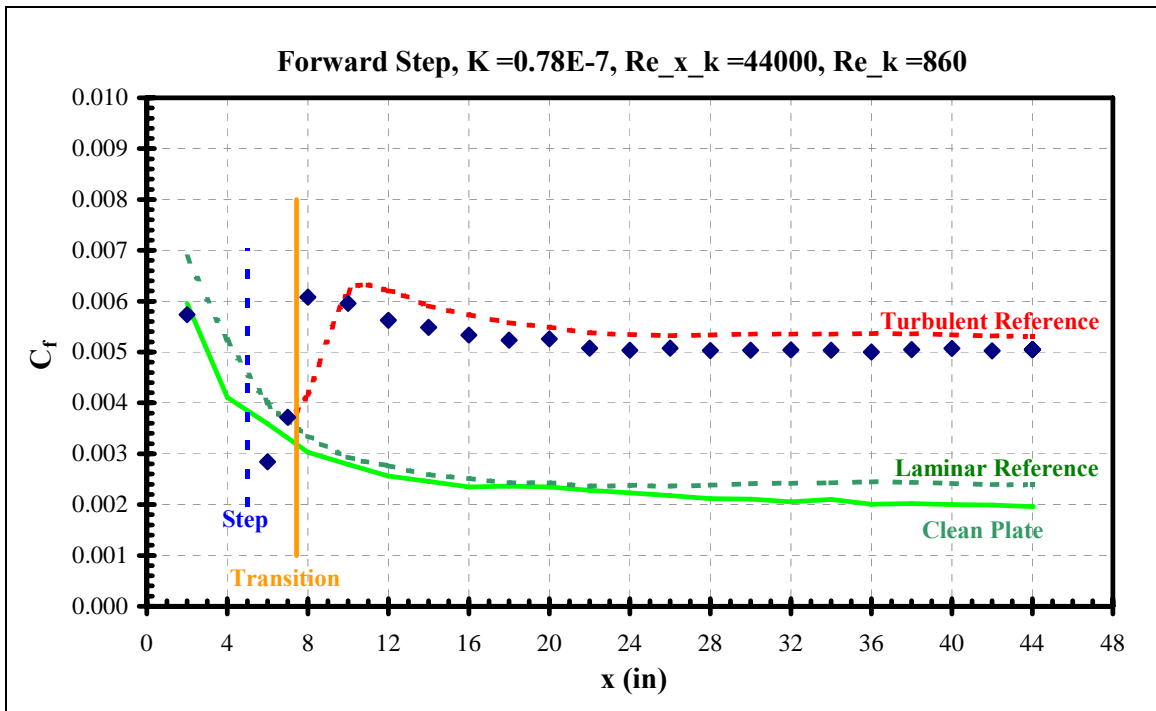




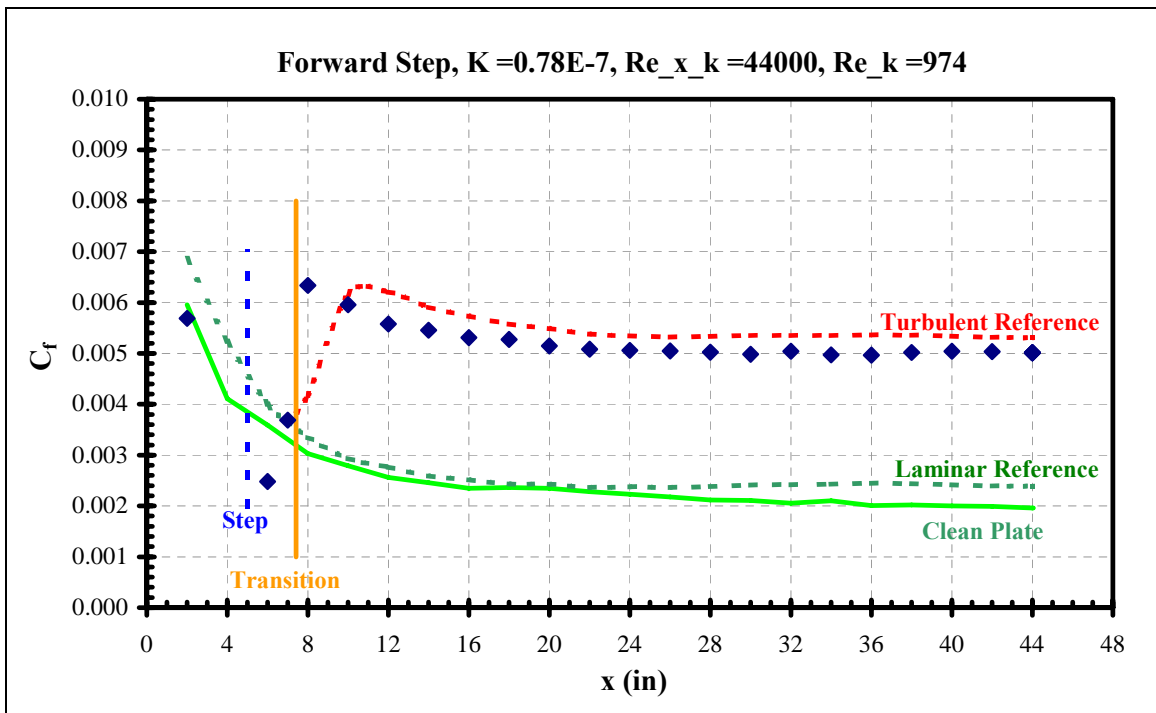
**Figure 260 Forward step skin friction distribution**



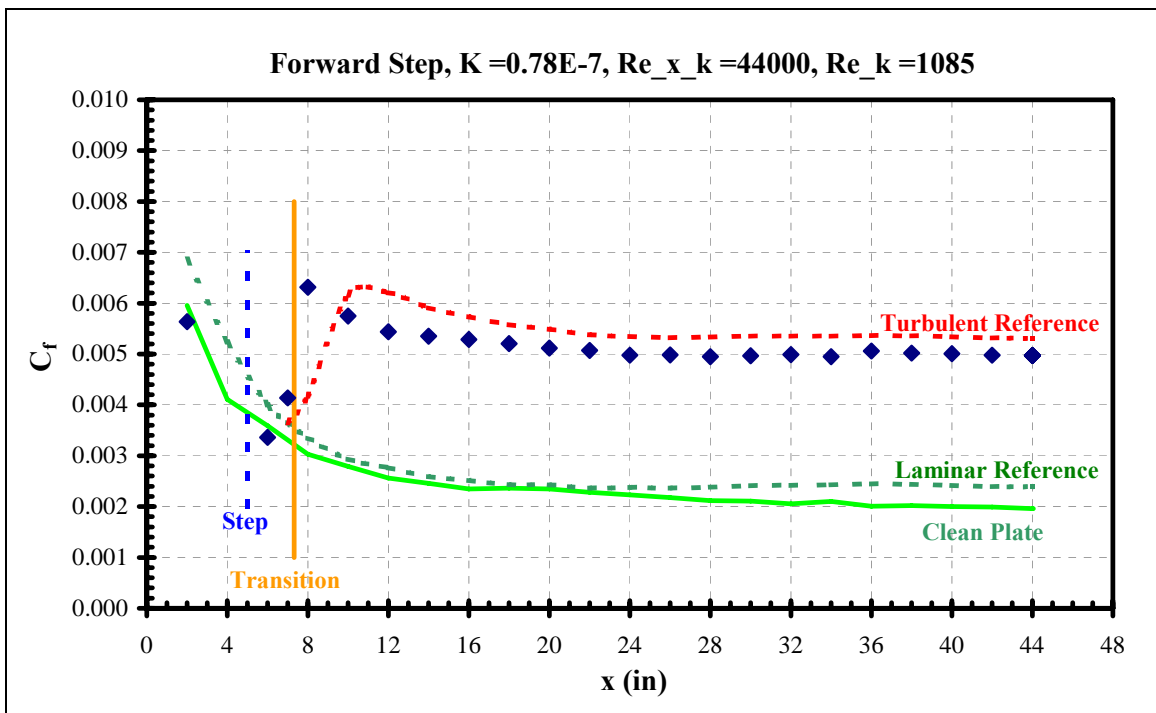
**Figure 261 Forward step skin friction distribution**



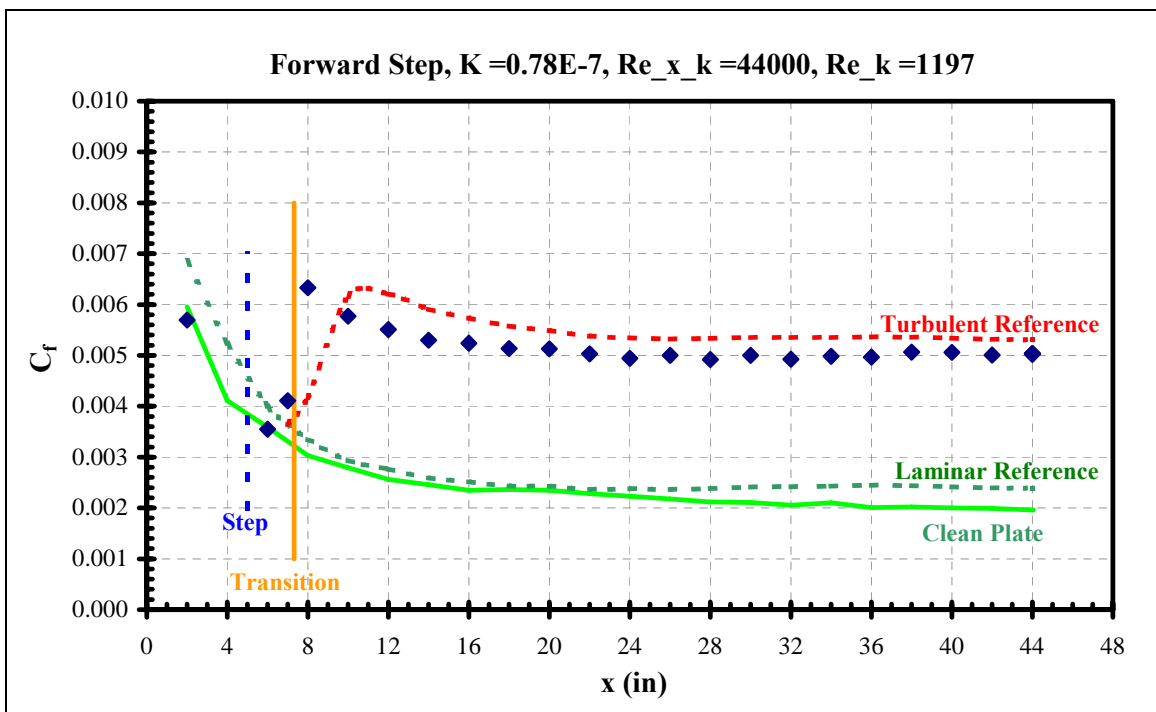
**Figure 262 Forward step skin friction distribution**



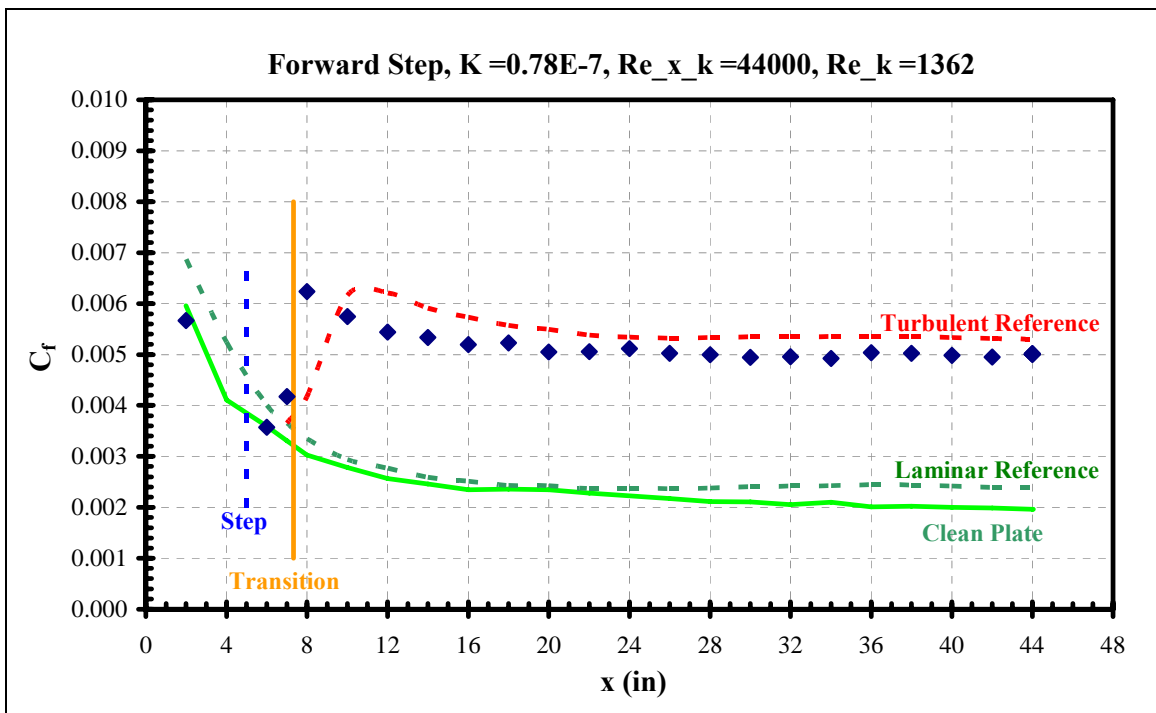
**Figure 263 Forward step skin friction distribution**



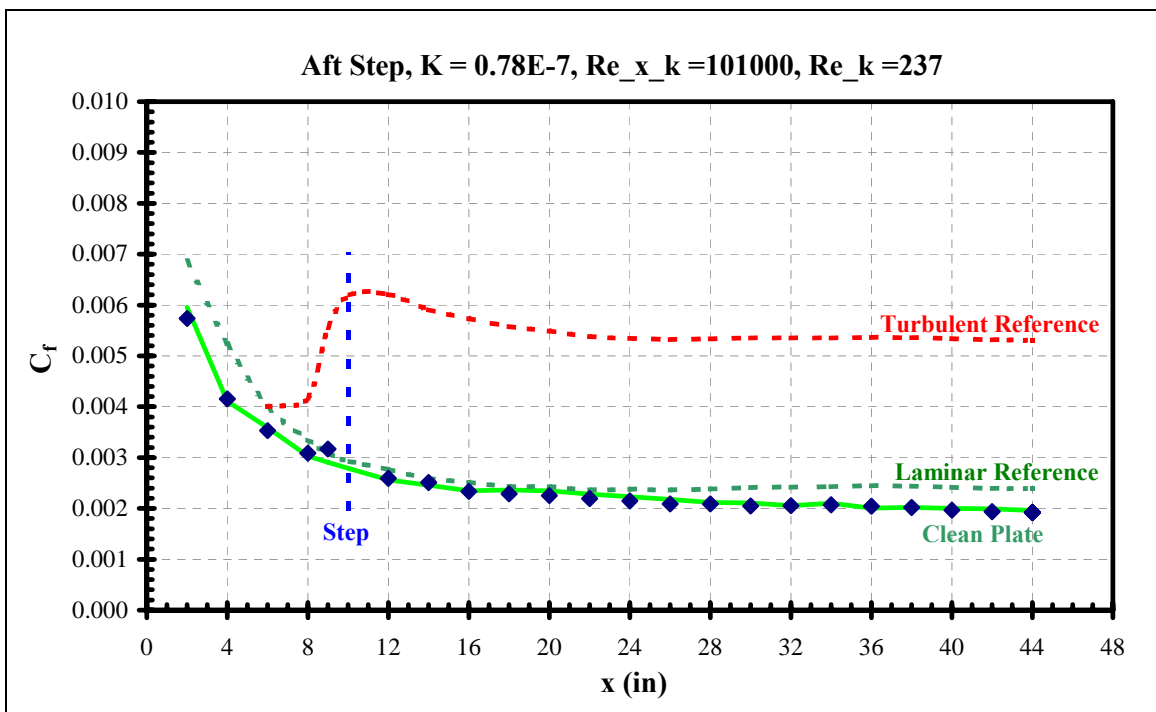
**Figure 264 Forward step skin friction distribution**



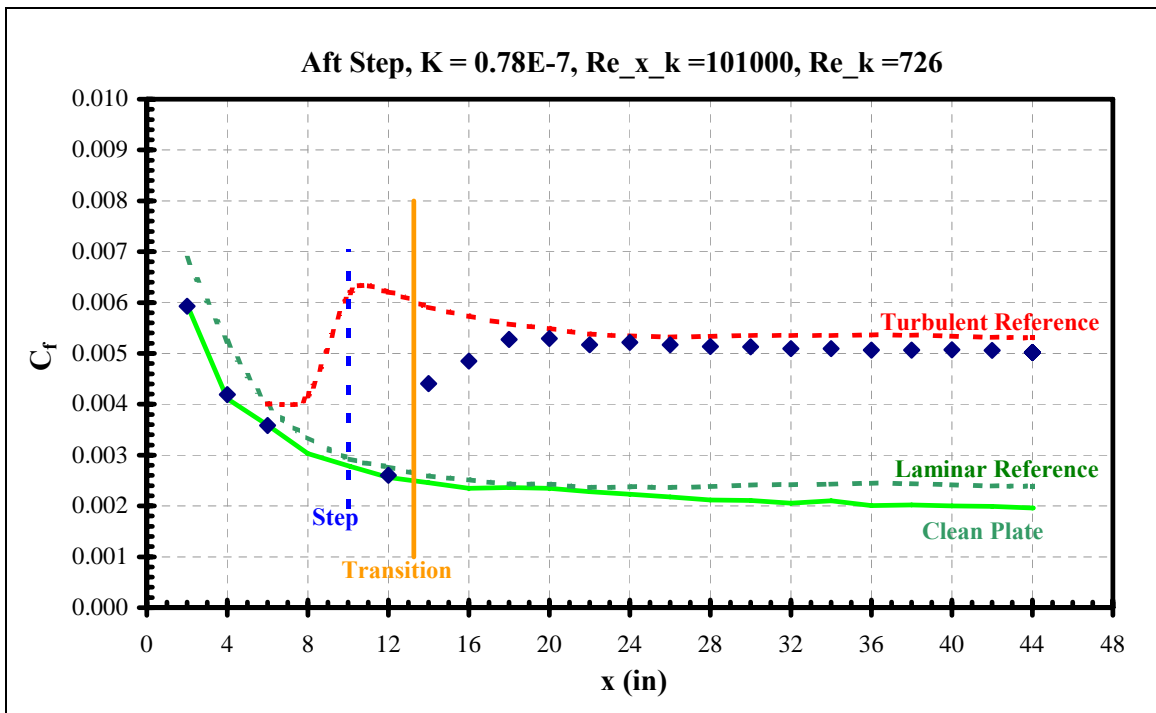
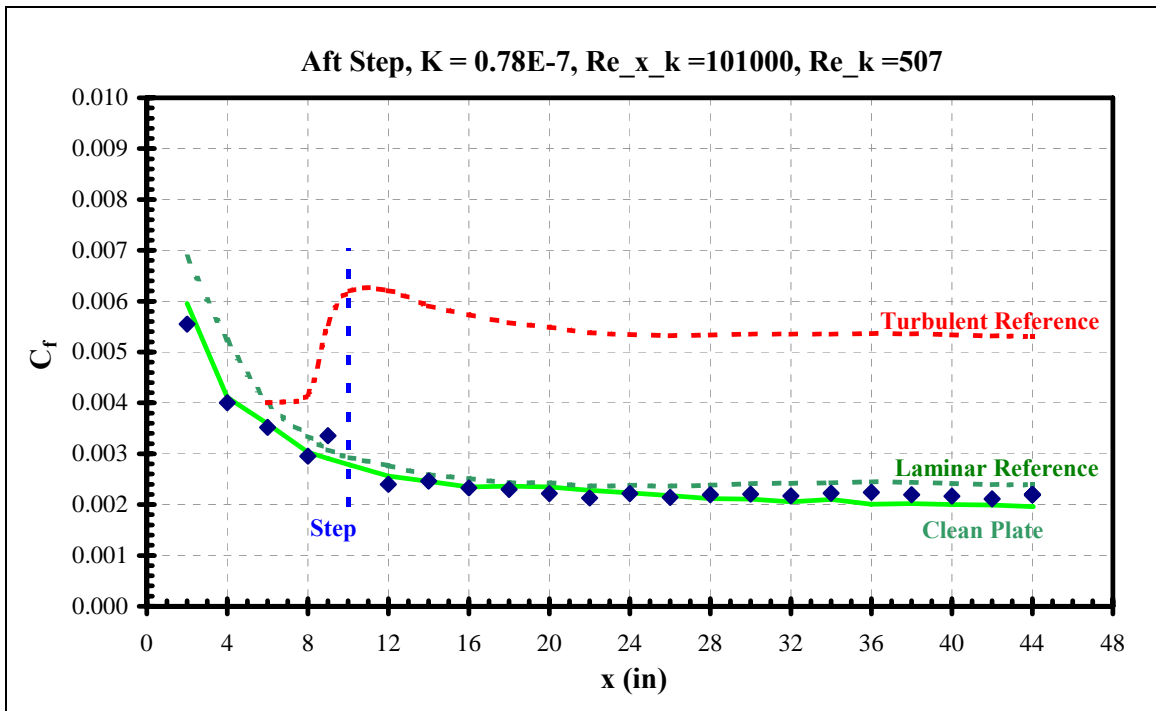
**Figure 265 Forward step skin friction distribution**



**Figure 266 Forward step skin friction distribution**



**Figure 267 Aft step skin friction distribution**



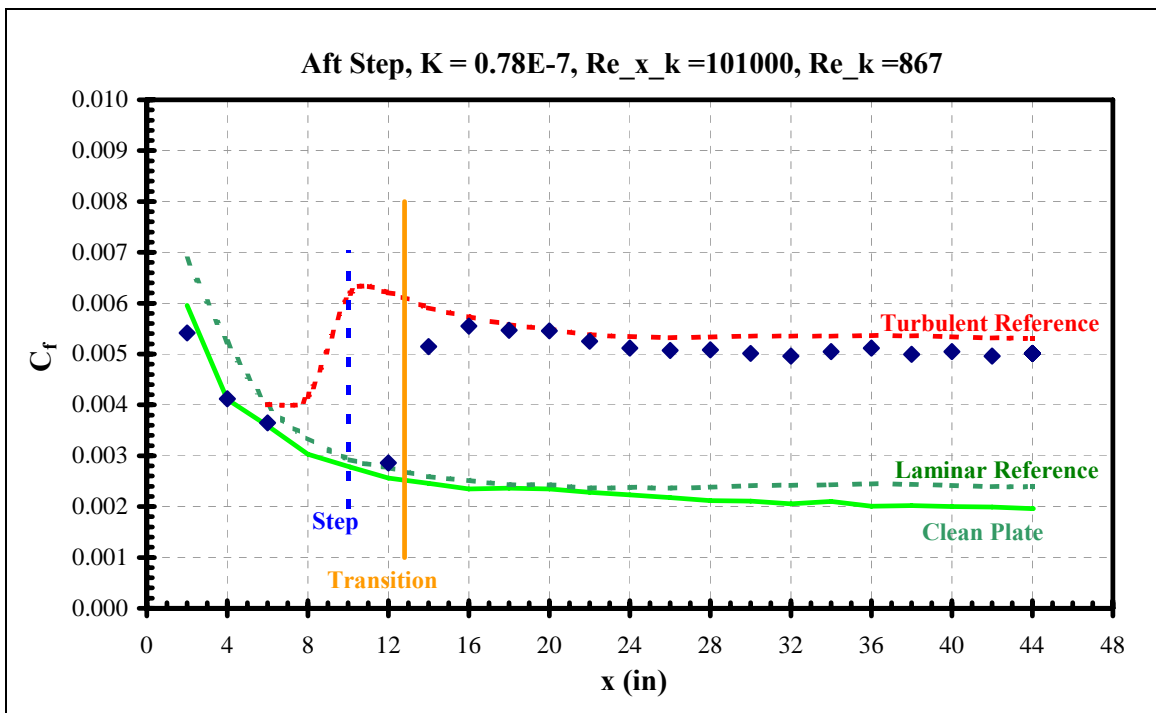


**Figure 270 Aft step skin friction distribution**

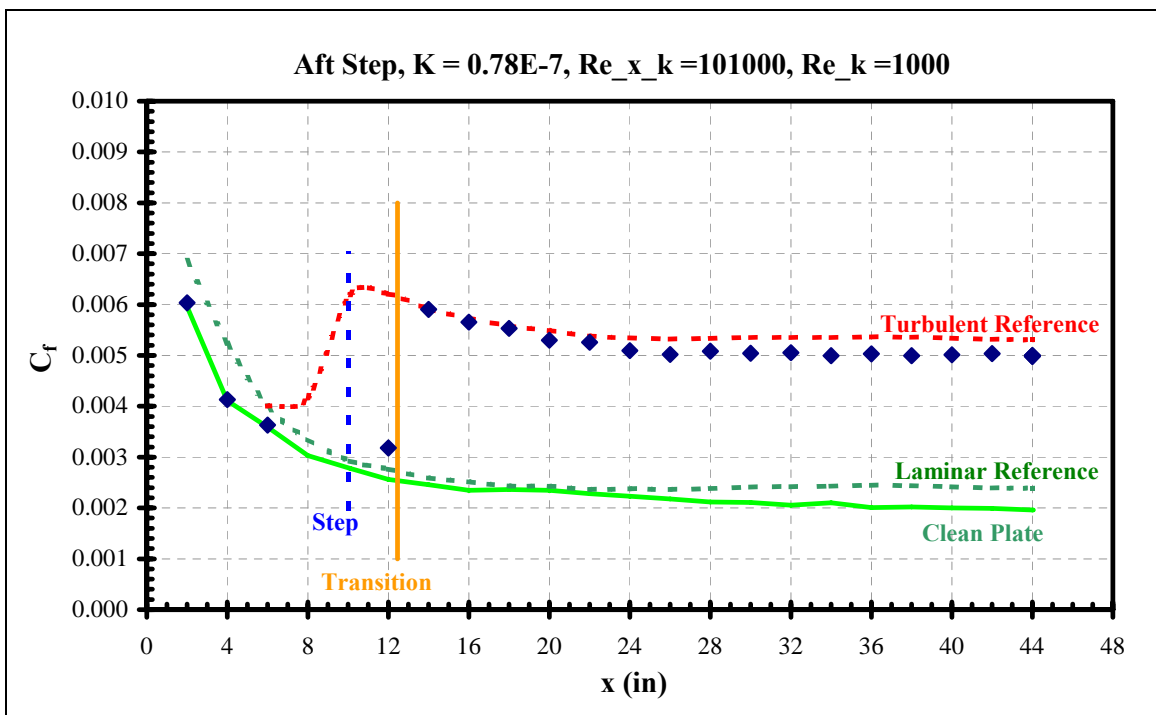


**Figure 271 Aft step skin friction distribution**

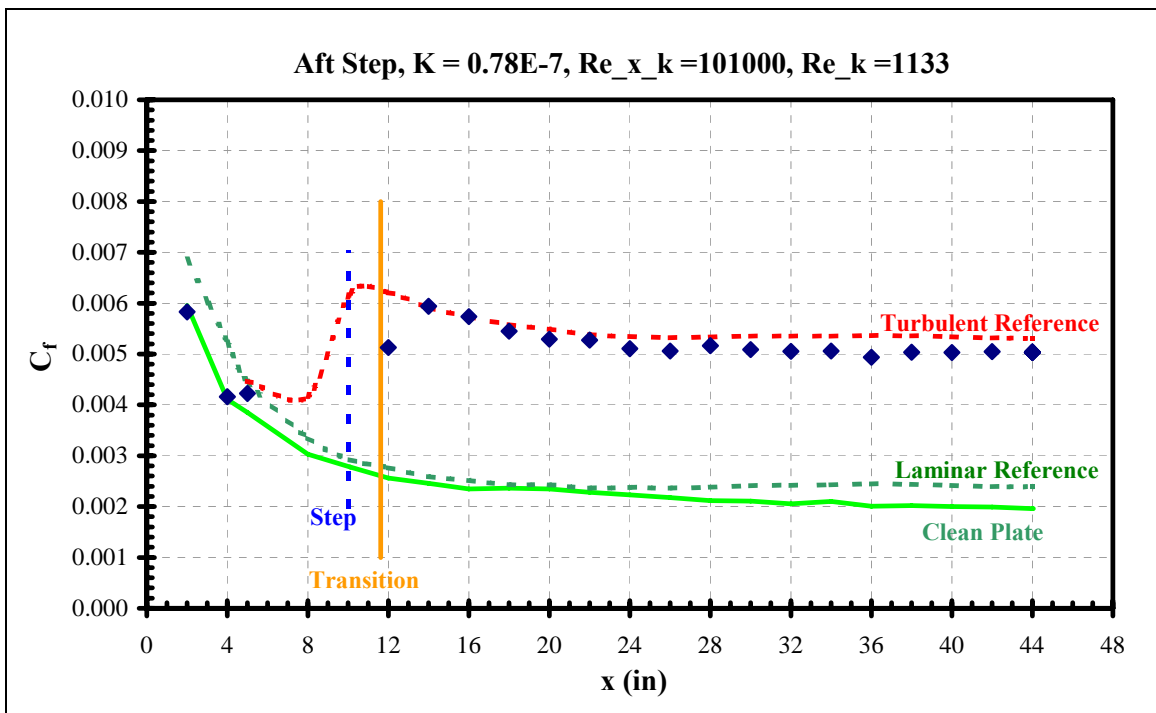


**Figure 272 Aft step skin friction distribution**

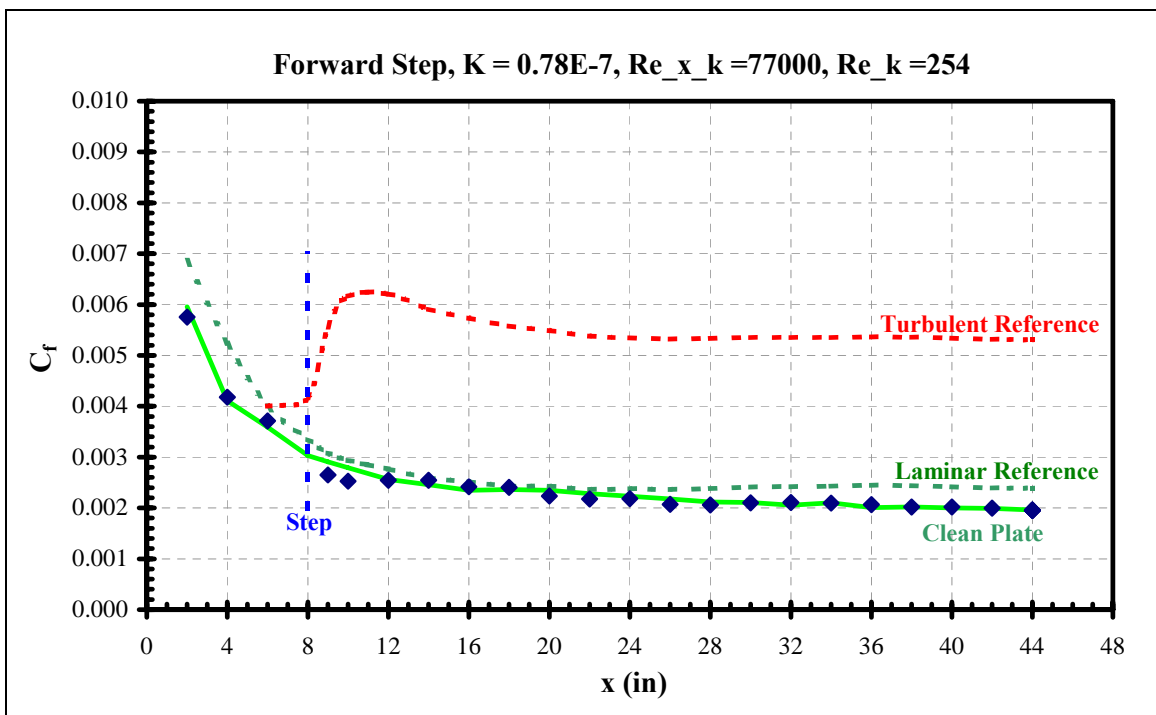


**Figure 273 Forward step skin friction distribution**

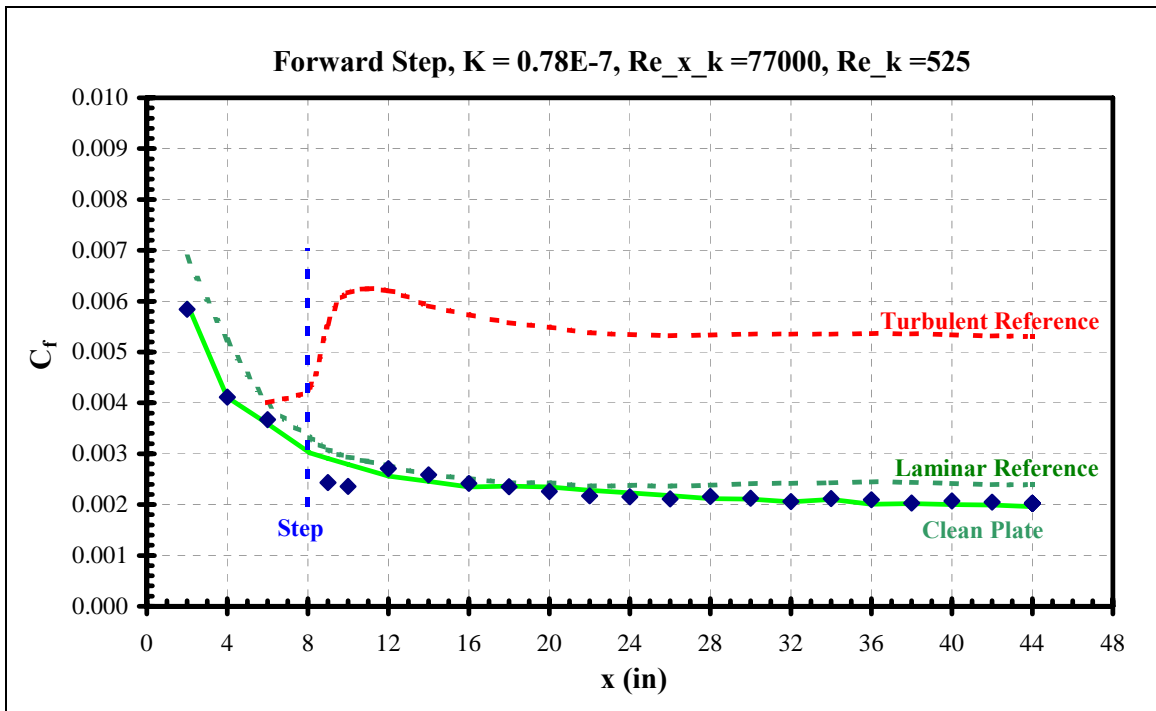


**Figure 274 Forward step skin friction distribution**

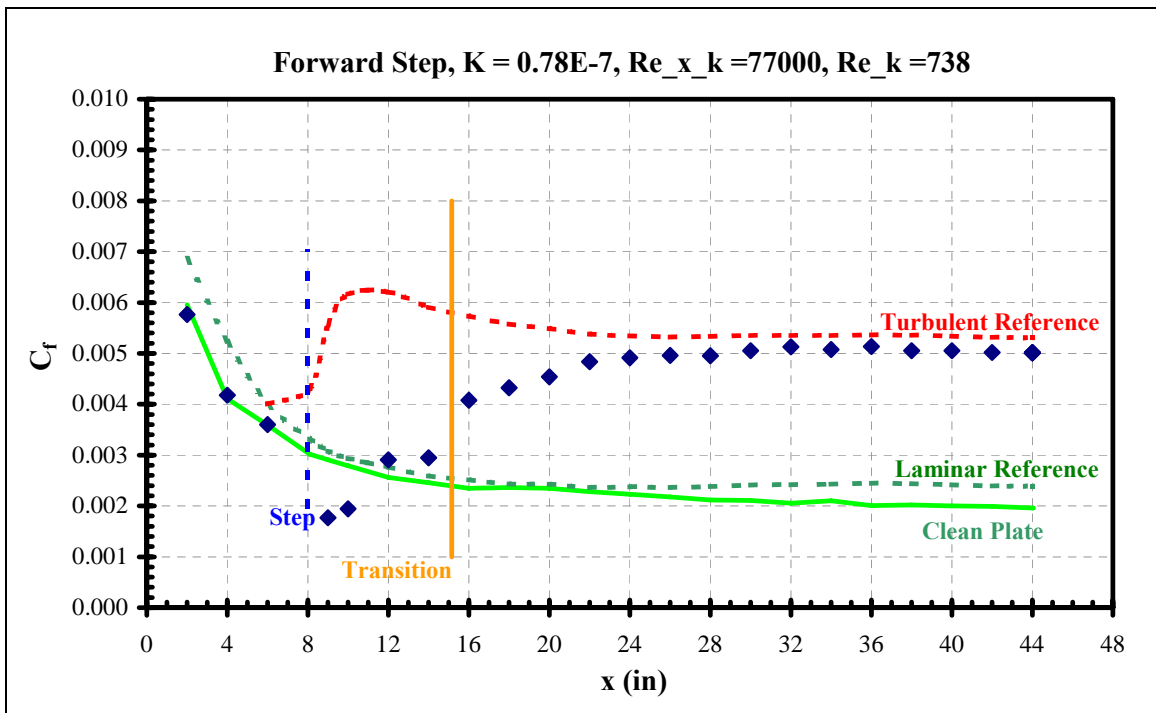


**Figure 275 Forward step skin friction distribution**



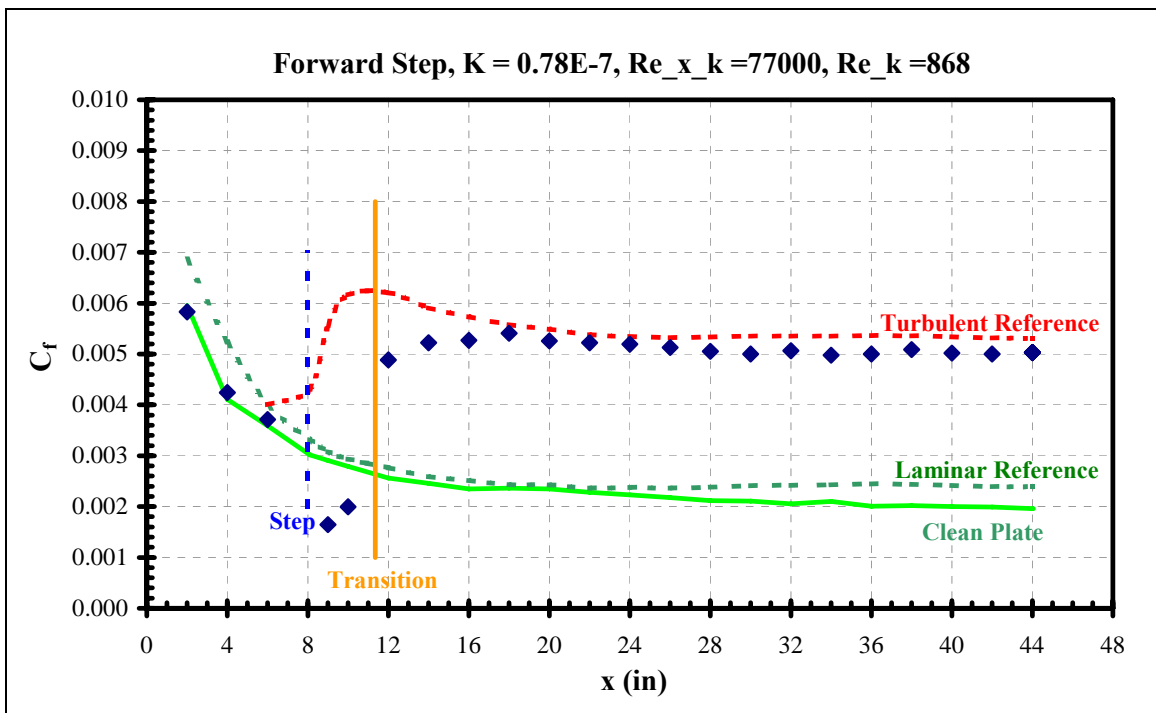


**Figure 276 Forward step skin friction distribution**

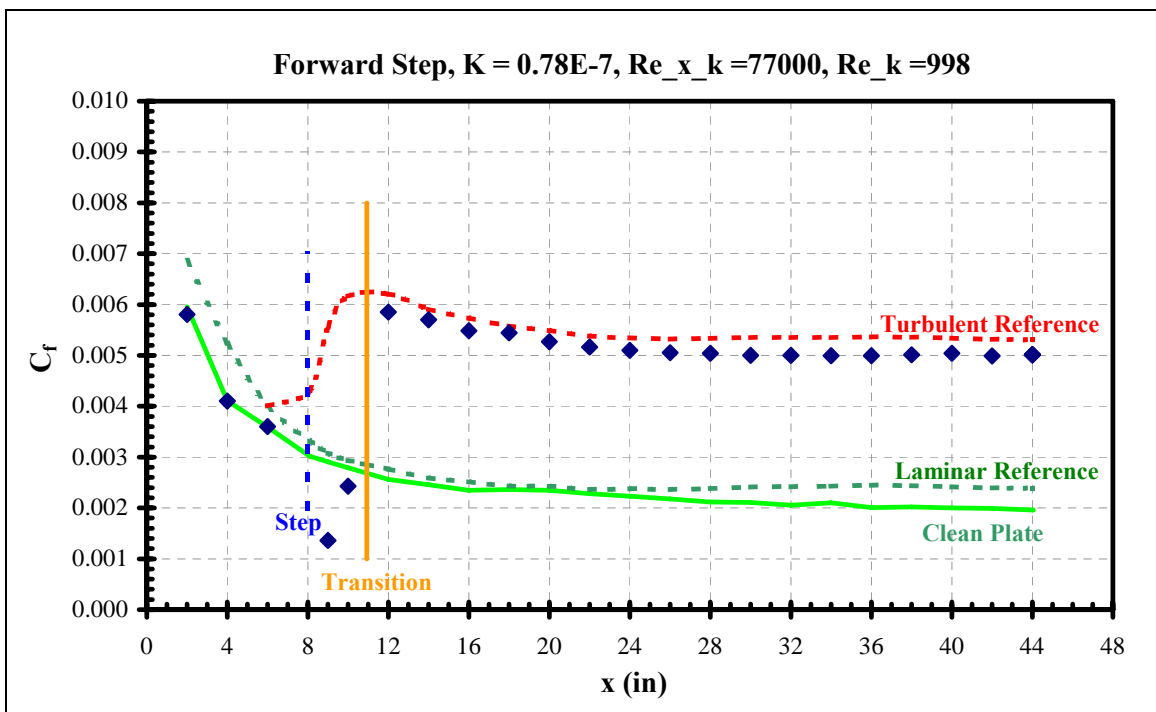


**Figure 277 Forward step skin friction distribution**

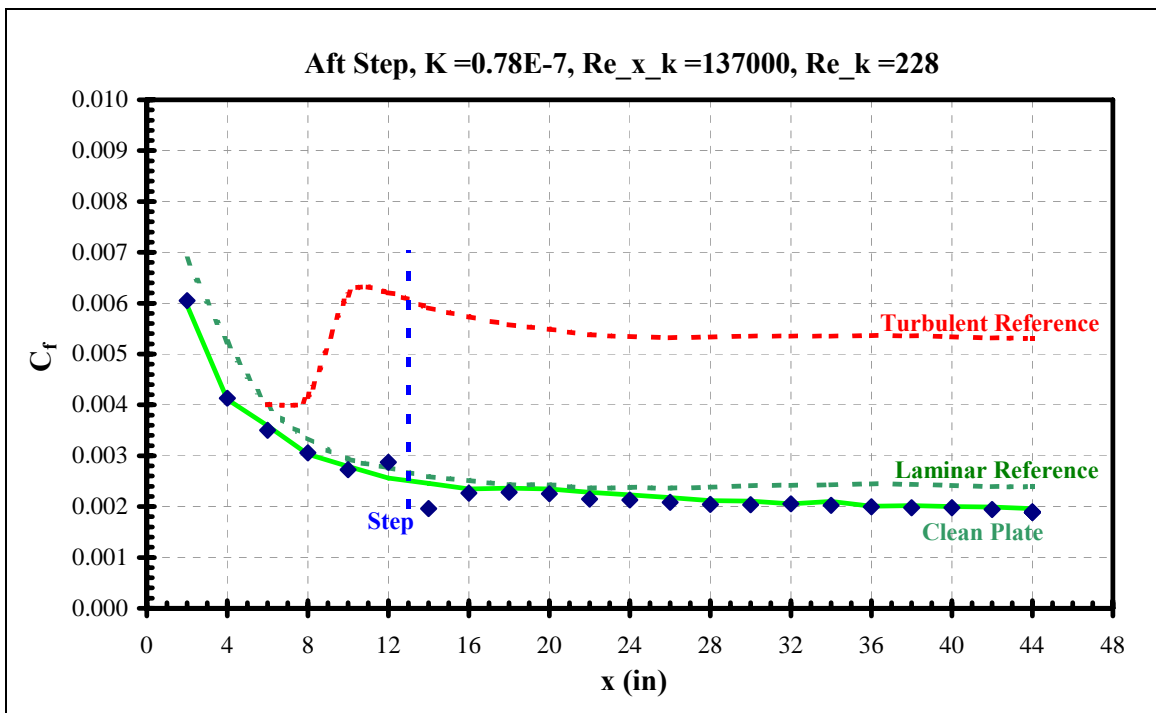


**Figure 278 Aft step skin friction distribution**

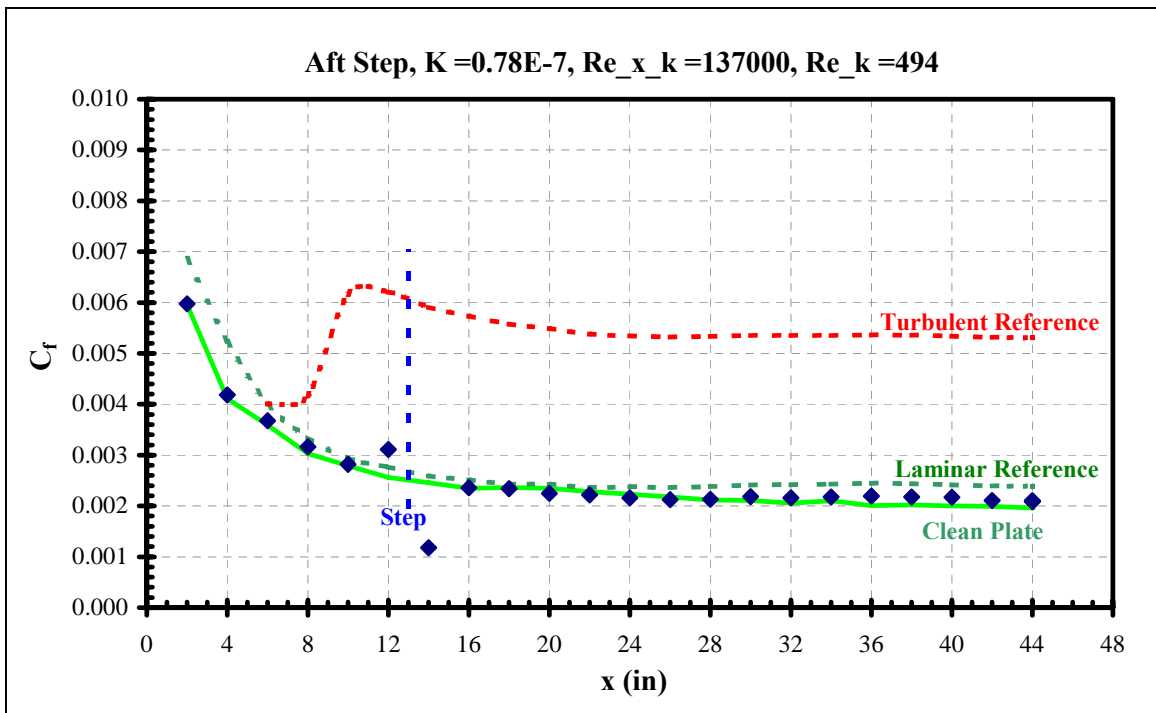


**Figure 279 Aft step skin friction distribution**

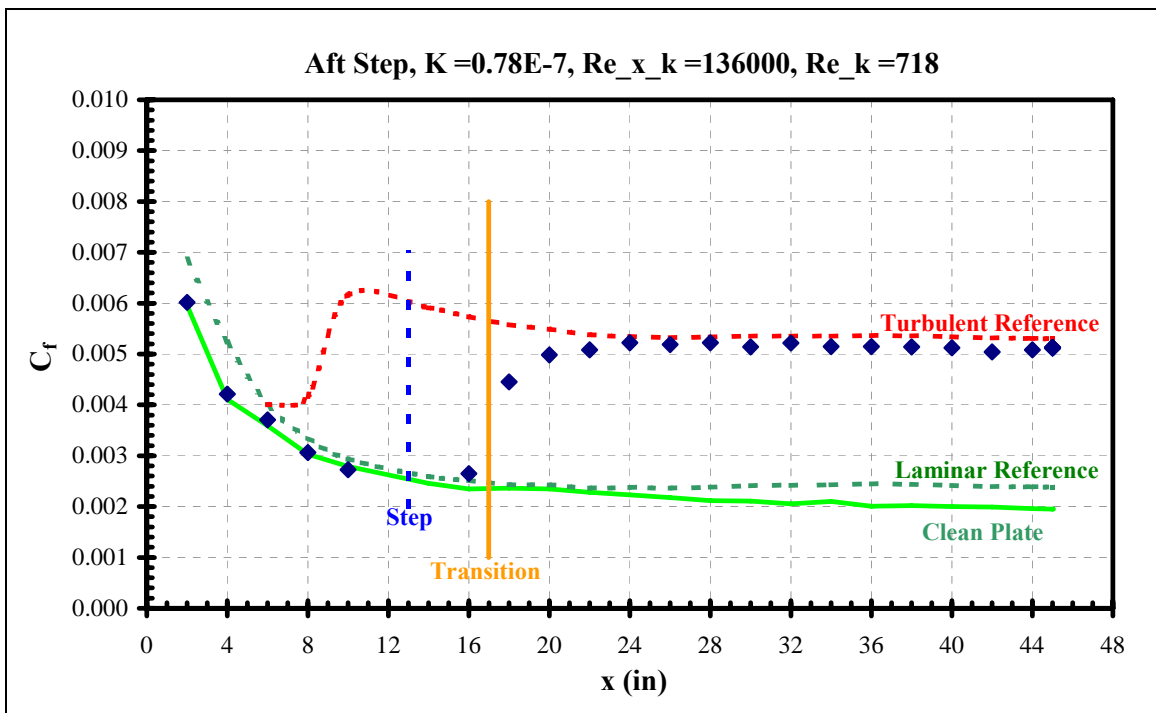


**Figure 280 Aft step skin friction distribution**

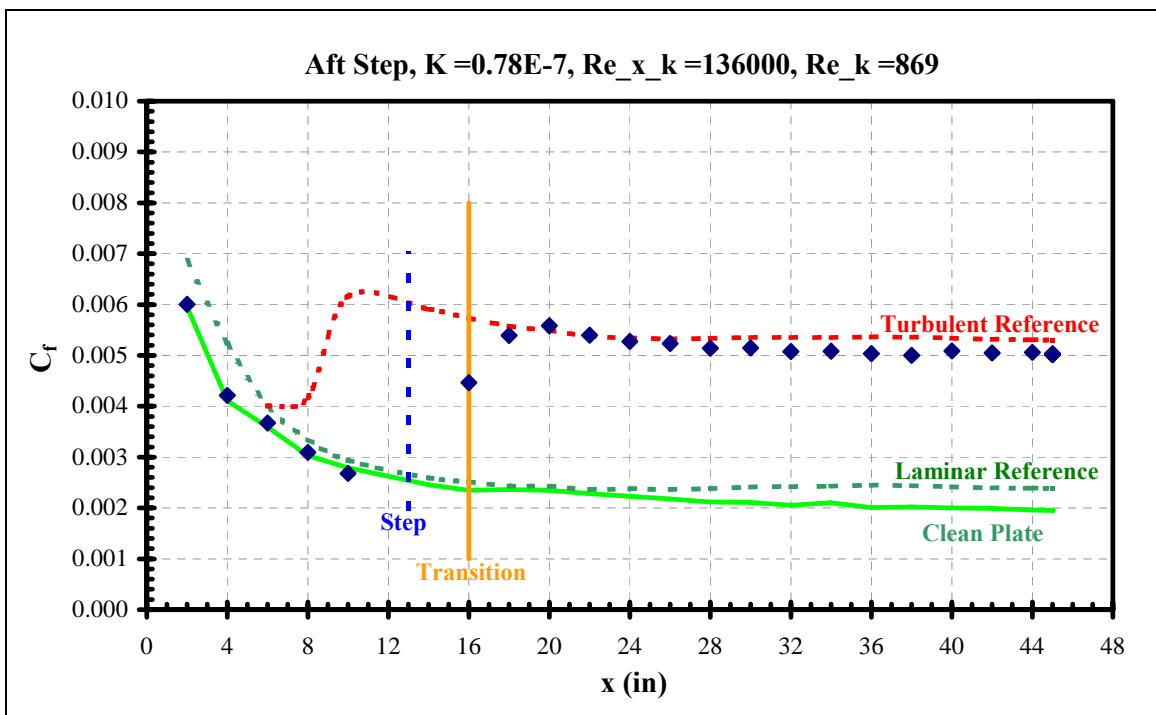


**Figure 281 Aft step skin friction distribution**

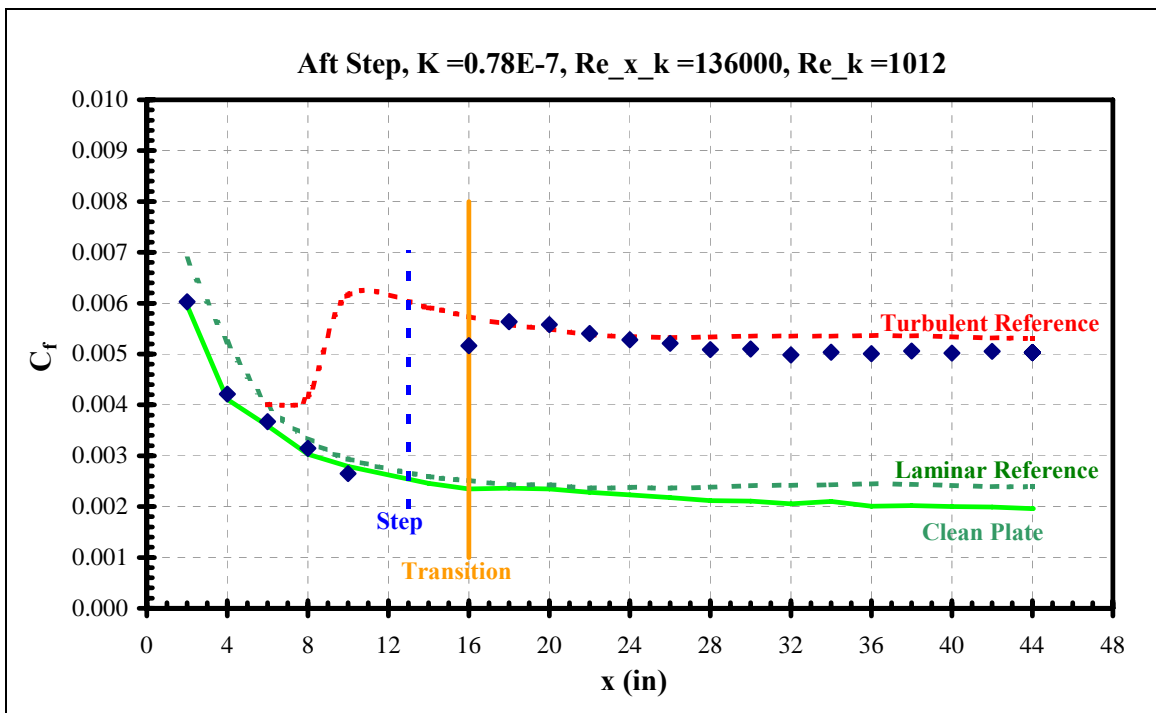


Figure 282 Aft step skin friction distribution

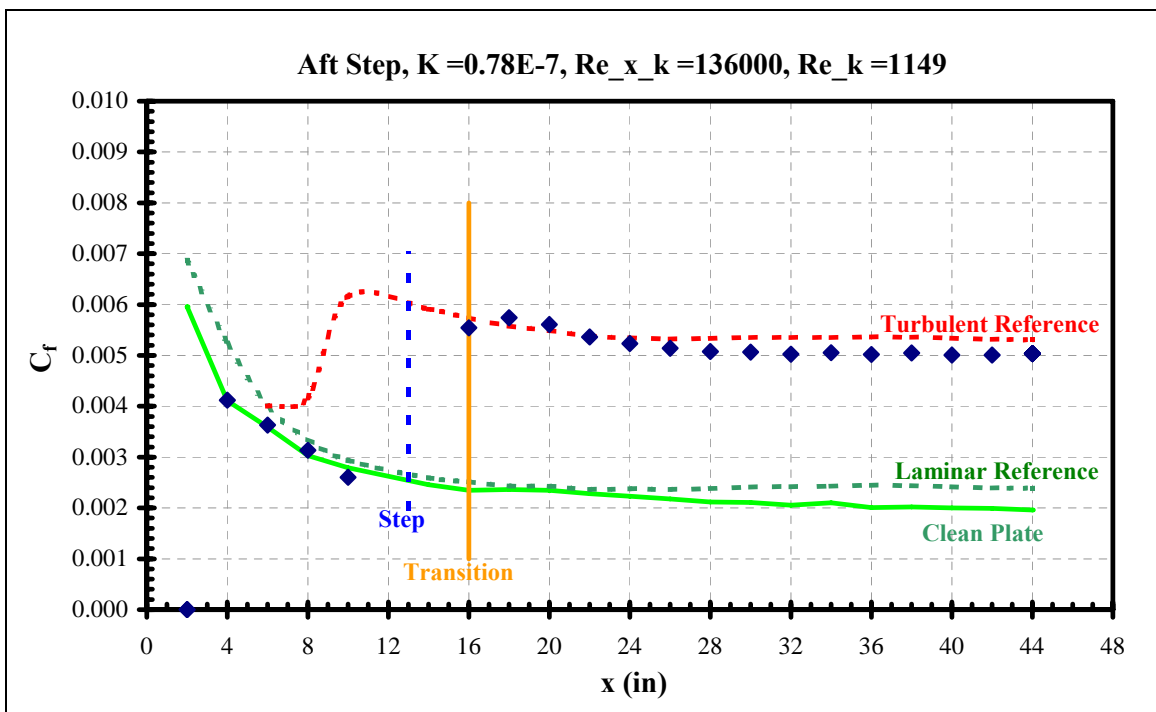
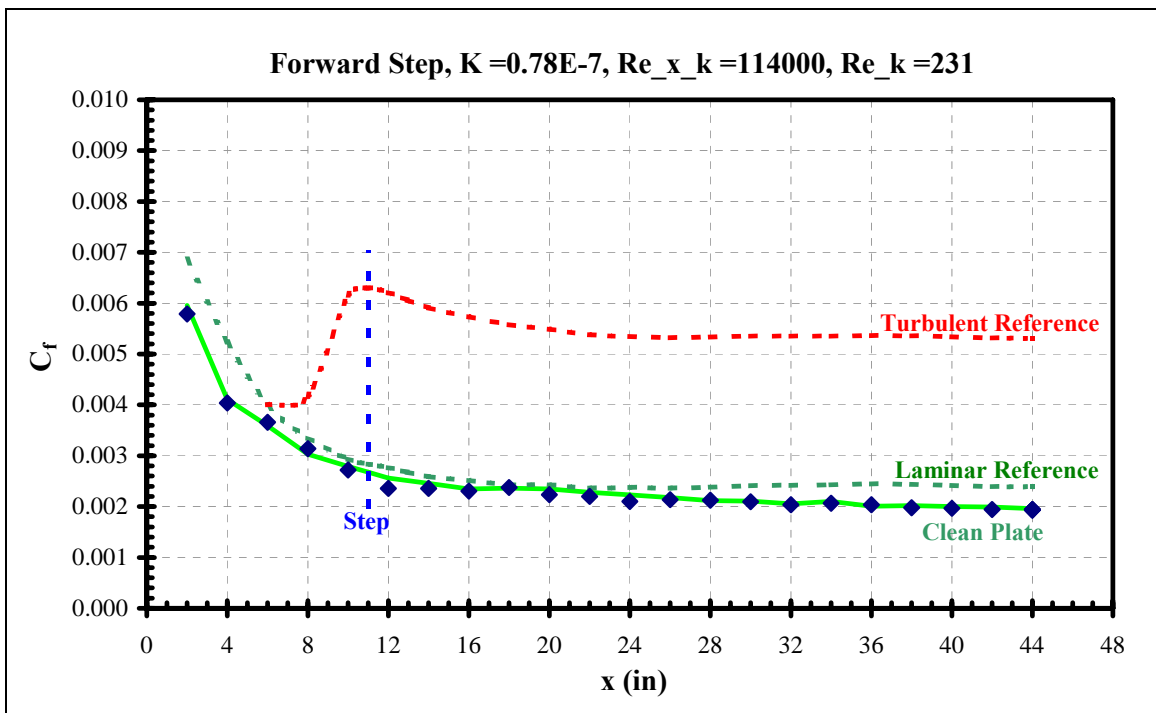
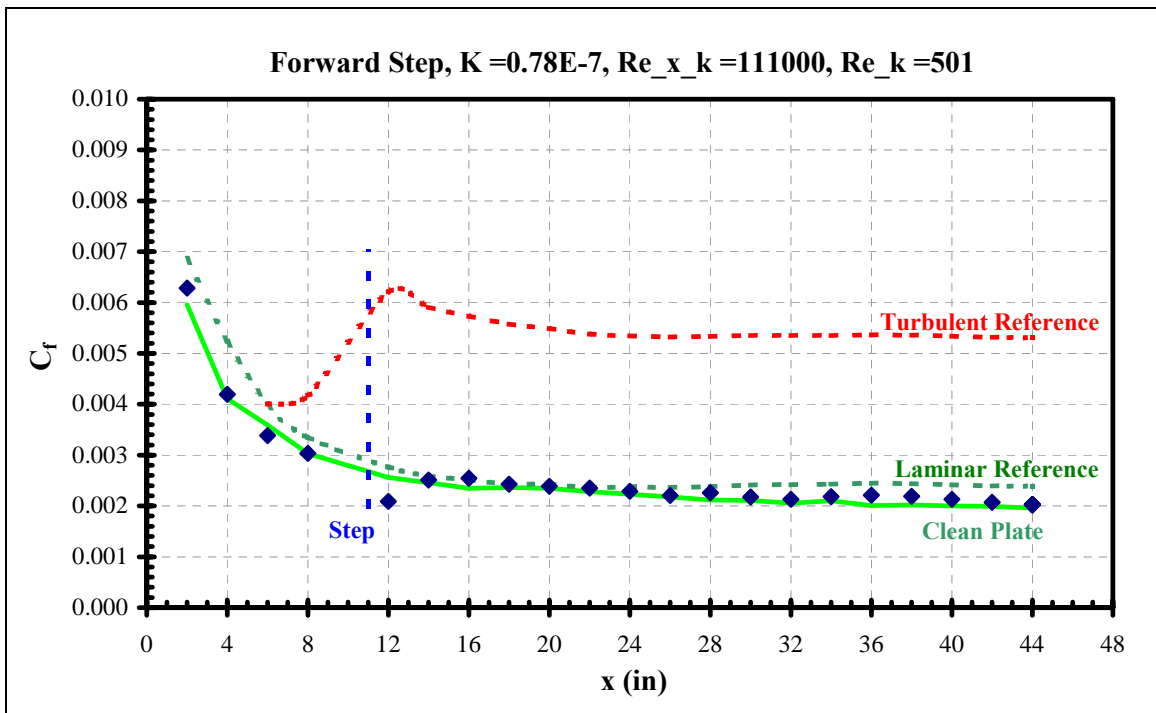


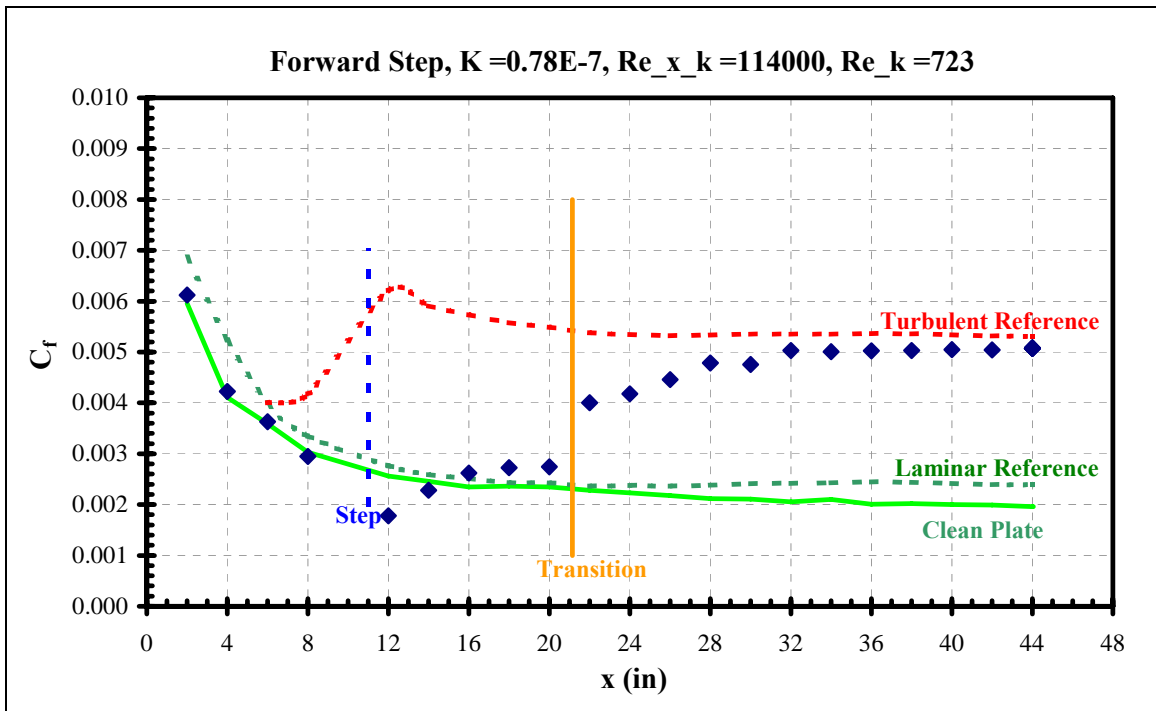
Figure 283 Aft step skin friction distribution



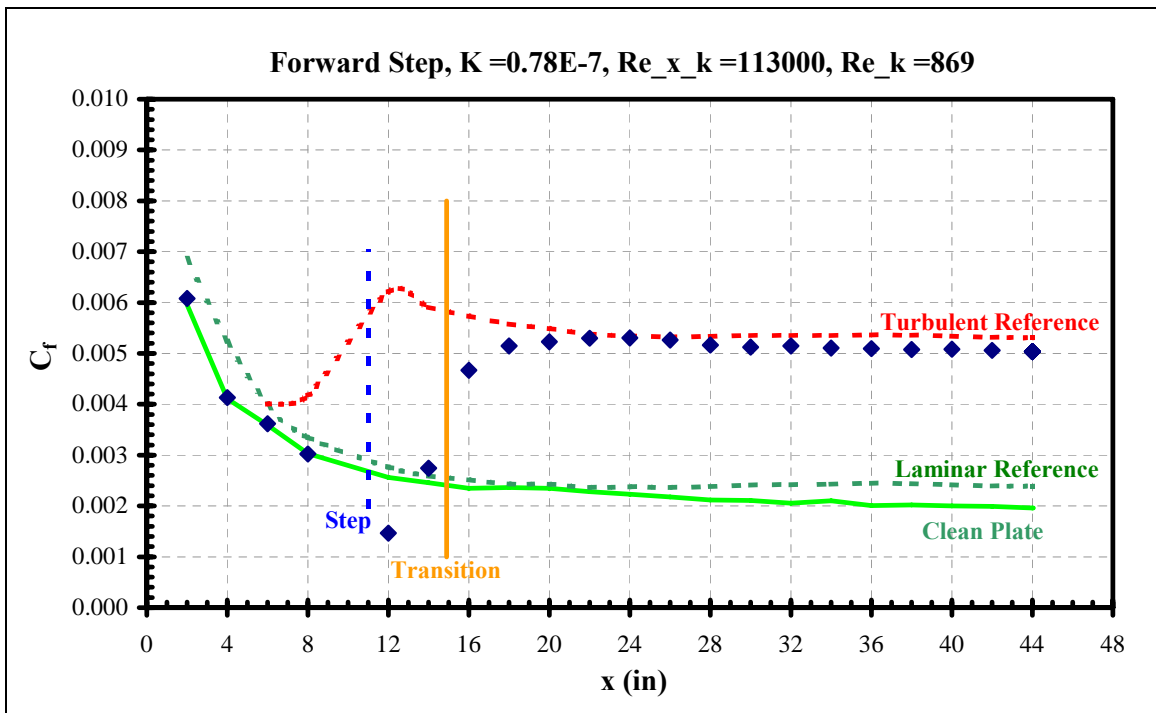
**Figure 284 Forward step skin friction distribution**



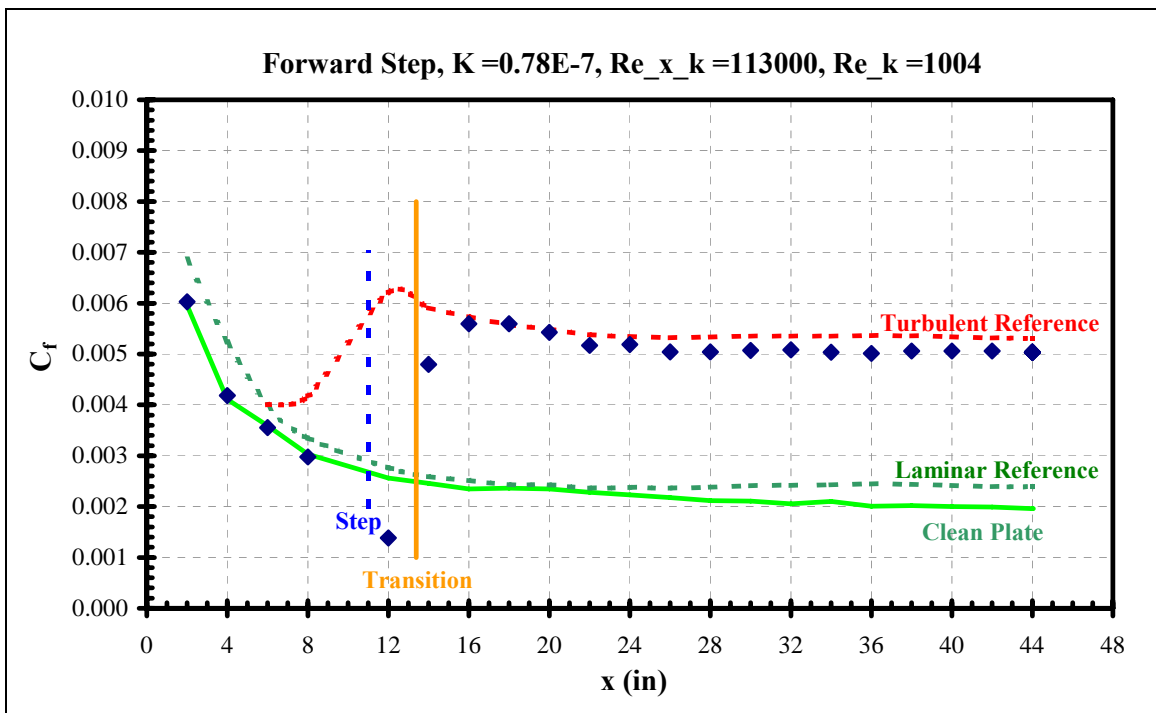
**Figure 285 Forward step skin friction distribution**



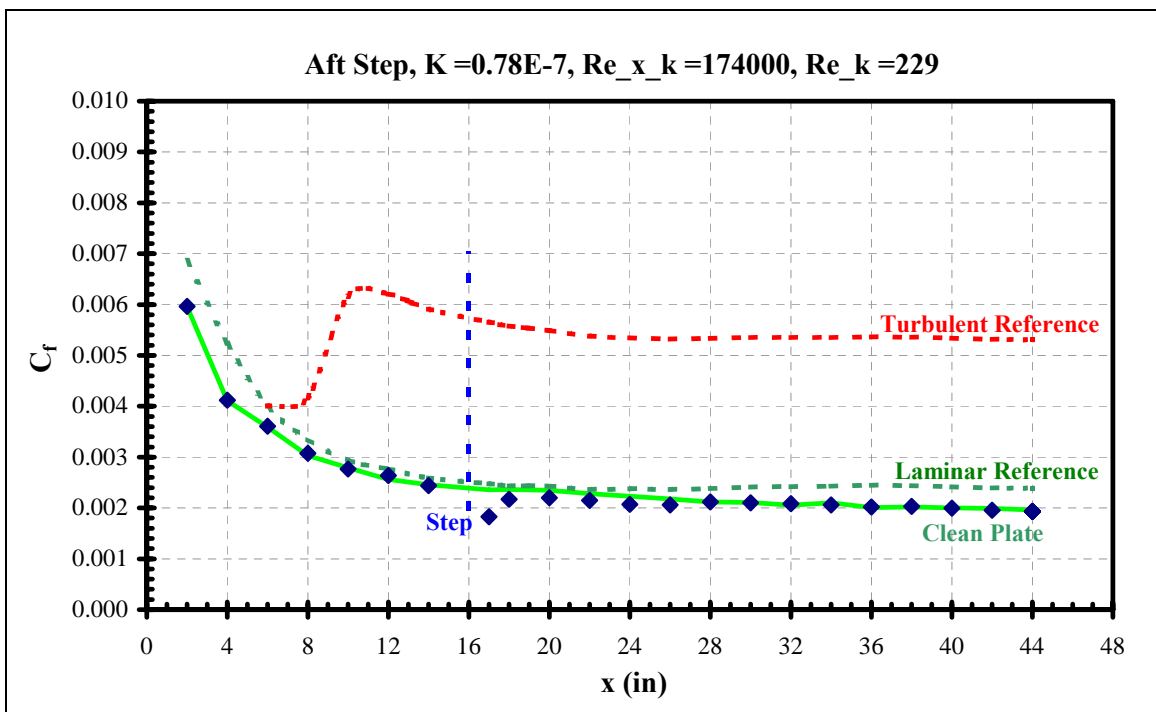
**Figure 286 Forward step skin friction distribution**



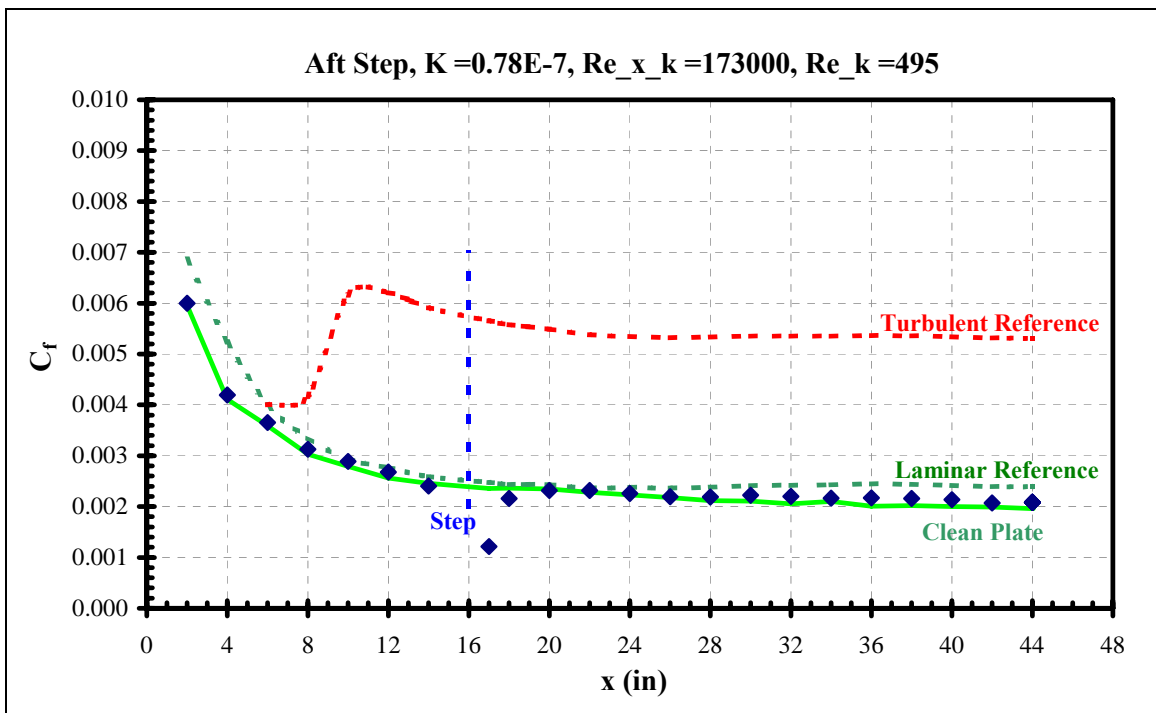
**Figure 287 Forward step skin friction distribution**



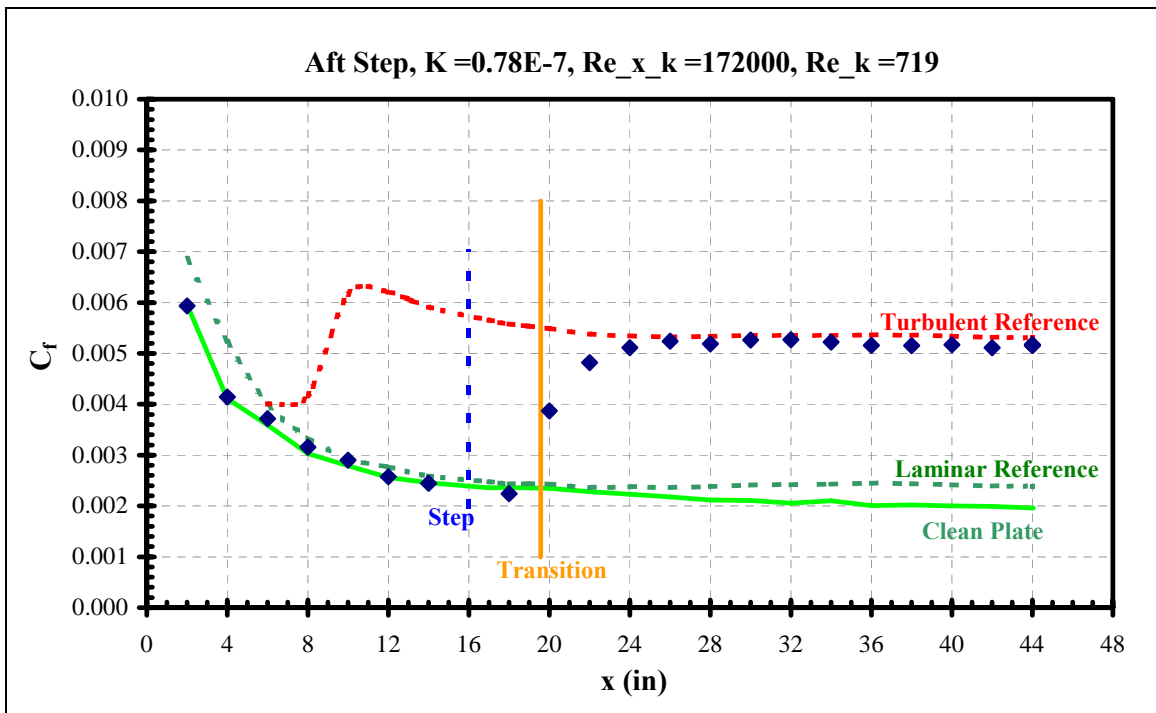
**Figure 288 Forward step skin friction distribution**



**Figure 289 Aft step skin friction distribution**

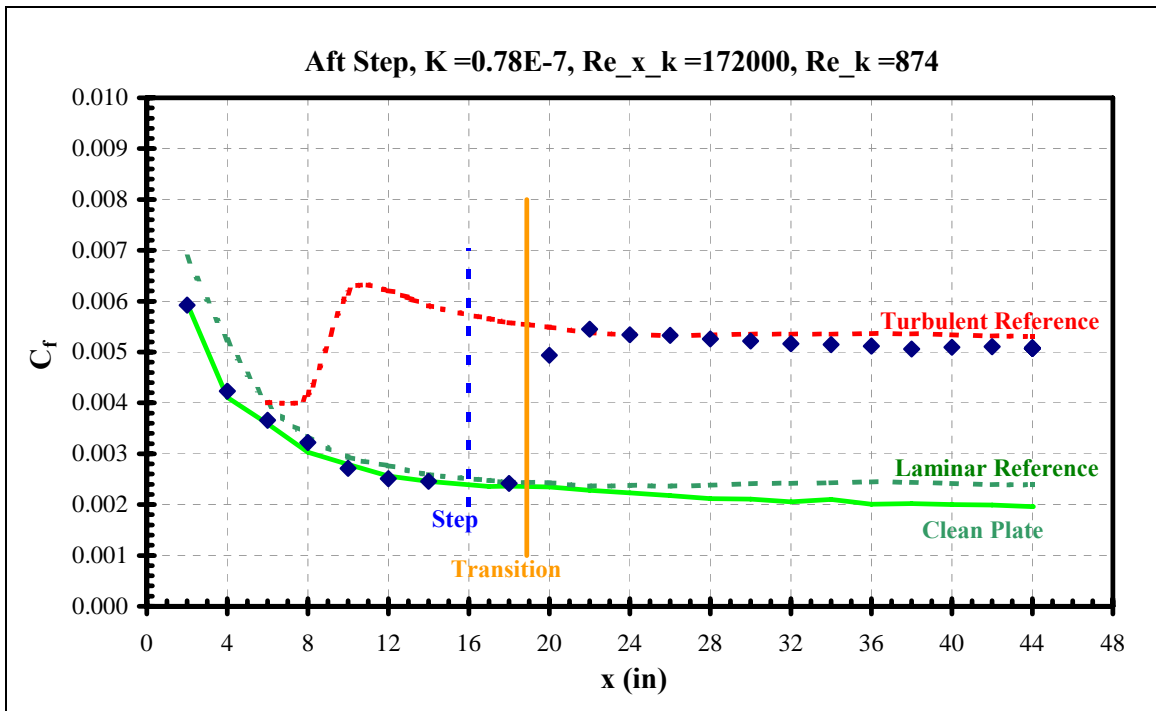


**Figure 290 Aft step skin friction distribution**

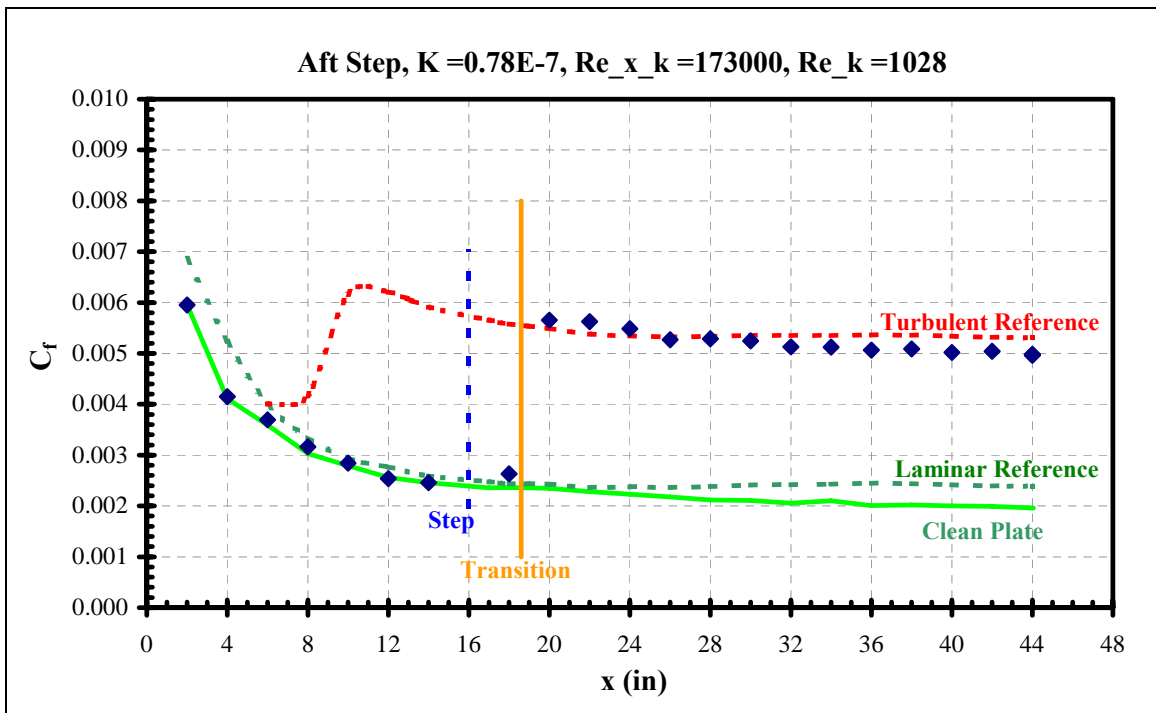


**Figure 291 Aft step skin friction distribution**

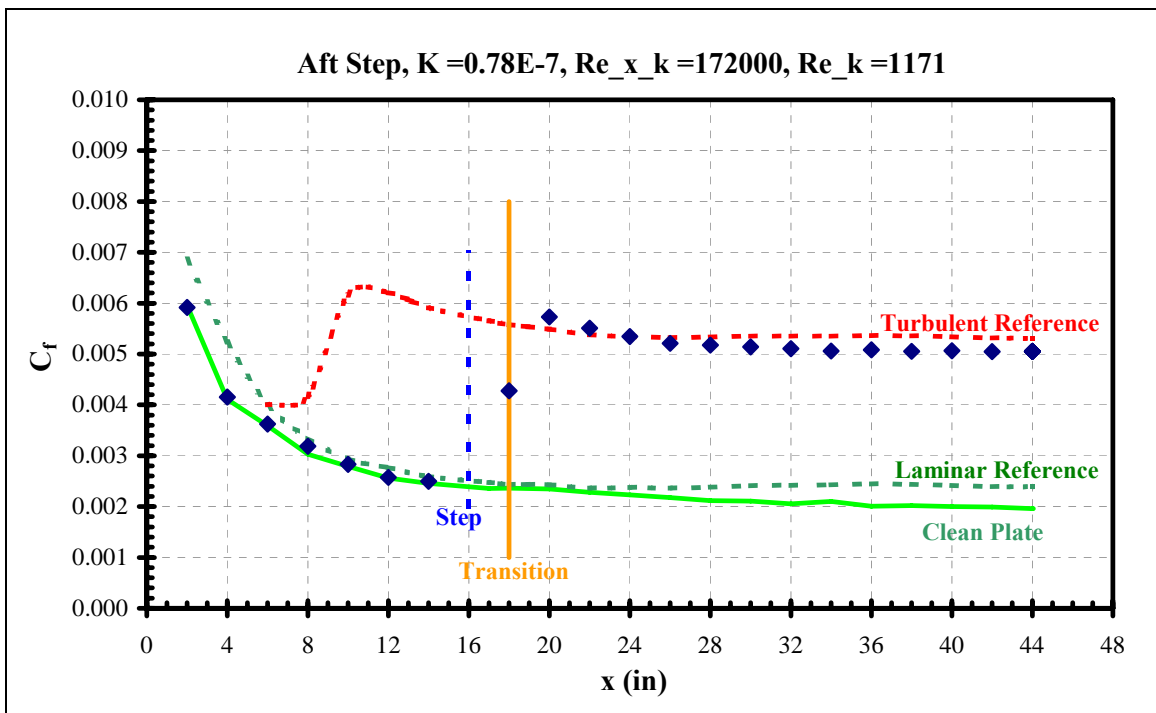




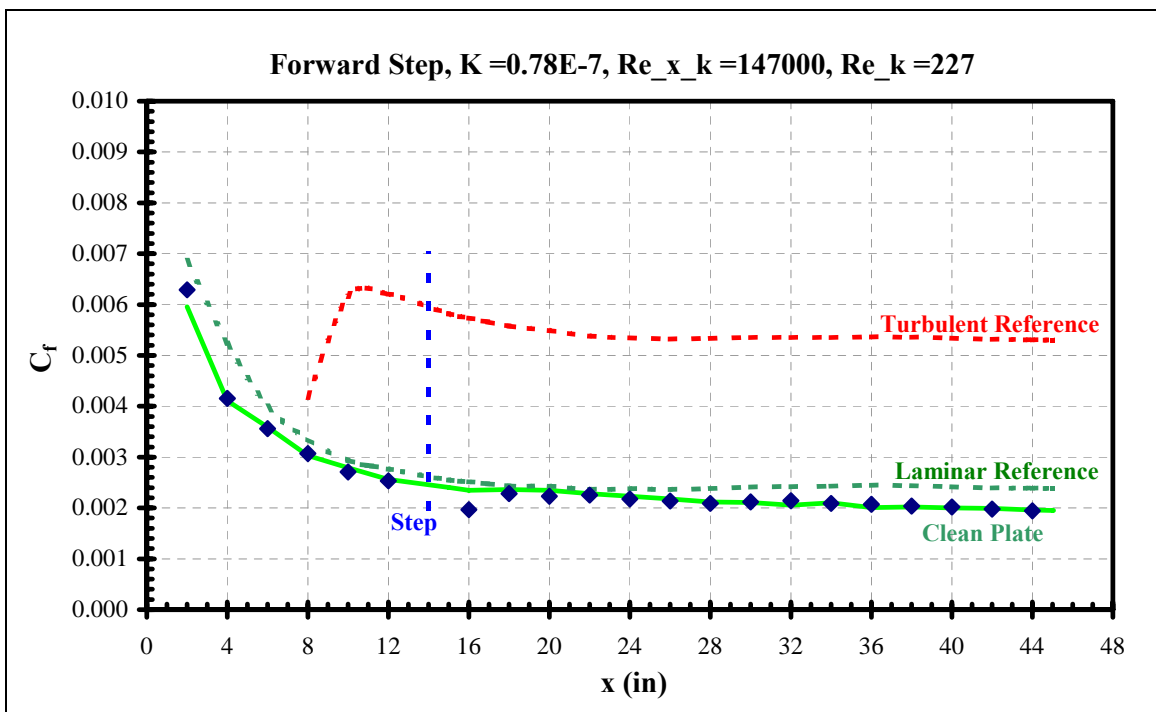
**Figure 292 Aft step skin friction distribution**



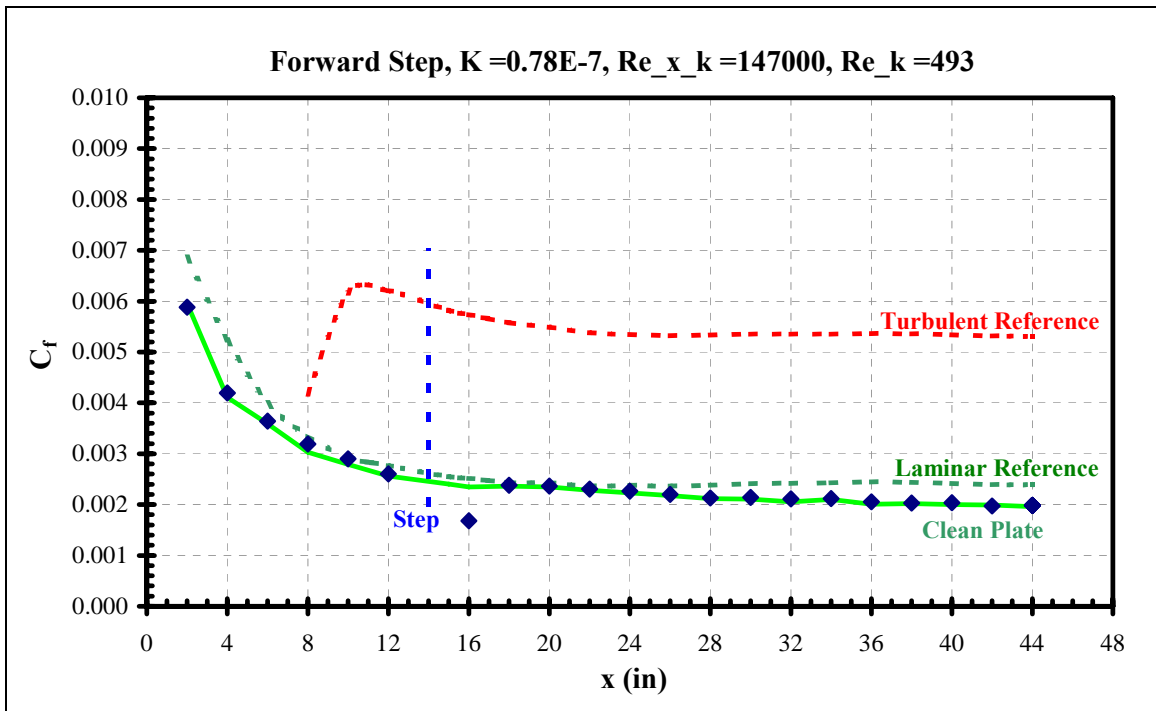
**Figure 293 Aft step skin friction distribution**



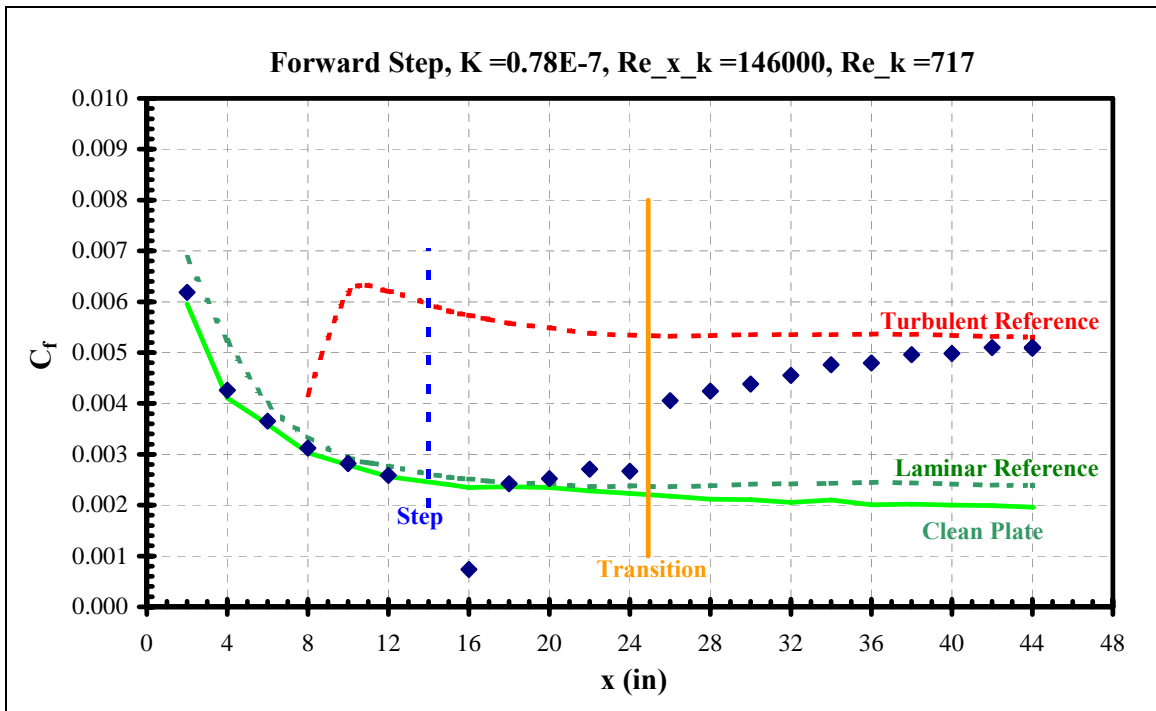
**Figure 294 Aft step skin friction distribution**



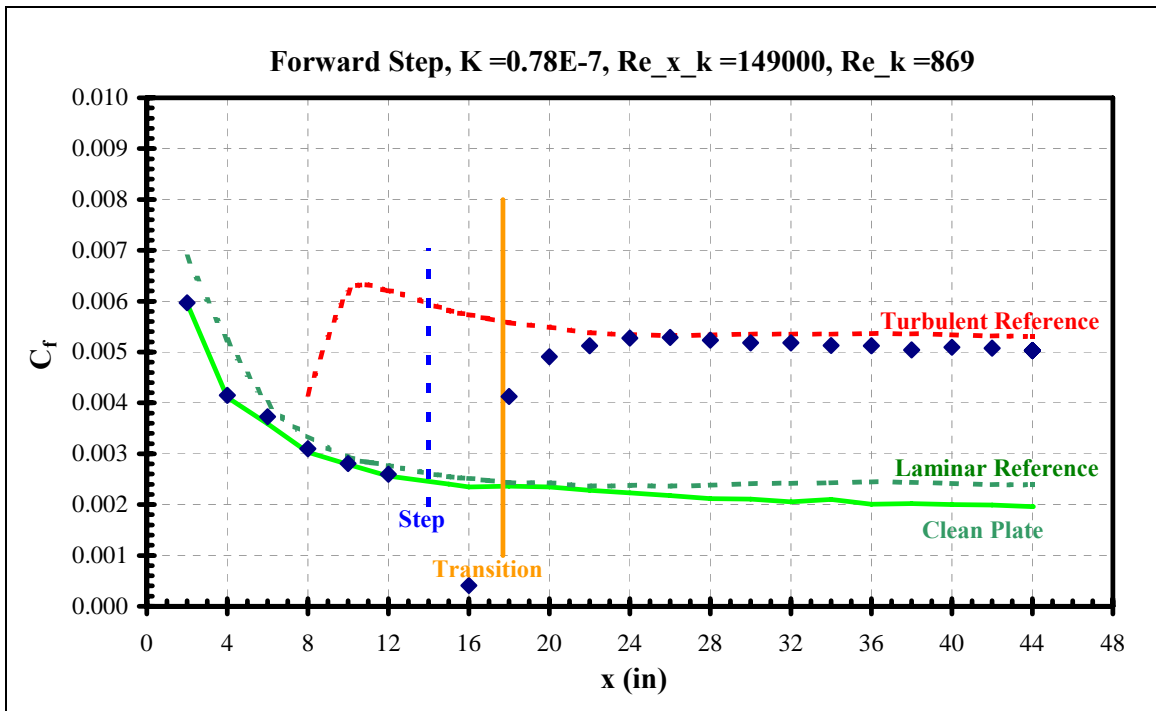
**Figure 295 Forward step skin friction distribution**



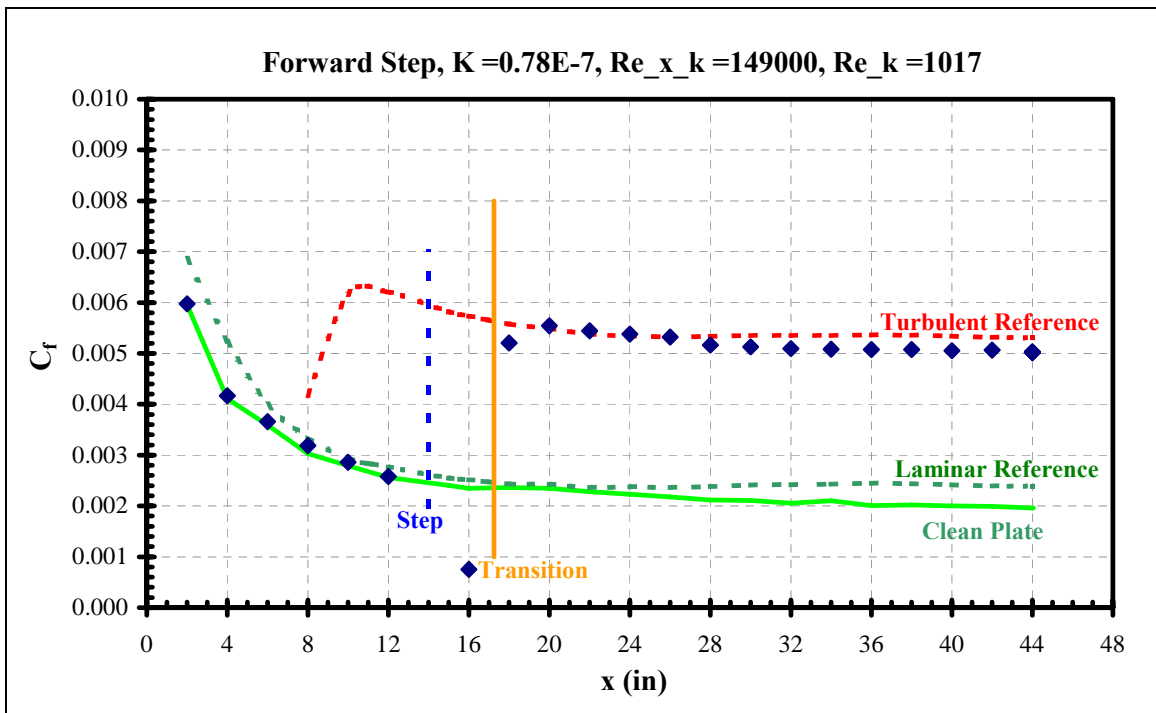
**Figure 296 Forward step skin friction distribution**



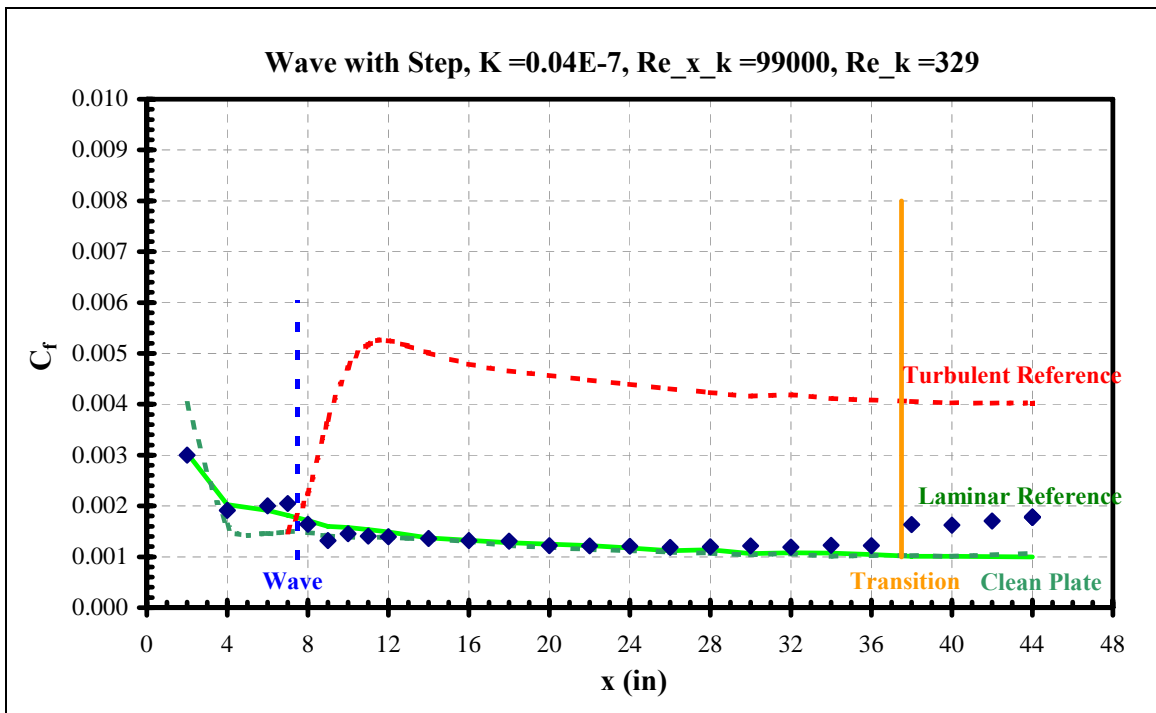
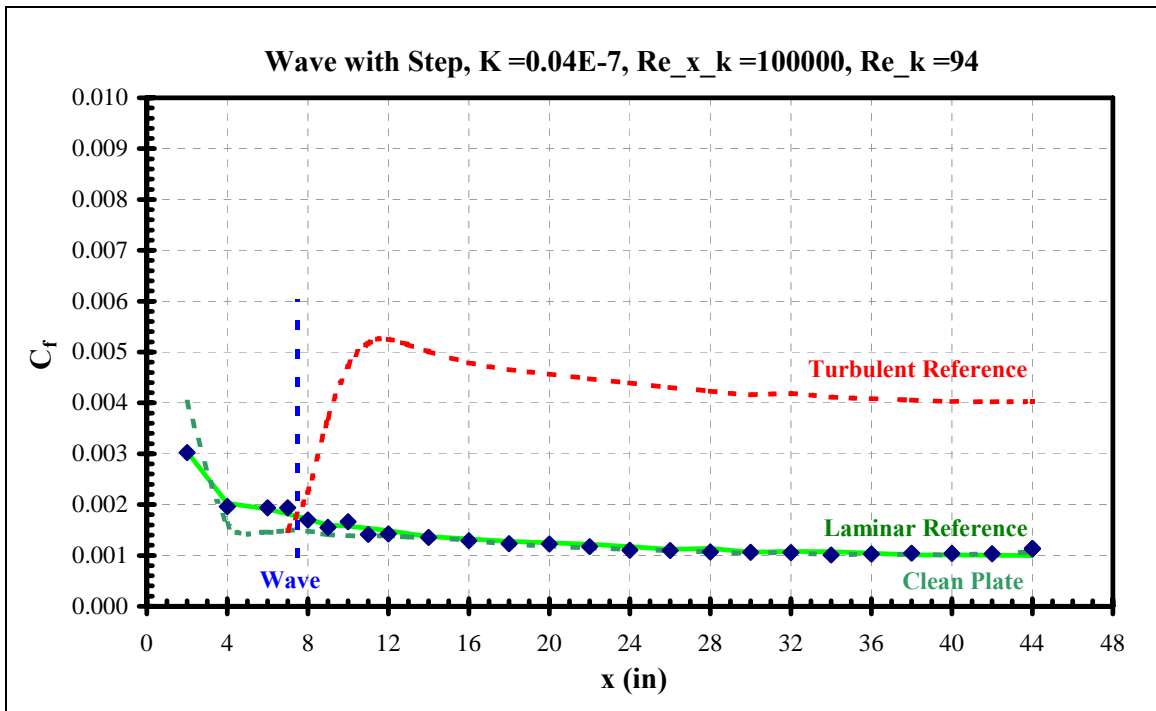
**Figure 297 Forward step skin friction distribution**

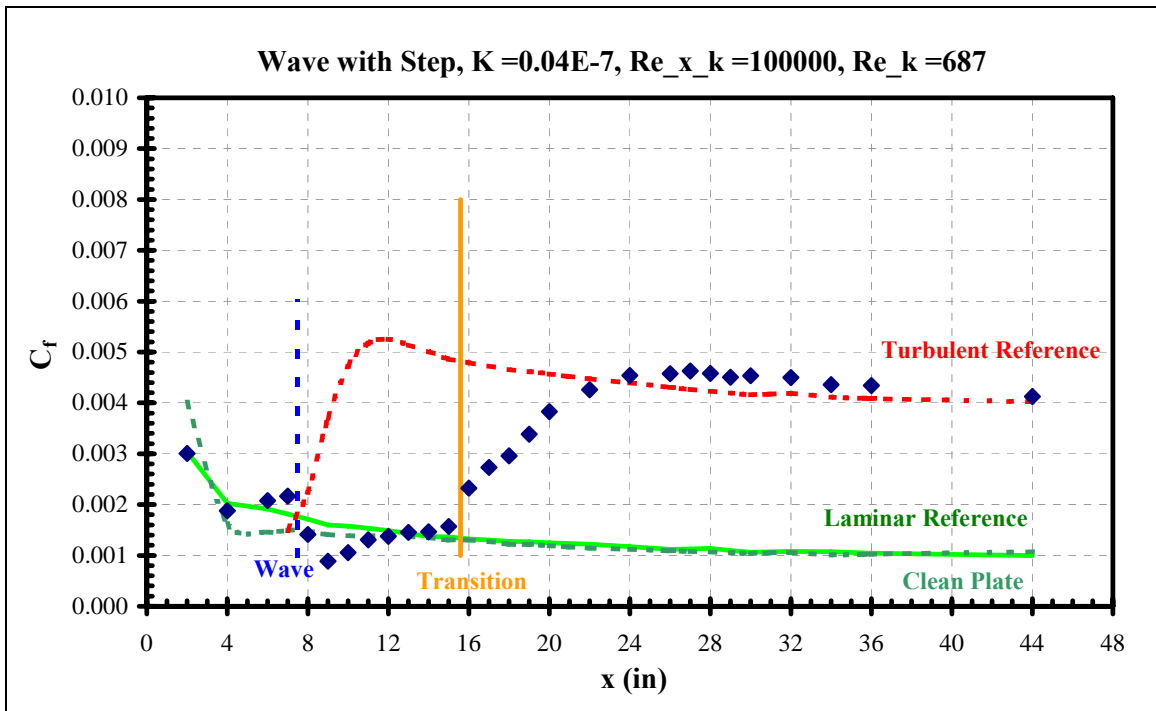


**Figure 298 Forward step skin friction distribution**

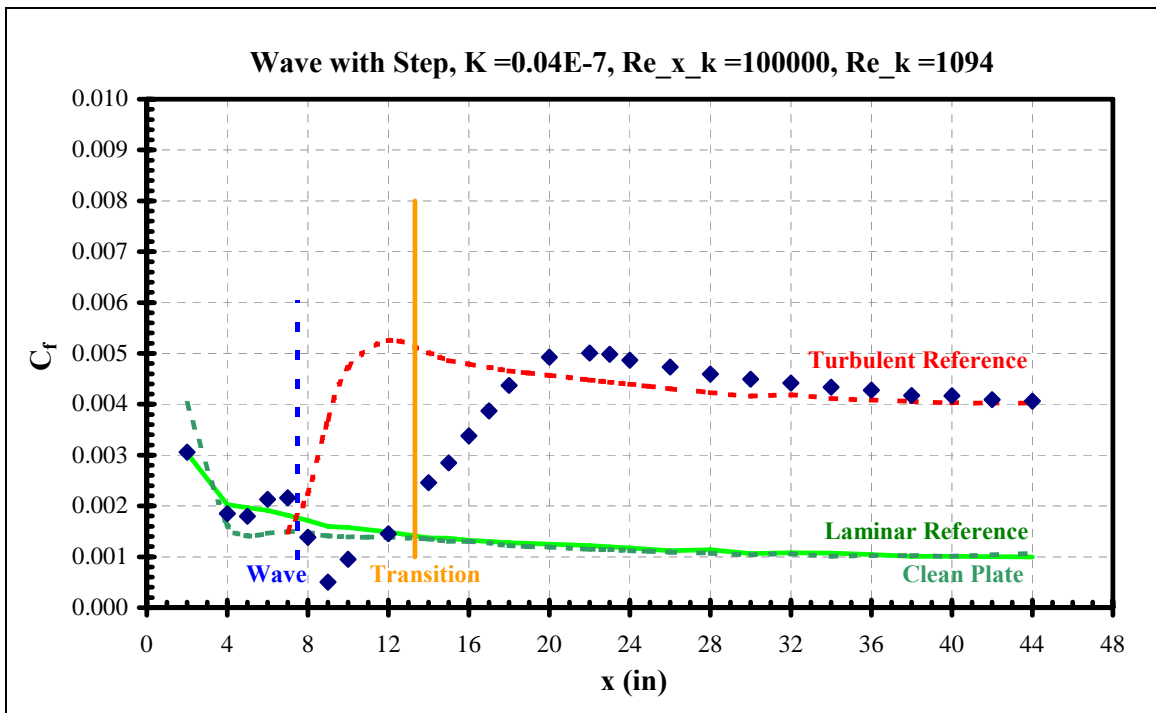


**Figure 299 Forward step skin friction distribution**

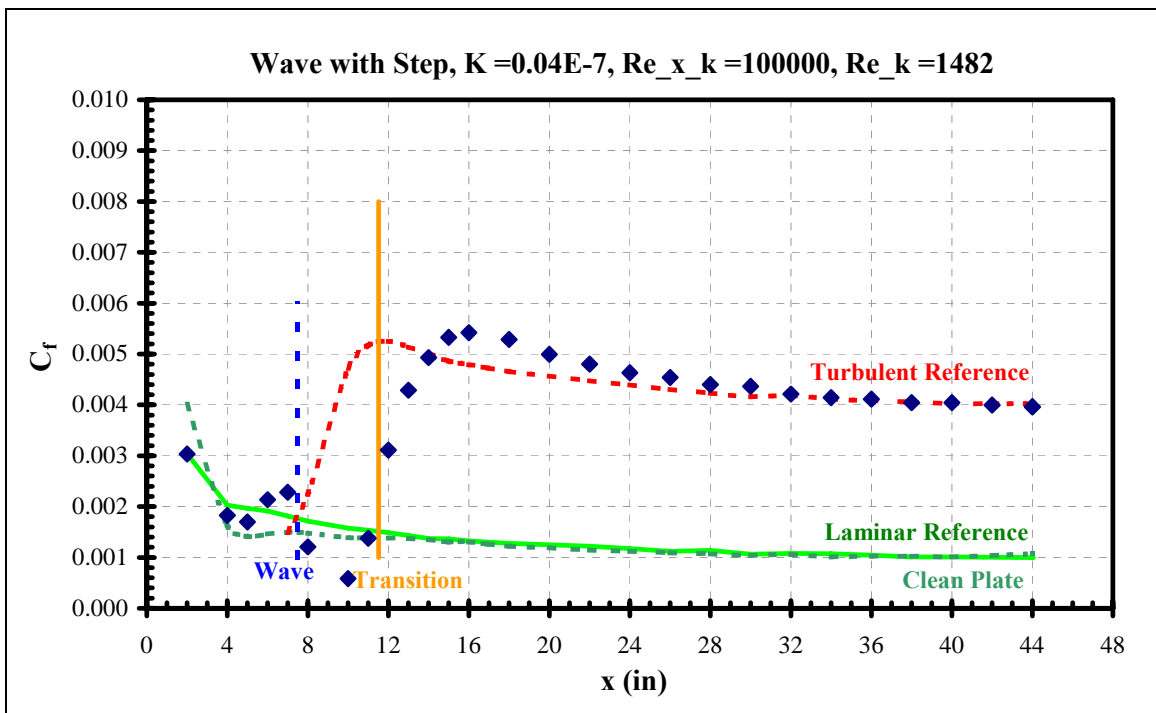




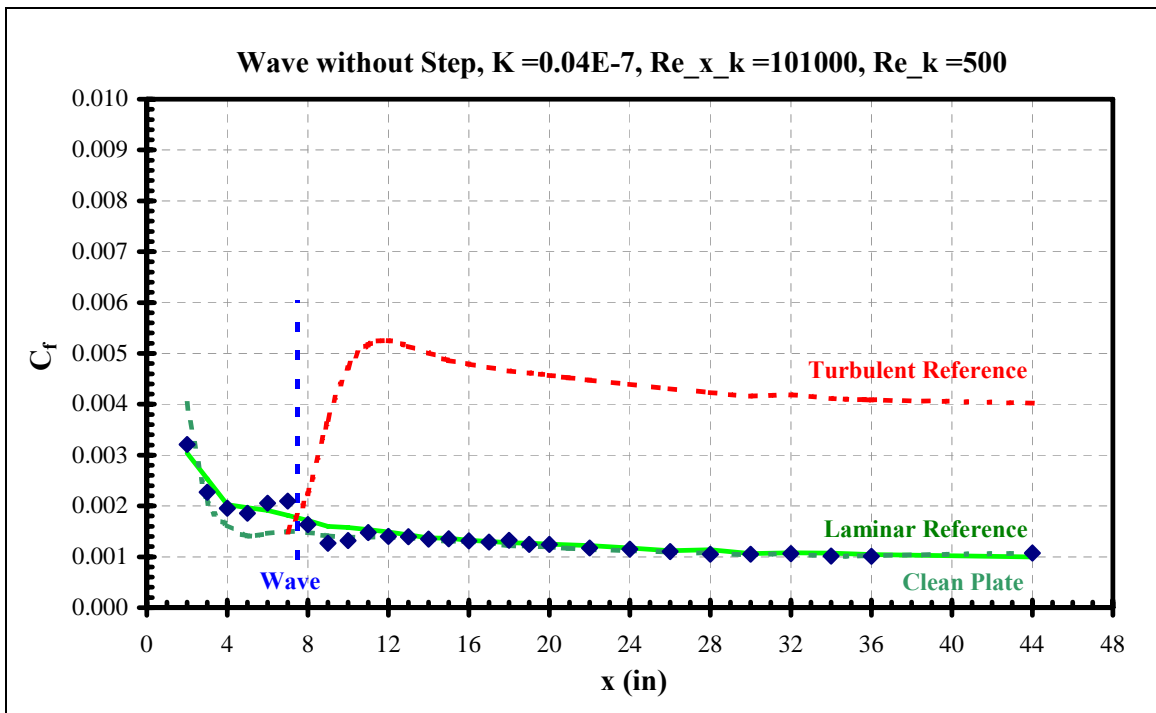
**Figure 302 Wave with step skin friction distribution**



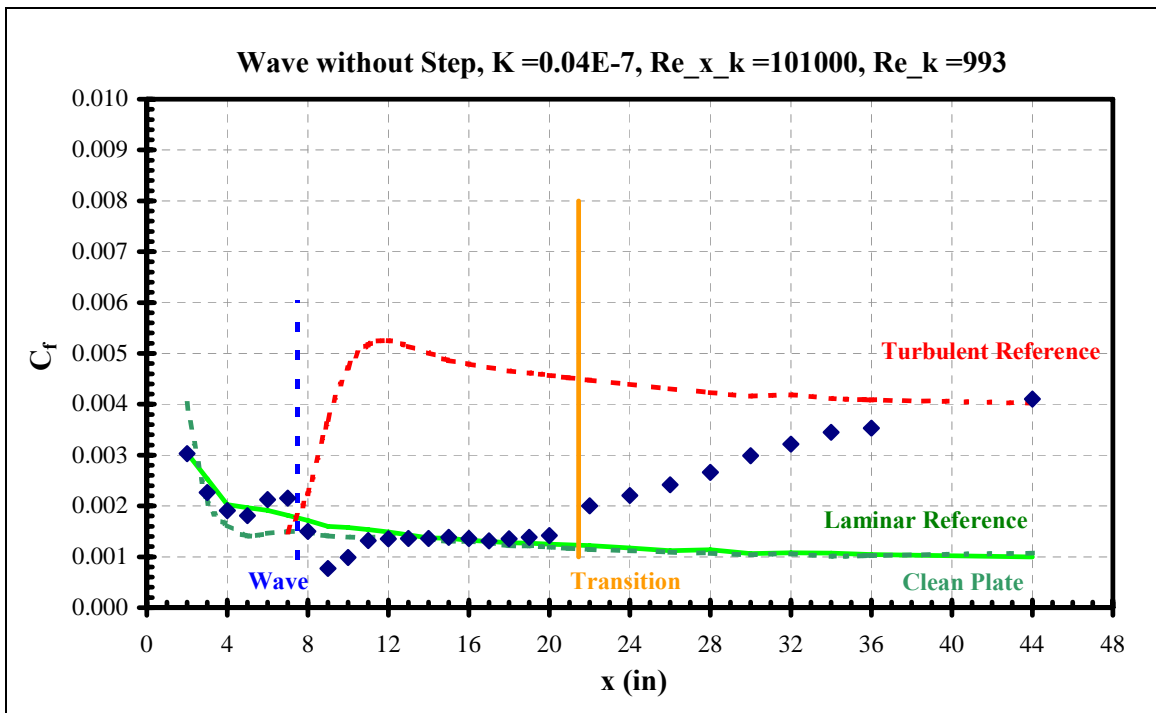
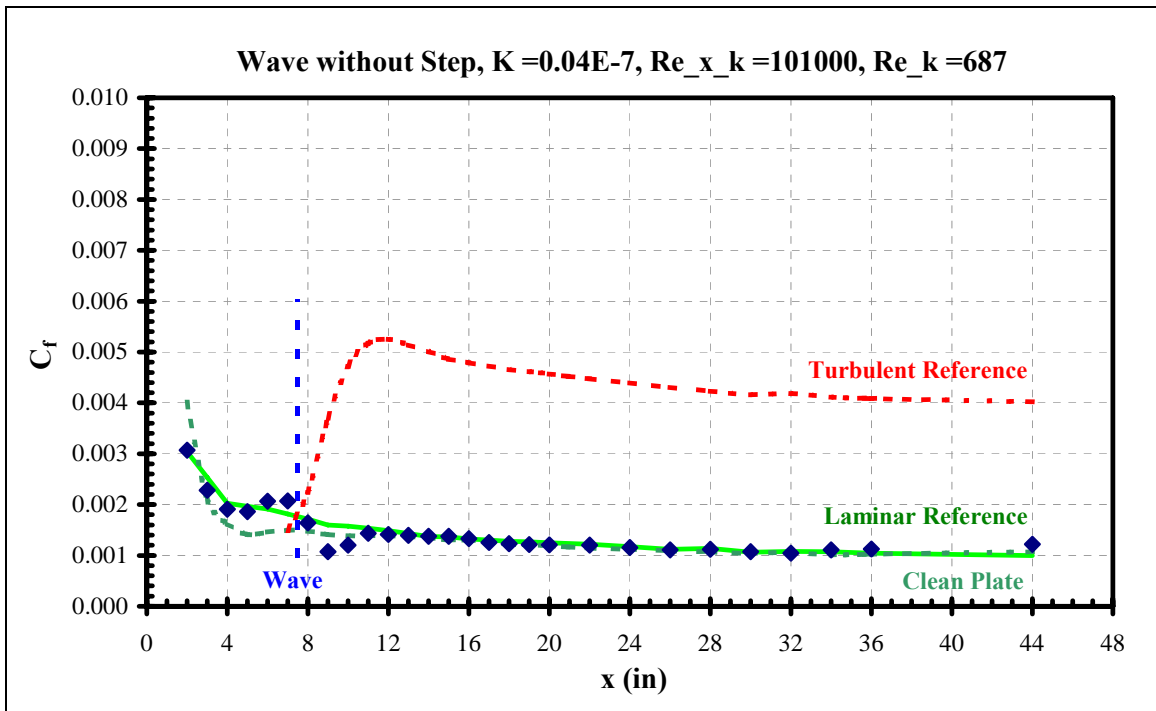
**Figure 303 Wave with step skin friction distribution**



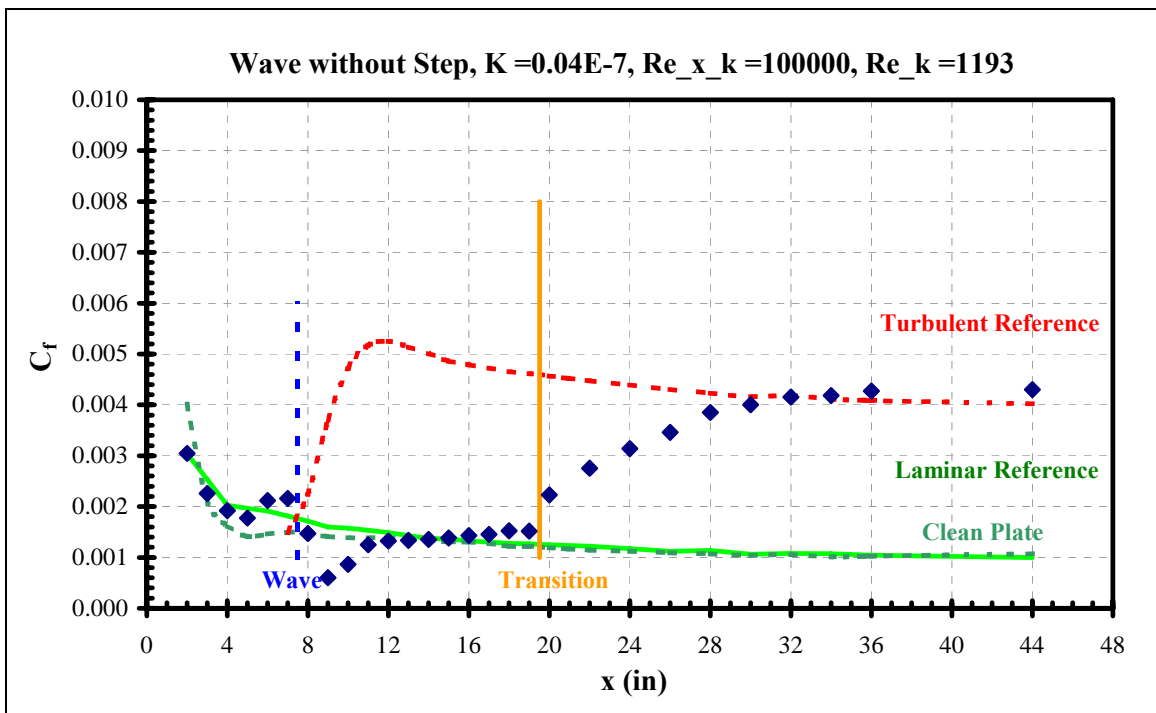
**Figure 304 Wave with step skin friction distribution**



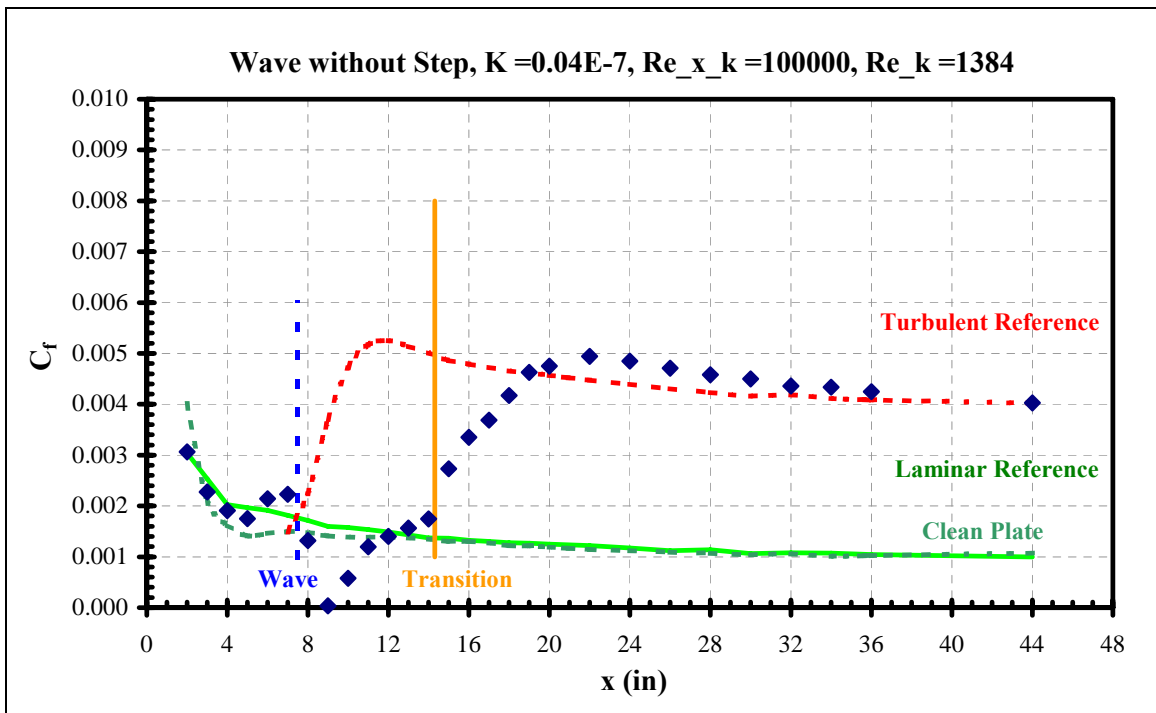
**Figure 305 Wave without step skin friction distribution**



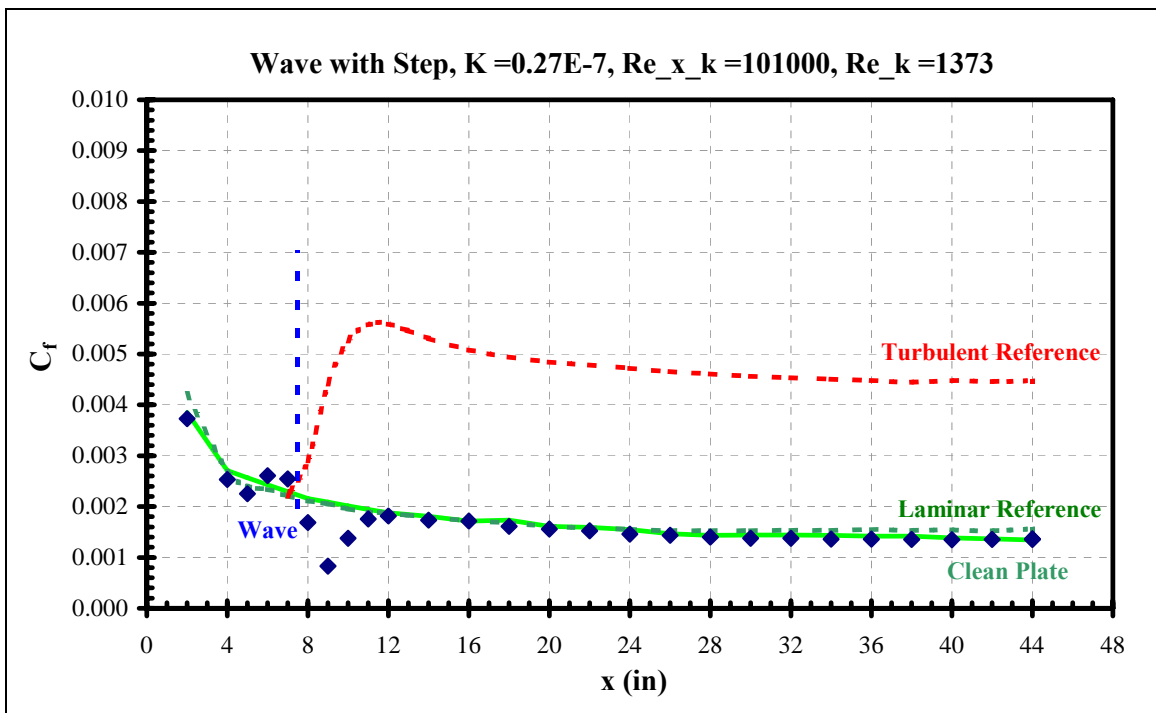




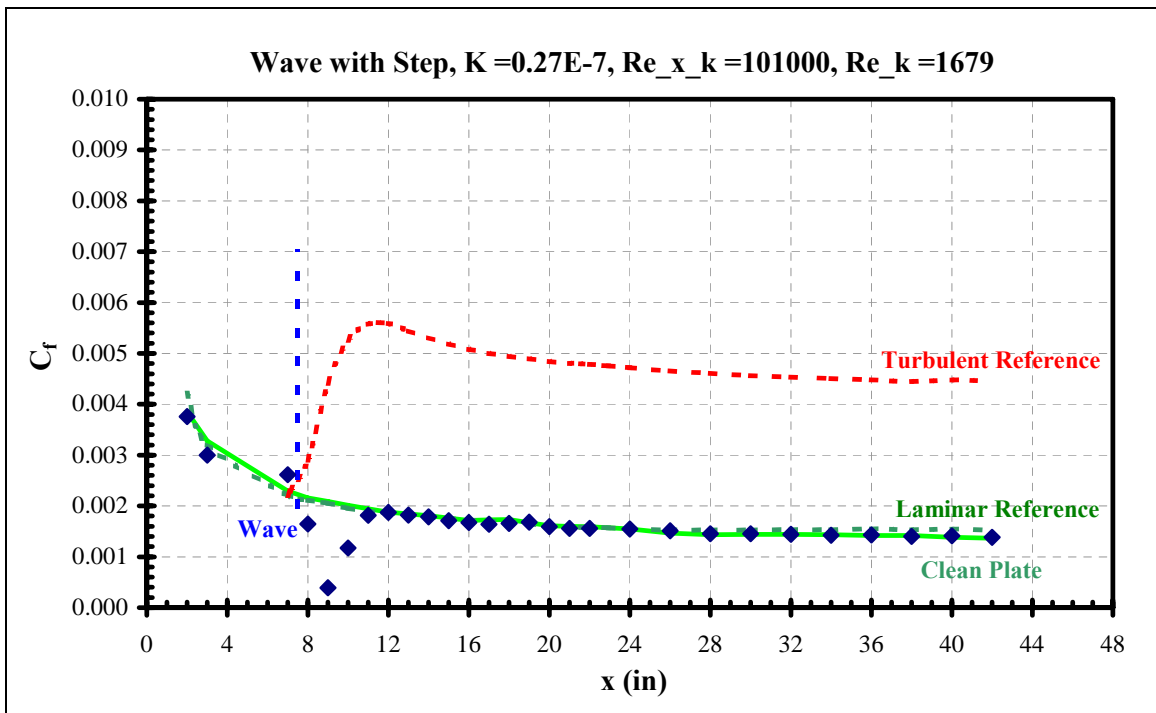
**Figure 308 Wave without step skin friction distribution**



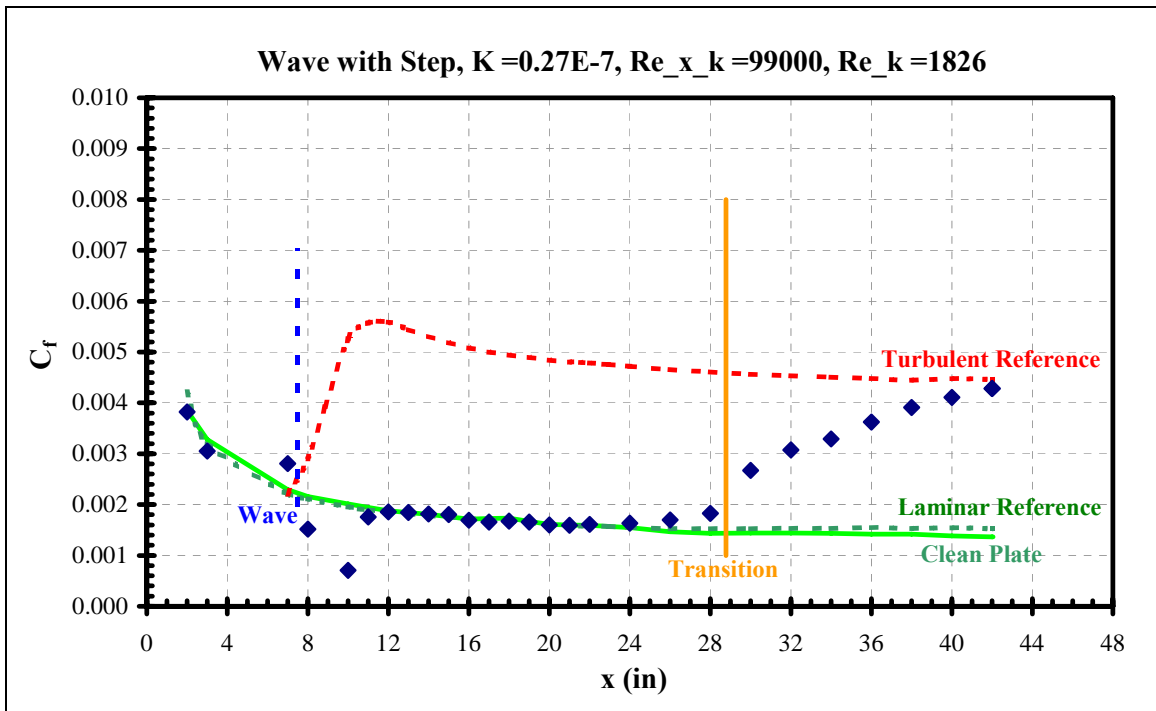
**Figure 309 Wave without step skin friction distribution**



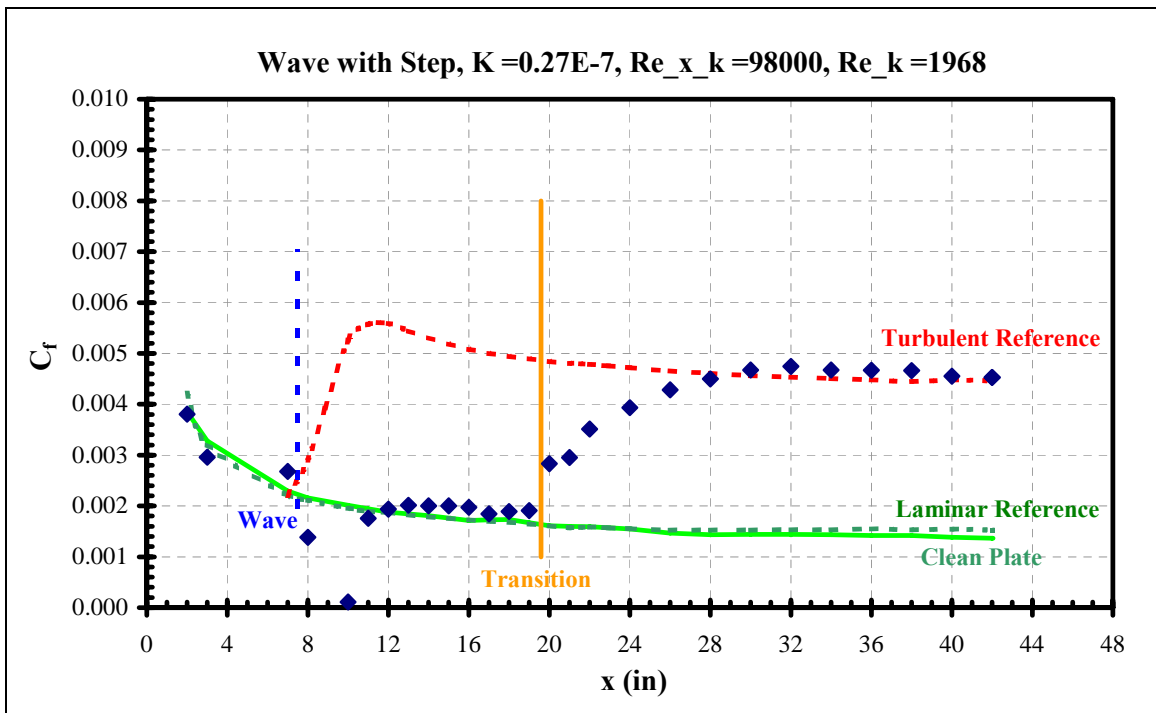
**Figure 310 Wave with step skin friction distribution**



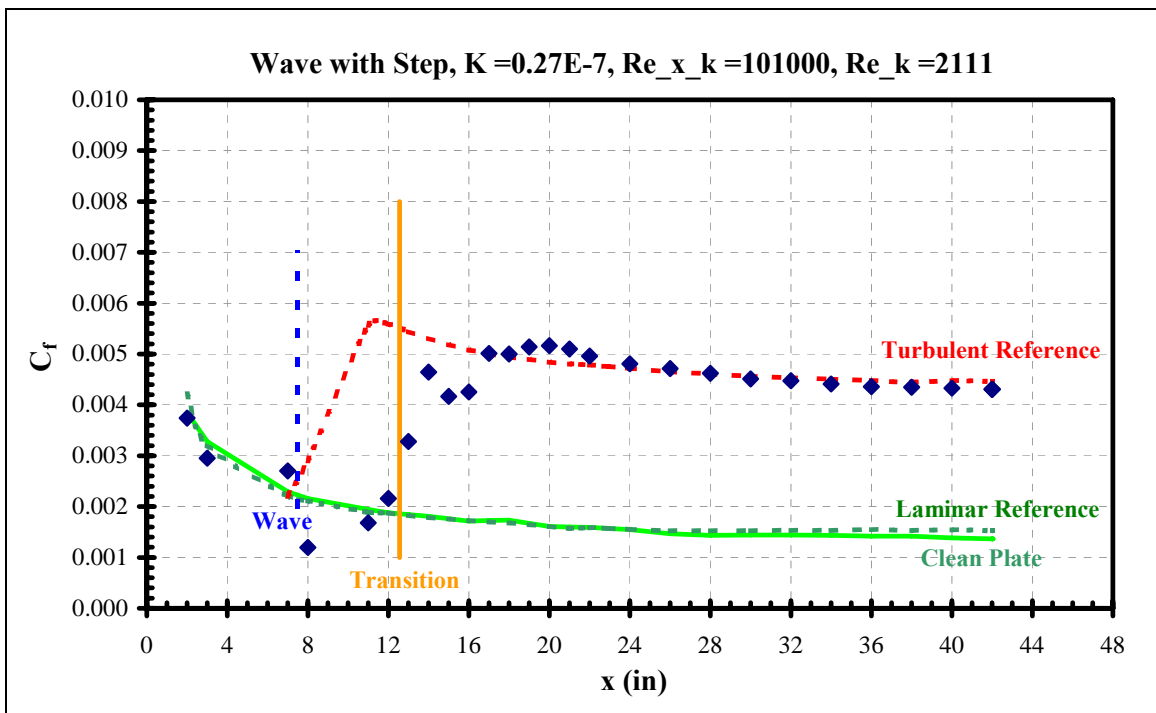
**Figure 311 Wave with step skin friction distribution**



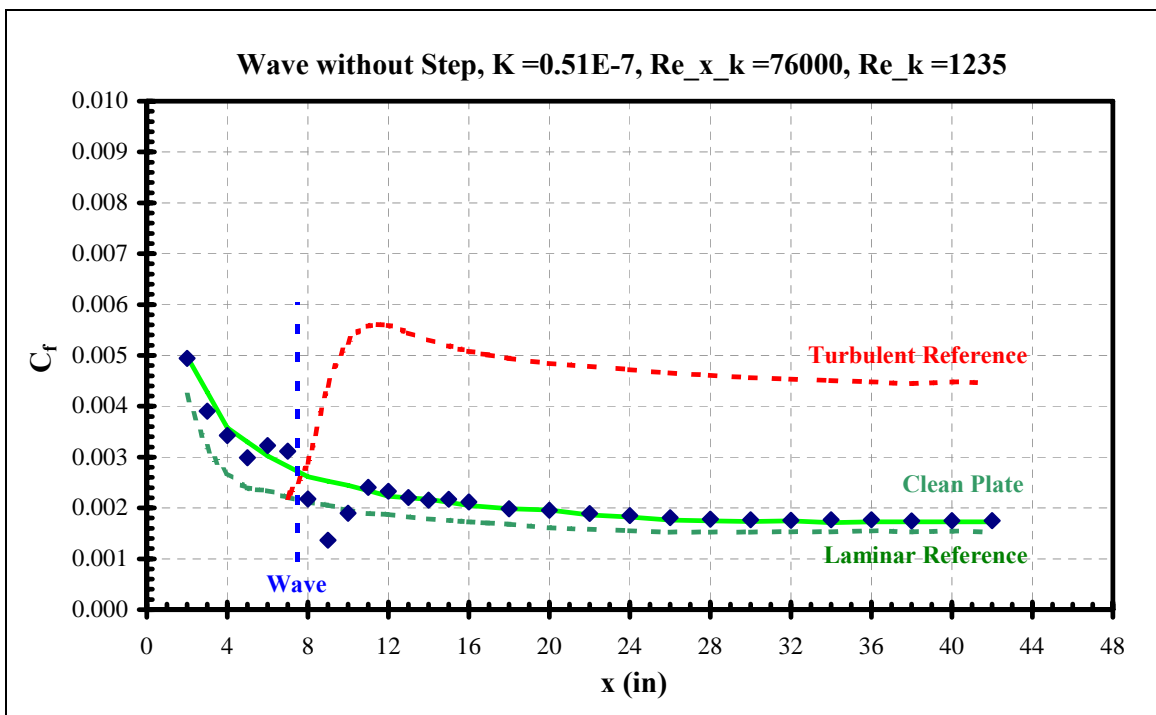
**Figure 312 Wave with step skin friction distribution**



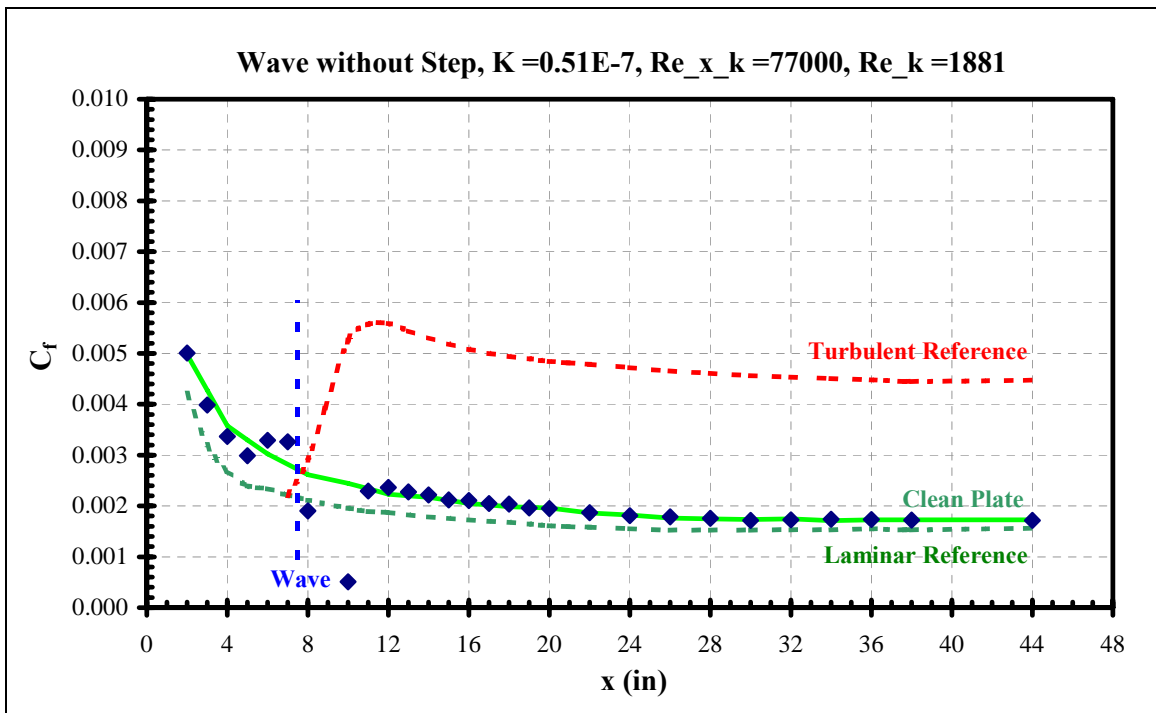
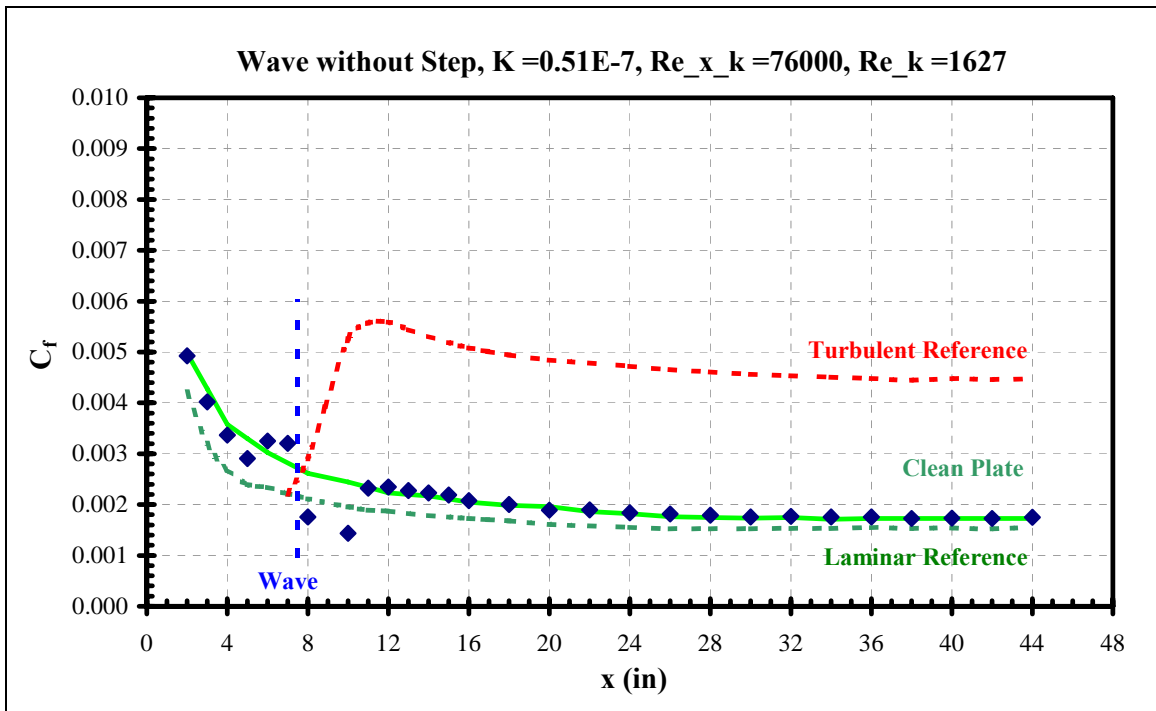
**Figure 313 Wave with step skin friction distribution**

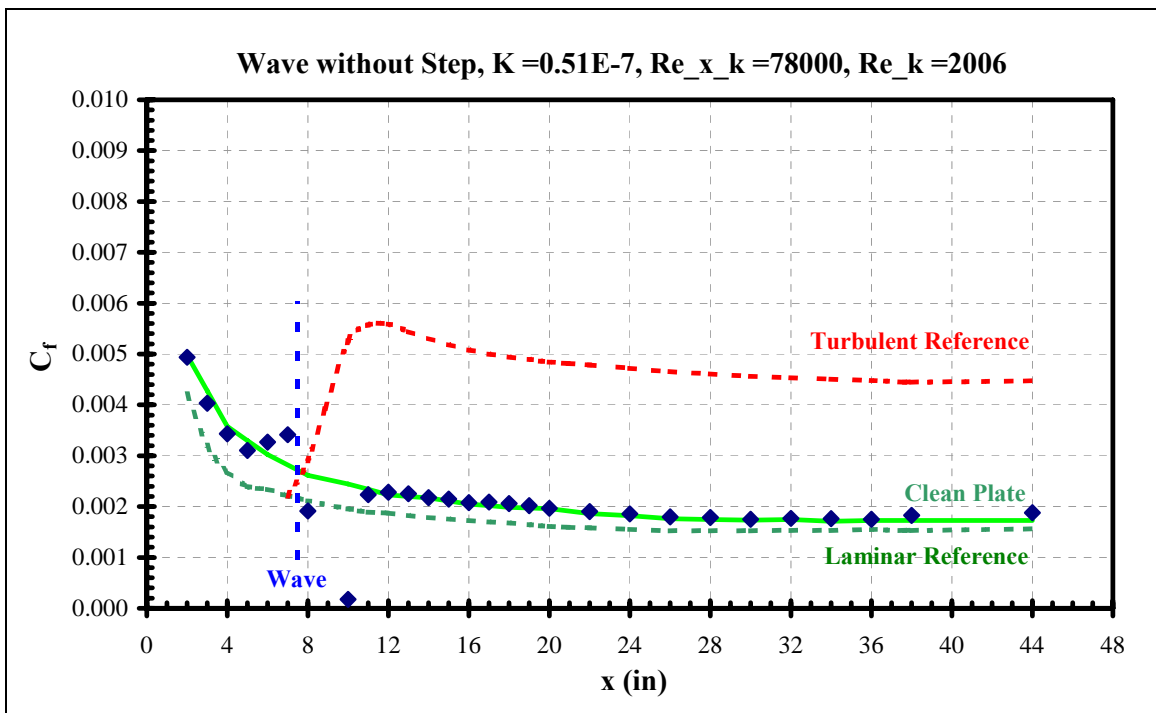


**Figure 314 Wave with step skin friction distributio.**

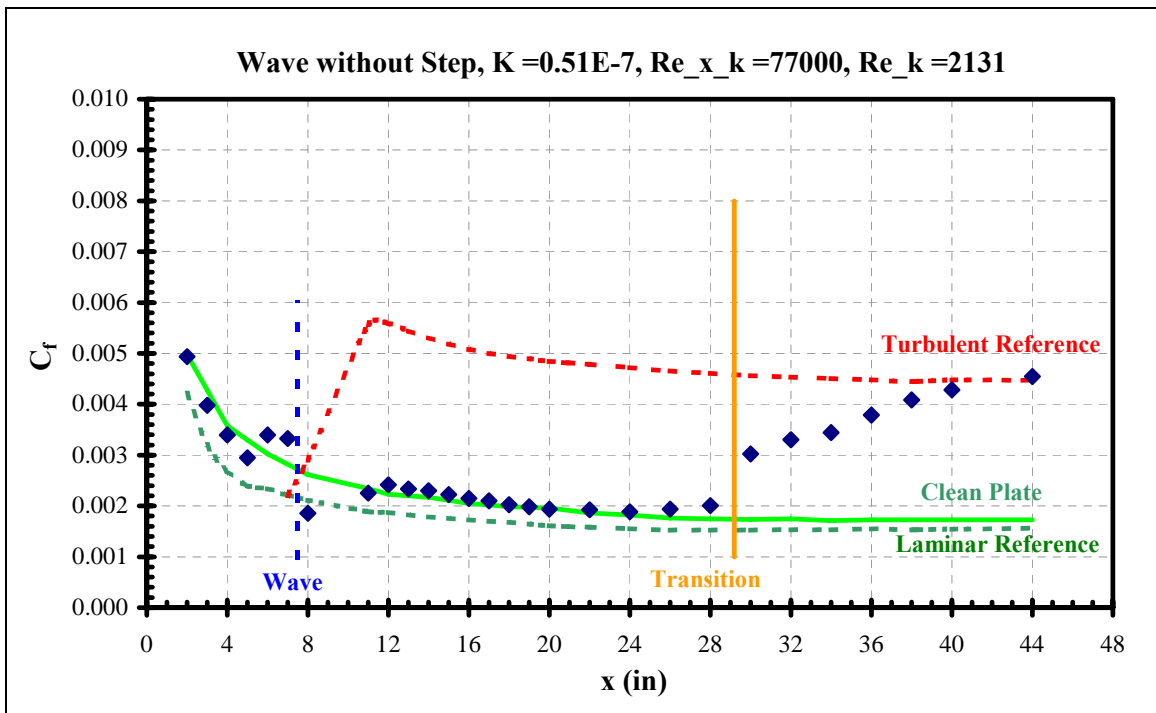


**Figure 315 Wave without step skin friction distribution**

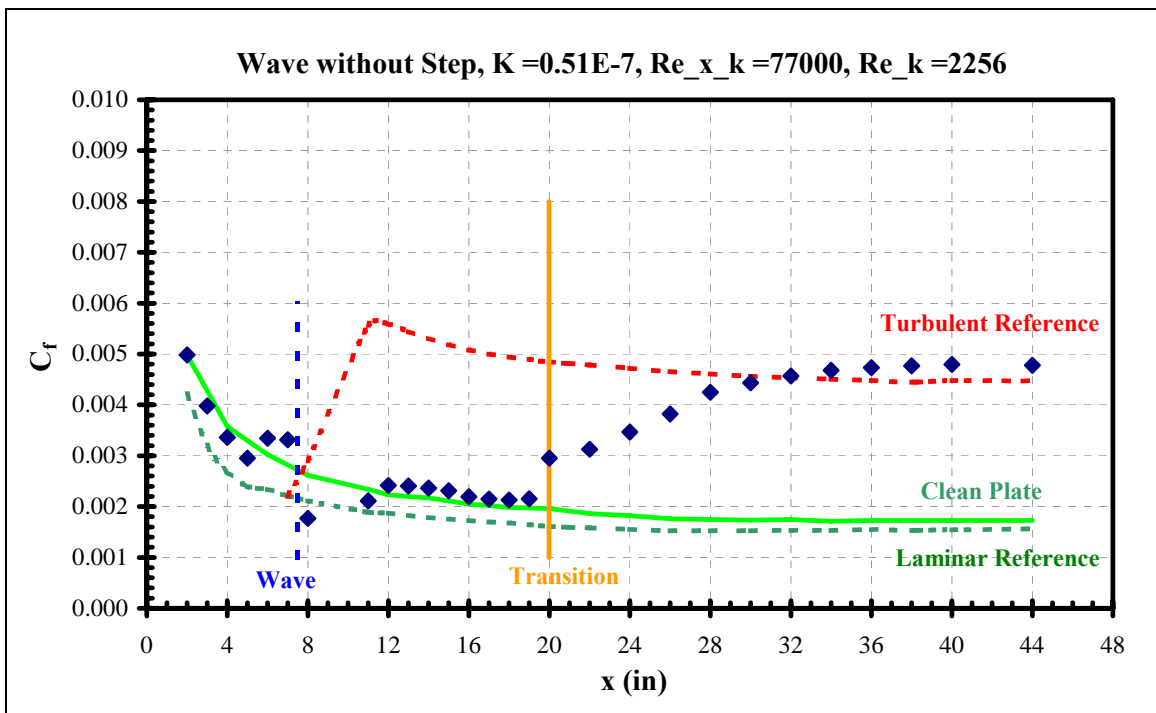




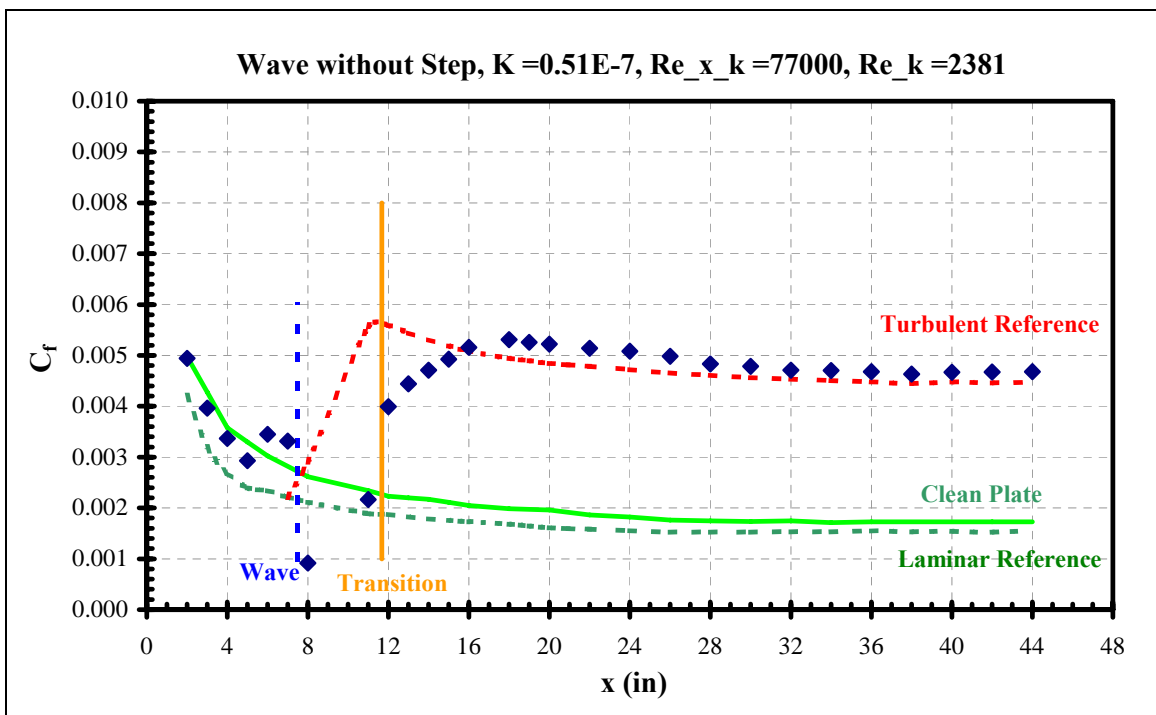
**Figure 318 Wave without step skin friction distribution**



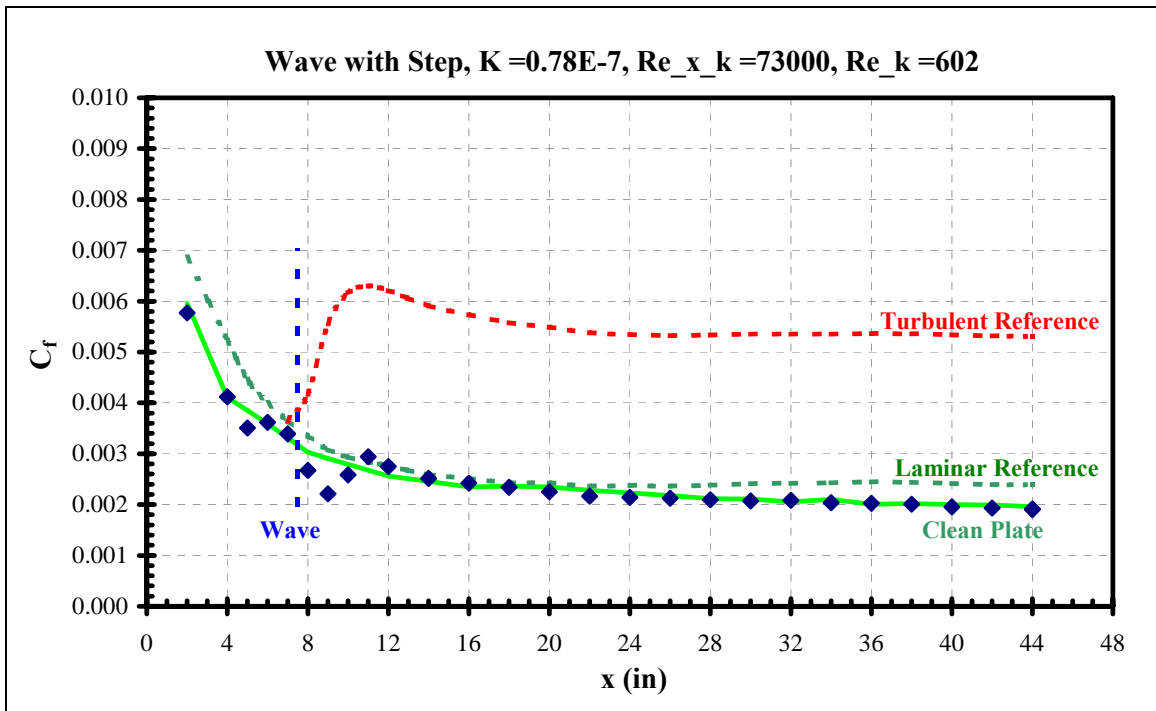
**Figure 319 Wave without step skin friction distribution**



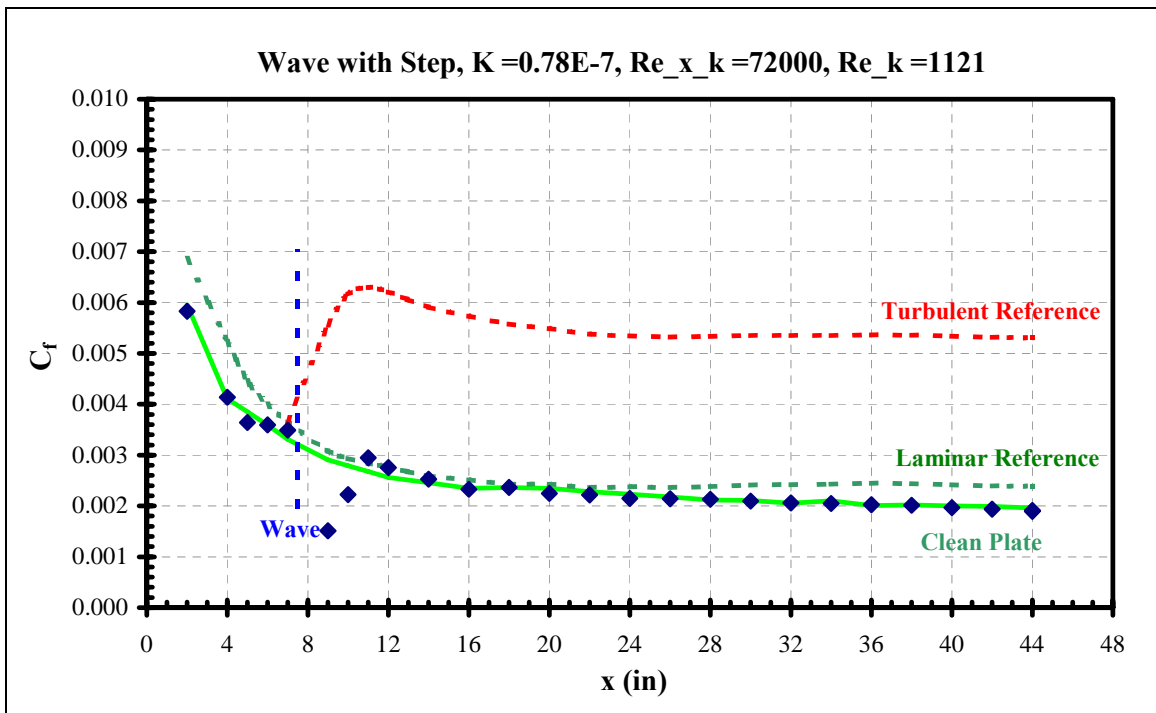
**Figure 320 Wave without step skin friction distribution**



**Figure 321 Wave without step skin friction distribution**

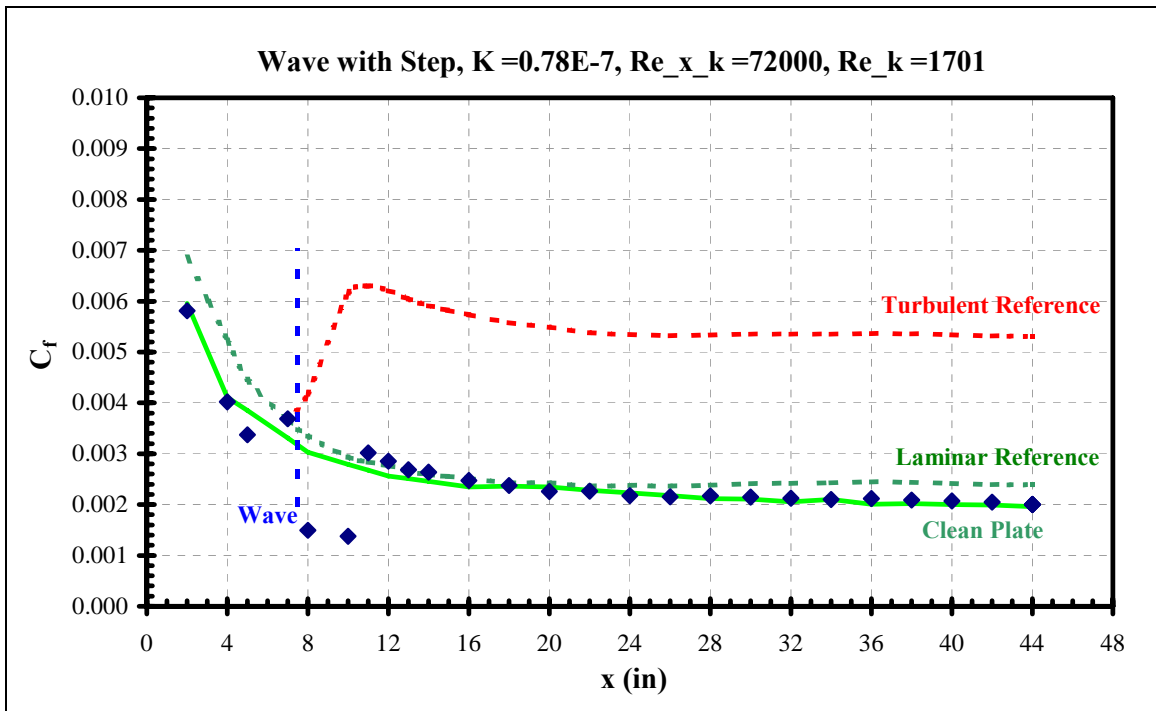


**Figure 322 Wave with step skin friction distribution**

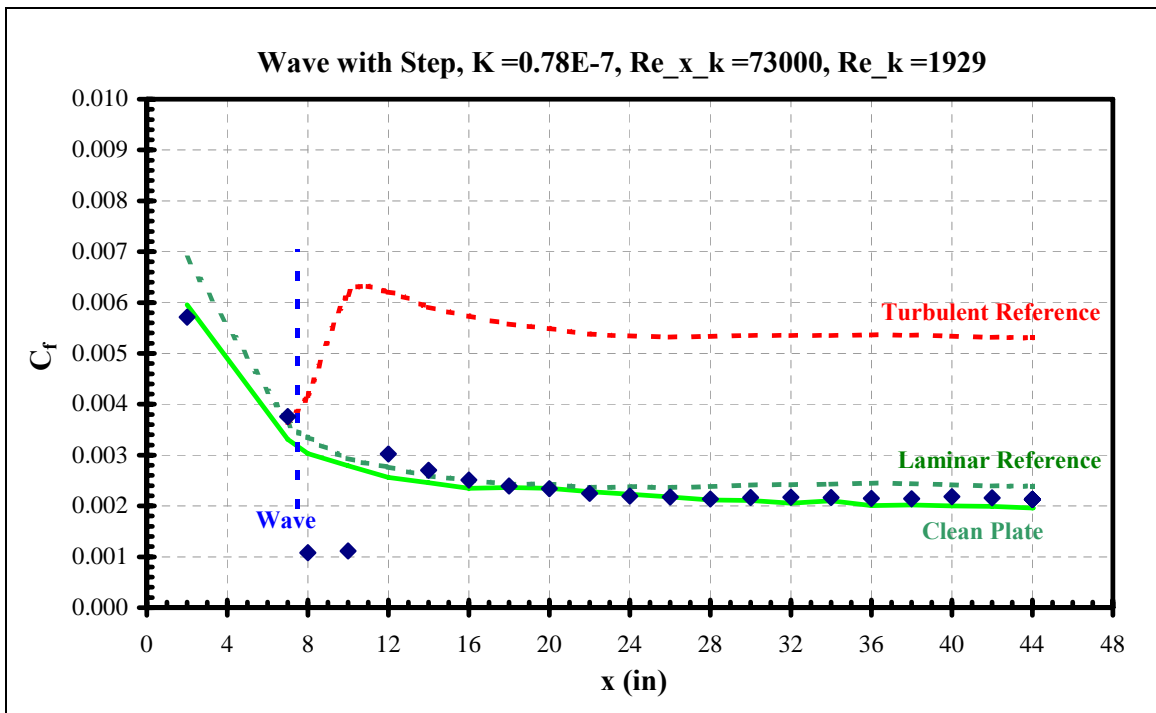


**Figure 323 Wave with step skin friction distribution**

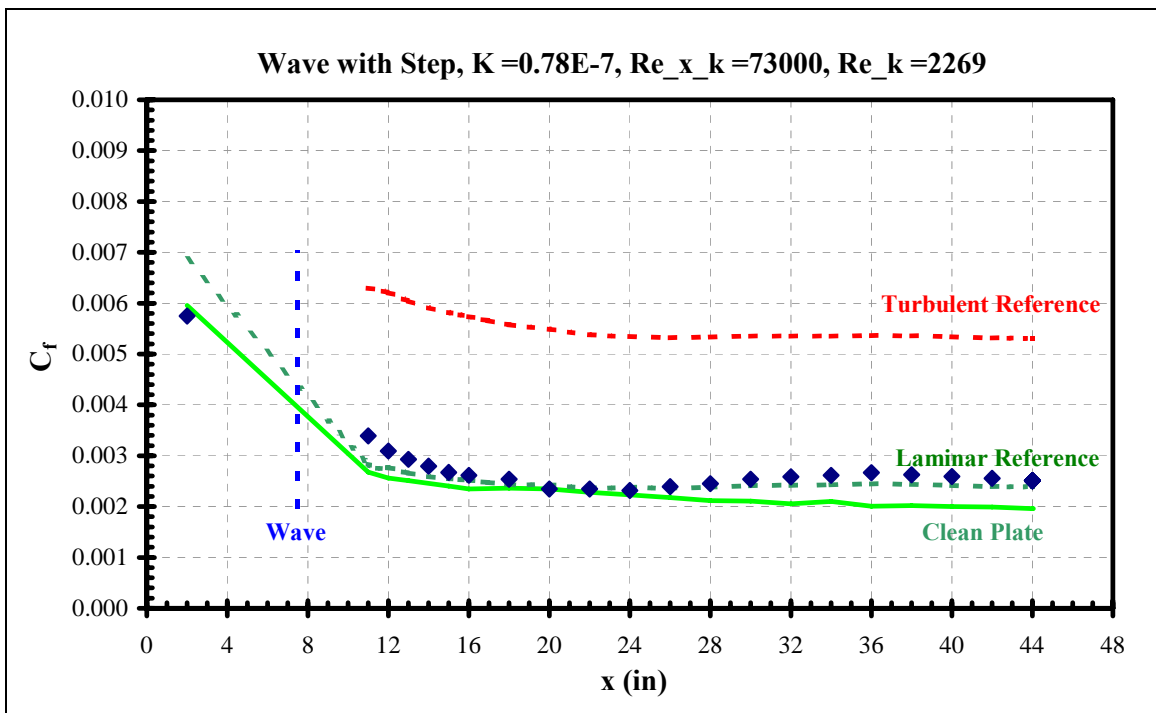




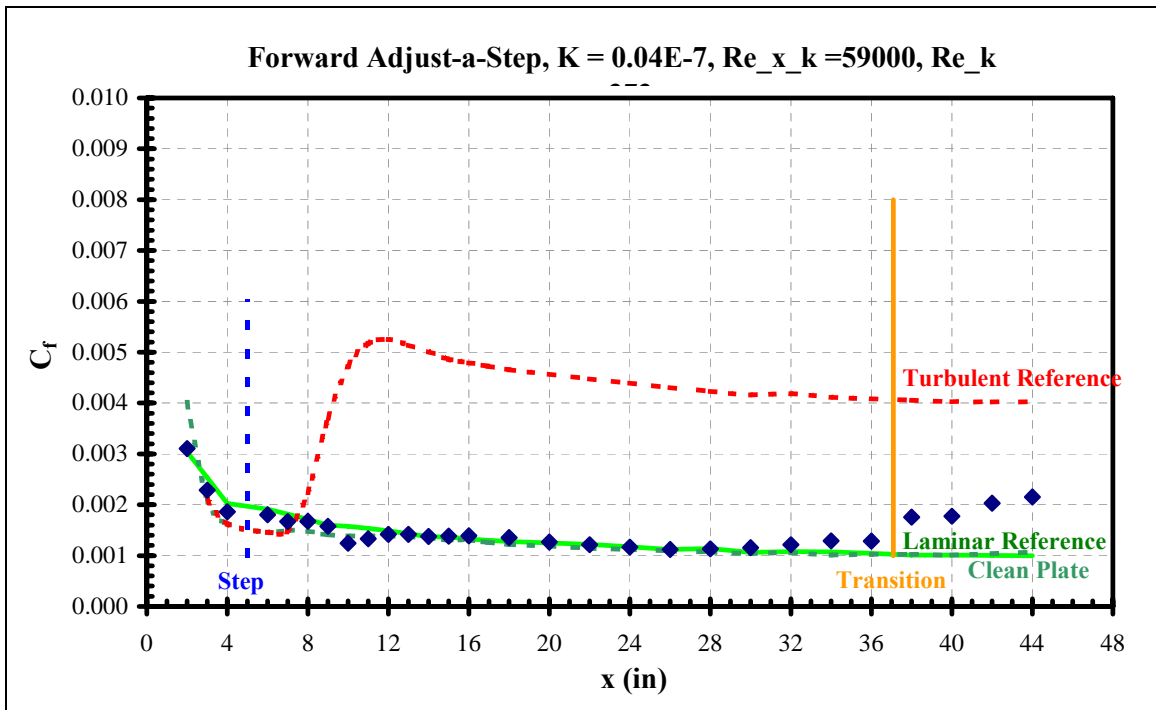
**Figure 324 Wave with step skin friction distribution**



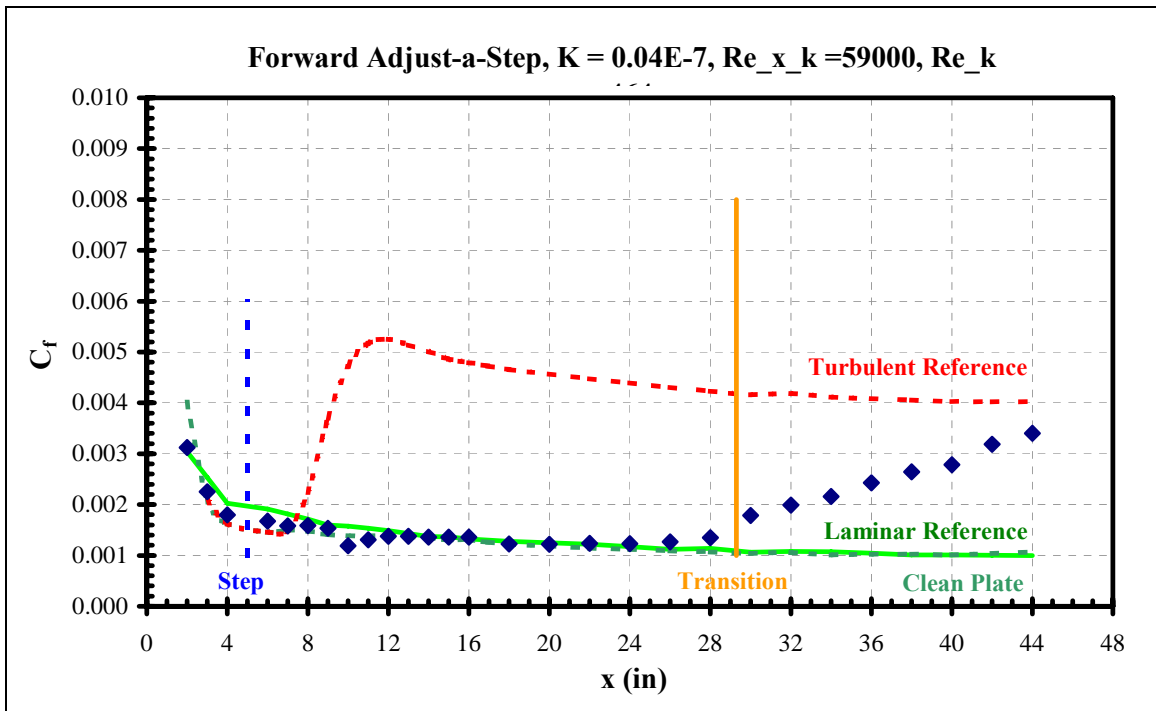
**Figure 325 Wave with step skin friction distribution**



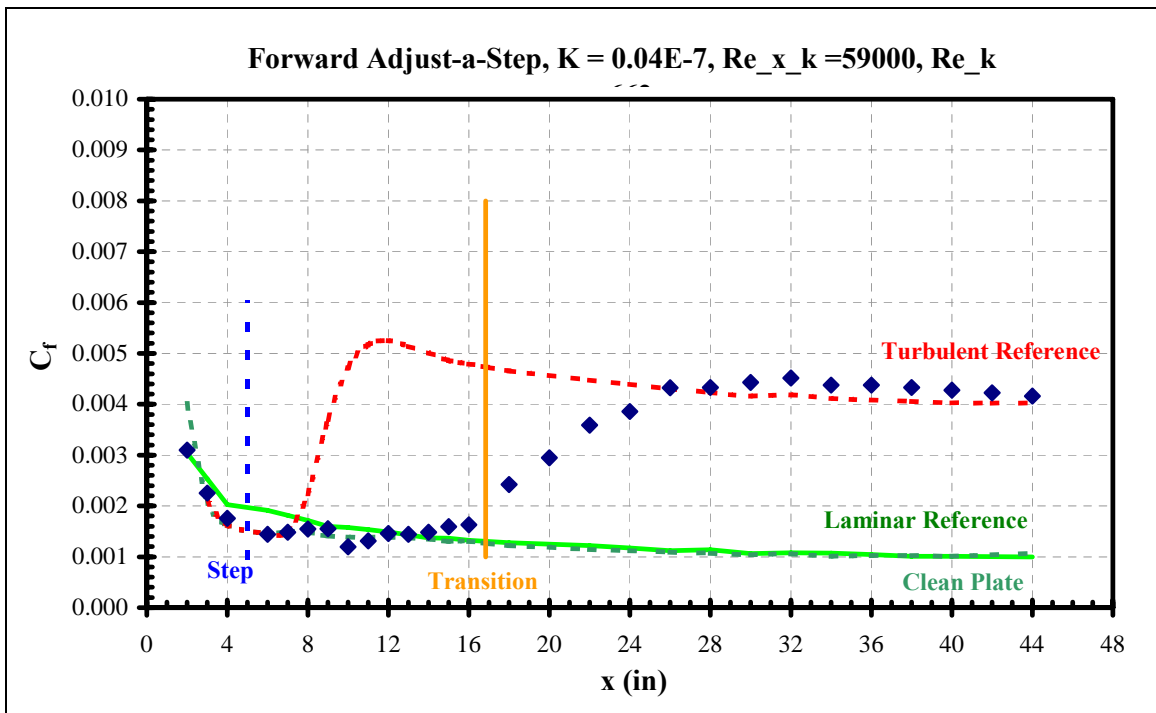
**Figure 326 Wave with step skin friction distribution**



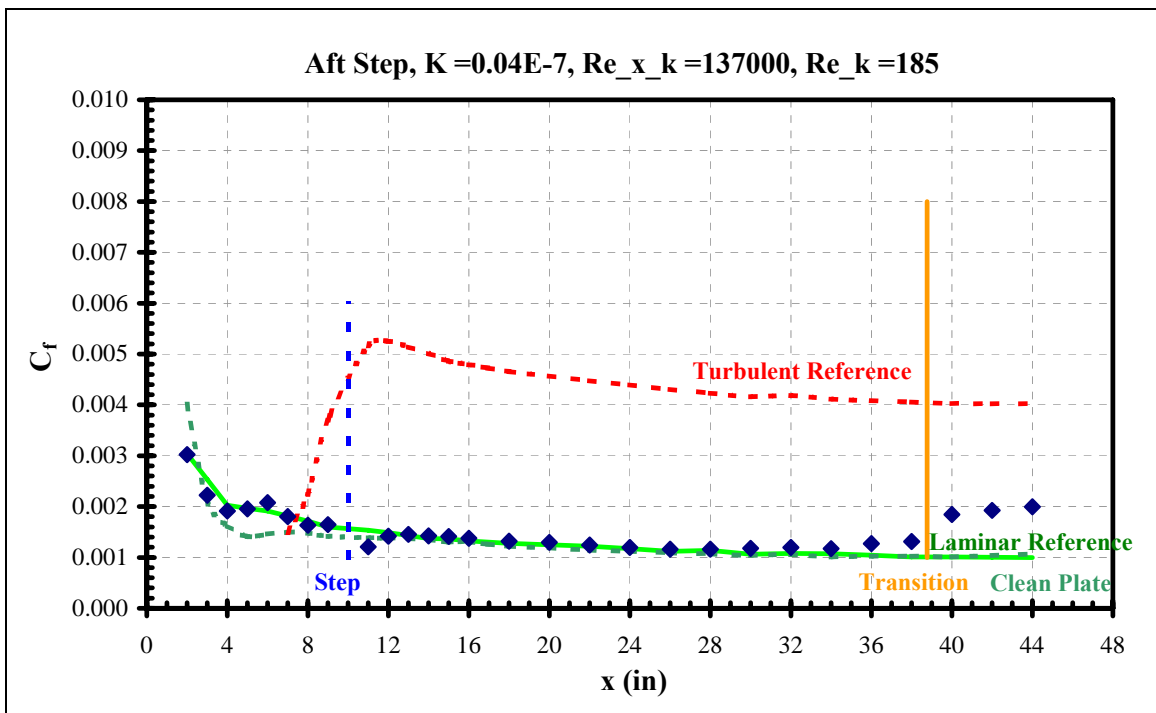
**Figure 327 Forward Adjust-a-Step skin friction distribution**



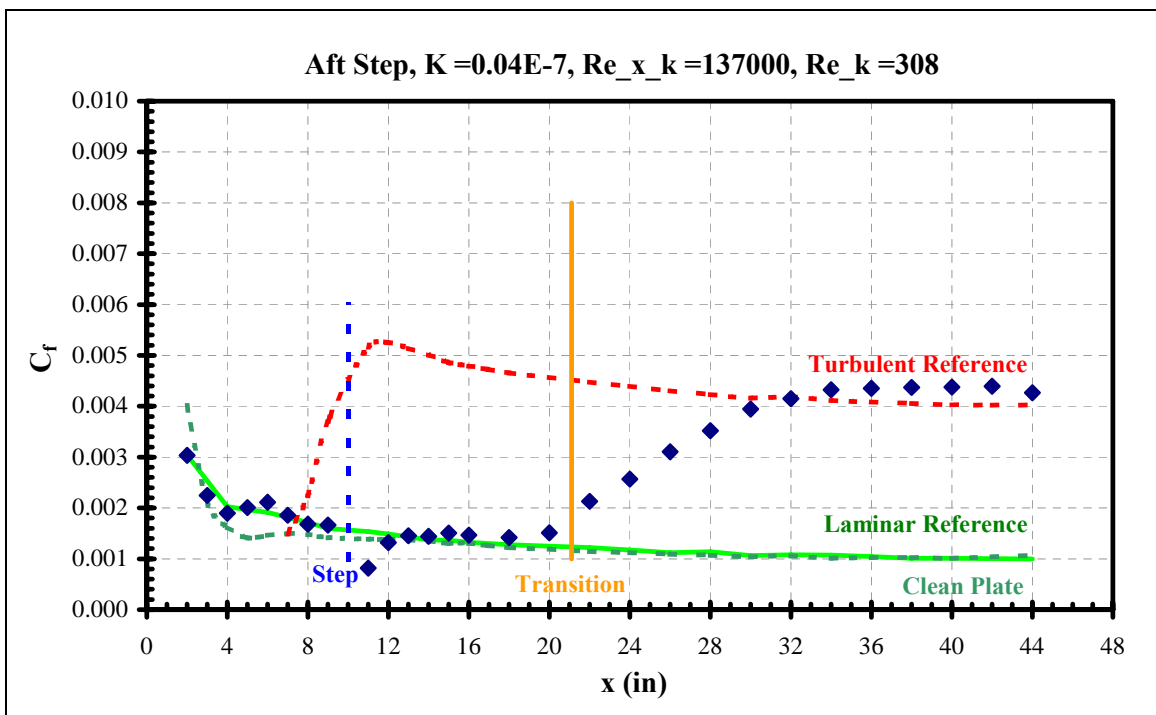
**Figure 328 Forward Adjust-a-Step skin friction distribution**



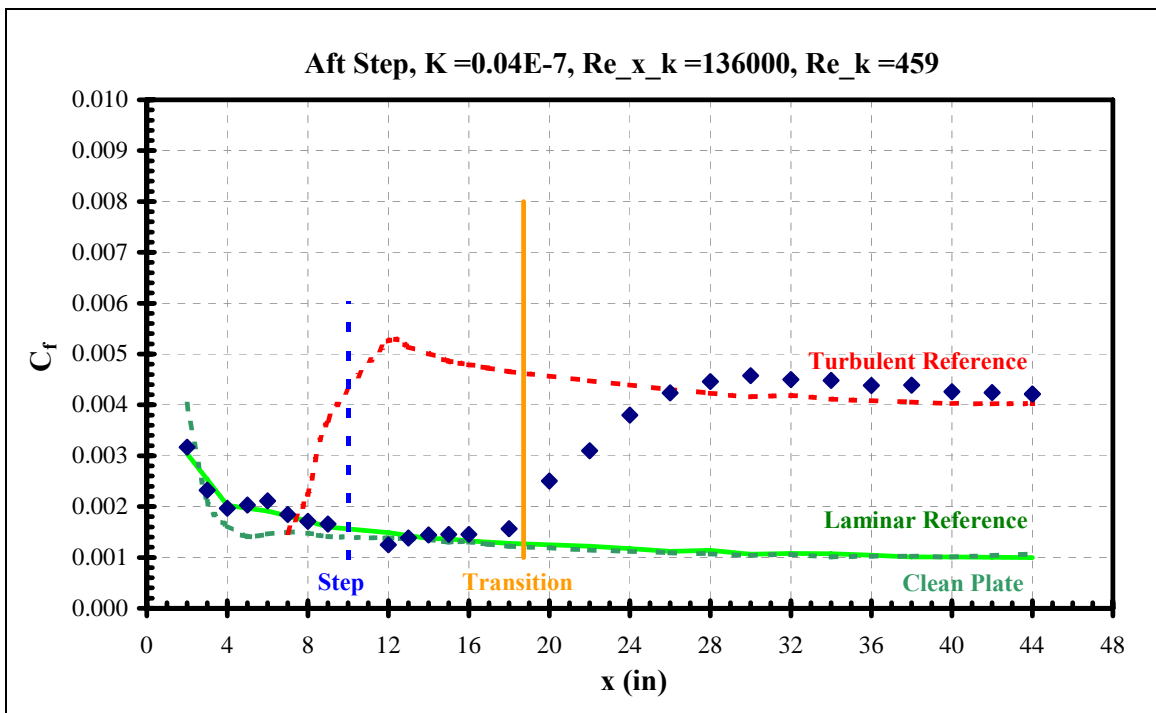
**Figure 329 Forward Adjust-a-Step skin friction distribution**



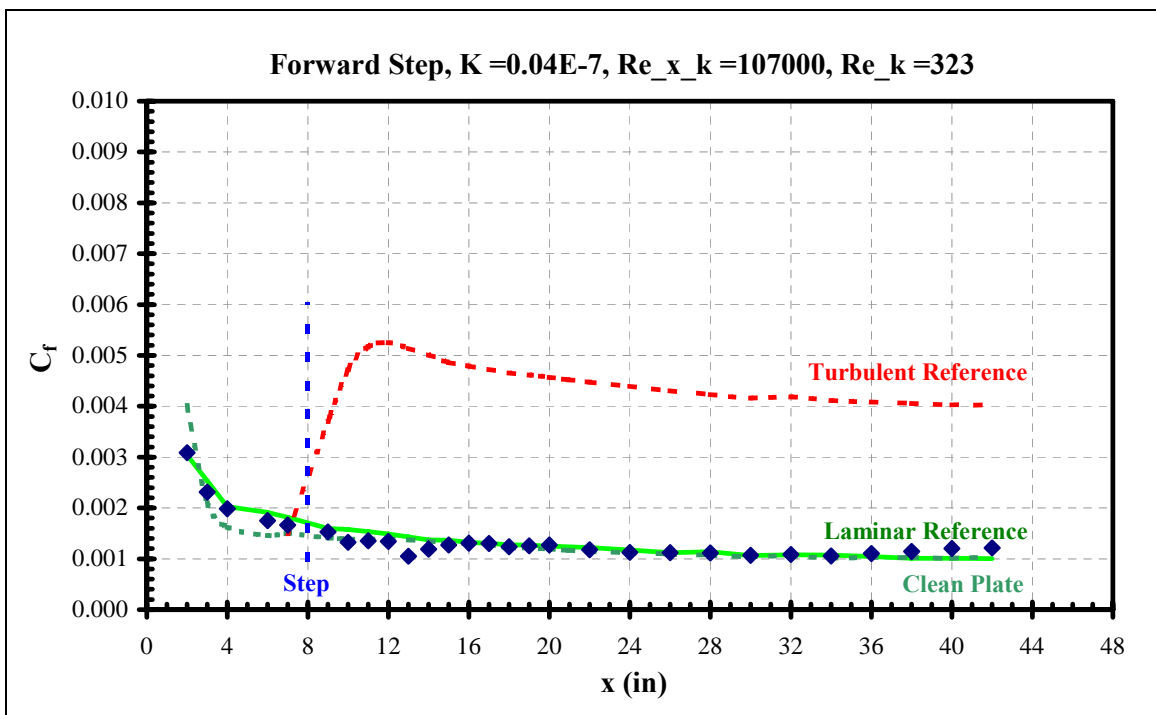
**Figure 330 Aft Adjust-a-Step skin friction distribution**



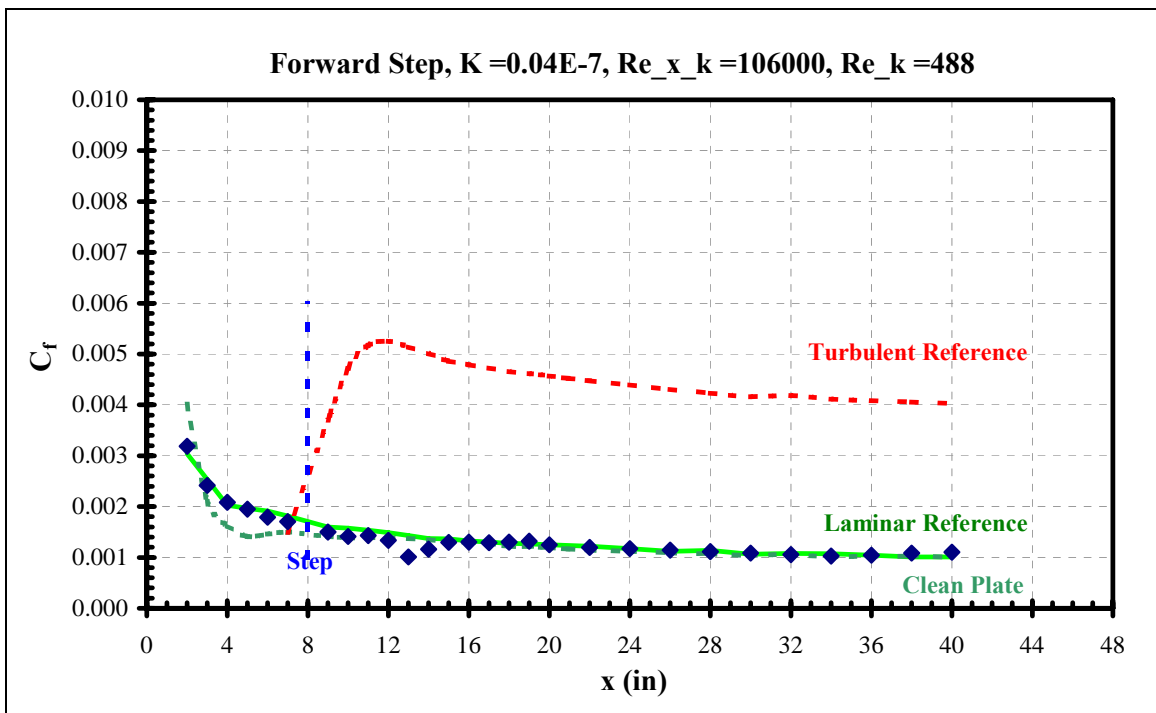
**Figure 331 Aft Adjust-a-Step skin friction distribution**



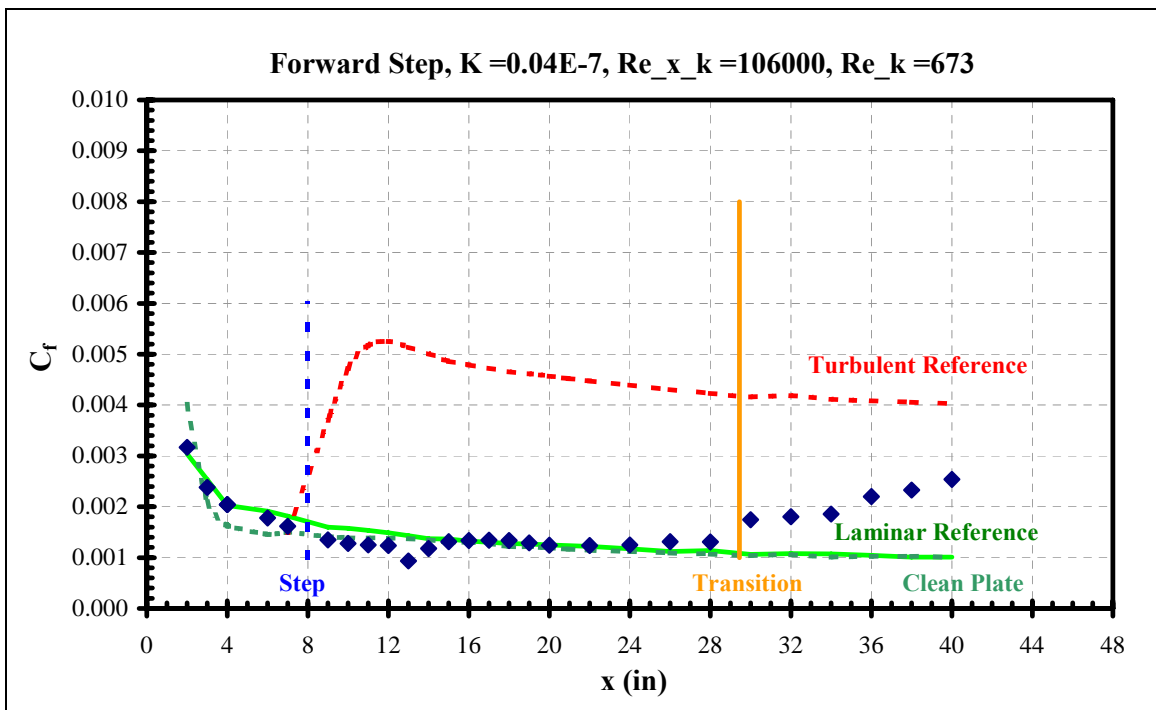
**Figure 332 Aft Adjust-a-Step skin friction distribution**



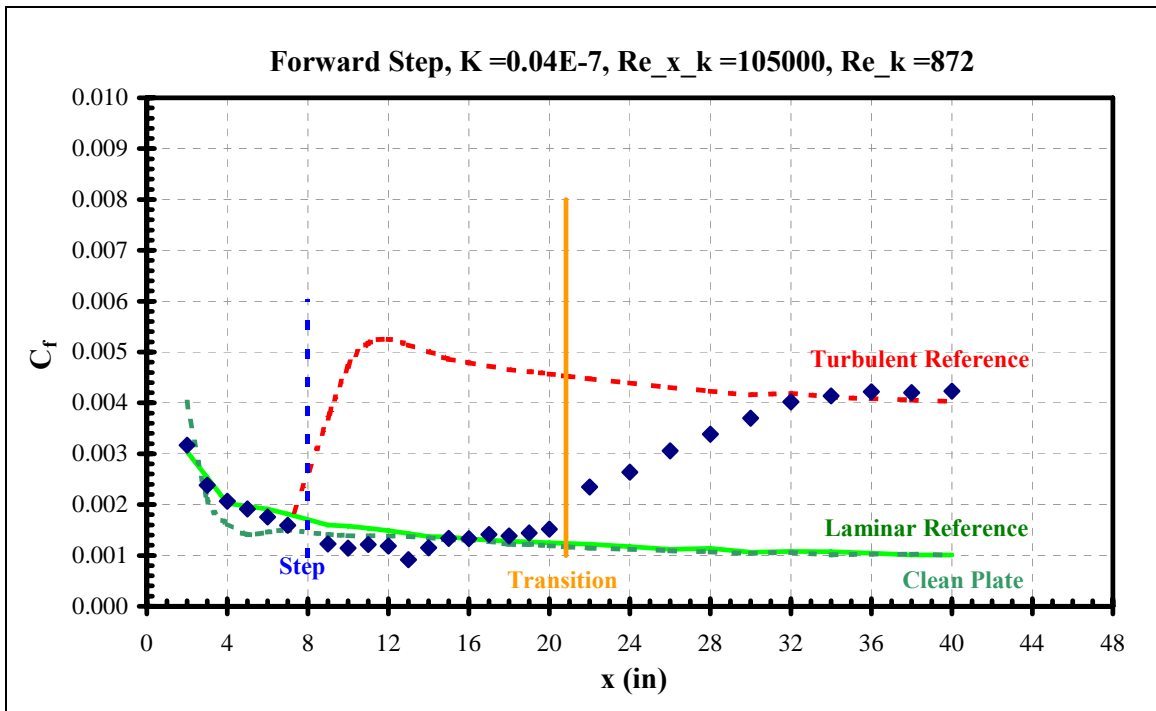
**Figure 333 Forward Adjust-a-Step skin friction distribution**



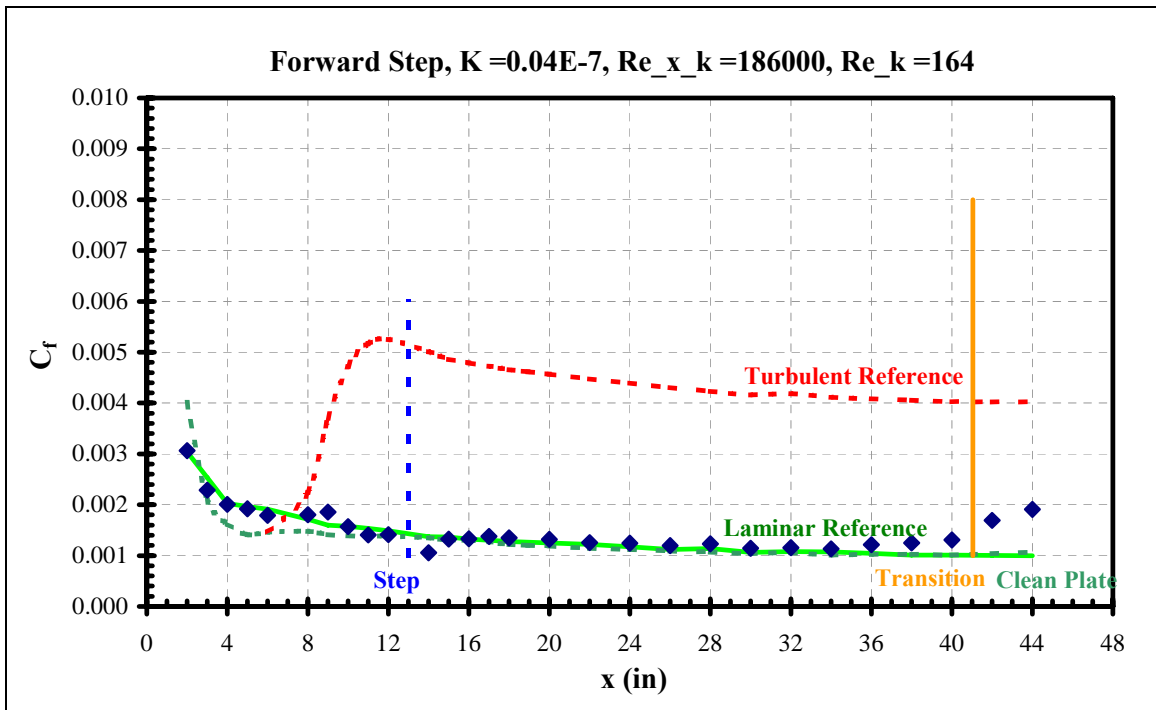
**Figure 334 Forward Adjust-a-Step skin friction distribution**



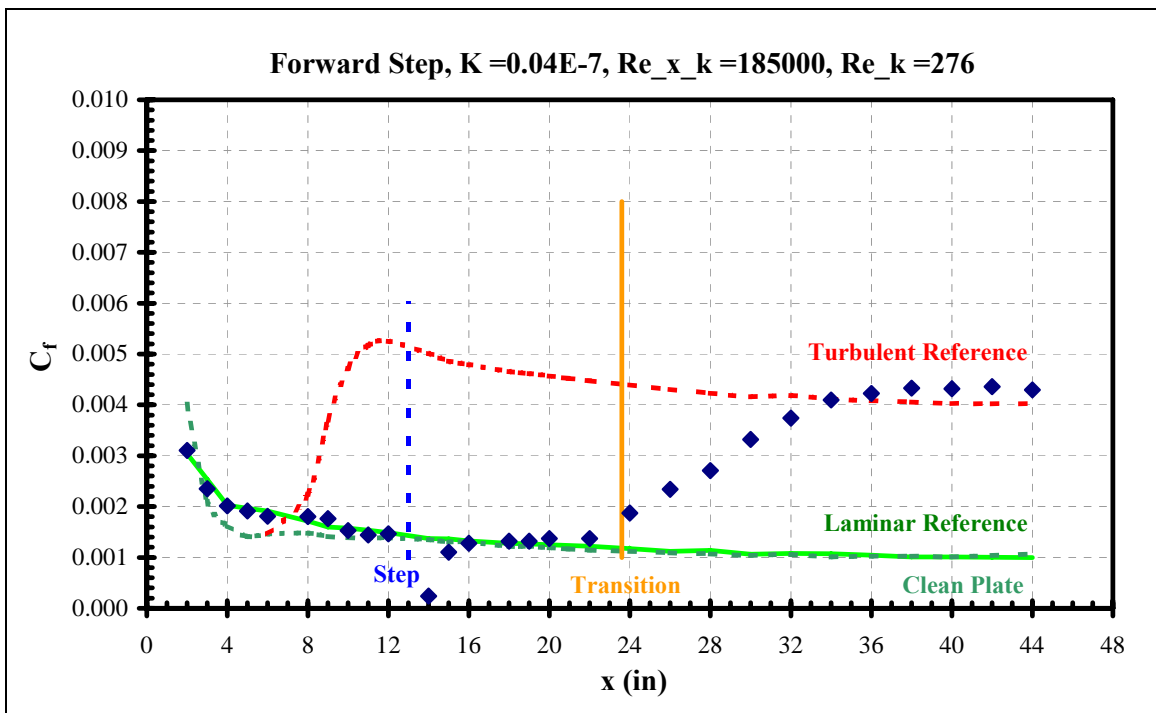
**Figure 335 Forward Adjust-a-Step skin friction distribution**



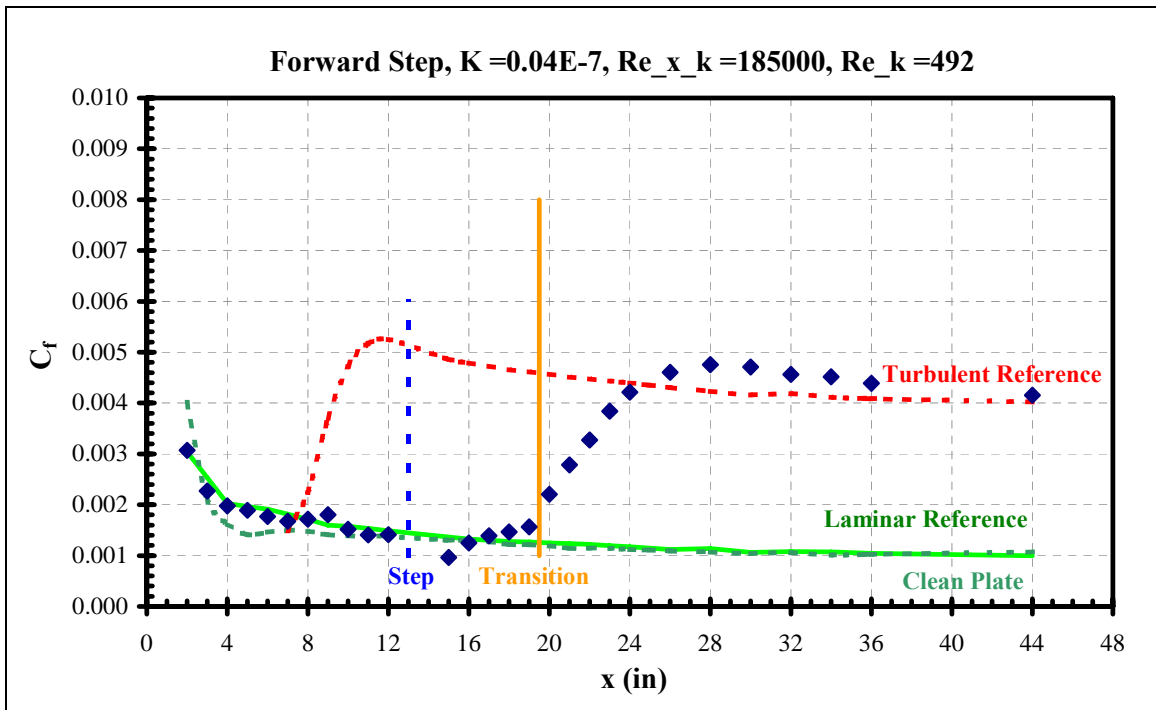
**Figure 336 Forward Adjust-a-Step skin friction distribution**



**Figure 337 Forward Adjust-a-Step skin friction distribution**

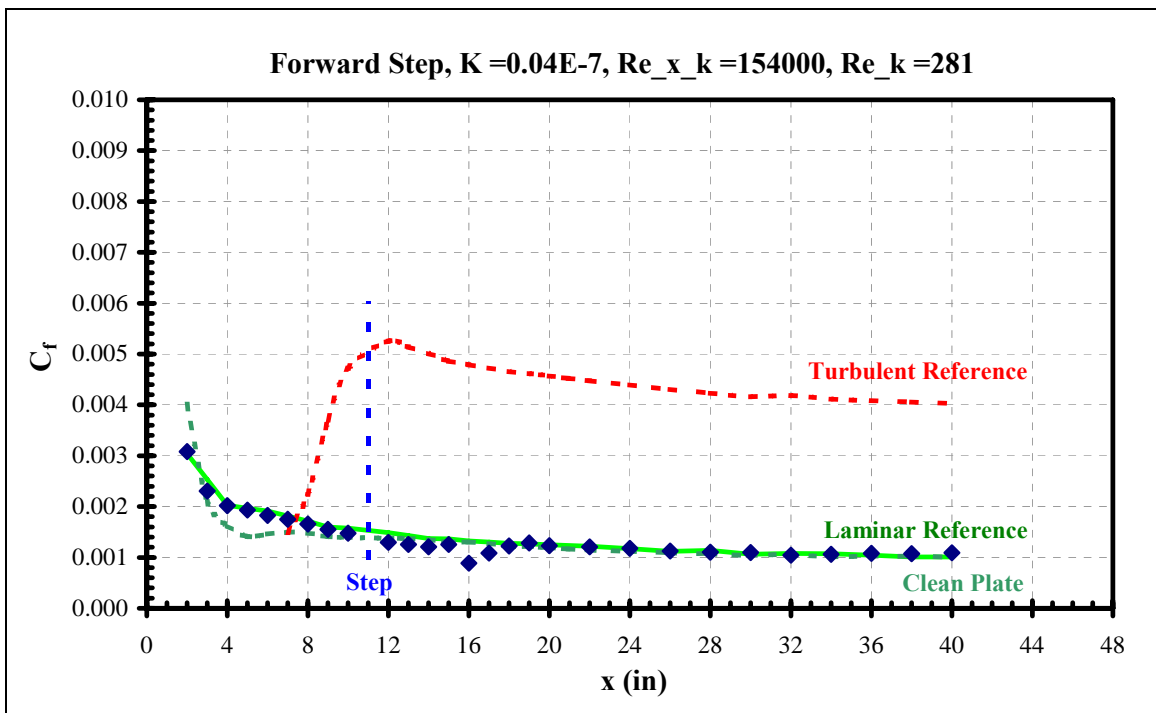


**Figure 338 Forward Adjust-a-Step skin friction distribution**

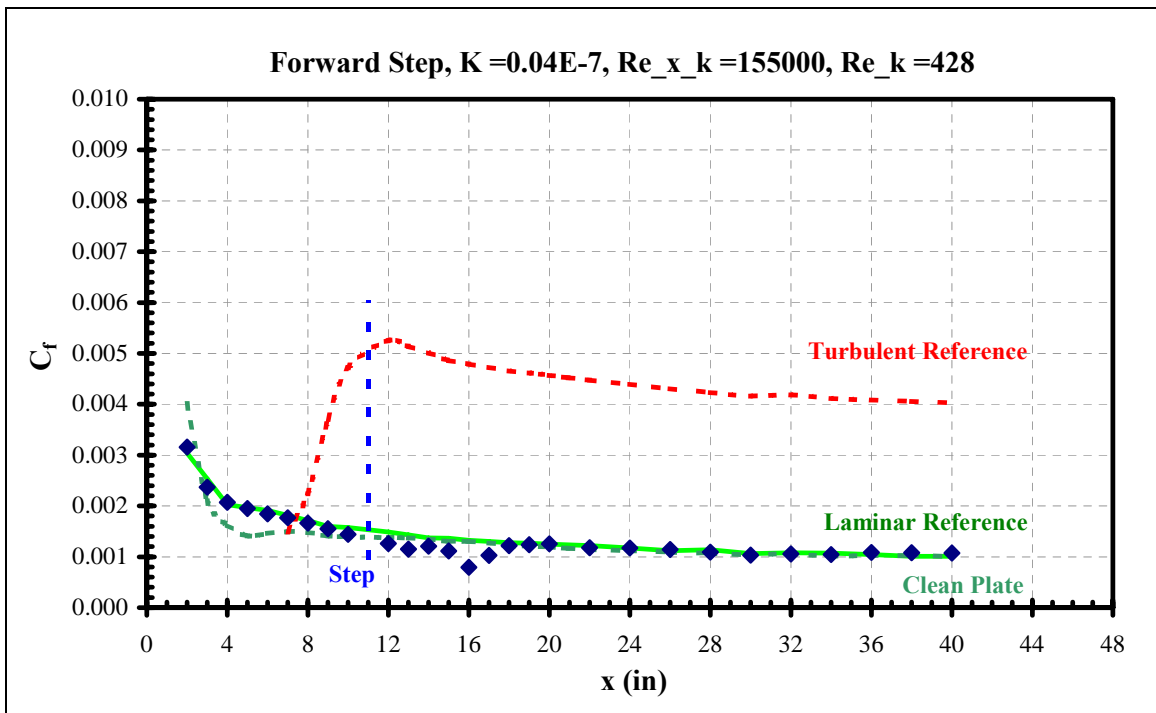


**Figure 339 Forward Adjust-a-Step skin friction distribution**

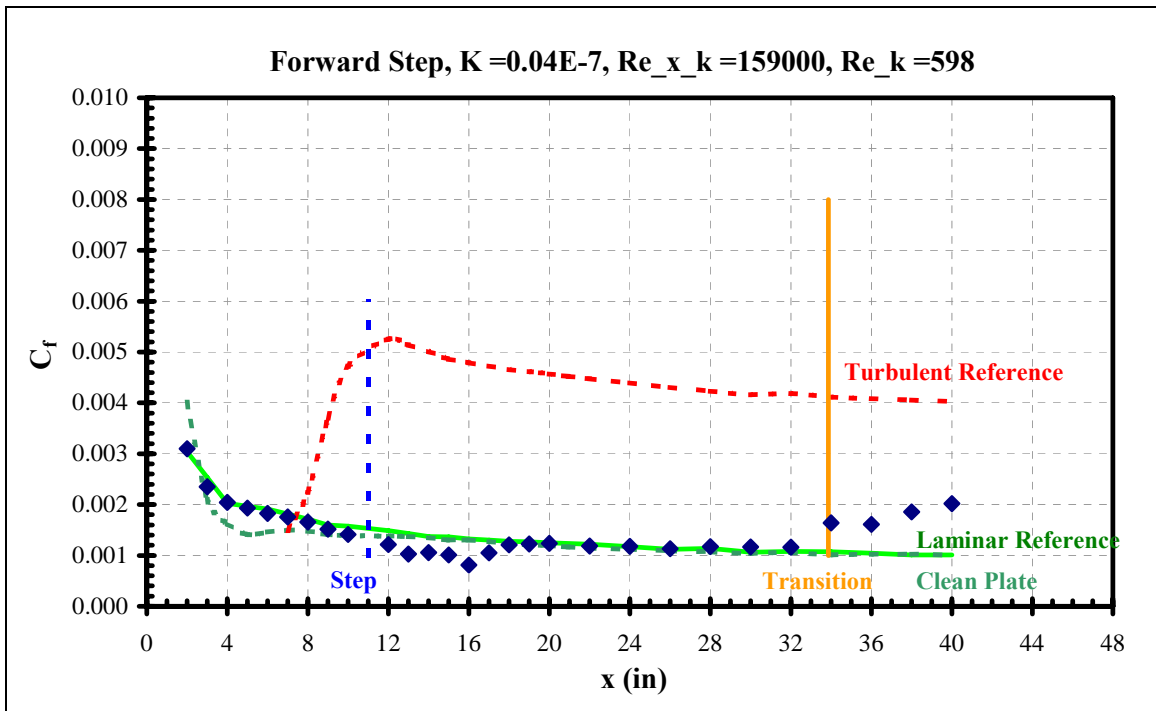




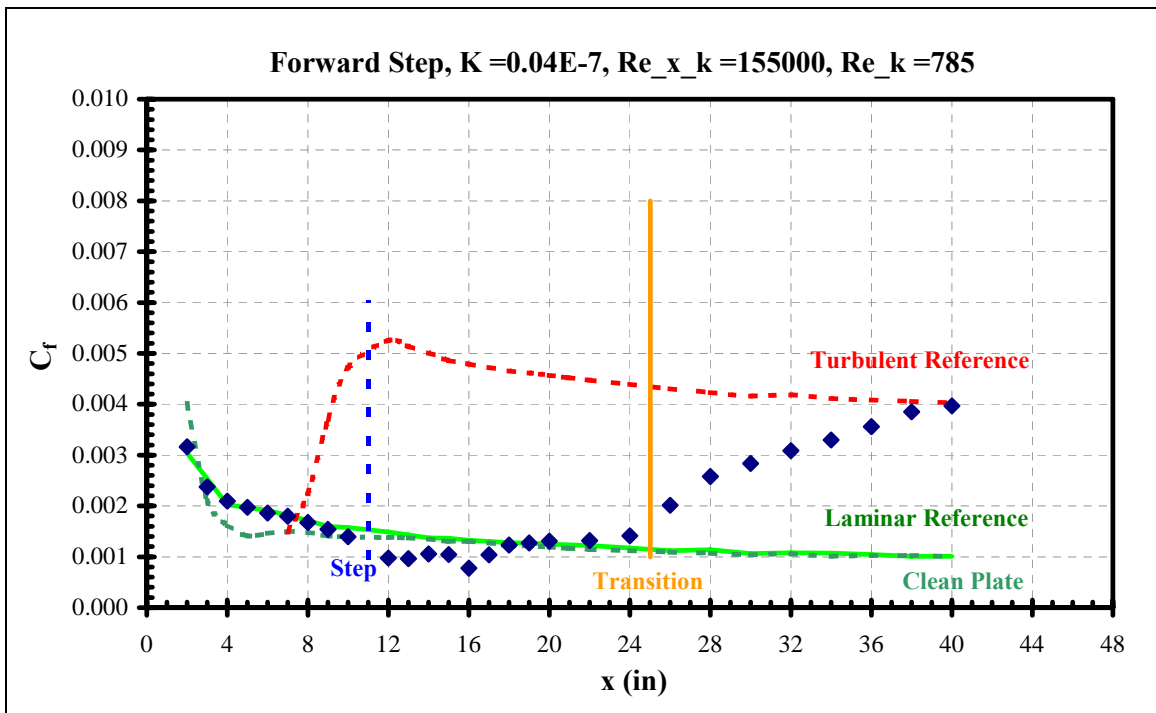
**Figure 340 Forward Adjust-a-Step skin friction distribution**



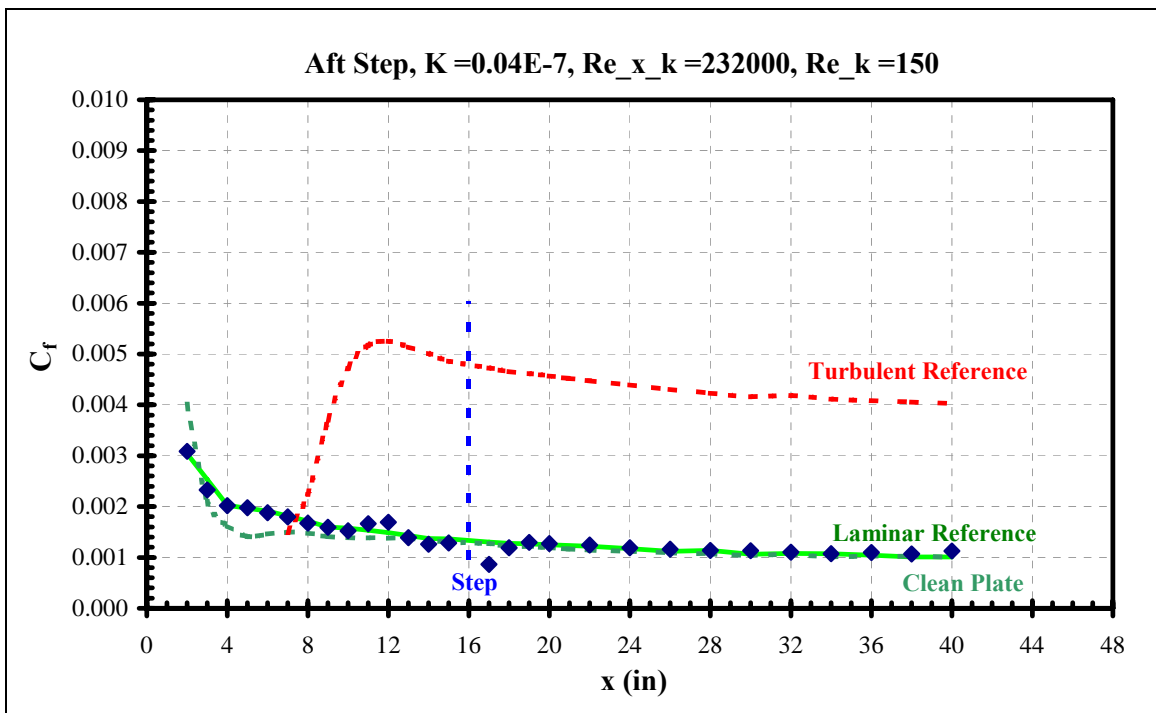
**Figure 341 Forward Adjust-a-Step skin friction distribution**



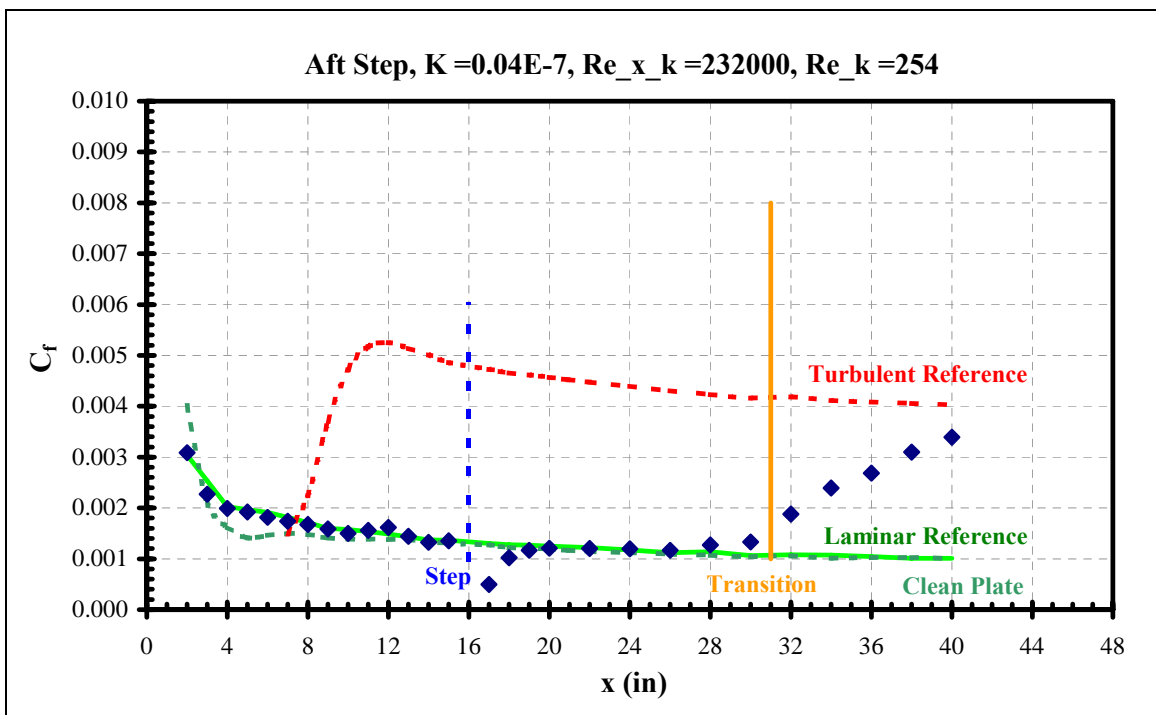
**Figure 342 Forward Adjust-a-Step skin friction distribution**



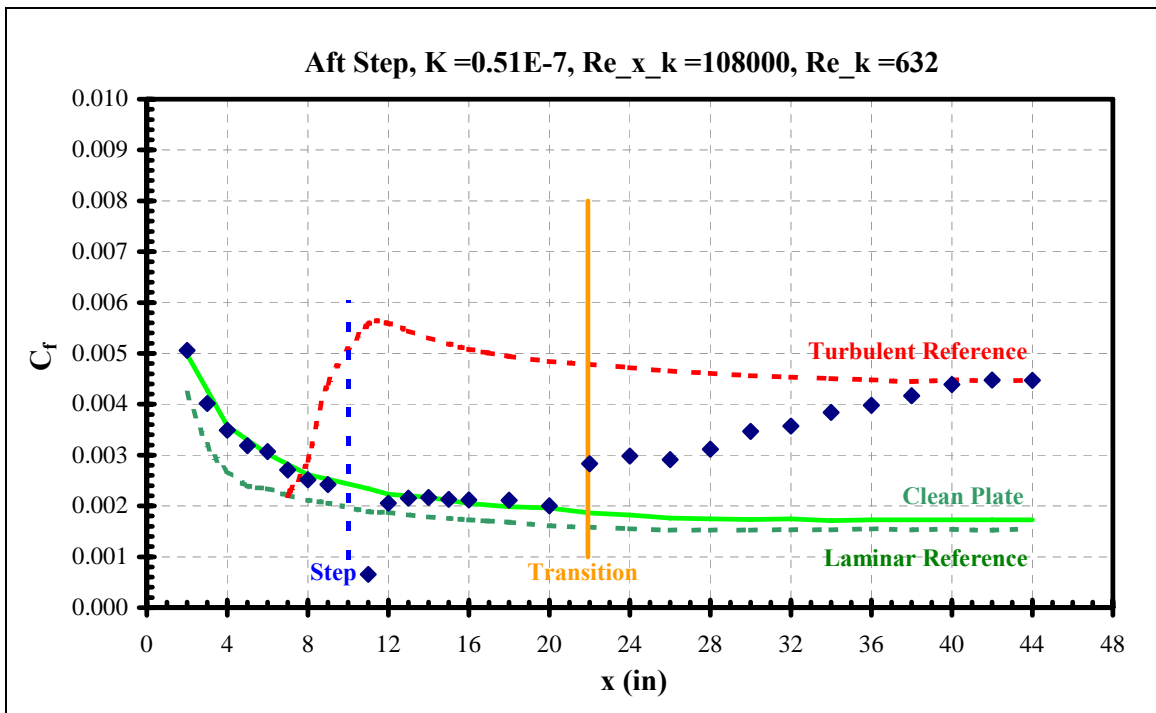
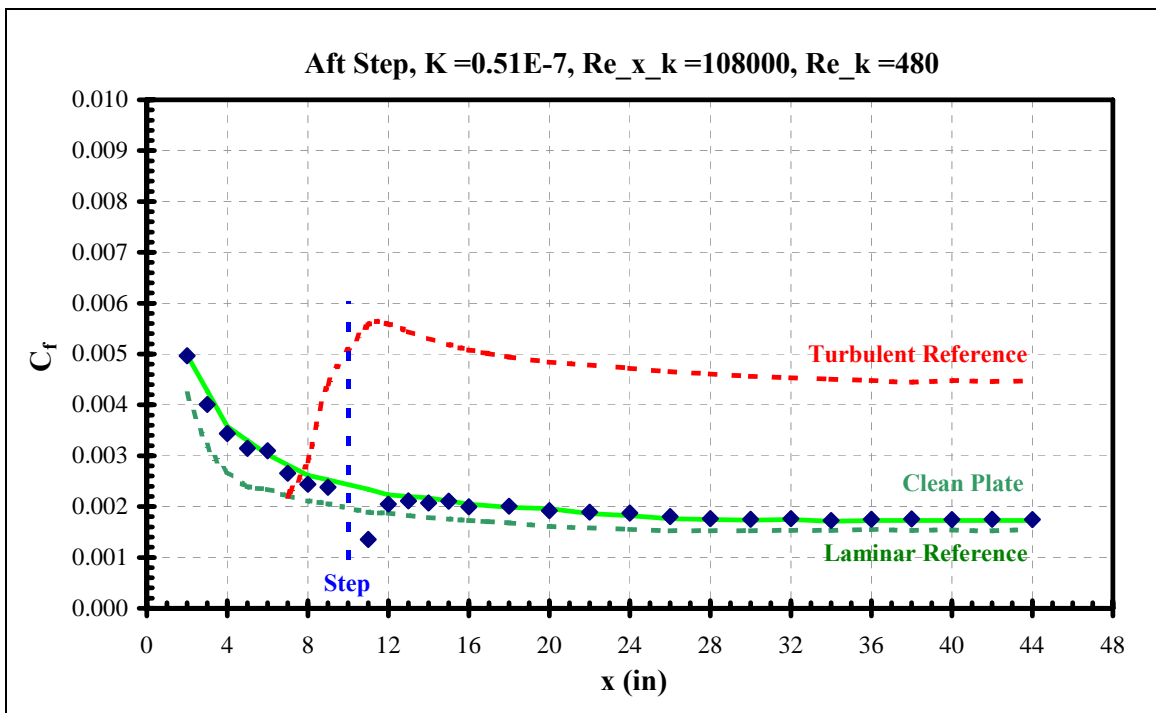
**Figure 343 Forward Adjust-a-Step skin friction distribution**



**Figure 344 Aft Adjust-a-Step skin friction distribution**



**Figure 345 Aft Adjust-a-Step skin friction distribution**



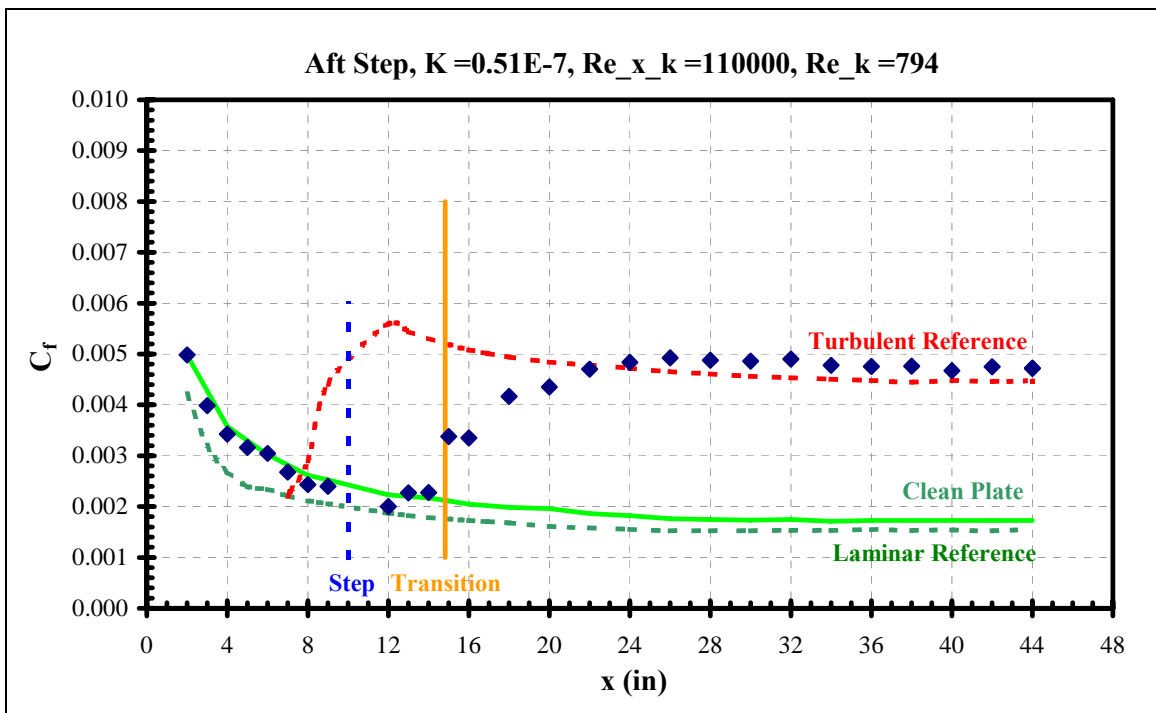


**Figure 348 Aft Adjust-a-Step skin friction distribution**

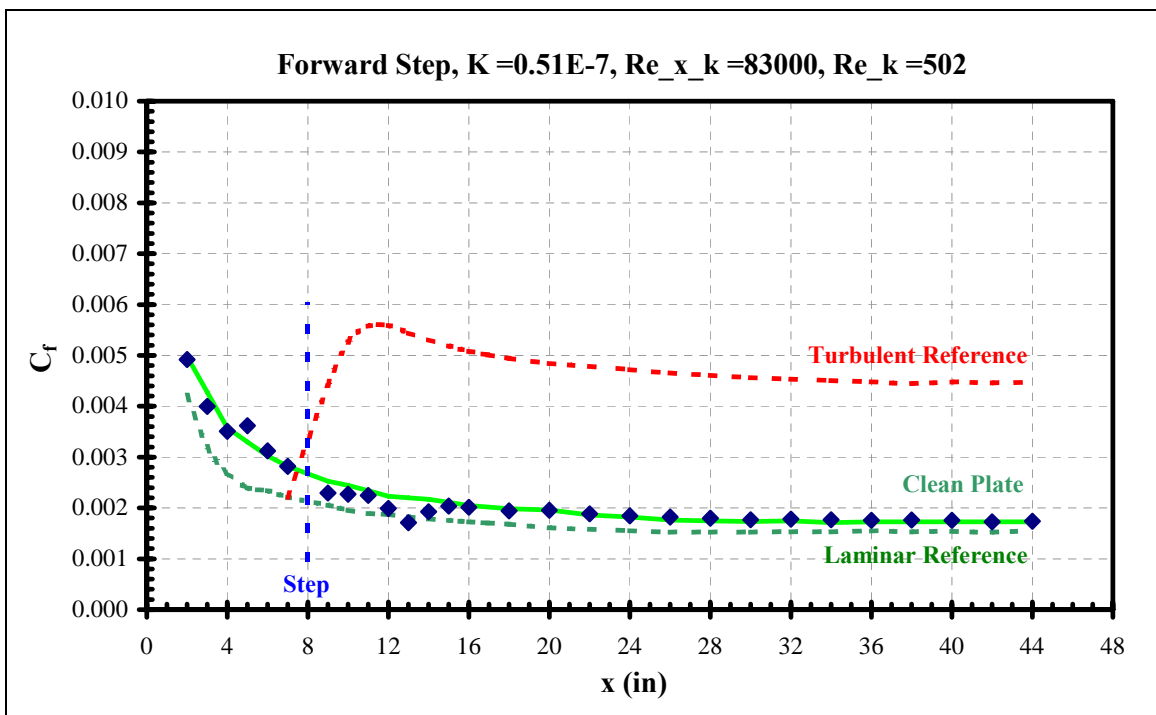


**Figure 349 Forward Adjust-a-Step skin friction distribution**

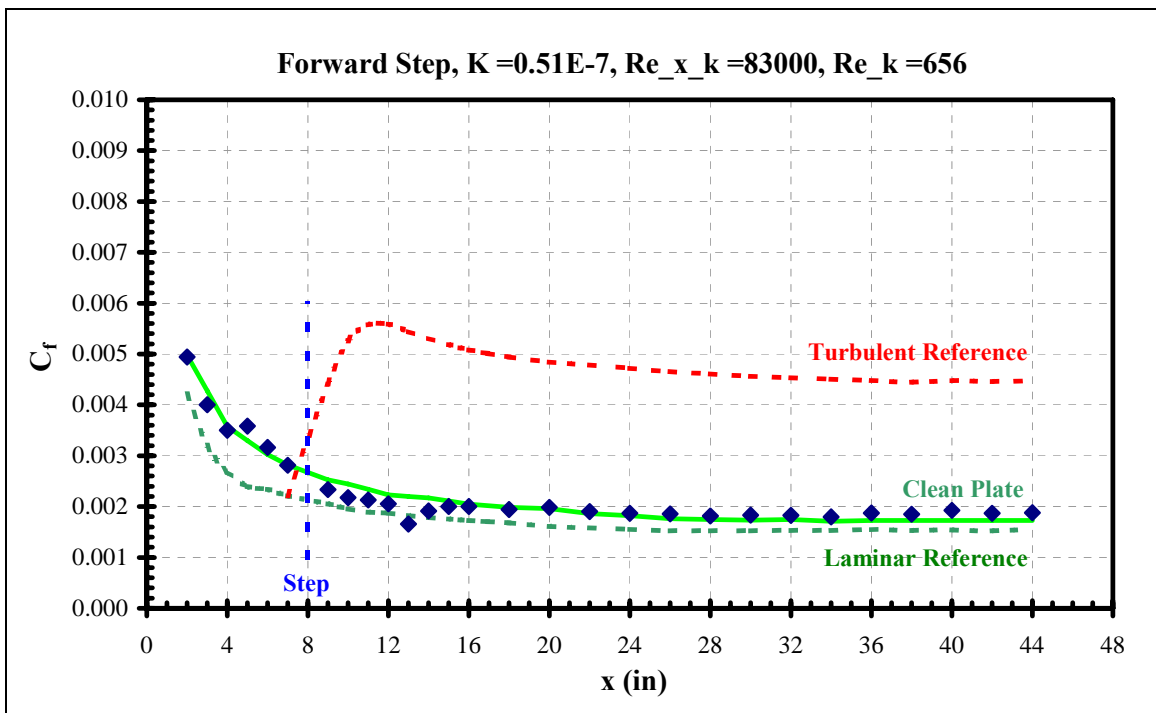


**Figure 350 Forward Adjust-a-Step skin friction distribution**

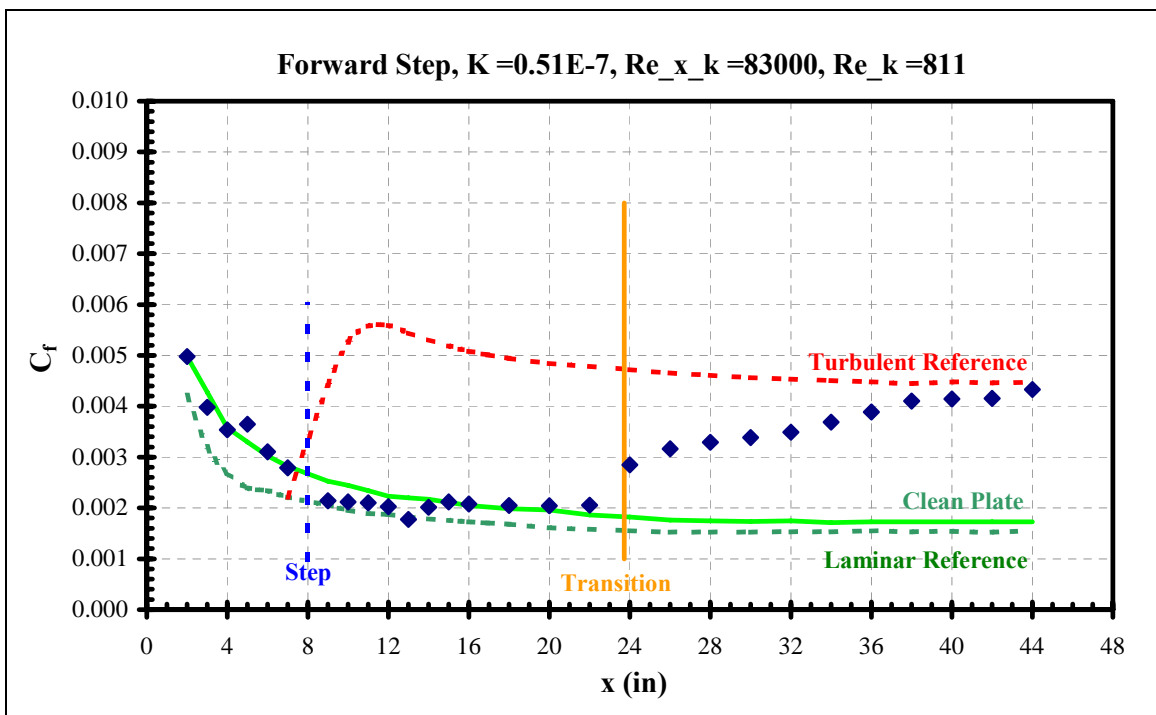


**Figure 351 Forward Adjust-a-Step skin friction distribution**

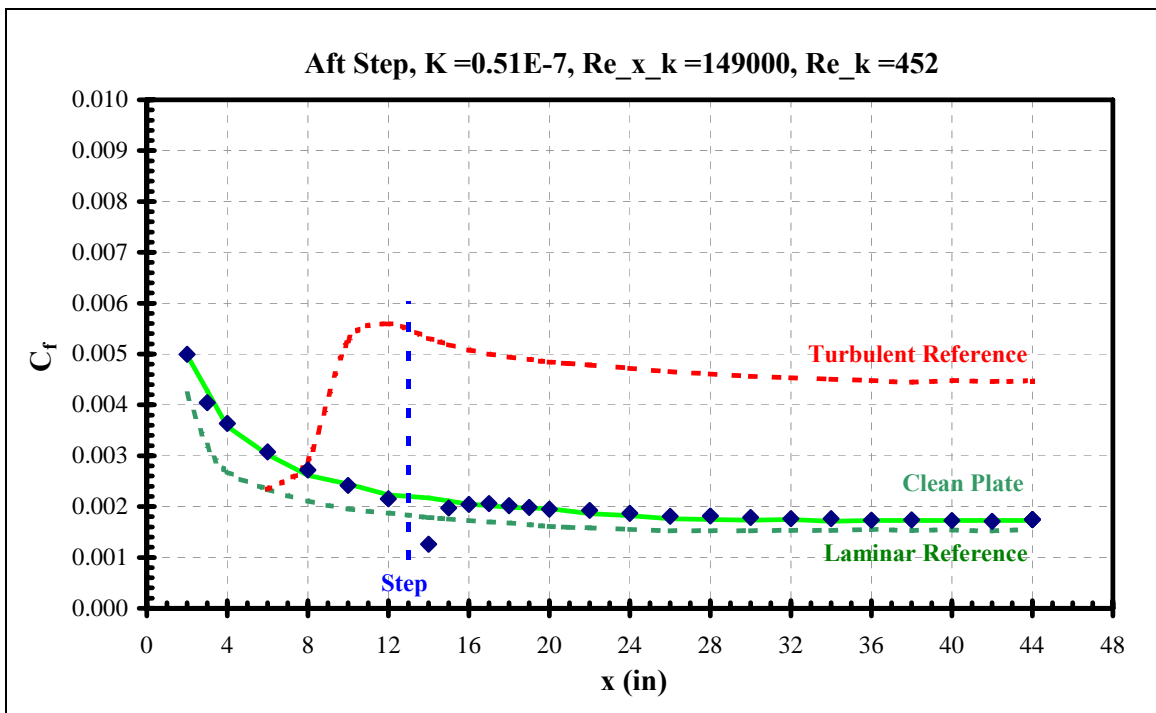


**Figure 352 Aft Adjust-a-Step skin friction distribution**

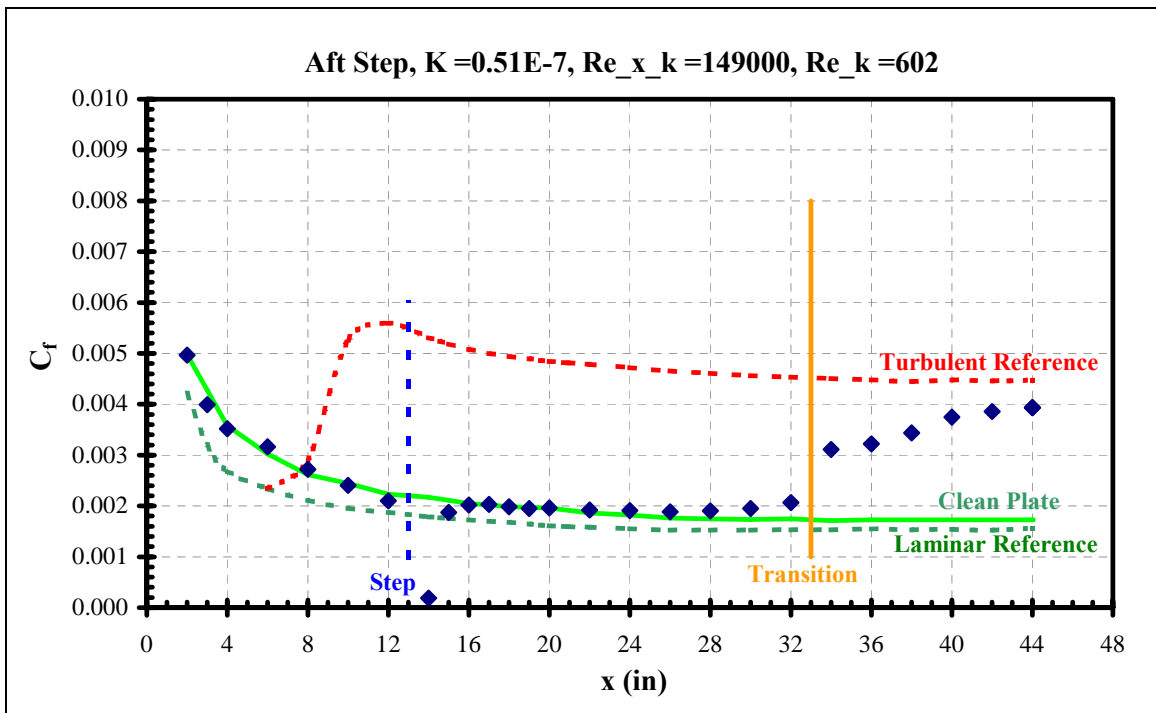


**Figure 353 Aft Adjust-a-Step skin friction distribution**

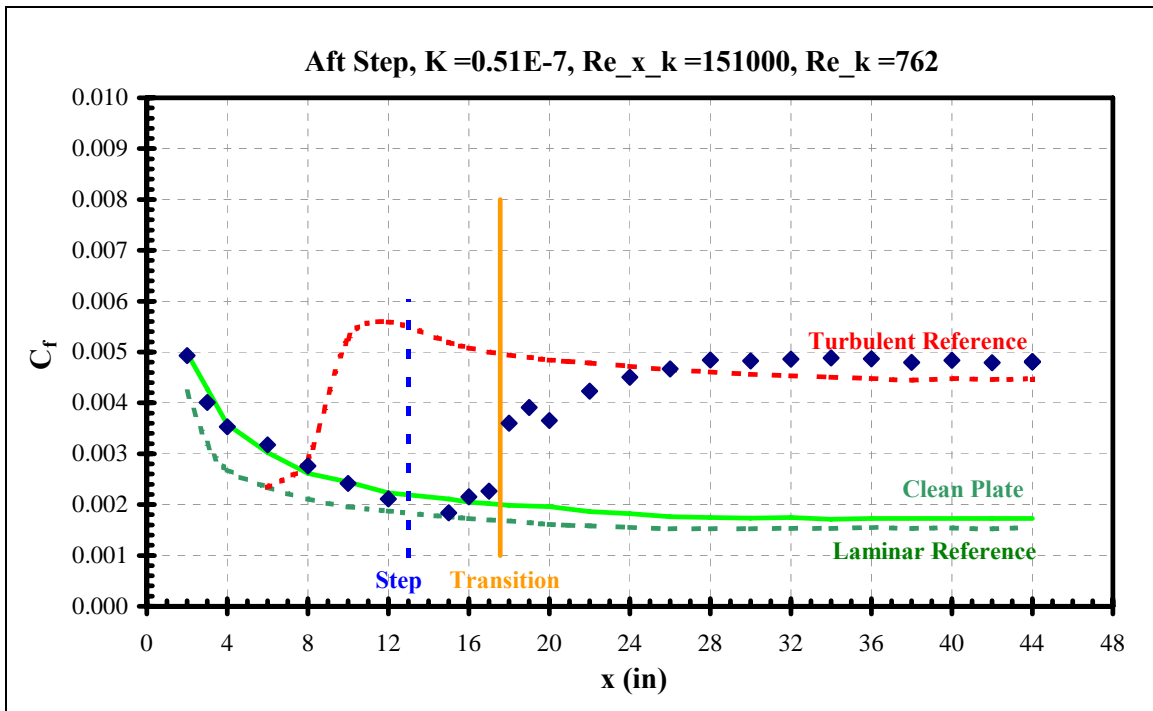


**Figure 354 Aft Adjust-a-Step skin friction distribution**

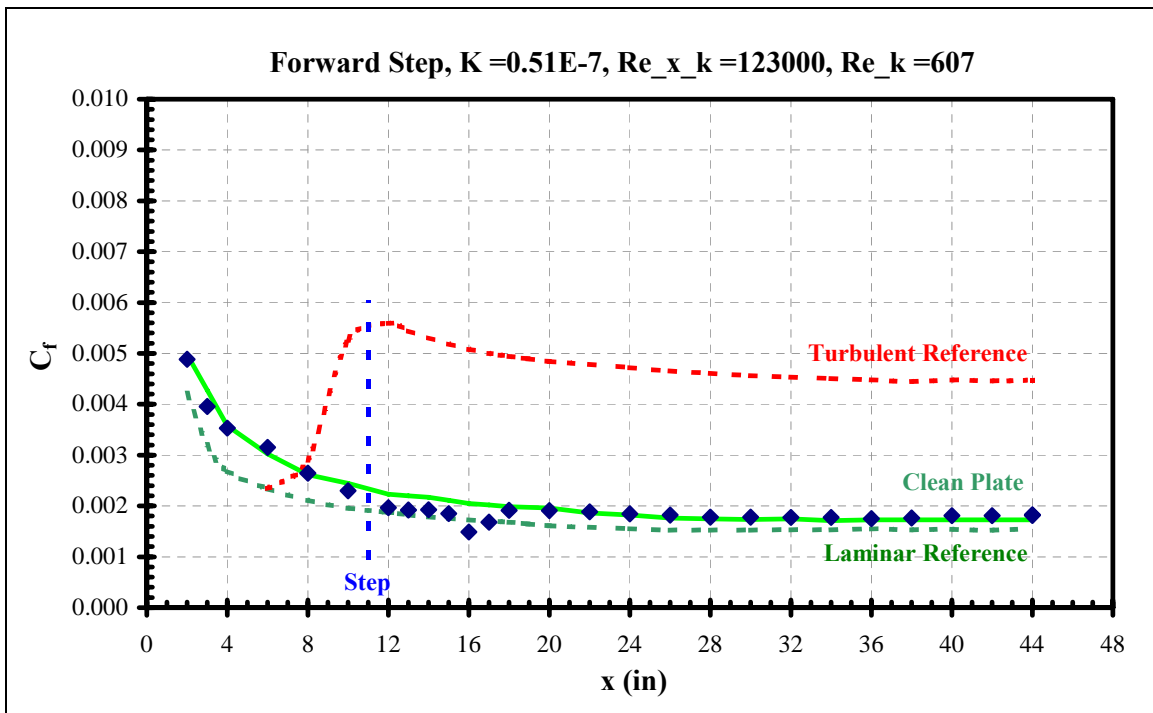


**Figure 355 Forward Adjust-a-Step skin friction distribution**



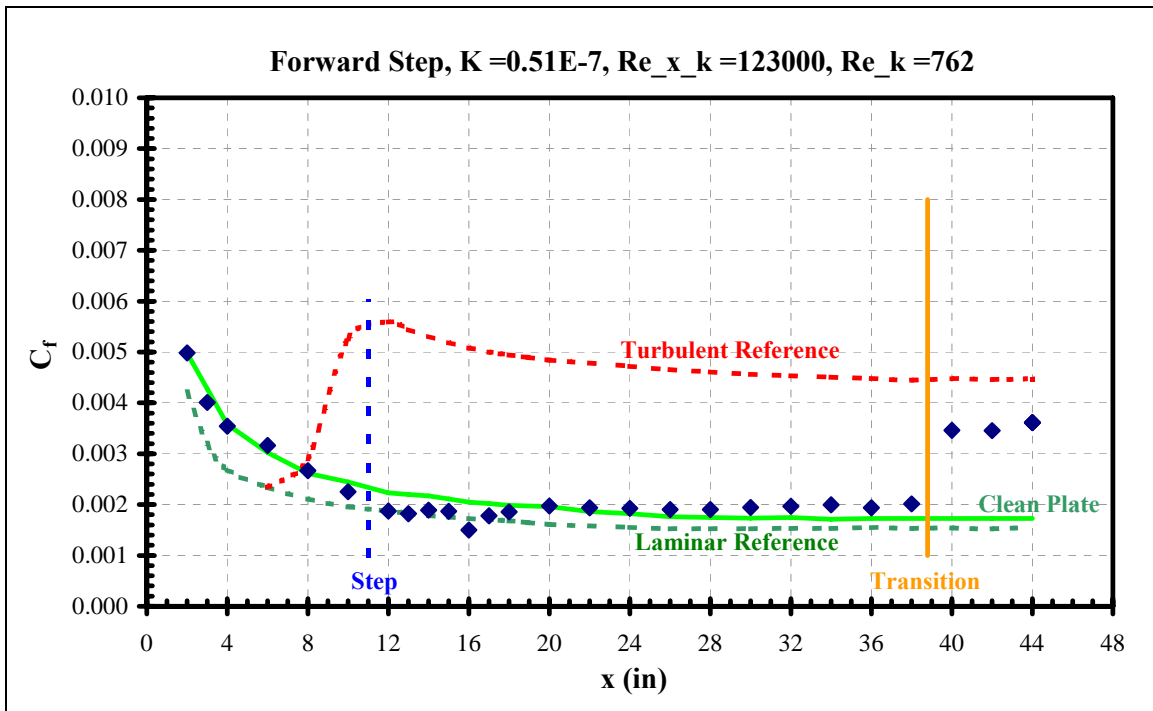


**Figure 356 Forward Adjust-a-Step skin friction distribution**

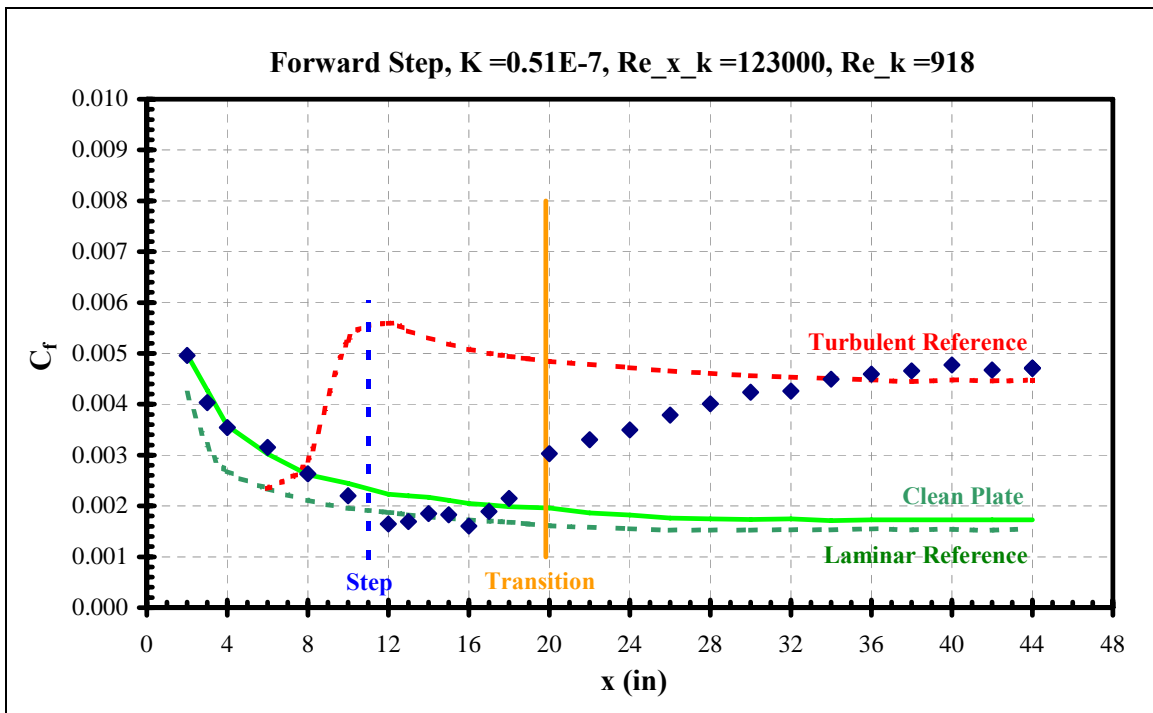


**Figure 357 Forward Adjust-a-Step skin friction distribution**

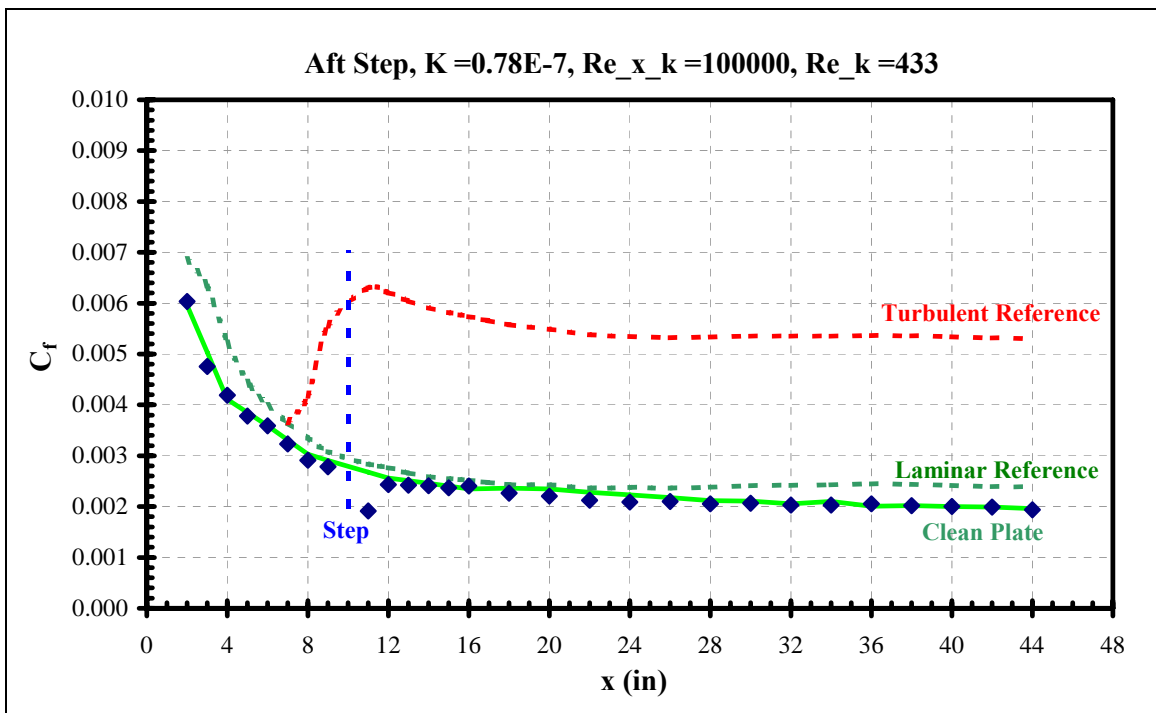


**Figure 358 Aft Adjust-a-Step skin friction distribution**

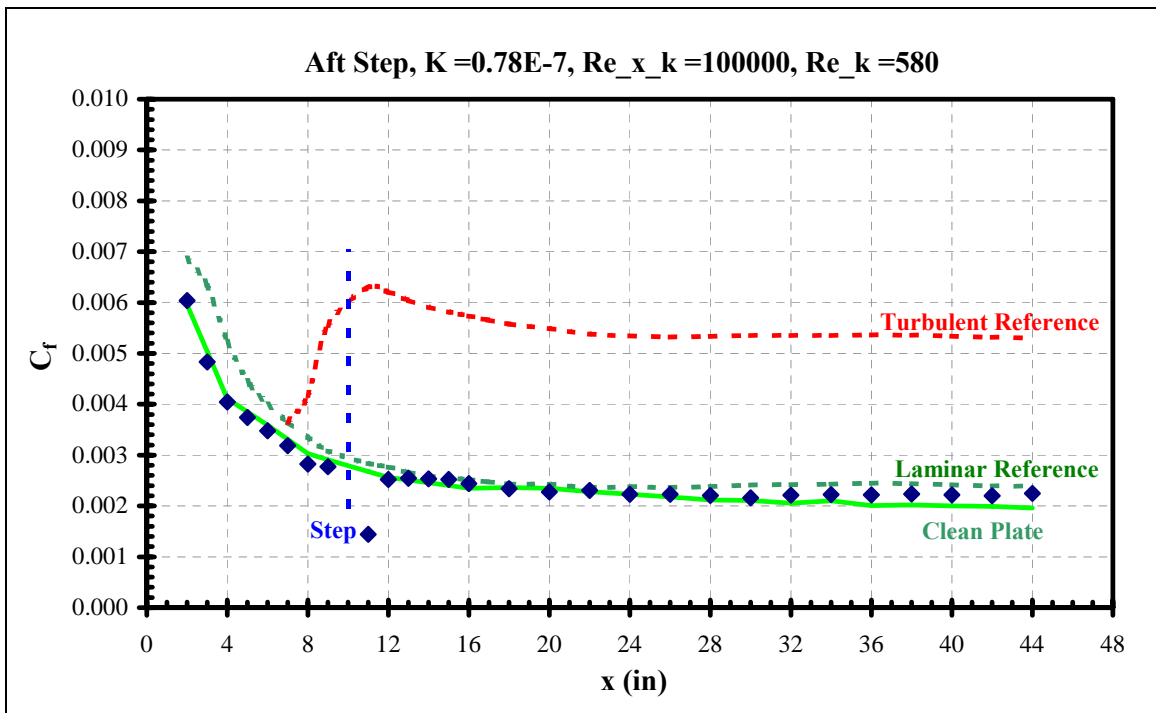


**Figure 359 Aft Adjust-a-Step skin friction distribution**

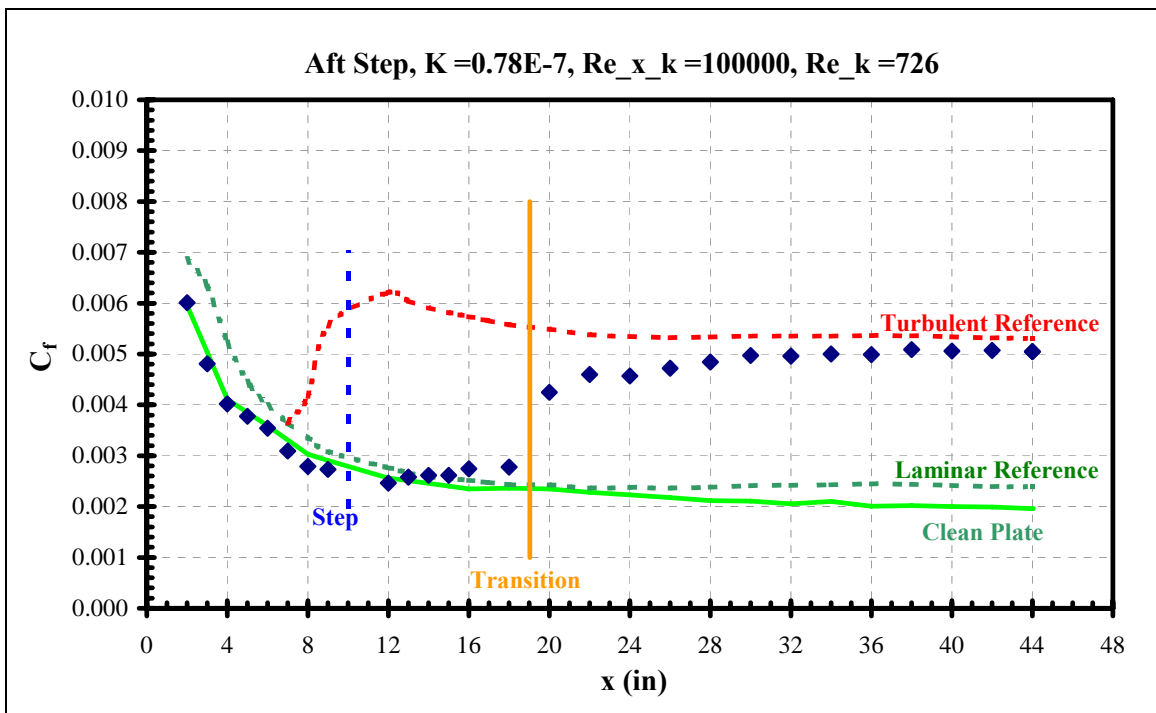


**Figure 360 Aft Adjust-a-Step skin friction distribution**

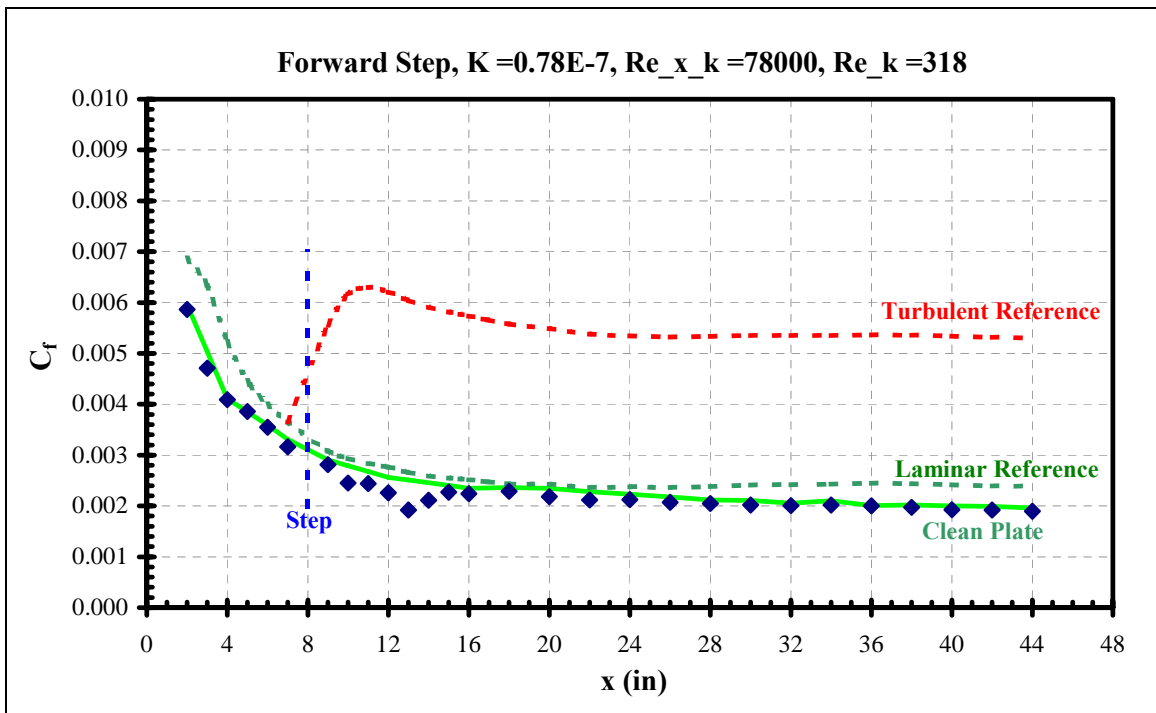


**Figure 361 Forward Adjust-a-Step skin friction distribution**

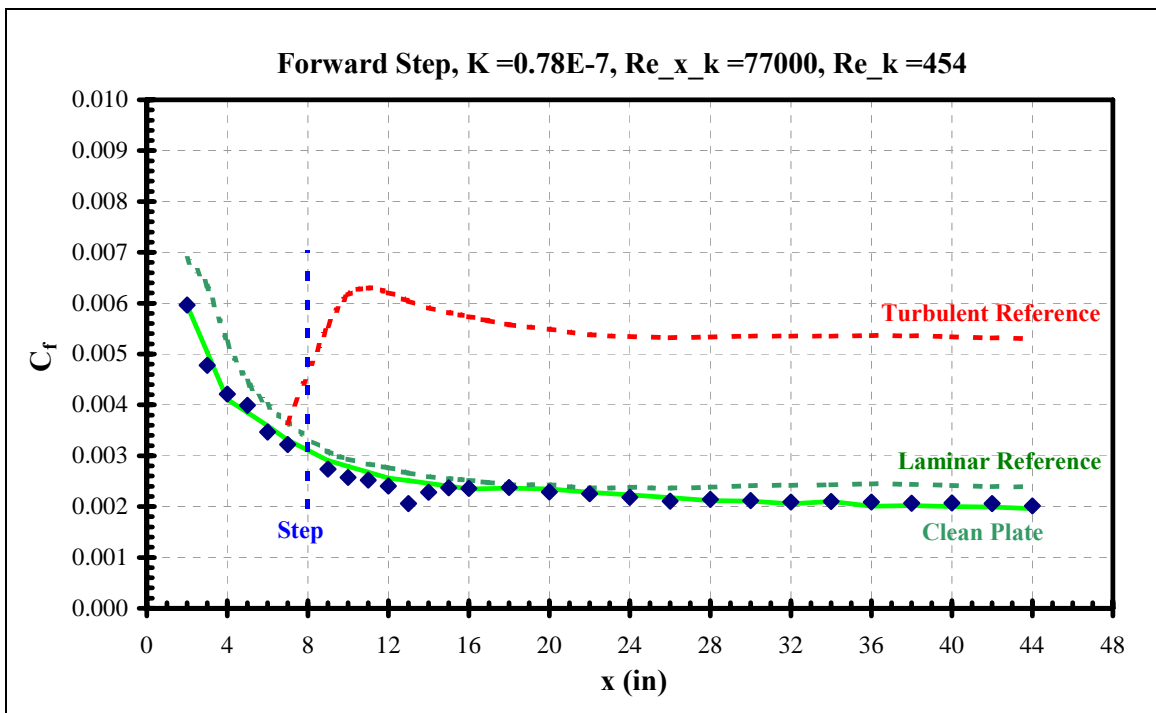


**Figure 362 Forward Adjust-a-Step skin friction distribution**

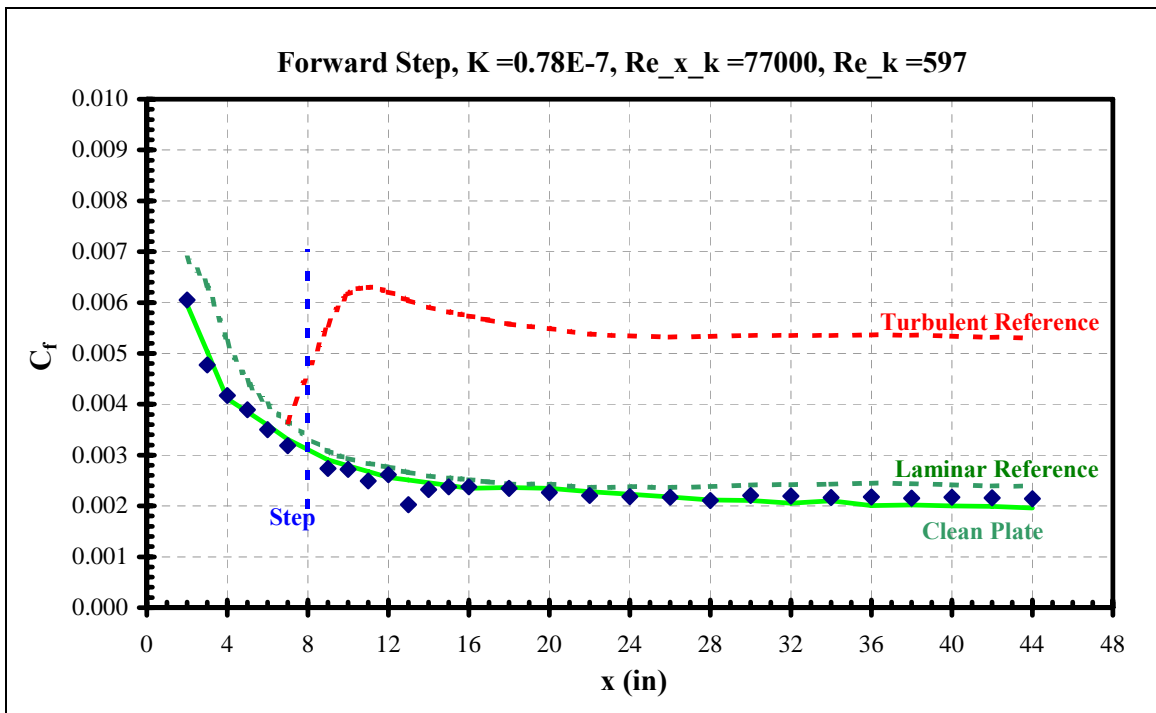


**Figure 363 Forward Adjust-a-Step skin friction distribution**

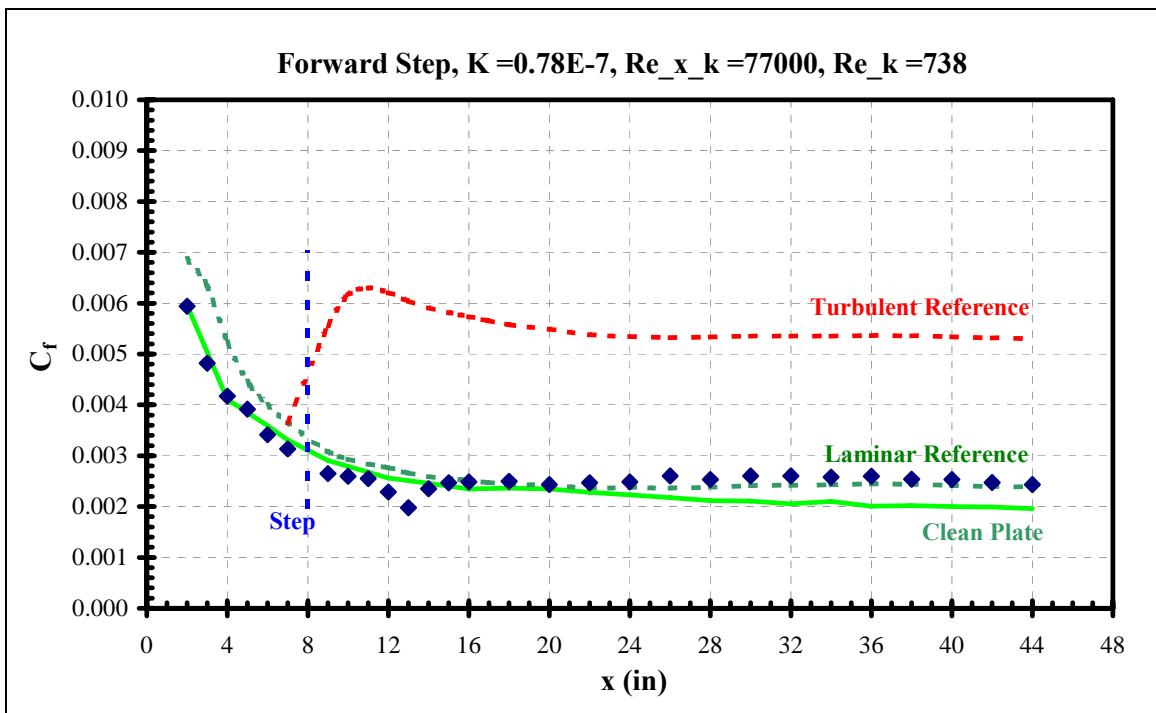


**Figure 364 Forward Adjust-a-Step skin friction distribution**

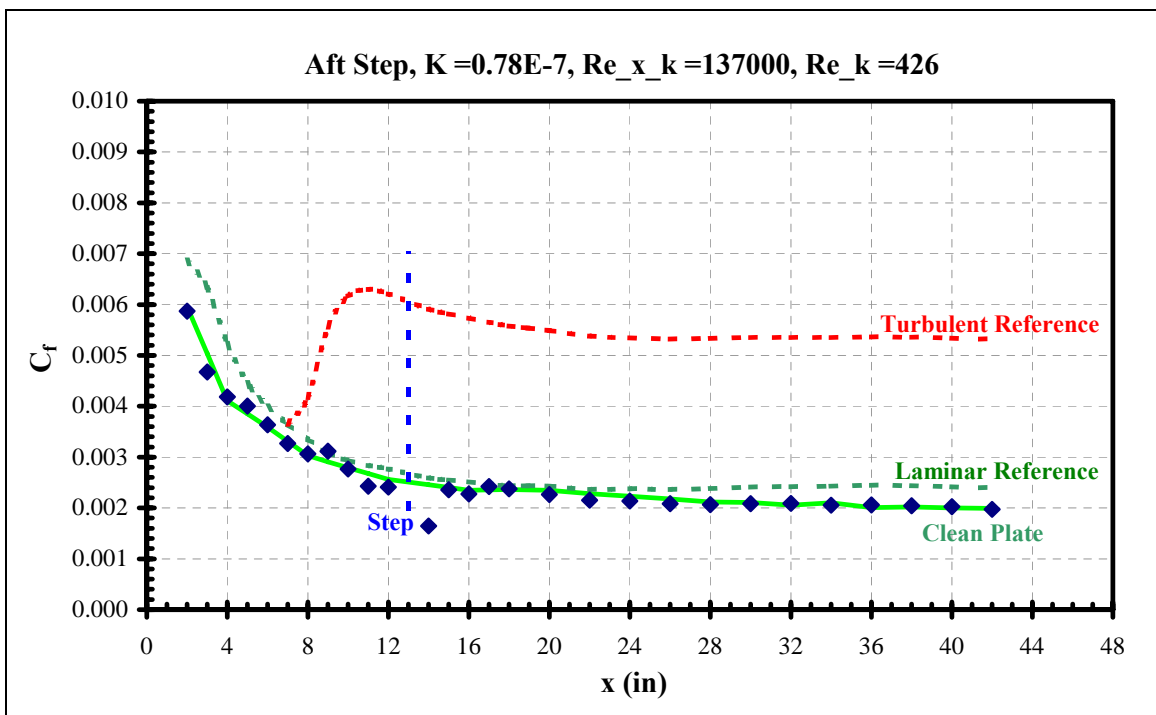


**Figure 365 Aft Adjust-a-Step skin friction distribution**

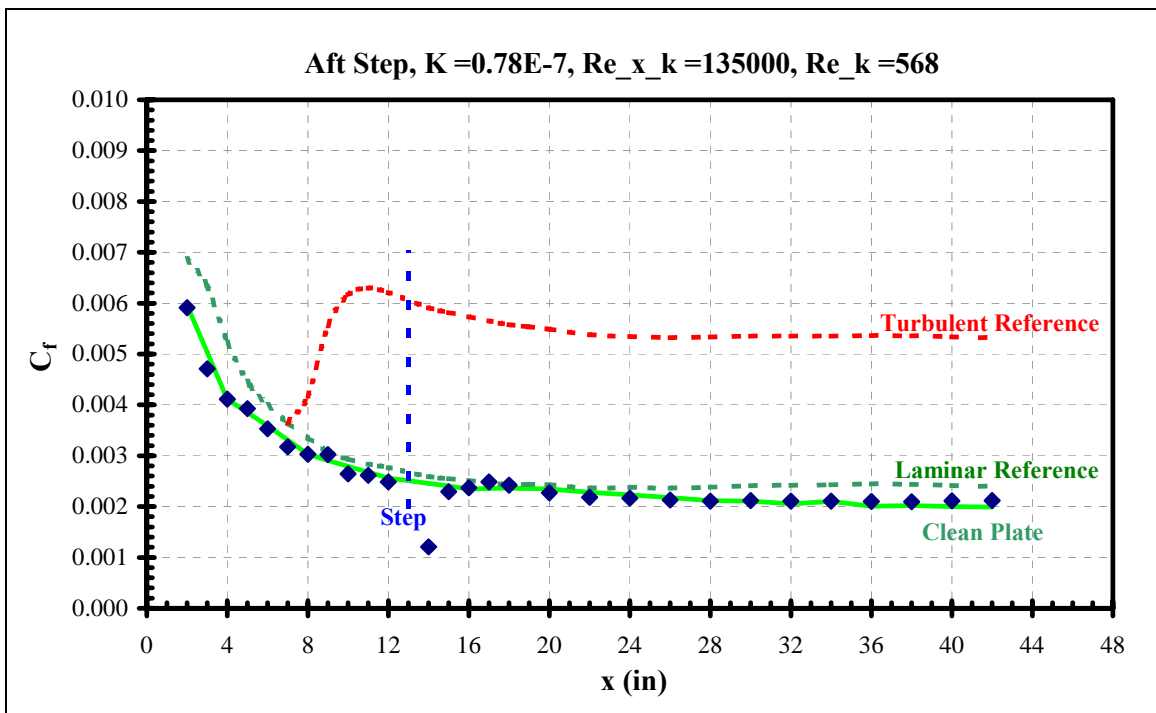


**Figure 366 Aft Adjust-a-Step skin friction distribution**

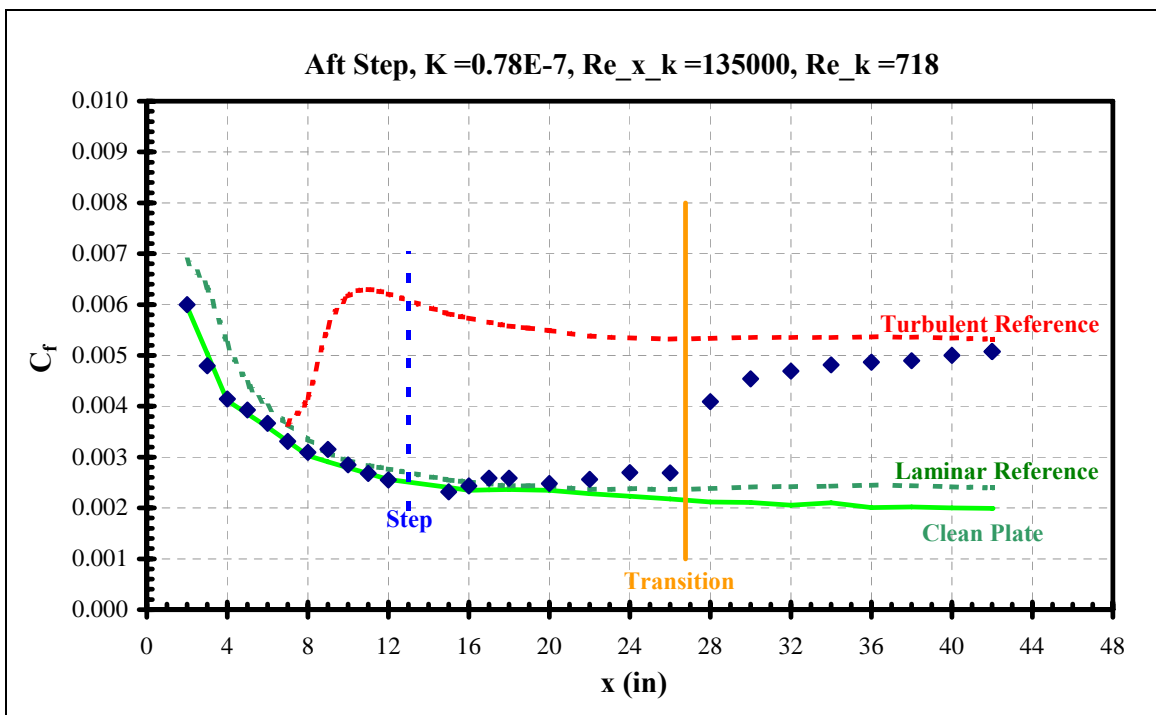


**Figure 367 Aft Adjust-a-Step skin friction distribution**

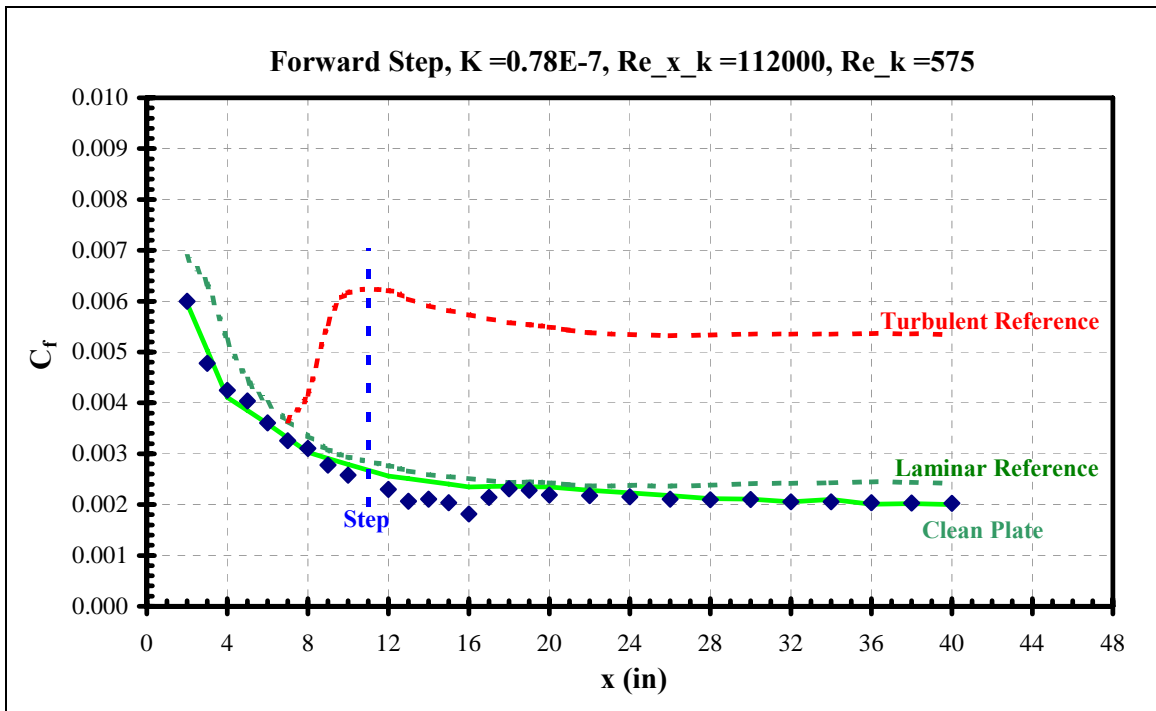


**Figure 368 Forward Adjust-a-Step skin friction distribution**

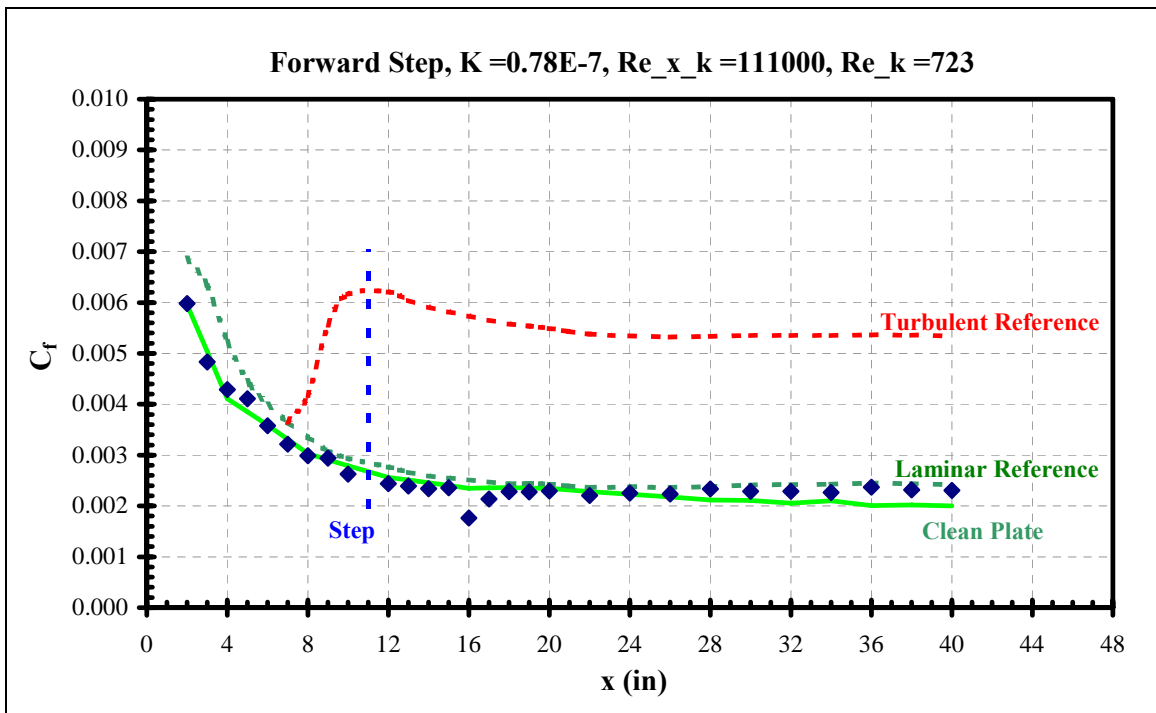


**Figure 369 Forward Adjust-a-Step skin friction distribution**

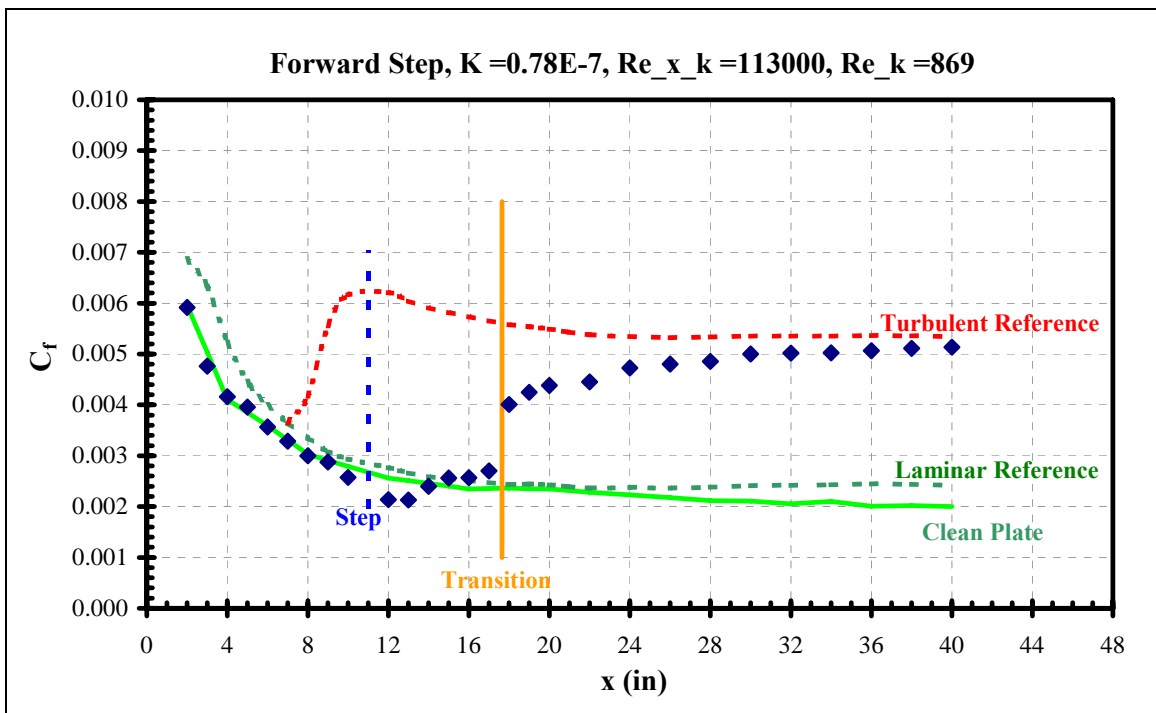
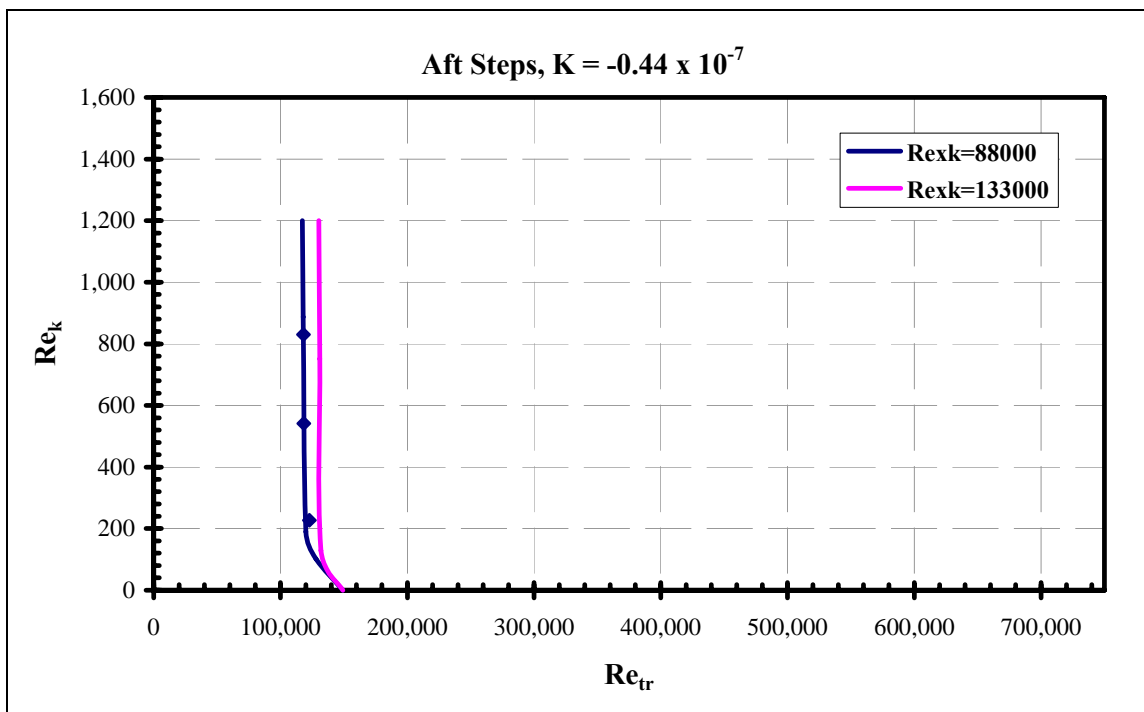


Figure 370 Forward Adjust-a-Step skin friction distribution



### 2.3.5 Boundary Layer Transition Trends

The following boundary layer transition trend plots show the transition trends for a family of  $Re_{xk}$  values for the given excrescence type and pressure gradient. Data points shown are transition locations from the skin friction distribution plots. The transition location criteria is defined as the location where the skin friction coefficient was greater than 1.5 times the measured clean plate skin friction coefficient. The data points were curve-fit as shown in the plots.



**Figure 371 Boundary layer transition trend**

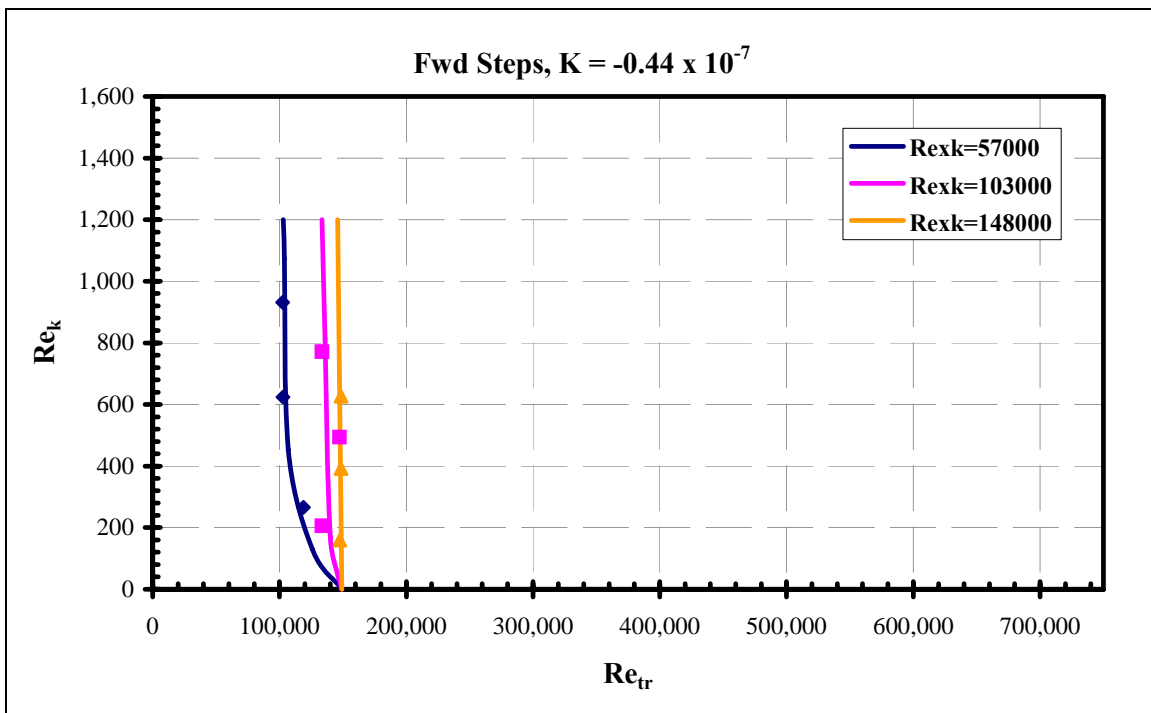


**Figure 372 Boundary layer transition trend**

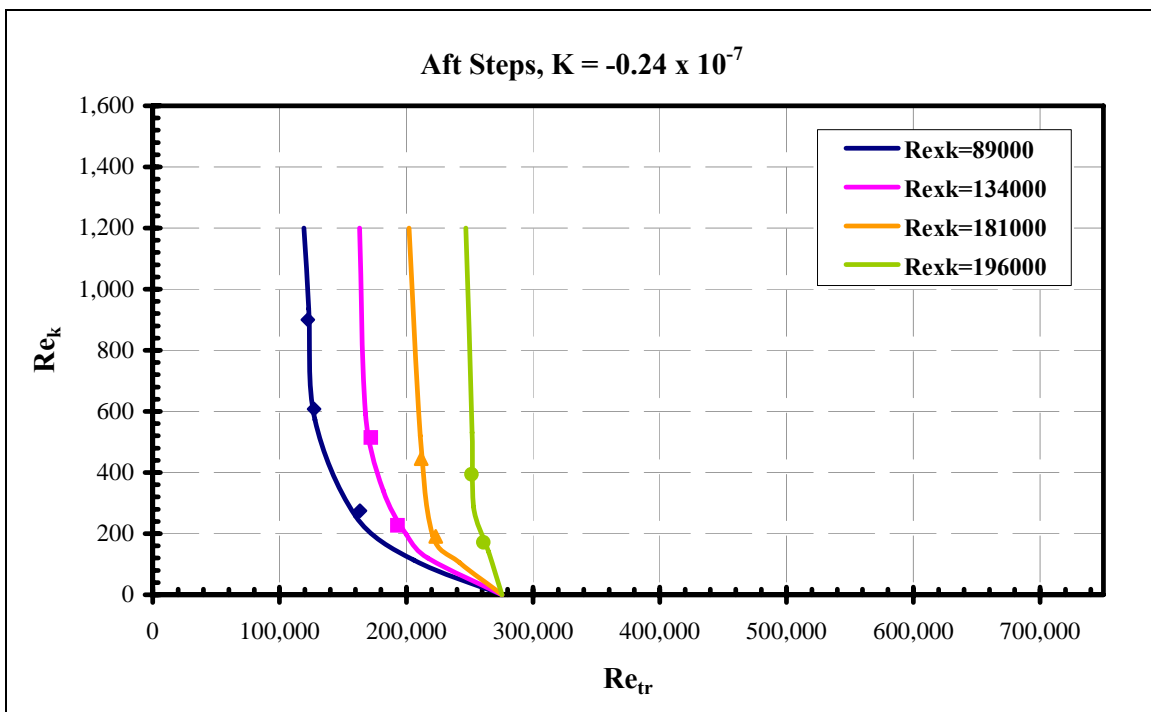


**Figure 373 Boundary layer transition trend**

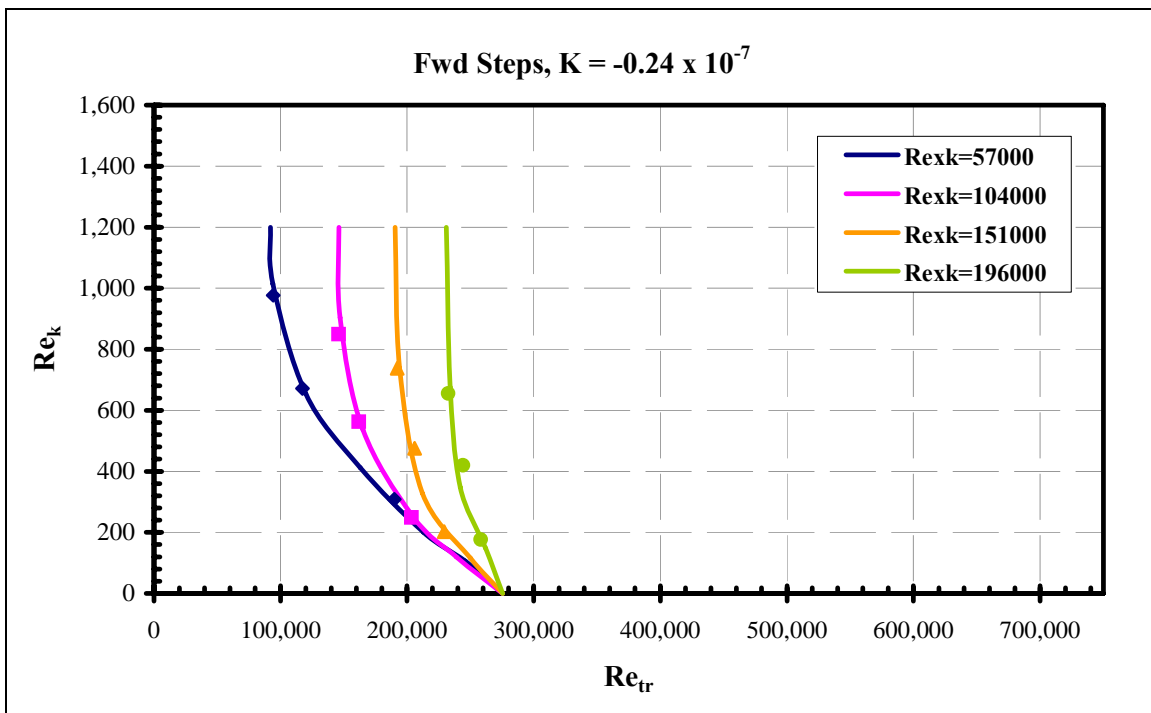


**Figure 374 Boundary layer transition trend**

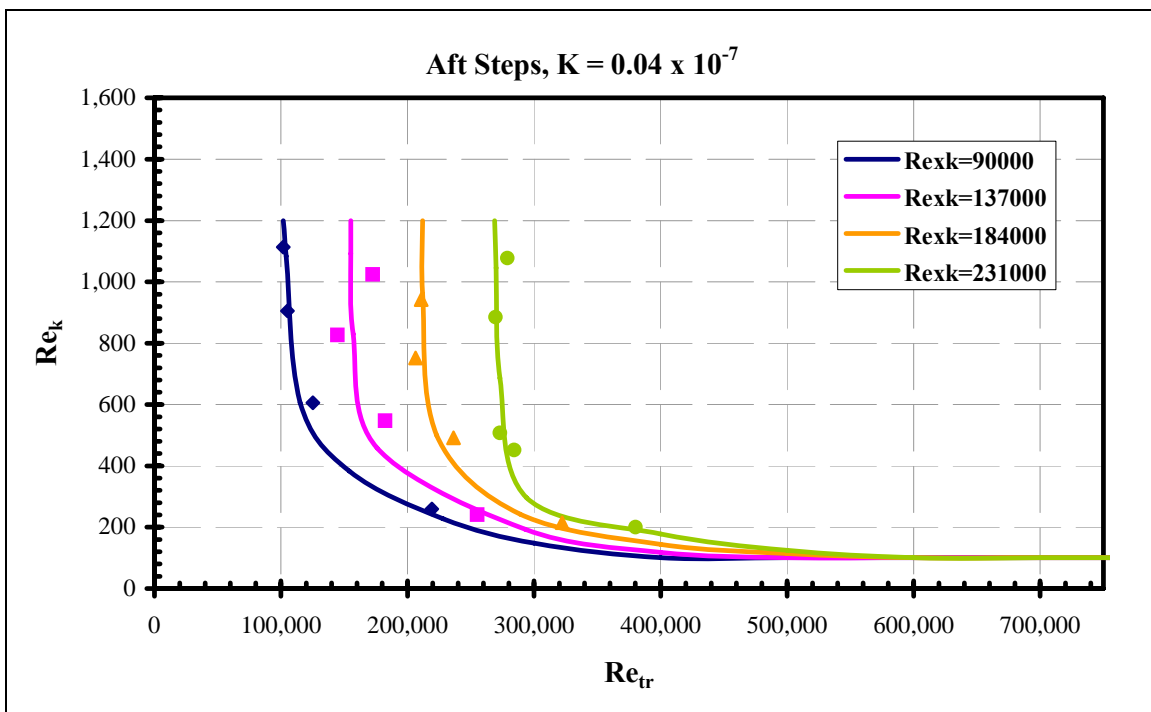


**Figure 375 Boundary layer transition trend**

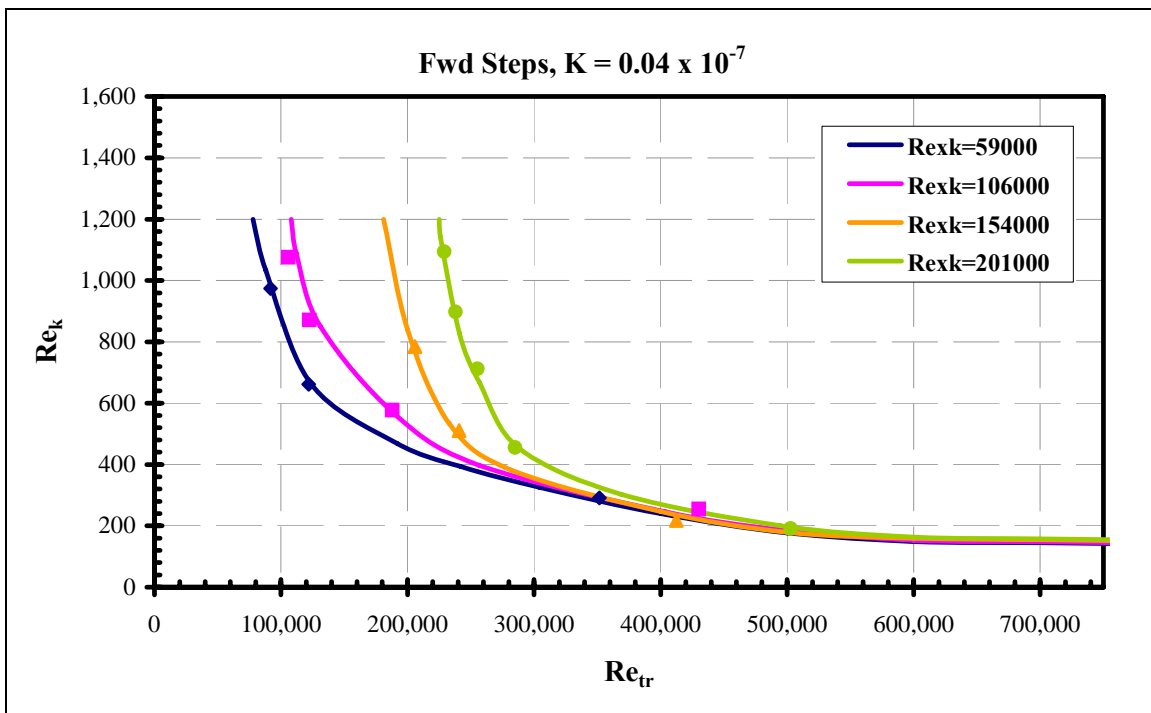


**Figure 376 Boundary layer transition trend**

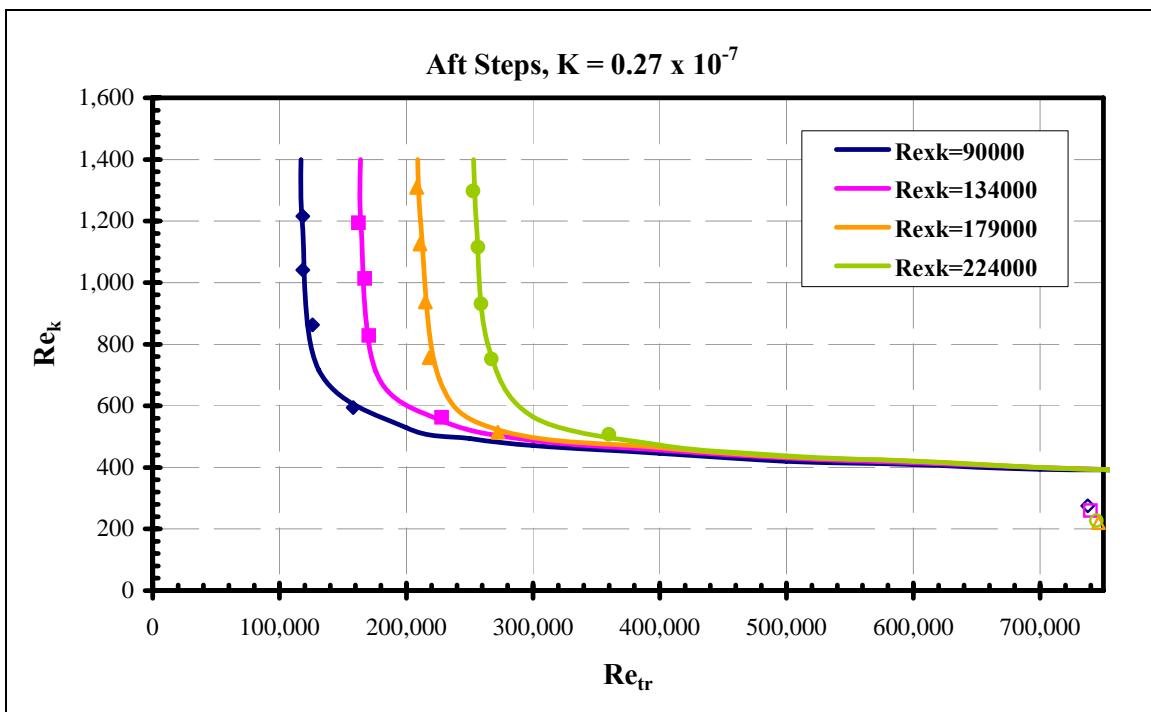


**Figure 377 Boundary layer transition trend**

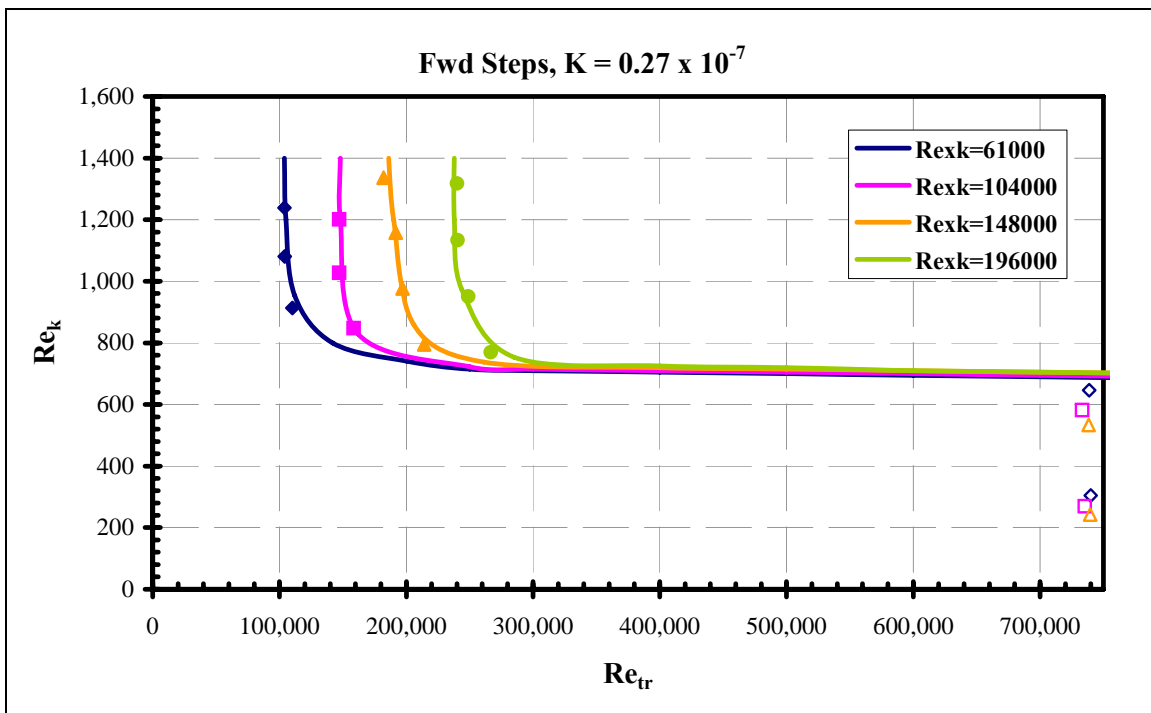


**Figure 378 Boundary layer transition trend**

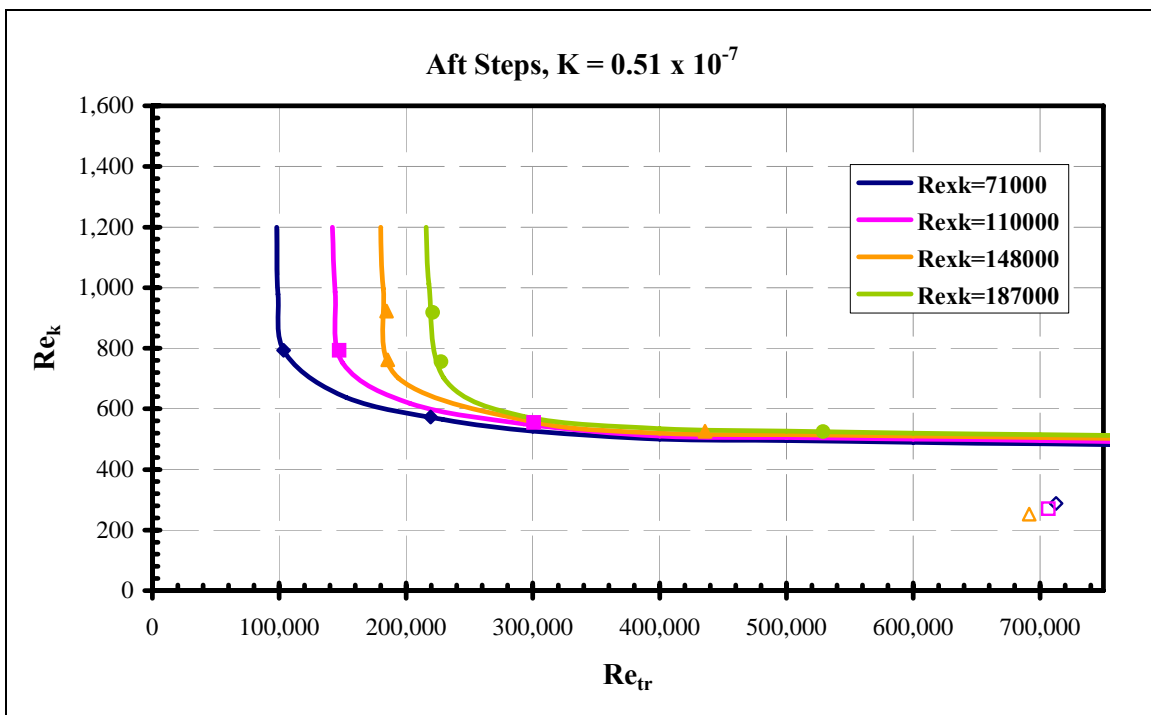


**Figure 379 Boundary layer transition trend**

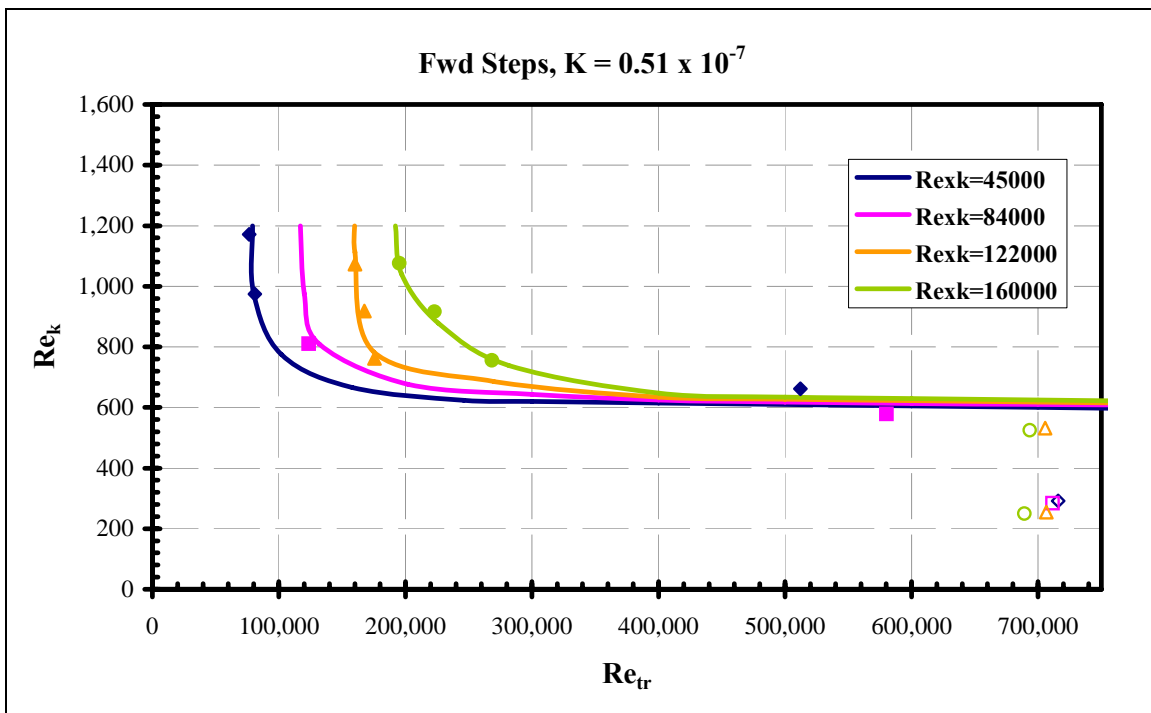


**Figure 380 Boundary layer transition trend**

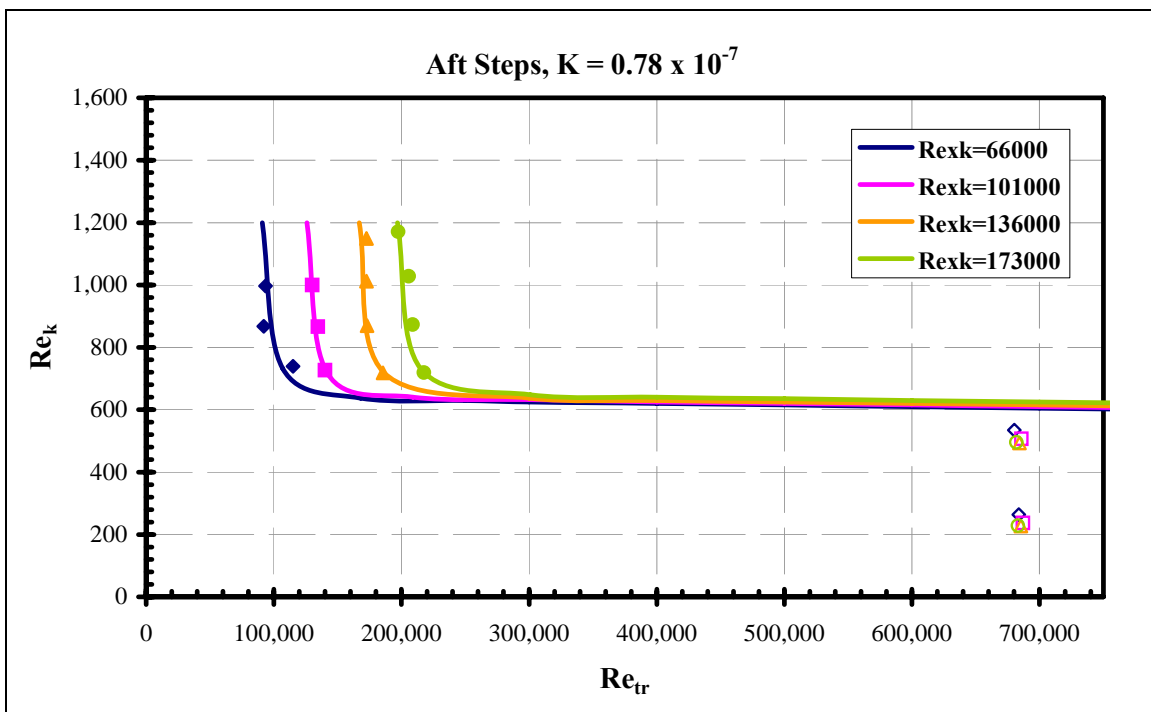


**Figure 381 Boundary layer transition trend**

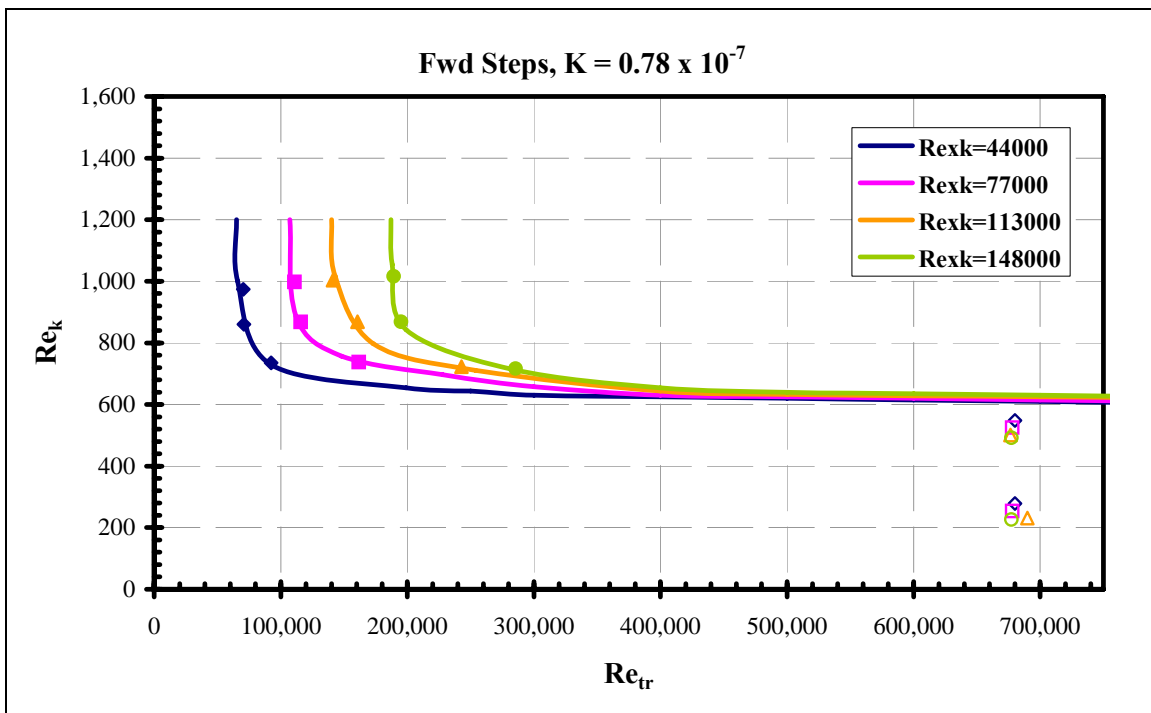


**Figure 382 Boundary layer transition trend**

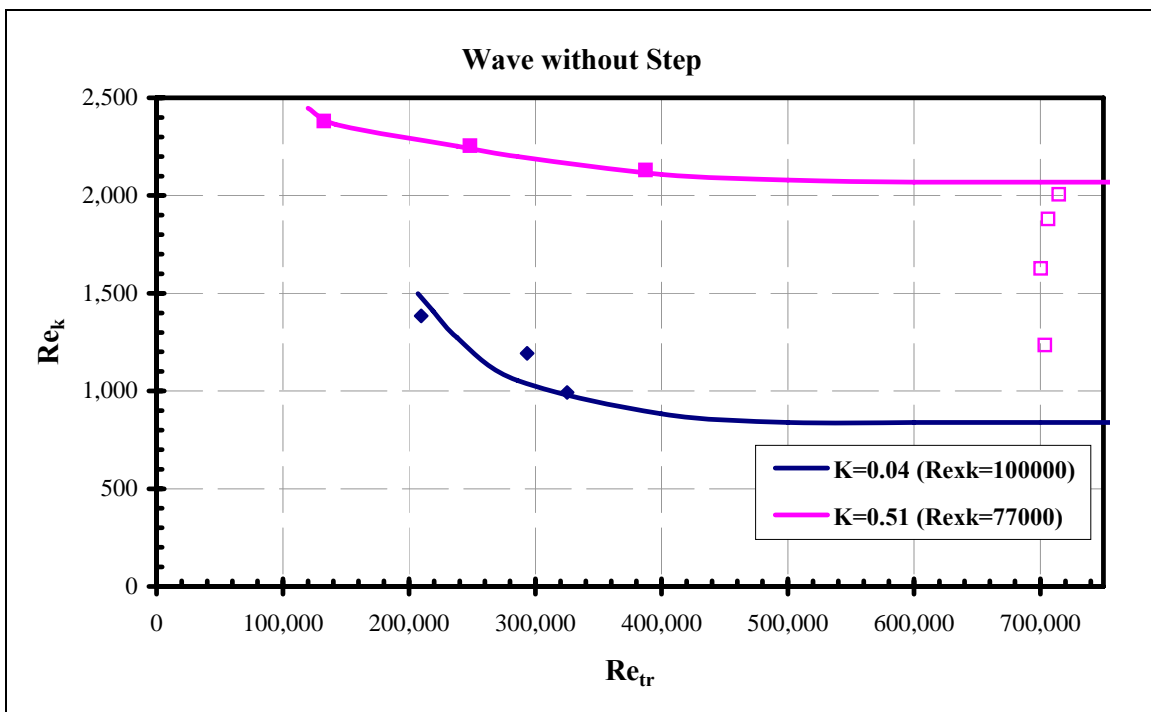


**Figure 383 Boundary layer transition trend**

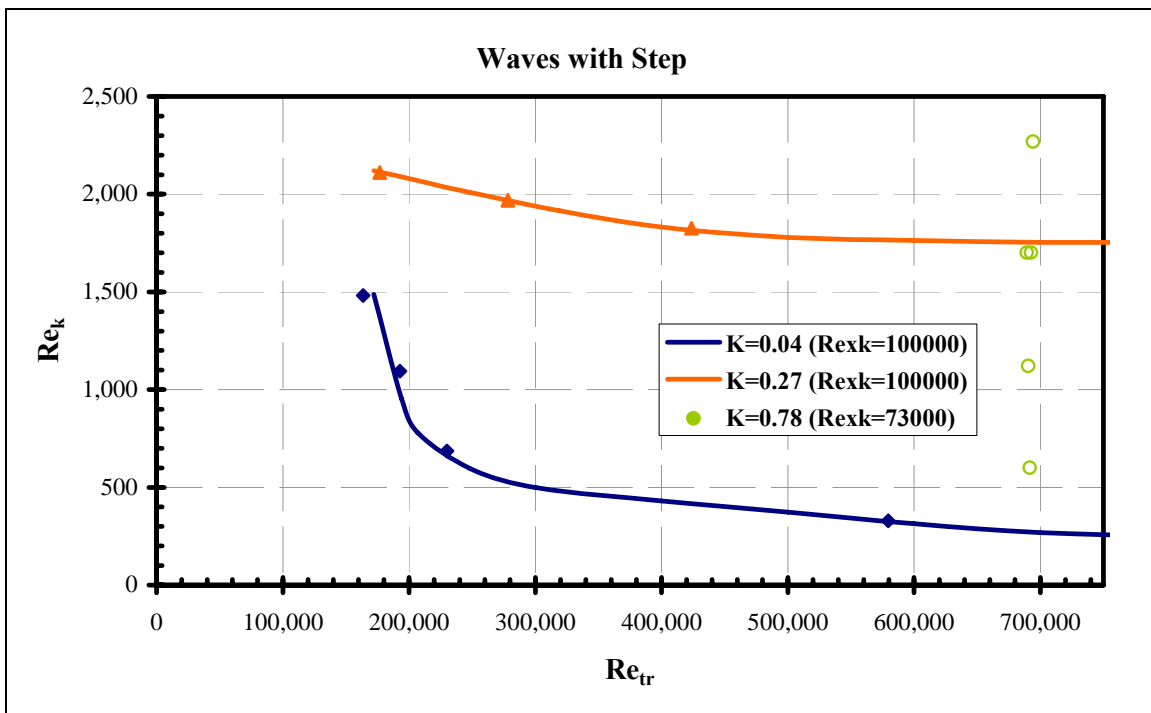


**Figure 384 Boundary layer transition trend**

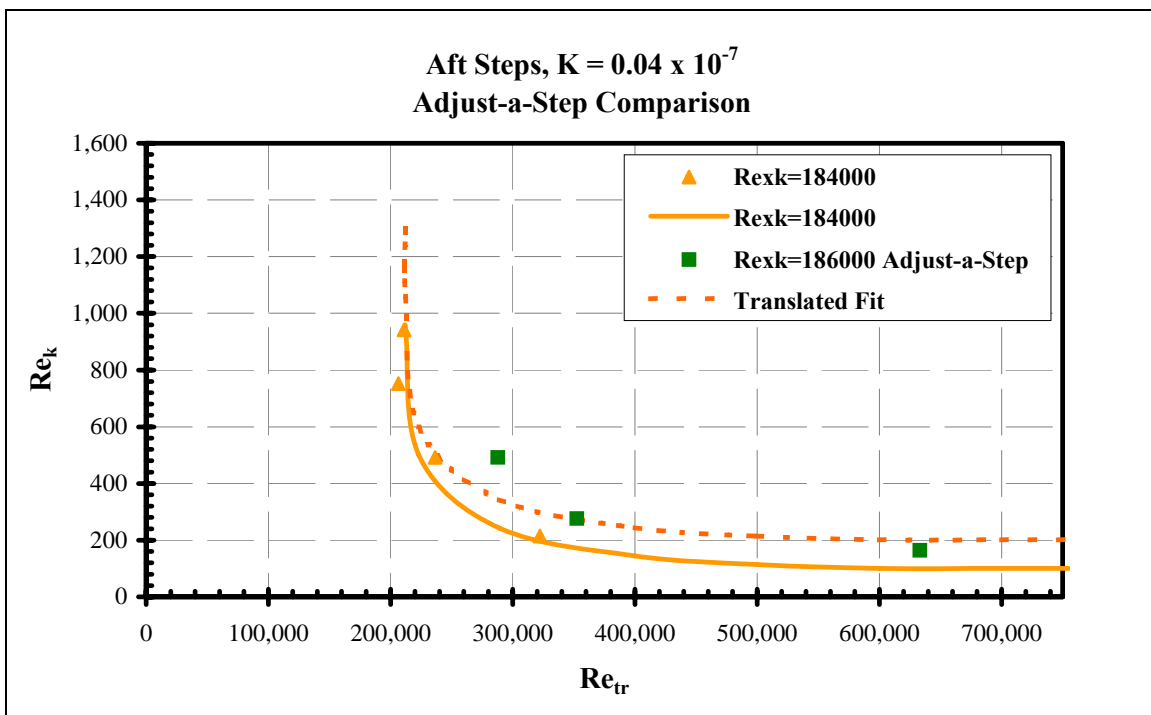


**Figure 385 Boundary layer transition trend**



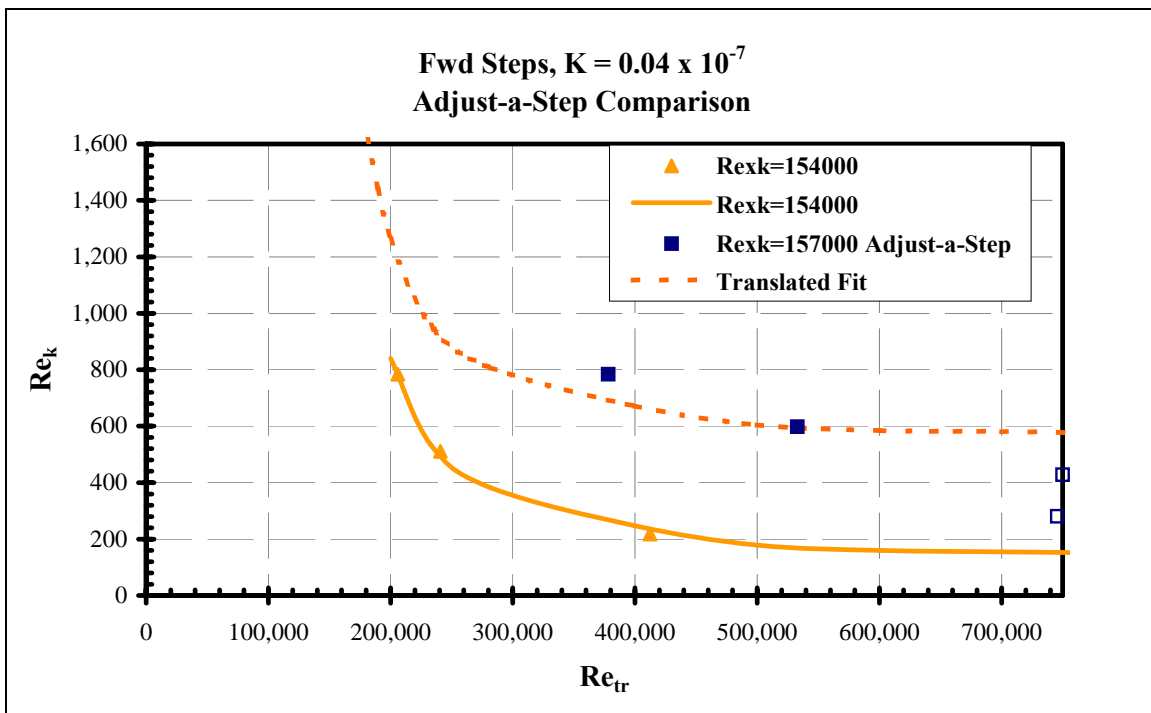


**Figure 386 Boundary layer transition trend**

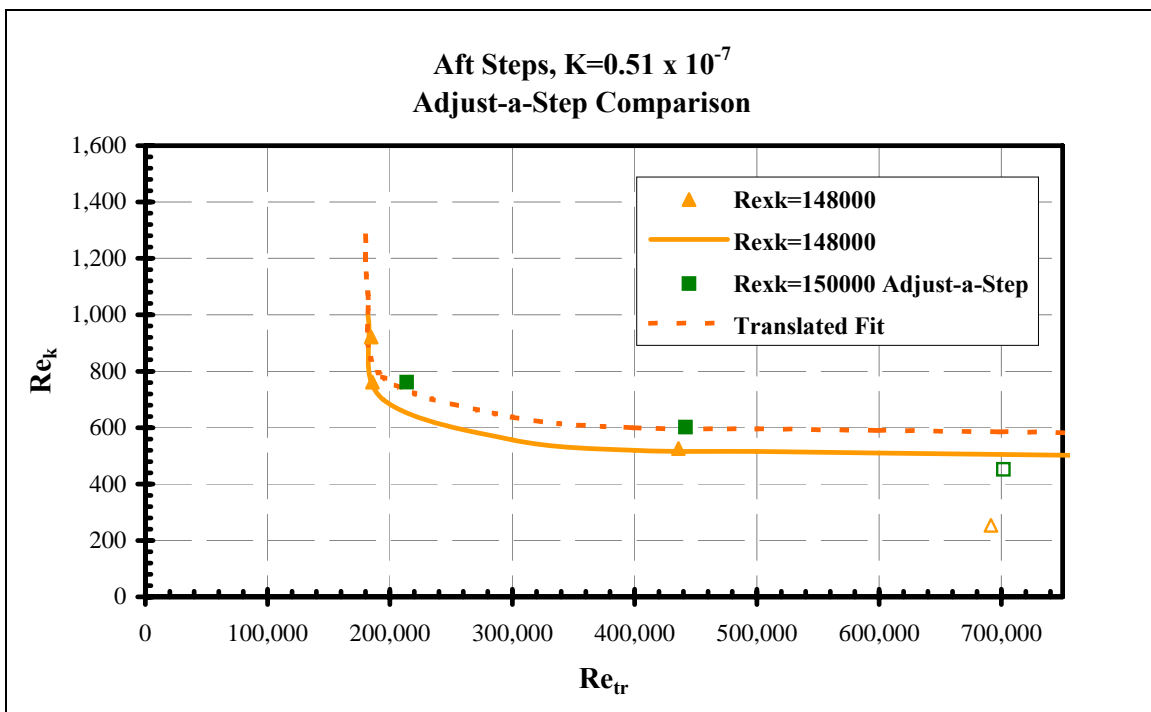


**Figure 387 Boundary layer transition trend**

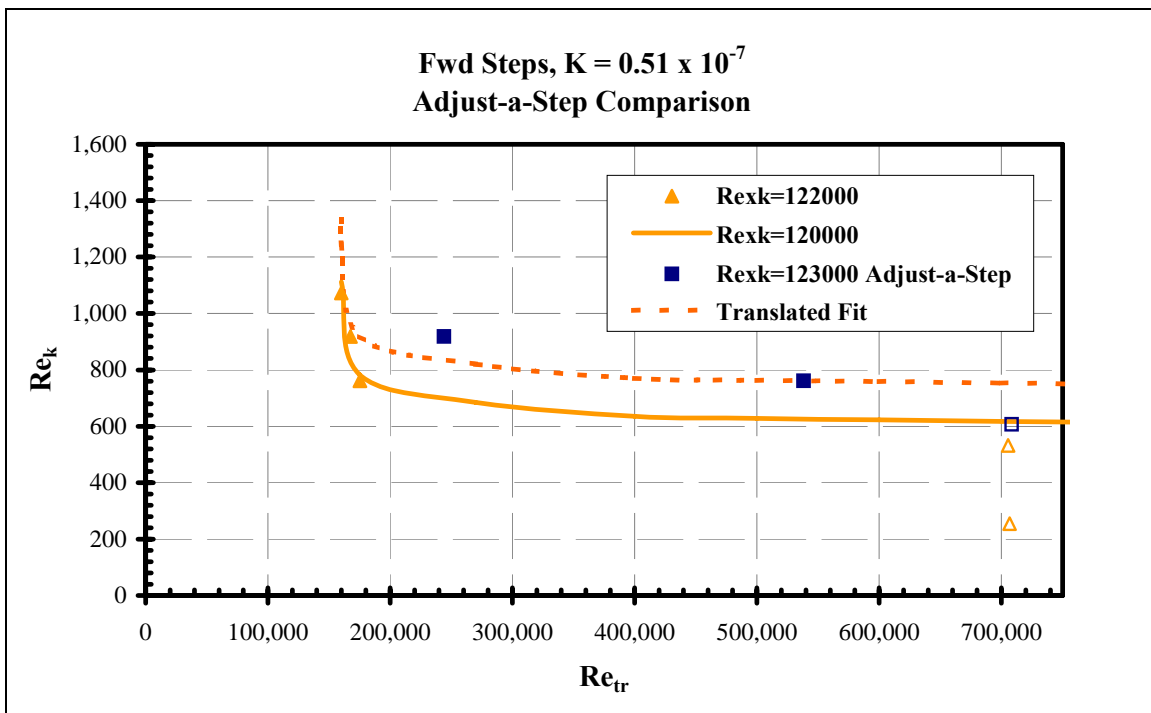


**Figure 388 Boundary layer transition trend**

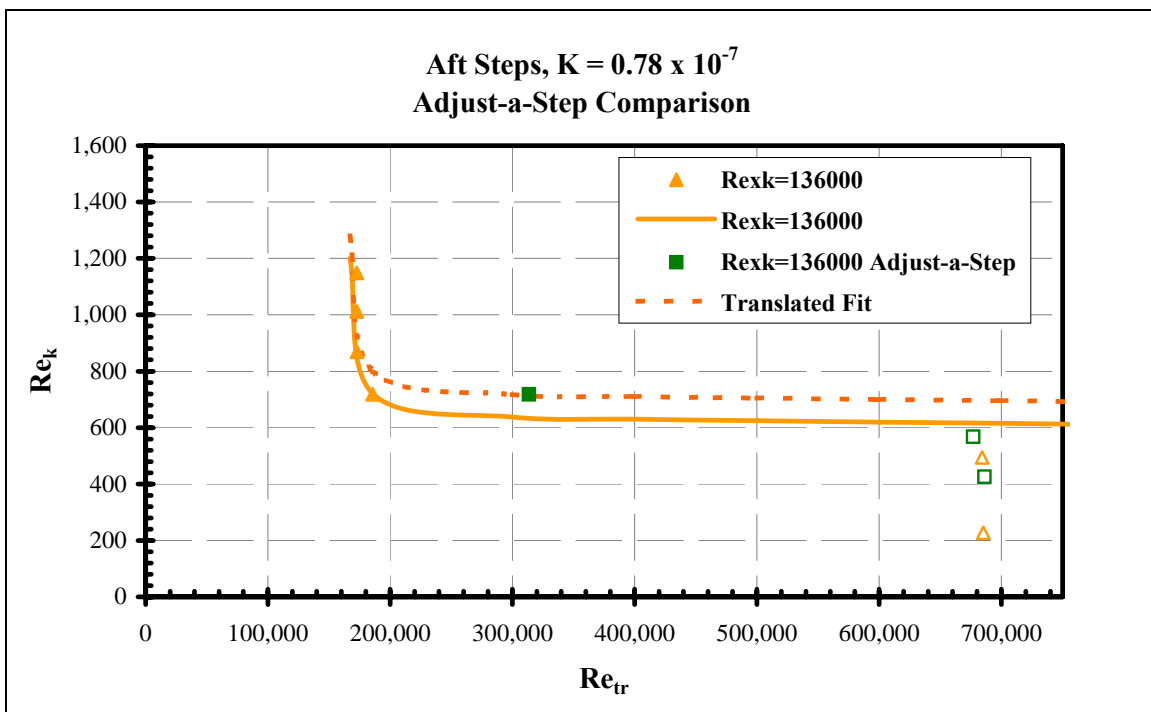


**Figure 389 Boundary layer transition trend**

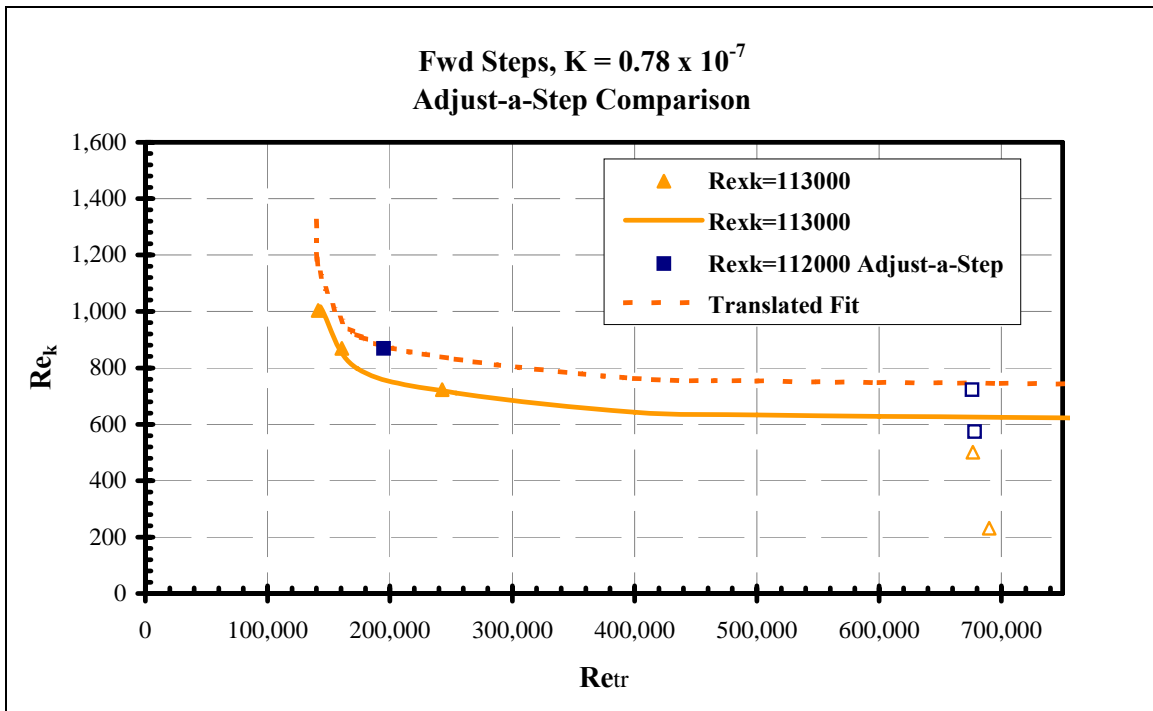


**Figure 390 Boundary layer transition trend**

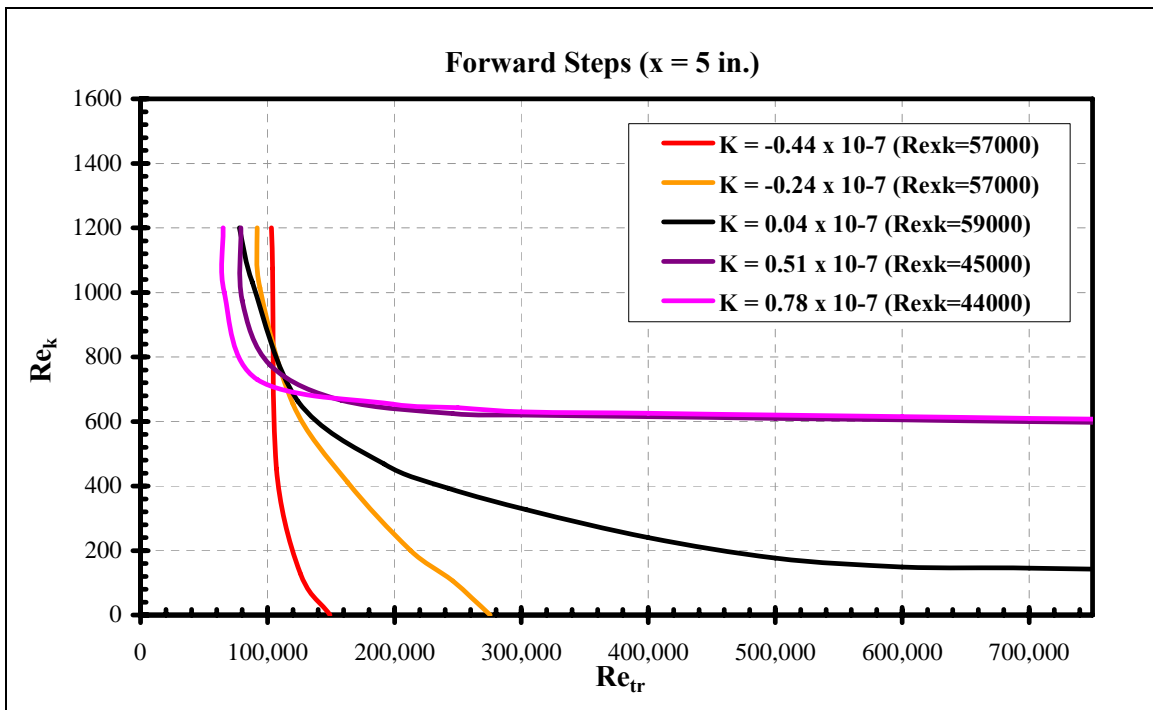


**Figure 391 Forward-facing step effect on boundary layer transition for  $x_k = 5$  inches**

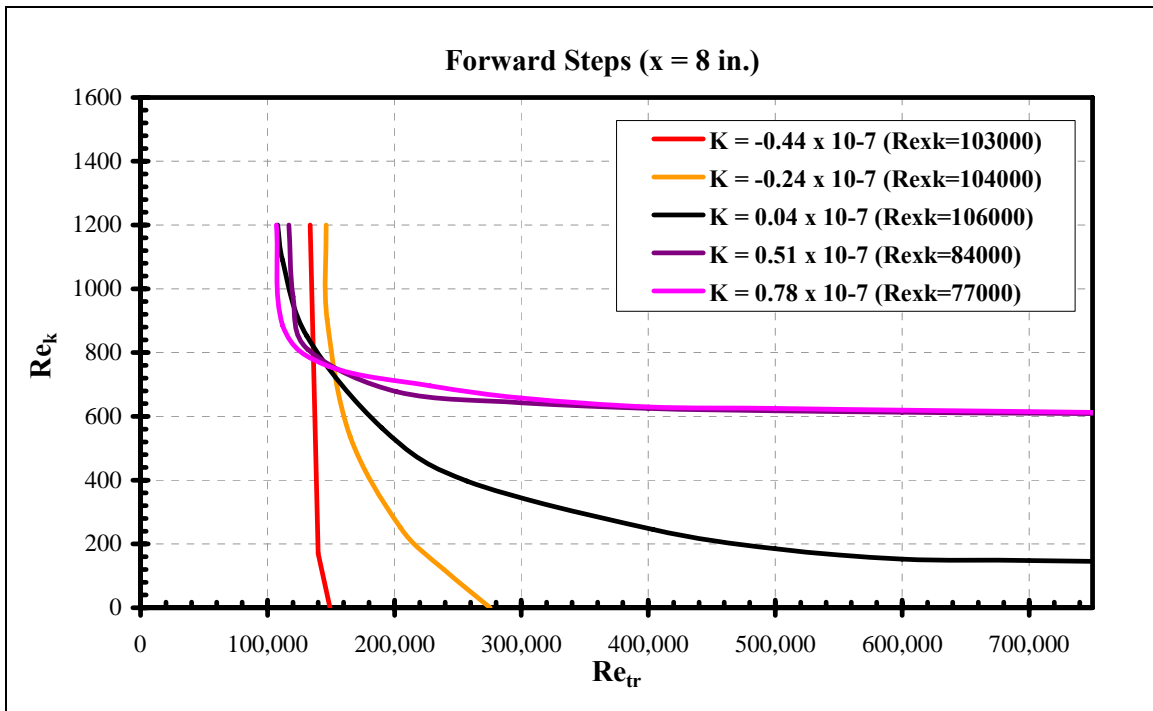


**Figure 392 Forward-facing step effect on boundary layer transition for  $x_k = 8$  inches**

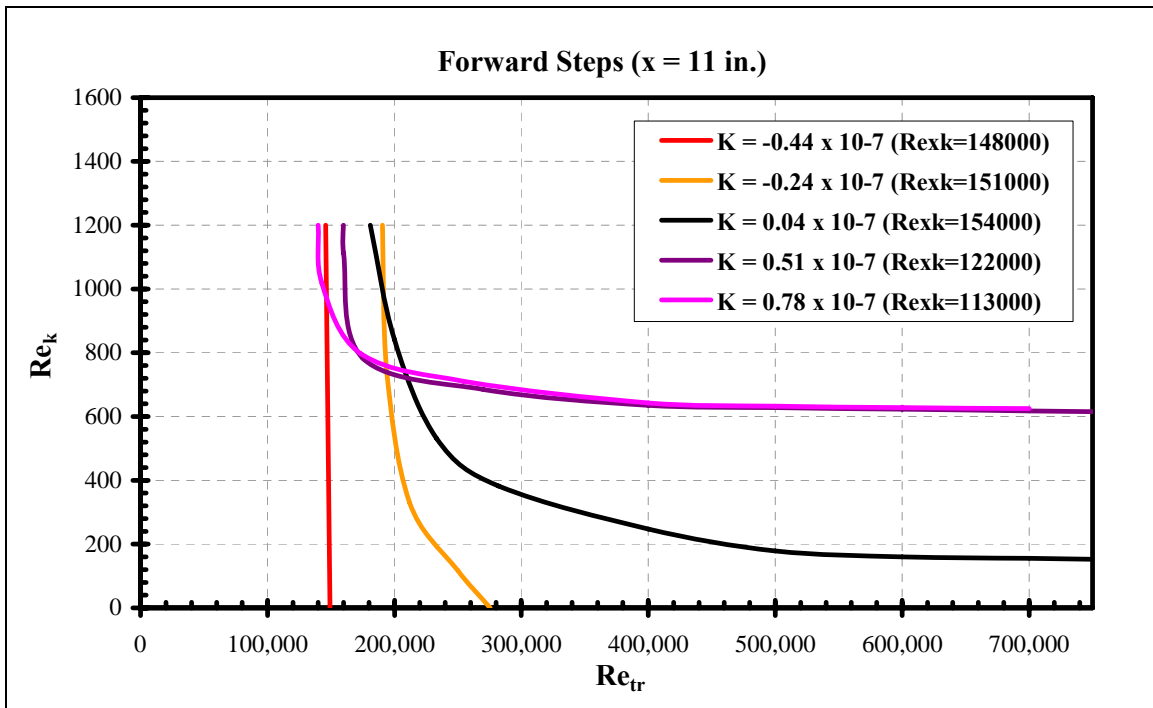


**Figure 393 Forward-facing step effect on boundary layer transition for  $x_k = 11$  inches**

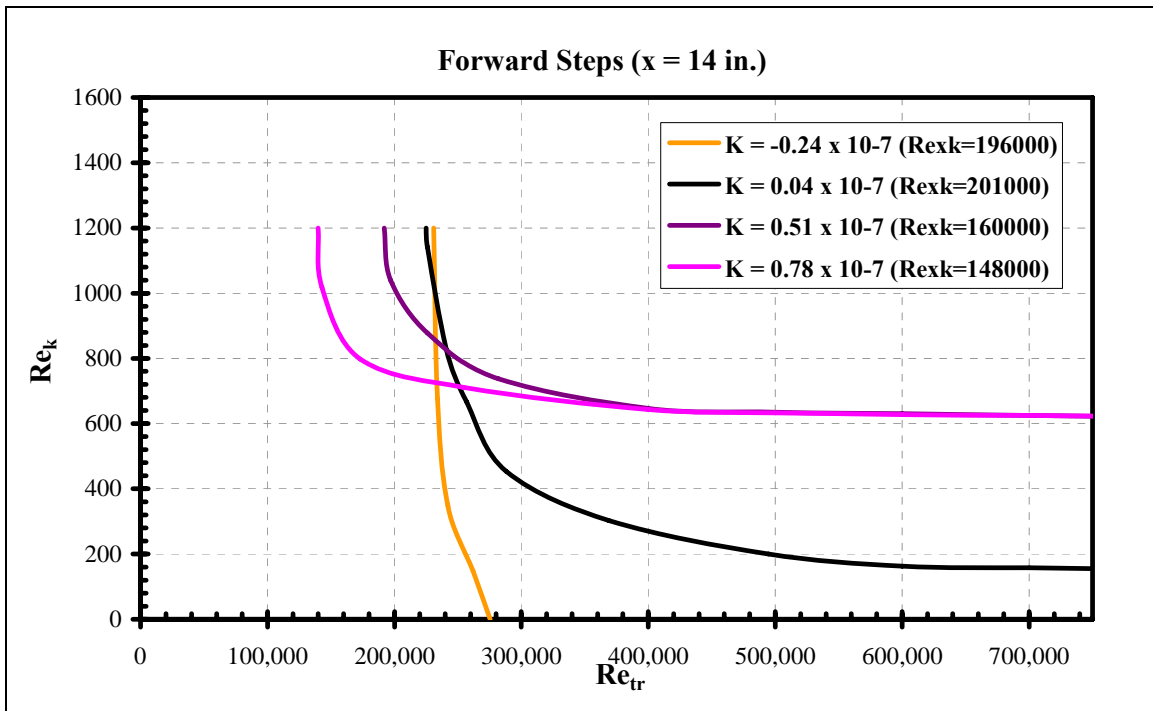


Figure 394 Forward-facing step effect on boundary layer transition for  $x_k = 14$  inches

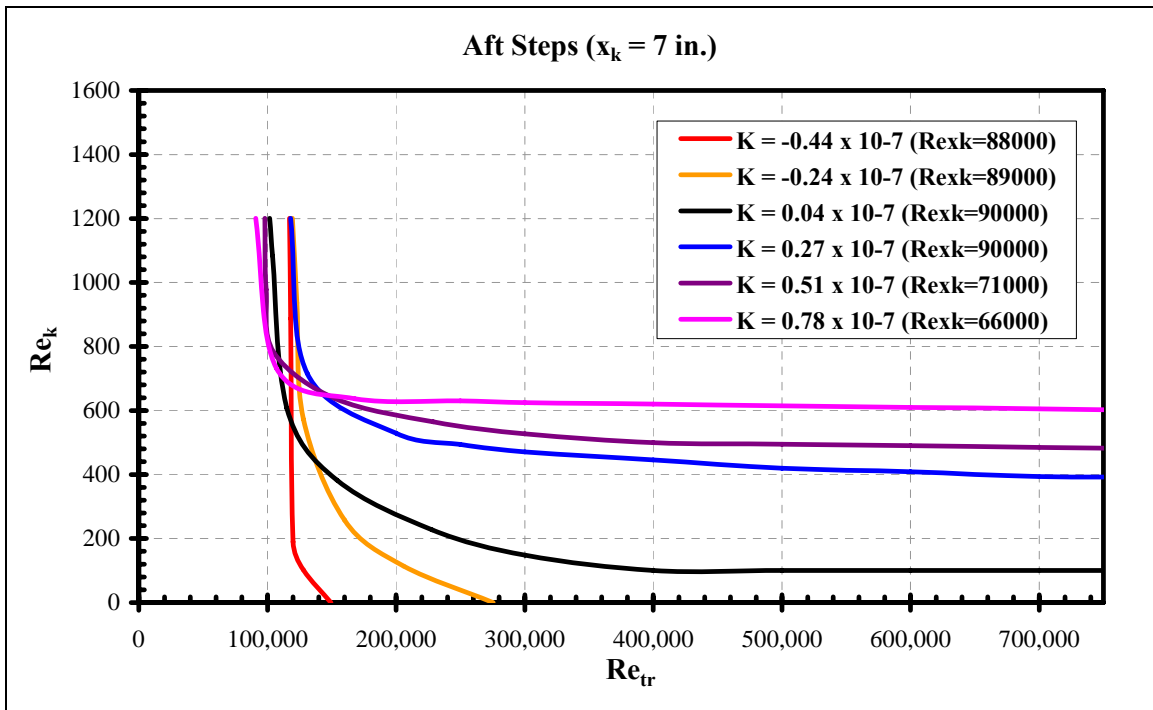
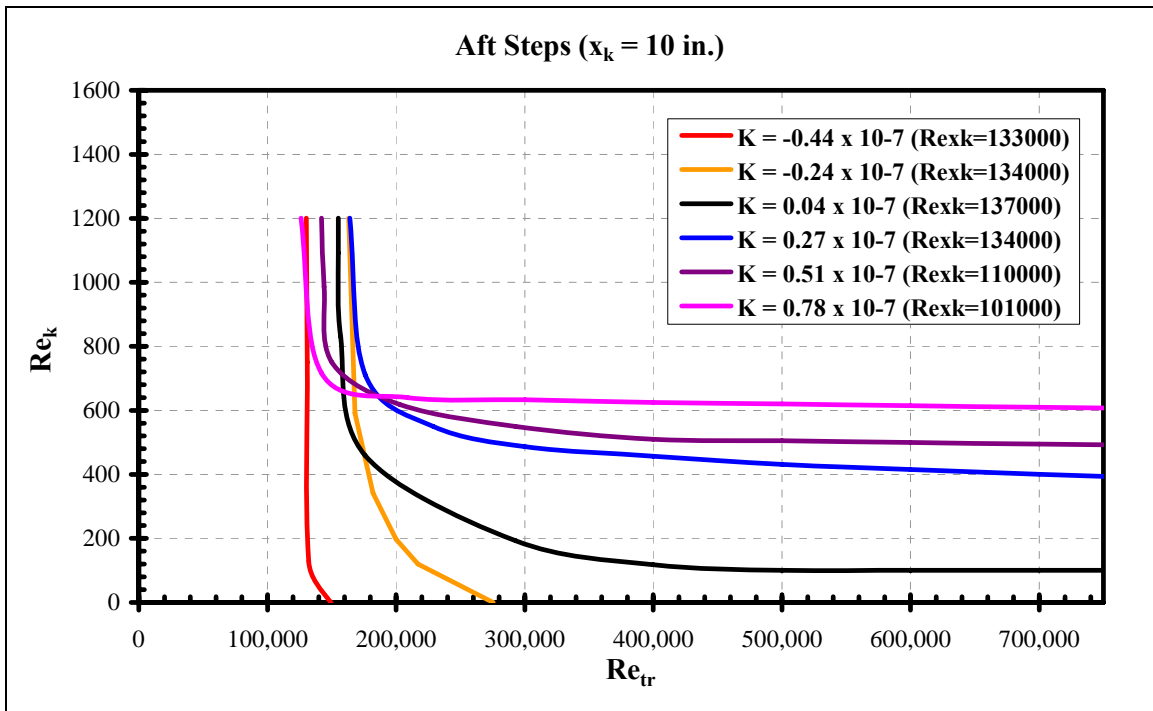
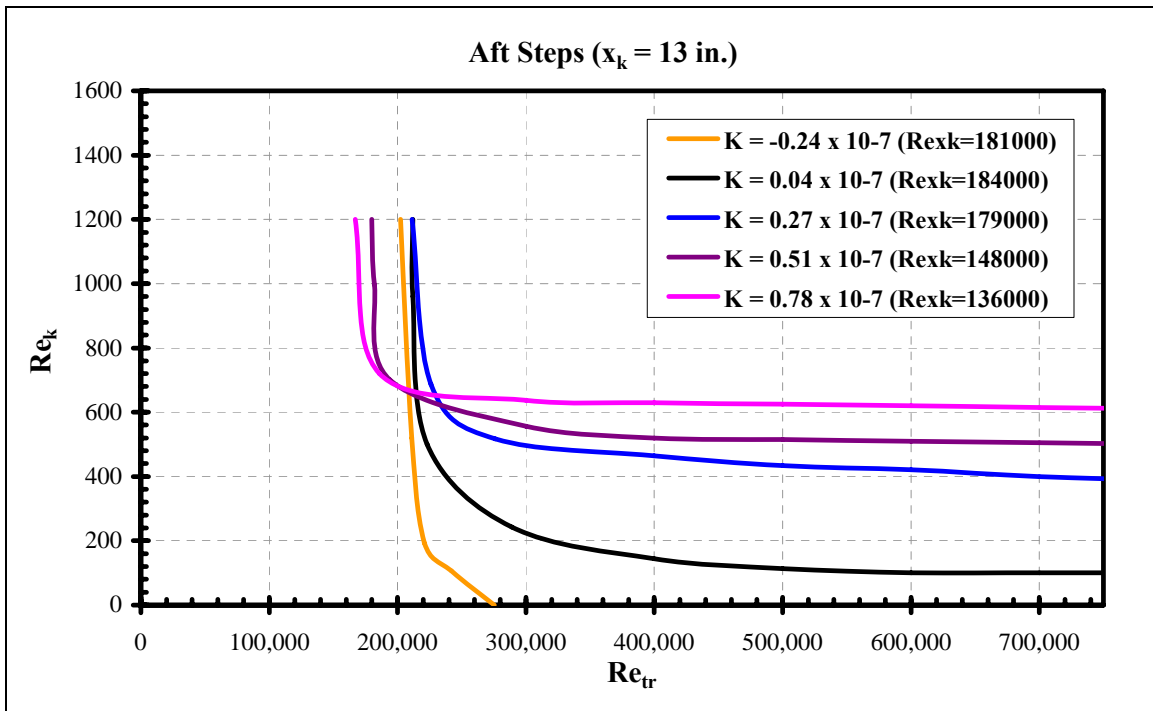


Figure 395 Aft-facing step effect on boundary layer transition for  $x_k = 7$  inches



**Figure 396 Aft-facing step effect on boundary layer transition for  $x_k = 10$  inches**



**Figure 397 Aft-facing step effect on boundary layer transition for  $x_k = 13$  inches**

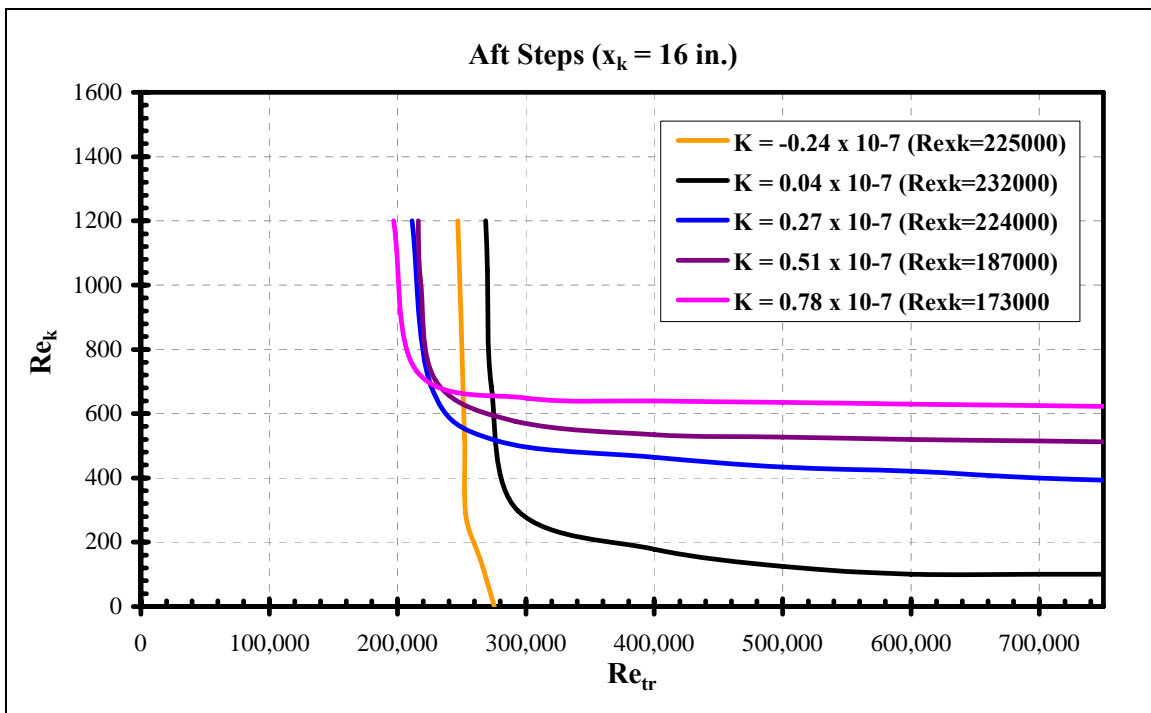


**Figure 398 Aft-facing step effect on boundary layer transition for  $x_k = 16$  inches**

### 3.0 Computational Examination of Excrescence Flow Fields

The goal of the computational study was to develop initial wing design guidelines regarding surface quality. Two-dimensional computational fluid dynamics (CFD) simulations were utilized to develop a detailed understanding of the flow fields associated with a subset of the surface disturbances examined experimentally. Geometric and flow parameters were systematically varied to determine what specific flow field features are associated with a given disturbance type, how they vary with disturbance geometry and flow parameters, and what their impact may be on boundary layer transition.

#### 3.1 CFD Modeling the Clean Plate in the Tunnel

The first task of the CFD study was to simulate the flat plate without excrescences for the various tunnel wall positions at the conditions tested. The immediate goal was to match the pressure gradients observed experimentally on the plate's upper surface. This was not a trivial task.

Figure 399 shows the conceptual design of the plate lower surface. On the actual hardware, the trough around the leading edge pressure tap lines did not widen and was filled in flush with the surrounding outer mold line. In the 2-D CFD model, the lower surface was approximated as flat, so the aft waffle construction was not included. The impact of this omission is uncertain. It probably altered the circulation around the plate to some degree.

Version 4.64 of Northrop Grumman's proprietary Generalized Compressible Navier-Stokes (GCNS) code was used for all computational analysis. Menter's  $k-\omega$  shear stress transport turbulence model was used for all cases. Laminar to turbulent transition regions were user-specified via boundary conditions.



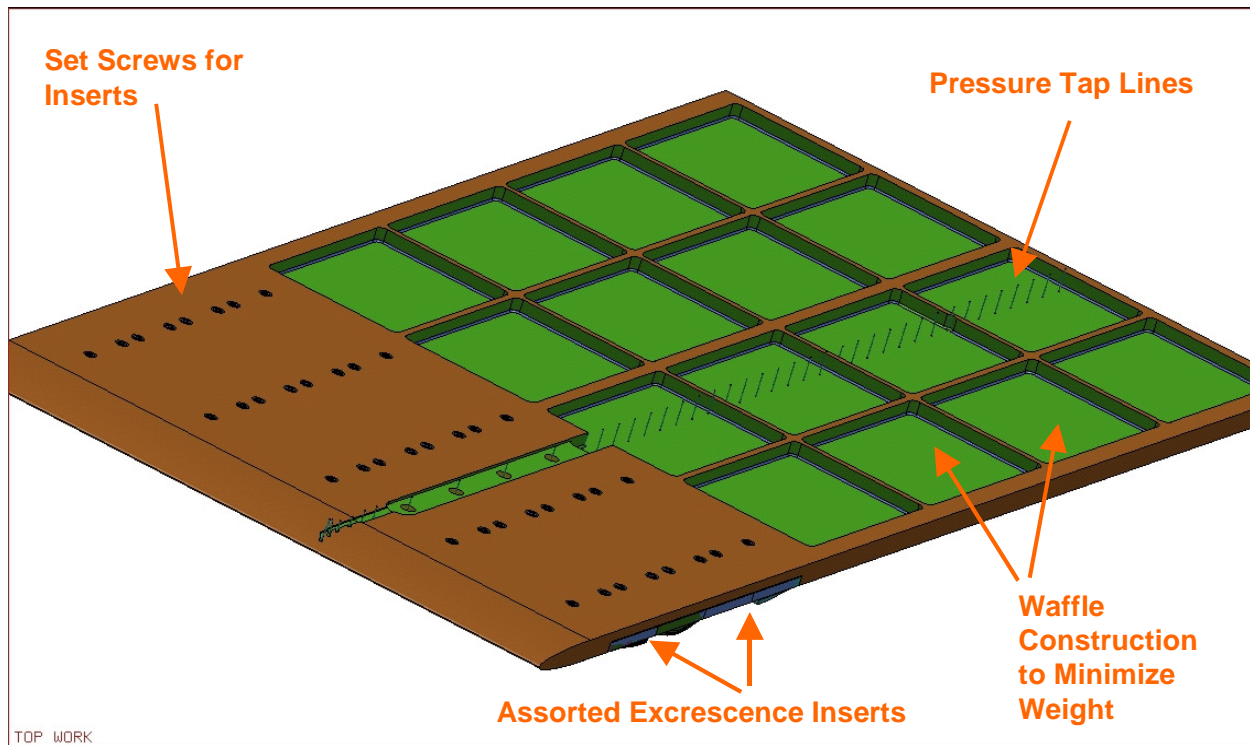


**Figure 399 Conceptual plate lower surface design detail**

Structured overset grids were generated for each wall geometry. The CFD model included the test section and a plenum beginning outside the test section and extending downstream. The grid for P6 shown in Figure 400 features 6 blocks and 788,298 grid points. All communication to the pink downstream plenum block was via patched interfaces. Overset grids were used within the test section. Minimum spacing off the plate surface was 0.001 inch, which corresponds to a  $y^+$  value of 1 at the test conditions. The view of test section identifies the grid point closest the location of the probe used to establish reference conditions in the experiment (14 inches upstream and 5.5 inches above the plate leading edge). The closest point in the grid varied with the tunnel wall geometry but was within about 0.07 inch of the desired location.

The GCNS solution is nondimensionalized by input Mach number, static temperature, and unit Reynolds number. Using the experimental reference conditions and applying exhaust

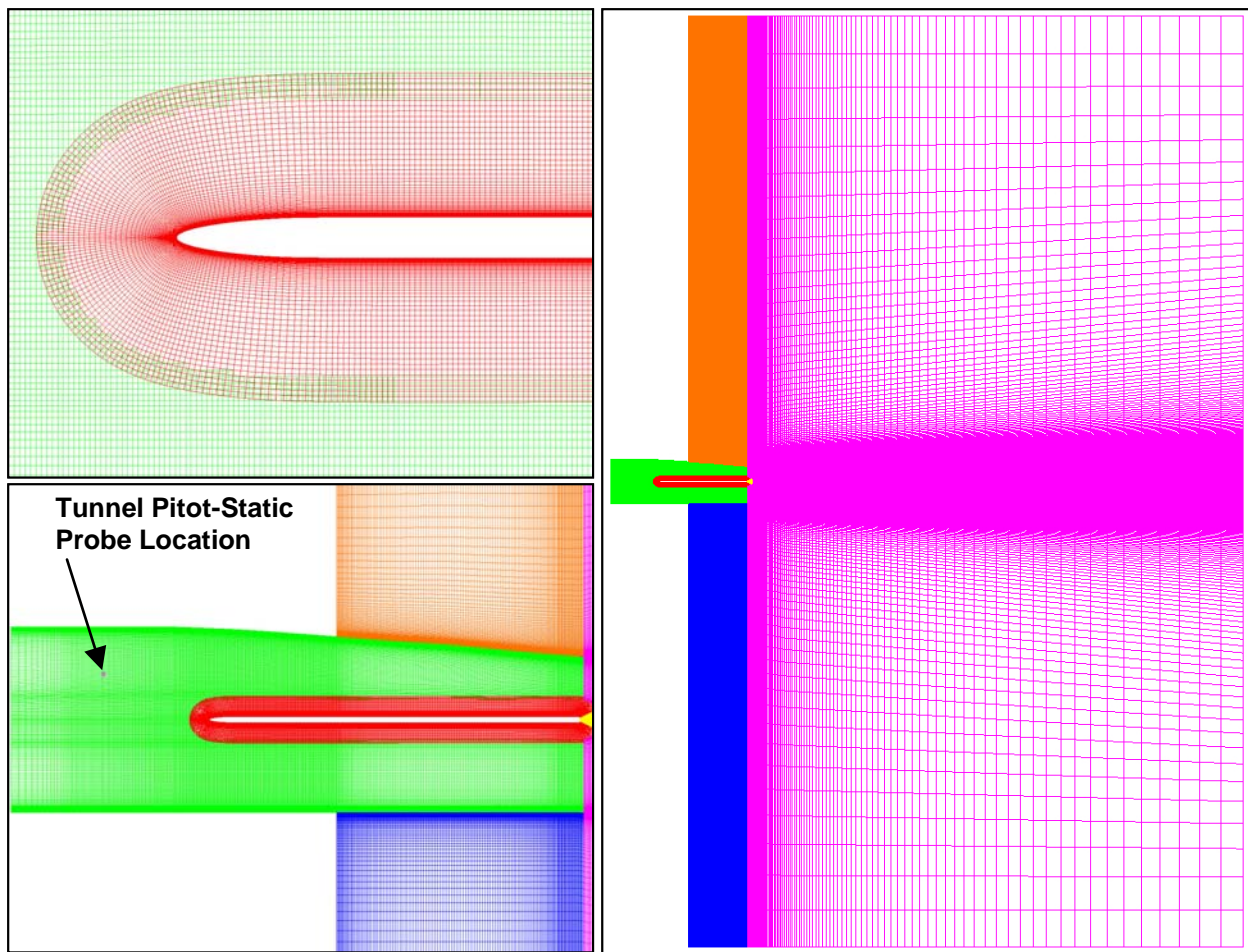


**Figure 400 Leading edge, test section, and complete 2-D grid for clean plate P6**

boundary conditions at the upstream end of the test section block will not produce the desired conditions at the probe location. Instead, the GCNS input Mach number was set to 0.001, the input static temperature was set to the experimental value, and the input Reynolds number was set to the experimental value divided by the experimental Mach number and multiplied by 0.001. An exhaust boundary condition with nozzle pressure and temperature ratios (local total to input static) of 1 were applied at the upstream surfaces of the plenum (orange and blue blocks) to simulate ambient pressure. Slip wall conditions were applied at the top and bottom of the plenum. Viscous turbulent walls were used on both the internal and external tunnel walls (red, orange, and blue blocks) except for the first nine cells, where slip walls were used to allow the flow to orient before encountering a boundary layer. An extrapolation condition was used on the downstream end of the pink plenum block. The nozzle temperature ratio applied at the test section upstream boundary was based on the experimental probe Mach number and static temperature. Isentropic relationships were assumed to determine the initial nozzle pressure ratio (NPR) applied at that same boundary. Runs were conducted assuming a fully turbulent boundary layer on the plate, and repeated with the driving NPR adjusted until the Mach number and temperature at the probe point were close to the desired values. The runs were repeated assuming laminar flow on both the plate upper and lower surfaces.

Each of those cases assumed steady flow and was run 6,000 iterations on 2 levels of grid sequencing, 6,000 iterations on 1 level of grid sequencing, then 10,000 iterations on the fine

mesh. Force convergence tended to exhibit damped oscillations, and some of the cases converged better than others. The comparison of the resultant values at the probe location to the wind tunnel values appears in Table 8. Results for selected cases with alternate transition locations are also included and will be revisited later.

The CFD pressure coefficients were renormalized from the GCNS input values to the values at the probe. Better correlation with experiment was obtained by referencing the CFD values at the probe location rather than to the experimental wind tunnel values. The CFD pressure coefficients were obtained using the following equation:

$$C_P \equiv (P - P_R)/q_R = (P/P_I)(P_I/q_R) - (P_R/q_R) = (P/P_I)\{P_I/[P_R^* M_R^{2*\gamma/2}]\} - \{1/(M_R^{2*\gamma/2})\}, \quad (14)$$

where the I subscript corresponds to the GCNS input values and the R subscript corresponds to the reference values at the probe location.  $P/P_I$  is the normalized static pressure PLOT3D function.  $P_I$  can be calculated from the GCNS input values for Mach number, static temperature, and unit Reynolds number.

**Table 8 Comparison of clean plate wind tunnel reference values to CFD with various transition**

Wall	Model	$Tr_{UP}$ (in)	$Tr_{LO}$ (in)	$M_R$	$T_R$ (R)	$P_R$ (psi)	$Re_R/in$	$Q_R$ (psi)
P2	WT			0.0254949	533.07	14.464486	14341.253	0.00658124
	TURB	0	0	0.0254432	533.07	14.498055	14310.431	0.00656979
	LAM	48	48	0.0257206	533.07	14.498009	14466.408	0.00671380
P3	WT			0.0254975	532.71	14.489049	14379.821	0.00659376
	TURB	0	0	0.0253914	532.71	14.501181	14296.814	0.00654447
	LAM	48	48	0.0256727	532.71	14.501021	14455.043	0.00669021
P0	WT			0.0255846	532.71	14.489049	14428.935	0.00663889
	TURB	0	0	0.0252943	532.71	14.524580	14265.122	0.00650500
	LAM	48	48	0.0256394	532.71	14.524464	14459.632	0.00668365
	TRAN9 /TRAN9	9	9	0.0259264	532.70	14.524377	14621.755	0.00683408
	LAM/TRAN9	48	9	0.0260861	532.71	14.524275	14711.362	0.00691848
P11	WT			0.0252087	533.07	14.518514	14233.694	0.00645834
	TURB	0	0	0.0251936	533.07	14.555159	14225.857	0.00646689
	LAM	48	48	0.0255039	533.07	14.555014	14400.928	0.00662711
P10	WT			0.0249225	533.07	14.550438	14102.818	0.00632641
	TURB	0	0	0.0249233	533.07	14.588187	14105.163	0.00634282
	LAM	48	48	0.0252257	533.07	14.588041	14276.161	0.00649803
P6	WT			0.0243840	533.07	14.557806	13804.942	0.00605904
	TURB	0	0	0.0243813	533.07	14.597324	13807.064	0.00607414
	LAM	48	48	0.0246463	533.07	14.597178	13956.993	0.00620684
	TRAN9/TRAN9	9	9	0.0247518	533.06	14.597033	14016.937	0.00626003
	LAM/TRAN9	48	9	0.0247727	533.06	14.597033	14028.772	0.00627060
P8	WT			0.0238748	533.25	14.555354	13508.590	0.00580765
	TURB	0	0	0.0238369	533.25	14.594361	13490.163	0.00580474
	LAM	48	48	0.0238715	533.25	14.597425	13512.581	0.00582282
	TRAN9 /TRAN9	9	9	0.0239572	533.25	14.597279	13560.956	0.00586465
	LAM/TRAN9	48	9	0.0240239	533.25	14.597279	13598.712	0.00589735

The Mach contours for the various tunnel wall geometries with turbulent flow on the plate are shown in Figure 401. Note how the acceleration around the plate leading edge shifts from the upper to the lower surface as the tunnel wall position changes from the P2 case to the P8 case. The plotting scale is truncated in a few cases to facilitate comparison. The peak Mach number for the P8 case was 0.053. The plate upper surface boundary layer is noticeably thicker for the adverse gradient cases (P2 & P3). Corresponding surface pressure coefficients for P2 and P3 are compared to the all laminar and wind tunnel values in Figures 402 and 403

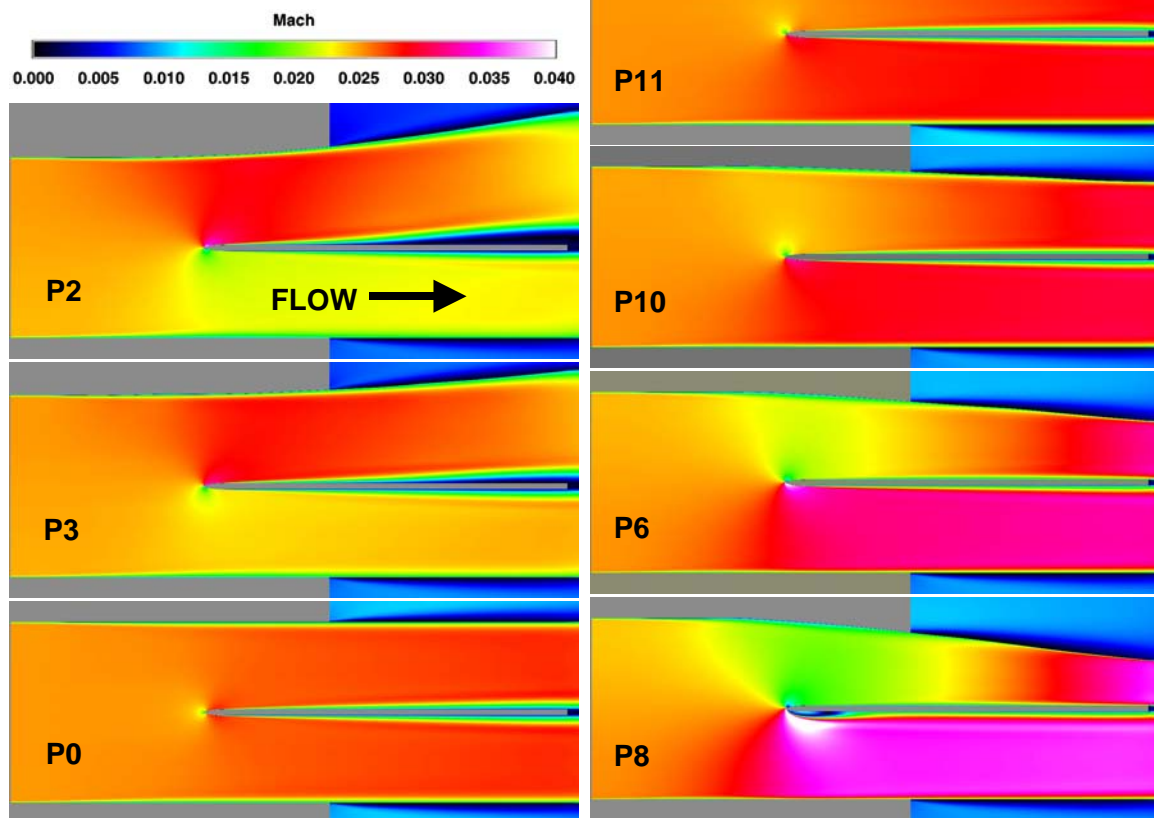


**Figure 401 Clean plate turbulent solutions used to select boundary conditions**

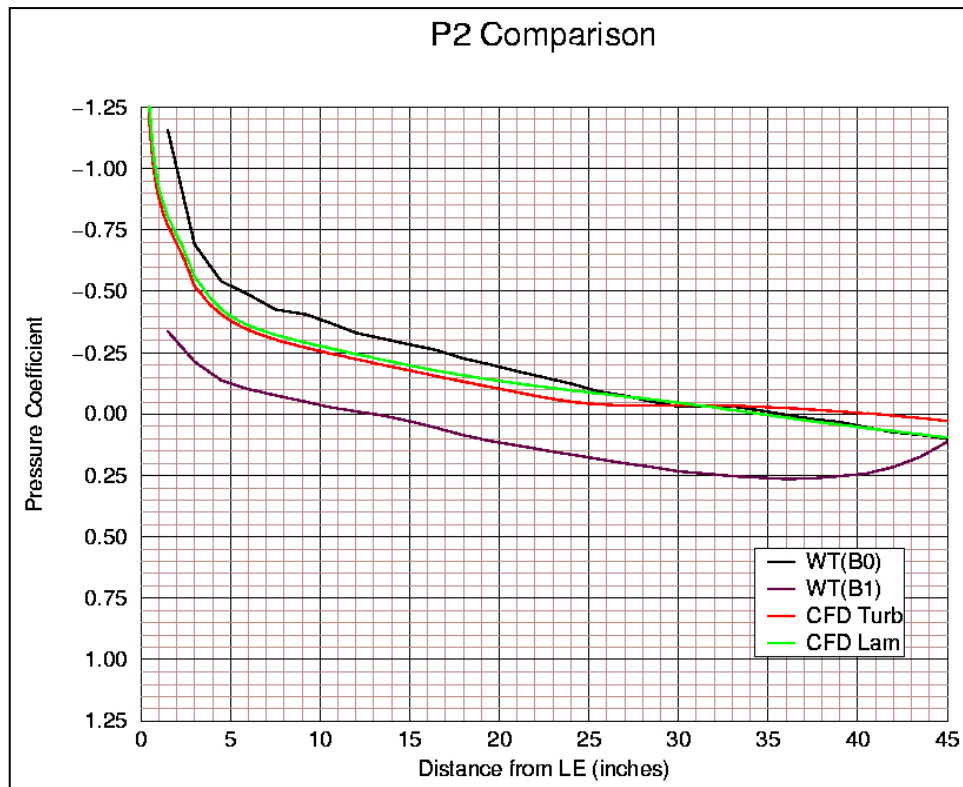


**Figure 402 P2 Wind tunnel, CFD turbulent and laminar  $C_p$**

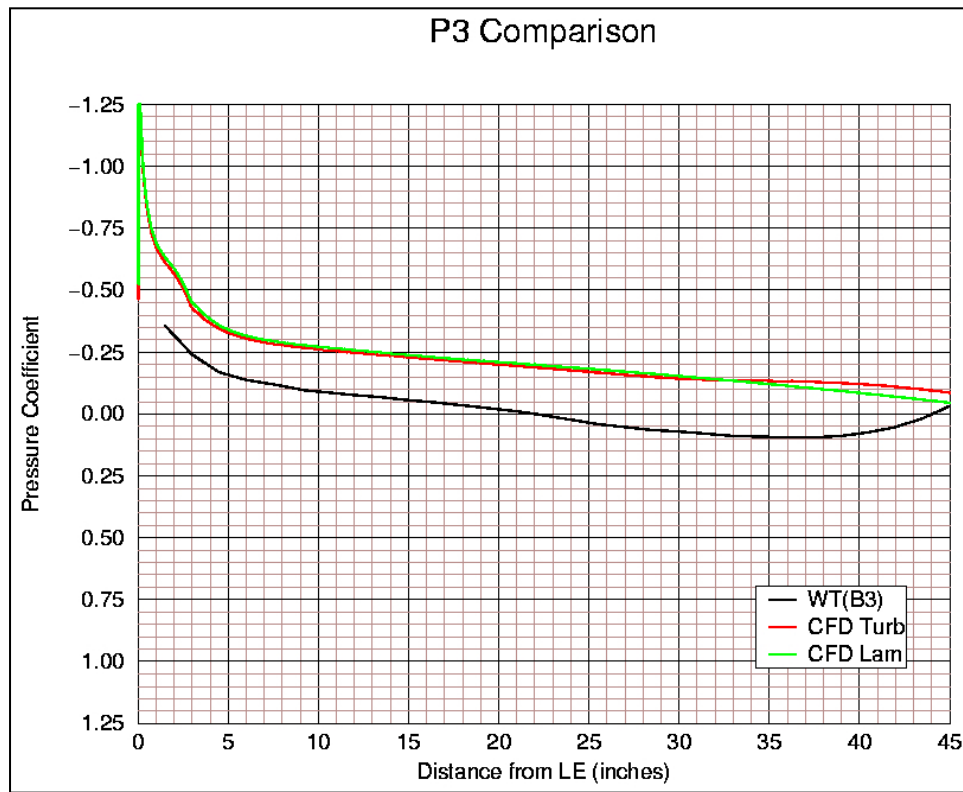


**Figure 403 P3 Wind tunnel, CFD turbulent and laminar  $C_p$**

For the P2 case, the black curve is the wind tunnel data for one run with no downstream blockage. The magenta curve is the nominal (averaged) wind tunnel data with a board (blockage 1) introduced at the upper wind tunnel wall trailing edge. Recall that the purpose of that modification was to alter the circulation and move the leading edge stagnation point because oil flows indicated that a leading edge separation bubble was preventing laminar flow downstream. The blocked configuration was used for P2 excrescence testing, but no matching CFD model was generated. Hence the fully laminar and fully turbulent CFD calculations are most comparable to the P2(B0) curve. The CFD gradients are generally flatter than the experimental values. The effect of alternate transition patterns was not investigated.

For the P3 case in Figure 403, the wind tunnel data are the nominal values with blockage 3. No data without blockage was available for a fair comparison with the CFD. The slopes are milder than for P2. The CFD gradients are generally similar to the experiment, but deviate more near the aft end.

Both the fully turbulent and fully laminar CFD clean plate boundary layers for the P2 geometry are compared in Figures 404 through 408 to determine whether GCNS also predicts a leading edge separation bubble. Figure 404 shows that the leading edge stagnation point is independent of the transition pattern with respect to the grid point distribution employed, although the vectors suggest it might be just a bit further downstream for the laminar case. Figure 405 shows a view of the first 0.13 inch of the plate, with very similar accelerated flow about the leading edge for either pattern. Figures 404 and 405 have identical length scales, but the vectors in the latter figure are one tenth as large to minimize overlap where the grid is clustered.



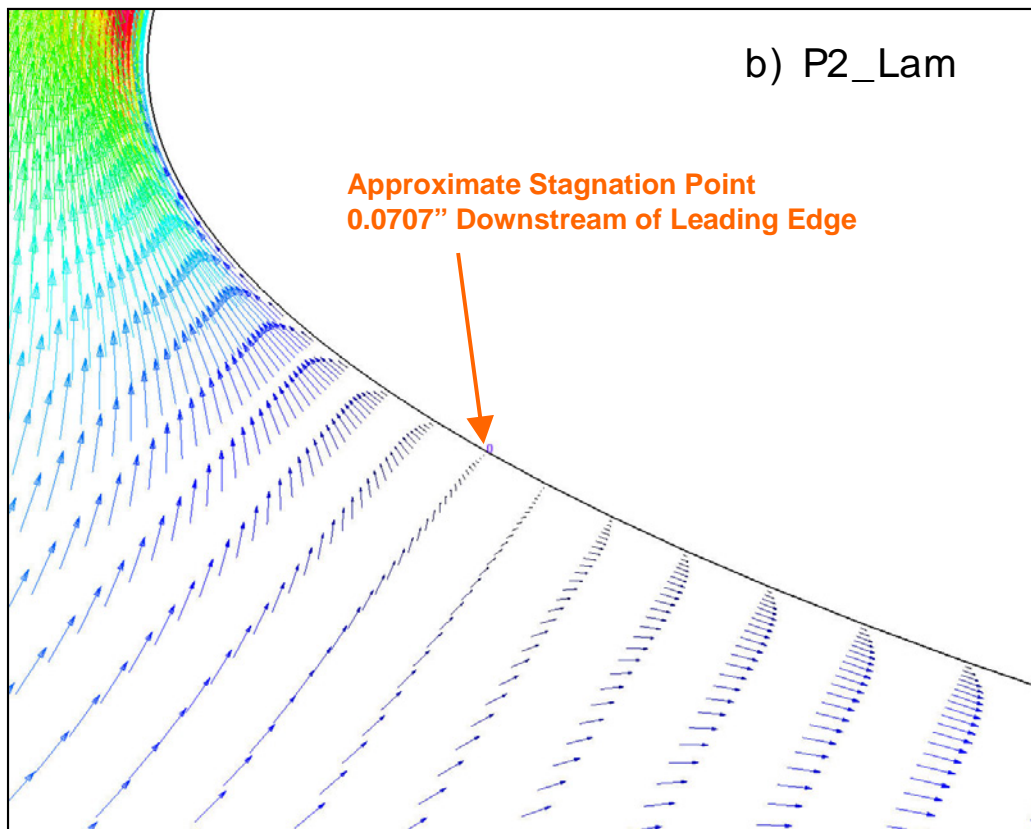
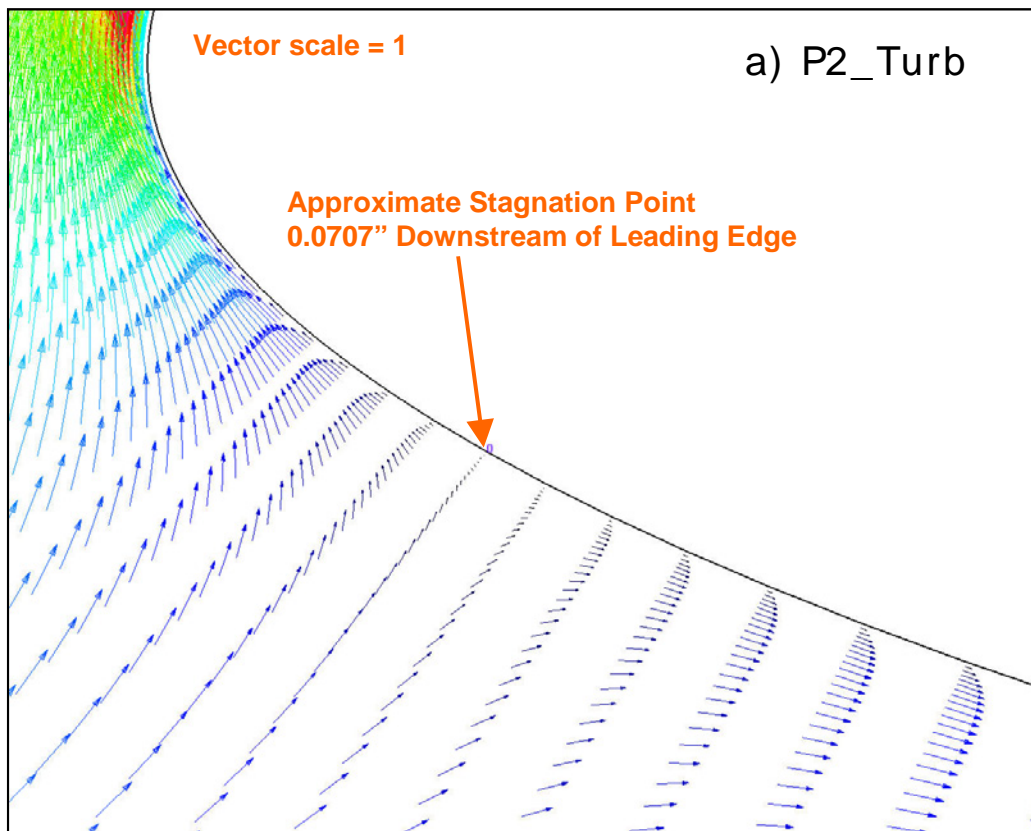
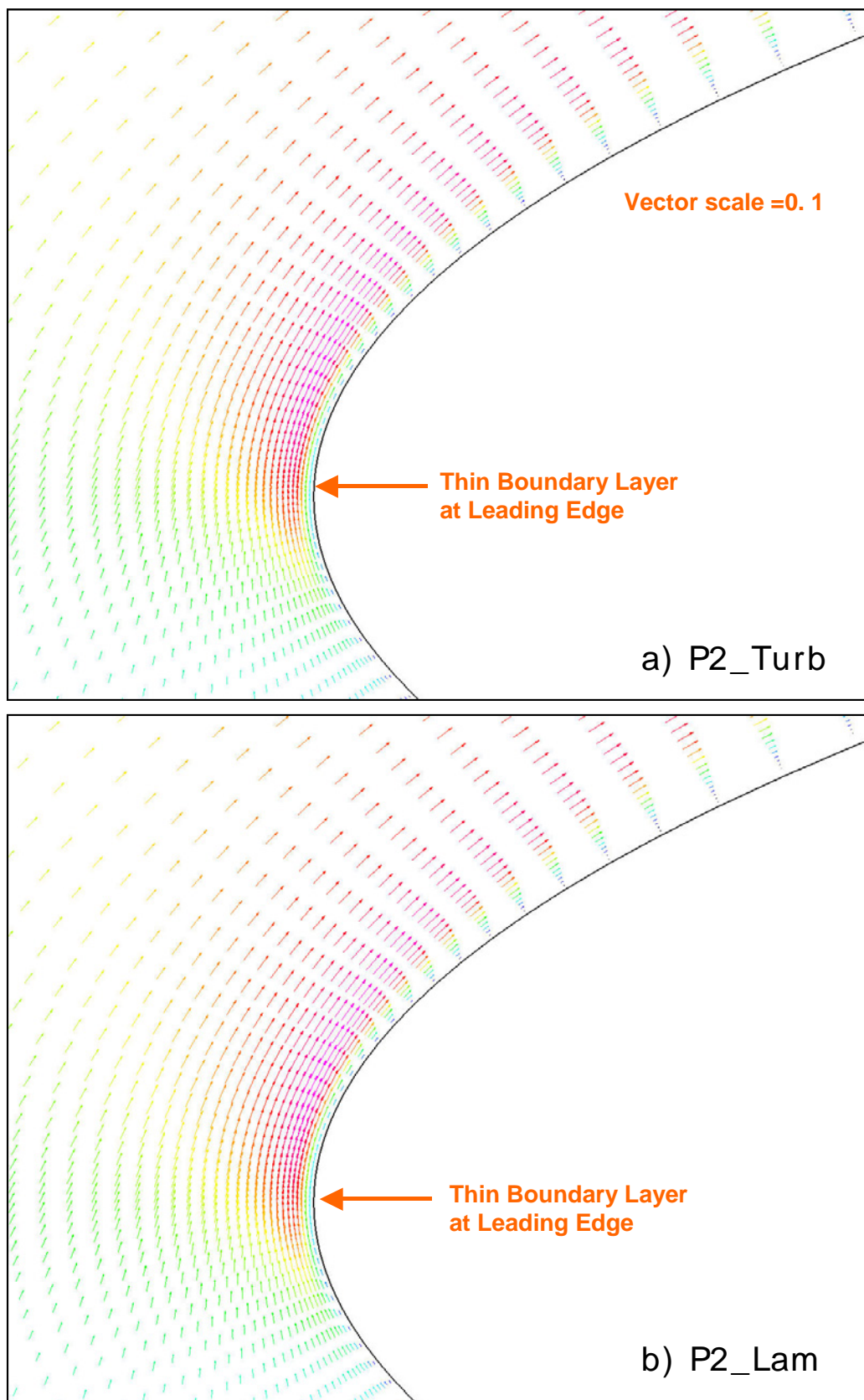


Figure 404 CFD P2 Fully turbulent and fully laminar stagnation point locations





**Figure 405 CFD P2 Fully turbulent and fully laminar leading edge vectors**

Figure 406 preserves both the original length and vector scale to accentuate any reversal of the boundary layer. Reversed flow is in fact evident on the first few grid cells off the plate surface 0.1705 inch downstream (along the plate major axis) from the leading edge.

Figure 407 is a view on the same scale that shows the upper surface from 0.1705 to 0.1946 inch from the leading edge. In this view, the reversed region is clearly thicker for the laminar case. This view almost captures the entire bubble (only about 0.002 inch high) for the turbulent case.

Different length and vector scales are employed in Figure 408 to illustrate the length of the bubble for each pattern. The bubble for the laminar case grew downstream to a maximum thickness of about 0.0147 inch (about 12 grid points). While the initial testing (i.e., without the wall board) of this configuration did not exhibit laminar flow downstream of the bubble as imposed in the GCNS solution, the CFD results do show the relative susceptibility of a laminar leading edge to bubble formation for this adverse pressure gradient case and are therefore qualitatively consistent with the experimental observations of the original configuration.

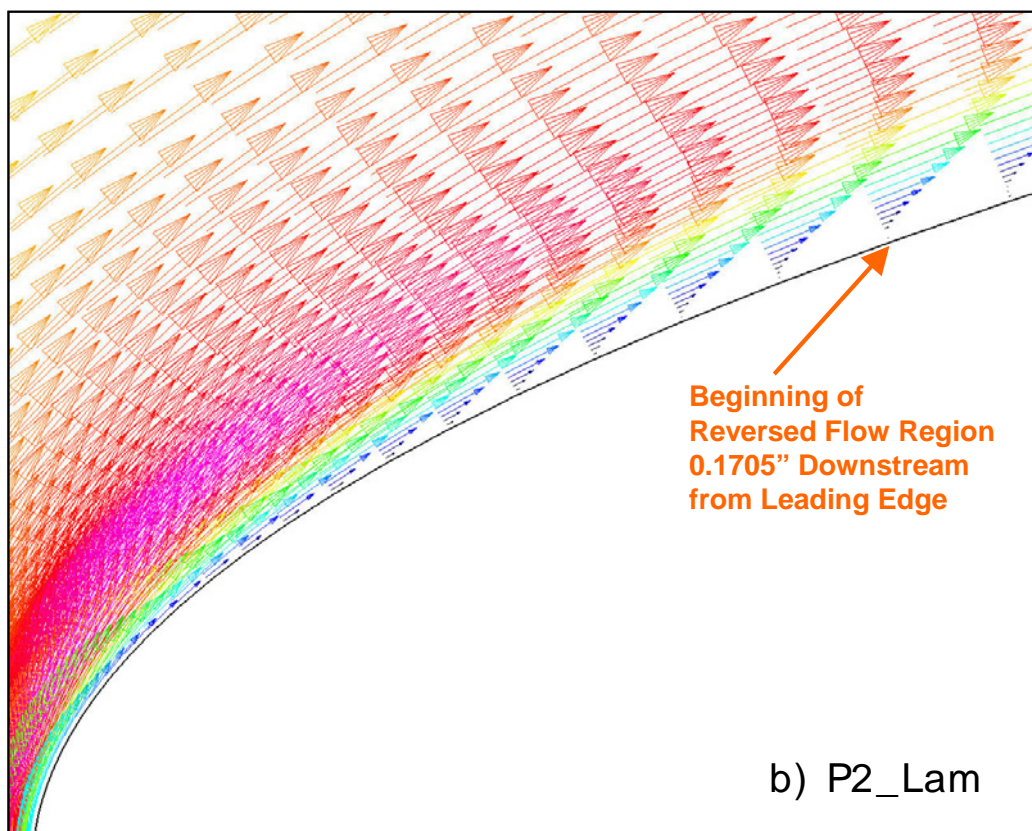
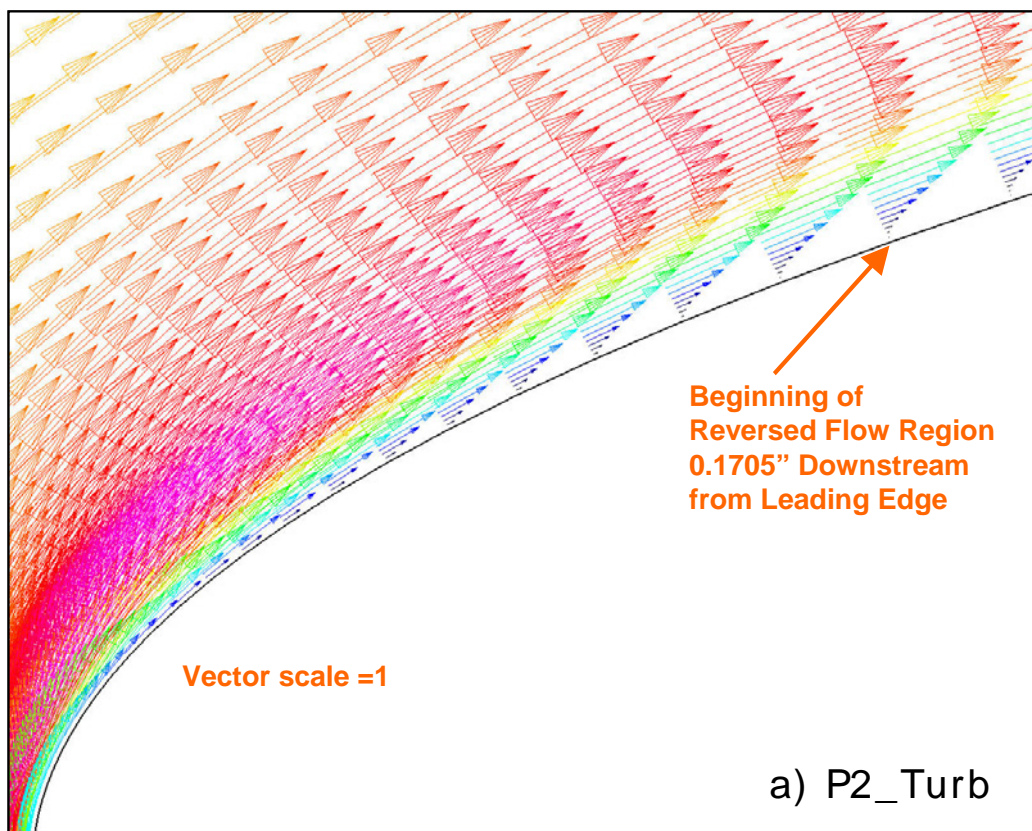


**Figure 406 CFD P2 Fully turbulent and fully laminar leading edge vectors**



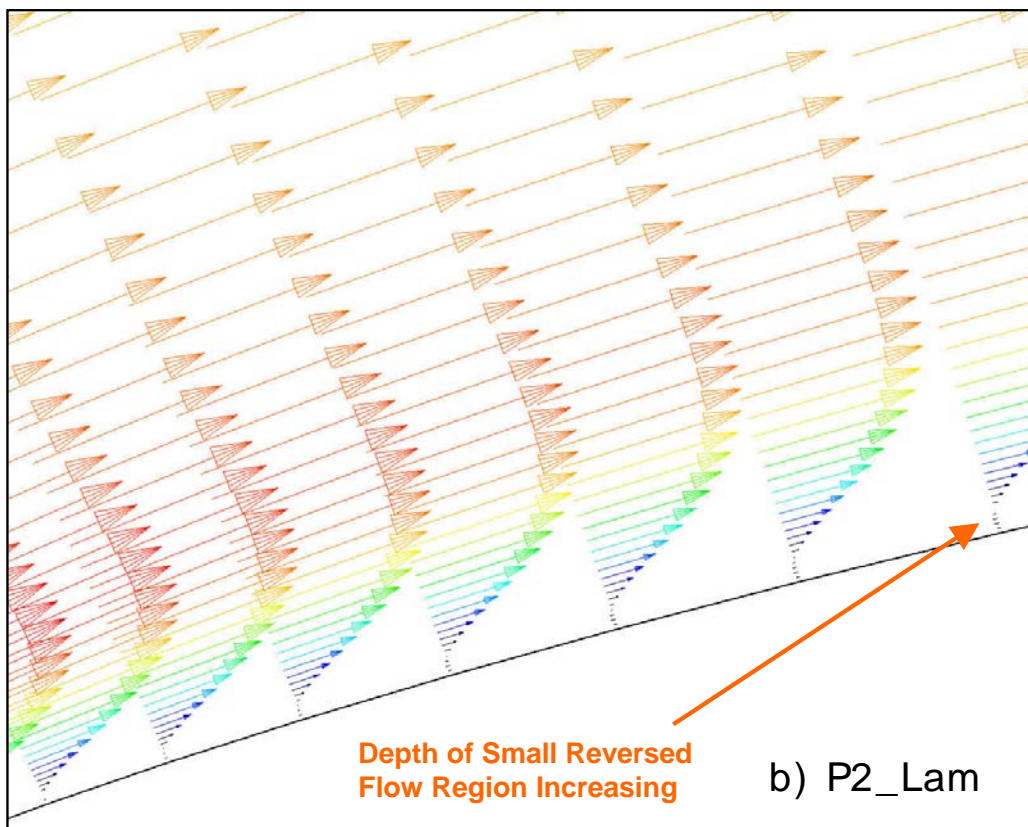
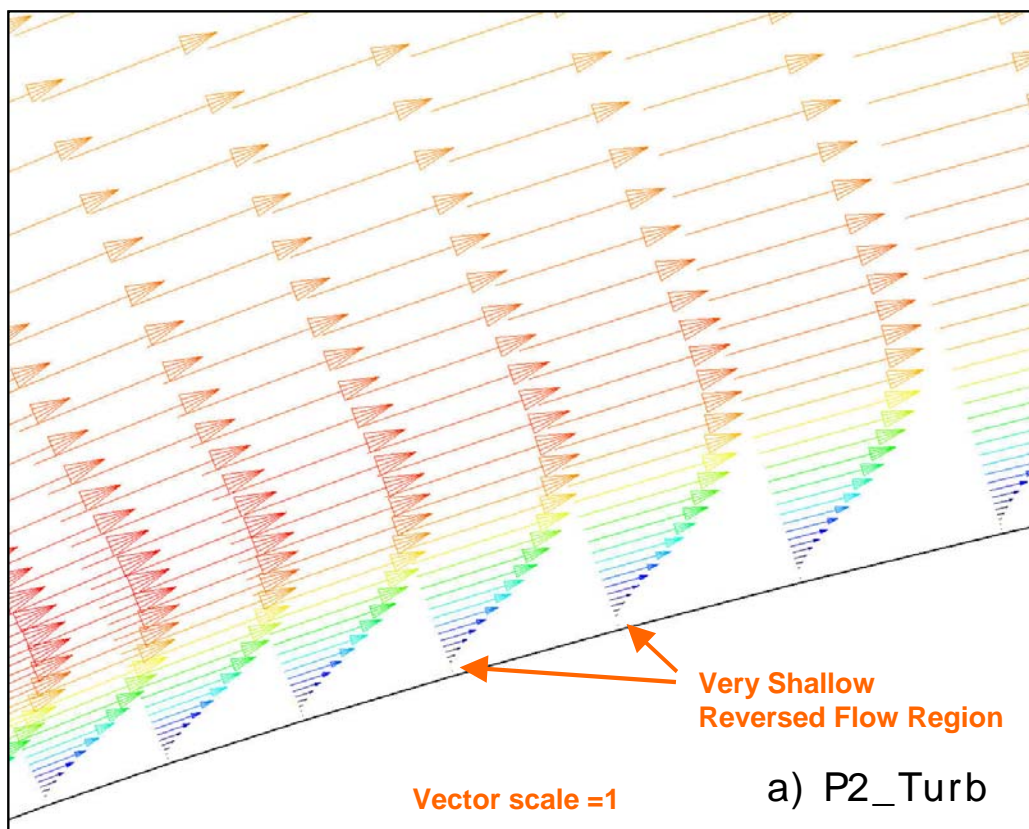


**Figure 407 CFD P2 Fully turbulent and fully laminar leading edge vectors**

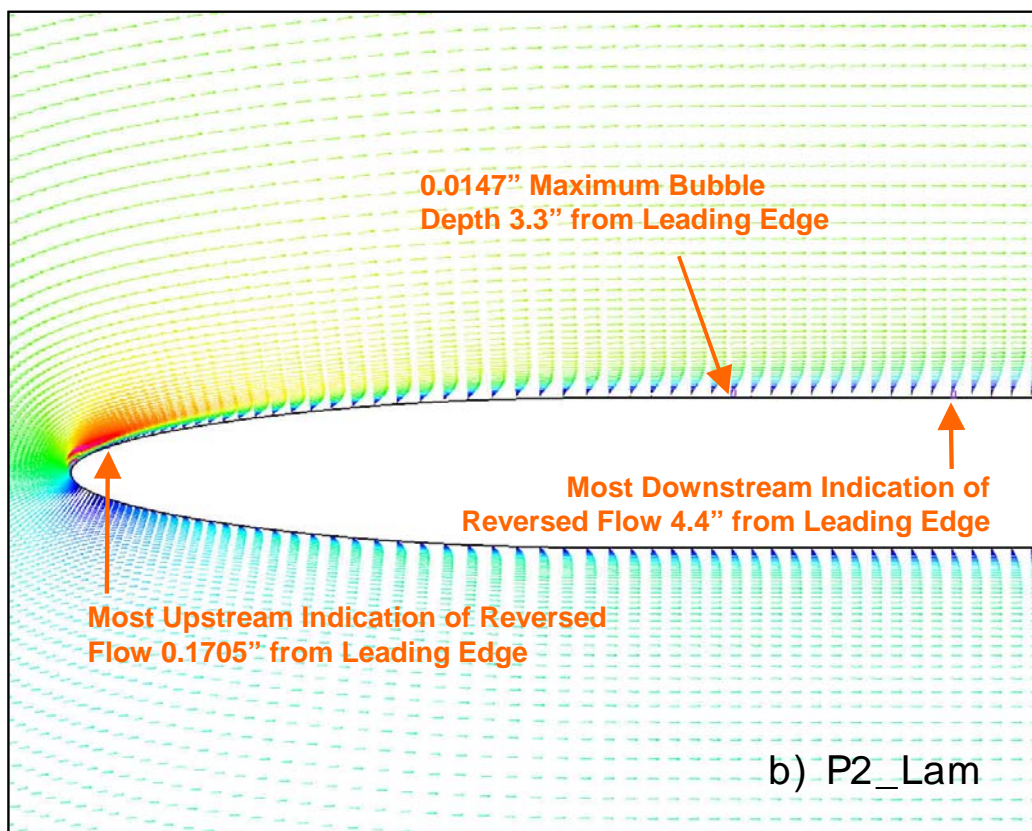
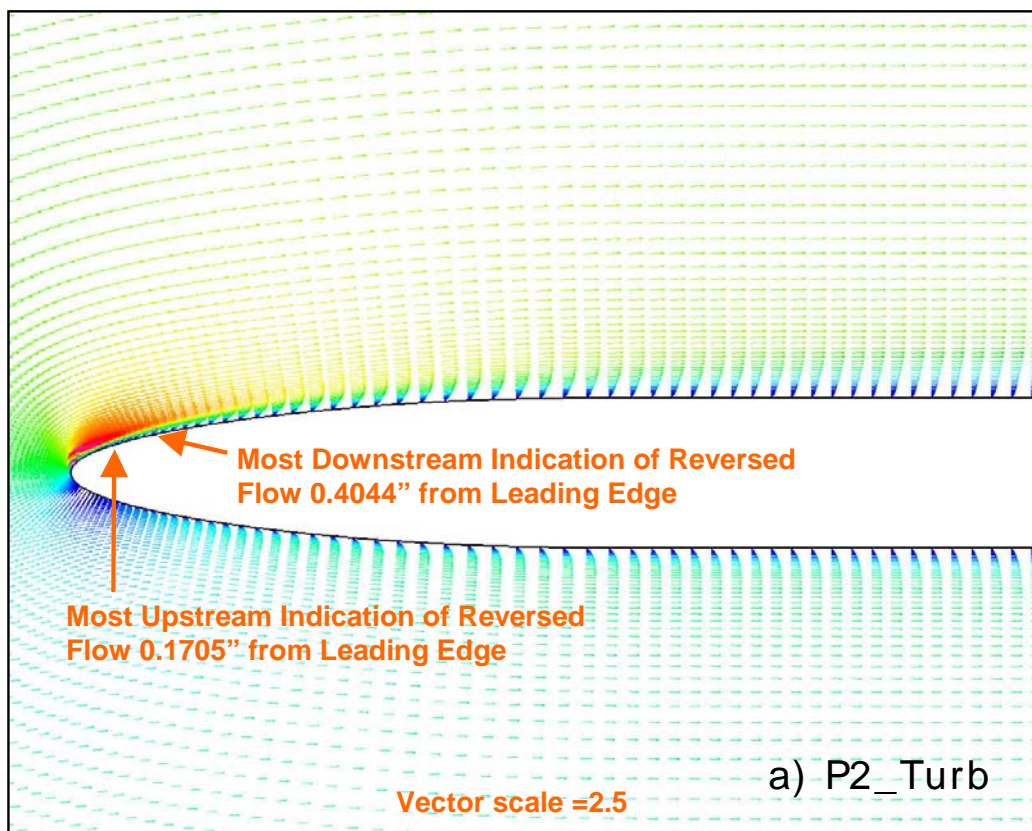


**Figure 408 CFD P2 Fully turbulent and fully laminar leading edge vectors**

No blockage was employed for the other wind tunnel wall geometries. Figure 409 shows a comparison for the undeflected wall case P0. The CFD values line up fairly well with the test values except near the leading edge. CFD results for a flat plate in free air at the test conditions were used as another check on the coefficient renormalization procedure, and are included here to illustrate the effect of the tunnel walls and their boundary layer on the gradient. A closeup of the same plot is shown in Figure 410 to facilitate comparison of the gradients. In this view, it is clear that the CFD gradients are steeper than the wind tunnel values.

In contrast, the CFD estimates are slightly offset for the mildly favorable upper surface gradient case P11, but the agreement in slope is much better (Figure 411). A similar comparison was obtained for case P10 (Figure 412), although the CFD gradient is flatter near the trailing edge. For case P6 (Figure 413) the offset between CFD and experiment is reduced but the downstream slope discrepancy persists. Finally, for P8 (Figure 414) the offset is again evident but the gradient agreement is somewhat better.

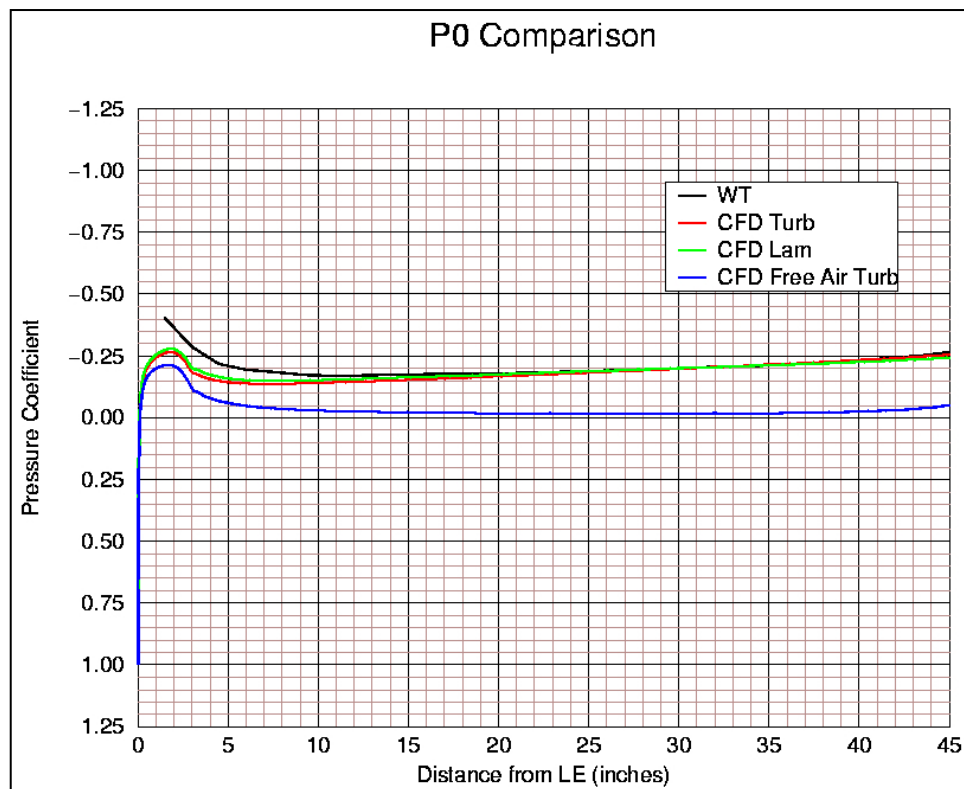
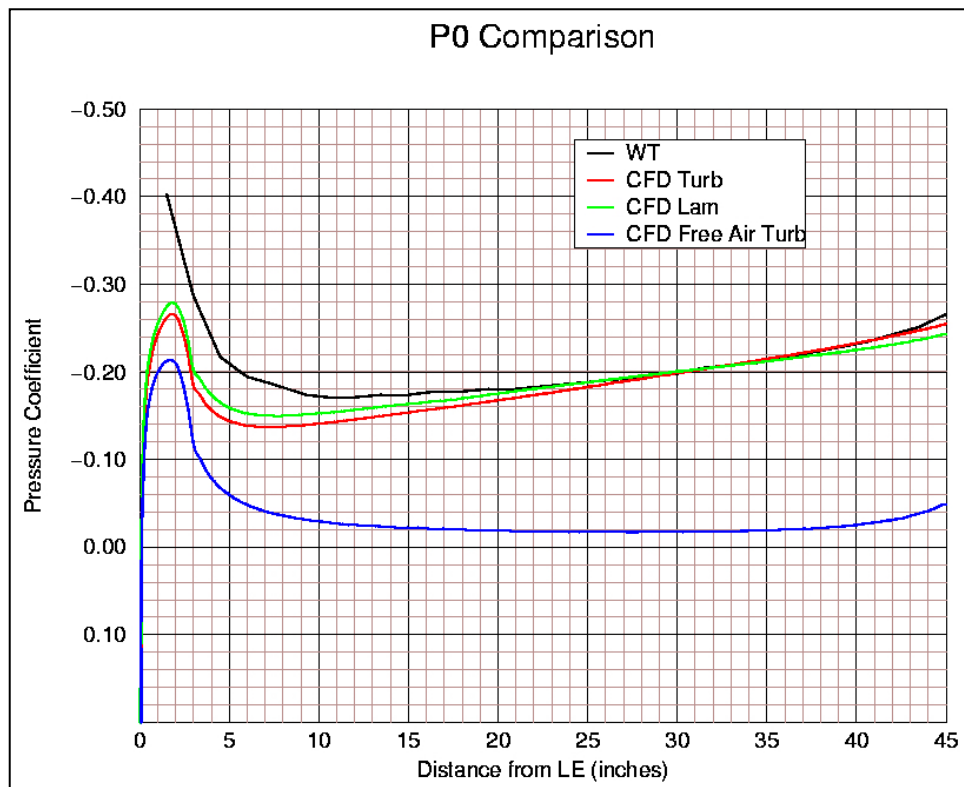
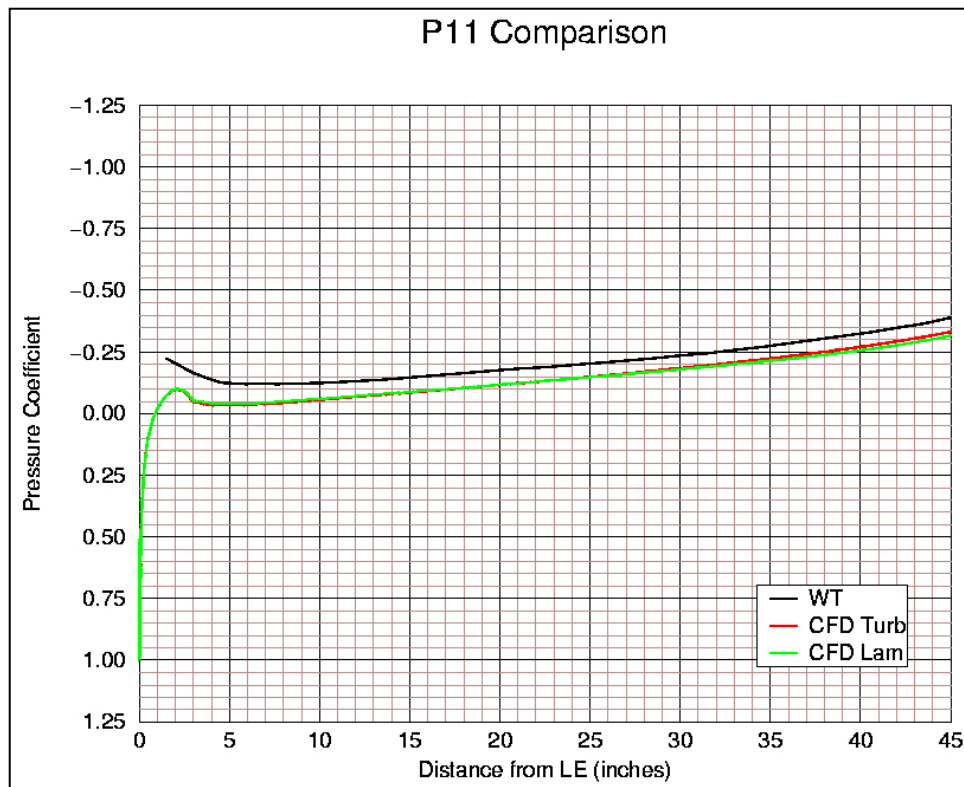


Figure 409 P0 Wind tunnel, CFD turbulent, and laminar  $C_p$





**Figure 410 P0 Wind tunnel, CFD turbulent, and laminar  $C_p$  (Finer Scale)**



**Figure 411 P11 Wind tunnel, CFD turbulent, and laminar  $C_p$**

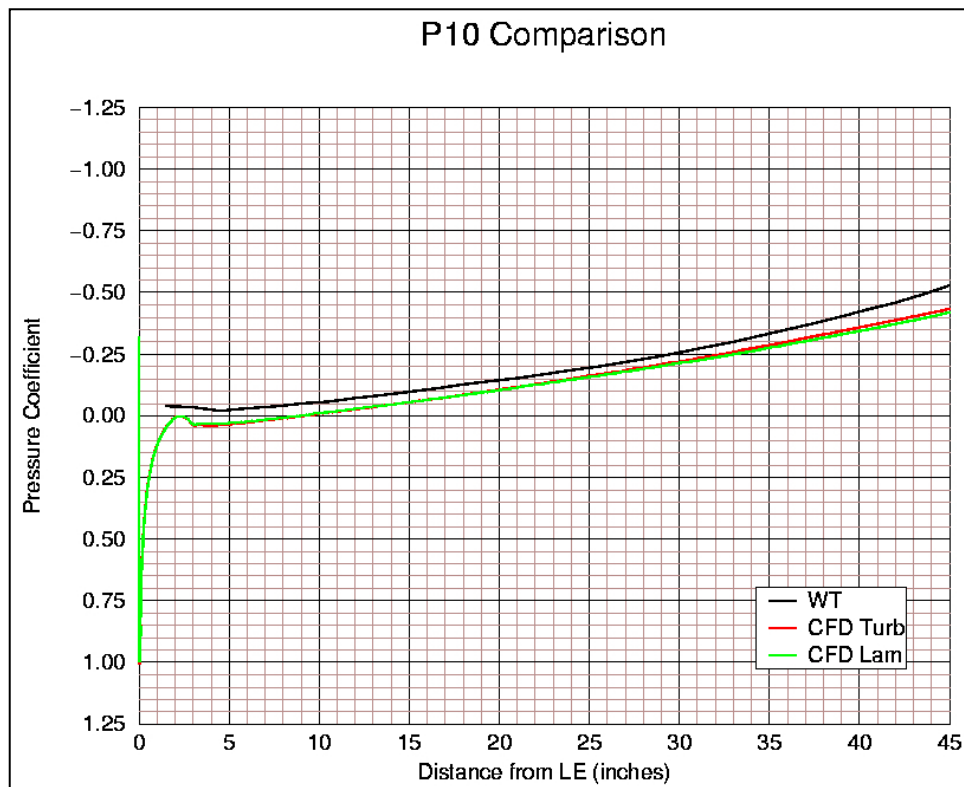


**Figure 412 P10 Wind tunnel, CFD turbulent, and laminar  $C_p$**

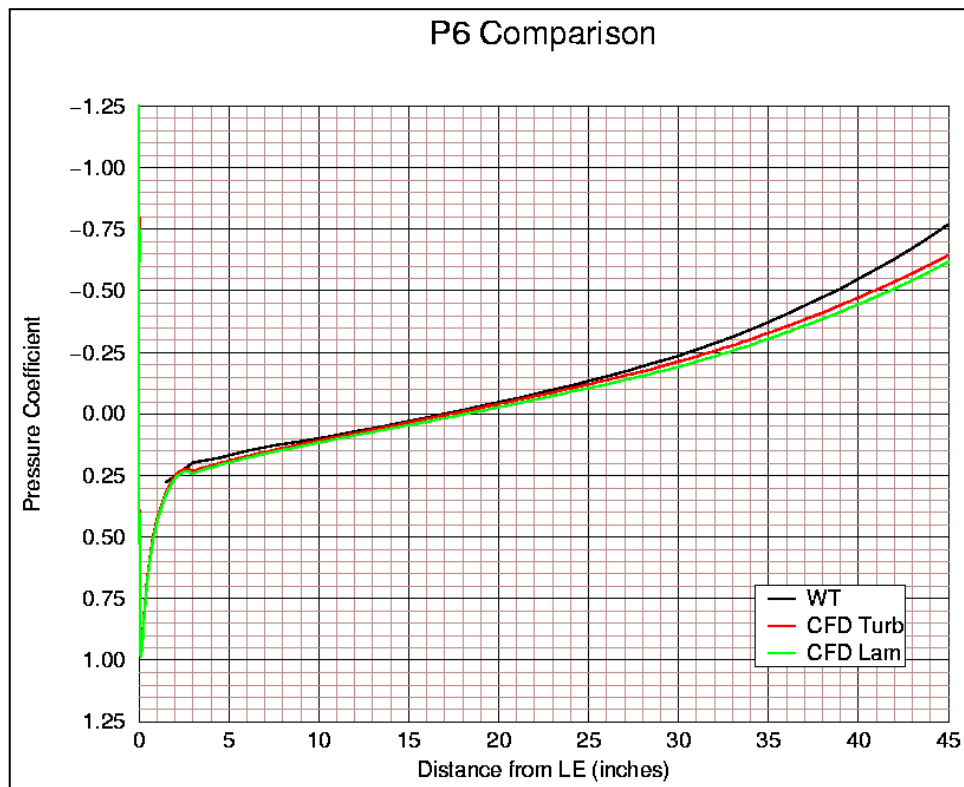


**Figure 413 P6 Wind tunnel, CFD turbulent, and laminar  $C_p$**



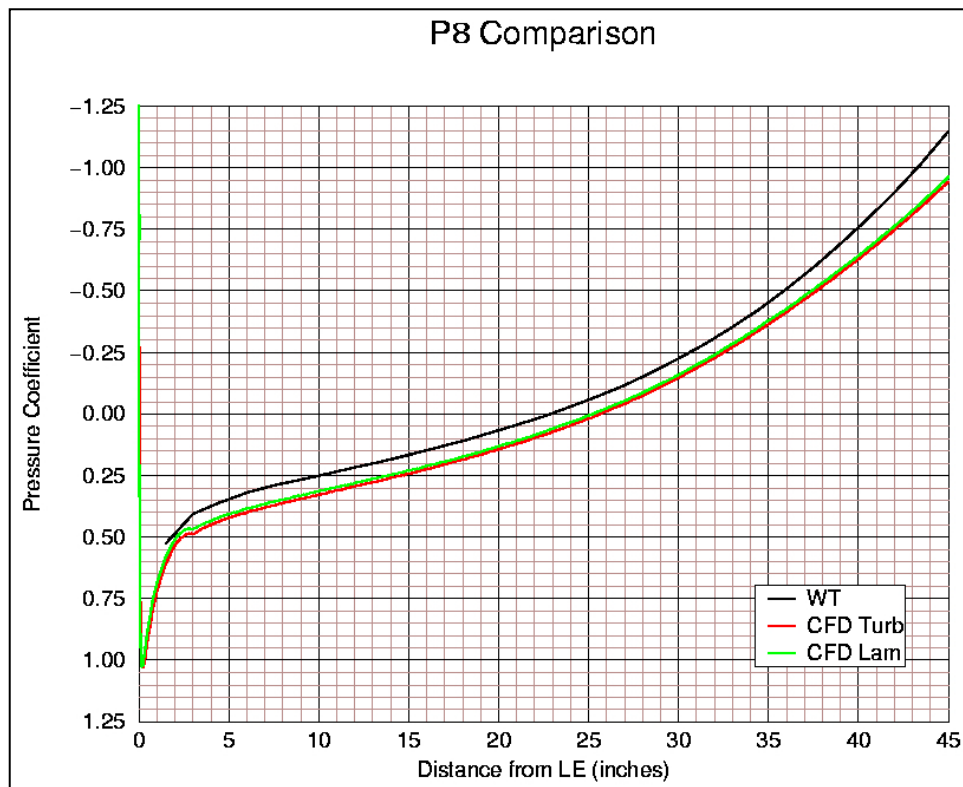


**Figure 414 P8 Wind tunnel, CFD turbulent, and laminar  $C_p$**

After reviewing these initial results, the decision was made to focus the computational study only on cases P0, P6, and P8 for subsequent runs with excrescences. It was deemed that these cases offered a reasonable comparison to test and the highest potential for identifying major differences in flow structures from which parametric correlations might be established.

First, these cases were re-run in the same manner with the established driving boundary conditions, but with transition 9 inches from the plate leading edge on the lower surface, and with the upper surface either laminar or with transition also at 9 inches from the leading edge. These cases are indicated as Lam/Tran9 or Tran9/Tran9, respectively.

The P8 solution was examined after performing the same number of iterations as before assuming steady flow. A rather large separation bubble was evident on the lower leading edge surface as shown in the left hand side of Figure 415. Oscillations persisted in the drag convergence. The solution was run an additional 6,000 iterations in pseudotime accurate mode, which limits the time step in larger grid cells to a constant but allows the solution in the boundary layer to proceed as under the steady flow assumption. This technique is often used to help determine whether oscillations in the steady convergence are an indication of significant unsteadiness or a numerical artifact. In this case, this approach damped out the oscillations in the drag convergence. The right hand side of Figure 415 shows how the bubble moved aft and increased in thickness for the converged solution. The presence of this bubble was experimentally confirmed later. Figure 416 shows how the offset from the wind tunnel data was reduced with the additional iterations, but the flatter aft gradient remained. The same iteration approach was executed for the P8 case with transition 9 inches from the leading edge on both the

upper and lower surfaces. The updated results are collected in Figure 417, normalized by the probe values listed in Table 8.

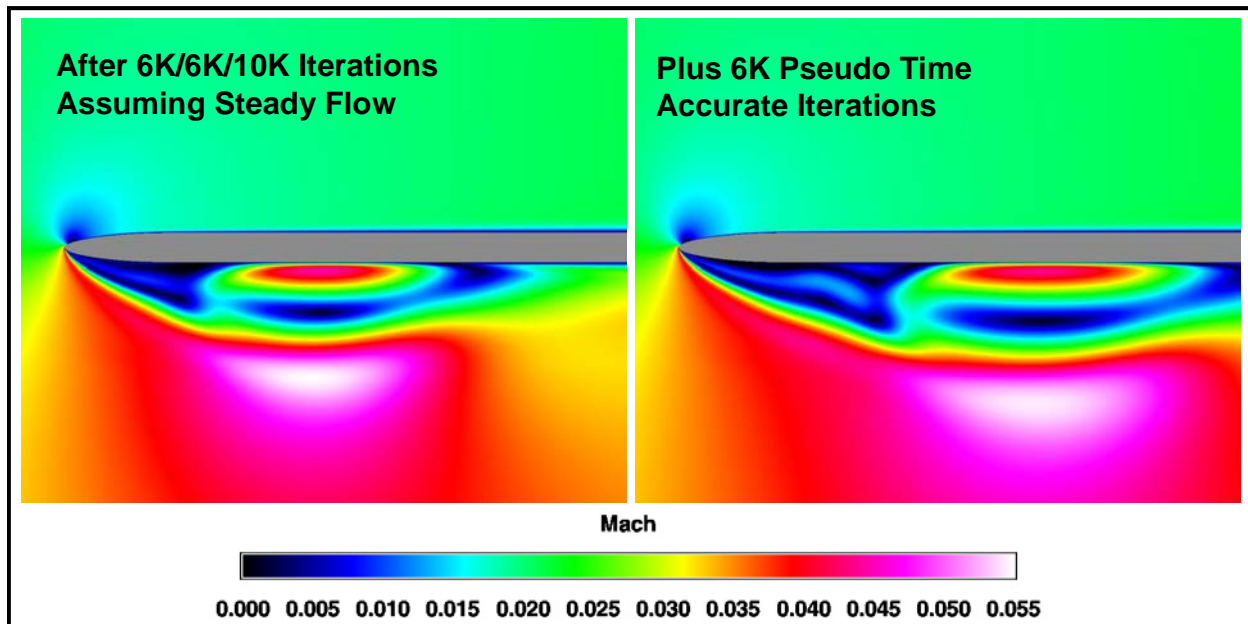


Figure 415 Movement of P8 lam/tran9 leading edge separation bubble in CFD solution

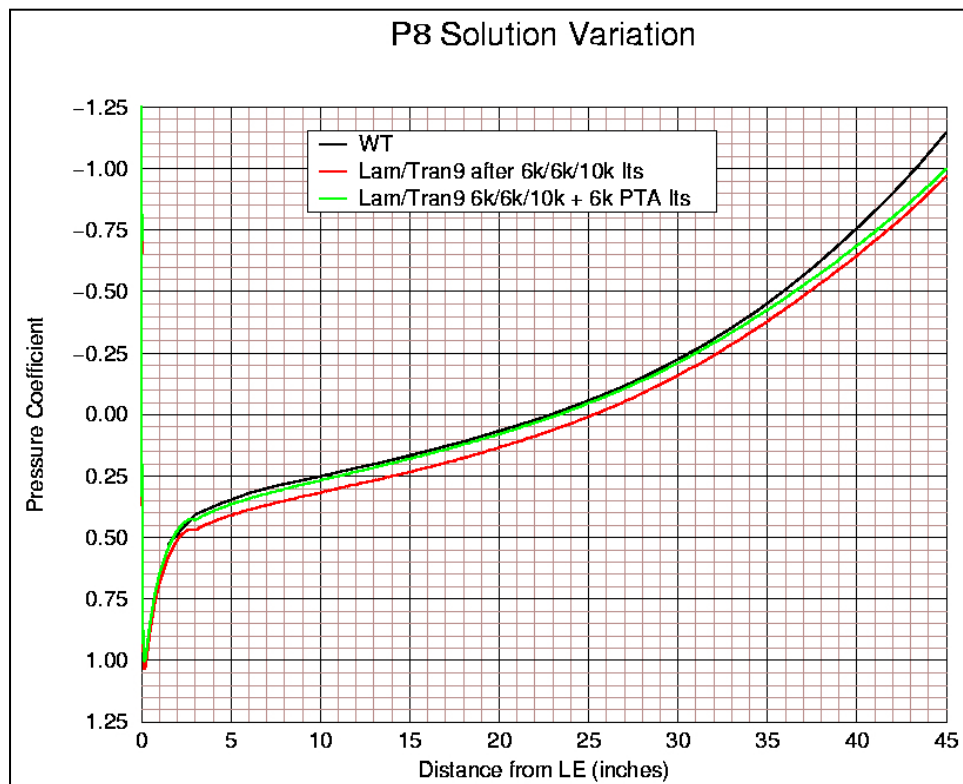
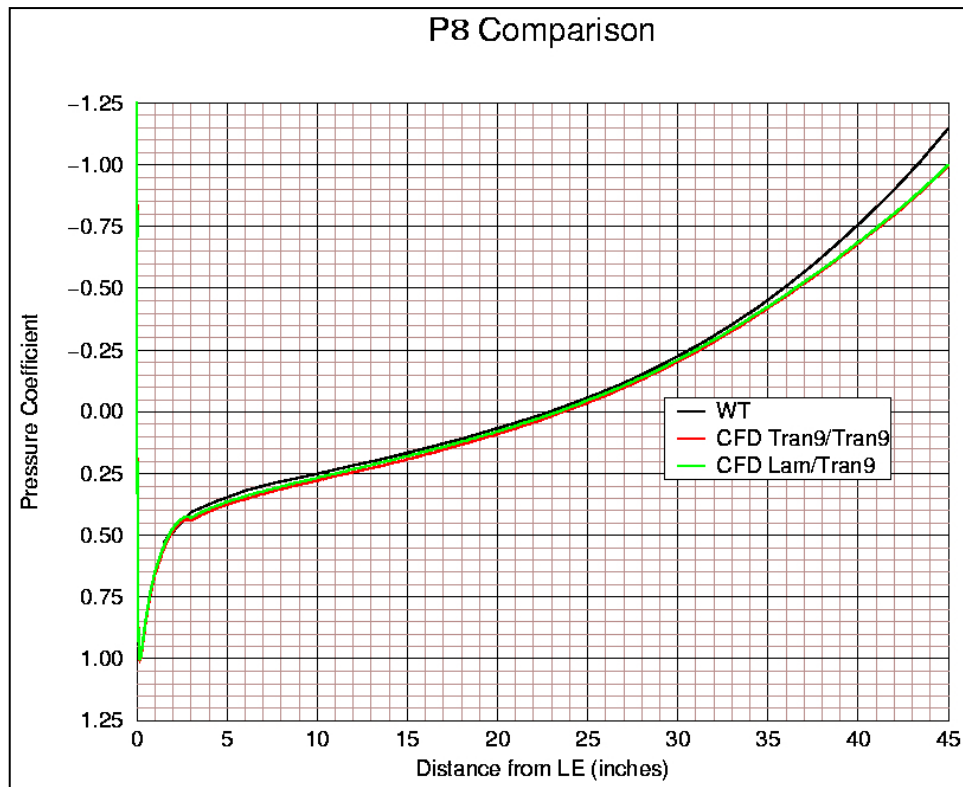


Figure 416 Variation of P8 CFD surface  $C_p$  with additional pseudotime accurate iterations



**Figure 417 P8 Wind tunnel, CFD transition at 9 inches on lower only and on both upper and lower**

For the P6 case with the new transition locations, the same number of steady iterations were performed followed by 8,000 pseudotime accurate iterations to obtain convergence. A comparison of Figures 413 and 418 show how the combination of the alternate transition patterns and additional iterations introduced a slight offset from the test data.

The same number of steady iterations were followed by 10,000 pseudotime accurate iterations for the P0 cases with the alternate transition locations. Compared to the earlier results for fully laminar or fully turbulent flow in Figures 409 and 410, the CFD results are now offset from the test data but the gradients are much more consistent. The force convergence for this case exhibited a tendency to drift, and running additional iterations (up to 70,000 more) did not improve correlation.

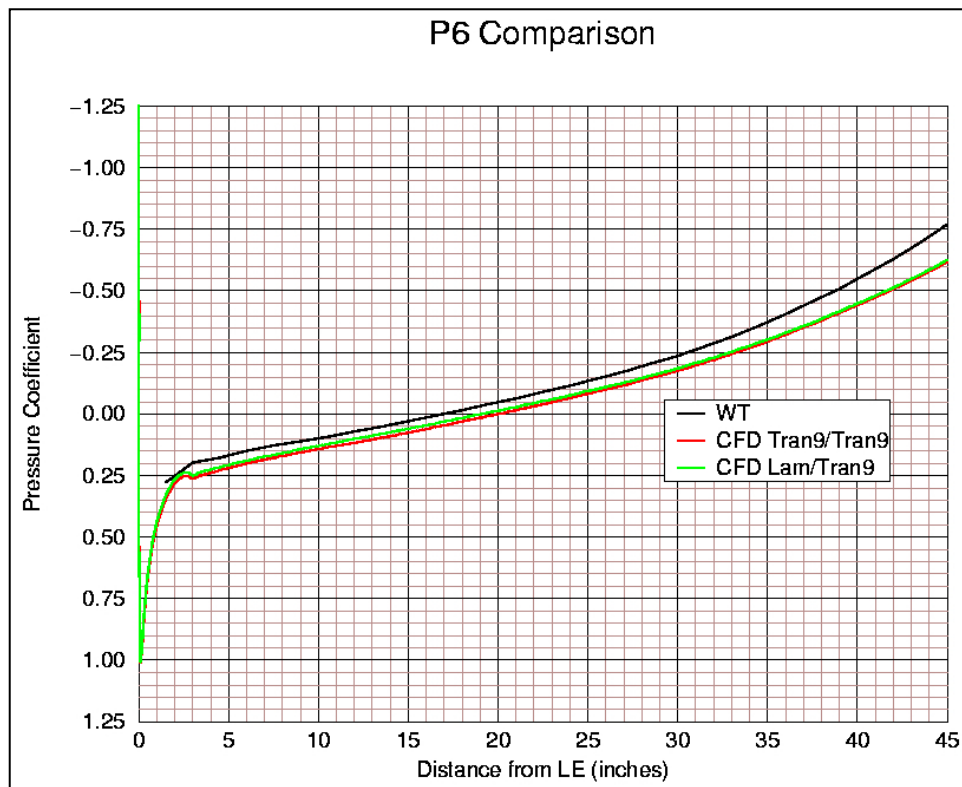


**Figure 418 P6 Wind tunnel, CFD transition at 9 inches on lower only and on both upper and lower**

Running the additional iterations for these cases consistently resulted in slightly faster calculated flow at the reference probe location, but the differences were not large enough to justify another round of iterations on the driving boundary conditions. These reference values are included with those for the shorter fully laminar and fully turbulent runs in Figure 410

The P0, P6, and P8 results for the Lam/Tran9 and Tran9/Tran9 transition patterns were used as the CFD baselines for assessing the impact of excrescences.

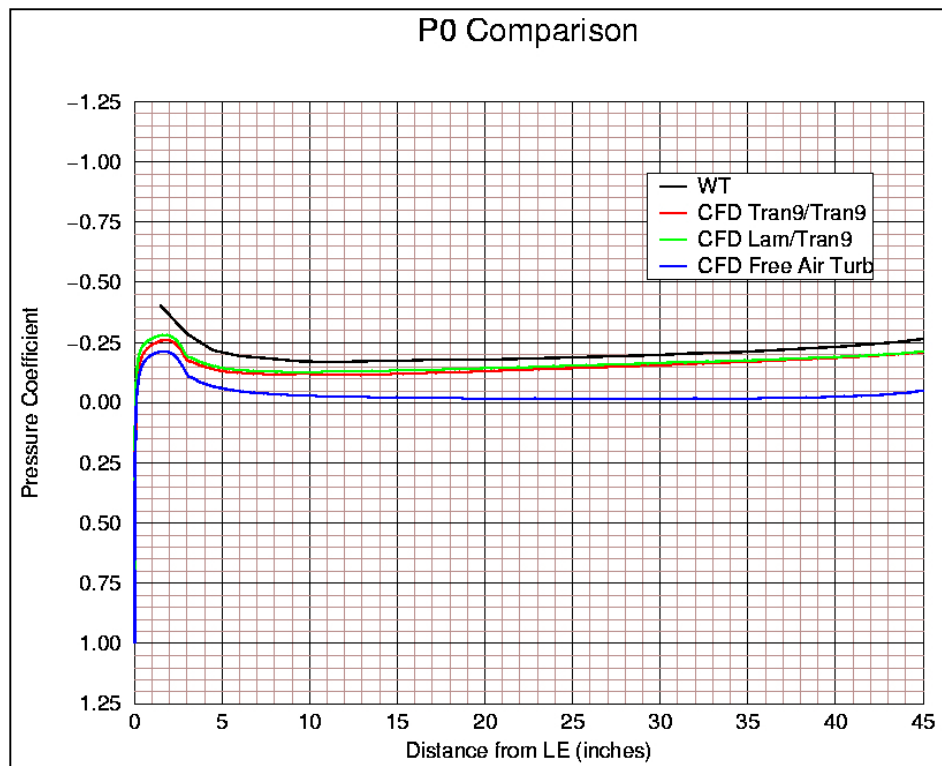


**Figure 419 P0 Wind tunnel, CFD transition at 9 inches on lower only and on both upper and lower**

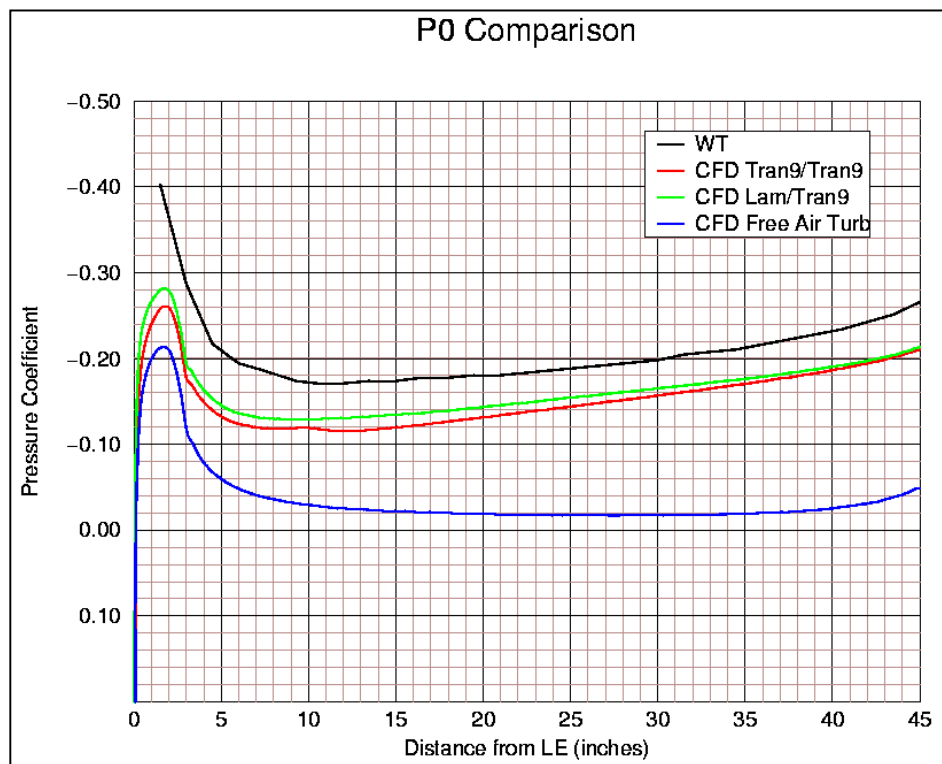


**Figure 420 P0 Wind tunnel, CFD transition at 9 inches on lower only and on both upper and lower (fine scale)**

### 3.2 CFD Modeling of Plate with Excrescences

With CFD runs for the clean flat plate completed, overset grid blocks were introduced with the excrescences so changes in the boundary layer character could be assessed and potentially correlated to the experimentally observed transition locations. These CFD runs for each wall geometry were conducted using the same input values and driving boundary conditions as the cases in Section 3.1. They were ran in the same manner and for the same number of iterations as the final runs (i.e., including the pseudo-time accurate iterations). The excrescences modeled were forward and aft facing steps, with a 0.25-inch-long flat step top blended into the clean flat plate upper surface by a 1.75-inch-long sinusoid. Lower surface transition was imposed via boundary condition at 9 inches from the leading edge for all cases. Upper surface transition was imposed at the closest grid point to the experimentally observed values listed in Table 9. These settings were within 0.21 inch from the desired values. Run times ranged from 7 ½ to 9 ½ hours on 2 SGI Origin 300 (600 MHz) processors for the 7 block 811,353 point grids.

**Table 9. CFD Case identification, step heights, and upper Surface transition location**

Case I.D.	Pressure Gradient	Insert	Step Direction	Step Location* (in)	Step Height (in)	Upper Transition* (in)
P0bfwd020	P0	b	fwd	8	0.020	43
P0bfwd035	P0	b	fwd	8	0.035	39
P6bfwd045	P6	b	fwd	8	0.045	43
P6bfwd060	P6	b	fwd	8	0.060	36
P8bfwd015	P8	b	fwd	8	0.015	40
P8bfwd035	P8	b	fwd	8	0.035	30
P0cfwd020	P0	c	fwd	11	0.020	41
P0cfwd035	P0	c	fwd	11	0.035	35
P6cfwd045	P6	c	fwd	11	0.045	46
P6cfwd060	P6	c	fwd	11	0.060	42
P8cfwd015	P8	c	fwd	11	0.015	40
P8cfwd035	P8	c	fwd	11	0.035	30
P6caft045	P6	c	aft	13	0.045	42
P6caft060	P6	c	aft	13	0.060	32
P0daft020	P0	d	aft	16	0.020	38
P0daft035	P0	d	aft	16	0.035	31

\* Measured from plate leading edge

Plots of velocity vectors colored by normalized velocity were generated for the clean plate and the steps. Here the reference velocity is based on the GCNS input conditions (not the value at the probe), which vary slightly for each wind tunnel wall setting, but are within 0.05 percent of 1.131275 feet/second.

First, the effect of the pressure gradient on a laminar nominal plate upper surface boundary layer is illustrated at each of the four step locations prior to step introduction in Figures 421 through 424. The view designations correspond to distances from the plate leading edge. The scale is the preserved for all vector plots in this section, so it is shown only once. These plots consistently

illustrate the fuller boundary layer profiles associated with increasingly favorable gradients. With the exception of the most downstream station, they also illustrate the reduction in the view's top edge velocity with increasingly favorable gradients. Consistent with the degree of change in pressure gradient between the three cases, the differences between profiles for P6 and P8 are more difficult to distinguish than between P0 and P6. For a given gradient, the top edge velocity also decreases with increasing distance from the leading edge as the boundary layer thickens.

The effect of the pressure gradient on a turbulent nominal plate upper surface boundary layer is shown at the most downstream step location in Figure 425. The differences with gradient are slightly more difficult to identify than for the laminar case in Figure 424.

For each pressure gradient and step location, plots are grouped to compare profiles for the clean upper surface with laminar flow and transition 9 inches from the plate leading edge, and profiles for two step heights with their associated downstream transition locations.

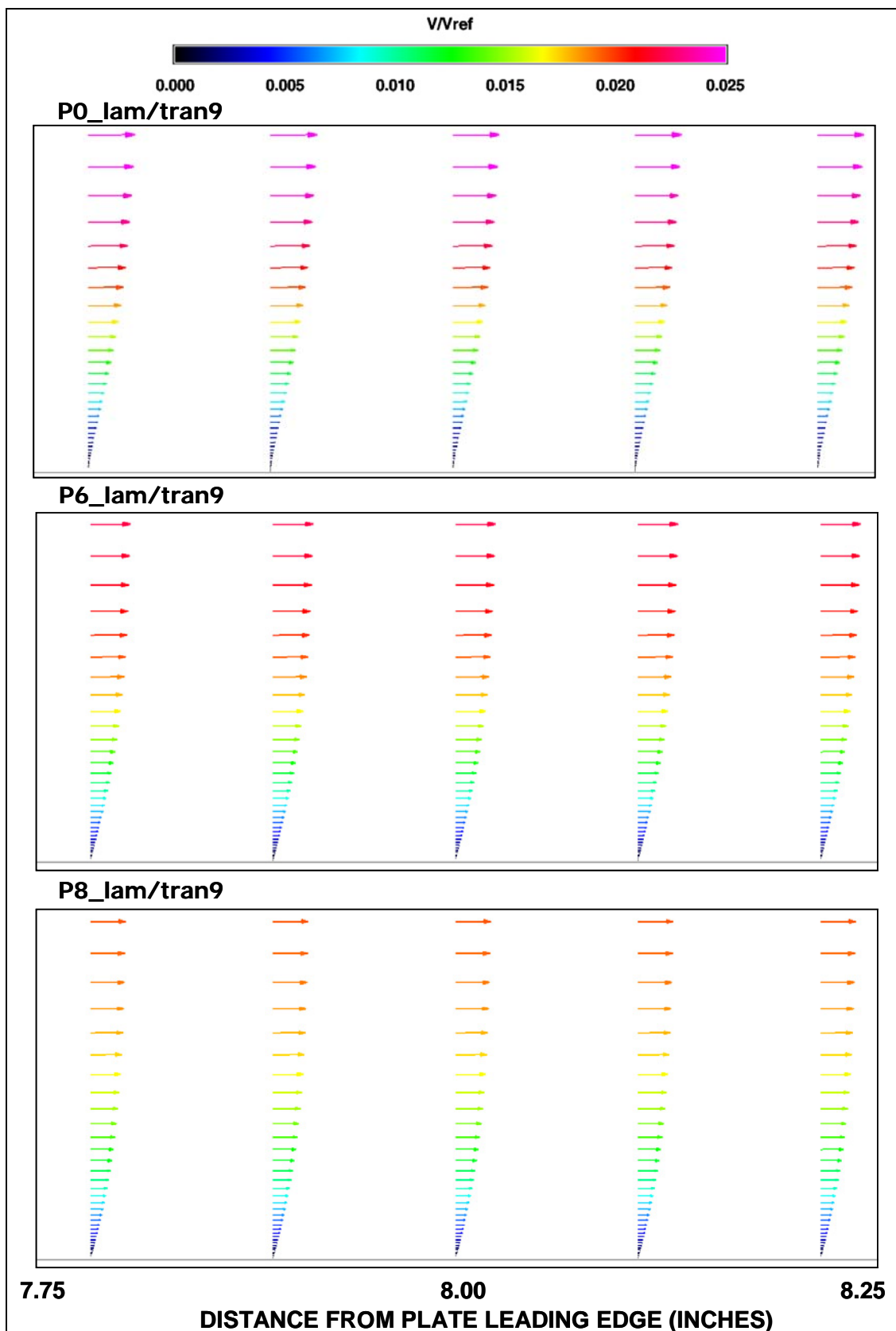


**Figure 421 Variation of clean laminar upper surface profiles with pressure gradient (view BFWD)**



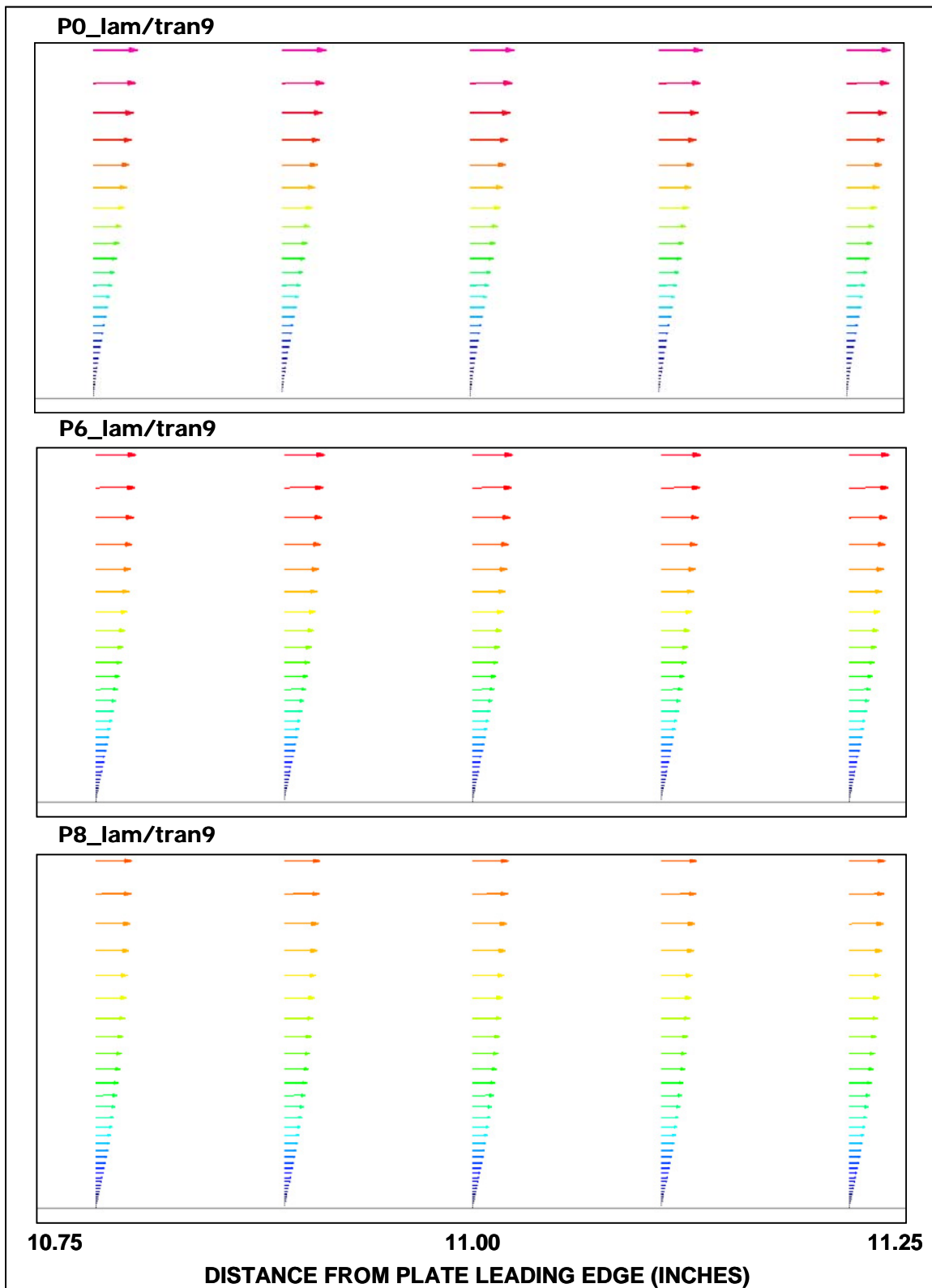


Figure 422 Variation of clean laminar upper surface profiles with pressure gradient (view CFWD)

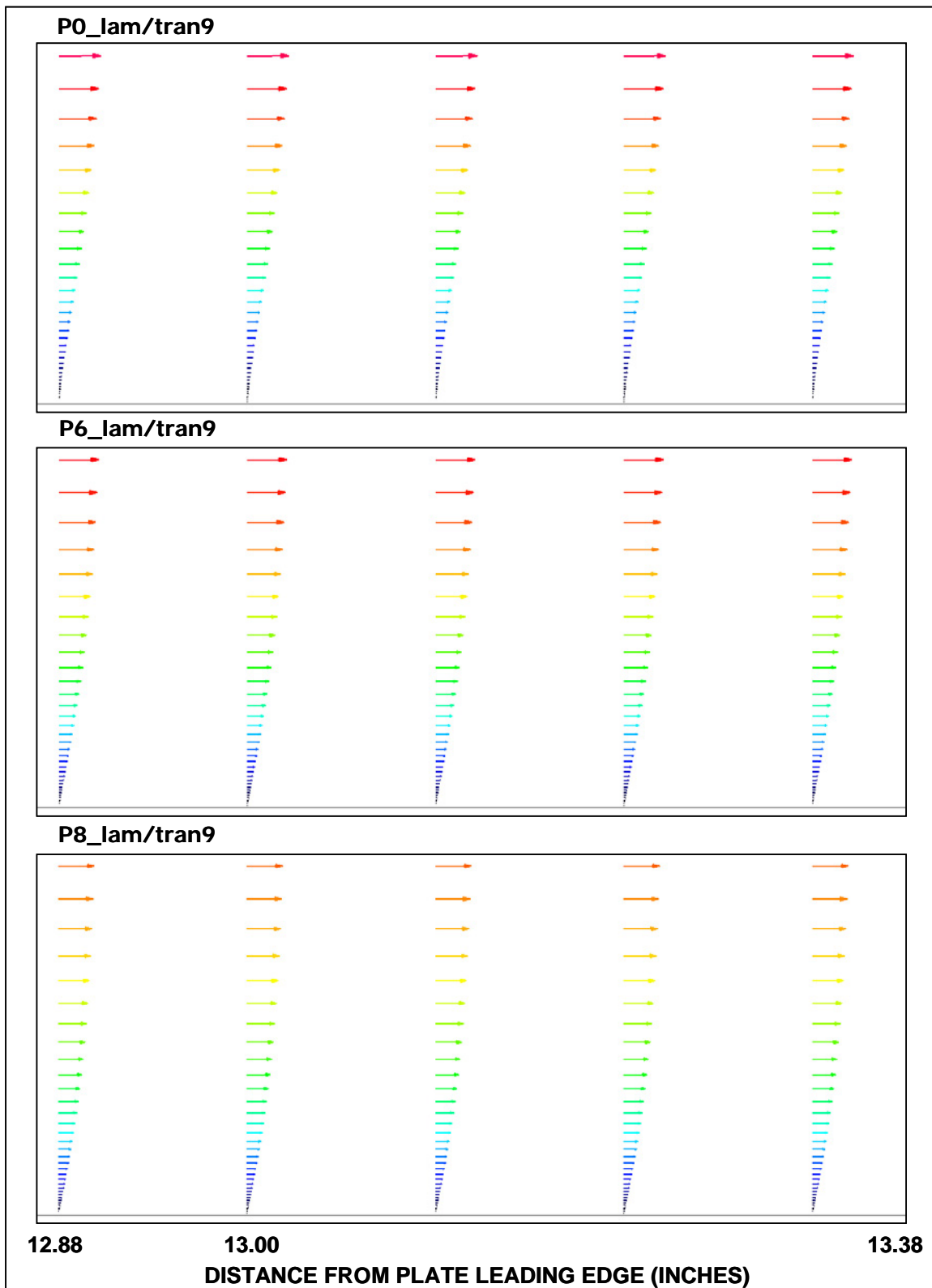


Figure 423 Variation of clean laminar upper surface profiles with pressure gradient (view CAFT)

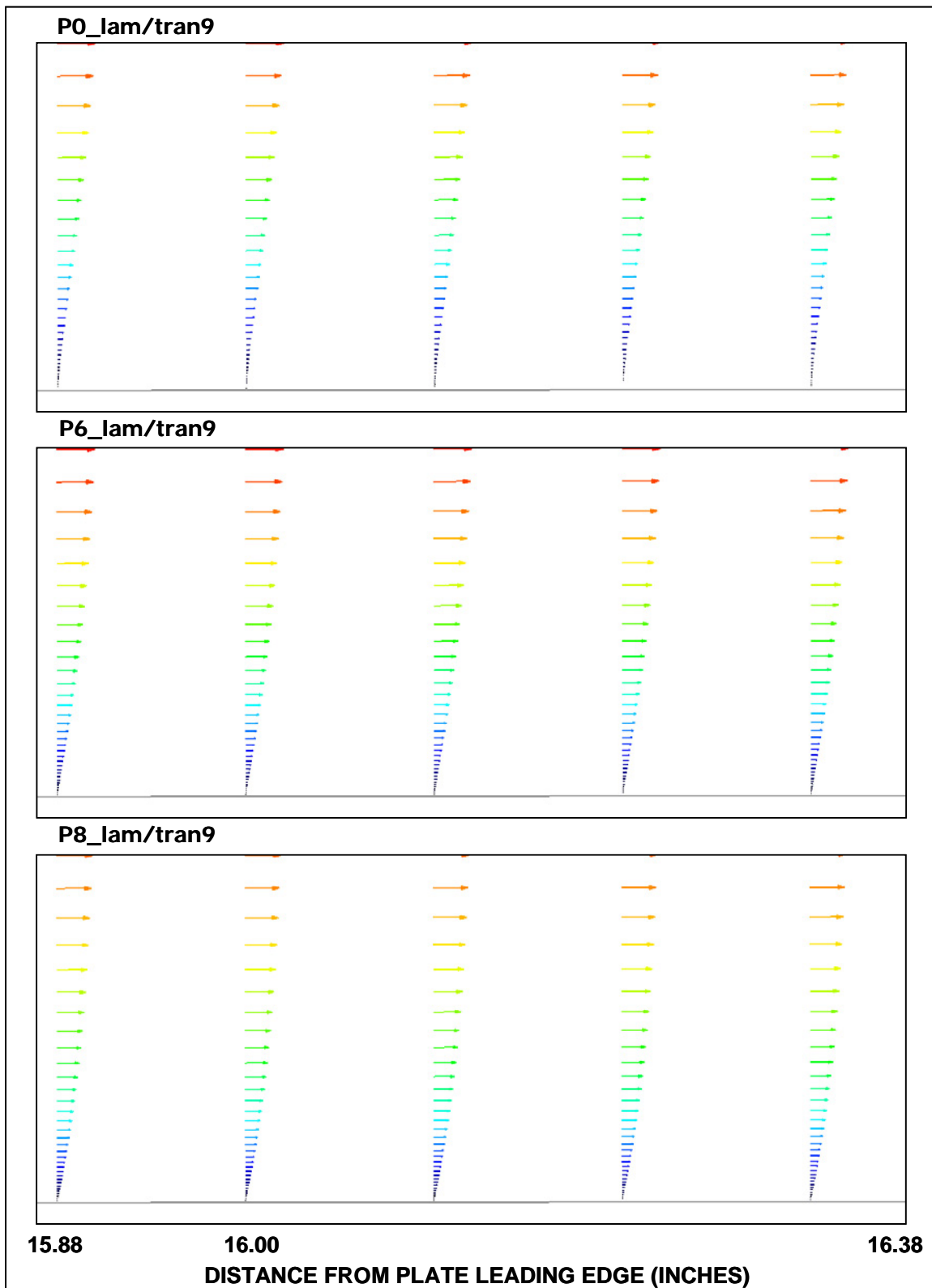
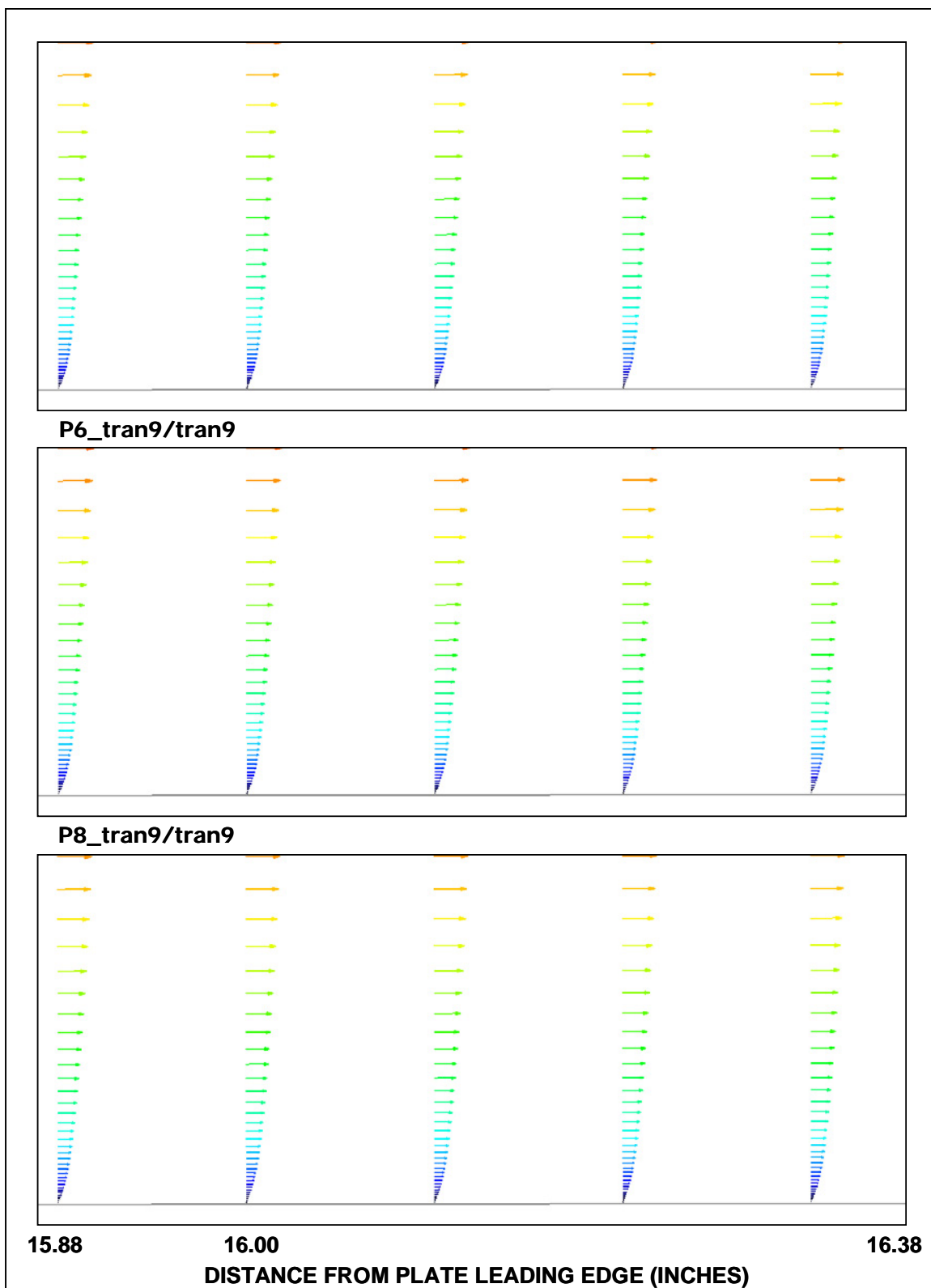
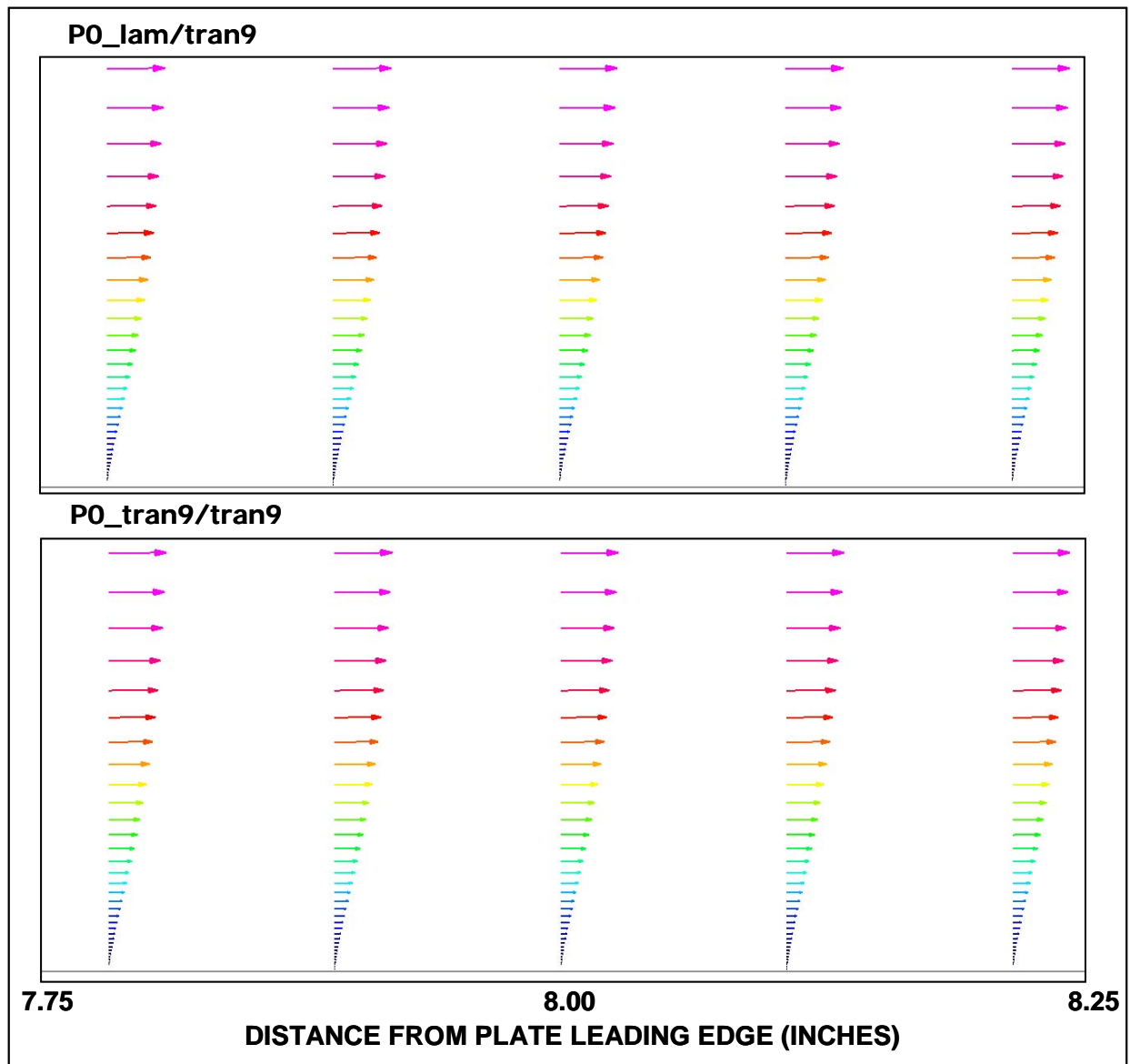


Figure 424 Variation of clean laminar upper surface profiles with pressure gradient (view DAFT)



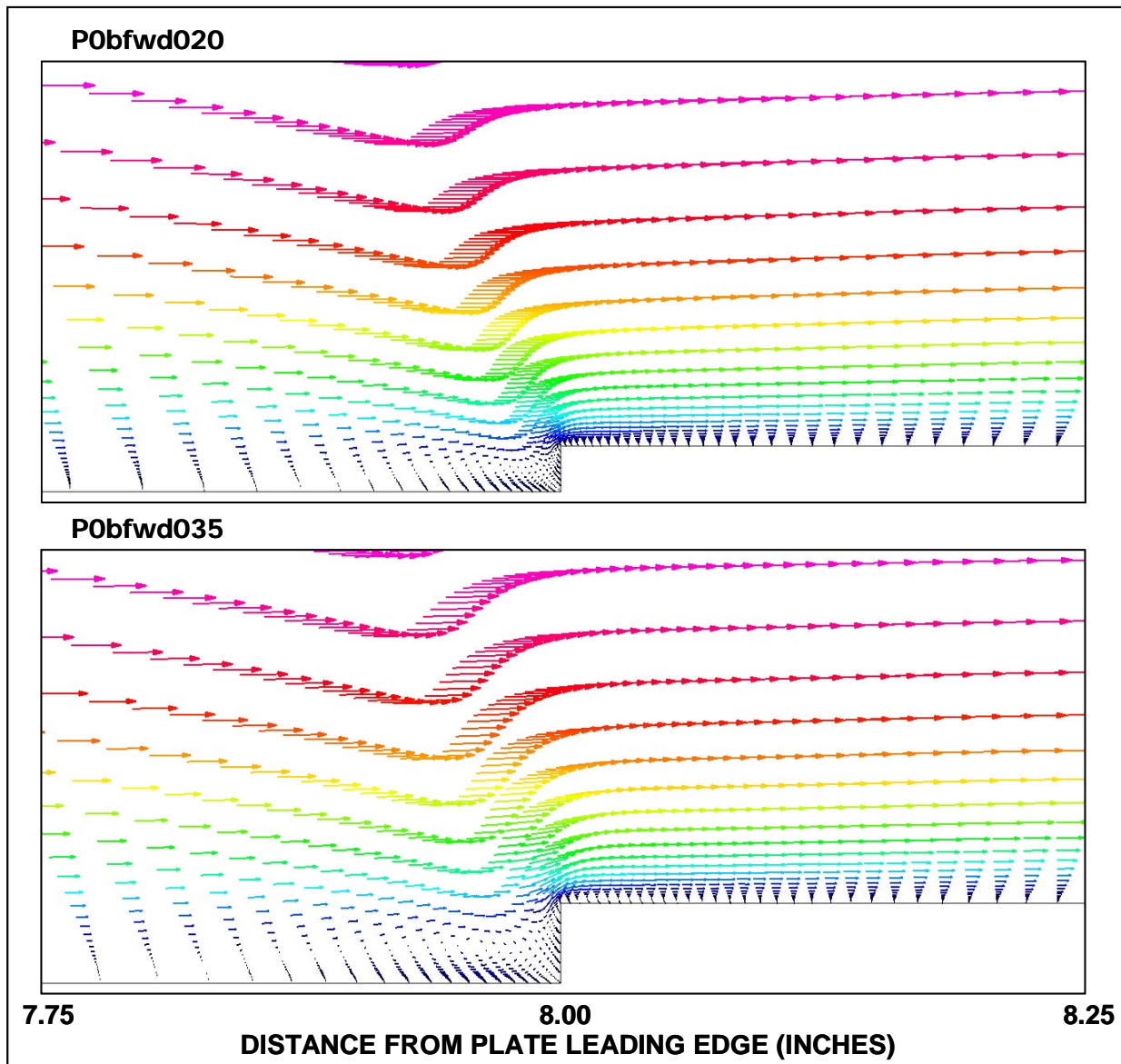
**Figure 425 Variation of clean turbulent upper surface profiles with pressure gradient (view DAFT)**

Not surprisingly, Figure 426 shows no obvious impact on the velocity vector profiles just upstream of the imposed transition at 9 inches.



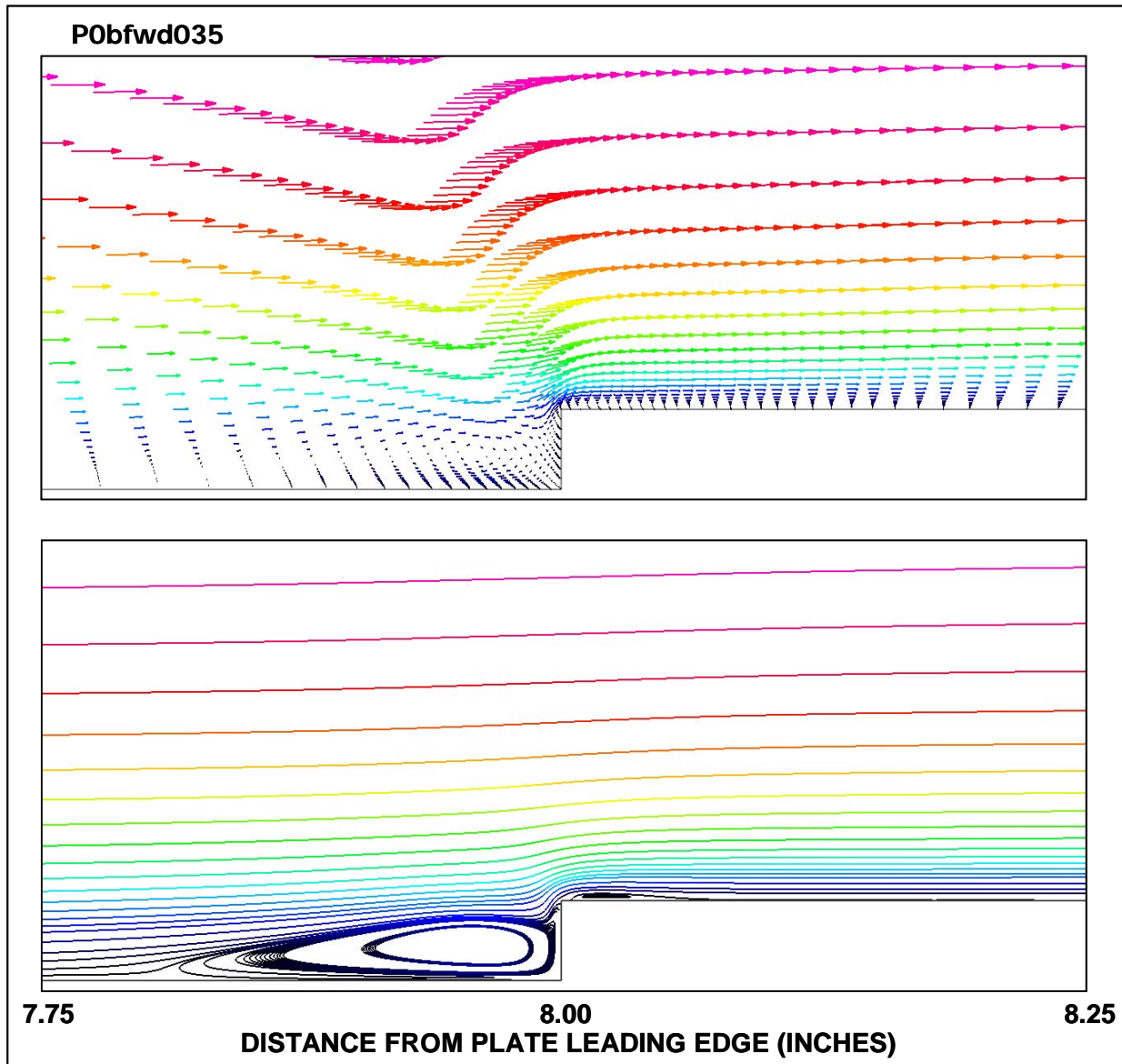
**Figure 426 P0 Clean velocity profiles for laminar and turbulent upper surfaces (view BFWD)**

In Figure 427, steps have been introduced. The slant and wave of the vector origins correspond to the grid that wraps around the step. Regions of reversed flow are evident just upstream of the step and immediately downstream (on top) of the step as the flow attempts to smooth out the turn.



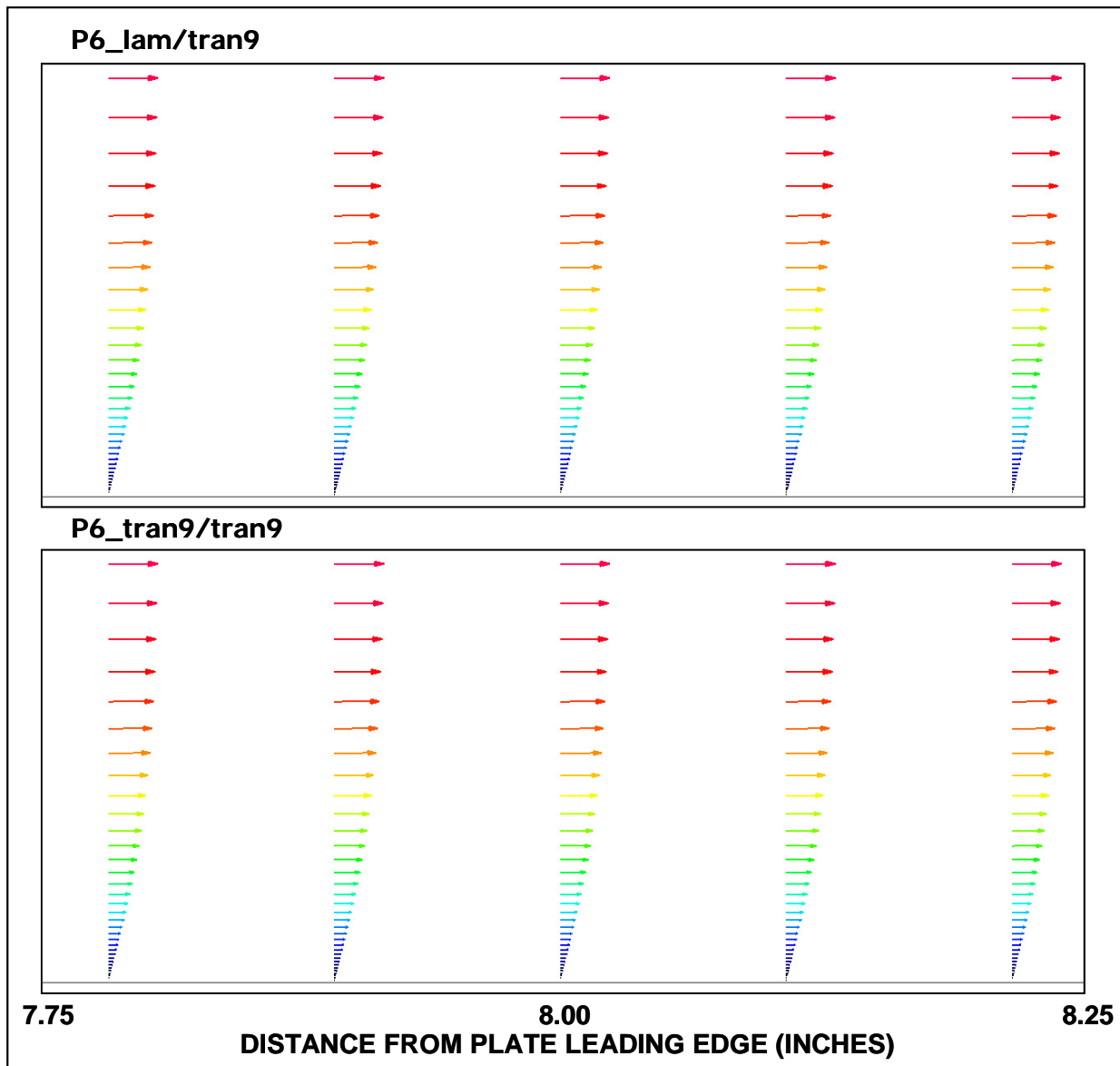
**Figure 427 P0 CFD velocity profiles for 0.020-inch and 0.035-inch-high position B forward steps (view BFWD)**

Figure 428 combines the velocity vectors of the previous figure with particle traces colored by normalized velocity on the same scale. The vectors indicate direction and relative speed within the boundary layer. The particle traces more clearly show the bubble just upstream of the step and the much shorter bubble immediately downstream. These structures are apparent for all forward steps examined in CFD.



**Figure 428 P0 Velocity vectors and particle traces for 0.035-inch-high position B forward step (view BFWD)**

The insensitivity of the profiles to variation of transition imposed just downstream does not change with the introduction of the favorable pressure gradient P6 (Figure 429).



**Figure 429 P6 Clean velocity profiles for laminar and turbulent upper surfaces (view BFW)**



In Figure 430, the largest steps analyzed in CFD are shown. The sizes of the bubbles increase with step height but do not change qualitatively.

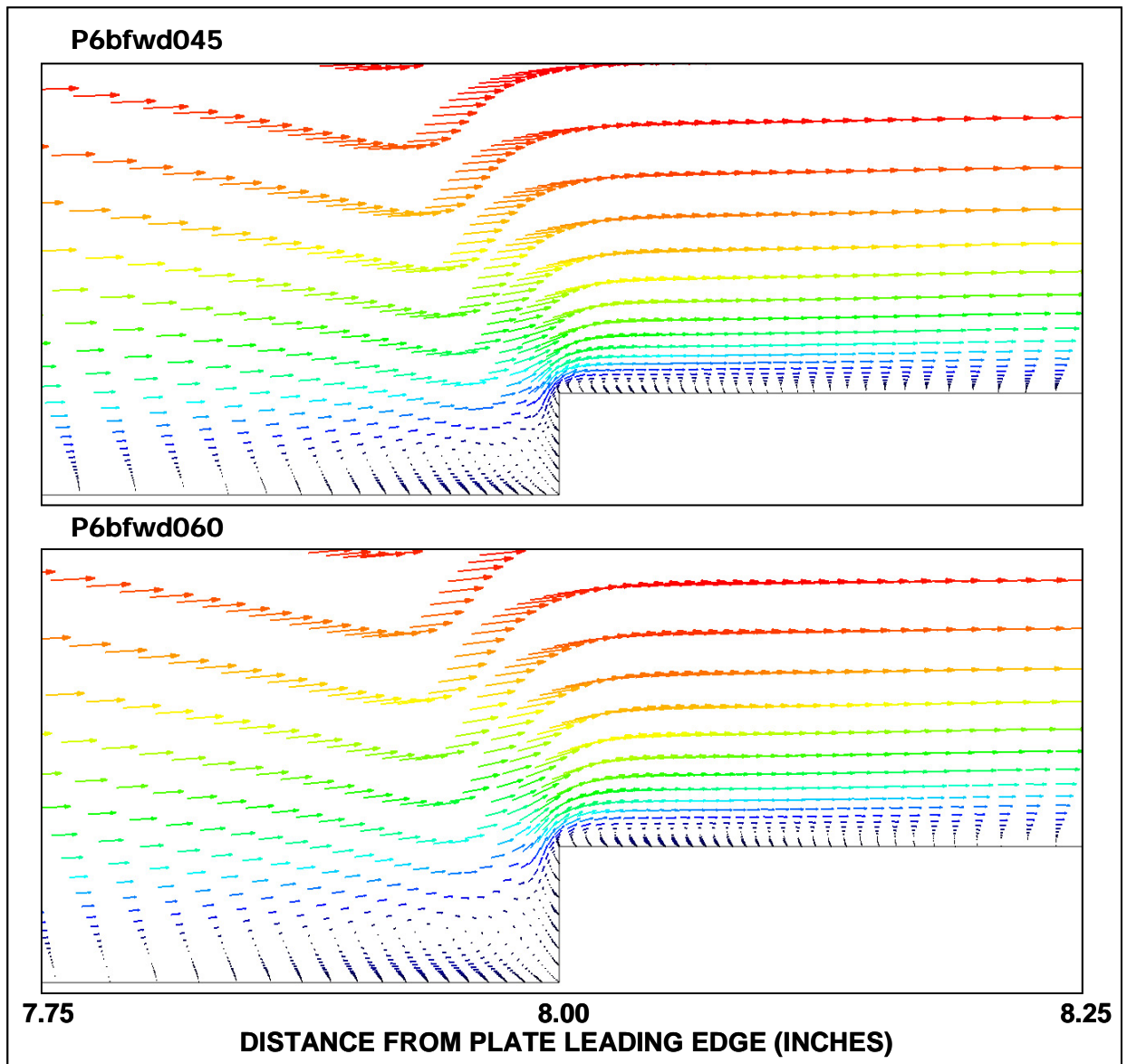


Figure 430 P6 CFD velocity profiles for 0.045-inch and 0.060-inch-high position B forward steps (view BFW)

Again, the insensitivity of the profiles to variation of transition imposed just downstream does not change with the introduction of the favorable pressure gradient P8 (Figure 431).

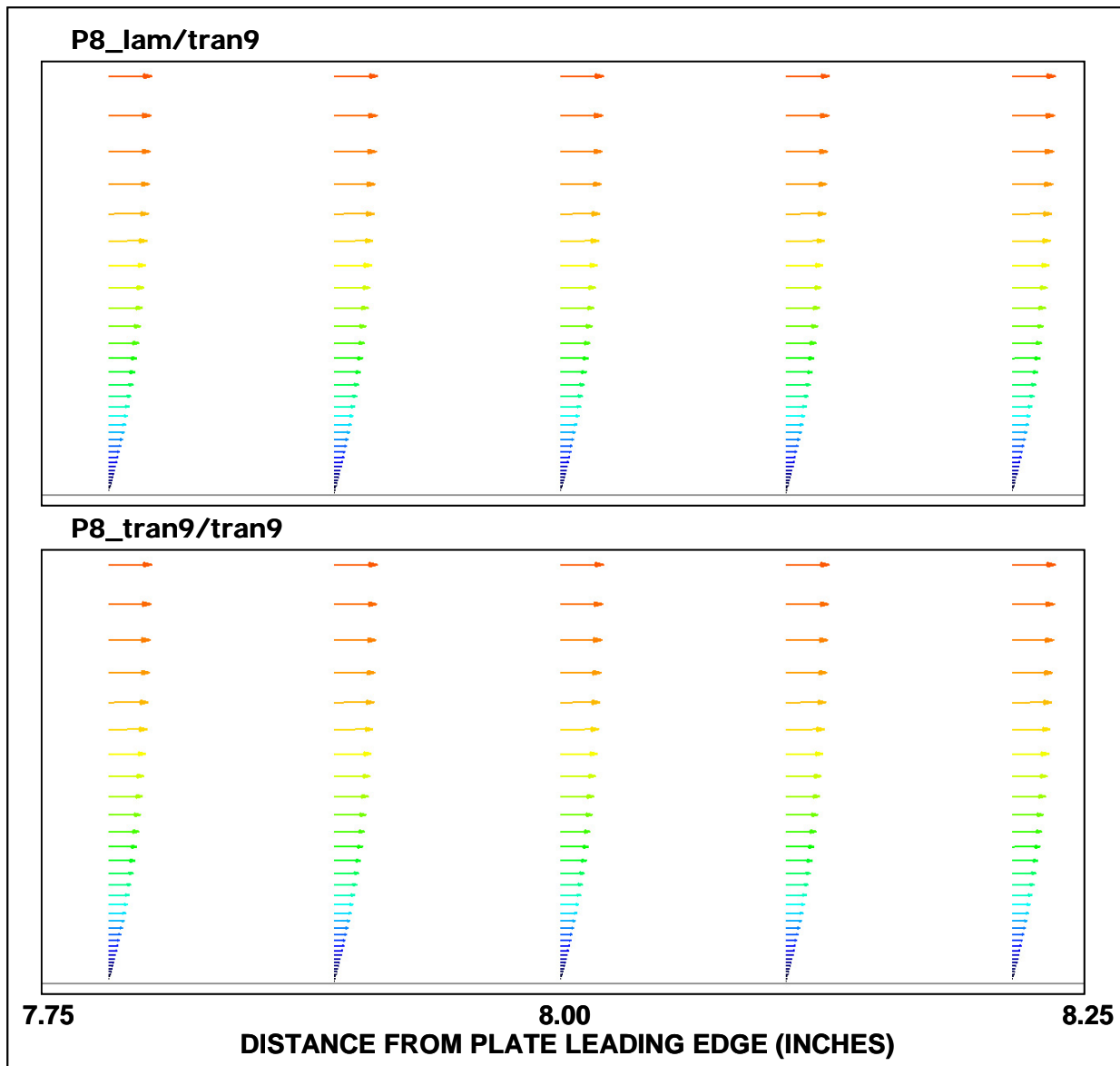


Figure 431 P8 Clean velocity profiles for laminar and turbulent upper surfaces (view BFWD)

In Figure 432, the characteristic bubbles again increase with step height but do not change qualitatively.

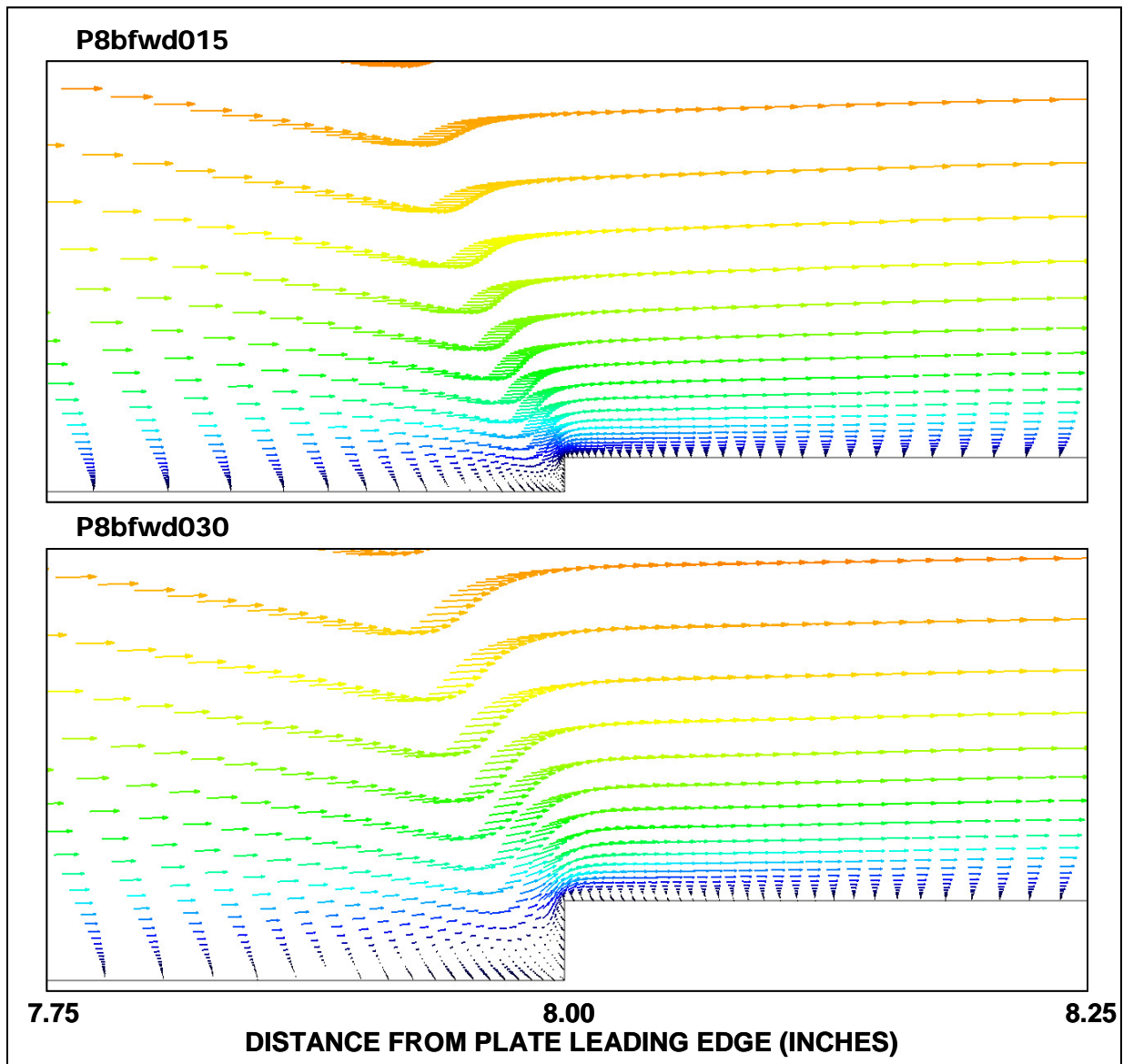
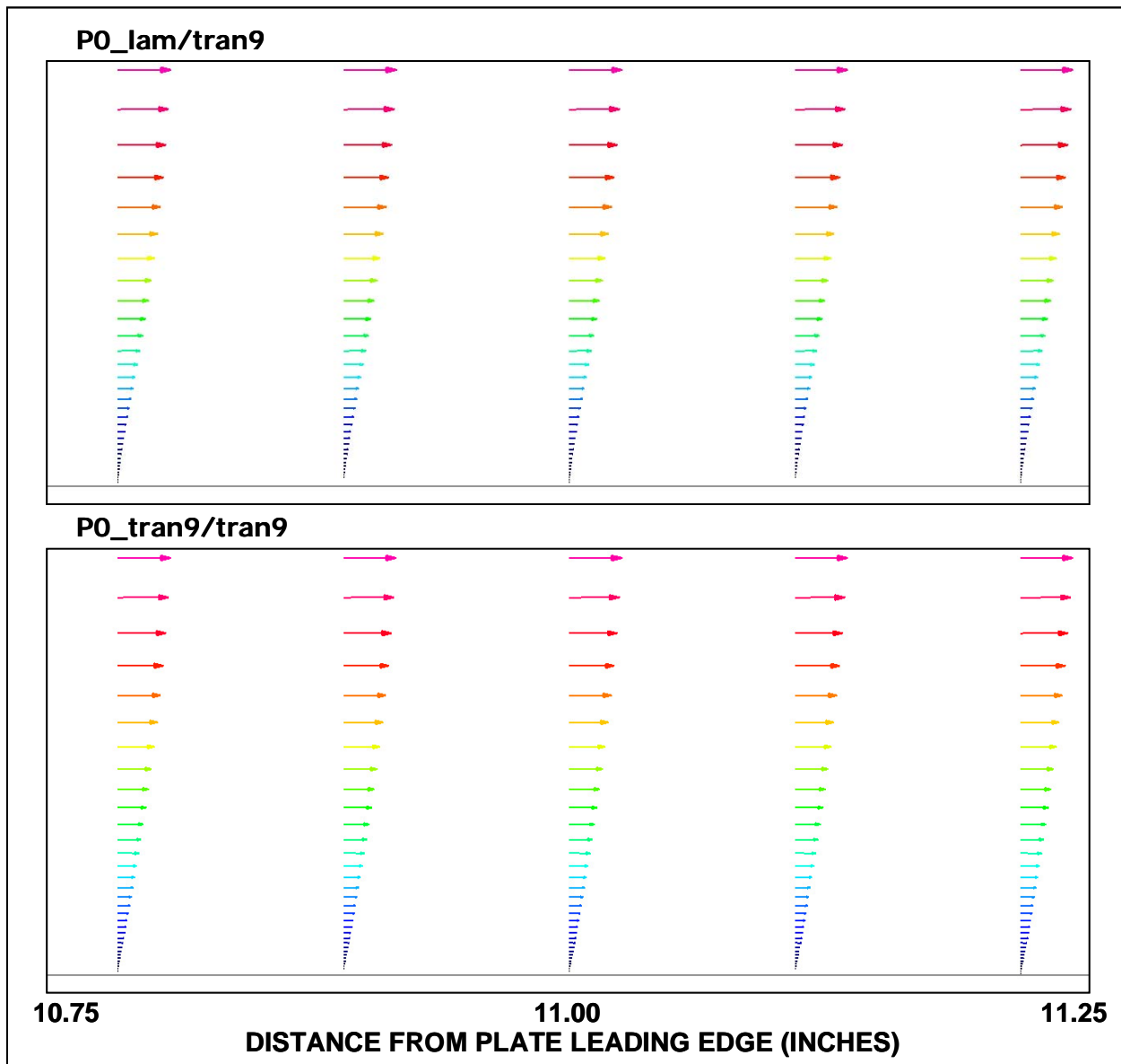


Figure 432 P8 CFD velocity profiles for 0.015-inch and 0.030-inch-high position B forward steps (View BFWD)

In Figure 433, just 3 inches downstream, slight differences appear at the base of the boundary layer with the imposition of transition 2 inches upstream.



**Figure 433 P0 Clean velocity profiles for laminar and turbulent upper surfaces (view CFWD)**

In Figure 434, the same characteristic bubbles are evident and the flow at the top of the view is slower for the larger step size.

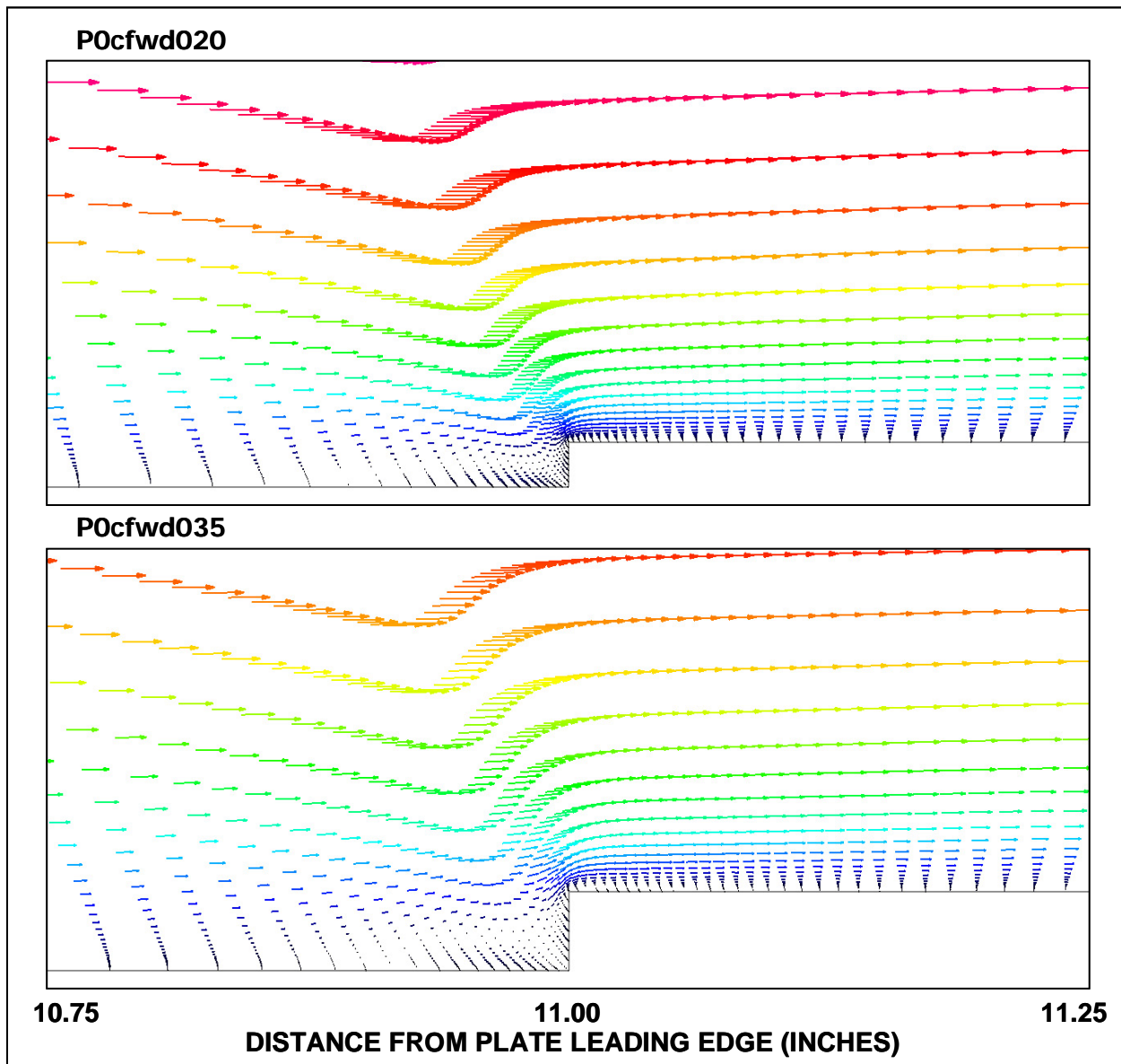


**Figure 434 P0 CFD Velocity profiles for 0.020-inch and 0.035-inch-high position C forward steps (View CFWD)**

In Figure 435, the upper surface profile at this location is just slightly fuller for the case with transition 2 inches upstream. The difference is not as apparent as it was for the P0 gradient.

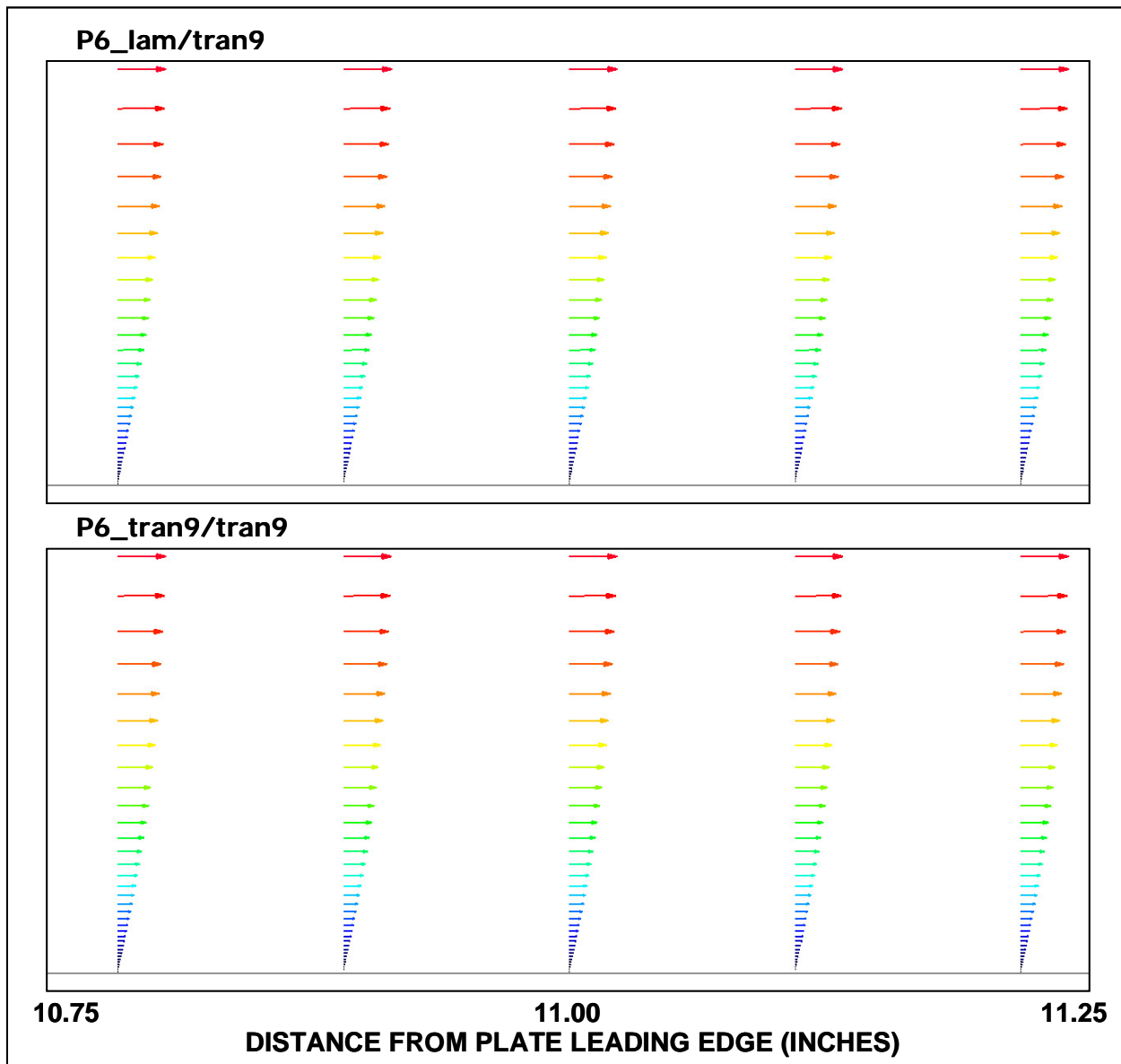


**Figure 435 P6 Clean velocity profiles for laminar and turbulent upper surfaces (view CFWD)**

In Figure 436, the characteristic bubbles are qualitatively similar.

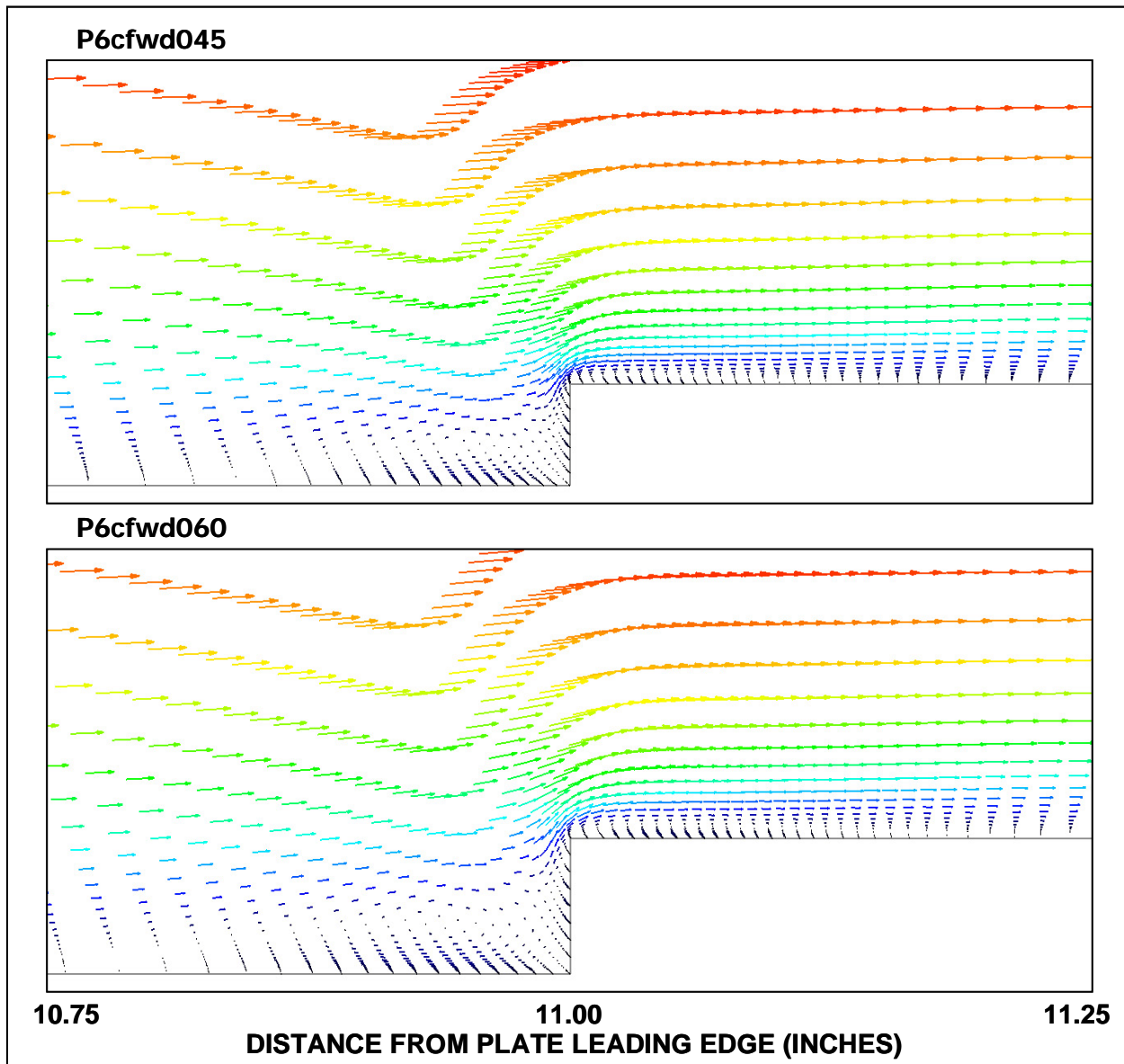
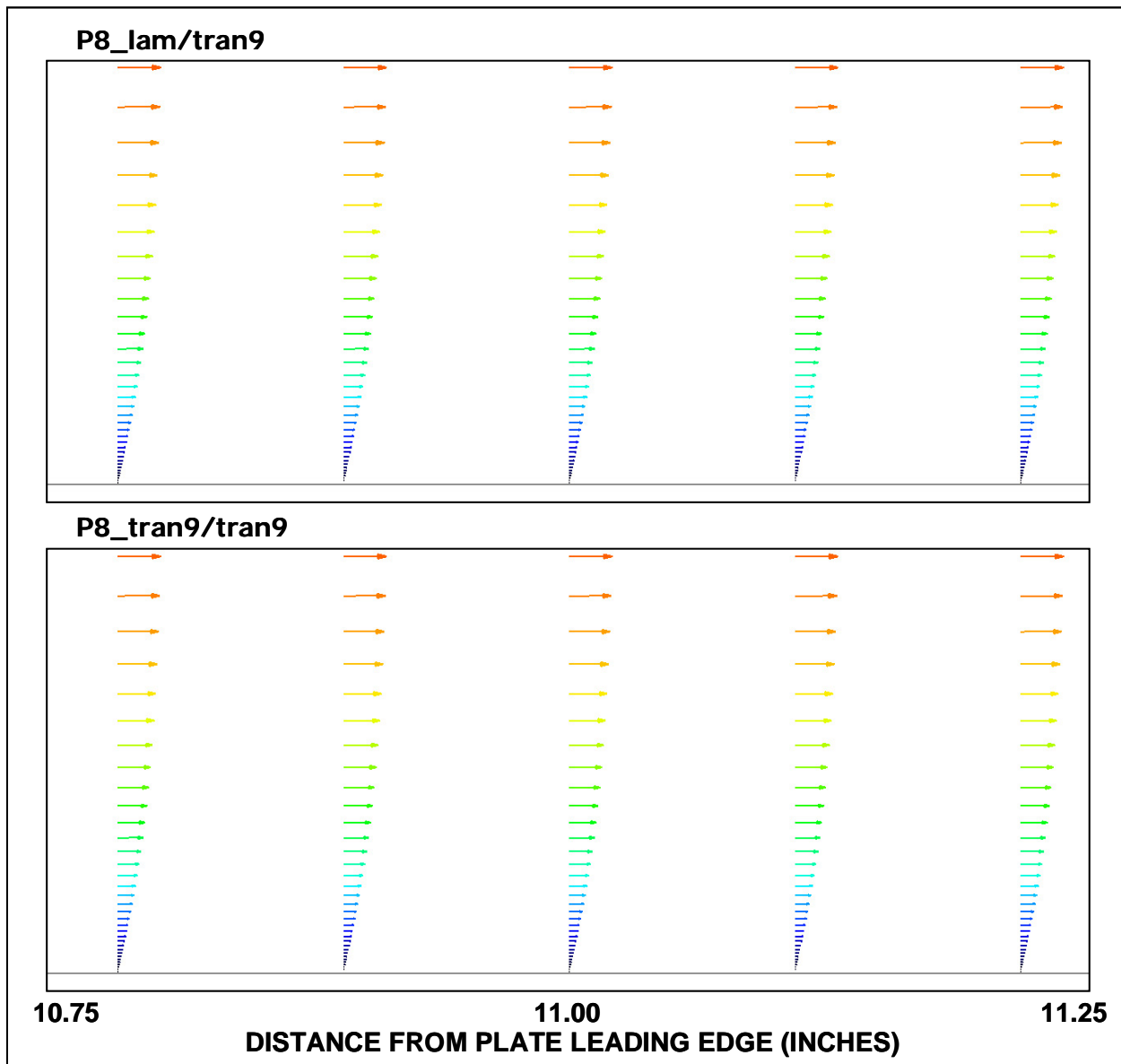


Figure 436 P6 CFD velocity profiles for 0.045-inch and 0.060-inch-high position C forward steps (view CFWD)

In Figure 437, differences in the clean profiles with transition at this position under the influence of the strongest favorable gradient are not readily apparent.



**Figure 437 P8 Clean velocity profiles for laminar and turbulent upper surfaces (view CFWD)**



In Figure 438, under the influence of the strong favorable gradient, the quality of the bubbles is again similar.

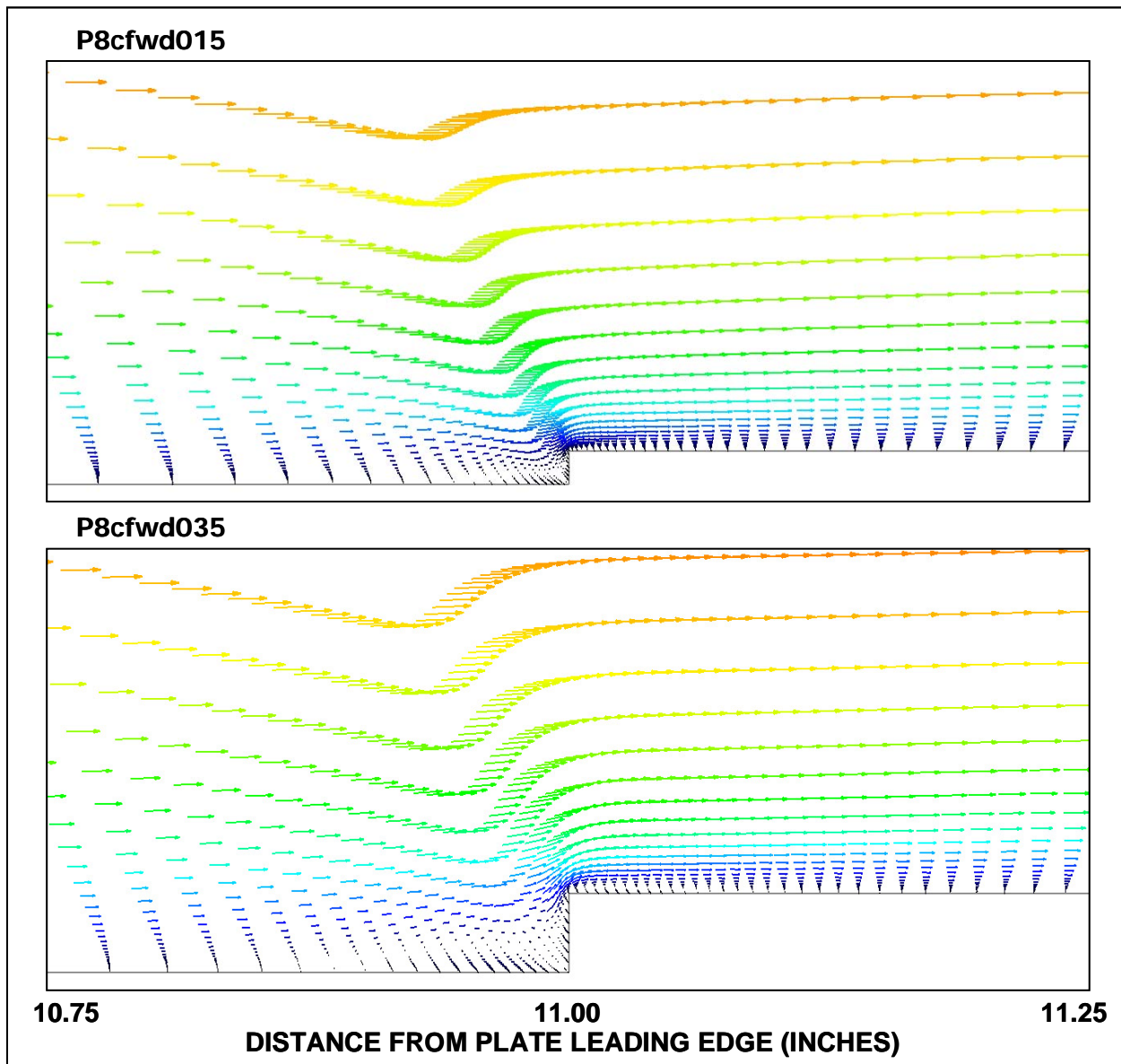


**Figure 438 P8 CFD velocity profiles for 0.015-inch and 0.030-inch-high position C forward steps (view CFWD)**

Further downstream (13 inches from the leading edge) under the influence of the P6 gradient, the boundary layer profile is more full when transition is introduced 4 inches upstream (Figure 439).

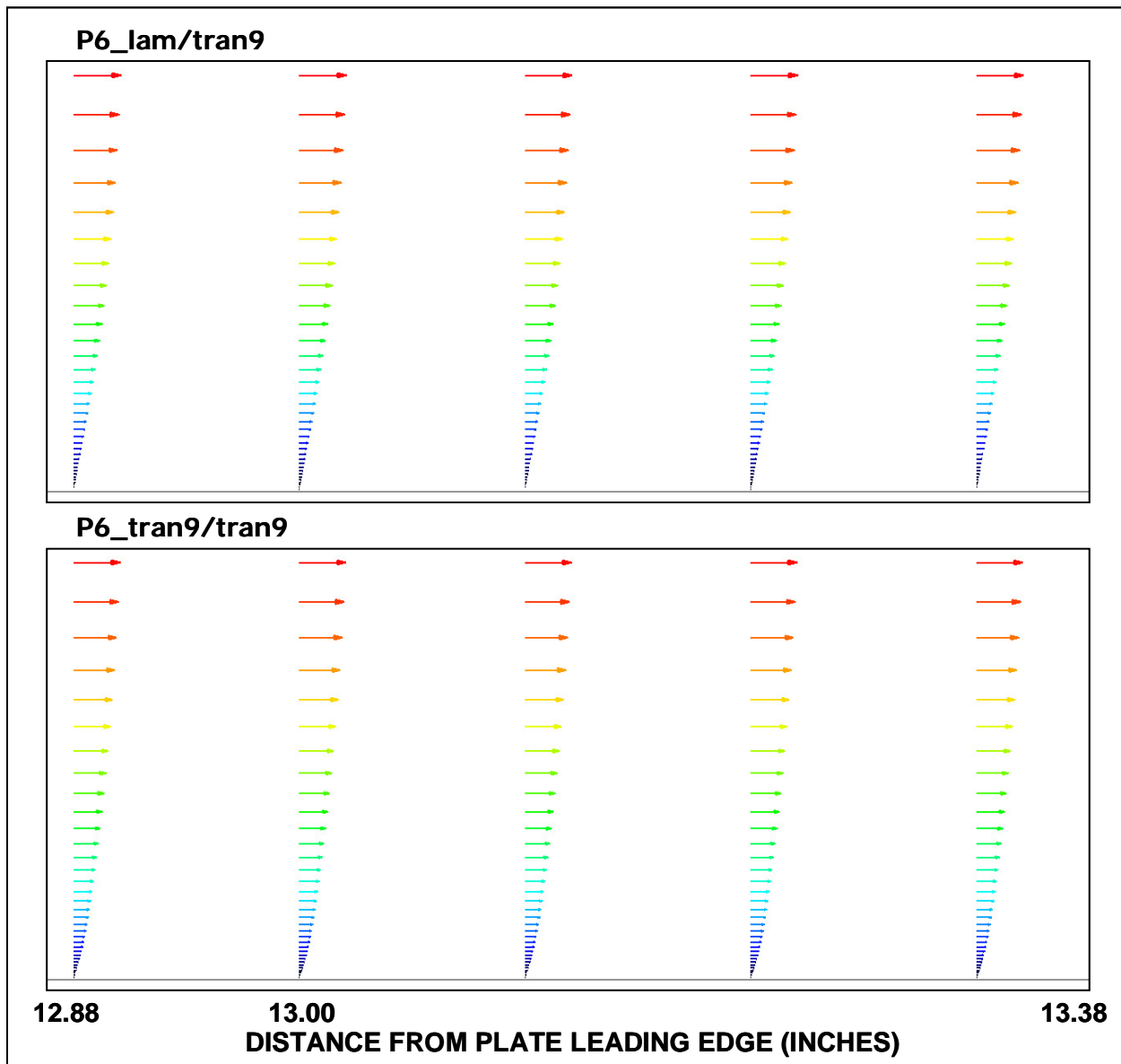
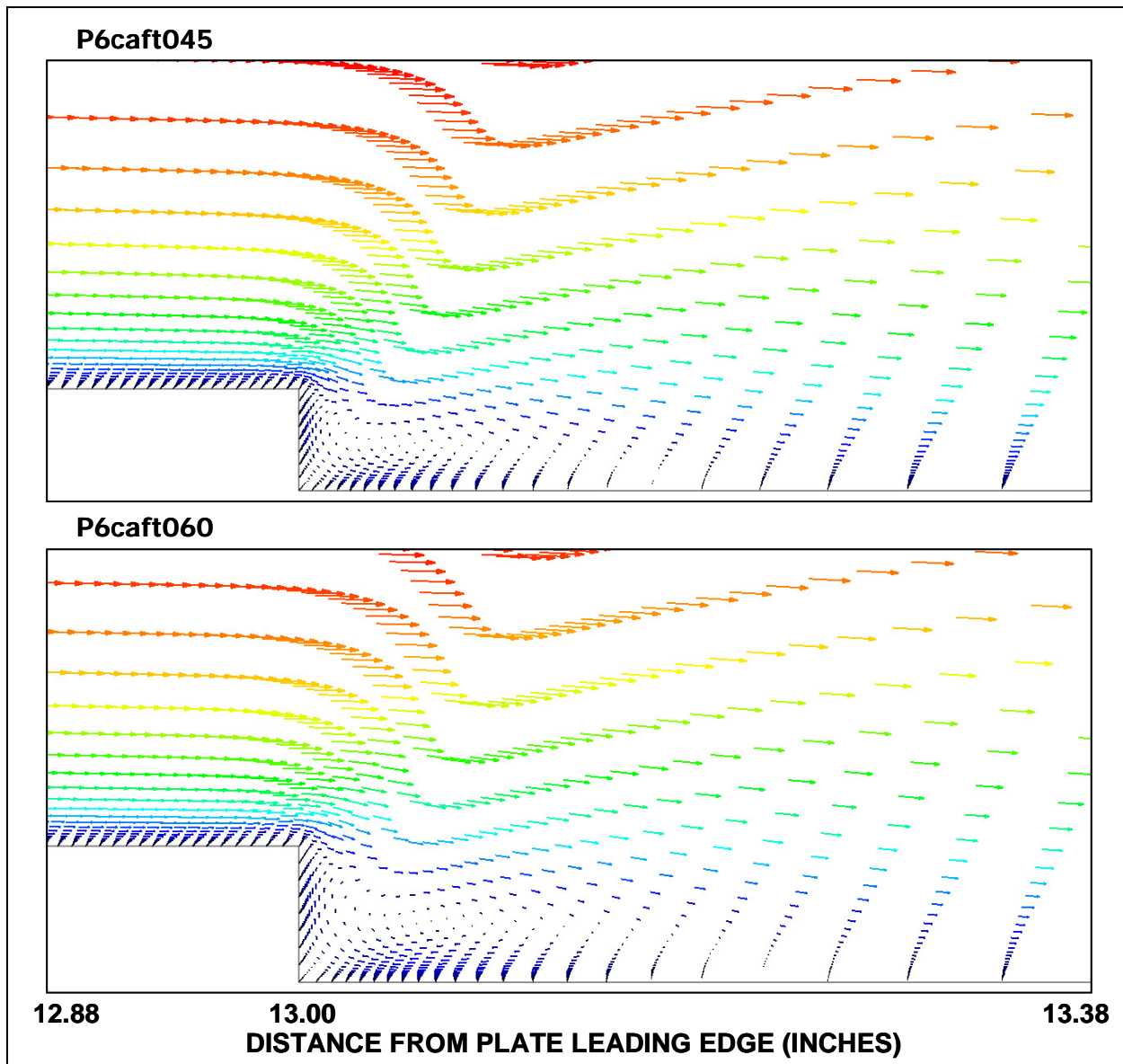


Figure 439 P6 Clean velocity profiles for laminar and turbulent upper surfaces (view CAFT)

At this same location, aft-facing steps for the two largest heights examined in CFD are shown. A bubble appears just downstream of the step in both cases. Recall that transition for these two cases was taken from the experiment and differs (Figure 420), but no qualitative change in the bubble shape is evident here (Figure 440).



**Figure 440 P6 CFD velocity profiles for 0.045-inch and 0.060-inch-high position C aft steps (view CAFT)**

Figure 441 compares the vectors for the 0.060-inch step from the previous figure with particle traces colored by the same normalized velocity scale. Other step sizes were modeled at this location for the P0 and P8 gradients and all had the same characteristic feature.

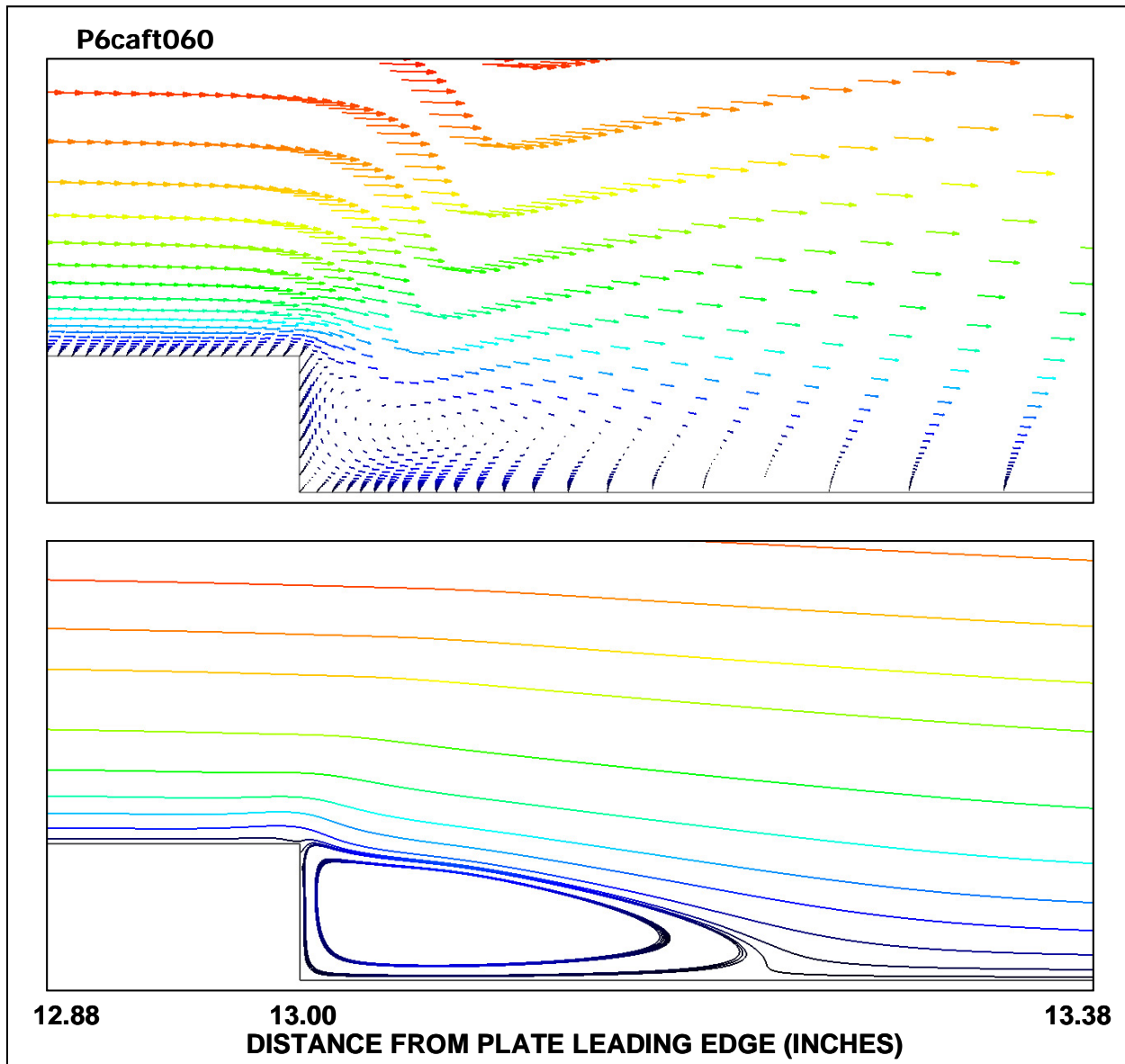
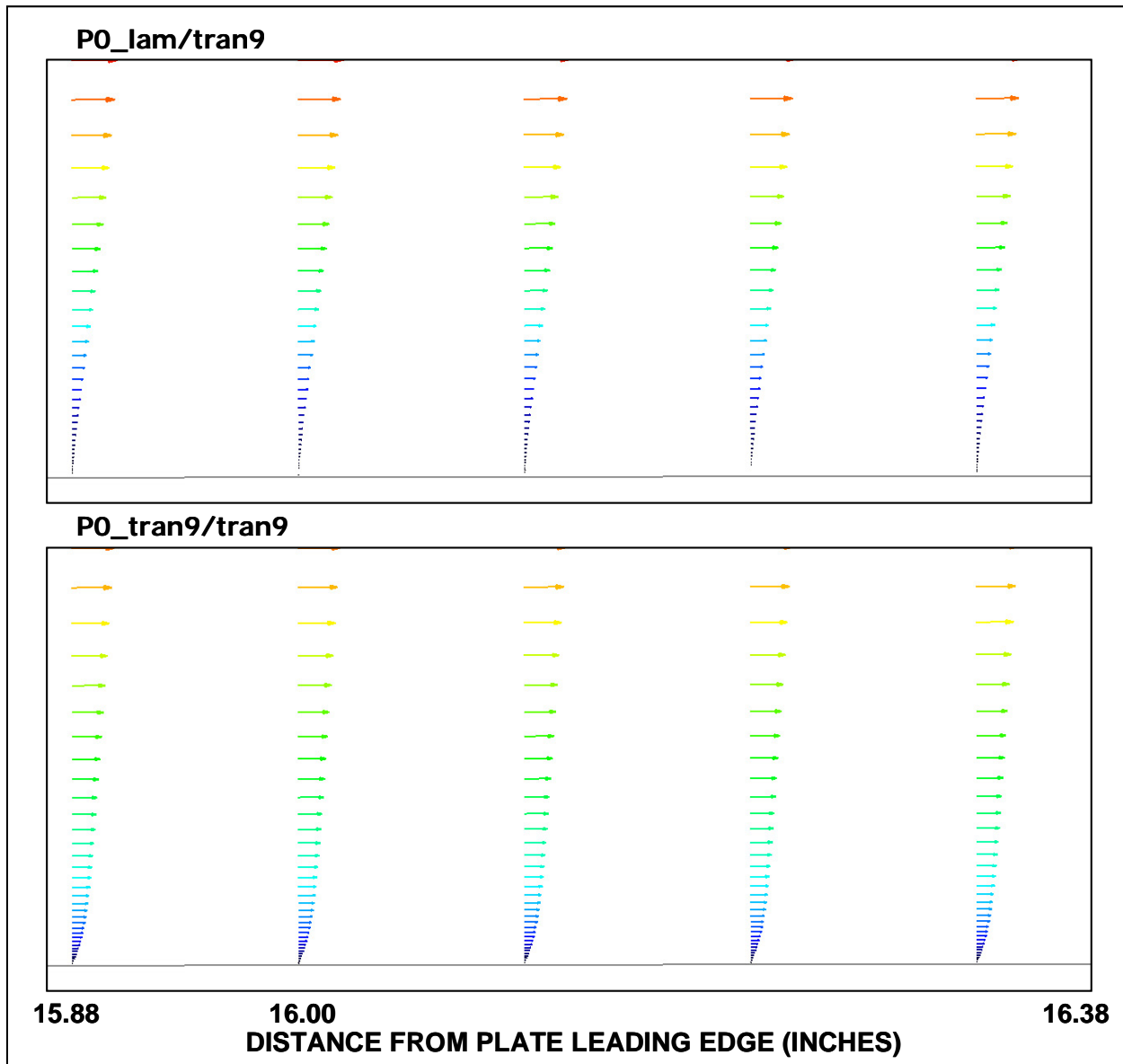


Figure 441 P6 CFD velocity profiles for 0.045-inch and 0.060-inch-high position C aft step (view CAFT)

Finally, Figure 442 shows the impact of upstream transition on the clean plate under the P0 gradient at the location of the most downstream step location tested. The fullness of the turbulent boundary layer is clearly evident.



**Figure 442 P0 Clean velocity profiles for laminar and turbulent upper surfaces (view DAFT)**

The boundary layer around the aft facing steps at this location exhibit a similar pattern (Figure 443).

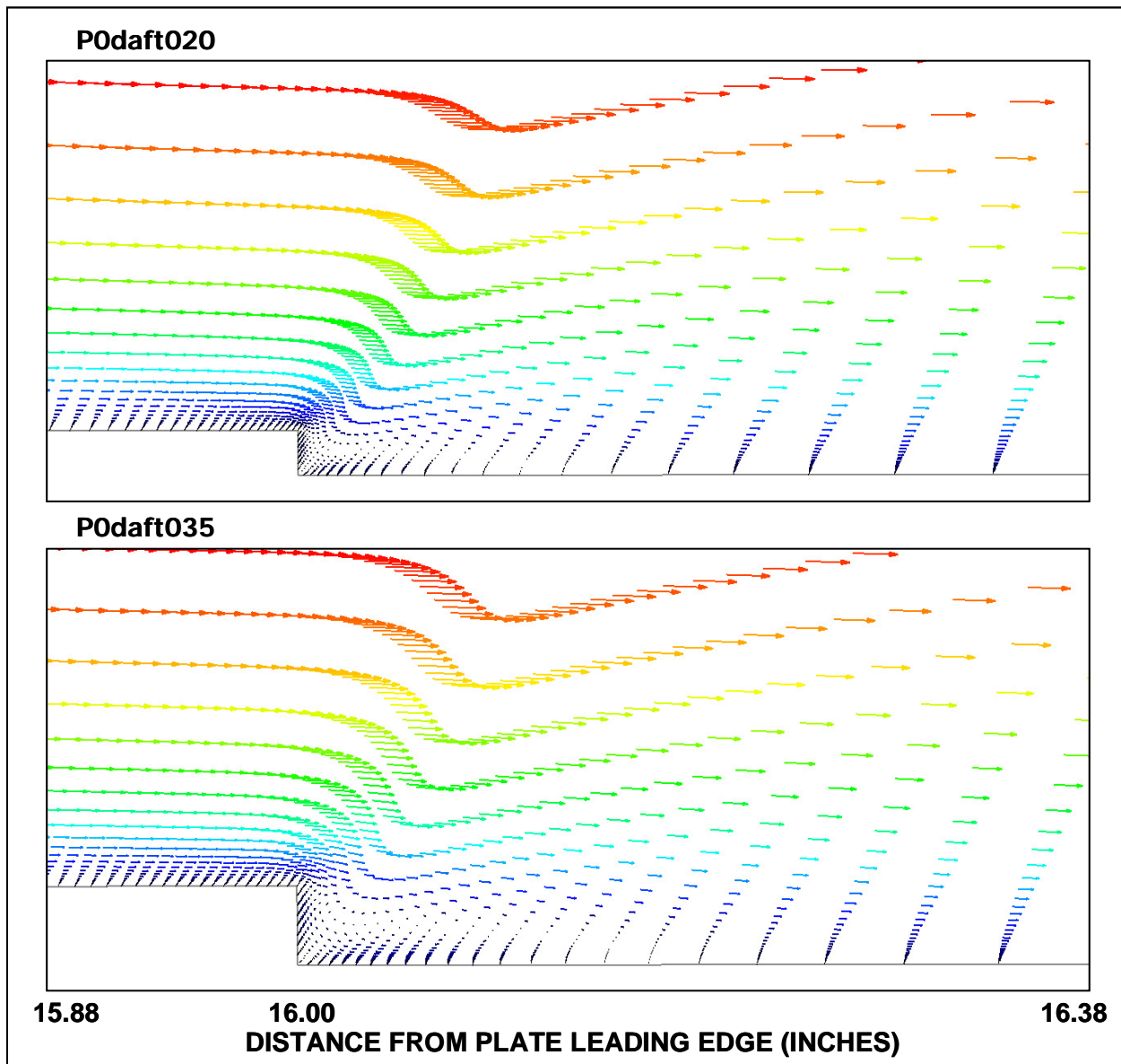


Figure 443 P0 CFD velocity profiles for 0.020-inch and 0.035-inch-high position D aft steps (view DAFT)

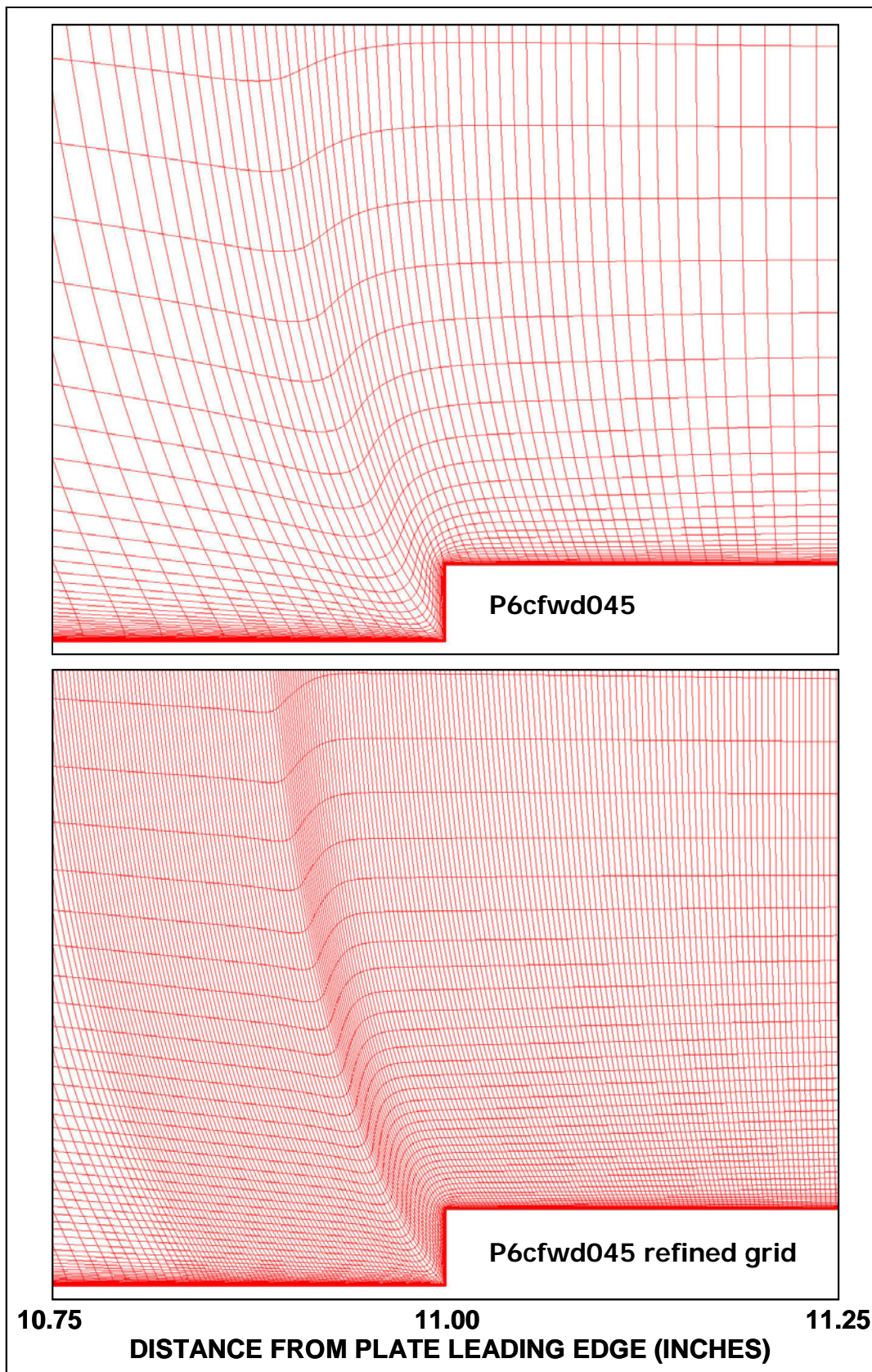
Since the basic bubble structure was similar for all of the forward facing steps and similar for all of the aft facing steps, quantitative aspects were compared next in hopes of uncovering a relationship to changes in downstream transition locations. Focus was limited to the forward facing steps at one location subject to the P6 pressure gradient, because the dual bubble structure for the forward steps was the most interesting. A series of relatively large steps were examined, with some downstream transition locations determined experimentally and others interpolated as indicated in Table 10. For each step height, the bubble lengths were calculated by determining the extent of reversed flow at the grid point nearest the surface. To improve the accuracy of this assessment, the grid block around the step was refined (primarily in the streamwise direction) as shown in Figure 444. The resulting 7-block 2-D grid had 848,553 points and required about 6 ½ hours on 4 SGI Origin 300 processors for each run in the same manner as before.

**Table 10 Run matrix for bubble size parametric study**

Case I.D.	Pressure Gradient	Step Dir.	Step Location* (in)	Step Height (in)=k	Upper Transition* (in)=x_tr	x_tr Origin	Re <sub>k</sub>	Re <sub>tr</sub>
P6cfwd045	P6	forward	11	0.045	48.00	Interp.	388	706,023
P6cfwd055	P6	forward	11	0.055	48.00	Test	532	705,468
P6cfwd060	P6	forward	11	0.060	37.40	Interp.	607	528,466
P6cfwd065	P6	forward	11	0.065	26.16	Interp.	684	351,875
P6cfwd070	P6	forward	11	0.070	15.12	Test	762	175,349
P6cfwd080	P6	forward	11	0.080	14.58	Test	918	167,540

\* Distance from plate leading edge

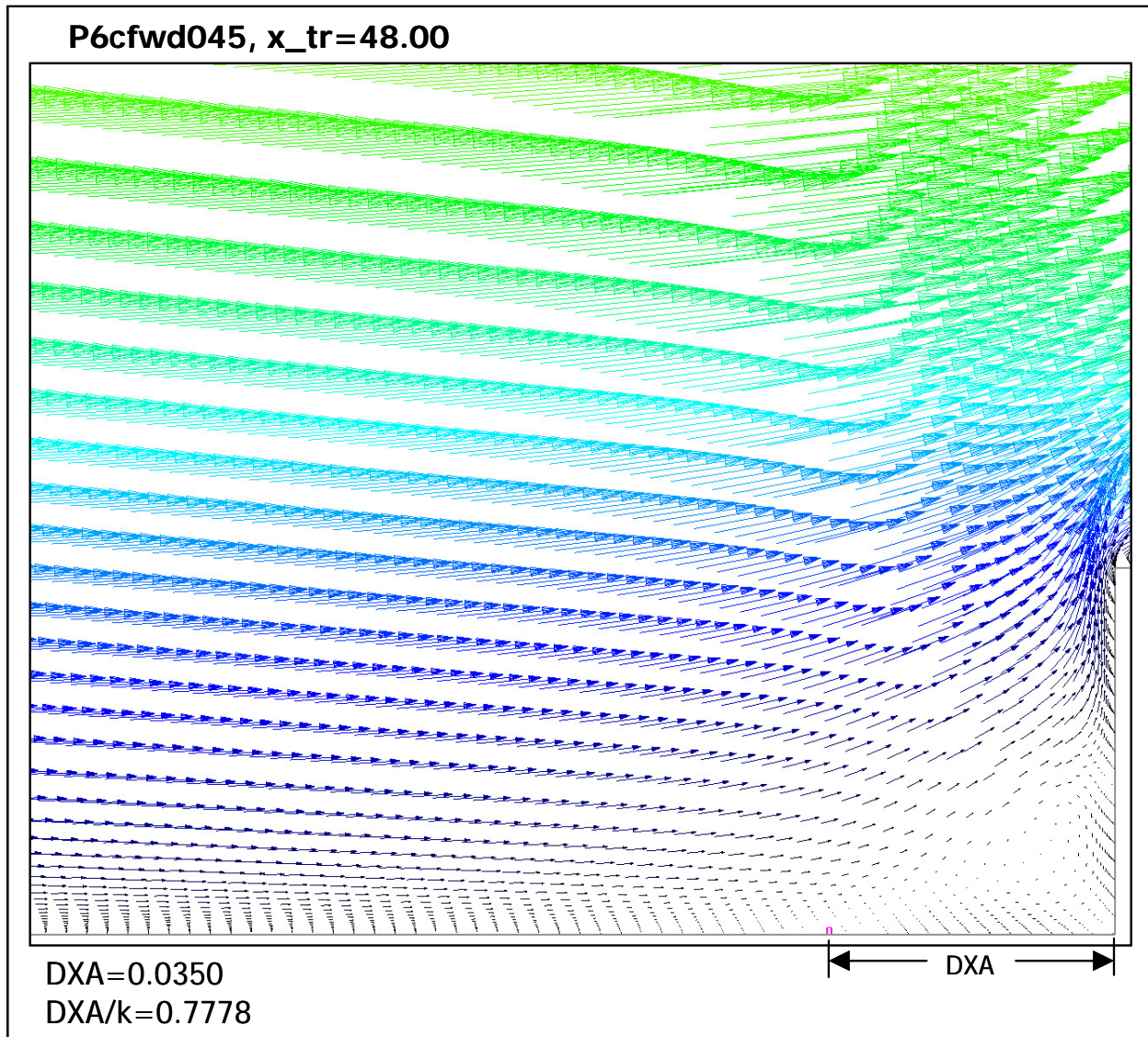




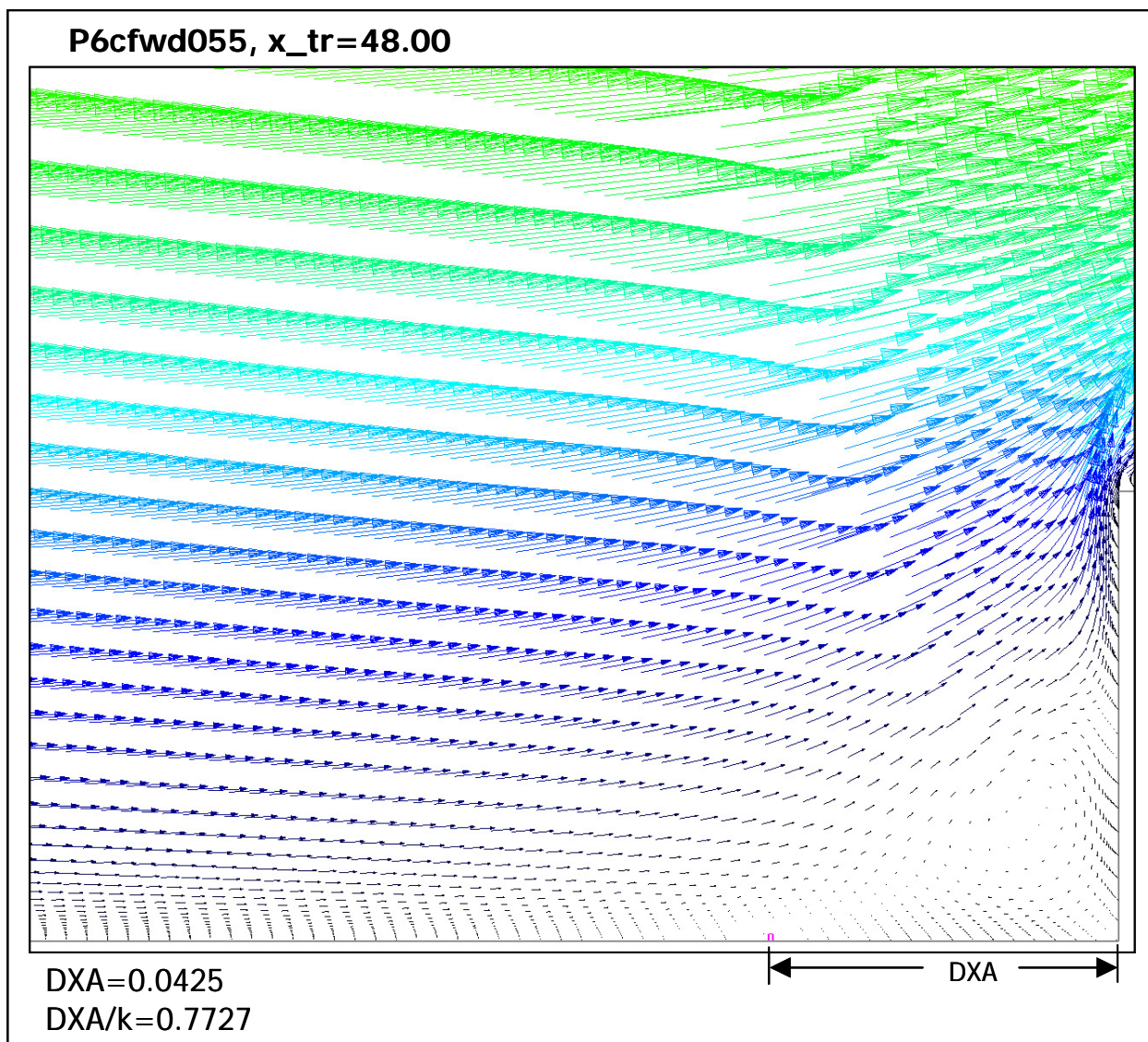
**Figure 444 Comparison of original and refined grid density In P6cfwd045 block (view BFWD)**



Figure 445 is a much closer view focused on the bubble just forward of the step. The pink O indicates the most upstream edge of reversed flow for the grid density shown. DXA is the length of the bubble. DXA/k is that length divided by the step height. Similar plots for other heights with the different downstream transition locations are shown in Figures 446 through 450.



**Figure 445 P6 CFD velocity profiles in front of 0.045-inch-high position C forward step (view CFWD5)**



**Figure 446 P6 CFD velocity profiles in front of 0.055-inch-high position C forward step (view CFWD5)**



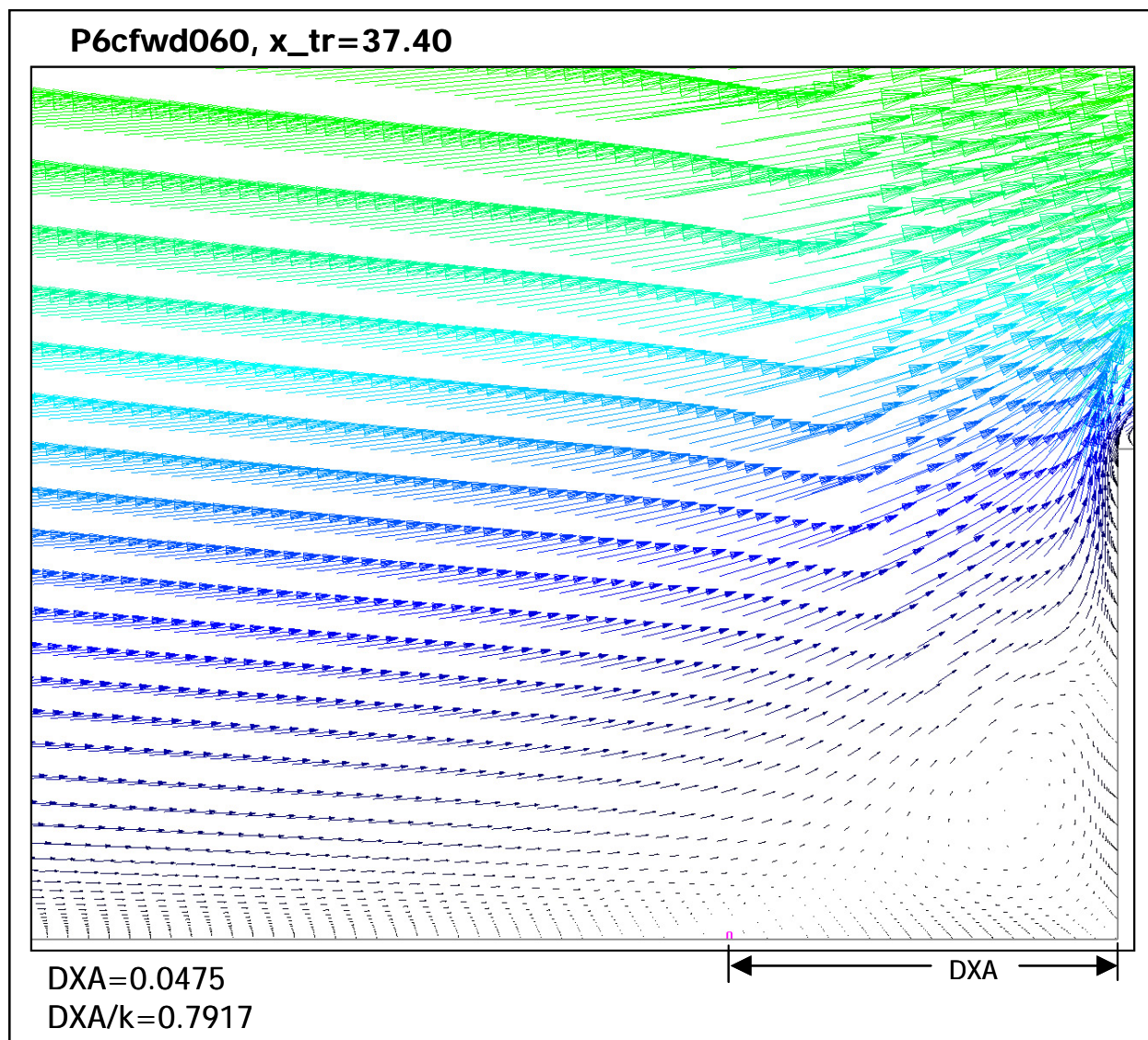


**Figure 447 P6 CFD velocity profiles in front of 0.060-inch-high position C forward step (view CFWD5)**

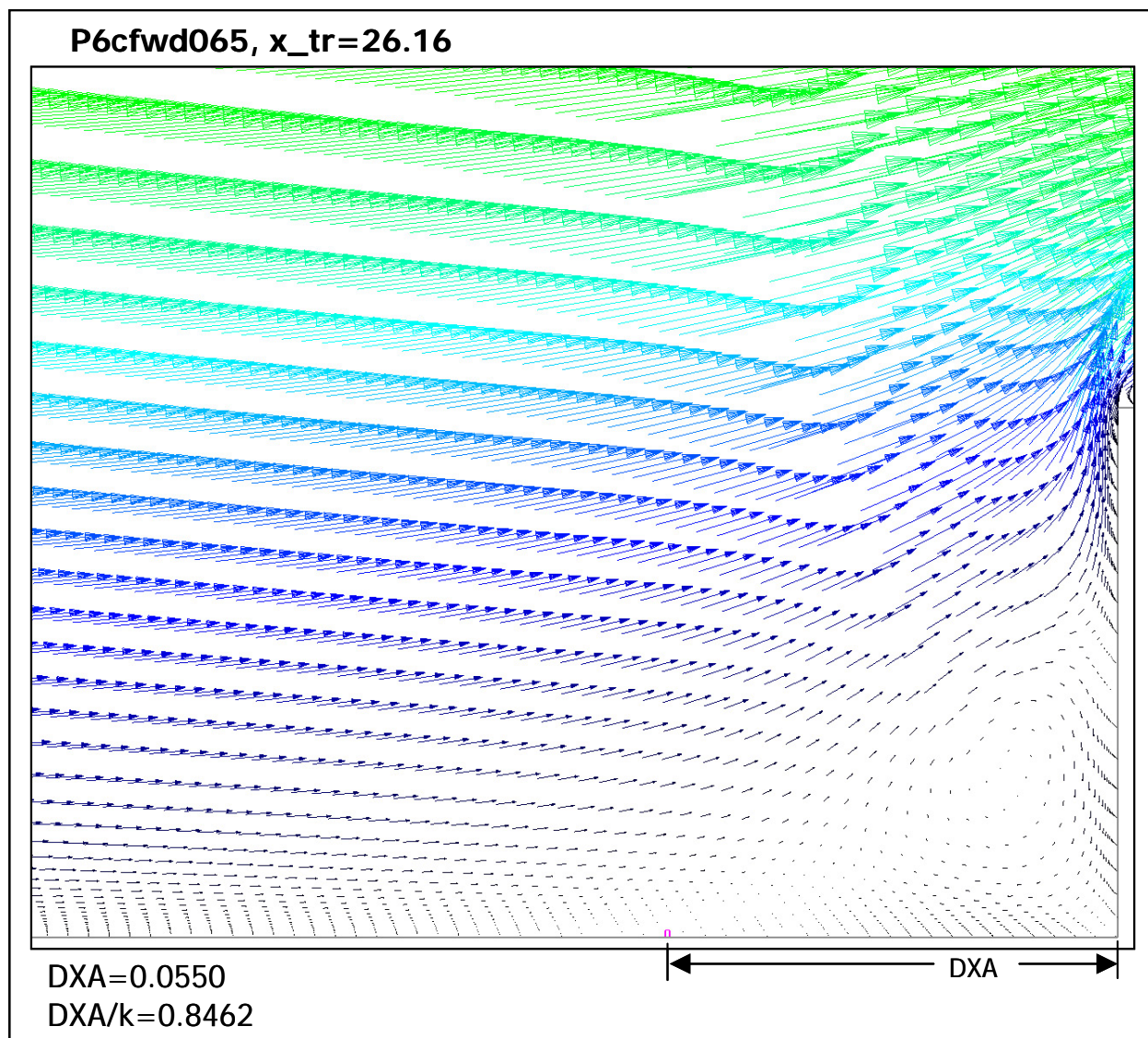


**Figure 448 P6 CFD velocity profiles in front of 0.065-inch-high position C forward step  
(view CFWD5)**



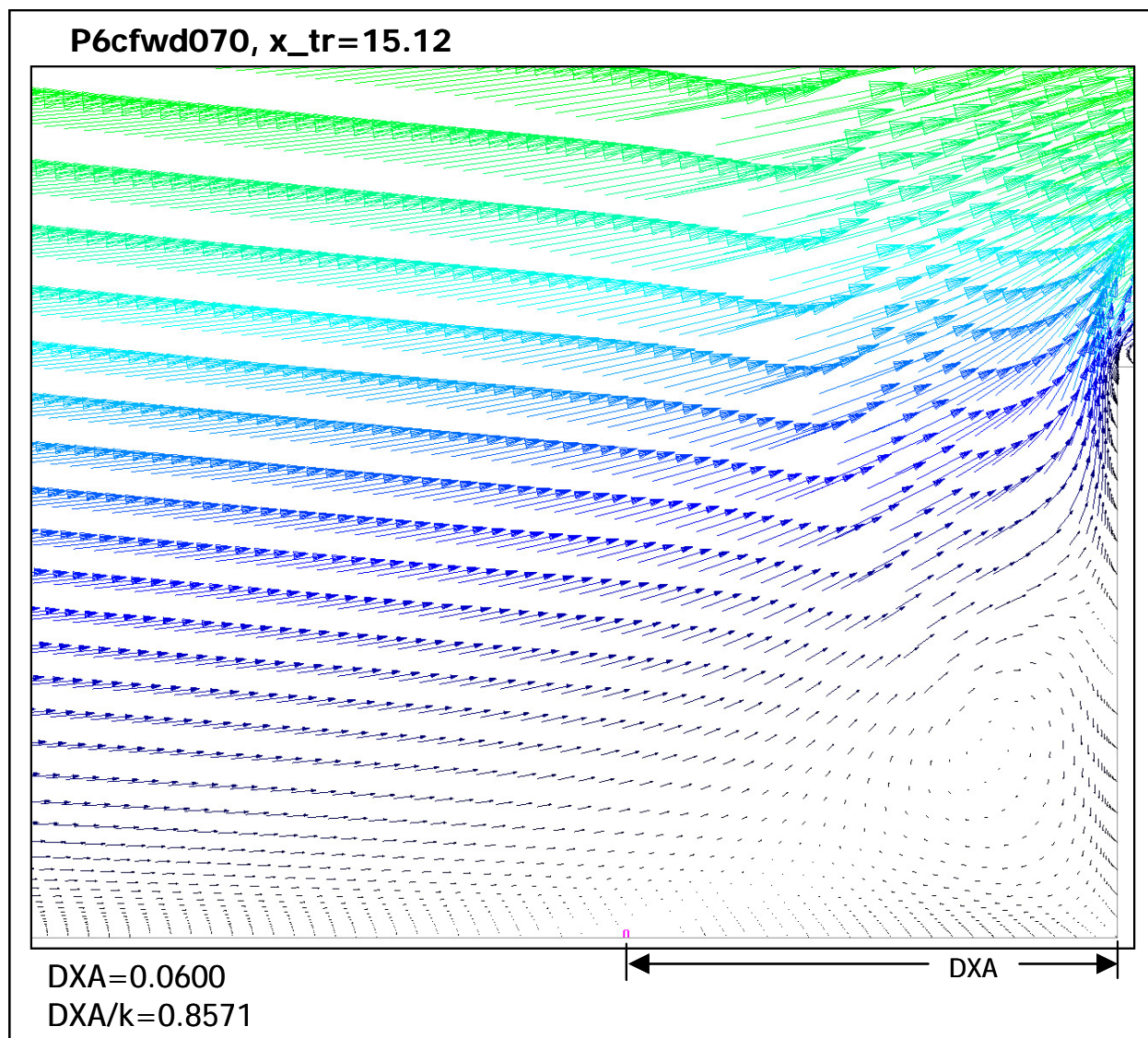


**Figure 449 P6 CFD velocity profiles in front of 0.070-inch-high position C forward step (view CFWD5)**

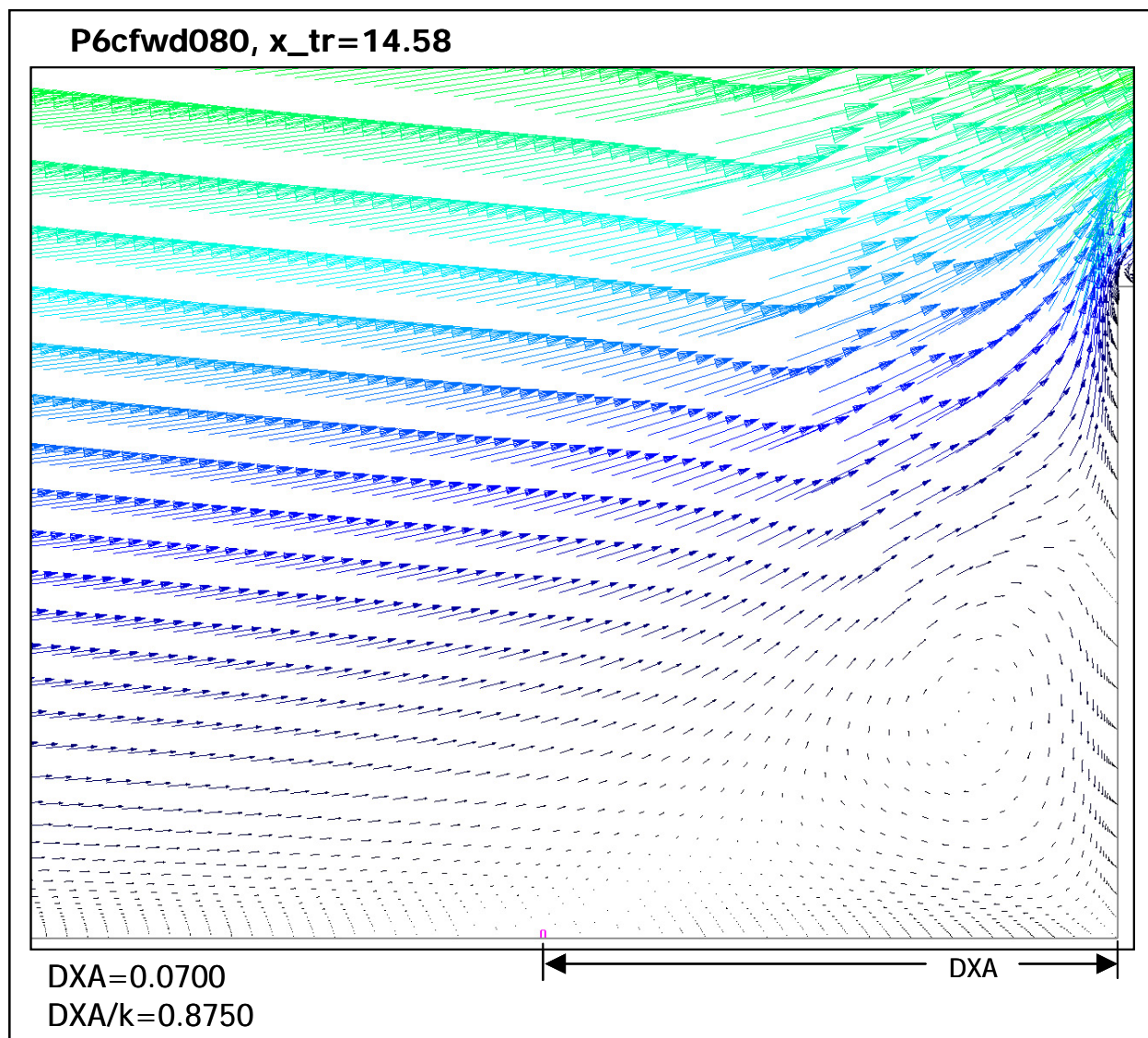


**Figure 450 P6 CFD velocity profiles in front of 0.080-inch-high position C forward step  
(view CFWD5)**

Figures 451 through 456 are the corresponding plots on the same scale focused on the short bubble on top of the step. The pink O indicates the most downstream edge of reversed flow for the grid density shown. DXB is the length of the bubble. DXB/k is that length divided by the step height.

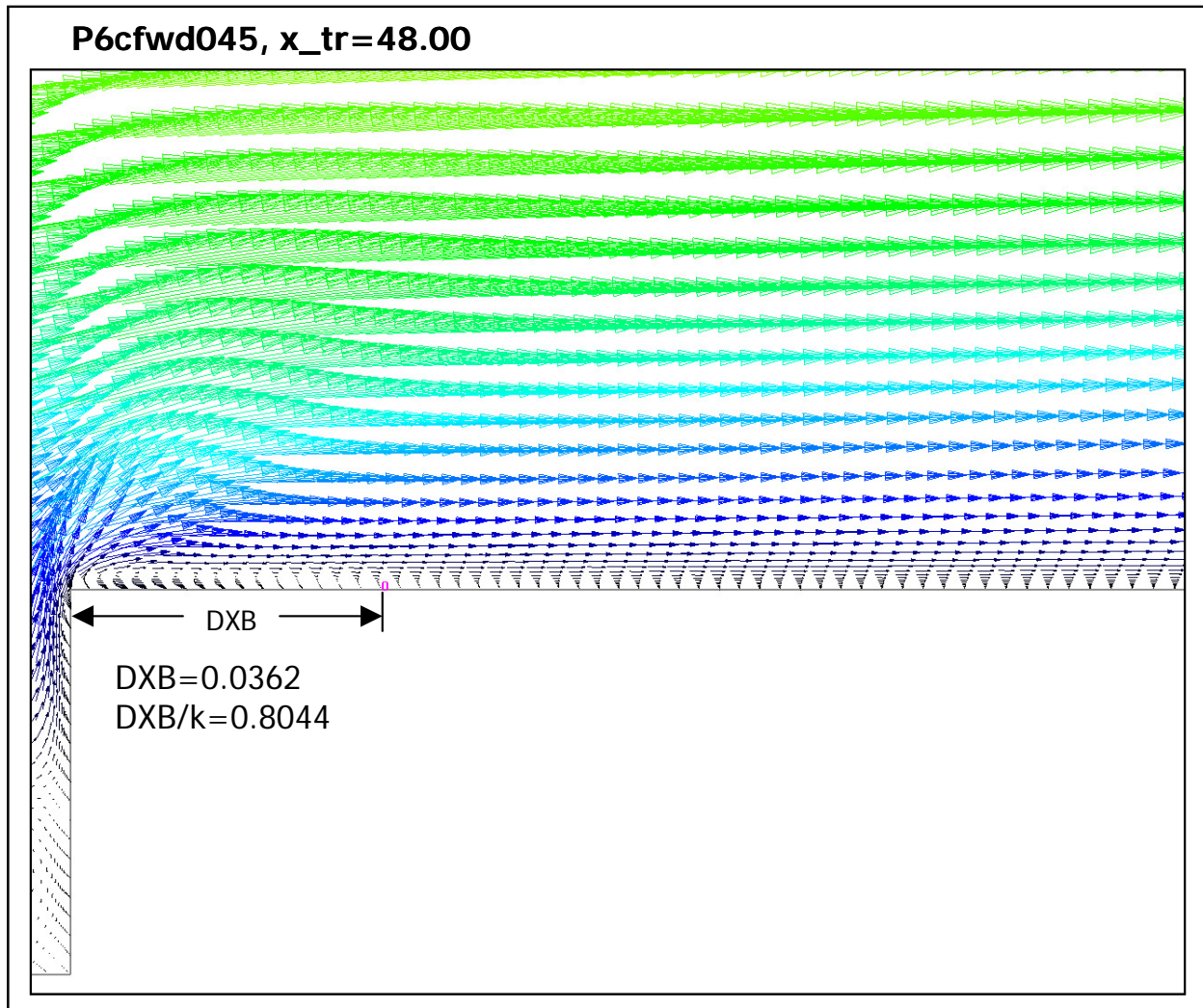


**Figure 451 P6 CFD velocity profiles on top of 0.045-inch-high position C forward step (view CFWD6)**



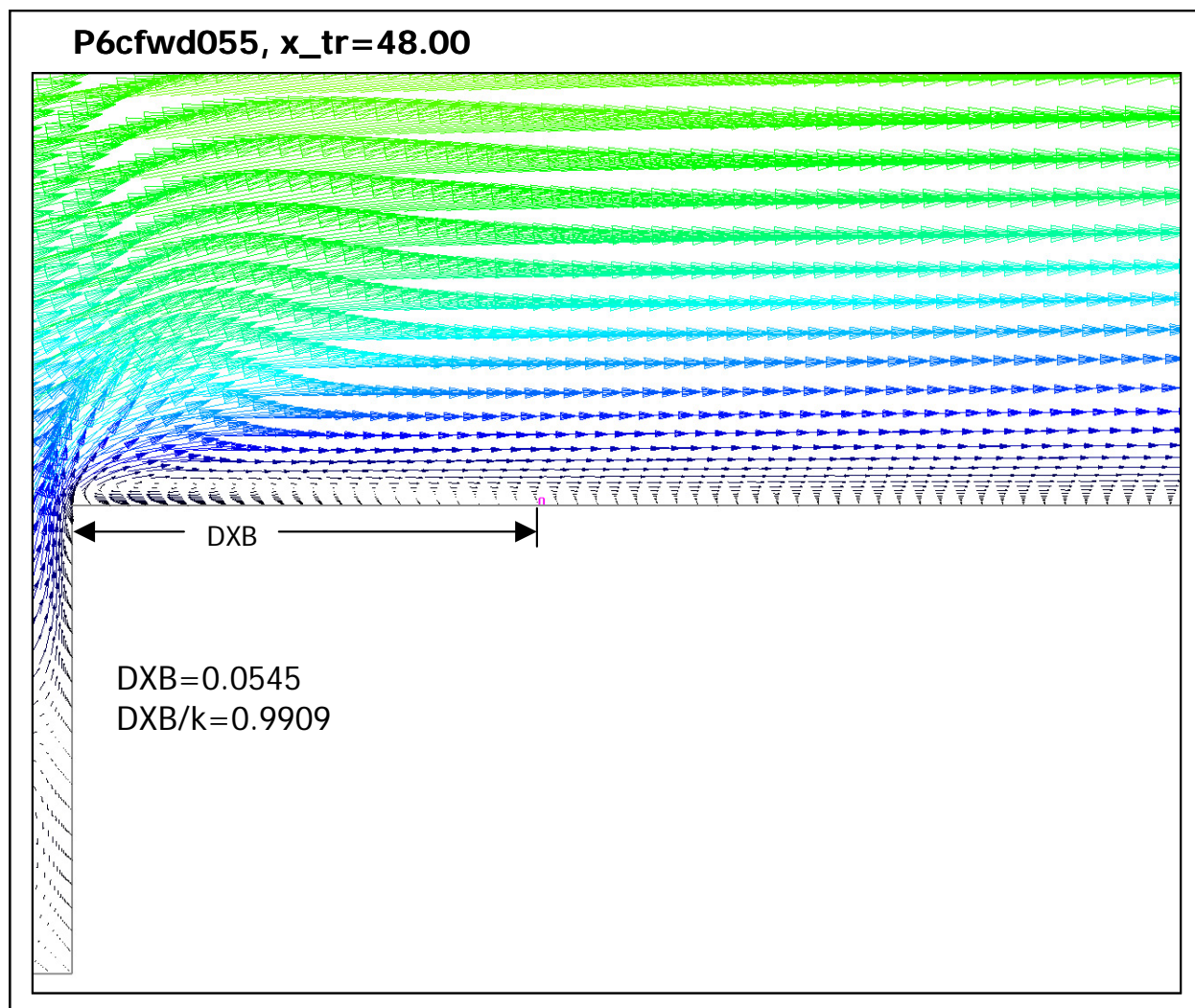


**Figure 452 P6 CFD velocity profiles on top of 0.055-inch-high position C forward step (view CFWD6)**



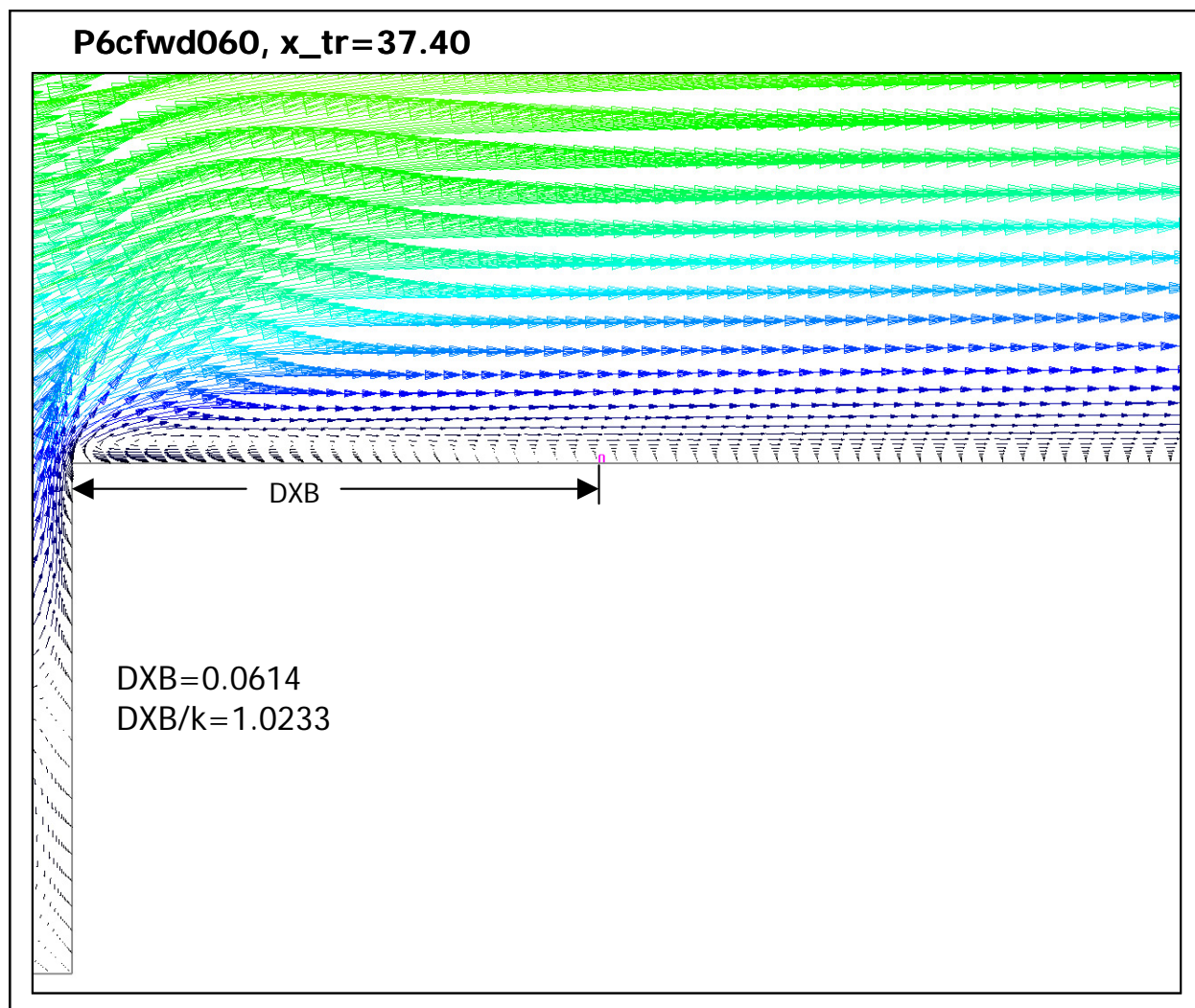


**Figure 453 P6 CFD velocity profiles on top of 0.060-inch-high position C forward step (view CFWD6)**

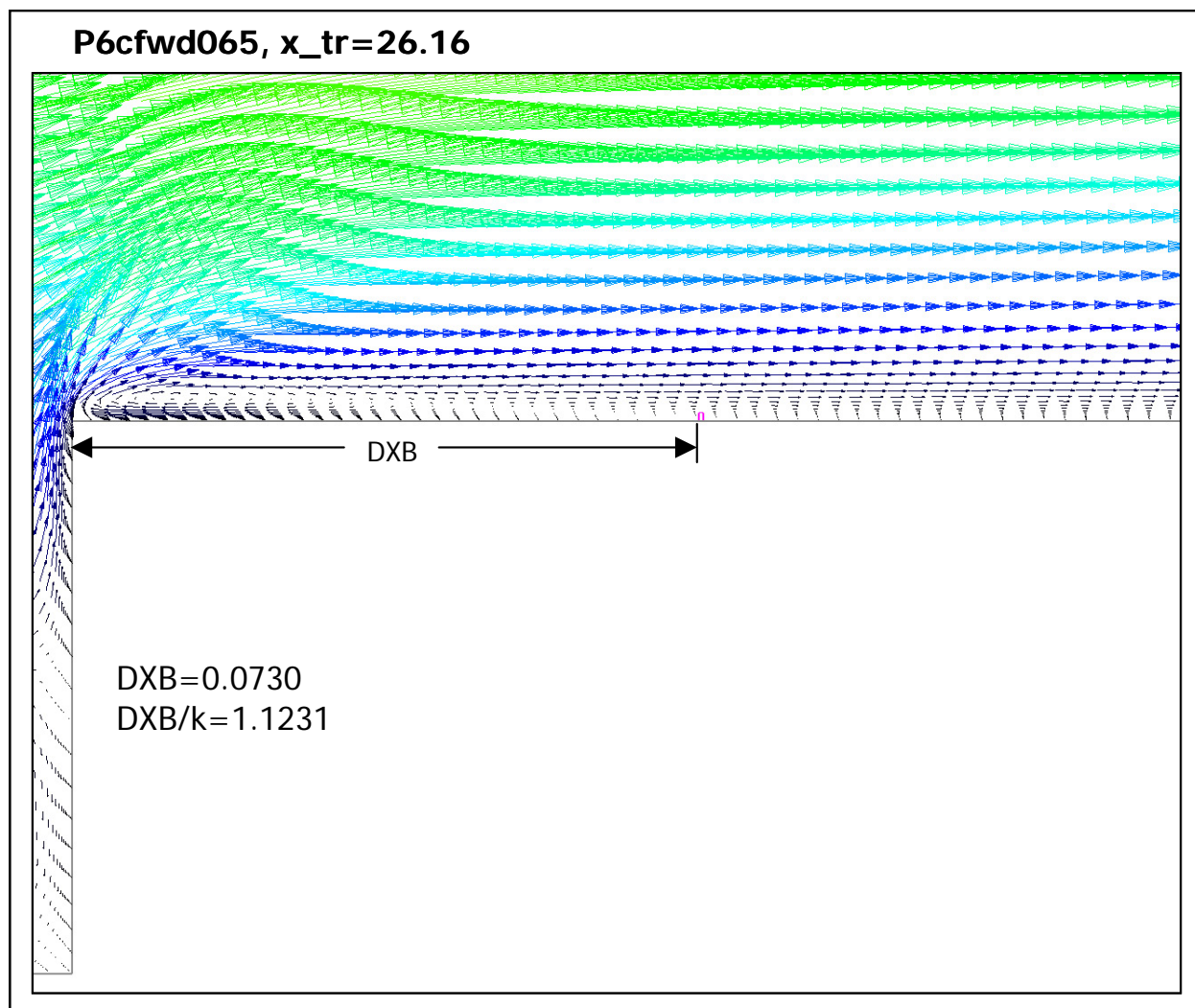


**Figure 454 P6 CFD velocity profiles on top of 0.065-inch-high position C forward step (view CFWD6)**

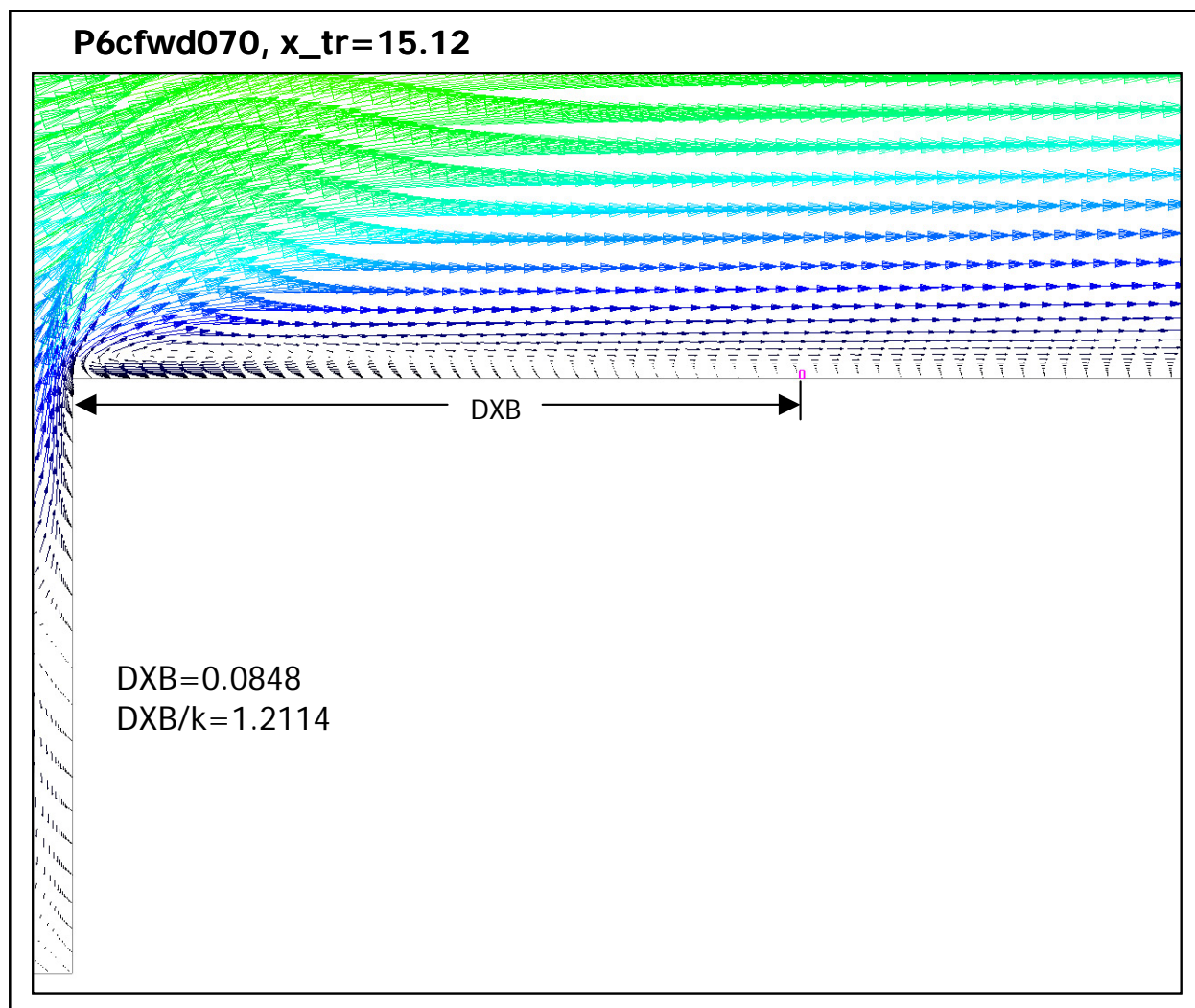


**Figure 455 P6 CFD velocity profiles on top of 0.070-inch-high position C forward step (view CFWD6)**

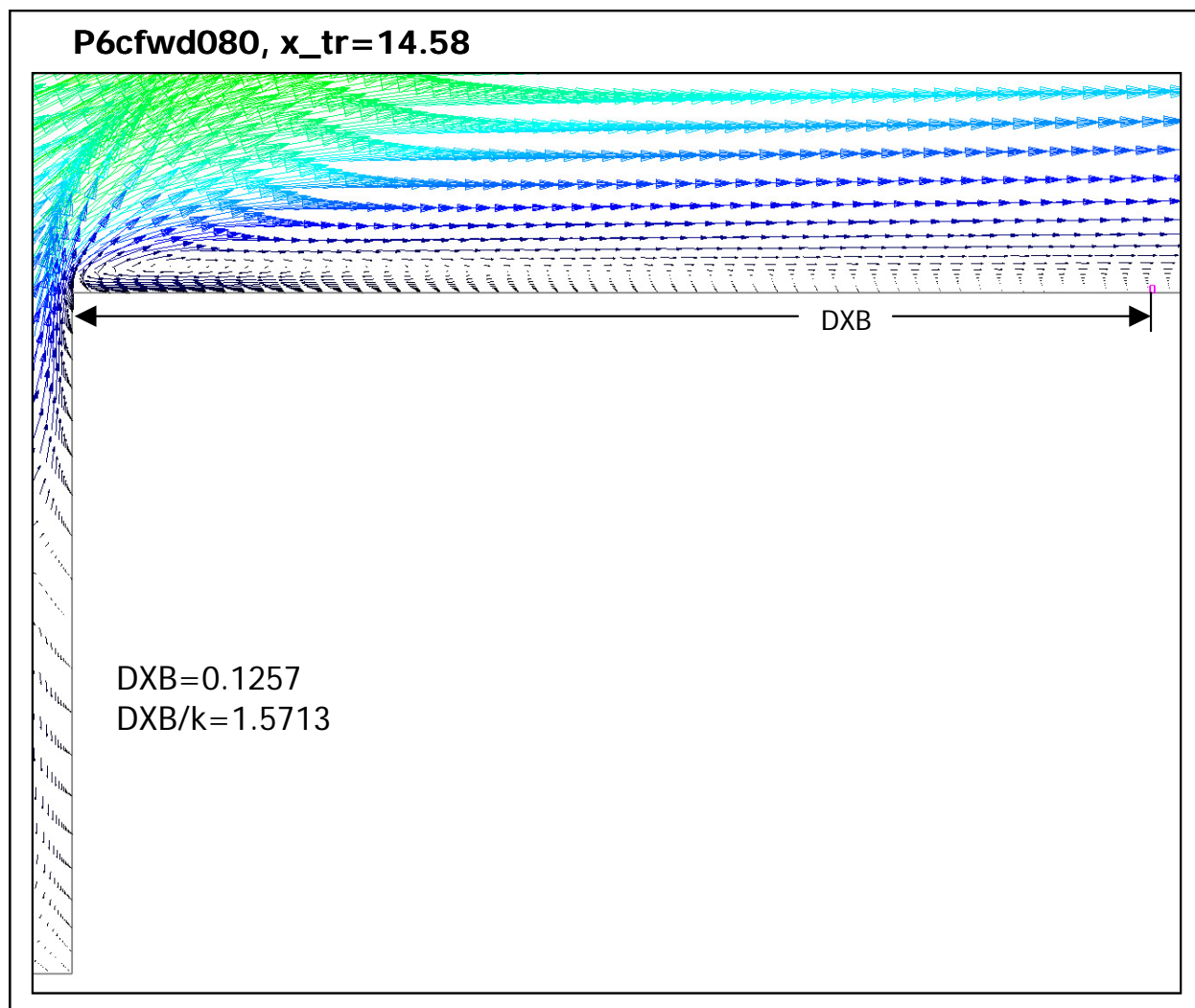


**Figure 456 P6 CFD velocity profiles on top of 0.080-inch-high position C forward step (view CFWD6)**

The normalized bubble lengths extracted from Figures 445 through 456 are collected in Table 11 next to experimentally determined values of step-height and transition Reynolds numbers.

**Table 11 Summary of nondimensional parameters extracted from P6 position C forward step CFD**

Case I.D.	Step Location* (in)	Step Height (in)=k	Upper Transition* (in)=x_tr	Re <sub>k</sub>	Re <sub>tr</sub>	DXA / k	DXB / k
P6cfwd045	11	0.045	48.00	388	706,023	0.7778	0.8044
P6cfwd055	11	0.055	48.00	532	705,468	0.7727	0.9909
P6cfwd060	11	0.060	37.40	607	528,466	0.7917	1.0233
P6cfwd065	11	0.065	26.16	684	351,875	0.8462	1.1231
P6cfwd070	11	0.070	15.12	762	175,349	0.8571	1.2114
P6cfwd080	11	0.080	14.58	918	167,540	0.8750	1.5713

\* Distance from plate leading edge

Recall that the step-height Reynolds number (Re<sub>k</sub>) is based on the step height (k) and flow values a clean plate would have at the step location a height k above the surface. The transition Reynolds number (Re<sub>tr</sub>) is based on an integration of the flow properties along the path from the stagnation point to the transition location at a height corresponding to 99 percent of the local inviscid velocity. Figure 457 is a plot of the nondimensionalized upstream bubble length with these two Reynolds numbers. The slope variation of the purple S curve is sufficiently gentle to discourage a clear relationship between step height and transition. Nor does the relatively straight purple line for the bubble immediately aft (on top of the step) in Figure 458 offer any clues to a parametric trigger for transition.

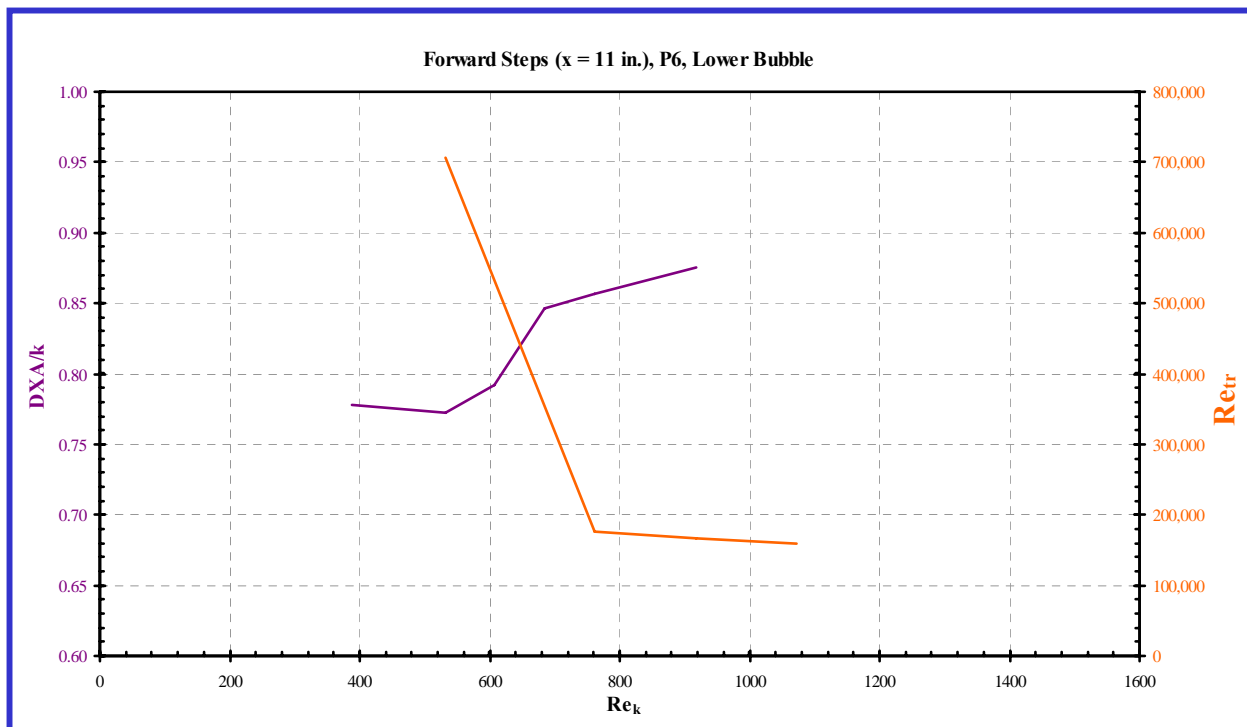


**Figure 457 Comparison of bubble length in front of step with height and transition Reynolds number**

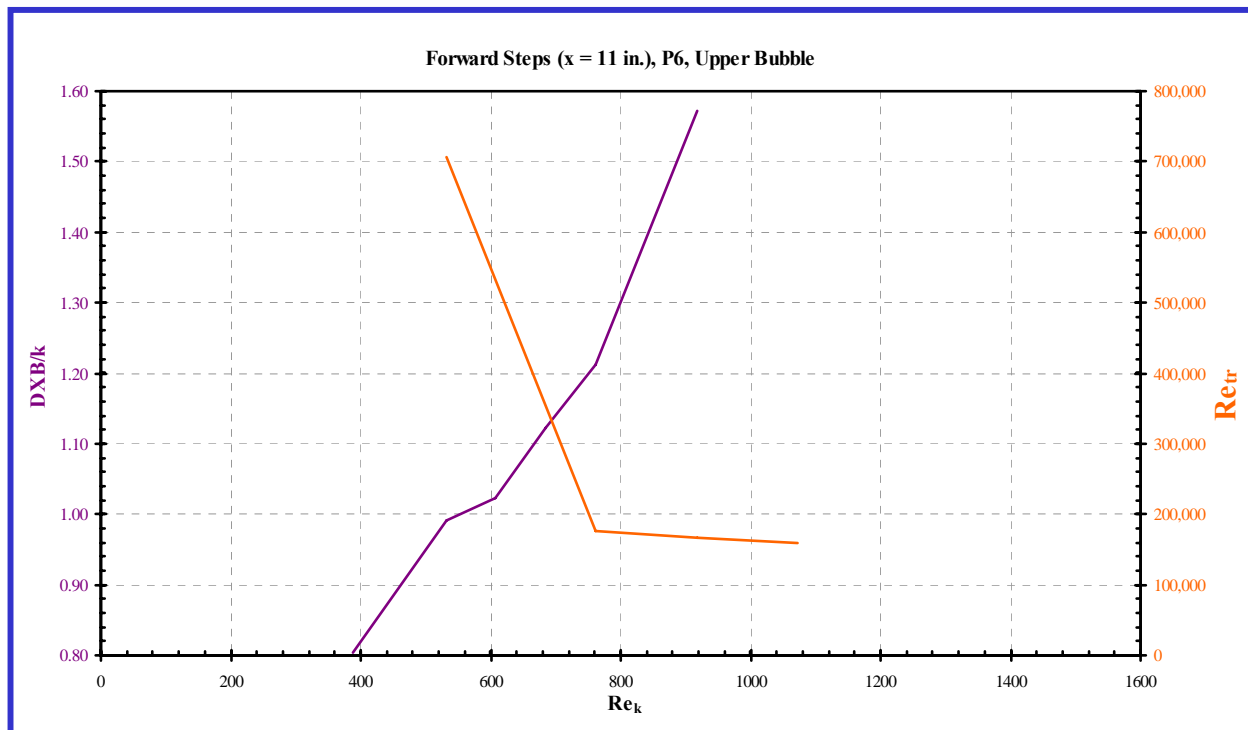


**Figure 458 Comparison of bubble length on top of step with height and transition Reynolds number**

### 3.3 Assessment of Computational Study

The pressure gradients obtained from the CFD correlate reasonably well with experiment considering the limited geometric and condition discrepancies. Detailed examination of the boundary layer passed all checks for reason. On a clean plate, laminar profiles appeared slightly more sensitive to changes in pressure gradient than turbulent profiles. Qualitatively similar separation bubbles were evident in the vicinity of a given step type, and limited parametric comparisons revealed no feature clearly linked to downstream transition.

## 4.0 Conclusions

The present study has shown that there is a pronounced effect of pressure gradient on boundary layer transition induced by surface excrescences. This has important ramifications for laminar flow aircraft, as many laminar flow wings feature mild favorable pressure gradients over large portions of the chord.

The effect of favorable pressure gradient is, as expected, beneficial in that the size of surface excrescences that can be tolerated without impacting the boundary layer transition location is greater than in a zero pressure gradient situation. This effect is pronounced, even in the cases of very mild favorable gradients.

The effects of adverse gradient were observed to increase the susceptibility of the boundary layer to surface excrescences. This result was expected, though it is of less practical importance to the aerodynamic designer since it is often assumed that the boundary layer will transition once the pressure gradient becomes adverse, irrespective of surface excrescences.

The results documented herein cover the full applicable  $K$  (pressure gradient) range for real systems but fall short—in some cases, significantly—of full-scale Reynolds number. For decisions on allowable manufacturing tolerances to be made with confidence, further work must be undertaken to increase the Reynolds number range and introduce other effects, such as compressibility.

### 4.1 Allowable Excrescences for Global Hawk-Type Aircraft

The previous recommended maximum allowable step heights for a laminar flow wing on an aircraft like Global Hawk have been revisited. In light of the fact that the bulk of the region intended for a laminar boundary layer has a favorable pressure gradient, new  $Re_k$  values—based on the results of the previous section—have been used to determine allowable step heights for representative flight conditions. The favorable gradient allows the use of an  $Re_k$  of 550 for forward-facing steps and an  $Re_k$  of 300 for aft-facing steps, in comparison with 150 and 80 previously used from flat plate characteristics. Figures 459 and 460 show the marked effect such changes have, essentially doubling the allowable step height. While the results of this study are insufficient to be the sole basis of such a large relaxation in tolerances, they are highly suggestive.

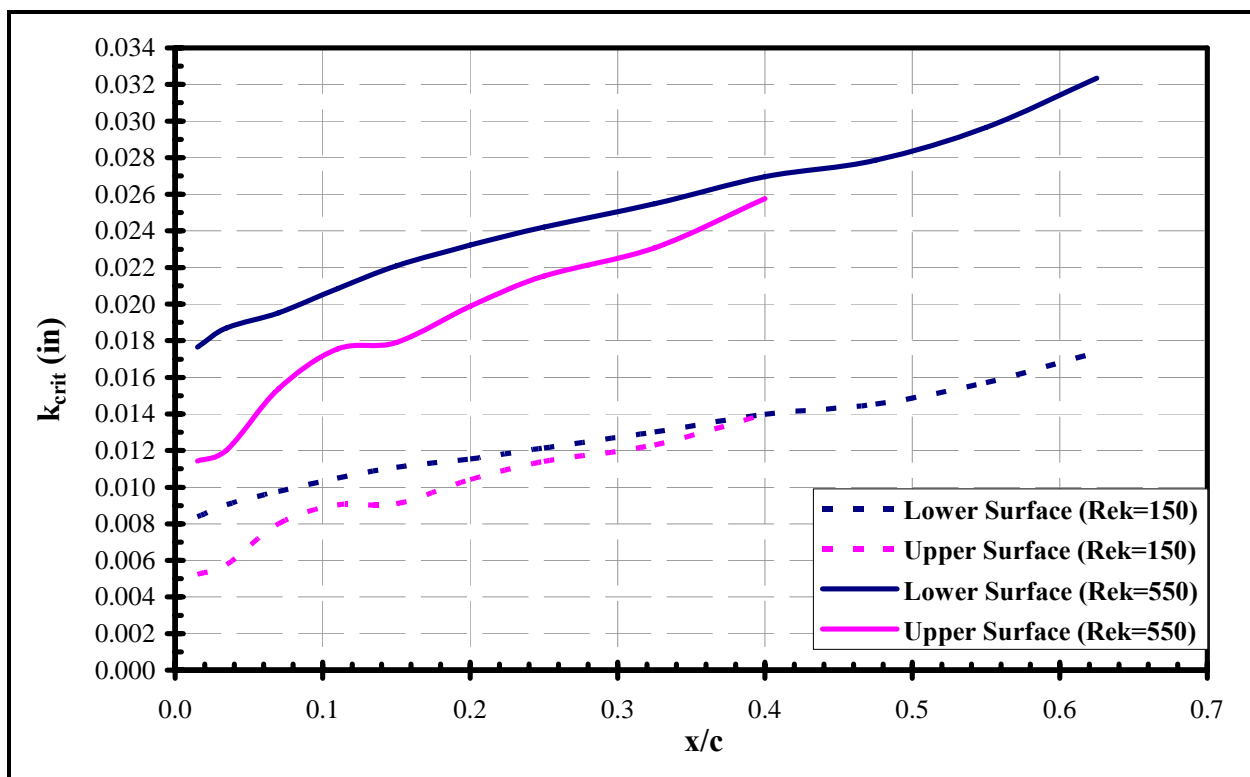


**Figure 459** Allowable forward-facing step height for a Global Hawk-type wing.

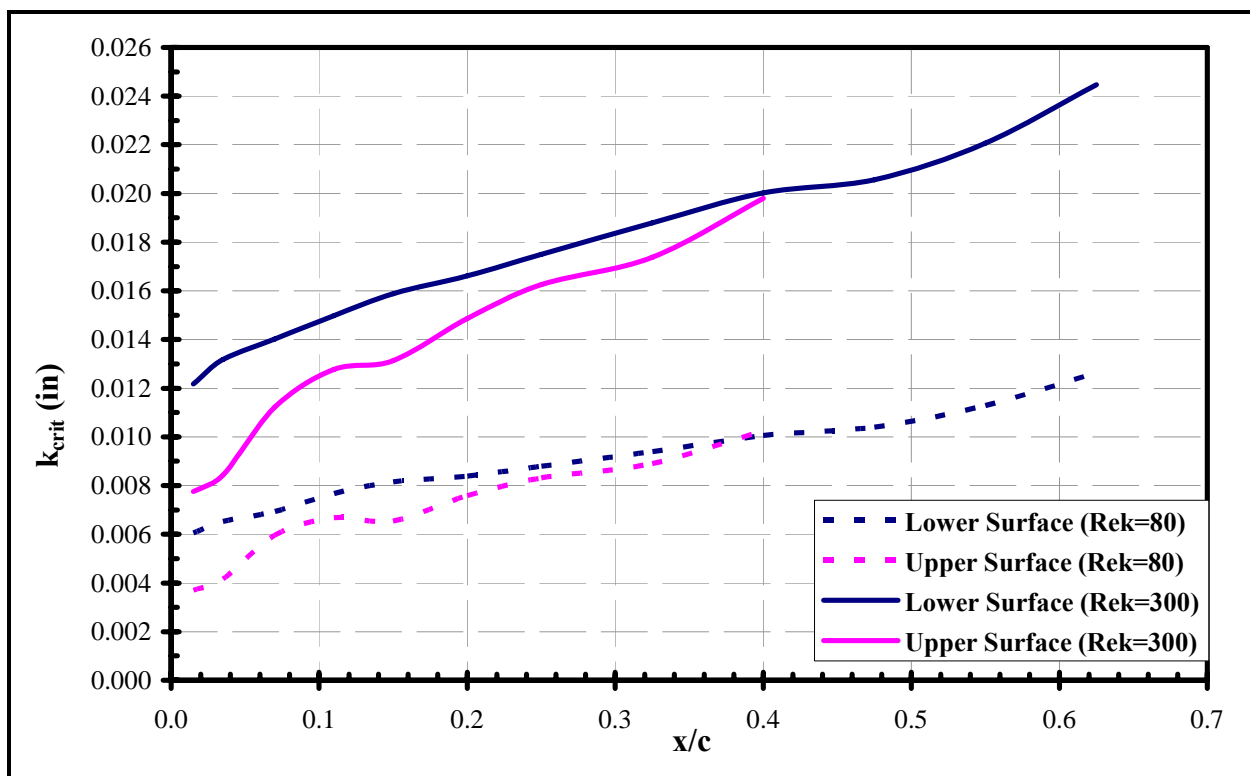


**Figure 460** Allowable aft-facing step height for a Global Hawk-type wing.



## 5.0 Recommended Follow-On Activities

### 5.1 Experimental Investigation at Full-Scale Reynolds Numbers

An investigation structured similarly to the present study but conducted in a facility capable of testing at higher Reynolds numbers would provide a very valuable next step in understanding excrescence effects. The single greatest impediment to the use of the current results is their limited Reynolds number range.

A test structured to allow testing at clean plate  $Re_{tr}$ s in the neighborhood of  $4-5 \times 10^6$ , would suffice to verify the asymptotic nature of the  $Re_{tr}$  v.  $Re_k$  relation and cover the Reynolds number region of greatest interest. Such a test should be feasible in simple low-cost facilities: the Northrop Grumman Research Wind Tunnel could be modified with improved flow conditioning to perform such a test; and the WSU Contractionless Research Wind Tunnel likely could be modified to increase the Reynolds number range.

### 5.2 Assessment of Compressibility Effects

The effects of compressibility are present for virtually every envisioned implementation of laminar flow wing designs. An experimentally based assessment of compressibility effects is necessary to understand how compressibility influences the relations between surface excrescences and boundary layer transition. The goal of the task is to identify and quantify trends in the allowable excrescence size criteria due to compressibility effects.

This investigation could be conducted in a small transonic wind tunnel, such as the NASA Ames Fluid Mechanics Lab (Figure 461). The Mach number of the experiments would be high enough to allow extrapolation to flight conditions of interest. The results of the experiment will also be applicable to Global Hawk, which cruises at a Mach number of 0.55.

There would be multiple test models for this transonic wind tunnel test. The models will all have airfoil shapes (Figure 462), which will be used to reproduce key pressure distribution characteristics that were identified from the preceding low-speed testing. This approach will allow a direct comparison to the incompressible results. From the wind tunnel data and subsequent analysis, compressibility effects can be taken into account in the criteria for allowable excrescence size.

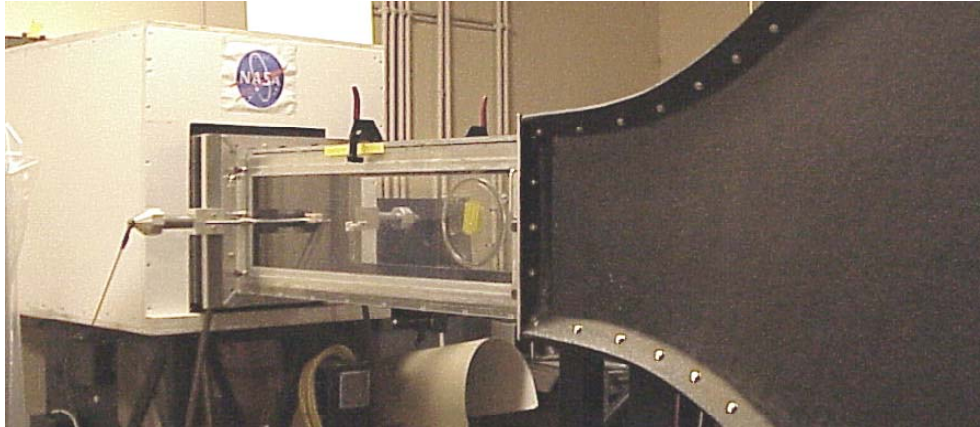


**Figure 461 NASA Ames Fluid Mechanics Laboratory (FML) Test Cell 3 wind tunnel.**

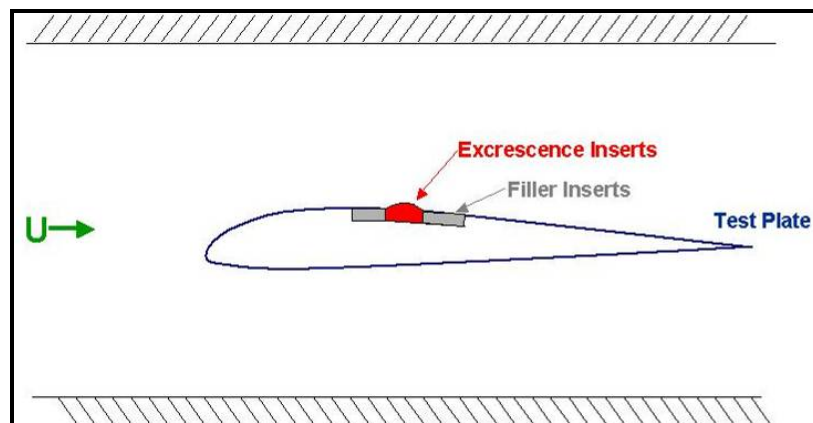


**Figure 462 Assessment of compressibility effects setup concept.**

### **5.3 Initial Experimental Assessment of Sweep Effects**

Because wing sweep changes the nature of the boundary layer disturbances that cause transition, there is the potential for significant differences in the interaction between surface excrescences and boundary layer transition on wings with significant sweep. To begin to understand these effects, a low speed experimental assessment of sweep effects should be undertaken. The goal of the task would be to get a preliminary feel for trends in the allowable excrescence size criteria due to sweep angle. The sweep angles tested will include a sweep angle of 30 degrees so that the results will be directly applicable to SensorCraft, and may include other moderate sweep angles as well.

The test article could be similar in concept to that used in the initial experimental studies, with the . The new swept test article (Figure 463) will use various replaceable leading edge and upper surface pieces. One leading edge attachment piece will be used to change the leading edge radius. Other upper surface pieces will be used to modify the sweep angle, as well. A slot in the upper surface pieces will keep the excrescences parallel to the leading edge (the leading edge and excrescence sweep angles are not independent). A contour attached to the upper wall will again be used to impose 3-D pressure gradients.

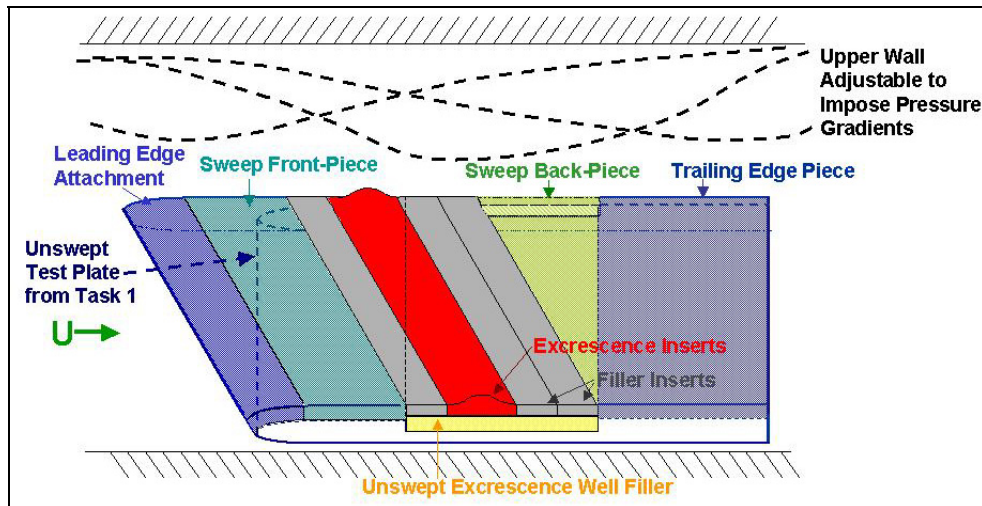


**Figure 463 Assessment of sweep effects setup concept.**

This task is intended to be only a limited assessment of sweep effects. It will, however, lay the groundwork for a more comprehensive test as a further follow-on activity. It is expected that this work will identify salient trends in sweep effects so a plan for a more comprehensive investigation can be made.

## 5.4 Integrated Demonstration of Critical Results

A desired follow-on activity for the program is the demonstration of the critical results that were developed during the previous activities. The goal of this follow-on activity would be to demonstrate the behavior of critical height excessances on the Global Hawk wing in a wind tunnel test.

The wind tunnel test would be conducted in the NASA Ames 11-foot Unitary Wind Tunnel and would use the existing Global Hawk airfoil model as the test specimen. An assortment of relevantly sized surface excessances at various locations would be tested.

The purpose of the activity would be to demonstrate and further validate the excessance criteria specifically for Global Hawk in a relevant environment.



**Figure 464 Global Hawk airfoil model in NASA Ames 11-ft wind tunnel**

## **5.5 Investigation of Combined Sweep and Compressibility Effects**

Another desirable follow-on activity is an experimental investigation of combined sweep and compressibility effects. The goal of the activity would be to identify and quantify trends in the allowable excrescence size criteria due to simultaneous Mach number and sweep effects.

The approach would be very similar to the approach for assessment of compressibility effects. Like the unswept investigation, multiple wing models would be used in a small transonic wind tunnel and the Mach numbers would be high enough to allow extrapolation to flight conditions of interest.

The purpose of the activity would be to further augment the database of excrescence effects to include compressibility and sweep in combination, which would make the results more applicable to a wider range of future vehicles.

## 6.0 References

1. Keller and Wang, "Flow and heat Transfer Behavior in Transitional Boundary Layers with Streamwise Acceleration" *ASME* v.118, Apr. 1996.
2. Fage, A., "The Smallest Size of a Spanwise Surface Corrugation Which Affects Boundary-Layer Transition on an Aerofoil" *RAE R&M* 2120, Jan, 1943.
3. Braslow, A. L., "Review of the Effect of Distributed Surface Roughness on Boundary Layer Transition" *AGARD Report* 254, 1960.
4. Smith, A. M. O., and D. W. Clutter, "The Smallest Height of Roughness Capable of Affecting Boundary-Layer Transition in Low-Speed Flow" *Douglas Aircraft Co. Engineering Report* ES 26803, 1954.
5. Drake, A., R. V. Westphal, F. A. Zuniga, R. A. Kennelly, and D. J. Koga, "Wing Leading Edge Joint Laminar Flow Tests" *NASA TM* 4762, 1996.
6. Hood, M. J., "The Effects of Surface Waviness and of Rib Stitching on Wing Drag" *N.A.C.A. Technical Note* No. 724, Aug. 1939.
7. NOR-59-438 (BLC-123) "Surface Waviness Criteria for Swept and Unswept Laminar Suction Wings," 1959.
8. Bryer and Pankhurst "Pressure-probe methods for determining wind speed and direction" *Her Majesty's Stationary Office*, London, 1971.
9. McKeon, Li, Jiang, Morrison, and Smits "Pitot probe corrections in fully developed turbulent pipe flow" *Measurement Science and Technology*, vol. 14, 2003, pp1449-1458.
10. Murphy, J. D. and Davies, C.A., "Users Guide – Ames Inlet Boundary Layer Program MK I" *NASA TM* X-62211, Jan. 1973.
11. Preston, M. A., "The Determination of Turbulent Skin Friction by Means of Pitot Tubes" *J. of the Royal Aeronautical Society*, v58, Feb. 1954, pp. 109-121.
12. Patel, V. C., "Calibration of the Preston Tube and Limitations on Its Use in Pressure Gradients" *J. Fluid Mech.*, v23, part 1, 1963, pp. 185-208.
13. Poll, D. I. A., "A Note on the Use of Surface Pitot Tubes for the Measurement of Skin Friction in Laminar Boundary Layers" *Cranfield College of Aeronautics Report* 8307, March 1983.

## LIST OF ACRONYMS, ABBREVIATIONS, AND SYMBOLS

ACRONYM	DESCRIPTION
2-D	two-dimensional
3-D	three-dimensional
CFD	computational fluid dynamics
CFM	cubic feet per minute
GCNS	generalized compressible Navier-Stokes
GH	Global Hawk
Hz	Hertz
LAM	laminar
NACA	National Advisory Committee for Aeronautics
NASA	National Aeronautics and Space Administration
NPR	nozzle pressure ratio
OML	outer mold line
Re	Reynolds Number
SC	SensorCraft
TURB	turbulent
WSU	Washington State University
WT	wind tunnel
C	Chord
$C_f$	skin friction coefficient
$C_l$	2-D lift coefficient
$C_p$	Coefficient of pressure
DXA	Length of upstream separation bubble
DXB	Length of downstream separation bubble
K	Pressure gradient parameter
k	Excrescence height
$Re_k$	Excrescence height Reynolds number
$Re_{krit}$	Critical excrescence height Reynolds number
$Re_{tr}$	Transition Reynolds number
$Re_{xk}$	Excrescence location Reynolds number
$s_k$	Surface distance of excrescence from the leading edge
U	Velocity
$U_e$	Boundary layer edge velocity
$U_k$	Undisturbed boundary layer velocity at height k
$x_k$	Chordwise location of excrescence
$x_{tr}$	Transition location Reynolds number
$\nu_k$	Viscosity at excrescence location